

# **ADDITION OF VANADIUM AND NIOBIUM TO PLATINUM-BASED ALLOYS**

**Bernard Okich Odera**

A thesis submitted to the Faculty of Engineering and the Built Environment, University of the Witwatersrand, in fulfilment of the requirements for the degree of Doctor of Philosophy.

**Johannesburg, 2012**

## **DECLARATION**

I, Bernard Okich Odera, declare that this thesis is my own work, except where otherwise acknowledged. It is being submitted for the degree of Doctor of Philosophy in Engineering at the University of the Witwatersrand, Johannesburg. It has not been submitted previously at this, or any other university for any degree or examination.

---

Signature

---

Date

## **ACKNOWLEDGEMENTS**

I would like to thank the following people and institutions for the assistance they gave during this work:

- My supervisor, Prof. Lesley Cornish, for guidance and encouragement.
- AMSEN for funding the bursary that enabled me to undertake the research.
- The Wits DST/NRF Centre of Excellence in Strong Materials for support and administration of the AMSEN bursary.
- Mintek for allowing me access to some of their laboratory facilities.
- Dr. Jones Papo for facilitating my work at Mintek laboratories.
- Richard Couperthwaite for countless hours at the SEM.
- Edson Muhuma for assisting me with melting at the arc furnace.
- And last, but not least, my dear wife Lilian, children Sarah, Cedric and Vanessa for their understanding and support throughout the project.

## ABSTRACT

The ternary systems, Pt-Al-V at the Pt-rich corner and Pt-Cr-V were investigated. Phase equilibria data were obtained using scanning electron microscopy with energy dispersive X-ray spectroscopy and X-ray diffraction analyses. The alloys were studied in the as-cast condition, as well as after annealing at 1000°C for 1500 h. Solidification projections were constructed and liquidus surface projections derived for the two systems. Isothermal sections at 1000°C were also determined for the two systems. Two ternary phases were found in the Pt-Al-V system and one in the Pt-Cr-V system. It was concluded that all the phase regions were identified correctly since the results were self-consistent. Four invariant reactions were identified in the Pt-Cr-V system.

Four Pt-Al-Cr-Ru-V and two Pt-Al-Cr-Ru-V-Nb alloys were also investigated and data obtained using scanning electron microscopy with energy dispersive X-ray spectroscopy and X-ray diffraction analyses. The alloys were studied in the as-cast condition, as well as after annealing at 1000°C for 1500 h. The compositions of the alloys were based on a quaternary alloy,  $\text{Pt}_{82}:\text{Al}_{12}:\text{Cr}_4:\text{Ru}_2$ , which had been identified as one of the alloys having optimum properties in an earlier investigation. Four of the as-cast alloys had a two-phase structure of  $\sim\text{Pt}_3\text{Al}$  and (Pt), while two had a single phase,  $\sim\text{Pt}_3\text{Al}$ . Vanadium partitioned more to  $\sim\text{Pt}_3\text{Al}$  compared to (Pt). There was an improvement in hardness compared to the quaternary alloys which had been identified as having optimum properties.

About 64% of as-cast Pt-Al-V alloys had Vickers hardnesses higher than 500  $\text{HV}_{0.3}$  while  $\sim 70\%$  of the annealed alloys had hardness higher than 500  $\text{HV}_{0.3}$ . More than 60% of both as-cast and annealed Pt-Cr-V alloys had hardness values higher than 600  $\text{HV}_{0.3}$ . There was a general increase in hardness after annealing Pt-Cr-V alloys. Hardness increased with V content in the higher order alloys, and also the annealed alloys had higher hardness compared to the as-cast ones.



# TABLE OF CONTENTS

DECLARATION.....	i
ACKNOWLEDGEMENTS.....	ii
ABSTRACT.....	iii
CHAPTER 1: INTRODUCTION AND BACKGROUND.....	1
CHAPTER 2: LITERATURE REVIEW .....	4
2.1 Pt-Al-V and Pt-Cr-V Ternary Systems .....	8
2.1.1 Pt-Al binary phase diagram.....	8
2.1.2 The binary Pt-V phase diagram .....	14
2.1.3 The binary Al-V phase diagram.....	17
2.1.4 Cr-Pt binary phase diagram.....	24
2.1.5 Cr-V binary phase diagram .....	31
2.2 Pt-Al-Nb and Pt-Cr-Nb Ternary Systems .....	34
2.2.1 Nb-Pt binary system.....	34
2.2.2 The Binary Nb-Al System.....	41
2.2.3 The Binary Cr-Nb System.....	45
2.3 Review of Selected Quaternary Alloys from the Pt-Al-Cr-Ru System.....	50
2.3.1 $Pt_{84}:Al_{11}:Cr_3:Ru_2$ .....	51
2.3.2 $Pt_{85}:Al_{11}:Cr_2:Ru_2$ .....	52
2.3.3 $Pt_{78}:Al_{15.5}:Cr_{4.5}:Ru_2$ .....	52
2.3.4 $Pt_{82}:Al_{12}:Cr_4:Ru_2$ .....	53
2.3.5 $Pt_{80}:Al_{14}:Cr_3:Ru_3$ .....	55
2.3.6 $Pt_{78}:Al_{11}:Cr_6:Ru_5$ .....	56
CHAPTER 3: EXPERIMENTAL PROCEDURE .....	57
CHAPTER 4: Pt-Al-V ALLOYS .....	60
4.1 AS-CAST ALLOYS .....	60
4.1.1 As-cast Alloy 1, Average Composition $Pt_{64.3}:Al_{26.6}:V_{9.1}$ (at.%).....	60
4.1.2 As-cast Alloy 2, Average Composition $Pt_{59.1}:Al_{23.1}:V_{17.8}$ (at.%).....	63
4.1.3 As-cast Alloy 3, Average Composition $Pt_{57.3}:Al_{6.7}:V_{26}$ (at.%) .....	66
4.1.4 As-cast Alloy 4A, Average Composition $Pt_{76.2}:Al_{17.4}:V_{6.4}$ (at.%) .....	68
4.1.5 As-cast Alloy 4B, Average Composition $Pt_{69.8}:Al_{22.3}:V_{7.9}$ (at.%) .....	71

4.1.6	As-cast Alloy 10, Average Composition $\text{Pt}_{83.9}:\text{Al}_{6.0}:\text{V}_{10.1}$ (at.%).....	74
4.1.7	As-cast Alloy 11, Average Composition $\text{Pt}_{80.9}:\text{Al}_{4.3}:\text{V}_{14.8}$ (at.%) .....	77
4.1.8	As-cast Alloy 12, Average Composition $\text{Pt}_{52.5}:\text{Al}_{22.6}:\text{V}_{24.9}$ (at.%) .....	79
4.1.9	As-cast Alloy 13, Average Composition $\text{Pt}_{53.7}:\text{Al}_{8.8}:\text{V}_{37.5}$ (at.%) .....	82
4.1.10	As-cast Alloy 14, Average Composition $\text{Pt}_{84}:\text{Al}_{12}:\text{V}_4$ (at.%) .....	85
4.1.11	As-cast Alloy 15, Average Composition $\text{Pt}_{72.4}:\text{Al}_{13.7}:\text{V}_{13.9}$ (at.%).....	87
4.1.12	As-cast Alloy 16, Average Composition $\text{Pt}_{56.9}:\text{Al}_{25.4}:\text{V}_{17.7}$ (at.%).....	90
4.1.13	Solidification Projection of the Pt-Al-V System at the Pt-rich corner .....	94
4.1.14	Liquidus Surface Projection of the Pt-Al-V at the Pt-rich Corner .....	95
4.2	ALLOYS ANNEALED AT 1000°C FOR 1500 HOURS .....	98
4.2.1	Annealed Alloy 1H, Average Composition $\text{Pt}_{64.7}:\text{Al}_{26.2}:\text{V}_{9.1}$ (at.%).....	98
4.2.2	Annealed Alloy 2H, Average Composition $\text{Pt}_{61.8}:\text{Al}_{21.1}:\text{V}_{17.1}$ (at.%).....	100
4.2.3	Annealed Alloy 3H, Average Composition $\text{Pt}_{63.7}:\text{Al}_{10.8}:\text{V}_{25.5}$ (at.%).....	103
4.2.4	Annealed Alloy 4BH, Average Composition $\text{Pt}_{69.7}:\text{Al}_{23.2}:\text{V}_{7.1}$ (at.%).....	105
4.2.5	Annealed Alloy 10H, Average Composition $\text{Pt}_{83.9}:\text{Al}_{5.8}:\text{V}_{10.3}$ (at.%).....	108
4.2.6	Annealed Alloy 11H, Average Composition $\text{Pt}_{85.2}:\text{Al}_{3.4}:\text{V}_{11.4}$ (at.%).....	110
4.2.7	Annealed Alloy 12H, Average Composition $\text{Pt}_{60.5}:\text{Al}_{18.6}:\text{V}_{20.9}$ (at.%).....	113
4.2.8	Annealed Alloy 13H, Average Composition $\text{Pt}_{59.2}:\text{Al}_{8.4}:\text{V}_{32.4}$ (at.%).....	115
4.2.9	Annealed Alloy 14H, Average Composition $\text{Pt}_{81.6}:\text{Al}_{14.5}:\text{V}_{3.7}$ (at.%).....	117
4.2.10	Annealed Alloy 15H, Average Overall Composition $\text{Pt}_{72.3}:\text{Al}_{13.5}:\text{V}_{14.2}$ (at.%).....	119
4.2.11	Annealed Alloy 16H, Average Composition $\text{Pt}_{51.0}:\text{Al}_{31.1}:\text{V}_{17.9}$ (at.%).....	122
4.2.12	Combined Plot and isothermal section of the Pt-Al-V System at 1000°C at the Pt-rich corner	124
4.2.13	Derived ternary phase, $\tau_1$ , peaks in the XRD patterns .....	126
CHAPTER 5:	Pt-Cr-V ALLOYS .....	129
5.1	AS-CAST ALLOYS .....	129
5.1.1	As-cast Alloy 5, Average Composition $\text{Pt}_{73.8}:\text{Cr}_{16.9}:\text{V}_{9.3}$ (at.%) .....	129
5.1.2	As-cast Alloy 6, Average Composition $\text{Pt}_{72.3}:\text{Cr}_{8.3}:\text{V}_{19.4}$ (at.%) .....	131
5.1.3	As-cast Alloy 7, Average Composition $\text{Pt}_{33.4}:\text{Cr}_{45.8}:\text{V}_{20.8}$ (at.%).....	133
5.1.4	As-cast Alloy 8, Average Composition $\text{Pt}_{53.0}:\text{Cr}_{22.4}:\text{V}_{24.5}$ (at.%).....	135
5.1.5	As-cast Alloy 17, Average Composition, $\text{Pt}_{68.5}:\text{Cr}_{16.2}:\text{V}_{15.3}$ (at.%).....	138
5.1.6	As-cast Alloy 18, Average Composition $\text{Pt}_{32.8}:\text{Cr}_{28.6}:\text{V}_{38.6}$ (at.%).....	141

5.1.7	As-cast Alloy 19, Average Composition Pt <sub>25.8</sub> :Cr <sub>42.9</sub> :V <sub>31.3</sub> (at.%) .....	144
5.1.8	As-cast Alloy 20, Average Composition Pt <sub>38.8</sub> :Cr <sub>14.2</sub> :V <sub>47.0</sub> (at.%) .....	146
5.1.9	As-cast Alloy 21, Average Composition Pt <sub>16.8</sub> :Cr <sub>13.4</sub> :V <sub>69.8</sub> (at.%) .....	149
5.1.10	As-cast Alloy 22, Average Composition Pt <sub>28.7</sub> :Cr <sub>27.2</sub> :V <sub>44.1</sub> (at.%) .....	151
5.1.11	As-cast Alloy 23, Average Composition Pt <sub>16.5</sub> :Cr <sub>56.1</sub> :V <sub>27.4</sub> (at.%) .....	154
5.1.12	As-cast Alloy 24, Average Composition Pt <sub>14.9</sub> :Cr <sub>73.7</sub> :V <sub>11.4</sub> (at.%) .....	156
5.1.13	As-cast Alloy 25, Average Composition Pt <sub>34.1</sub> :Cr <sub>57.4</sub> :V <sub>8.5</sub> (at.%) .....	159
5.1.14	Solidification Projection of the Pt-Cr-V System .....	162
5.1.15	Liquidus Surface Projection of the Pt-Cr-V System .....	162
5.2	ALLOYS ANNEALED AT 1000°C FOR 1500 HOURS .....	164
5.2.1	Annealed Alloy 5H, Average Composition Pt <sub>76.2</sub> :Cr <sub>16.1</sub> :V <sub>7.7</sub> (at.%) .....	164
5.2.2	Annealed Alloy 6H, Average Composition Pt <sub>77.3</sub> :Cr <sub>6.6</sub> :V <sub>16.1</sub> (at.%) .....	166
5.2.3	Annealed Alloy 7H, Average Composition Pt <sub>35.7</sub> :Cr <sub>45.1</sub> :V <sub>19.2</sub> (at.%) .....	168
5.2.4	Annealed Alloy 8H, Average Composition Pt <sub>52.3</sub> :Cr <sub>23.4</sub> :V <sub>24.3</sub> (at.%) .....	170
5.2.5	Annealed Alloy 17H, Average Composition Pt <sub>70.2</sub> :Cr <sub>15.4</sub> :V <sub>14.4</sub> (at.%) .....	173
5.2.6	Annealed Alloy 18H, Average Composition Pt <sub>34.0</sub> :Cr <sub>28.3</sub> :V <sub>37.7</sub> (at.%) .....	175
5.2.7	Annealed Alloy 19H, Average Composition Pt <sub>25.1</sub> :Cr <sub>43.5</sub> :V <sub>31.5</sub> (at.%) .....	177
5.2.8	Annealed Alloy 20H, Average Composition Pt <sub>37.2</sub> :Cr <sub>14.6</sub> :V <sub>48.2</sub> (at.%) .....	178
5.2.9	Annealed Alloy 21H, Average Composition Pt <sub>16.5</sub> :Cr <sub>13.2</sub> :V <sub>70.3</sub> (at.%) .....	181
5.2.10	Annealed Alloy 22H, Average Composition Pt <sub>27.1</sub> :Cr <sub>26.8</sub> :V <sub>46.1</sub> (at.%) .....	182
5.2.11	Annealed Alloy 23H, Average Composition Pt <sub>14.5</sub> :Cr <sub>58.1</sub> :V <sub>27.4</sub> (at.%) .....	184
5.2.12	Annealed Alloy 24H, Average Composition Pt <sub>14.2</sub> :Cr <sub>75.8</sub> :V <sub>10.0</sub> (at.%) .....	187
5.2.13	Annealed Alloy 25H, Average Composition Pt <sub>33.6</sub> :Cr <sub>57.7</sub> :V <sub>8.7</sub> (at.%) .....	189
5.2.14	Isothermal Section of the Pt-Cr-V System at 1000°C .....	191
5.2.15	Tabulated Positions of the Ternary Phase, $\tau$ , in the XRD Pattern .....	192
CHAPTER 6: HIGHER ORDER ALLOYS OF THE Pt-Al-Cr-Ru-V AND Pt-Al-Cr-Ru-V-Nb SYSTEMS		193
6.1	AS-CAST ALLOYS .....	194
6.1.1	As-cast Alloy 26, Average Composition Pt <sub>63.9</sub> :Al <sub>12.2</sub> :Cr <sub>4.3</sub> :Ru <sub>0.7</sub> :V <sub>18.9</sub> (at.%) .....	194
6.1.2	As-cast Alloy 27, Average Overall Composition Pt <sub>69.5</sub> :Al <sub>11.5</sub> :Cr <sub>4.2</sub> :Ru <sub>0.6</sub> :V <sub>14.2</sub> (at.%) .....	196
6.1.3	As-cast Alloy 28, Average Composition Pt <sub>75.2</sub> :Al <sub>11.2</sub> :Cr <sub>4.0</sub> :Ru <sub>0.6</sub> :V <sub>9.5</sub> (at.%) .....	198
6.1.4	As-cast Alloy 29, Average Composition Pt <sub>78.7</sub> :Al <sub>12.2</sub> :Cr <sub>3.8</sub> :Ru <sub>0.6</sub> :V <sub>5.2</sub> (at.%) .....	200

6.1.5	As-cast Alloy 30, Average Composition $\text{Pt}_{63.2}\text{:Al}_{12.9}\text{:Cr}_{4.0}\text{:Ru}_{0.7}\text{:V}_{19.0}\text{:Nb}_{0.6}$ (at.%) .....	202
6.1.6	As-cast Alloy 31, Average Composition $\text{Pt}_{71.7}\text{:Al}_{12.8}\text{:Cr}_{4.9}\text{:Ru}_{1.1}\text{:V}_{9.9}\text{:Nb}_{0.3}$ (at.%) .....	204
6.2	ALLOYS ANNEALED AT 1000°C FOR 1500 HOURS .....	206
6.2.1	Annealed Alloy 26H, Average Composition $\text{Pt}_{61.7}\text{:Al}_{13.9}\text{:Cr}_{4.1}\text{:Ru}_{0.6}\text{:V}_{19.6}$ (at.%) .....	206
6.2.2	Annealed Alloy 27H, Average Composition $\text{Pt}_{69.8}\text{:Al}_{11.4}\text{:Cr}_{4.4}\text{:Ru}_{0.5}\text{:V}_{14.1}$ (at.%) .....	208
6.2.3	Annealed Alloy 28H, Average Composition $\text{Pt}_{83.0}\text{:Al}_{10.1}\text{:Cr}_{3.7}\text{:Ru}_{0.8}\text{:V}_{9.0}$ (at.%) .....	210
6.2.4	Annealed Alloy 29H, Average Composition $\text{Pt}_{83.0}\text{:Al}_{18.7}\text{:Cr}_{3.7}\text{:Ru}_{0.8}\text{:V}_{4.3}$ (at.%) .....	212
6.2.5	Annealed Alloy 30H, Average Composition $\text{Pt}_{53.9}\text{:Al}_{18.0}\text{:Cr}_{4.3}\text{:Ru}_{1.4}\text{:V}_{21.9}\text{:Nb}_{1.0}$ (at.%) .....	214
6.2.6	Annealed Alloy 31H, Average Composition $\text{Pt}_{74.1}\text{:Al}_{11.5}\text{:Cr}_{4.5}\text{:Ru}_{0.5}\text{:V}_{9.3}\text{:Nb}_{0.3}$ (at.%) .....	216
CHAPTER 7:	MICROHARDNESS .....	219
7.1	Experimental Procedure .....	219
7.2	Alloys of the Pt-Al-V System .....	219
7.2.1	As-cast Alloys of the Pt-Al-V System .....	219
7.2.2	Pt-Al-V Alloys Annealed at 1000°C for 1500 Hours .....	226
7.3	Alloys of the Pt-Cr-V System .....	233
7.3.1	As-cast Pt-Cr-V Alloys .....	233
7.3.2	Pt-Cr-V Alloys Annealed at 1000°C for 1500 Hours .....	243
7.4	Higher Order Alloys .....	251
7.4.1	As-cast Higher Order Alloys .....	251
7.4.2	Higher Order Alloys Annealed at 1000°C for 1500 Hours .....	256
7.4.3	Variation of Hardness Values with Vanadium Content .....	260
CHAPTER 8:	DISCUSSION .....	262
8.1	Pt-Al-V ALLOYS .....	262
8.2	Pt-Cr-V ALLOYS .....	266
8.3	HIGHER ORDER ALLOYS .....	269
9.	CONCLUSIONS AND RECOMMENDATIONS .....	272
9.1	CONCLUSIONS .....	272
9.1.1	The Pt-Al-V System at the Pt-rich Corner .....	272
9.1.2	The Pt-Cr-V System .....	272
9.1.3	Higher Order Alloys .....	273
9.2	RECOMMENDATIONS .....	273
REFERENCES	.....	275



## LIST OF FIGURES

Figure 2.1. Binary Al-Pt equilibrium phase diagram [1990Mas]. .....	9
Figure 2.2. Pt-rich portion of the Pt-Al phase diagram according to Oya, Mishima and Suzuki [1986Mis, 1987Oya]. .....	14
Figure 2.3. Assessed binary Pt-V equilibrium phase diagram, [1990Mas]. .....	15
Figure 2.4. Assessed binary Al-V equilibrium phase diagram by [1990Mas]. .....	18
Figure 2.5. Assessed binary Cr-Pt diagram by Murray, [1990Mas]. .....	25
Figure 2.6. Calculated Cr-Pt phase diagram after Oikawa [2001Oik]. .....	26
Figure 2.7. Proposed refinement (dotted lines) of the phase diagram showing the two ordered phases in separate phase regions and the disordered region between them after Zhao [2005Zha] .....	26
Figure 2.8. Comparison between calculated Cr-Pt phase diagram and experimentally determined data [2008Zha]. .....	27
Figure 2.9. Assessed binary Cr-Pt phase diagram by Okamoto [2009Oka]. .....	30
Figure 2.10. Binary phase equilibria of Cr-V [1959Car, 1969Rud1, 1977Koc] – after [1982Smi]. .....	32
Figure 2.11. Calculated Cr-V phase equilibrium diagram [1982Smi]. .....	33
Figure 2.12. Lattice parameter as a function of composition for Cr-V alloys [1982Smi], where the data are from independent investigators. ....	33
Figure 2.13. Assessed Nb-Pt phase diagram [1995Tri]. .....	35
Figure 2.14. Nb-Al phase diagram after Jorda et al. [1980Jor]: ○, single phase; Φ, two phases; ●, levitation thermal analysis (LTA); Δ, DTA; □, microprobe analysis; x, phase boundary determination by X-ray analysis. ....	43
Figure 2.15 (a). Calculated Al-Nb phase diagram [2009Wit] along with experimental data from [2008Zhu], [1980Jor] and [1971Wic]; (b) enlarged part in the vicinity of NbAl <sub>3</sub> (ε-phase). ....	44
Figure 2.16. Assessed phase diagram of Cr-Nb after Venkatraman and Neumann [1986Van]. .....	46
Figure 2.17 (a). Calculated Cr-Nb phase diagram by Costa Neto <i>et al.</i> [1993Net] where dark symbols are used in the optimisation and light are not. ....	47
Figure 2.18 (a). SEM-BSE image of unetched, annealed Pt <sub>82</sub> :Al <sub>12</sub> :Cr <sub>4</sub> :Ru <sub>2</sub> (at.%), showing ~Pt <sub>3</sub> Al precipitates in light (Pt) matrix [2008Sho], (b). Optical microscope image of annealed Pt <sub>82</sub> :Al <sub>12</sub> :Cr <sub>4</sub> :Ru <sub>2</sub> (at.%) after electrolytic etching in HCl/NaCl solution, showing ~Pt <sub>3</sub> Al precipitates in light (Pt) matrix as well as a eutectic. The scale is 10 μm. [2012Ode1]. ....	54
Figure 2.19. TEM micrograph for nominal Pt <sub>82</sub> :Al <sub>12</sub> :Cr <sub>4</sub> :Ru <sub>2</sub> (at.%) showing ~Pt <sub>3</sub> Al (marked A) with channels of (Pt) matrix [2012Sho]. .....	55
Figure 4.1. SEM-BSE image of as-cast Alloy 1 showing medium contrast dendrites (~Pt <sub>3</sub> Al) with a dark thin layer (~Pt <sub>2</sub> V), light needles (~Pt <sub>5</sub> Al <sub>3</sub> ), and a eutectic. ....	61
Figure 4.2. Plot of overall and phase compositions of Alloy 1, average composition Pt <sub>64.3</sub> :Al <sub>26.6</sub> :V <sub>9.1</sub> (at.%). .....	62
Figure 4.3. XRD pattern of Alloy 1, average composition Pt <sub>64.3</sub> :Al <sub>26.6</sub> :V <sub>9.1</sub> (at.%). .....	62

Figure 4.4 (a). SEM-BSE image of Alloy 2 showing medium grey dendrites ( $\sim\text{Pt}_2\text{V}$ ), a light phase ( $\sim\text{Pt}_5\text{Al}_3$ ), and a eutectic ( $\sim\text{PtAl} + \sim\text{Pt}_5\text{Al}_3$ ), (b). SEM-BSE image of Alloy 2 showing medium grey dendrites ( $\sim\text{Pt}_2\text{V}$ ), a light phase ( $\sim\text{Pt}_5\text{Al}_3$ ) and the cellular precipitation ( $\sim\text{PtAl}$ ).	64
Figure 4.5. Plot of overall and phase compositions of as-cast Alloy 2, average composition $\text{Pt}_{59.1}:\text{Al}_{23.1}:\text{V}_{17.8}$ (at.%).	65
Figure 4.6. XRD pattern of as-cast Alloy 2, average composition $\text{Pt}_{59.1}:\text{Al}_{23.1}:\text{V}_{17.8}$ (at.%).	65
Figure 4.7. (a). SEM-BSE image of as-cast Alloy 3, $\text{Pt}_{57.3}:\text{Al}_{6.7}:\text{V}_{26}$ (at.%), showing dendrites ( $\sim\text{Pt}_3\text{V}$ ) and a light phase ( $\sim\text{Pt}_3\text{Al}$ ) and (b). SEM-BSE image of as-cast Alloy $\text{Pt}_{57.3}:\text{Al}_{6.7}:\text{V}_{26}$ (at.%) dendrites ( $\sim\text{Pt}_3\text{V}$ ), a light phase ( $\sim\text{Pt}_3\text{Al}$ ) and a dark phase ( $\sim\text{Pt}_2\text{Al}$ ) in between the dendrites.	66
Figure 4.8. Plot of overall and phase compositions of as-cast Alloy 3, average composition $\text{Pt}_{57.3}:\text{Al}_{6.7}:\text{V}_{26}$ (at.%).	67
Figure 4.9. XRD pattern of as-cast Alloy 3, average composition $\text{Pt}_{57.3}:\text{Al}_{6.7}:\text{V}_{26}$ (at.%).	68
Figure 4.10. SEM-BSE image of as-cast Alloy 4A, average composition $\text{Pt}_{76.2}:\text{Al}_{17.4}:\text{V}_{6.4}$ (at.%), showing a single phase ( $\sim\text{Pt}_3\text{Al}$ ) with grains at different orientations.	69
Figure 4.11. Plot of composition of as-cast Alloy 4A, average composition $\text{Pt}_{76.2}:\text{Al}_{17.4}:\text{V}_{6.4}$ .	70
Figure 4.12. XRD pattern of as-cast Alloy 4A, average overall composition $\text{Pt}_{76.2}:\text{Al}_{17.4}:\text{V}_{6.4}$ (at.%).	71
Figure 4.13. SEM-BSE image of as-cast Alloy 4B, average composition $\text{Pt}_{69.8}:\text{Al}_{22.3}:\text{V}_{7.9}$ (at.%), showing a light grey phase ( $\sim\text{Pt}_3\text{Al}$ ), a medium grey phase ( $\sim\text{Pt}_3\text{Al}$ ) and a thin dark grey phase ( $\sim\text{Pt}_2\text{Al}$ ). The scale bar is 30 $\mu\text{m}$ .	72
Figure 4.14. Plot of Alloy 4B, average composition $\text{Pt}_{69.8}:\text{Al}_{22.3}:\text{V}_{7.9}$ (at.%).	73
Figure 4.15. XRD pattern of Alloy 4B, average composition $\text{Pt}_{69.8}:\text{Al}_{22.3}:\text{V}_{7.9}$ (at.%).	74
Figure 4.16. SEM-BSE image of as-cast Alloy 10, average composition $\text{Pt}_{83.9}:\text{Al}_6:\text{V}_{10.1}$ (at.%), showing a medium grey phase (Pt), a fine eutectic ((Pt) + $\sim\text{Pt}_3\text{Al}$ ) and porosity dark spots, scale bar is 30 $\mu\text{m}$ .	75
Figure 4.17. Plot of as-cast Alloy 10, average composition $\text{Pt}_{83.9}:\text{Al}_6:\text{V}_{10.1}$ (at.%).	76
Figure 4.18. XRD pattern of as-cast Alloy 10, average composition $\text{Pt}_{83.9}:\text{Al}_6:\text{V}_{10.1}$ (at.%).	76
Figure 4.19 (a). SEM-BSE image of as-cast Alloy 11, $\text{Pt}_{80.9}:\text{Al}_{4.3}:\text{V}_{14.8}$ , showing medium grey dendrites and a eutectic which appears dark and (b). SEM-BSE image of as-cast Alloy 11, $\text{Pt}_{80.9}:\text{Al}_{4.3}:\text{V}_{14.8}$ , at a higher magnification, showing medium grey dendrites and a eutectic which appears dark.	77
Figure 4.20. Plot of the overall and phase compositions of Alloy 11, average composition $\text{Pt}_{80.9}:\text{Al}_{4.3}:\text{V}_{14.8}$ (at.%).	78
Figure 4.21. XRD pattern of as-cast Alloy 11, average composition $\text{Pt}_{80.9}:\text{Al}_{4.3}:\text{V}_{14.8}$ (at.%).	78
Figure 4.22. (a). SEM-BSE image of as-cast Alloy 12, $\text{Pt}_{52.5}:\text{Al}_{22.6}:\text{V}_{24.9}$ showing light medium dendrites and a thin ternary eutectic and (b). SEM-BSE image of as-cast alloy $\text{Pt}_{52.5}:\text{Al}_{22.6}:\text{V}_{24.9}$ , at a higher magnification showing dark $\sim\text{PtV}$ , darker medium $\sim\text{PtV}_3$ , medium and light needles ( $\text{Pt}_5\text{Al}_3$ ).	80
Figure 4.23. Plot of overall and phase compositions of alloy 12, average composition $\text{Pt}_{52.5}:\text{Al}_{22.6}:\text{V}_{24.9}$ (at.%).	81
Figure 4.24. XRD pattern of as-cast Alloy 12, average composition $\text{Pt}_{52.5}:\text{Al}_{22.6}:\text{V}_{24.9}$ (at.%).	82
Figure 4.25 (a). SEM-BSE image of alloy $\text{Pt}_{53.7}:\text{Al}_{8.8}:\text{V}_{37.5}$ (at.%) medium dendrites ( $\sim\text{PtV} + \sim\text{PtV}_3$ ), a light phase ( $\tau_1$ ) and dark porosity and (b). SEM-BSE image of Alloy 13, $\text{Pt}_{53.7}:\text{Al}_{8.8}:\text{V}_{37.5}$ (at.%), at a higher magnification showing medium dendrites ( $\sim\text{PtV} + \sim\text{PtV}_3$ ), a light phase ( $\tau_1$ ) and a sparse eutectic of $\tau_1$ (which decomposed to $\sim\text{PtV}_3 + \text{Pt}_5\text{Al}_3$ ) + $\sim\text{PtV}_3$ .	83
Figure 4.26. Plot of overall and phase compositions for as-cast Alloy 13, average composition $\text{Pt}_{53.7}:\text{Al}_{8.8}:\text{V}_{37.5}$ (at.%).	84

Figure 4.27. XRD pattern for as-cast Alloy 13, average composition $\text{Pt}_{53.7}:\text{Al}_{8.8}:\text{V}_{37.5}$ (at.%).	84
Figure 4.28. SEM-BSE image of as-cast Alloy 14, average composition $\text{Pt}_{84}:\text{Al}_{12}:\text{V}_4$ (at.%), showing light (Pt) dendrites with $\sim\text{Pt}_3\text{Al}$ pptn. in some areas and a eutectic of (Pt) + $\sim\text{Pt}_3\text{Al}$ .	85
Figure 4.29. Plot of overall and phase compositions for as-cast Alloy 14, average composition $\text{Pt}_{84}:\text{Al}_{12}:\text{V}_4$ (at.%).	86
Figure 4.30. XRD pattern of as-cast Alloy 14, average composition $\text{Pt}_{84}:\text{Al}_{12}:\text{V}_4$ (at.%).	87
Figure 4.31. SEM-BSE image of as-cast Alloy 15, average composition $\text{Pt}_{72.4}:\text{Al}_{13.7}:\text{V}_{13.9}$ (at.%), showing medium contrast $\sim\text{Pt}_3\text{Al}$ and light contrast $\sim\text{Pt}_2\text{Al}$ , with light and dark areas due to different grain orientations.	88
Figure 4.32. Plot of as-cast Alloy 15, average composition $\text{Pt}_{72.4}:\text{Al}_{13.7}:\text{V}_{13.9}$ (at.%).	89
Figure 4.33. XRD pattern for as-cast Alloy 15, average composition $\text{Pt}_{72.4}:\text{Al}_{13.7}:\text{V}_{13.9}$ (at.%).	89
Figure 4.34. (a). SEM-BSE image of Alloy 16, average composition $\text{Pt}_{56.9}:\text{Al}_{25.4}:\text{V}_{17.7}$ (at.%), showing no contrast and (b) optical microscope image of etched Alloy 16, average composition $\text{Pt}_{56.9}:\text{Al}_{25.4}:\text{V}_{17.7}$ (at.%), showing single ternary phase, $\tau_2$ , with grains at different orientations.	90
Figure 4.35. Plot of Alloy 16, average composition $\text{Pt}_{56.9}:\text{Al}_{25.4}:\text{V}_{17.7}$ (at.%).	91
Figure 4.36 (a). XRD pattern of Alloy 16, average composition $\text{Pt}_{56.9}:\text{Al}_{25.4}:\text{V}_{17.7}$ (at.%), presumed to be from $\tau_2$ .	92
Figure 4.37. Solidification projection of the Pt-Al-V system at the Pt-rich corner (at.%).	95
Figure 4.38. Liquidus surface projection of the Pt-Al-V system at the Pt-rich corner (at.%).	97
Figure 4.39. SEM-BSE image of annealed Alloy 1H, average composition $\text{Pt}_{64.7}:\text{Al}_{26.2}:\text{V}_{9.1}$ (at.%), showing a medium grey phase ( $\sim\text{Pt}_3\text{Al}$ ), a light phase ( $\sim\text{Pt}_5\text{Al}_3$ ), a dark ( $\sim\text{Pt}_2\text{V}$ ) phase, a eutectoid ( $\sim\text{PtAl} + \text{Pt}_5\text{Al}_3$ ).	98
Figure 4.40. Plot of the overall and phase compositions of the annealed Alloy 1H, average composition $\text{Pt}_{64.7}:\text{Al}_{26.2}:\text{V}_{9.1}$ (at.%).	99
Figure 4.41. XRD pattern of Alloy 1H, average composition $\text{Pt}_{64.7}:\text{Al}_{26.2}:\text{V}_{9.1}$ (at.%).	100
Figure 4.42. (a). SEM-BSE image of annealed Alloy 2H, average composition $\text{Pt}_{61.8}:\text{Al}_{21.1}:\text{V}_{17.1}$ (at.%), showing a dark phase ( $\sim\text{PtV}$ ), a light phase ( $\sim\text{Pt}_5\text{Al}_3$ ) and dark precipitates in the light phase, scale bar is 30 $\mu\text{m}$ and (b). SEM-BSE image of annealed Alloy $\text{Pt}_{61.8}:\text{Al}_{21.1}:\text{V}_{17.1}$ (at.%) showing a dark phase ( $\sim\text{PtV}$ ), a light phase ( $\sim\text{Pt}_5\text{Al}_3$ ), dark precipitates within the light phase and light precipitates in the dark phase, scale bar is 10 $\mu\text{m}$ .	101
Figure 4.43. Plot of overall and phase compositions of annealed Alloy 2H, average composition $\text{Pt}_{61.8}:\text{Al}_{21.1}:\text{V}_{17.1}$ (at.%).	102
Figure 4.44. XRD pattern of annealed Alloy 2H, average composition $\text{Pt}_{61.8}:\text{Al}_{21.1}:\text{V}_{17.1}$ (at.%).	102
Figure 4.45. (a). SEM-BSE image of annealed Alloy 3H, $\text{Pt}_{63.7}:\text{Al}_{10.8}:\text{V}_{25.5}$ (at.%) showing a medium grey phase ( $\sim\text{Pt}_2\text{V}$ ), a light phase ( $\sim\text{Pt}_3\text{Al}$ ) and a dark phase ( $\sim\text{PtV}$ ) and (b). SEM-BSE image of annealed Alloy 3H, $\text{Pt}_{63.7}:\text{Al}_{10.8}:\text{V}_{25.5}$ (at.%) showing a medium grey phase ( $\sim\text{Pt}_2\text{V}$ ), a light phase ( $\sim\text{Pt}_3\text{Al}$ ), a dark phase ( $\sim\text{PtV}$ ) and 2-phase dendrites.	103
Figure 4.46. Plot of overall and phase compositions of annealed Alloy 3H, average composition $\text{Pt}_{63.7}:\text{Al}_{10.8}:\text{V}_{25.5}$ (at.%).	104
Figure 4.47. XRD pattern of annealed Alloy 3H, average composition $\text{Pt}_{63.7}:\text{Al}_{10.8}:\text{V}_{25.5}$ (at.%).	105
Figure 4.48. (a). SEM-BSE image of Alloy 4BH, $\text{Pt}_{69.7}:\text{Al}_{23.2}:\text{V}_{7.1}$ (at.%) showing a dark phase, a medium grey phase and a light phase ( $\sim\text{Pt}_2\text{Al}$ ). The dark phase and the medium grey phases are the same phase	



(~Pt <sub>3</sub> Al) seen from different orientations and (b). SEM-BSE image of Alloy 4BH, Pt <sub>69.7</sub> :Al <sub>23.2</sub> :V <sub>7.1</sub> (at.%) showing a dark phase, a medium grey phase and a light phase at a higher magnification. ....	106
Figure 4.49. Plot of the overall and phase compositions of annealed Alloy 4BH, average composition Pt <sub>69.7</sub> :Al <sub>23.2</sub> :V <sub>7.1</sub> (at.%).....	107
Figure 4.50. XRD pattern of alloy 4BH, average composition Pt <sub>69.7</sub> :Al <sub>23.2</sub> :V <sub>7.1</sub> (at.%) . ....	107
Figure 4.51 (a). SEM-BSE image of annealed Alloy 10H, Pt <sub>83.9</sub> :Al <sub>6</sub> :V <sub>10.1</sub> (at.%) showing a light grey phase, a dark phase and a eutectic and (b). SEM-BSE image of annealed Alloy 10H, Pt <sub>83.9</sub> :Al <sub>6</sub> :V <sub>10.1</sub> (at.%) showing a light grey phase and a eutectic at a higher magnification. ....	108
Figure 4.52. Plot of overall and phase compositions of annealed Alloy 10H, average composition Pt <sub>83.9</sub> :Al <sub>5.8</sub> :V <sub>10.3</sub> (at.%) . ....	109
Figure 4.53. XRD pattern of alloy 10H, average composition Pt <sub>83.9</sub> :Al <sub>5.8</sub> :V <sub>10.3</sub> (at.%) . The unlabelled peaks are due to the resin mounting (Appendix 1A).....	110
Figure 4.54. (a). SEM-BSE image of annealed Alloy 11H showing a light phase (Pt) and a dark eutectic, (Pt) + ~Pt <sub>3</sub> Al and (b). SEM-BSE image of annealed Alloy 11H at a higher magnification, showing a light phase (Pt) and a dark eutectic, (Pt) + ~Pt <sub>3</sub> Al. ....	111
Figure 4.55. Plot of overall and phase compositions of annealed Alloy 11H, average composition Pt <sub>85.2</sub> :Al <sub>3.4</sub> :V <sub>11.4</sub> (at.%).....	112
Figure 4.56. XRD pattern of annealed Alloy 11H, average composition Pt <sub>85.2</sub> :Al <sub>3.4</sub> :V <sub>11.4</sub> (at.%) . ....	112
Figure 4.57. SEM-BSE image of Alloy 12H, average composition Pt <sub>60.5</sub> :Al <sub>18.6</sub> :V <sub>20.9</sub> (at.%) showing a medium phase (~PtV), a dark phase (~PtV <sub>3</sub> ) and the light phase (~Pt <sub>5</sub> Al <sub>3</sub> ). ....	113
Figure 4.58. Plot of average and phase compositions of annealed Alloy 12H, average composition Pt <sub>60.5</sub> :Al <sub>18.6</sub> :V <sub>20.9</sub> (at.%) . ....	114
Figure 4.59. XRD pattern of annealed Alloy 12H, average composition Pt <sub>60.5</sub> :Al <sub>18.6</sub> :V <sub>20.9</sub> (at.%).....	114
Figure 4. 60. SEM-BSE image of annealed Alloy 13H, average composition Pt <sub>59.2</sub> :Al <sub>8.4</sub> :V <sub>32.4</sub> (at.%) showing a medium contrast phase ~PtV, a dark phase ~PtV <sub>3</sub> and a light phase (~Pt <sub>5</sub> Al <sub>3</sub> ). ....	115
Figure 4.61. Plot of overall and phase compositions of annealed Alloy 13H, average composition Pt <sub>59.2</sub> :Al <sub>8.4</sub> :V <sub>32.4</sub> (at.%).....	116
Figure 4.62. XRD pattern of annealed Alloy 13H, average composition Pt <sub>59.2</sub> :Al <sub>8.4</sub> :V <sub>32.4</sub> (at.%).....	116
Figure 4.63. SEM-BSE image of Alloy 14H, average composition Pt <sub>81.6</sub> :Al <sub>14.5</sub> :V <sub>3.7</sub> (at.%), showing light dendrites, (~Pt), having dark pptn. within, medium phase (~Pt <sub>3</sub> Al) with light pptn. (~Pt <sub>3</sub> Al) within. ....	117
Figure 4.64. Plot of the overall and phase compositions of annealed Alloy 14H, average composition Pt <sub>81.6</sub> :Al <sub>14.5</sub> :V <sub>3.7</sub> (at.%).....	118
Figure 4.65. XRD pattern of annealed Alloy 14H, average composition Pt <sub>81.6</sub> :Al <sub>14.5</sub> :V <sub>3.7</sub> (at.%) . ....	119
Figure 4.66. SEM-BSE image of annealed Alloy 15H, average composition Pt <sub>72.3</sub> :Al <sub>13.5</sub> :V <sub>14.2</sub> (at.%) , showing single phase ~Pt <sub>3</sub> Al with grains at different orientations. ....	120
Figure 4.67. Plot of annealed Alloy 15H, average composition Pt <sub>72.3</sub> :Al <sub>13.5</sub> :V <sub>14.2</sub> (at.%) . ....	121
Figure 4.68. XRD pattern of annealed Alloy 15H, average composition Pt <sub>72.3</sub> :Al <sub>13.5</sub> :V <sub>14.2</sub> (at.%) . ....	121
Figure 4 69. SEM-BSE image of annealed Alloy 16H, average composition Pt <sub>51.0</sub> :Al <sub>31.1</sub> :V <sub>17.9</sub> (at.%) , showing dark ~PtV and light ~PtAl. ....	122
Figure 4.70. Plot of annealed Alloy 16H, average composition Pt <sub>51.0</sub> :Al <sub>31.1</sub> :V <sub>17.9</sub> (at.%).....	123
Figure 4.71. XRD pattern for annealed Alloy 16H, average composition Pt <sub>51.0</sub> :Al <sub>31.1</sub> :V <sub>17.9</sub> (at.%).....	123
Figure 4.72. Combined plot of the Pt-Al-V system at 1000°C at the Pt-rich corner. ....	124
Figure 4.73. Isothermal section of the Pt-Al-V system at 1000°C at the Pt-rich corner.....	125

Figure 4.74. Plot of annealed Alloys 12H and 13H, average compositions $\text{Pt}_{60.5}:\text{Al}_{18.6}:\text{V}_{20.9}$ and $\text{Pt}_{59.2}:\text{Al}_{8.4}:\text{V}_{32.4}$ (at.%) respectively. ....	126
---	-----

Figure 5.1. SEM-BSE image of as-cast Alloy 5, average composition $\text{Pt}_{73.8}:\text{Cr}_{16.9}:\text{V}_{9.3}$ (at.%), showing single phase, $\sim\text{Pt}_3\text{V}$ , with grains at different orientations. ....	129
Figure 5.2. Plot of compositions of Alloy 5, average overall composition $\text{Pt}_{73.8}:\text{Cr}_{16.9}:\text{V}_{9.3}$ (at.%). ....	130
Figure 5.3. XRD pattern of Alloy 5, average composition $\text{Pt}_{73.8}:\text{Cr}_{16.9}:\text{V}_{9.3}$ (at.%). ....	130
Figure 5.4. SEM-BSE image of Alloy 6, average composition $\text{Pt}_{72.3}:\text{Cr}_{8.3}:\text{V}_{19.4}$ (at.%) showing single phase $\sim\text{Pt}_3\text{V}$ with grains at different orientations. ....	131
Figure 5.5. Plot of composition of Alloy 6, average composition $\text{Pt}_{72.3}:\text{Cr}_{8.3}:\text{V}_{19.4}$ (at.%). ....	132
Figure 5.6. XRD pattern of Alloy 6, average composition $\text{Pt}_{72.3}:\text{Cr}_{8.3}:\text{V}_{19.4}$ (at.%). ....	132
Figure 5.7. SEM-BSE image of as-cast Alloy 7, average composition $\text{Pt}_{33.4}:\text{Cr}_{45.8}:\text{V}_{20.8}$ (at.%) showing $\sim\text{Cr}_3\text{Pt}$ dendrites, medium contrast $\text{Al}_5(\sim\text{Cr}_3\text{Pt})$ , a eutectic of $\sim\text{Cr}_3\text{Pt} + \tau$ and porosity. ....	133
Figure 5.8. Plot of composition of Alloy 7, average composition $\text{Pt}_{33.4}:\text{Cr}_{45.8}:\text{V}_{20.8}$ (at.%). ....	134
Figure 5.9. XRD pattern of as-cast Alloy 7, average composition $\text{Pt}_{33.4}:\text{Cr}_{45.8}:\text{V}_{20.8}$ (at.%). ....	135
Figure 5.10(a). SEM-BSE image of Alloy 8, average composition $\text{Pt}_{53.0}:\text{Cr}_{22.4}:\text{V}_{24.5}$ (at.%) showing medium $\sim\text{Cr}_3\text{Pt}$ and light $\sim\text{CrPt}$ dendrites, a eutectic of $\tau + \sim\text{CrPt}$ and $\tau + \sim\text{Cr}_3\text{Pt}$ and porosity. (b). SEM-BSE image of Alloy 8, average composition $\text{Pt}_{53.0}:\text{Cr}_{22.4}:\text{V}_{24.5}$ (at.%), at higher magnification, showing medium $\sim\text{Cr}_3\text{Pt}$ and light $\sim\text{CrPt}$ dendrites and a eutectic of $\tau + \sim\text{CrPt}$ and $\tau + \sim\text{Cr}_3\text{Pt}$ and porosity. ....	136
Figure 5.11. Plot of Alloy 8, average composition $\text{Pt}_{53.0}:\text{Cr}_{22.4}:\text{V}_{24.5}$ (at.%). ....	137
Figure 5.12. XRD pattern of Alloy 8, average composition $\text{Pt}_{53.0}:\text{Cr}_{22.4}:\text{V}_{24.5}$ (at.%). ....	138
Figure 5.13. SEM-BSE image of Alloy 17, average composition $\text{Pt}_{68.5}:\text{Cr}_{16.2}:\text{V}_{15.3}$ (at.%) showing single phase $\sim\text{Pt}_3\text{V}$ with grains at different orientations. ....	139
Figure 5.14. Plot of Alloy 17, average composition $\text{Pt}_{68.5}:\text{Cr}_{16.2}:\text{V}_{15.3}$ (at.%). ....	140
Figure 5.15. XRD pattern of Alloy 17, average composition $\text{Pt}_{68.5}:\text{Cr}_{16.2}:\text{V}_{15.3}$ (at.%). ....	141
Figure 5.16. SEM-BSE image of Alloy 18, average composition $\text{Pt}_{32.8}:\text{Cr}_{28.6}:\text{V}_{38.6}$ (at.%), showing dark $\tau$ dendrites, light $\sim\text{Cr}_3\text{Pt}$ , and a sparse eutectic of small dark $\tau + \sim\text{Cr}_3\text{Pt}$ . ....	142
Figure 5.17. Plot of Alloy 18, average composition $\text{Pt}_{32.8}:\text{Cr}_{28.6}:\text{V}_{38.6}$ (at.%). ....	143
Figure 5.18. XRD pattern of Alloy 18, average composition $\text{Pt}_{32.8}:\text{Cr}_{28.6}:\text{V}_{38.6}$ (at.%). ....	143
Figure 5.19(a). SEM-BSE image of Alloy 19, average composition $\text{Pt}_{25.8}:\text{Cr}_{42.9}:\text{V}_{31.3}$ (at.%), showing medium $\tau$ dendrites, light $\sim\text{Cr}_3\text{Pt}$ and dark porosity and oxide (b). SEM-BSE image of Alloy 19, at a higher magnification, showing a eutectic between the light and a light medium phase. ....	144
Figure 5.20. Plot of Alloy 19, average composition $\text{Pt}_{25.8}:\text{Cr}_{42.9}:\text{V}_{31.3}$ (at.%). ....	145
Figure 5.21. XRD pattern of Alloy 19, average composition $\text{Pt}_{25.8}:\text{Cr}_{42.9}:\text{V}_{31.3}$ (at.%). ....	146
Figure 5.22. SEM-BSE image of Alloy 20, average composition $\text{Pt}_{38.8}:\text{Cr}_{14.2}:\text{V}_{47.0}$ (at.%), showing light cored $\sim\text{PtV}$ dendrites, medium $\sim\text{PtV}_3$ and a eutectic of dark $\tau +$ medium $\text{PtV}_3$ . ....	147
Figure 5.23. Plot of Alloy 20, average composition $\text{Pt}_{38.8}:\text{Cr}_{14.2}:\text{V}_{47.0}$ (at.%). ....	148
Figure 5.24. XRD pattern for Alloy 20, average overall composition $\text{Pt}_{38.8}:\text{Cr}_{14.2}:\text{V}_{47.0}$ (at.%). ....	148
Figure 5.25(a). SEM-BSE image of Alloy 21, average composition $\text{Pt}_{16.8}:\text{Cr}_{13.4}:\text{V}_{69.8}$ (at.%) showing medium contrast (V,Cr) dendrites, light contrast $\sim\text{PtV}_3$ and solid state precipitates $\sim\text{PtV}_3$ in (V,Cr). (b). ....	

SEM-BSE image of Alloy 21, average composition $\text{Pt}_{16.8}:\text{Cr}_{13.4}:\text{V}_{69.8}$ (at.%) showing medium contrast (V,Cr) dendrites, light contrast $\sim\text{PtV}_3$ , solid state precipitates $\sim\text{PtV}_3$ in (V,Cr) and a thin dark ternary phase, $\tau$ , at the boundary of (V,Cr) and $\sim\text{PtV}_3$ .....	149
Figure 5.26. Plot of Alloy 21, average composition $\text{Pt}_{16.8}:\text{Cr}_{13.4}:\text{V}_{69.8}$ (at.%).....	150
Figure 5.27. XRD pattern of Alloy 21, average composition $\text{Pt}_{16.8}:\text{Cr}_{13.4}:\text{V}_{69.8}$ (at.%).....	151
Figure 5.28(a). SEM-BSE image of Alloy 22, average composition $\text{Pt}_{28.7}:\text{Cr}_{27.2}:\text{V}_{44.1}$ (at.%) showing medium dendrites, a light phase and a eutectic. (b). SEM-BSE image of Alloy 22 at a higher magnification showing a different shade of medium contrast at the extremities of dendrites. ....	152
Figure 5.29. Plot of Alloy 22, average composition $\text{Pt}_{28.7}:\text{Cr}_{27.2}:\text{V}_{44.1}$ (at.%).....	153
Figure 5.30. XRD pattern for Alloy 22, average composition $\text{Pt}_{28.7}:\text{Cr}_{27.2}:\text{V}_{44.1}$ (at.%).....	153
Figure 5.31. SEM-BSE image of Alloy 23, average composition $\text{Pt}_{16.5}:\text{Cr}_{56.1}:\text{V}_{27.4}$ (at.%), showing medium contrast (Cr) dendrites, light A15( $\sim\text{Cr}_3\text{Pt}$ ), A15( $\sim\text{Cr}_3\text{Pt}$ ) + (Cr) eutectic and dark oxide.....	154
Figure 5.32. Plot of Alloy 23, average composition $\text{Pt}_{16.5}:\text{Cr}_{56.1}:\text{V}_{27.4}$ (at.%).....	155
Figure 5.33. XRD pattern of Alloy 23, average composition $\text{Pt}_{16.5}:\text{Cr}_{56.1}:\text{V}_{27.4}$ (at.%).....	156
Figure 5.34 (a). SEM-BSE image of Alloy 24, average composition $\text{Pt}_{14.9}:\text{Cr}_{73.7}:\text{V}_{11.4}$ (at.%), showing medium cored dendrites, (V,Cr), light A15( $\sim\text{Cr}_3\text{Pt}$ ), sparse eutectic of (Cr) + A15( $\sim\text{Cr}_3\text{Pt}$ ) and rounded dark porosity and oxides. (b). SEM-BSE image of Alloy 24, average composition $\text{Pt}_{14.9}:\text{Cr}_{73.7}:\text{V}_{11.4}$ (at.%), showing medium cored dendrites, (V,Cr), light A15( $\sim\text{Cr}_3\text{Pt}$ ), multi-phase area with a dark component and rounded dark porosity and oxides. ....	157
Figure 5.35. Plot of Alloy 24, average composition $\text{Pt}_{14.9}:\text{Cr}_{73.7}:\text{V}_{11.4}$ (at.%).....	158
Figure 5.36. XRD pattern of Alloy 24, average composition $\text{Pt}_{14.9}:\text{Cr}_{73.7}:\text{V}_{11.4}$ (at.%).....	159
Figure 5.37. SEM-BSE image of Alloy 25, average composition $\text{Pt}_{34.1}:\text{Cr}_{57.4}:\text{V}_{8.5}$ (at.%), showing light $\sim\text{Cr}_3\text{Pt}$ cored dendrites, medium contrast A15( $\sim\text{Cr}_3\text{Pt}$ ) and dark oxide.....	160
Figure 5.38. Plot of Alloy 25, average composition $\text{Pt}_{34.1}:\text{Cr}_{57.4}:\text{V}_{8.5}$ (at.%).....	161
Figure 5.39. XRD pattern of Alloy 25, average composition $\text{Pt}_{34.1}:\text{Cr}_{57.4}:\text{V}_{8.5}$ (at.%).....	161
Figure 5.40. Solidification projection of the Pt-Cr-V system (at.%).....	162
Figure 5.41. Liquidus surface projection of the Pt-Cr-V system (at.%).....	163
Figure 5.42. SEM-BSE image of annealed Alloy 5H, average composition $\text{Pt}_{76.2}:\text{Cr}_{16.1}:\text{V}_{7.7}$ (at.%), showing single phase $\sim\text{Pt}_3\text{V}$ with grains at different orientations.....	164
Figure 5.43. Plot of annealed Alloy 5H, average composition $\text{Pt}_{76.2}:\text{Cr}_{16.1}:\text{V}_{7.7}$ (at.%).....	165
Figure 5.44. XRD pattern of annealed Alloy 5H, average composition $\text{Pt}_{76.2}:\text{Cr}_{16.1}:\text{V}_{7.7}$ (at.%).....	165
Figure 5.45. SEM-BSE image of annealed Alloy 6H, average composition $\text{Pt}_{77.3}:\text{Cr}_{6.6}:\text{V}_{16.1}$ (at.%), showing single phase $\sim\text{Pt}_3\text{V}$ with grains at different orientations.....	166
Figure 5.46. Plot of annealed Alloy 6H, average composition $\text{Pt}_{77.3}:\text{Cr}_{6.6}:\text{V}_{16.1}$ (at.%).....	167
Figure 5.47. XRD pattern of annealed Alloy 6H, average composition $\text{Pt}_{77.3}:\text{Cr}_{6.6}:\text{V}_{16.1}$ (at.%).....	167
Figure 5.48. SEM-BSE image of annealed Alloy 7H, average composition $\text{Pt}_{35.7}:\text{Cr}_{45.1}:\text{V}_{19.2}$ (at.%), showing darker medium contrast A15( $\sim\text{Cr}_3\text{Pt}$ ) (1), light medium contrast $\sim\text{CrPt}$ (2), medium contrast $\sim\text{Cr}_3\text{Pt}$ (3), light contrast (Pt) (4) and a eutectic of $\tau$ + $\sim\text{Cr}_3\text{Pt}$ (5). ....	168
Figure 5.49. Plot of annealed Alloy 7H, average composition $\text{Pt}_{35.7}:\text{Cr}_{45.1}:\text{V}_{19.2}$ (at.%).....	169
Figure 5.50. XRD pattern of annealed Alloy 7H, average composition $\text{Pt}_{35.7}:\text{Cr}_{45.1}:\text{V}_{19.2}$ (at.%), with unidentified peaks from $\tau$ .....	170
Figure 5.51. SEM-BSE image of annealed Alloy 8H, average composition $\text{Pt}_{52.3}:\text{Cr}_{23.4}:\text{V}_{24.3}$ (at.%), showing medium contrast $\sim\text{Cr}_3\text{Pt}$ , a eutectic of $\sim\text{Cr}_3\text{Pt}$ + $\tau$ and dark porosity.....	171

Figure 5.52. Plot of annealed Alloy 8H, average composition $\text{Pt}_{52.3}:\text{Cr}_{23.4}:\text{V}_{24.3}$ (at.%).	172
Figure 5.53. XRD pattern of annealed Alloy 8H, average composition $\text{Pt}_{52.3}:\text{Cr}_{23.4}:\text{V}_{24.3}$ (at.%), with unidentified peaks from $\tau$ .	172
Figure 5.54. SEM-BSE image of annealed Alloy 17H, average composition $\text{Pt}_{70.2}:\text{Cr}_{15.4}:\text{V}_{14.4}$ (at.%), showing single phase $\sim\text{Pt}_3\text{V}$ and dark porosity.	173
Figure 5.55. Plot of annealed Alloy 17H, average composition $\text{Pt}_{70.2}:\text{Cr}_{15.4}:\text{V}_{14.4}$ (at.%).	174
Figure 5.56. XRD pattern of annealed Alloy 17H, average composition $\text{Pt}_{70.2}:\text{Cr}_{15.4}:\text{V}_{14.4}$ (at.%).	174
Figure 5.57. SEM-BSE image of annealed Alloy 18H, average composition $\text{Pt}_{34.0}:\text{Cr}_{28.3}:\text{V}_{37.7}$ (at.%), showing a medium ternary phase, $\tau$ , light $\sim\text{PtV}$ , and medium $\sim\text{CrPt}$ within $\sim\text{PtV}$ .	175
Figure 5.58. Plot of annealed Alloy 18H, average composition $\text{Pt}_{34.0}:\text{Cr}_{28.3}:\text{V}_{37.7}$ (at.%).	176
Figure 5.59. XRD pattern of annealed Alloy 18H, average composition $\text{Pt}_{34.0}:\text{Cr}_{28.3}:\text{V}_{37.7}$ (at.%). The unidentified peaks originated from $\tau$ .	176
Figure 5.60(a). SEM-BSE image of Alloy 19H, average composition $\text{Pt}_{25.1}:\text{Cr}_{43.5}:\text{V}_{31.5}$ (at.%), showing dark dendrites, $\tau$ , light A15( $\sim\text{Cr}_3\text{Pt}$ ), and lightest $\sim\text{Cr}_3\text{Pt}$ . (b). SEM-BSE image of Alloy 19H, average composition $\text{Pt}_{25.1}:\text{Cr}_{43.5}:\text{V}_{31.5}$ (at.%), at a higher magnification showing dark dendrites, $\tau$ , light A15( $\sim\text{Cr}_3\text{Pt}$ ), and lightest $\sim\text{Cr}_3\text{Pt}$ .	177
Figure 5.61. Plot of Alloy annealed 19H, average composition $\text{Pt}_{25.1}:\text{Cr}_{43.5}:\text{V}_{31.5}$ (at.%).	178
Figure 5.62. SEM-BSE image of annealed Alloy 20H, average composition $\text{Pt}_{37.2}:\text{Cr}_{14.6}:\text{V}_{48.2}$ (at.%), showing medium contrast $\sim\text{PtV}_3$ , light $\text{PtV}$ and a eutectic of dark $\tau + \text{PtV}_3$ . Porosity and oxides are also of dark contrast.	179
Figure 5.63. Plot of annealed Alloy 20H, average composition $\text{Pt}_{37.2}:\text{Cr}_{14.6}:\text{V}_{48.2}$ (at.%).	180
Figure 5.64. XRD pattern of annealed Alloy 20H, average composition $\text{Pt}_{37.2}:\text{Cr}_{14.6}:\text{V}_{48.2}$ (at.%).	180
Figure 5.65. SEM-BSE image of annealed Alloy 21H, average composition $\text{Pt}_{16.5}:\text{Cr}_{13.2}:\text{V}_{70.3}$ (at.%), showing light $\sim\text{PtV}_3$ and light $\sim\text{PtV}_3$ solid state precipitates from medium contrast solid solution dendrites (V, Cr).	181
Figure 5.66. Plot of annealed Alloy 21H, average composition $\text{Pt}_{16.5}:\text{Cr}_{13.2}:\text{V}_{70.3}$ (at.%).	182
Figure 5.67. SEM-BSE image of annealed Alloy 22H, average composition $\text{Pt}_{27.1}:\text{Cr}_{26.8}:\text{V}_{46.1}$ (at.%), showing medium contrast dendrites ( $\tau$ ) with fine dark solid state precipitates (Cr), a medium phase ( $\sim\text{PtV}_3$ ), a eutectic of $\tau + (\text{Cr})$ and dark porosity.	183
Figure 5.68. Plot of annealed Alloy 22H, average composition $\text{Pt}_{27.1}:\text{Cr}_{26.8}:\text{V}_{46.1}$ (at.%).	184
Figure 5.69. SEM-BSE image of annealed Alloy 23H, average composition $\text{Pt}_{14.5}:\text{Cr}_{58.1}:\text{V}_{27.4}$ (at.%), showing (Cr) dendrites having light A15 ( $\sim\text{Cr}_3\text{Pt}$ ) solid state precipitates, light A15 ( $\sim\text{Cr}_3\text{Pt}$ ) and a eutectic of A15 ( $\sim\text{Cr}_3\text{Pt}$ ) and (V,Cr).	185
Figure 5.70. Plot of annealed Alloy 23H, average composition $\text{Pt}_{14.5}:\text{Cr}_{58.1}:\text{V}_{27.4}$ (at.%).	186
Figure 5.71. XRD pattern of annealed Alloy 23H, average composition $\text{Pt}_{14.5}:\text{Cr}_{58.1}:\text{V}_{27.4}$ (at.%).	186
Figure 5.72. SEM-BSE image of annealed Alloy 24H, average composition $\text{Pt}_{14.2}:\text{Cr}_{75.8}:\text{V}_{10.0}$ (at.%), showing medium contrast (Cr) dendrites having light A15 ( $\sim\text{Cr}_3\text{Pt}$ ) solid state precipitates, light contrast A15( $\sim\text{Cr}_3\text{Pt}$ ) and lightest contrast $\sim\text{Cr}_3\text{Pt}$ .	187
Figure 5.73. Plot of annealed Alloy 24H, average composition $\text{Pt}_{14.2}:\text{Cr}_{75.8}:\text{V}_{10.0}$ (at.%).	188
Figure 5.74. XRD pattern of annealed Alloy 24H, average composition $\text{Pt}_{14.2}:\text{Cr}_{75.8}:\text{V}_{10.0}$ (at.%).	188
Figure 5.75. SEM-BSE image of annealed Alloy 25H, average composition $\text{Pt}_{33.6}:\text{Cr}_{57.7}:\text{V}_{8.7}$ (at.%), showing light $\sim\text{CrPt}$ , light medium $\sim\text{Cr}_3\text{Pt}$ , darker medium A15 ( $\sim\text{Cr}_3\text{Pt}$ ), dark oxides and porosity.	189
Figure 5.76. Plot of annealed Alloy 25H, average composition $\text{Pt}_{33.6}:\text{Cr}_{57.7}:\text{V}_{8.7}$ (at.%).	190

Figure 5.77. XRD pattern of annealed Alloy 25H, average composition $\text{Pt}_{33.6}:\text{Cr}_{57.7}:\text{V}_{8.7}$ (at.%). ....	190
Figure 5.78. Isothermal section of the Pt-Cr-V system at 1000°C (at.%).....	191
Figure 6.1. SEM-BSE image of as-cast Alloy 26, average composition $\text{Pt}_{63.9}:\text{Al}_{12.2}:\text{Cr}_{4.3}:\text{Ru}_{0.7}:\text{V}_{18.9}$ (at.%), showing dark (Pt) and light $\sim\text{Pt}_3\text{Al}$ . ....	195
Figure 6.2. XRD pattern of Alloy 26, average composition $\text{Pt}_{63.9}:\text{Al}_{12.2}:\text{Cr}_{4.3}:\text{Ru}_{0.7}:\text{V}_{18.9}$ (at.%).....	196
Figure 6.3. SEM-BSE image of as-cast Alloy 27, average composition $\text{Pt}_{69.5}:\text{Al}_{11.5}:\text{Cr}_{4.2}:\text{Ru}_{0.6}:\text{V}_{14.2}$ (at.%), showing dark $\sim\text{Pt}_3\text{Al}$ and light (Pt). There are dark and light areas due to different orientations and irregular grain boundaries. ....	197
Figure 6.4. XRD pattern of Alloy 27, average composition $\text{Pt}_{69.5}:\text{Al}_{11.5}:\text{Cr}_{4.2}:\text{Ru}_{0.6}:\text{V}_{14.2}$ (at.%).....	198
Figure 6.5. SEM-BSE image of as-cast Alloy 28, average composition $\text{Pt}_{75.2}:\text{Al}_{11.2}:\text{Cr}_{4.0}:\text{Ru}_{0.6}:\text{V}_{9.5}$ (at.%), showing single phase, $\sim\text{Pt}_3\text{Al}$ , with grains at different orientations. ....	199
Figure 6.6. XRD pattern of Alloy 28, average composition $\text{Pt}_{75.2}:\text{Al}_{11.2}:\text{Cr}_{4.0}:\text{Ru}_{0.6}:\text{V}_{9.5}$ (at.%). ....	200
Figure 6.7. SEM-BSE image of as-cast Alloy 29, average composition $\text{Pt}_{78.7}:\text{Al}_{12.2}:\text{Cr}_{3.8}:\text{Ru}_{0.6}:\text{V}_{5.2}$ (at.%), showing single phase, $\sim\text{Pt}_3\text{Al}$ , with irregular grains at different orientations.....	201
Figure 6.8. XRD pattern of Alloy 29, average composition $\text{Pt}_{78.7}:\text{Al}_{12.2}:\text{Cr}_{3.8}:\text{Ru}_{0.6}:\text{V}_{5.2}$ (at.%). ....	202
Figure 6.9. SEM-BSE image of as-cast Alloy 30, average composition $\text{Pt}_{63.2}:\text{Al}_{12.9}:\text{Cr}_{4.0}:\text{Ru}_{0.7}:\text{V}_{19.0}:\text{Nb}_{0.6}$ (at.%), showing dark (Pt) dendrites and a eutectic of $\sim\text{Pt}_3\text{Al} + (\text{Pt})$ . ....	203
Figure 6.10. XRD pattern of Alloy 30, average composition $\text{Pt}_{63.2}:\text{Al}_{12.9}:\text{Cr}_{4.0}:\text{Ru}_{0.7}:\text{V}_{19.0}:\text{Nb}_{0.6}$ (at.%)....	204
Figure 6.11. SEM-BSE image of as-cast Alloy 31, average composition $\text{Pt}_{71.7}:\text{Al}_{12.8}:\text{Cr}_{4.9}:\text{Ru}_{1.1}:\text{V}_{9.9}:\text{Nb}_{0.3}$ (at.%), showing dark $\sim\text{Pt}_3\text{Al}$ and light (Pt). There are light and dark areas due to different orientations. ....	205
Figure 6.12. XRD pattern of Alloy 31, average composition $\text{Pt}_{71.7}:\text{Al}_{12.8}:\text{Cr}_{4.9}:\text{Ru}_{1.1}:\text{V}_{9.9}:\text{Nb}_{0.3}$ (at.%). ....	206
Figure 6.13. SEM-BSE image of annealed Alloy 26H, average composition $\text{Pt}_{61.7}:\text{Al}_{13.9}:\text{Cr}_{4.1}:\text{Ru}_{0.6}:\text{V}_{19.6}$ (at.%), showing a two phase structure of dark $\sim\text{Pt}_2\text{V}$ and light $\sim\text{Pt}_3\text{Al}$ .....	207
Figure 6.14. XRD pattern of annealed Alloy 26H, average composition $\text{Pt}_{61.7}:\text{Al}_{13.9}:\text{Cr}_{4.1}:\text{Ru}_{0.6}:\text{V}_{19.6}$ (at.%). ....	208
Figure 6.15. SEM-BSE image of annealed Alloy 27H, average composition $\text{Pt}_{69.8}:\text{Al}_{11.4}:\text{Cr}_{4.4}:\text{Ru}_{0.5}:\text{V}_{14.1}$ (at.%), showing single phase $\sim\text{Pt}_3\text{Al}$ with grains at different orientations.....	209
Figure 6.16. XRD pattern of annealed Alloy 27H, average composition $\text{Pt}_{69.8}:\text{Al}_{11.4}:\text{Cr}_{4.4}:\text{Ru}_{0.5}:\text{V}_{14.1}$ (at.%). ....	210
Figure 6.17. SEM-BSE image of annealed Alloy 28H, average composition $\text{Pt}_{83.0}:\text{Al}_{10.1}:\text{Cr}_{3.7}:\text{Ru}_{0.8}:\text{V}_{9.0}$ (at.%), showing single phase $\sim\text{Pt}_3\text{Al}$ with grains at different orientations.....	211
Figure 6.18. XRD pattern of annealed Alloy 28H, average composition $\text{Pt}_{83.0}:\text{Al}_{10.1}:\text{Cr}_{3.7}:\text{Ru}_{0.8}:\text{V}_{9.0}$ (at.%). ....	212
Figure 6.19. SEM-BSE image of annealed Alloy 29H, average composition $\text{Pt}_{83.0}:\text{Al}_{8.7}:\text{Cr}_{3.7}:\text{Ru}_{0.8}:\text{V}_{4.3}$ (at.%).....	213
Figure 6.20. XRD pattern for annealed Alloy 29H, average composition $\text{Pt}_{83.0}:\text{Al}_{8.7}:\text{Cr}_{3.7}:\text{Ru}_{0.8}:\text{V}_{4.3}$ (at.%). ....	214
Figure 6.21(a). SEM-BSE image of annealed Alloy 30H, average composition $\text{Pt}_{53.9}:\text{Al}_{18.0}:\text{Cr}_{4.3}:\text{Ru}_{1.4}:\text{V}_{21.9}:\text{Nb}_{1.0}$ (at.%), showing a medium $\sim\text{Pt}_2\text{V}$ with a light solid state precipitate, dark $\sim\text{PtV}$ , coarsened eutectoid of $\sim\text{PtV} + \sim\text{Pt}_2\text{V}$ . (b). SEM-BSE image of annealed Alloy 30H, average	

composition $\text{Pt}_{53.9}:\text{Al}_{18.0}:\text{Cr}_{4.3}:\text{Ru}_{1.4}:\text{V}_{21.9}:\text{Nb}_{1.0}$ (at.%), at a higher magnification, showing a medium $\sim\text{Pt}_2\text{V}$ with a light solid state precipitate, dark $\sim\text{PtV}$ , coarsened eutectoid of $\sim\text{PtV} + \sim\text{Pt}_2\text{V}$ .....	215
Figure 6.22. XRD pattern of annealed Alloy 30H, average composition $\text{Pt}_{53.9}:\text{Al}_{18.0}:\text{Cr}_{4.3}:\text{Ru}_{1.4}:\text{V}_{21.9}:\text{Nb}_{1.0}$ (at.%).....	216
Figure 6.23. SEM-BSE image of annealed Alloy 31H, average composition $\text{Pt}_{74.1}:\text{Al}_{11.5}:\text{Cr}_{4.5}:\text{Ru}_{0.5}:\text{V}_{9.3}:\text{Nb}_{0.3}$ (at.%), showing single phase $\sim\text{Pt}_3\text{Al}$ with grains at different orientations. ....	217
Figure 6.24. XRD pattern of annealed Alloy 31H, average composition $\text{Pt}_{74.1}:\text{Al}_{11.5}:\text{Cr}_{4.5}:\text{Ru}_{0.5}:\text{V}_{9.3}:\text{Nb}_{0.3}$ (at.%).....	218
 Figure 7.2 Vickers hardness indentation on as-cast Alloy 1, average composition $\text{Pt}_{64.3}:\text{Al}_{26.6}:\text{V}_{9.1}$ (at.%). ....	220
Figure 7.1.Vickers hardness indentation on as-cast Alloy 2, average composition $\text{Pt}_{59.1}:\text{Al}_{23.1}:\text{V}_{17.8}$ (at.%). ....	220
Figure 7.3. Vickers hardness indentation on as-cast Alloy 3, average composition $\text{Pt}_{69.3}:\text{Al}_{9.6}:\text{V}_{21.1}$ (at.%) (a)one area (b) image from a different area .....	221
Figure 7.4. Vickers hardness indentation on as-cast Alloy 4B average composition $\text{Pt}_{69.8}:\text{Al}_{22.3}:\text{V}_{7.9}$ (at.%) (a) low magnification (b) higher magnification. ....	221
Figure 7.5. Vickers hardness indentation on as-cast Alloy 10, average composition $\text{Pt}_{83.9}:\text{Al}_6:\text{V}_{10.1}$ (at.%) (a) low magnification (b) higher magnification. ....	222
Figure 7.6. Vickers hardness indentation on as-cast Alloy 11, average composition $\text{Pt}_{80.9}:\text{Al}_{4.3}:\text{V}_{14.8}$ (at.%) (a) low magnification (b) higher magnification. ....	222
Figure 7.7. Vickers hardness indentation on as-cast Alloy 12, average composition $\text{Pt}_{52.5}:\text{Al}_{22.6}:\text{V}_{24.9}$ (at.%) (a) low magnification (b) higher magnification. ....	223
Figure 7.8. Vickers hardness indentation on as-cast Alloy 14, average composition $\text{Pt}_{84}:\text{Al}_2:\text{V}_4$ (at.%) (a) low magnification (b) higher magnification. ....	223
Figure 7.9. Vickers hardness indentation on as-cast Alloy 15, average composition $\text{Pt}_{72.4}:\text{Al}_{13.7}:\text{V}_{13.9}$ (at.%) with (a) low magnification (b) higher magnification showing minor cracks at three corners. ....	224
Figure 7.10. Vickers hardness indentation on as-cast Alloy 16, average composition $\text{Pt}_{56.9}:\text{Al}_{25.4}:\text{V}_{17.7}$ (at.%)with (a) low magnification (b) higher magnification showing minor cracks at three corners. ....	224
Figure 7.11. Hardness values ( $\text{HV}_{0.3}$ ) of as-cast Pt-Al-V alloys superposed on solidification projection (at.%).....	226
Figure 7.12. Vickers hardness indentation on annealed Alloy 1H, average composition $\text{Pt}_{64.3}:\text{Al}_{26.6}:\text{V}_{9.1}$ (at.%).....	228
Figure 7.13. Vickers hardness indentation on annealed Alloy 2H, average composition $\text{Pt}_{59.1}:\text{Al}_{23.1}:\text{V}_{17.8}$ (at.%).....	229
Figure 7.14. Vickers hardness indentation on annealed Alloy 3H, average composition $\text{Pt}_{69.3}:\text{Al}_{9.6}:\text{V}_{21.1}$ (at.%).....	229
Figure 7.15. Vickers hardness indentation on annealed Alloy 4BH, average composition $\text{Pt}_{69.8}:\text{Al}_{22.3}:\text{V}_{7.9}$ (at.%).....	230
Figure 7.16. Vickers hardness indentation on annealed Alloy 10H, average composition $\text{Pt}_{83.9}:\text{Al}_6:\text{V}_{10.1}$ (at.%).....	230

Figure 7.17. Vickers hardness indentation on annealed Alloy 11H, average composition Pt <sub>80.9</sub> :Al <sub>4.3</sub> : ....	231
Figure 7.18. Vickers hardness indentation on annealed Alloy 12H, average composition Pt <sub>52.5</sub> :Al <sub>22.6</sub> :V <sub>24.9</sub> (at.%).	231
Figure 7.19. Vickers hardness indentation on annealed Alloy 13H, average composition Pt <sub>53.7</sub> :Al <sub>8.8</sub> :V <sub>37.5</sub> (at.%).	231
Figure 7.20. Vickers hardness indentation on annealed Alloy 14H, average composition Pt <sub>81.6</sub> :Al <sub>14.5</sub> :V <sub>3.7</sub> (at.%).	232
Figure 7.21. Vickers hardness indentation on annealed Alloy 15H, average composition Pt <sub>72.4</sub> :Al <sub>13.7</sub> :V <sub>13.9</sub> (at.%).	232
Figure 7.22. Hardness values (HV <sub>0.3</sub> ) of annealed Pt-Al-V alloys superposed on isothermal section at 1000°C (at.%).	233
Figure 7.23. Vickers hardness indentation on as-cast Alloy 5, average composition Pt <sub>73.8</sub> :Cr <sub>16.9</sub> :V <sub>9.3</sub> (at.%), with (a) low magnification (b) a higher magnification showing two minor cracks at the corners. ....	235
Figure 7.24. Vickers hardness indentation on as-cast Alloy 6, average composition Pt <sub>72.3</sub> :Cr <sub>8.3</sub> :V <sub>19.4</sub> (at.%), with (a) low magnification (b) a higher magnification. ....	235
Figure 7.25. Vickers hardness indentation on as-cast Alloy 7, average composition Pt <sub>33.4</sub> :Cr <sub>45.8</sub> :V <sub>20.8</sub> (at.%), with (a) low magnification (b) a higher magnification. ....	236
Figure 7.26. Vickers hardness indentation on as-cast Alloy 8, average composition Pt <sub>53.0</sub> :Cr <sub>22.4</sub> :V <sub>24.5</sub> (at.%), with (a) one area (b) a different area .....	236
Figure 7.27. Vickers hardness indentation on as-cast Alloy 17, average composition Pt <sub>68.5</sub> :Cr <sub>16.2</sub> :V <sub>15.3</sub> (at.%), with (a) low magnification (b) a higher magnification. ....	237
Figure 7.28. Vickers hardness indentation on as-cast Alloy 18, average composition Pt <sub>32.8</sub> :Cr <sub>28.6</sub> :V <sub>38.6</sub> (at.%), with (a) low magnification (b) a higher magnification. ....	237
Figure 7.29. Vickers hardness indentation on as-cast Alloy 19, average composition Pt <sub>25.8</sub> :Cr <sub>42.9</sub> :V <sub>31.3</sub> (at.%), (a) low magnification (b) a higher magnification. ....	238
Figure 7.30. Vickers hardness indentation on as-cast Alloy 20, average composition Pt <sub>16.8</sub> :Cr <sub>13.4</sub> :V <sub>69.8</sub> (at.%), (a) one area (b) a different area .....	238
Figure 7.31. Vickers hardness indentation on as-cast Alloy 21, average composition Pt <sub>16.8</sub> :Cr <sub>13.4</sub> :V <sub>69.8</sub> (at.%), (a) low magnification (b) a higher magnification. ....	239
Figure 7.32. Vickers hardness indentation on as-cast Alloy 22, average composition Pt <sub>28.7</sub> :Cr <sub>27.2</sub> :V <sub>44.1</sub> (at.%), (a) low magnification (b) a higher magnification. ....	239
Figure 7.33. Vickers hardness indentation on as-cast Alloy 23, average composition Pt <sub>16.5</sub> :Cr <sub>56.1</sub> :V <sub>27.4</sub> (at.%), (a) low magnification (b) a higher magnification. ....	240
Figure 7.34. Vickers hardness indentation on as-cast Alloy 24, average composition Pt <sub>14.9</sub> :Cr <sub>73.7</sub> :V <sub>11.4</sub> (at.%), with (a) low magnification (b) a higher magnification. ....	240
Figure 7.35. Vickers hardness indentation on as-cast Alloy 25, average composition Pt <sub>34.1</sub> :Cr <sub>57.4</sub> :V <sub>8.5</sub> (at.%), (a) low magnification (b) a higher magnification. ....	241
Figure 7.36. Hardness values (HV <sub>0.3</sub> ) of as-cast Pt-Cr-V alloys superposed on the solidification projection (at.%).	243
Figure 7.37. Vickers hardness indentation on annealed Alloy 5H, average composition Pt <sub>73.8</sub> :Cr <sub>16.9</sub> :V <sub>9.3</sub> (at.%), (a) low magnification with the indentation showing pin cushioning, (b) a higher magnification with the indentation showing that the diamond indenter is damaged. ....	246

Figure 7.38. Vickers hardness indentation on annealed Alloy 6H, average composition $\text{Pt}_{72.3}:\text{Cr}_{8.3}:\text{V}_{19.4}$ (at.%), (a) low magnification with the indentation showing pin cushioning, (b) at a higher magnification with the indentation showing that the diamond indenter is damaged. ....	246
Figure 7.39. Vickers hardness indentation on annealed Alloy 7H, average composition $\text{Pt}_{33.4}:\text{Cr}_{45.8}:\text{V}_{20.8}$ (at.%), (a) low magnification (b) a higher magnification. ....	247
Figure 7.40. Vickers hardness indentation on annealed Alloy 8H, average composition $\text{Pt}_{53.0}:\text{Cr}_{22.4}:\text{V}_{24.5}$ (at.%), (a) low magnification (b) a higher magnification. ....	247
Figure 7.41. Vickers hardness indentation on annealed Alloy 17H, average composition $\text{Pt}_{68.5}:\text{Cr}_{16.2}:\text{V}_{15.3}$ (at.%), (a) low magnification (b) a higher magnification. ....	248
Figure 7.42. Vickers hardness indentation on annealed Alloy 18H, average composition $\text{Pt}_{32.8}:\text{Cr}_{28.6}:\text{V}_{38.6}$ (at.%) with (a) low magnification and (b) higher magnification. ....	248
Figure 7.43. Vickers hardness indentation on annealed Alloy 20H, average composition $\text{Pt}_{38.8}:\text{Cr}_{14.2}:\text{V}_{47.0}$ (at.%) with (a) low magnification and (b) higher magnification. ....	249
Figure 7.44. Vickers hardness indentation on annealed Alloy 23H, average composition $\text{Pt}_{16.5}:\text{Cr}_{56.1}:\text{V}_{27.4}$ (at.%) with (a) low magnification and (b) higher magnification. ....	249
Figure 7.45. Vickers hardness indentation on annealed Alloy 24H, average composition $\text{Pt}_{14.9}:\text{Cr}_{73.7}:\text{V}_{11.4}$ (at.%) with (a) low magnification and (b) higher magnification. ....	250
Figure 7.46. Vickers hardness indentation on annealed Alloy 25H, average composition $\text{Pt}_{34.1}:\text{Cr}_{57.4}:\text{V}_{8.5}$ (at.%) with (a) low magnification and (b) higher magnification. ....	250
Figure 7.47. Hardness values (HV0.3) of annealed Pt-Cr-V alloys superposed on isothermal section at 1000°C (at.%). ....	251
Figure 7.48. Vickers hardness indentation on as-cast Alloy 26, average composition $\text{Pt}_{63.9}:\text{Al}_{12.2}:\text{Cr}_{4.3}:\text{Ru}_{0.7}:\text{V}_{18.9}$ (at.%) with (a) low magnification and (b) higher magnification. ....	253
Figure 7.49. Vickers hardness indentation on as-cast Alloy 27, average composition $\text{Pt}_{69.5}:\text{Al}_{11.5}:\text{Cr}_{4.2}:\text{Ru}_{0.6}:\text{V}_{14.2}$ (at.%) with (a) low magnification and (b) higher magnification with indentation showing pin-cushioning. ....	253
Figure 7.50. Vickers hardness indentation on as-cast Alloy 28, average composition $\text{Pt}_{75.2}:\text{Al}_{11.2}:\text{Cr}_{4.0}:\text{Ru}_{0.6}:\text{V}_{9.5}$ (at.%) with (a) low magnification and (b) higher magnification. ....	254
Figure 7.51. Vickers hardness indentation on as-cast Alloy 29, average composition $\text{Pt}_{78.7}:\text{Al}_{12.2}:\text{Cr}_{3.8}:\text{Ru}_{0.6}:\text{V}_{5.2}$ (at.%) with (a) low magnification and (b) higher magnification. ....	254
Figure 7.52. Vickers hardness indentation on as-cast Alloy 30, average composition $\text{Pt}_{63.2}:\text{Al}_{12.9}:\text{Cr}_{4.0}:\text{Ru}_{0.7}:\text{V}_{19.0}:\text{Nb}_{0.6}$ (at.%) with (a) low magnification and (b) higher magnification with the indentation showing pin-cushioning. ....	255
Figure 7.53. Vickers hardness indentation on as-cast Alloy 31, average composition $\text{Pt}_{71.7}:\text{Al}_{12.8}:\text{Cr}_{4.9}:\text{Ru}_{1.1}:\text{V}_{9.9}:\text{Nb}_{0.3}$ (at.%) with (a) low magnification and (b) higher magnification. ....	255
Figure 7.54. Vickers hardness indentation on Alloy 26H, average composition $\text{Pt}_{63.9}:\text{Al}_{12.2}:\text{Cr}_{4.3}:\text{Ru}_{0.7}:\text{V}_{18.9}$ (at.%) with (a) low magnification and (b) higher magnification with pin-cushioning. ....	258
Figure 7.55. Vickers hardness indentation on annealed Alloy 27H, average composition $\text{Pt}_{69.5}:\text{Al}_{11.5}:\text{Cr}_{4.2}:\text{Ru}_{0.6}:\text{V}_{14.2}$ (at.%) with (a) low magnification and (b) higher magnification. ....	258
Figure 7.56. Vickers hardness indentation on annealed Alloy 28H, average composition $\text{Pt}_{75.2}:\text{Al}_{11.2}:\text{Cr}_{4.0}:\text{Ru}_{0.6}:\text{V}_{9.5}$ (at.%) with (a) low magnification and (b) higher magnification. ....	259
Figure 7.57. Vickers hardness indentation on annealed Alloy 30H, average composition $\text{Pt}_{63.2}:\text{Al}_{12.9}:\text{Cr}_{4.0}:\text{Ru}_{0.7}:\text{V}_{19.0}:\text{Nb}_{0.6}$ (at.%) with (a) lower magnification and (b) higher magnification. ....	259



Figure 7.58. Vickers hardness indentation on annealed Alloy 31H, average composition Pt <sub>71.7</sub> :Al <sub>12.8</sub> :Cr <sub>4.9</sub> :Ru <sub>1.1</sub> :V <sub>9.9</sub> :Nb <sub>0.3</sub> (at.%) with (a) low magnification and (b) higher magnification. ....	260
Figure 7.59. Hardness values (HV <sub>0.3</sub> ) plotted against vanadium content (at.%) for as-cast and annealed higher order alloys. ....	261

## List of Tables

Table 2.1. Al-Pt crystal structure data [1990Mas].....	10
Table 2.2. Reactions on cooling in the Pt-Al system [1990Mas].....	13
Table 2.3. Reactions on cooling in the Pt-V system, experimental, after [1989Smi].....	16
Table 2.4. Reactions on cooling in the Pt-V system, calculated [2008Wan].....	16
Table 2.5. Crystallographic data for Pt-V intermediate phases [1973Wat1].....	17
Table 2.6. Special points of the assessed Al-V phase diagram [1989Mur].....	19
Table 2.7. Reported invariant reactions for Al-rich alloys [1989Mur].....	21
Table 2.8. Al-V crystal structure data [1989Mur].....	23
Table 2.9. Al-V Lattice Parameter Data [1989Mur].....	24
Table 2.10. Crystal structure data of Cr-Pt.....	28
Table 2.11. Invariant Equilibria of Cr-Pt [1990Mas].....	31
Table 2.12. Reactions in the assessed Nb-Pt Diagram [1995Tri].....	36
Table 2.13. Crystallographic data for Nb-Pt system [1995Tri].....	37
Table 2.14. Lattice parameters of intermediate phases and terminal solid solutions in Nb-Pt system – after [1985Wat].....	38
Table 2.15. Summary of results before Jorda [1980Jor] for the Nb-Al system – after [1980Jor].42	
Table 2.16. Equilibria reactions in the Nb-Al system [1980Jor].....	43
Table 2.17. Eutectic temperatures and compositions in the Cr-Nb system [1986Van].....	48
Table 2.18. Crystal structure data for phases in Cr-Nb system [1986Van].....	49
Table 2.19. The six selected alloys with hardness values and precipitate volume percent.....	51
Table 4.1. Overall and phase compositions of Alloy 1, average composition $Pt_{64.3}:Al_{26.6}:V_{9.1}$ (at.%) determined by EDX. ....	61
Table 4.2. Overall and phase compositions of Alloy 2, average composition $Pt_{59.1}:Al_{23.1}:V_{17.8}$ (at.%) determined by EDX. ....	64
Table 4.3. Overall and phase compositions of Alloy 3, average composition $Pt_{69.3}:Al_{9.6}:V_{21.1}$ (at.%) as determined by EDX. ....	67
Table 4.4. Compositions of Alloy 4A, average composition $Pt_{76.2}Al_{17.4}V_{6.4}$ (at.%) determined by EDX... 69	
Table 4.5. EDX composition analysis data of Alloy 4B, average composition $Pt_{69.8}:Al_{22.3}:V_{7.9}$ (at.%) ....	72
Table 4.6. Compositions of as-cast Alloy 10, average composition $Pt_{83.9}:Al_6:V_{10.1}$ (at.%) as determined by EDX. ....	75
Table 4.7. Compositions of as-cast Alloy 11, average composition $Pt_{80.9}:Al_{4.3}:V_{14.8}$ (at.%), determined by EDX. ....	77
Table 4.8. EDX composition analysis data of as-cast Alloy 12, average composition $Pt_{52.5}:Al_{22.6}:V_{24.9}$ (at.%).....	80
Table 4.9. Compositions of as-cast Alloy 13, average composition $Pt_{53.7}:Al_{8.8}:V_{37.5}$ (at.%) as determined by EDX. ....	83
Table 4.10. Compositions of as-cast Alloy 14, average composition $Pt_{84}:Al_{12}:V_4$ (at.%) determined by EDX. ....	85
Table 4.11. EDX composition analysis data for as-cast Alloy 15, average composition $Pt_{72.4}:Al_{13.7}:V_{13.9}$ (at.%).....	88

Table 4.12. EDX composition analysis data for as-cast alloy 16, average composition Pt <sub>56.9</sub> :Al <sub>25.4</sub> :V <sub>17.7</sub> (at.%).....	91
Table 4.13. Invariant reactions on the Pt-Al-V liquidus surface at the Pt-rich corner.....	97
Table 4.14. Overall and phase compositions of annealed Alloy 1H, average composition Pt <sub>64.7</sub> :Al <sub>26.2</sub> :V <sub>9.1</sub> (at.%) as determined by EDX.....	99
Table 4.15. Overall and phase compositions of annealed Alloy 2H, average composition Pt <sub>61.8</sub> :Al <sub>21.1</sub> :V <sub>17.1</sub> (at.%) as determined by EDX.....	101
Table 4.16. Overall and phase compositions of annealed Alloy 3H, average composition Pt <sub>63.7</sub> :Al <sub>10.8</sub> :V <sub>25.5</sub> (at.%) determined by EDX.....	104
Table 4.17. Overall and phase compositions of annealed Alloy 4BH, average composition Pt <sub>69.7</sub> :Al <sub>23.2</sub> :V <sub>7.1</sub> (at.%) as determined by EDX.....	106
Table 4.18. Overall and phase compositions of annealed Alloy 10H, average overall composition Pt <sub>83.9</sub> :Al <sub>5.8</sub> :V <sub>10.3</sub> (at.%) as determined by EDX.....	109
Table 4.19. Overall and phase compositions of annealed Alloy 11H, average composition Pt <sub>85.2</sub> :Al <sub>3.4</sub> :V <sub>11.4</sub> (at.%), determined by EDX.....	111
Table 4.20. Overall and phase compositions of Alloy 12H, average composition Pt <sub>60.5</sub> :Al <sub>18.6</sub> :V <sub>20.9</sub> (at.%), determined by EDX.....	113
Table 4.21. Overall and phase compositions of Alloy 13H, average composition Pt <sub>59.2</sub> :Al <sub>8.4</sub> :V <sub>32.4</sub> (at.%), determined by EDX.....	115
Table 4.22. Overall and phase compositions of Alloy 14H, average composition Pt <sub>81.6</sub> :Al <sub>14.5</sub> :V <sub>3.7</sub> (at.%), determined by EDX.....	118
Table 4.23. EDX composition analysis for annealed Alloy 15H, average composition Pt <sub>72.3</sub> :Al <sub>13.5</sub> :V <sub>14.2</sub> (at.%).....	120
Table 4.24. EDX composition analysis data for annealed Alloy 16H, average composition Pt <sub>51.0</sub> :Al <sub>31.1</sub> :V <sub>17.9</sub> (at.%).....	122
Table 4.25. Position (2 Theta) and corresponding <i>d</i> spacing of the $\tau_1$ peaks in the XRD pattern of Alloys 12 and 13.....	127.
Table 4.26. Solidification and cooling reactions of the Pt-Al-V alloys.....	127
Table 5.1. Compositions of Alloy 5, average composition Pt <sub>73.8</sub> :Cr <sub>16.9</sub> :V <sub>9.3</sub> (at.%) as determined by EDX. ....	129
Table 5.2. EDX composition analysis of Alloy 6, average overall composition Pt <sub>72.3</sub> :Cr <sub>8.3</sub> :V <sub>19.4</sub> (at.%)..	131
Table 5.3. EDX composition analysis of Alloy 7, average composition Pt <sub>33.4</sub> :Cr <sub>45.8</sub> :V <sub>20.8</sub> (at.%).....	134
Table 5.4. EDX composition analysis of Alloy 8, average composition Pt <sub>53.0</sub> :Cr <sub>22.4</sub> :V <sub>24.5</sub> (at.%).....	137
Table 5.5. EDX composition analysis of Alloy 17, average composition Pt <sub>68.5</sub> :Cr <sub>16.2</sub> :V <sub>15.3</sub> (at.%).....	139
Table 5.6. EDX composition analysis of Alloy 18, average composition Pt <sub>32.8</sub> :Cr <sub>28.6</sub> :V <sub>38.6</sub> (at.%).....	142
Table 5.7. EDX composition analysis of Alloy 19, average composition Pt <sub>25.8</sub> :Cr <sub>42.9</sub> :V <sub>31.3</sub> (at.%).....	145
Table 5.8. EDX composition analysis of Alloy 20, average composition Pt <sub>38.8</sub> :Cr <sub>14.2</sub> :V <sub>47.0</sub> (at.%).....	147
Table 5.9. EDX composition analysis of Alloy 21, average composition Pt <sub>16.8</sub> :Cr <sub>13.4</sub> :V <sub>69.8</sub> (at.%).....	150
Table 5.10. EDX composition analysis of Alloy 22, average composition Pt <sub>28.7</sub> :Cr <sub>27.2</sub> :V <sub>44.1</sub> (at.%).....	152

Table 5.11. EDX composition analysis of Alloy 23, average composition $\text{Pt}_{16.5}:\text{Cr}_{56.1}:\text{V}_{27.4}$ (at.%). .....	155
Table 5.12. EDX composition analysis of Alloy 24, average overall composition $\text{Pt}_{14.9}:\text{Cr}_{73.7}:\text{V}_{11.4}$ (at.%). .....	157
Table 5.13. EDX composition analysis of Alloy 25, average composition $\text{Pt}_{34.1}:\text{Cr}_{57.4}:\text{V}_{8.5}$ (at.%). .....	160
Table 5.14. EDX composition analysis data for annealed Alloy 5H, average composition $\text{Pt}_{76.2}:\text{Cr}_{16.1}:\text{V}_{7.7}$ (at.%). .....	164
Table 5.15. EDX composition analysis data for annealed Alloy 6H, average composition $\text{Pt}_{77.3}:\text{Cr}_{6.6}:\text{V}_{16.1}$ (at.%). .....	166
Table 5.16. EDX composition analysis for annealed Alloy 7H, average composition $\text{Pt}_{35.7}:\text{Cr}_{45.1}:\text{V}_{19.2}$ (at.%). .....	169
Table 5.17. EDX composition analysis data for annealed Alloy 8H, average composition $\text{Pt}_{52.3}:\text{Cr}_{23.4}:\text{V}_{24.3}$ (at.%). .....	171
Table 5.18. EDX composition analysis data for annealed Alloy 17H, average composition $\text{Pt}_{70.2}:\text{Cr}_{15.4}:\text{V}_{14.4}$ (at.%). .....	173
Table 5.19. EDX composition analysis data for annealed Alloy 18H, average composition $\text{Pt}_{34.0}:\text{Cr}_{28.3}:\text{V}_{37.7}$ (at.%). .....	175
Table 5.20. EDX composition analysis data for Alloy 19H, average composition $\text{Pt}_{25.1}:\text{Cr}_{43.5}:\text{V}_{31.5}$ (at.%). .....	177
Table 5.21. EDX composition analysis data for annealed Alloy 20H, average composition $\text{Pt}_{37.2}:\text{Cr}_{14.6}:\text{V}_{48.2}$ (at.%). .....	179
Table 5. 22. EDX composition analysis data for annealed Alloy 21H, average composition $\text{Pt}_{16.5}:\text{Cr}_{13.2}:\text{V}_{70.3}$ (at.%). .....	181
Table 5.23. EDX composition analysis data of annealed Alloy 22H, average composition $\text{Pt}_{27.1}:\text{Cr}_{26.8}:\text{V}_{46.1}$ (at.%). .....	183
Table 5.24. EDX composition analysis data for annealed Alloy 23H, average composition $\text{Pt}_{14.5}:\text{Cr}_{58.1}:\text{V}_{27.4}$ (at.%). .....	185
Table 5.25. EDX composition analysis data for annealed Alloy 24H, average composition $\text{Pt}_{14.2}:\text{Cr}_{75.8}:\text{V}_{10.0}$ (at.%). .....	187
Table 5.26. EDX composition analysis data for Alloy 25H, average composition $\text{Pt}_{33.6}:\text{Cr}_{57.7}:\text{V}_{8.7}$ (at.%). .....	189
Table 5.27. Positions (2 Theta) of the ternary phase, $\tau$ , in the XRD pattern.....	192
Table 5.28. Solidification and cooling reactions of the Pt-Cr-V alloys.....	191
Table 6.1. EDX composition analysis data for as-cast Alloy 26, average composition $\text{Pt}_{63.9}:\text{Al}_{12.2}:\text{Cr}_{4.3}:\text{Ru}_{0.7}:\text{V}_{18.9}$ (at.%). .....	196
Table 6.2. EDX composition analysis data for as-cast Alloy 27, average composition $\text{Pt}_{69.5}:\text{Al}_{11.5}:\text{Cr}_{4.2}:\text{Ru}_{0.6}:\text{V}_{14.2}$ (at.%). .....	197
Table 6.3. EDX composition analysis data for as-cast Alloy 28, average composition $\text{Pt}_{75.2}:\text{Al}_{11.2}:\text{Cr}_{4.0}:\text{Ru}_{0.6}:\text{V}_{9.5}$ (at.%). .....	199
Table 6.4. EDX composition analysis data for as-cast Alloy 29, average composition $\text{Pt}_{78.7}:\text{Al}_{12.2}:\text{Cr}_{3.8}:\text{Ru}_{0.6}:\text{V}_{5.2}$ (at.%). .....	201
Table 6.5. EDX composition analysis data for as-cast Alloy 30, average composition $\text{Pt}_{63.2}:\text{Al}_{12.9}:\text{Cr}_{4.0}:\text{Ru}_{0.7}:\text{V}_{19.0}:\text{Nb}_{0.6}$ (at.%). .....	203
Table 6.6. EDX composition analysis data for as-cast Alloy 31, average composition $\text{Pt}_{71.7}:\text{Al}_{12.8}:\text{Cr}_{4.9}:\text{Ru}_{1.1}:\text{V}_{9.9}:\text{Nb}_{0.3}$ (at.%). .....	205

Table 6.7. EDX composition analysis data for annealed Alloy 26H, average composition Pt <sub>61.7</sub> :Al <sub>13.9</sub> :Cr <sub>4.1</sub> :Ru <sub>0.6</sub> :V <sub>19.6</sub> (at.%). .....	207
Table 6.8. EDX composition analysis data for Alloy 27H, average composition Pt <sub>69.8</sub> :Al <sub>11.4</sub> :Cr <sub>4.4</sub> :Ru <sub>0.5</sub> :V <sub>14.1</sub> (at.%). .....	209
Table 6.9. EDX composition analysis data for Alloy 28H, average composition Pt <sub>83.0</sub> :Al <sub>10.1</sub> :Cr <sub>3.7</sub> :Ru <sub>0.8</sub> :V <sub>9.0</sub> (at.%). .....	211
Table 6.10. EDX composition analysis data for Alloy 29H, average composition Pt <sub>83.0</sub> :Al <sub>8.7</sub> :Cr <sub>3.7</sub> :Ru <sub>0.8</sub> :V <sub>4.3</sub> (at.%). .....	213
Table 6.11. EDX composition analysis data for annealed Alloy 30H, average composition Pt <sub>53.9</sub> :Al <sub>18.0</sub> :Cr <sub>4.3</sub> :Ru <sub>1.4</sub> :V <sub>21.9</sub> :Nb <sub>1.0</sub> (at.%). .....	215
Table 6.12. EDX composition annealed analysis for Alloy 31H, average composition Pt <sub>74.1</sub> :Al <sub>11.5</sub> :Cr <sub>4.5</sub> :Ru <sub>0.5</sub> :V <sub>9.3</sub> :Nb <sub>0.3</sub> (at.%). .....	217
 Table 7.1. Hardness values (HV <sub>0.3</sub> ) of annealed Pt-Al-V alloys compared to as-cast alloys. ....	225
Table 7.2. Hardness values (HV <sub>0.3</sub> ) of annealed Pt-Cr-V alloys compared to as-cast alloys. ....	242
Table 7.3. Hardness values (HV <sub>0.3</sub> ) of annealed higher order alloys compared to as-cast alloys. ....	256

## CHAPTER 1: INTRODUCTION AND BACKGROUND

Nickel-based superalloys (NBSAs) have been successfully used in turbine components since the late 1940s. Approximately 70% of the weight in a modern jet turbine comprises NBSAs, and their success is due to their high yield stress and excellent resistance to environmental attack at high temperatures [1987Sim]. The high yield stresses are possible because the microstructure is composed of fine, coherent, ordered precipitates in a compatible matrix. The precipitates are coherent with the matrix since they have very similar structure, so that the misfit between the lattice parameters of the matrix and the precipitate is very low. The precipitates are ordered (specific atom types, e.g. Ni or Al, prefer specific sites), whereas the matrix is random or disordered (the atoms have no site preference). In NBSAs, the precipitates have the  $L1_2$  structure: they are in an ordered fcc structure and thus very closely related to the fcc matrix phases [1987Sim].

Alloy deformation is made more difficult because dislocations are slowed, since they must move through many precipitates to pass through the component as stress is applied. The coherent nature of the precipitates means that the particles are very stable, even at high temperatures, because there is very low surface energy per unit area of precipitate/matrix interface. The surface energy is always low, even for the high surface areas of fine precipitates, and there is very little driving force for particle coarsening. This is very advantageous because the precipitates remain fine and the high strength of the alloys are retained. If the precipitates did coarsen, the dislocations would move through the material more easily and the yield stresses would be much lower. These microstructures also give very good creep properties as reported by Völkl *et al.* [2003Völ]. Additionally, Sims *et al.* state that  $Ni_3Al$  has good intrinsic strength at high temperatures and this increases with increasing temperature [1987Sim].

Although the NBSAs have excellent properties, they are hindered by their maximum application temperature, which is limited by the melting point of the nickel solid-solution matrix. Currently, the maximum temperature at which NBSAs operate is  $\sim 1100^\circ\text{C}$ , which is approximately  $\sim 90\%$  of their melting temperature [1987Sim]. If the operating temperatures could be increased, there are a number of advantages. Higher temperatures improve the efficiency of the turbine engines,

and this enables greater thrust, improved fuel efficiency and reduced pollution. Although thermal-barrier coatings can be used to increase the application temperature, the component is still restricted by the melting point of the substrate, for safety reasons the maximum attainable temperatures are still limited [1998Gow].

There is increasing interest in using a different alloy system with a much higher melting point. Intermetallic compounds have been considered because of their high-temperature strengths but the inherent room temperature brittleness of these materials remains problematic [1996Wol]. Ceramic materials had also been considered at one time, but their low environmental resistance and limited toughness prevents their widespread use [1987Sim]. One solution would be to base the new materials on alloys with high melting points and use the naturally occurring precipitates of that system. This should also help keep the processing cost to a minimum. Thus, the systems developed would be similar in structure to the NBSAs with a matrix and a fine dispersion of small, preferably coherent, and stable precipitates. Face-centred cubic structures (like nickel) are advantageous because, being close-packed, they are more creep resistant. Refractory metals (niobium, molybdenum and tungsten) have been considered because of their high melting points (2477°C, 2623°C and 3422°C respectively), but their more open body-centred cubic structures are more susceptible to creep. Additionally, they are prone to rapid oxidation, even at relatively low temperatures [1994Bri]. Platinum-group metals (platinum, iridium and rhodium) were targeted because they have high melting points, good environmental resistance and a mostly fcc structure [1996Yam, 2000Wol].

The first work undertaken on platinum-group metals (PGM)-based superalloys was on Rh- and Ir- based alloys [1996Yam]. The rationale was that these elements not only have the fcc structure, which could permit a similar microstructure to the NBSAs, but also have higher melting points than the NBSAs: 1964°C and 2466°C for Rh and Ir, respectively. Additionally, the alloys based on Rh and Ir have superior environmental resistance [1998Gu]. Workers at the National Institute for Materials (NIMS) in Japan have achieved promising results for both Ir- and Rh-based alloys [1997Yam1, 1997Yam2, 1997Yam3 and 1998Yam]. However, it was later realised that these alloys have a major drawback in their brittleness [2005Vol]. Since then, researchers at NIMS, Japan, have continued work on Ir- and Rh-based superalloys but with additions of Pt and Ni replacing some Ir and Rh to improve toughness and reduce

density[2000Yu, 2003Hua]. Although the use of Pt-based alloys as a replacement for Ni-based superalloys is limited due to their higher price and higher density, it is possible that they could be used for critical components, or as corrosion resistant coatings [2009Süs].

### **Specific Objectives of the Study**

- A study of the two ternary systems, Pt-Al-V and Pt-Cr-V through microstructural characterisation, phase identification and microhardness testing and using some of the data obtained to plot and derive solidification projection, isothermal section at 1000°C and liquidus surface projection.
- Microstructural characterisation of the higher order alloys, phase identification and microhardness testing, which is an attempt to improve on the properties of some identified optimum quaternary alloys. Literature survey has established that certain quaternary alloys had microstructure and properties approaching NBSAs and there is a need to improve on these properties.



## CHAPTER 2: LITERATURE REVIEW

It is generally accepted that the  $L_{12}$  structure of the  $\gamma'$  phase is a prerequisite for the success of the Ni-based superalloys. Due to close crystallographic relationship, precipitates with ordered face centered cubic (fcc),  $L_{12}$ , can have coherent interfaces with the surrounding fcc matrix. Coherent  $\gamma/\gamma'$  interfaces with small lattice misfit lead to low interfacial energies, thus inhibiting fast coarsening of  $\gamma'$  [1987Sim].

The success of the Ni-based superalloys leads one to seek succeeding generations of high-temperature alloys that make use of the precepts of a high-volume fraction of finely dispersed, coherent precipitates within a ductile matrix. Analogous  $\gamma/\gamma'$  systems with higher melting points, based on  $L_{12}$  precipitates (ordered fcc) in an fcc matrix (the matrix usually has the higher melting point) are however limited in number. Some of the platinum group metals are almost unique among the high-melting-point metals in that they have fcc structures. Moreover, they have excellent environmental resistance that enables them to be considered for high temperature use [1998Yam]. Systems based on iridium, rhodium and platinum have attracted attention that has led to the suggestion that they form a class of alloys to be named ‘refractory superalloys’ [1997Yam3].

Alloys based on Pt-Al turned out to have the highest potential, not only because of possible precipitation strengthening through  $Pt_3Al$ , but also due to high oxidation and corrosion resistance. The resistance to oxidation and corrosion is attributed to the formation of a protective Al oxide scale [2001Hil1]. At least 11 at.% Al is needed to form a thin protective oxide coating at high temperatures [2001Süs1].

Pt is similar to Ni in crystal structure (fcc) and chemistry. The important differences are the higher melting point (1768.3°C for Pt compared to 1455°C for Ni) and much better corrosion resistance [2002Süs]. Thus, similar phases to  $L_{12}$   $Ni_3Al$  could be used to give mechanisms similar to those found in the Ni-based superalloys. Although platinum-based alloys are unlikely to replace all Ni-based superalloys on account of both higher price and density, it is likely that they could be used for the highest application temperature components [2002Süs].

However, phase diagrams of the Pt-Al system reported by Mishima, Oya and Suzuki

[1986Mis, 1987Oya] show that the  $L1_2$  phase, which co-exists with (Pt) at high temperatures, transforms to tetragonal  $\sim\text{Pt}_3\text{Al}$  at lower temperatures of 340°C and 127°C. The phase diagram assessed by Massalski [1990Mas] and which was largely based on the work of McAlister and Kahan [1986McA] shows the transformation taking place at 1290°C. This transformation has been reported as being martensitic [1986Mis]. The formation of a coherent two-phase structure between a cubic and a tetragonal phase is likely to be more difficult than between two cubic phases. In addition, repeated transformation during temperature cycles would certainly degrade the thermo-mechanical fatigue resistance. Therefore, the transformation of  $\text{Pt}_3\text{Al}$  at the Pt-rich side of stoichiometry to the tetragonal low temperature allotrope should be avoided [2005Vol].

Douglas *et al.* [2007Dou] investigated the microstructure and crystal structure of the tetragonally distorted  $\text{Pt}_3\text{Al}$  precipitates in a binary Pt-Al alloy of nominal composition 86 at.% Pt and 14 at.% Al. They observed a two-phase microstructure consisting of  $\text{Pt}_3\text{Al}$  precipitates in a (Pt) solid solution. The precipitates consisted of a number of stacked plates with thickness 200-400 nm. This kind of microstructure is similar to that observed for precipitates in other materials where an fcc-to-tetragonal distortion has taken place, such as  $\text{Ni}_3\text{V}$  as described by Tanner [1968Tan] and  $\text{D}_{023}\text{Al}_{11}\text{Ti}_5$  investigated by Tian *et al.* [2002Tia]. Douglas *et al.* [2007Dou] found the stacked plates to be twin related with specific orientation relationship with the matrix and concluded that this could be justified by misfit considerations. The stacked plates in the  $\text{Pt}_3\text{Al}$  precipitates exhibited sets of narrow parallel lines, or platelets, perpendicular to the [001] directions in the stacked plates.

Under the auspices of the Platinum Development Initiative in South Africa, platinum-based superalloys have been investigated and developed for high temperature and special applications requiring good corrosion and oxidation resistance. Ternary alloys based on the Pt-Al system, where the ternary additions comprised chromium, iridium, molybdenum, nickel, rhenium, ruthenium, tantalum, titanium and tungsten were tested. As well as phase characterisation work, mechanical and oxidation tests were undertaken. The best systems were found to be Pt-Al-Cr and Pt-Al-Ru [2009Cor]. The microstructures were similar to nickel-based superalloys, and comprised  $\sim\text{Pt}_3\text{Al}$  precipitates in a Pt-based matrix. However, the volume fraction of  $\sim\text{Pt}_3\text{Al}$  was only  $\sim 40\%$  instead of the  $\sim 70\text{-}80\%$  found in the Ni-based superalloys [1987Sim].

Chromium was found to stabilise the cubic form of the  $\sim\text{Pt}_3\text{Al}$  phase, whereas ruthenium acted as a solid solution strengthener [2007Süs, 2009Mul, 2009Cor]. In order to exploit the additional benefits from the two ternary additions (Cr and Ru), quaternary alloys were made comprising both. A number of these quaternary alloys have been investigated extensively. They exhibited a two-phase  $\gamma/\gamma'$  structures analogous to the Ni-based superalloys [2002Cor].

In an investigation of some Pt-Al-Cr-Ru alloys, it was found that both Ru and Cr partition preferentially to the (Pt). The solubility ranges of Ru and Cr were found to be 0.5 to 0.7 at.% Ru and 1.3 to 1.8 at.% Cr in the precipitates, while for (Pt) phase it was between 1.2 to 2.4 at.% Ru and 2.7 to 4.6 at.% Cr [2008Sho]. This may explain the limited stabilising effect of Cr on the cubic  $\sim\text{Pt}_3\text{Al}$  precipitate, as well as the relatively low volume fraction ( $\sim 30\%$  or less) at room temperature. This has led to the thinking that a quinary addition to an optimum quaternary alloy from the Pt-Al-Cr-Ru system may improve the melting temperature, stability and volume fraction of  $\sim\text{Pt}_3\text{Al}$ . This will improve mechanical properties, such as hardness and strength, at high temperatures, while maintaining the oxidation and corrosion resistance in these aggressive environments.

Huang *et al.* [2004Hua] investigated the structure of the  $\sim\text{Pt}_3\text{Al}$  phase in the quaternary Pt-Al-Ir-Nb and ternary Pt-Al-Nb alloys. The specific alloys in this study were 69.4 at.% Pt, 19.3 at.% Al, 8.2 at.% Ir, 3.1 at.% Nb and 86 at.% Pt, 10 at.% Al, 4 at.% Nb. The stabilisation of the  $\text{L}_{12}$   $\sim\text{Pt}_3\text{Al}$  structure at room temperature was attributed to Nb. It has been reported [1986Mis] that the phase transformation from  $\text{L}_{12}$  to  $\text{D0}'_c$  of  $\text{Pt}_3\text{Al}$  in a Pt-Al system should basically be the one from fcc to fct, where a platinum atom is systematically displaced from its original position with a movement of less than one interatomic spacing. This indicated that the transformation is martensitic in nature [2004Hua]. According to the binary phase diagram of Pt-Al, the cubic  $\text{L}_{12}$   $\sim\text{Pt}_3\text{Al}$  phase with 70-73 at.% Pt can be stable down to room temperature [1986McA]. This suggested that in the  $\text{Pt}_3\text{Al}$  stoichiometric composition, when all Al atoms fully occupied all their corner positions in the  $\text{L}_{12}$   $\sim\text{Pt}_3\text{Al}$  crystal, the fcc structure could not convert to fct because the Al atoms around the Pt atoms limit the movement of Pt atoms [2005Vol]. It seems conceivable that in the hypo-stoichiometric composition, when a third element with high solubility in  $\text{L}_{12}$   $\sim\text{Pt}_3\text{Al}$  fills the empty sites of Al, this could have the same effect as Al on limitation of the movement of Pt atoms. The work by Hill *et al.* [2002Hil] provides support for this. The  $\text{L}_{12}$

$\sim\text{Pt}_3\text{Al}$  phase composition results of ternary alloys Pt-Al-X (X = Ti, Cr, Ta), where the atomic percent of (Al+X) was 22.4, 22.7 and 23.1 for samples  $\text{Pt}_{86}:\text{Al}_{10}:\text{Ti}_4$ ,  $\text{Pt}_{86}:\text{Al}_{10}:\text{Cr}_4$  and  $\text{Pt}_{86}:\text{Al}_{10}:\text{Ta}_4$  respectively was close to the stoichiometric composition of  $\text{Pt}_3\text{Al}$ . This indicated that the high solubility of a third element substituting for Al in the  $\text{Pt}_3\text{Al}$  may be the main factor in stabilisation of the  $\text{L}_{12}$ .

The solubility of Nb in the  $\text{L}_{12} \sim\text{Pt}_3\text{Al}$  phase could not be obtained directly in the ternary alloy  $\text{Pt}_{86}:\text{Al}_{10}:\text{Nb}_4$  because of the small sizes of the phases [2004Hua]. However, a comparison of Nb and Ta indicated that Nb and Ta have the same atomic radius as Al and a similar electronic structure. They are in the same group in the periodic table of elements. These similarities would cause them to have similar solubility characteristics. The solubility of Ta in the  $\text{L}_{12} \sim\text{Pt}_3\text{Al}$  phase was reported to be high (5 at.%); accordingly, a high solubility is expected for Nb in  $\text{L}_{12} \sim\text{Pt}_3\text{Al}$  phase [2004Hua]. Another reason for targeting Nb is because it has the potential to increase the melting temperature of the alloy for additions up to  $\sim 10$  at.%. Niobium has been added to Ni-based superalloys to improve creep strength of components in jet gas turbines [2000Car, 2008Had]. Alloying with Nb, which is a slow diffusing element, retards the coarsening rate of the  $\gamma'$  phase [2004Hua].

There are no reported data on the Pt-Al-V system. However, the reasons given above justifying the addition of Nb may also apply to V since it is in the same group in the periodic table. The Pt-V phase diagram [1990Mas] shows high solubility of V in the (Pt) phase, being  $\sim 20$  at.% V at  $700^\circ\text{C}$  and rising to  $\sim 57$  at.% at  $1720^\circ\text{C}$ . Thus, V may also act as a solid solution strengthener. In another investigation, addition of Nb, Ta and Ti to Pt-based alloys resulted in elevated strengths at high temperatures through precipitation-hardening [2008Wen]. The polycrystalline Pt-based alloys containing 5 at.% Nb or Ta were stronger than the single-crystal Ni-based superalloy CMSX-4 in (001) orientation above  $1200^\circ\text{C}$  [2008Wen]. Vanadium is near Nb, Ta and Ti in the periodic table and is smaller in size compared to Nb and Ta. Therefore, V may act as a precipitation hardener in addition to solid solution strengthening.

The binary phase diagrams of Nb-Pt and Pt-V have the melting point of (Pt) increasing with increasing additions of Nb and V respectively [1990Mas]. This could counteract the effect of the Al-Pt eutectic with the decreasing (Pt) melting point.

Several workers have been attempting to build Pt-based alloys databases. Some have calculated the phase diagrams using Calphad and others from first principles. Watson *et al.* [2006Wat] undertook a preliminary assessment of the Cr-Pt-Ru system using a combination of Pandat and MTDATA software. In their review, Cornish *et al.* [2007Cor] reported on the work being undertaken at Mintek, the University of Leeds and the University of Bayreuth to build up a thermodynamic database for Pt-Al-Cr-Ru system. At the University of Bayreuth, Preussner *et al.* [2008Pre] used thermodynamic calculations based on first principles to deal with the problem of sparse data.

## **2.1 Pt-Al-V and Pt-Cr-V Ternary Systems**

In the development of alloys, especially new alloys, knowledge of the phases and their proportions are required. This is because the phases define the properties, and for multi-phase alloys, the properties are also affected by the proportion and distribution of those phases. A survey of literature has established that while some phase diagram work has been done on the ternary systems Pt-Al-Nb by Ndlovu [2006Ndl, 2010Sam] and Pt-Cr-Nb by Mulaudzi [2009Mul], nothing had been published on the ternary systems Pt-Al-V and Pt-Cr-V.

A clear understanding of the binary systems which constitute the ternary systems is important. These are Pt-Al, Pt-V and Al-V in the case of the ternary system Pt-Al-V and Pt-Cr, Pt-V and Cr-V in the case of Pt-Cr-V ternary system.

### **2.1.1 Pt-Al binary phase diagram**

The Pt-Al phase diagram is complex and the Pt-rich end has been problematic. McAlister and Kahan reviewed the Pt-Al system in 1986 [1986McA] for the Bulletin of Alloy Phase Diagrams and Massalski assessed the same system for ASM International in 1990 [1990Mas]. The assessed phase diagram (Fig. 2.1) was based on the work of Huch [1964Huc], Darling [1970Dar], Chattopadhyay [1975Cha, 1976Cha], Bhan [1978Bha] and Piatti [1980Pia]. Table 2.1 gives crystal data while Table 2.2 summarises the reactions that occur on cooling in the Pt-Al system [1990Mas].

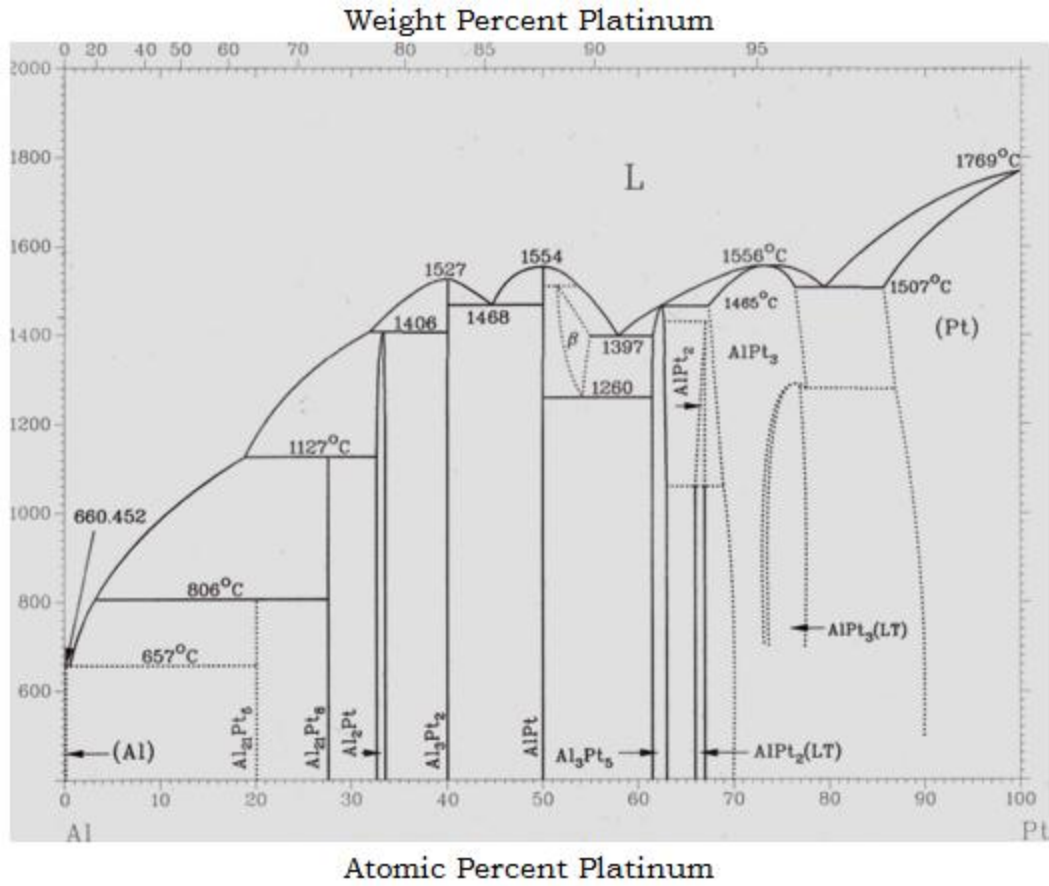


Figure 2.1. Binary Al-Pt equilibrium phase diagram [1990Mas].

## The Solid Phases

Table 2.1. Al-Pt crystal structure data [1990Mas].

Phase	Composition (at.% Pt)	Pearson symbol	Space group	Struktur- Bericht Designation	Prototype
(Al)	0	<i>cF4</i>	<i>Fm<math>\bar{3}m</math></i>	A1	Cu
Pt <sub>5</sub> Al <sub>21</sub>	19.2	Cubic	-	-	-
Pt <sub>8</sub> Al <sub>21</sub>	27	<i>tI116</i>	<i>I<math>\bar{4}_1a</math></i>	-	-
PtAl <sub>2</sub>	31.5 - 33.5	<i>cF12</i>	<i>Fm<math>\bar{3}m</math></i>	C1	CaF <sub>2</sub>
Pt <sub>2</sub> Al <sub>3</sub>	40	<i>hP5</i>	<i>P<math>\bar{3}m\bar{1}</math></i>	-	-
PtAl	50	<i>cP8</i>	<i>P<math>\bar{2}_1\bar{3}</math></i>	B20	FeSi
$\beta$	~52 - ~56	<i>cP2</i>	<i>Pm<math>\bar{3}m</math></i>	B2	CsCl
Pt <sub>5</sub> Al <sub>3</sub>	~61.5 - 63	<i>oP16</i>	<i>Pbam</i>		Rh <sub>5</sub> Ge <sub>3</sub>
Pt <sub>2</sub> Al	~66 - ~67	<i>oP12</i>	<i>Pnma</i>	C23	PbCl <sub>2</sub>
Pt <sub>2</sub> Al(LT)	~66 - ~67	<i>oP24</i>	<i>Pmma</i>		Pt <sub>2</sub> Ga(LT)
Pt <sub>3</sub> Al	~67.3 - ~77.7	<i>cP4</i>	<i>Pm<math>\bar{3}m</math></i>	L1 <sub>2</sub>	AuCu <sub>3</sub>
Pt <sub>3</sub> Al(LT)	~73.5 - 100	<i>tP16</i>	<i>P<math>\bar{4}/mbm</math></i>	D0'c	Pt <sub>3</sub> Ga(LT)
(Pt)	~83.8 - 100	<i>cF4</i>	<i>Fm<math>\bar{3}m</math></i>	A1	Cu
<b>Metastable phases</b>					
$\alpha'$		<i>cF4</i>	<i>Fm<math>\bar{3}m</math></i>	A1	Cu
PtAl <sub>4</sub>	~20				
PtAl <sub>6</sub>	~14				
$\varepsilon'$					
$\lambda'$	10 - 25				

## Phase Equilibria

**Table 2.2. Reactions on cooling in the Pt-Al system [1990Mas].**

Reaction	Reaction phase compositions (at.% Pt)	Temperature (°C)	Reaction Type
$L \rightarrow (Pt) + Pt_3Al$	79.4 76.4 85.7	1507	Eutectic
$PtAl + L \rightarrow \beta$	50 53.7 51.5	1510	Peritectic
$L \rightarrow Pt_2Al_3 + PtAl$	44.7 40 50	1468	Eutectic
$L + Pt_3Al \rightarrow Pt_5Al_3$	62.3 67.3 62.5	1465	Peritectic
$Pt_3Al + Pt_5Al_3 \rightarrow Pt_2Al$	67.5 62.5 67	1430	Peritectoid
$L + Pt_2Al_3 \rightarrow Pt_2Al$	31.8 40 33.3	1406	Peritectic
$L \rightarrow \beta + Pt_5Al_3$	55.7 57.9 66.5	1397	Eutectic
$\beta \rightarrow PtAl + Pt_5Al_3$	54.2 50 61.5	1260	Eutectoid
$L + Pt_2Al \rightarrow Pt_8Al_{21}$	18.8 32.6 27.5	1127	Peritectic
$Pt_2Al \rightarrow Pt_2Al(LT)$	67	1060	?
$L + Pt_8Al_{21} \rightarrow Pt_5Al_{21}$	3.1 27.5 19.2	806	Peritectic
$L \rightarrow (Al) + Pt_5Al_{21}$	0.4 0.0 19.2	657	Eutectic
$L \rightarrow Pt$	100	1769	Melting
$L \rightarrow Pt_3Al, \gamma'$	73.2	1556	Congruent
$L \rightarrow PtAl$	50	1554	Congruent
$L \rightarrow Pt_2Al_3$	40	1527	Congruent
$L \rightarrow Al$	0	660.4	Melting
$Pt_3Al, \gamma' \rightarrow Pt_3Al, \gamma'_1$		340	Martensitic
$Pt_3Al, \gamma'_1 \rightarrow Pt_3Al, \gamma'_2$		127	Martensitic

Huch [1964Huc] reported platinum to be practically insoluble in (Al), and observed the eutectic reaction  $L \rightarrow (Al) + Pt_5Al_{21}$  at 627°C. McAlister [1986McA] placed the eutectic composition at 0.44 at.% Pt which is in agreement with unidirectional solidification experimental work by Piatti



[1980Pia].  $\text{Pt}_5\text{Al}_{21}$  forms by a peritectic reaction from  $\text{Pt}_8\text{Al}_{21}$  at  $806^\circ\text{C}$  and has a complex cubic stoichiometric structure with very limited solubility. Huch [1964Huc] reported cubic ‘ $\text{PtAl}_4$ ’ with  $\sim 20\text{at.}\%$  Pt and suggested that the phase might be  $\text{Pt}_5\text{Al}_{21}$ . Piatti [1980Pia] confirmed this composition range, but noted a transformation from hexagonal to cubic phase after treatment at  $200^\circ\text{C}$  for several hours. Guex [1976Gue] also reported a complex cubic phase of either  $\text{PtAl}_4$  or  $\text{Pt}_5\text{Al}_{21}$ . Schaller [1979Sch] reported, without experimental detail, a hexagonal  $\text{Pt}_5\text{Al}_{21}$ . Ellner [1982Ell] confirmed a hexagonal phase and called it  $\text{PtAl}_4$ . Careful analysis by McAlister [1986McA] of thermal arrest data by Huch and Klemm [1964Huc], in conjunction with a  $\text{Pt}_6\text{Al}_{21}$  phase reported at this composition, confirmed the phase as  $\text{Pt}_5\text{Al}_{21}$ .  $\text{PtAl}_4$  and  $\text{Pt}_6\text{Al}_{21}$  have been suggested as metastable phases in the Pt-Al system [1986McA].

The stoichiometric  $\text{Pt}_8\text{Al}_{21}$  phase at  $27.5\text{ at.}\%$  Pt, forming peritectically from  $\text{PtAl}_2$  was confirmed by Edshammar [1968Eds] and Ellner *et al.* [1983Ell] after earlier reports by Huch [1964Huc] and Guex [1976Gue] of a  $\text{PtAl}_3$ -like structure. The structure of  $\text{Pt}_8\text{Al}_{21}$  has not been fully determined.

Huch [1964Huc], Guex [1976Gue] and Ellner [1982Ell] reported the  $\text{PtAl}_2$  phase, which forms peritectically at  $1406^\circ\text{C}$  from  $\text{Pt}_2\text{Al}_3$ . Guex reported the  $\text{PtAl}_2$  phase as a line compound, while Huch and Ellner reported a  $\sim 1\text{ at.}\%$  solubility range up to  $850^\circ\text{C}$ .

$\text{Pt}_2\text{Al}_3$  has a structure related to, but not isotypic with, hexagonal  $\text{Ni}_2\text{Al}_3$  and essentially no solubility range [1964Huc, 1976Gue, 1982Ell].  $\text{PtAl}$  is stoichiometric with a cubic  $\text{FeSi}$  structure and forms congruently at  $1554^\circ\text{C}$ .

Evidence of a  $\beta$  phase (B2 CsCl crystal structure) existing between  $1260 - 1500^\circ\text{C}$  with a solubility range from  $51$  to  $56\text{ at.}\%$  Pt was reported by Chattopadhyay [1975Cha] and Bhan [1978Bha]. McAlister and Kahan [1986McA] included these observations in their assessment and proposed a peritectic reaction:  $\text{L} + \text{PtAl} \rightarrow \beta$  with a eutectoid decomposition:  $\beta \leftrightarrow \text{PtAl} + \text{Pt}_5\text{Al}_3$  to correspond with a thermal arrest reported by Huch [1964Huc]. In their study of the Pt-Al-Ru ternary system, Prins *et al.* found evidence of the existence of the  $\beta$  phase [2005Pri].

Fig. 2.1 shows  $\text{Pt}_5\text{Al}_3$  as having a solubility range 61.5 – 63 at.% Pt as reported by Ellner [1982Ell] and Oya [1987Oya], although it was originally reported as a line compound by Huch [1964Huc] and Guex [1976Gue].

$\text{Pt}_2\text{Al}$  has been reported as having two crystal variants. Although the low temperature form has not been observed by all researchers, Tshawe *et al.* [2011Tsh] observed laths in the low temperature  $\text{Pt}_2\text{Al}$  after annealing at 1000°C. The presence of laths indicated that a martensitic transformation occurs above 1000°C and this agrees with the generally accepted transformation temperature of 1060°C.

$\text{Pt}_3\text{Al}$  forms congruently at 1556°C and eutectically with (Pt) at 1507°C. A martensitic transformation has been reported where ordered fcc  $\text{L}_{12}$  transforms to tetragonal  $\text{D0}'\text{c}$  during cooling [1986Mis]. Although this transformation has been previously reported as a congruent transformation at 1290°C or a eutectoid reaction at 1280°C, Biggs [2001Big] observed two low temperature martensitic transformations at ~130°C and ~320°C. Biggs' observation coincides with the  $\gamma' \rightarrow \gamma'_1 \rightarrow \gamma'_2$  transformations (Fig. 2.2) reported by Oya [1986Mis, 1987Oya]. Douglas *et al.* [2007Dou, 2009Dou] studied a binary Pt-Al alloy in an attempt to resolve the two different versions of the phase diagram. A modified  $\text{D0}'\text{c}$  tetragonal version of one of the lower temperature forms of  $\sim\text{Pt}_3\text{Al}$  was identified. The transformation producing the  $\text{D0}'\text{c}$  structure was confirmed as displacive, since there were distinct bands in the precipitates, which were identified as twins at higher magnifications [2009Dou]. Similar work at the University of Bayreuth, Germany [2011Cor2], determined that the transformation took place at a high temperature of ~1290°C as reported in [1990Mas]. The Pt used in the four different investigations were from different sources and the lower temperature transformations could have resulted from an impurity effect [2011Cor1].

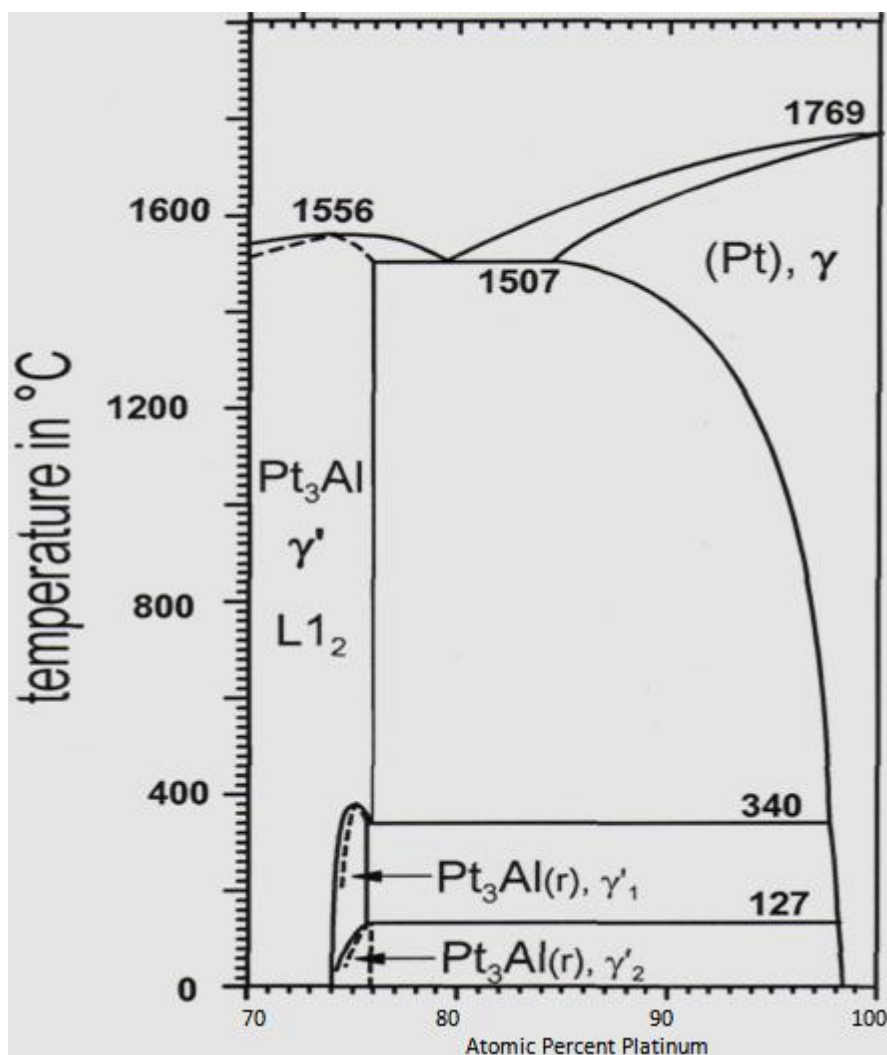


**Figure 2.2. Pt-rich portion of the Pt-Al phase diagram according to Oya, Mishima and Suzuki [1986Mis, 1987Oya].**

(Pt) dissolves ~14 at.% Al at 1510°C [1964Huc, 1970Dar]. Darling [1970Dar] suggested decreasing solubility of Al in (Pt) as temperature decreases and confirmed a ~10 at.% Al content at 1200°C by Bronger [1962Bro], and 10 and 5 at% Al at 1000°C and 300°C, respectively, by Schubert [1978Sch].

### 2.1.2 The binary Pt-V phase diagram

Vanadium is bcc, while platinum is fcc. Pt is soluble in (V) up to a maximum 12 at.% Pt at ~1800°C, while vanadium is soluble in (Pt) up to ~20.5 at.% V at 700°C and the solubility increases with temperature (Fig. 2.3). There are four stable intermetallic compounds:  $PtV_3$ ,  $PtV$ ,  $Pt_2V$ , and  $Pt_3V$  with finite homogeneity ranges [2008Wan]. Three of these,  $PtV$ ,  $Pt_2V$ , and  $Pt_3V$

form at lower temperatures from (Pt) in the solid state. The phase diagram was mainly investigated by Waterstrat [1973Wat1] using metallography, X-ray diffraction and electron microprobe. There is a congruent transformation from liquid to solid at  $\sim 1805^\circ\text{C}$  with an extremum at  $\sim 27$  at.% V. A congruent transformation implies no change in composition during the transformation.

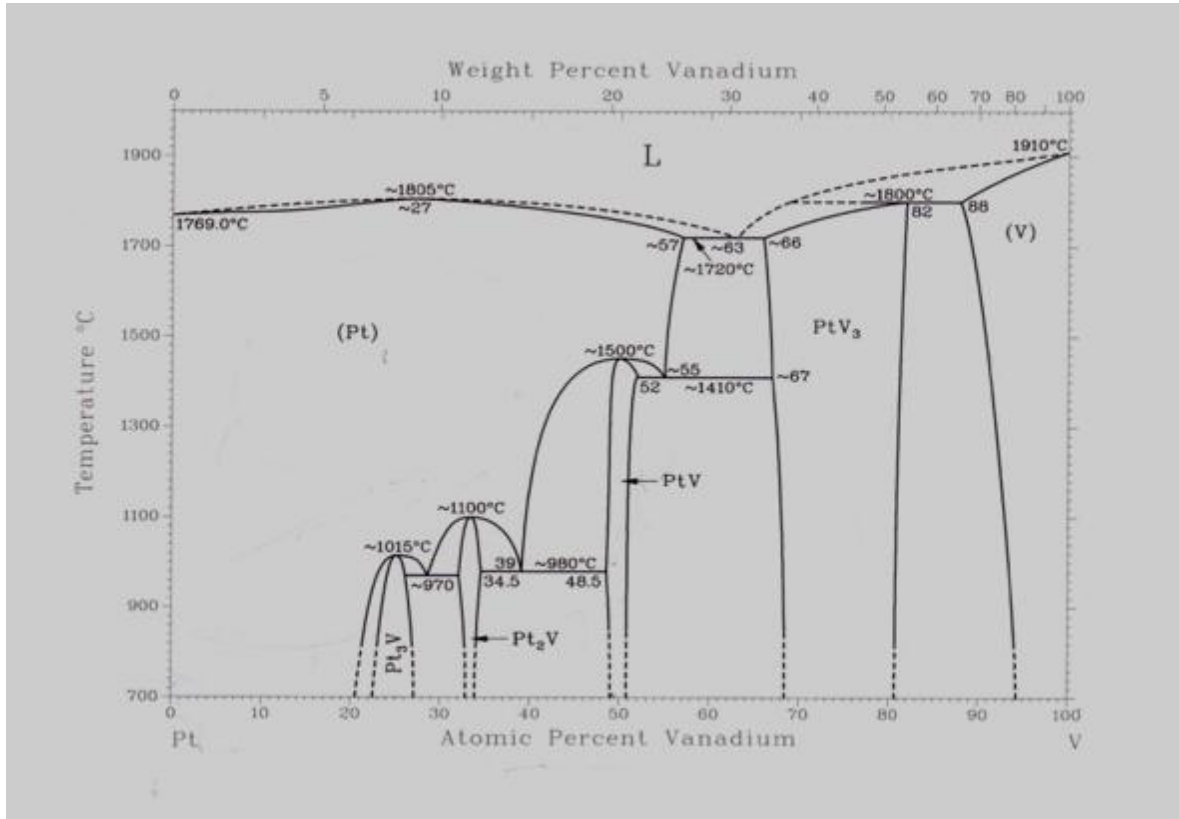


**Figure 2.3. Assessed binary Pt-V equilibrium phase diagram, [1990Mas].**

Schryvers and Amelinckx [1986Sch] reported that there is a phase, Pt<sub>8</sub>V, which was found to be ordered below  $810^\circ\text{C}$ . Later Smith [1989Smi] reviewed the phase diagram of Pt-V and the Pt<sub>8</sub>V was not included, because it was uncertain whether it was an equilibrium phase or not. Nxumalo and Lang [2006Nxu] reported that the stable Pt<sub>8</sub>V-ordered phase exists below  $810^\circ\text{C}$ , but the ordering kinetics was very sluggish, requiring an excess vacancy concentration for nucleation of the ordered phase. Wang *et al.* [2008Wan] left out Pt<sub>8</sub>V in their work, because its phase stability was not known. They compared their calculated results with experimental data of Smith [1989Smi] and found them in agreement (Tables 2.3 & 2.4). The crystallographic data for the intermediate phases are given in Table 2.5.

**Table 2.3. Reactions on cooling in the Pt-V system, experimental, after [1989Smi].**

Reaction	Reaction Type	Composition, at.% Pt	Temperature, °C
$L \leftrightarrow (Pt)$	Fusion	100 100	1769
$L \leftrightarrow (Pt)$	Congruent	~73 ~73	1805±10
$(Pt) \leftrightarrow Pt_3V$	Congruent	75 75	1015±5
$(Pt) \leftrightarrow Pt_3V + Pt_2V$	Eutectoid	~71.5 ~74 ~68	970±10
$(Pt) \leftrightarrow Pt_2V$	Congruent	66.7 66.7	1100±5
$(Pt) \leftrightarrow Pt_2V + PtV$	Eutectoid	~61 ~65.5 ~51.5	980±10
$(Pt) \leftrightarrow PtV$	Congruent	50 50	1500±10
$(Pt) \leftrightarrow PtV + PtV_3$	Eutectoid	~45 ~48 ~33	~1410
$L \leftrightarrow (Pt) + PtV_3$	Eutectic	~37 ~43 ~34	1720±10
$L + (V) \leftrightarrow PtV_3$	Peritectic	~31? ~12 ~18	1800±10
$L \leftrightarrow (V)$	Fusion	0 0	1910

**Table 2.4. Reactions on cooling in the Pt-V system, calculated [2008Wan].**

Reaction	Reaction Type	Composition, at.% Pt	Temperature, °C
$L \leftrightarrow (Pt)$	Fusion	100 100	1769
$L \leftrightarrow (Pt)$	Congruent	73.8 73.8	1804
$(Pt) \leftrightarrow Pt_3V$	Congruent	75 75	1012
$(Pt) \leftrightarrow Pt_3V + Pt_2V$	Eutectoid	72.7 74.5 68.2	972
$(Pt) \leftrightarrow Pt_2V$	Congruent	67.3 67.3	1100
$(Pt) \leftrightarrow Pt_2V + PtV$	Eutectoid	61 66.5 50	978
$(Pt) \leftrightarrow PtV$	Congruent	49.4 49.4	1501
$(Pt) \leftrightarrow PtV + PtV_3$	Eutectoid	44.1 48.1 32.5	1416
$L \leftrightarrow (Pt) + PtV_3$	Eutectic	39.7 43.5 32.7	1720
$L + (V) \leftrightarrow PtV_3$	Peritectic	21.4 10.6 19.4	1803
$L \leftrightarrow (V)$	Fusion	0 0	1910

**Table 2.5. Crystallographic data for Pt-V intermediate phases [1973Wat1].**

<b>Intermediate phase</b>	<b>Crystal system</b>	<b>Space group</b>	<b>Structure type</b>	<b>No. of atoms per unit cell</b>	<b>Composition limits, at.% V, Temp.</b>
$\beta\text{PtV}_3$	Cubic	$Pm\bar{3}n$	A15, $\text{Cr}_3\text{Si}$	8	68 – 81, 1300°C
$\xi\text{PtV}$	Orthorhombic	$Pmma$	B19, AuCd	4	48.5 – 51.5, 1300°C
$\delta\text{Pt}_2\text{V}$	Orthorhombic	$Immm$	MoPt <sub>2</sub>	6	32.5 – 34.0, 900°C
$\theta\text{Pt}_3\text{V}$	Tetragonal	$I\bar{4}/mmm$	$D0_{22}$ , TiAl <sub>3</sub>	8	23 – 27, 900°C
$\gamma'\text{Pt}_3\text{V}^*$	Cubic	$Pm\bar{3}m$	$L1_2$ , AuCu <sub>3</sub>	4	~22 – ~23, 900°C

\* The  $\gamma'$  phase is possibly metastable.

### 2.1.3 The binary Al-V phase diagram

The Al-V system has been studied by Bailey [1959 Bai] for invariant reactions, and by Wiley [1967Wil] and Eremenko [1981Ere] for the liquidus. The phase diagram assessed by Murray [1989Mur] is presented in Fig. 2.4. Reactions, compositions, and temperatures are summarised in Table 2.6. Aluminium is fcc while vanadium is bcc as had been stated earlier. On the V-rich side, high melting temperatures make the liquidus and solidus temperatures difficult to measure and also make equilibrium difficult to achieve in the solid state. On the Al-rich side, the melting reactions are of the peritectic type and therefore sluggish [1989Mur].

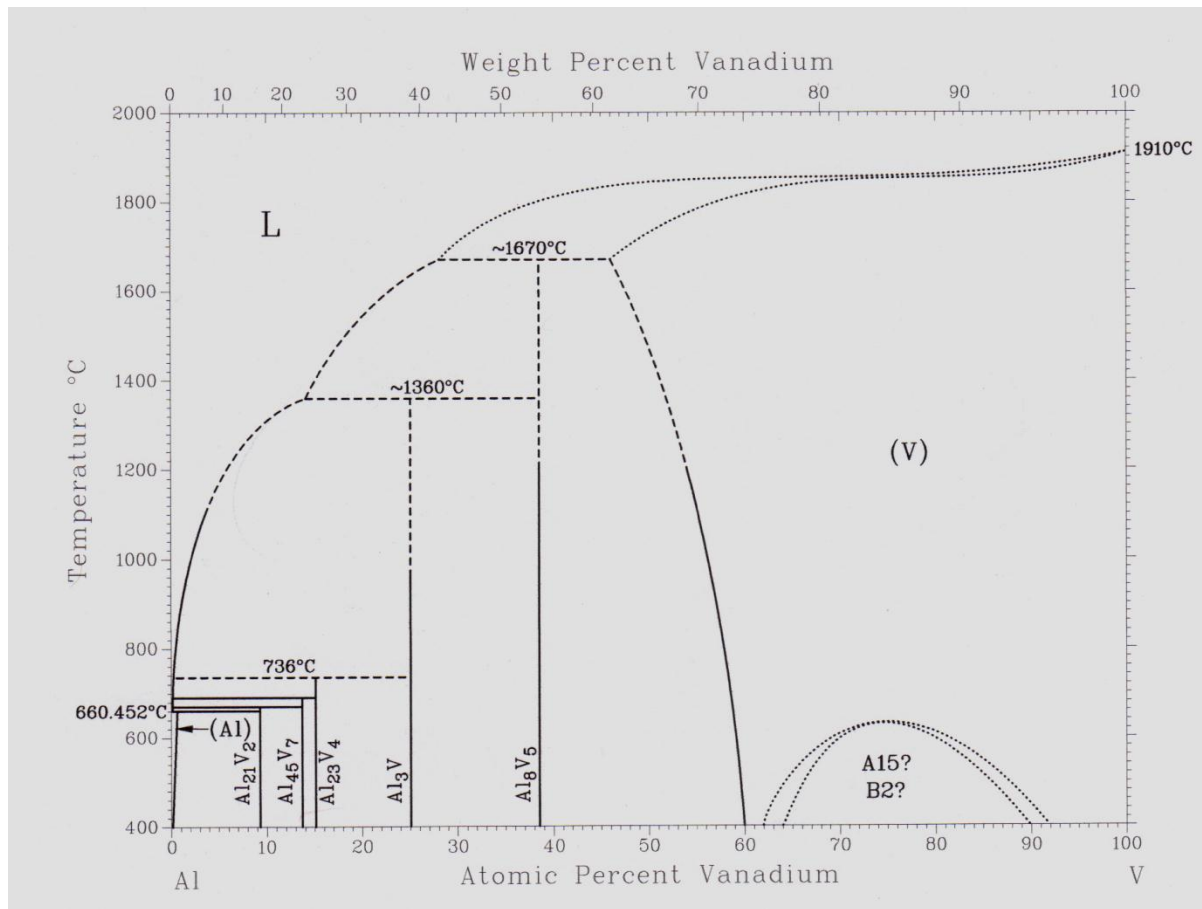


**Figure 2.4. Assessed binary Al-V equilibrium phase diagram by [1990Mas]**

Murray [1989Mur] described the solid equilibrium Al-V phases as follows:

- i) The fcc (Al) has a very narrow homogeneity range of 0 to 0.3 at.% V.
- ii) The bcc (V) has a wide homogeneity range of ~50 to 100 at.% V.
- iii) The Al-rich compounds – complex cubic  $V_2Al_{21}$  (also designated  $VAl_{11}$  or  $VAl_{10}$ ), monoclinic  $V_7Al_{45}$  (also designated  $VAl_7$ ), hexagonal  $V_4Al_{23}$  (also designated  $VAl_6$ ), and  $VAl_3$  with  $D0_{22}$  structure.
- iv)  $V_5Al_8$ , with cubic  $\gamma$  structure, which is thought to have some range of homogeneity at high temperature. This range, not being quantitatively known, is not indicated in Fig. 2.4.

- v) There is a low temperature phase forming congruently from (V). It is designated as either *A15* or *B2*. Its homogeneity range and transformation temperature has not been resolved.

**Table 2.6. Special points of the assessed Al-V phase diagram [1989Mur].**

Reaction	Composition, at.% V	Temperature, °C	Reaction type
$L \leftrightarrow (Al)$	0	660.452	Melting
$L + V_2Al_{21} \leftrightarrow (Al)$	0.09 8.7 0.3	662.1	Peritectic
$L + V_7Al_{45} \leftrightarrow V_2Al_{21}$	0.1 13.5 8.7	670	Peritectic
$L + V_4Al_{23} \leftrightarrow V_7Al_{45}$	0.13 14.8 13.5	688	Peritectic
$L + VAl_3 \leftrightarrow V_4Al_{23}$	0.22 25 14.8	736	Peritectic
$L + V_5Al_8 \leftrightarrow VAl_3$	14 38.5 25	~1360	Peritectic
$L + (V) \leftrightarrow V_5Al_8$	28 46 38.5	~1670	Peritectic
$L \leftrightarrow (V)$	100	1910	Melting

For the V-rich liquidus, melting points were determined by Rostoker and Yamamoto [1954Ros] and by Carlson *et al.* [1955Car] for alloys containing more than 5 at.% V. The melting point of pure V was reported by Carlson *et al.* [1955Car] as  $1845 \pm 10^\circ\text{C}$  (the assessed value is  $1910^\circ\text{C}$ ); therefore a somewhat larger uncertainty should be attributed to the V-rich alloys. Incongruent melting of  $V_5Al_8$  and  $VAl_3$  was reported at  $1670^\circ\text{C}$  and  $1360^\circ\text{C}$  respectively. By determination of incipient melting via optical pyrometry, Rostoker and Yamamoto [1954Ros] found the peritectic melting of  $VAl_3$  at about  $1370^\circ\text{C}$ , in good agreement with the Carlson value of  $1360^\circ\text{C}$  [1955Car].

### Al-Rich Alloys

The Al-rich alloys up to 3 at.% V have been investigated by Elliot [1955Ell], Gebhart and Joseph [1961Geb], Wiley [1967Wil] and Eremenko *et al.* [1981Ere]. Wiley, Eremenko *et al.* [1981Ere] and Elliot used chemical analysis of extracted equilibrated liquid, while Gebhart and Joseph used



thermal analysis on cooling. The results of Wiley [1967Wil], Eremenko *et al.* [1981Ere] and Elliot [1955Ell] are in reasonable agreement, with Eremenko's [1981Ere] being the lowest and Elliot's [1955Ell] the highest.

Four intermetallic compounds have been identified in Al-rich alloys :  $V_2Al_{21}$ ,  $V_7Al_{45}$ ,  $V_4Al_{23}$  and  $VA_3$ . Although there is reasonable agreement among temperatures of invariant reactions (Table 2.5), the interpretation of the reactions conflict. It is also possible that the reaction temperatures, being close together, could result in confusion, especially if reactions were missed, by intermediate reactions going to completion [1989Mur].

**Table 2.7. Reported invariant reactions for Al-rich alloys [1989Mur].**

Reaction	Reaction Temperature, °C	Reference
$L + VAl_3 \leftrightarrow V_2Al_{21}$	703	[1959Bai]
$L + Al_3V \leftrightarrow ?$	<1210	[1954Ros]
$L + VAl_3 \leftrightarrow V_4Al_{23}$	735	[1955Car]
$L + V_4Al_{23} \leftrightarrow V_2Al_{21}$	685	
$L + V_4Al_{23} \leftrightarrow V_2Al_{21}$	727	[1955Ell]
$L + VAl_3 \leftrightarrow V_4Al_{23}$	>850	
$L + VAl_3 \leftrightarrow V_4Al_{23}$	736	[1959Bai]
$L + V_4Al_{23} \leftrightarrow V_7Al_{45}$	688	
$L + V_7Al_{45} \leftrightarrow V_2Al_{21}$	670	
$L + VAl_3 \leftrightarrow V_4Al_{23}$	735	[1961Geb]
$L + V_4Al_{23} \leftrightarrow V_7Al_{45}$	689	
$L + V_7Al_{45} \leftrightarrow V_2Al_{21}$	680	

### V-Rich Alloys

Numerous attempts have been made to synthesise the  $A15$  compound,  $V_3Al$ , because of its potential as a superconducting material. Holleck *et al.* [1963Hol] reported  $A15$  structures made at 100°C in quartz tubes, with lattice parameters of 0.4812 nm and 0.4926 nm. Others [1955Car, 1964Ram, 1970Shi] reported that only the bcc phase was found in the V-rich alloys. Similar findings exist for samples annealed at 700°C and 1000°C as reported by Hatt *et al.* [1973Hat], but some evidence was reported for a martensitic transformation to an unknown pseudo-cubic structure after annealing at 1500°C [1973Hat]. Hexagonal  $\beta$   $V_3Al$ , with  $a = 0.7070$  nm and  $c = 0.9565$  nm, was reported to form under pressures greater than 30 kbar and above 1500°C and tetragonal  $\alpha$   $AlV_3$ , with  $a = 0.6167$  nm and  $c = 0.9481$  nm, appeared at lower temperatures and pressures [46]. No  $A15$  was found up to 70 kbar above 1000°C.

Hartsough and Hammond [1971Har] performed vacuum evaporation experiments using substrate temperatures of 350° to 450°C and found an A15 phase of lattice parameter 0.4829 nm. With increasing Al content, bcc + A15 and bcc phases were formed. The A15 phase decomposed at 700°C. This suggests that other attempts to synthesise V<sub>3</sub>Al were unsuccessful, because too high annealing temperatures were chosen.

It can be concluded tentatively that above 600°C and 700°C, the disordered bcc phase is stable in the binary system [1989Mur]. Small particles, undetected by XRD, of a second phase may form during quenching. The number of equilibrium phases is not definitely known, nor are the phase boundaries [1989Mur]. It was not known how or whether to include the hexagonal [1973Leg], tetragonal [1973Leg], and pseudo-cubic [1973Hat] structures at low pressures [1989Mur].

### **Metastable Phases**

The achievement of extended solubility of V in (Al) by rapid solidification has been reported [1969Var, 1968Mos, 1986Ino, 1987Kim] with the maximum value being 2 at.% V by splat quenching [1987Kim].

A quasi-crystalline icosahedral phase has been identified in a rapidly solidified alloys containing 13.9 at.% V [1987Kim] and 14.3 at.% V [1986Ino]. Kim and Froes [1987Kim] found the icosahedral phase as a minor constituent, with Al<sub>3</sub>V predominating, whereas Inoue *et al.* [1986Ino] reported higher volume fractions of the icosahedral phase, also together with Al<sub>3</sub>V. Inoue *et al.* [1986Ino] identified the composition of the icosahedral phase as approximately VAl<sub>4</sub> by EDX.

### **Crystal Structures and Lattice Parameters**

Crystal structures and lattice parameters are listed in Tables 2.7 and 2.8 respectively. The structures of Al<sub>21</sub>V<sub>2</sub>, Al<sub>23</sub>V<sub>4</sub> and Al<sub>45</sub>V<sub>7</sub> have an icosahedron as the basic structural unit [1977Bha]. The structure of Al<sub>21</sub>V<sub>2</sub> is the same as that of Al<sub>18</sub>Mg<sub>3</sub>Cr<sub>2</sub>. In the binary Al-V system, the structure occurs with vacancies on Al sites, hence the common designation Al<sub>10</sub>V. The structure of Al<sub>23</sub>V<sub>4</sub> is closely related to that of Al<sub>10</sub>Mn<sub>3</sub>, Al<sub>5</sub>Co<sub>2</sub>, Al<sub>9</sub>SiMn<sub>3</sub>, and Al<sub>10</sub>NiFe<sub>3</sub>.

**Table 2.8. Al-V crystal structure data [1989Mur].**

Phase	Composition, at.% V	Pearson symbol	Space group	Struktur- bericht designation	Prototype
(Al)	0 to 0.3	<i>cF4</i>	<i>Fm<math>\bar{3}m</math></i>	A1	Cu
V <sub>2</sub> Al <sub>21</sub>	~8.7 to 9.1	<i>cF176</i>	<i>Fd<math>\bar{3}m</math></i>		VAl <sub>10</sub>
V <sub>7</sub> Al <sub>45</sub>	~13.5	<i>mC104</i>	<i>C<math>\bar{2}</math>/m</i>		V <sub>7</sub> Al <sub>45</sub>
V <sub>4</sub> Al <sub>23</sub>	~14.8	<i>hP54</i>	<i>P<math>\bar{6}_3</math>/mmc</i>		V <sub>4</sub> Al <sub>23</sub>
VAl <sub>3</sub>	~25	<i>tI8</i>	<i>I<math>\bar{4}</math>/mmm</i>	<i>D0<sub>22</sub></i>	Ti Al <sub>3</sub>
V <sub>5</sub> Al <sub>8</sub>		<i>cI52</i>	<i>I<math>\bar{4}\bar{3}m</math></i>	<i>D8<sub>2</sub></i>	Cu <sub>5</sub> Zn <sub>8</sub>
(V)	~46 to 100	<i>cI2</i>	<i>Im<math>\bar{3}m</math></i>	A2	W
<b>Other possible phases</b>					
V <sub>3</sub> Al		<i>cP8</i>	<i>Pm<math>\bar{3}m</math></i>	A15	Cr <sub>3</sub> Si
β V <sub>3</sub> Al		<i>h**</i>			
α V <sub>3</sub> Al		<i>t**</i>			

**Table 2.9. Al-V Lattice Parameter Data [1989Mur].**

Phase	Composition, at.% V	Lattice parameters, nm		
		a	b	c
(Al)	0	0.40496		
V <sub>2</sub> Al <sub>21</sub>	9.1	1.4492		
V <sub>7</sub> Al <sub>45</sub>	13.5	2.54	0.759(a)	1.10
V <sub>4</sub> Al <sub>23</sub>	14.8	0.76928		1.7040
VAl <sub>3</sub>	25	0.3780		0.8321
V <sub>5</sub> Al <sub>8</sub>	39.5	0.92345		
(V)	100	0.30240		
<b>Other possible phases</b>				
V <sub>3</sub> Al	75			
βV <sub>3</sub> Al	75	0.7070		0.956
αV <sub>3</sub> Al	75	0.6167		0.9481

**2.1.4 Cr-Pt binary phase diagram**

The Cr-Pt phase diagram in Figure 2.5 was redrawn from that of Venkatraman and Neumann [1990Ven] and assessed by Massalski [1990Mas]. The phase diagram is based primarily on experimental work done by Müller [1930Mul] and Waterstrat [1973Wat2]. Oikawa *et al.* [2001Oik] produced a calculated diagram and Zhao *et al.* [2005Zha] proposed a refined version of the accepted diagram, based on thermal conductivity mapping. Another calculated version was presented by Preussner *et al.* [2008Pre]. Their modelled eutectic temperatures were in agreement with the results of Venkatraman and Neumann [1990Ven], within the stated experimental errors, rather than those of Oikawa *et al.* [2001Oik].

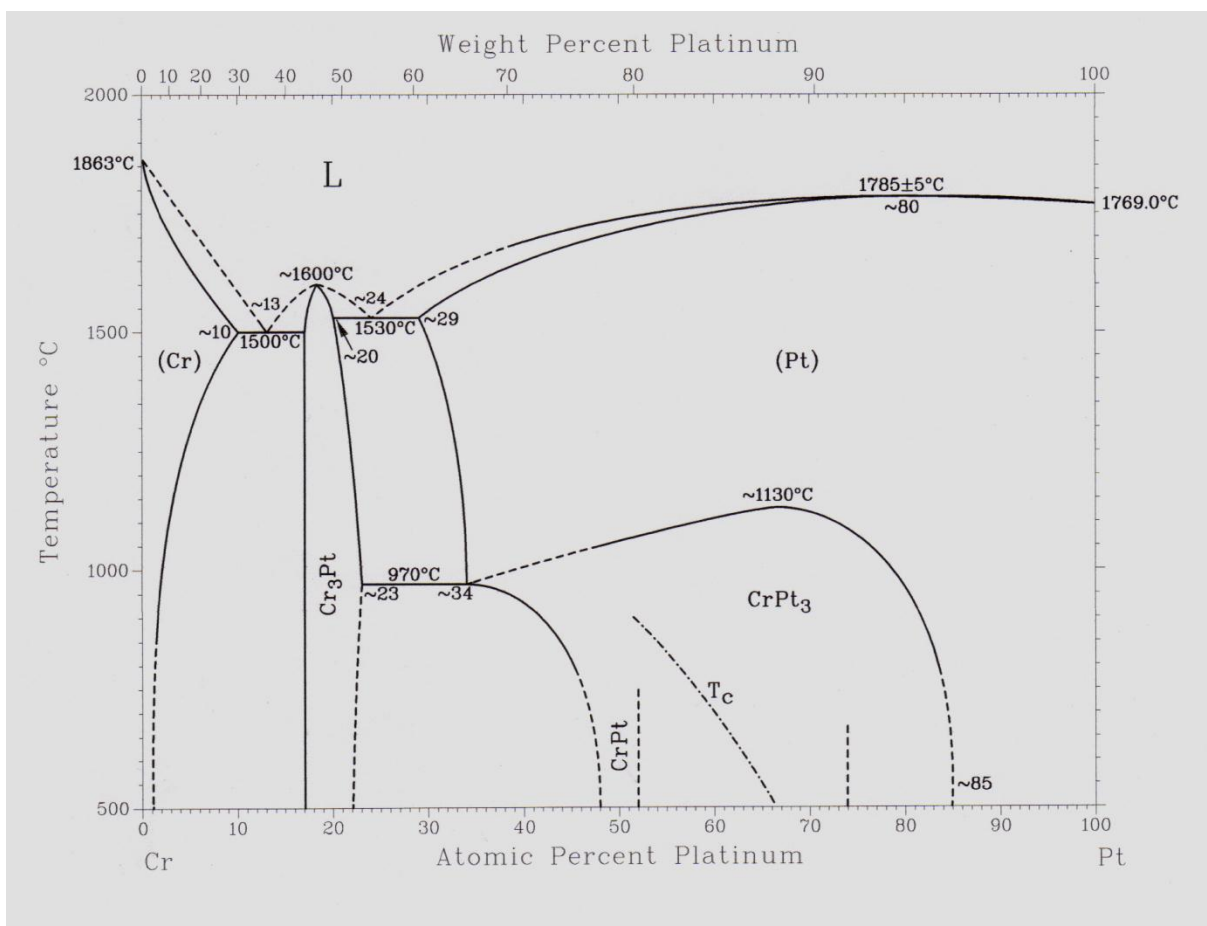


**Figure 2.5. Assessed binary Cr-Pt diagram by Murray, [1990Mas].**

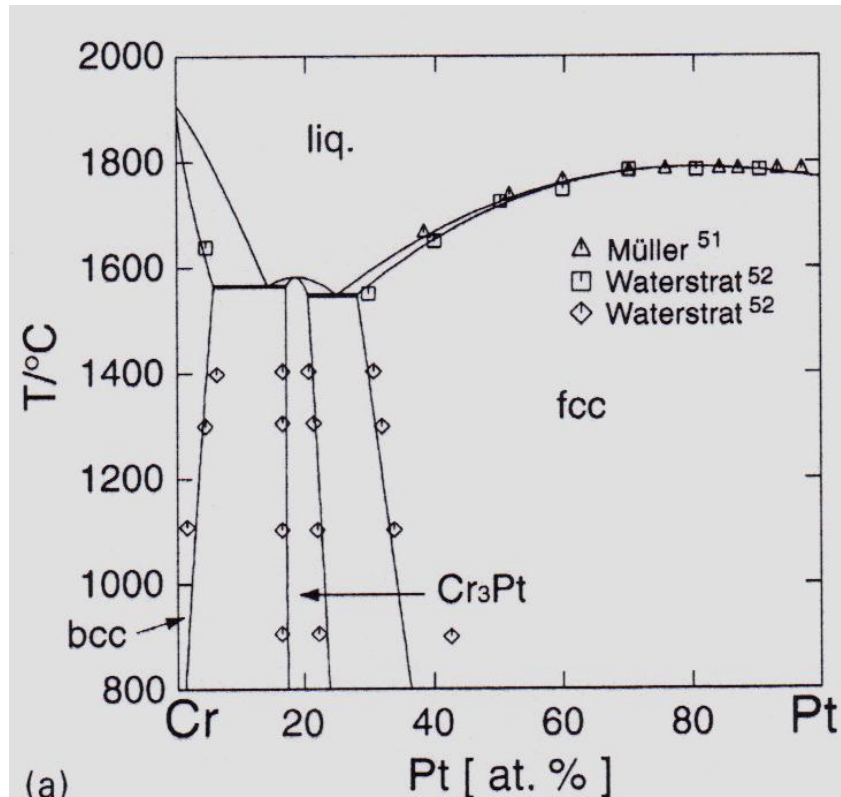


Figure 2.6. Calculated Cr-Pt phase diagram after Oikawa [2001Oik].

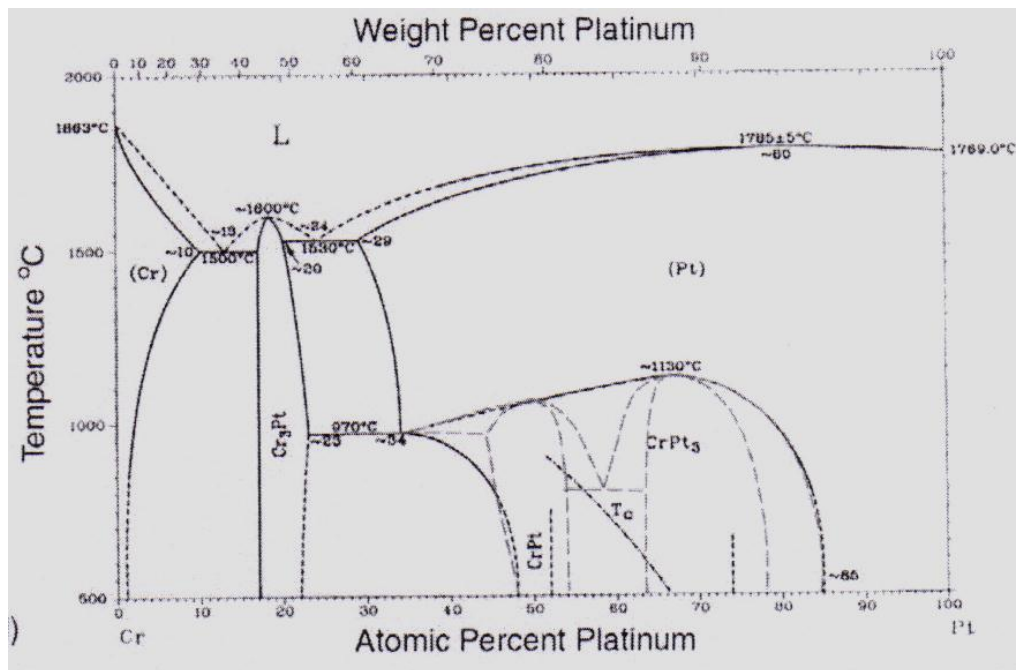


Figure 2.7. Proposed refinement (dotted lines) of the phase diagram showing the two ordered phases in separate phase regions and the disordered region between them after Zhao [2005Zha]

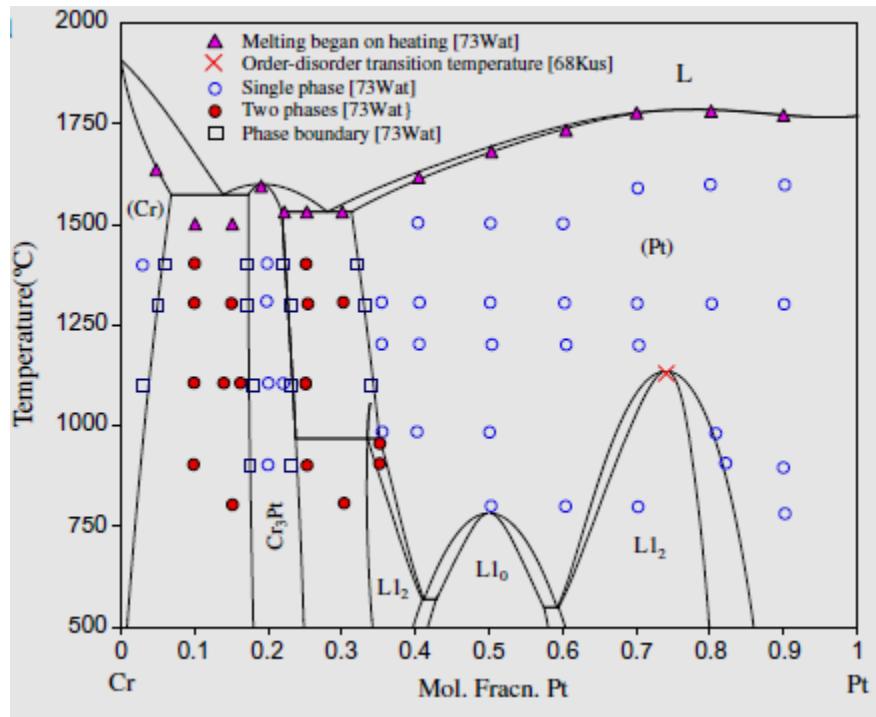


Figure 2.8. Comparison between calculated Cr-Pt phase diagram and experimentally determined data [2008Zha]



## Solid Phases

Table 2.10. shows the solid phases and their crystal data.

**Table 2.10. Crystal structure data of Cr-Pt**

Phase/Temperature Range, ( $^{\circ}\text{C}$ )	Pearson Symbol/Space Group/Strukturbericht/Prototype	Lattice Parameters (nm)	Reference
(Cr) <1863	$cI2$ $Im\bar{3}m$ A2 W	$a = 0.288$	[1985Vil1]
$\text{Cr}_3\text{Pt}$ <1600	$cP8$ $Pm\bar{3}n$ A15 $\text{Cr}_3\text{Si}$	$a = 0.471$	[1956Gre]
$\text{CrPt}$ <700	$tP4$ $P\bar{4}/mmm$ $L1_0$ AuCu	$a = 0.382$ $c = 0.381$	[1976Bag]
$\text{CrPt}$ <700	$cF4$ $Fm\bar{3}m$ A1 Cu	$a = 0.380$	[1985Vil2]
$\text{CrPt}$ <700	$cP8$ $Pm\bar{3}n$ A15 $\text{Cr}_3\text{Si}$	$a = 0.471$	[1978Bag]
$\text{CrPt}_3$ <1130	$cP4$ $Pm\bar{3}m$ $L1_2$ $\text{AuCu}_3$	$a = 0.387$	[1985Vil3]
(Pt) <1769	$cF4$ $Fm\bar{3}m$ A1 Cu	$a = 0.392$	[1985Vil3]

## Phase Equilibria

Figure 2.5 and Table 2.9 show the phase equilibria. The liquidus and solidus points from 20 at.% Pt to 100 at.% Pt are taken from Waterstrat and Müller [1973Wat2, 1930Mül]. They both found

a maximum melting point of (Pt) at ~80 at.% Pt at 1780°C and 1790°C respectively. Raub *et al.* [1940Rau] found that Cr<sub>3</sub>Pt probably melts congruently and not syntectically as suggested by Waterstrat [1973Wat2]. Both Raub [1940Rau] and Waterstrat [1973Wat2] established the presence of a eutectic reaction on both sides of Cr<sub>3</sub>Pt. These eutectic temperatures were taken from Waterstrat, as well as the solid-state boundaries of (Cr), Cr<sub>3</sub>Pt and (Pt). In agreement with previous studies [1930Mul, 1940Rau, 1934Nem, 1940Geb, 1935Fri], it was observed that (Pt) had a broad solubility range (~29 to 100 at.% Pt at 1530°C). Several investigators showed that ordered fcc CrPt<sub>3</sub> forms from disordered (Pt) below 1200°C [1934Rem, 1935Fri, 1940Geb, 1940Rau, 1956Gre, 1962Bro, 1963Pic, 1968Kus, 1973Wat2]. The high temperature (Pt) can only be obtained by quenching [1935Fri, 1940Rau, 1968Kus, 1973Wat2]. CrPt<sub>3</sub> remains cubic over its whole composition range from 50-85 at.% Pt [1935Fri, 1940Geb, 1940Rau, 1963Pic, 1973Bes, 1973Wat2, 1977Got]. L<sub>12</sub> CrPt<sub>3</sub> transforms to an L<sub>10</sub> type structure CrPt without the tetragonal distortion typical of this structure [1963Pic, 1973Bes, 1973Wat2, 1977Got]. Through thin-film studies, however, a tiny distortion as well as a CrPt/CrPt<sub>3</sub> two phase region was observed. More studies are required to resolve the latter two issues.

The relative temperatures of the two eutectics have also been controversial. The temperature of the eutectic on the Cr-rich side is specified in the assessed phase diagram [1990Mas] as 1500°C and the one on the Pt-rich side as 1530°C. Zhao [2005Zha] also gave the same temperatures. However, Oikawa's calculated phase diagram [2001Oik] shows that the temperature of the eutectic on the Cr-rich side is higher and this is in agreement with the work of Süss *et al.* [2006Süs, 2007Süs] and Zhang *et al.* [2008Zha]

In the refined version of the Cr-Pt diagram (Figure 2.7) [2005Zha], the two ordered phases (CrPt and CrPt<sub>3</sub>) are shown in two separate phase regions with the disordered fcc region in between them, i.e. (Pt) does not order to CrPt via CrPt<sub>3</sub>, but fcc (Pt) orders to either CrPt or CrPt<sub>3</sub> depending on the composition.

In his supplemental literature review, Okamoto [2009Oka] based his phase diagram (Figure 2.9) on that determined by thermodynamic modelling by Zhang [2008Zha] (Figure 2.8). The melting behavior of Cr<sub>3</sub>Pt, in the phase diagram given in [1990Mas], violated the Gibbs-Konovalov rule [1981Goo] and the phase boundaries of the low temperature ordered phases were ambiguous.

The problem was solved by the phase diagram calculated by Oikawa [2001Oik]. In the diagram presented by Okamoto [2009Oka],  $\text{Cr}_3\text{Pt}$  is shown as  $\text{Cr}_4\text{Pt}$ . The  $\text{L}_{12}$ -type  $\text{Cr}_3\text{Pt}$  has the peak at about  $1250^\circ\text{C}$  and at 25 at.% Pt in the metastable state. The peak is hidden due to the existence of a more stable phase  $\text{Cr}_4\text{Pt}$ .

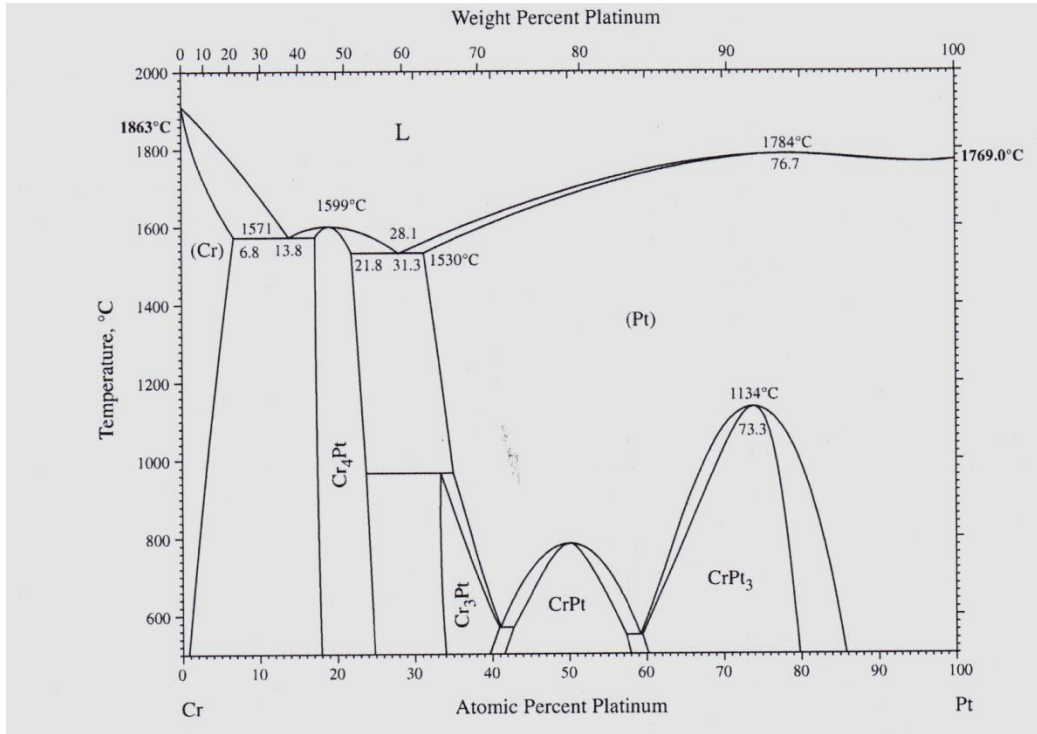


**Figure 2.9. Assessed binary Cr-Pt phase diagram by Okamoto [2009Oka].**

The phase  $\text{Cr}_4\text{Pt}$  in Figure 2.8 may need further clarification. Since the composition at the congruent melting point is 19.1 at.% Pt and the composition of the melting point should not be far away from the stoichiometric composition, and so the phase should be  $\text{Cr}_4\text{Pt}$  from the standpoint of its location. However, it has been well established that the phase has the  $\text{Cr}_3\text{Si}$  crystal structure [1991Vil]. In this regard  $\text{Cr}_3\text{Pt}$  may be a better designation for this phase. Nevertheless “ $\text{Cr}_4\text{Pt}$ ” was used to differentiate from the  $\text{L}_{12}$ -type  $\text{Cr}_3\text{Pt}$  [2009Oka]. In this investigation, it will be designated  $\text{A15}(\sim\text{Cr}_3\text{Pt})$  to distinguish it from the  $\sim\text{Cr}_3\text{Pt}$  formed by ordering (Pt).

**Table 2.11. Invariant Equilibria of Cr-Pt [1990Mas].**

Reaction	Temperature, °C	Reaction type	Composition, at.% Pt
$L \leftrightarrow Cr_3Pt$	~1600	Congruent	~18    ~18
$L \leftrightarrow Cr_3Pt + (Pt)$	1530	Eutectic	~24    ~20    ~29
$L \leftrightarrow (Cr) + Cr_3Pt$	1500	Eutectic	~13    ~10    ~17
$(Pt) \leftrightarrow Cr_3Pt$	~1130	Ordering	~67    ~67
$(Pt) \leftrightarrow Cr_3Pt + CrPt_3$	970	Eutectoid	~34    ~23    ?
$L \leftrightarrow (Pt)$	1785±5	Congruent	~80    ~80
$CrPt_3 \leftrightarrow CrPt$	<700?	Ordering	~50    ~50

### 2.1.5 Cr-V binary phase diagram

Three separate investigations of the V-Cr system have given somewhat different versions of the system [1982Smi]. All the three versions show a complete series of solid solutions. There was no evidence of ordering or compound formation [1982Smi]. The differences among the three proposed versions of the diagram are illustrated in Figure 2.9.

The earliest investigation by Carlson *et al.* [1959Car] indicated a minimum in the melting of V-Cr alloys near 70 at.% Cr and 1750°C. The second investigation by Rudy [1969Rud1] found no minimum or maximum in melting at any composition between pure V and pure Cr. The third investigation by Kocherzhinskii and Shishkin [1977Koc] reported a melting minimum, but on the other side of the system near 25 at.% Cr and 1759°C. Figure 2.9 includes the data points from Kocherzhinskii and Shishkin because the liquidus line in the figure has been modified from that of the original report to meet the thermodynamic requirement of tangential contact between liquidus and solidus at the melting minimum [1982Smi].

Support for the occurrence of a melting minimum in the system was provided by the calculated phase diagrams. One of these has been published by Molokanov *et al.* [1977Mol]. With melting points of 1907°C for V and 1877°C for Cr, the calculated phase of Molokanov *et al.* showed a melting minimum near 55 at.% Cr and 1819°C.

With the mounting evidence indicating a melting minimum in the system, but with uncertainty as to the composition and temperature of this minimum, it was decided that the effort to make a few

additional solidus determinations was warranted. Carlson made such determinations on a few alloys in the composition range 60 - 80 at.% Cr. The supplemental solidus determinations were believed to be representative of the purest V-Cr alloys that have been measured [1982Smi]. Melting temperatures between 1765°C and 1780°C were found, and, because these values were considerably below the melting point of V or Cr, the new measurements confirmed the existence of a melting minimum in the composition range 60 - 80 at.% Cr. A more precise definition of the coordinates of the melting minimum was then achieved by a new calculation of the phase diagram. This calculated phase diagram is shown in Figure 2.10 and was believed to be the best compromise for representing currently available data [1982Smi].

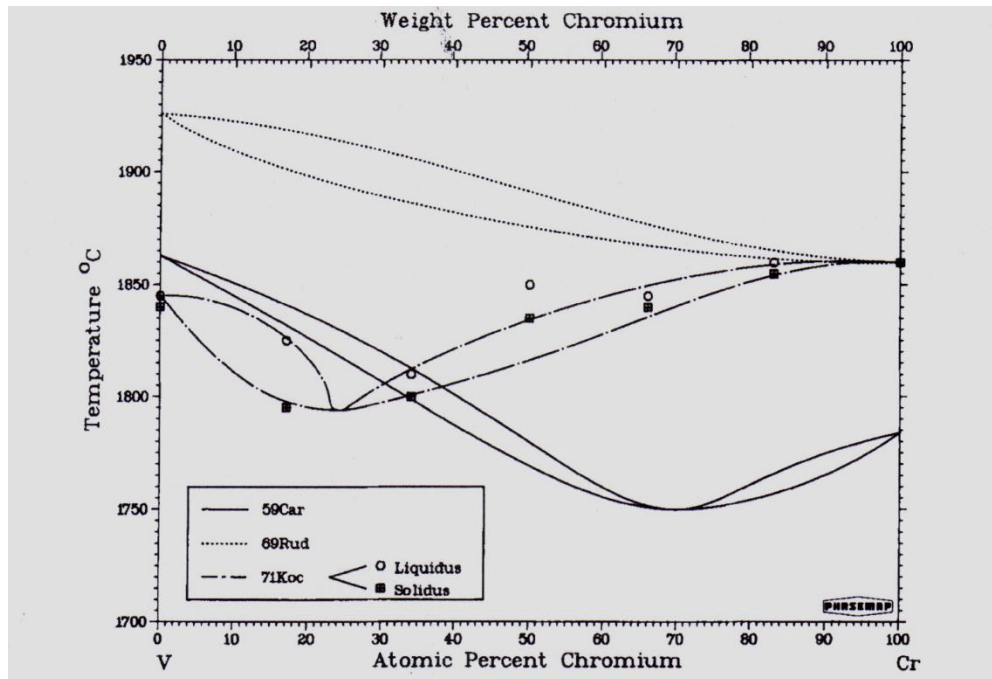


**Figure 2.10. Binary phase equilibria of Cr-V [1959Car, 1969Rud1, 1977Koc] – after [1982Smi].**

### Crystallography

V, Cr and their alloys crystallize with the bcc structure, of which W is the prototype. The room-temperature lattice parameter as a function of alloy composition is shown in Figure 2.11, which indicates a smooth monotonic increase in lattice parameter from pure Cr to pure V. Data for this plot are from several sources [1959Car, 1969Rud1, 1952Mar, 1959Sve].

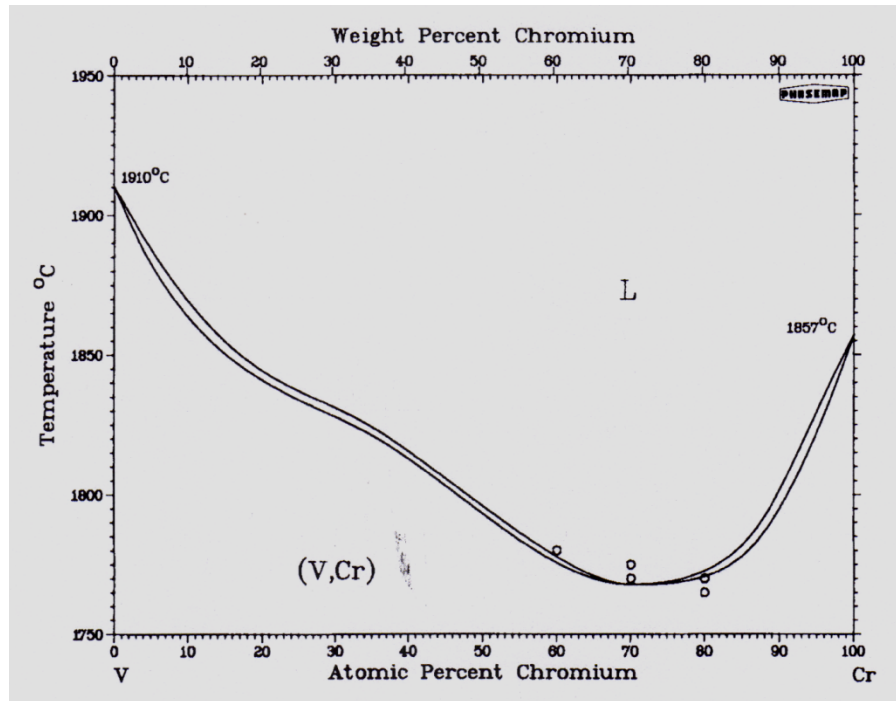
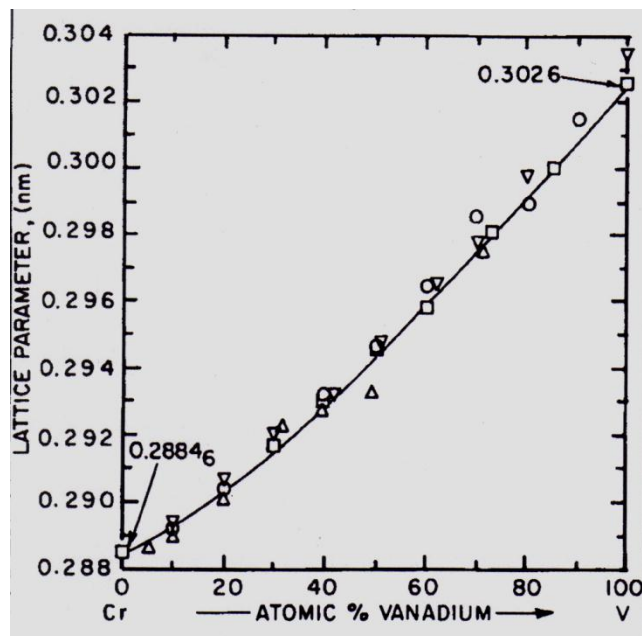


Figure 2.11. Calculated Cr-V phase equilibrium diagram [1982Smi].



▽ ≡ Carlson et al. [1959Car]

□ ≡ Rudy [1969Rud]

o ≡ Martens and Duwez [1952Mar]

Figure 2.12. Lattice parameter as a function of composition for Cr-V alloys [1982Smi], where the data are from independent investigators.

## 2.2 Pt-Al-Nb and Pt-Cr-Nb Ternary Systems

The binary systems which comprise the two ternary systems above are Pt-Al, Nb-Pt, Al-Nb, Pt-Cr, Cr-Nb and Nb-Pt. The binary systems Pt-Al and Pt-Cr have already been reviewed. The remaining systems are reviewed below.

### 2.2.1 Nb-Pt binary system

The phase boundaries and reaction temperatures presented in Figure 2.12 are based primarily on the work of Waterstrat [1985Wat], who investigated the system over the entire composition range between 1000°C and 2400°C by metallography, electron microprobe, XRD and thermal analysis of 35 arc-melted alloy samples prepared from 99.6% pure Nb and 99.9% pure Pt. The Nb-rich alloys up to 20 at.% Pt were given homogenization anneals in a vacuum furnace at 1900°C for 3 hours, and the other compositions were annealed at 1600°C to 1700°C for 6 to 12 hours and quenched at the rates of 30°C to 100°C per second. The compositions and temperatures in Figure 2.12 have an accuracy of  $\pm 1$  at.% and  $\pm 10^\circ\text{C}$ , respectively.

Six (at least partially) non-stoichiometric compounds exist:  $\text{Nb}_3\text{Pt}$ , “ $\sim\text{Nb}_2\text{Pt}$ ”,  $\text{Nb}_{1-x}\text{P}_{1+x}$ ,  $\alpha'\text{Pt}$ ,  $\text{NbPt}_2$  and  $\text{NbPt}_3$ . “ $\text{Nb}_2\text{Pt}$ ” is usually referred to as  $\sigma$  phase. The two Nb-rich phases,  $\text{Nb}_3\text{Pt}$  and  $\sigma$ , are known as Frank-Kasper phases [1995Tri] and comprise Kasper co-ordination polyhedral stacked differently.

The equilibrium phases of the Nb-Pt system are (1) the liquid, L; (2) the bcc solid solution of Pt in  $\alpha\text{Nb}$  phase with a maximum solubility of Pt up to  $\sim 12$  at.% at 2040°C; (3) the cubic  $\text{Nb}_3\text{Pt}$  crystallizing peritectically at 2040°C; (4) the tetragonal  $\sigma$  phase forming peritectically at 1800°C; (5) the orthorhombic  $\text{Nb}_{1-x}\text{P}_{1+x}$  phase crystallizing peritectically at 1750°C; (6) the high temperature  $\alpha'\text{Pt}$  phase of unknown structure, forming peritectically at 1780°C and decomposing eutectoidally at 1670°C; (7) the orthorhombic  $\text{NbPt}_2$  forming peritectically at 1990°C; (8) the  $\text{NbPt}_3$  phase solidifying congruently at 2040°C; and (9) the fcc solid solution of Nb in  $\alpha\text{Pt}$  with solubility up to  $\sim 20$  at.% Nb at 2000°C.

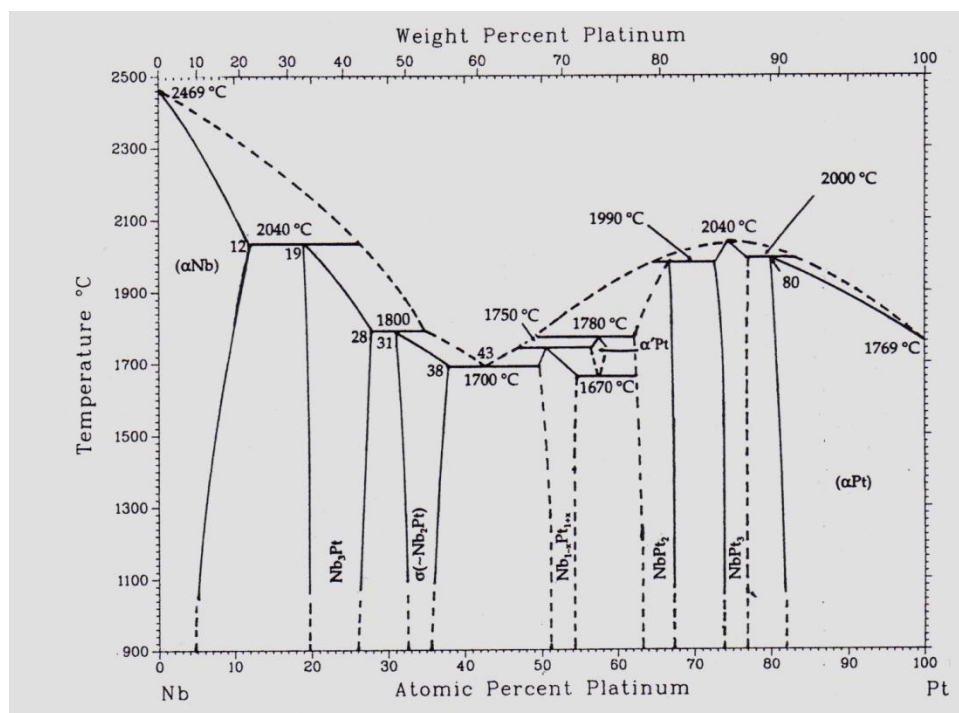


**Figure 2.13. Assessed Nb-Pt phase diagram [1995Tri].**

### Liquidus and Solidus

Melting point work done by Knapton [1960Kna] showed that the liquidus on the Pt-rich side of the phase diagram had a maximum near 75 at.% Pt. It was later confirmed by Waterstrat [1985Wat], who made an approximate determination of the liquidus by microscopic examination of the of the melting point samples with visual estimates of the relative amounts of solid and liquid phases present in each sample. Therefore, the liquidus in Figure 2.12 is shown by broken lines.

Waterstrat [1985Wat] determined the solidus boundaries using metallography, XRD and thermal methods for phase analysis of the samples quenched after homogenization anneals. The solidus temperatures were measured to an accuracy of  $\pm 10^\circ\text{C}$  and compositions within  $\pm 1$  at.% and are known with a high degree of confidence and therefore represented by solid lines. Nine invariant reactions, including eight three-phase equilibria were identified in addition to the normal melting of the pure end-members. The compositions of the phases involved in the invariant reactions and the temperatures of the respective equilibria are presented in Table 2.10.



**Table 2.12. Reactions in the assessed Nb-Pt Diagram [1995Tri].**

Reaction	Composition, at.% Pt	Temperature, °C	Reaction type
$L \leftrightarrow Nb$	0	2469	Melting
$L + (\alpha Nb) \leftrightarrow Nb_3Pt$	~26    ~12    ~19	2040	Peritectic
$L + Nb_3Pt \leftrightarrow \sigma$	36.4    28    31	1800	Peritectic
$L \leftrightarrow Nb_{1-x}Pt_{1+x} + \sigma$	43    51.2    38	1700	Eutectic
$L + \alpha'Pt \leftrightarrow Nb_{1-x}Pt_{1+x}$	47    57    52	1750	Peritectic
$L + NbPt_2 \leftrightarrow \alpha'Pt$	49    65    57	1780	Peritectic
$\alpha'Pt \leftrightarrow Nb_{1-x}Pt_{1+x} + NbPt_2$	57.5    54    66	1670	Eutectoid
$L + NbPt_3 \leftrightarrow NbPt_2$	66    74    67	1990	Peritectic
$L \leftrightarrow NbPt_3$	75	2040	Congruent
$L + NbPt_3 \leftrightarrow (\alpha Pt)$	82.5    76    80	2000	Peritectic
$L \leftrightarrow \alpha Pt$	100	1769	Melting

### Terminal Solid Solutions

Both terminal solid solutions of the system exhibit considerable solid solubility. Knapton [1960Kna] observed larger solid solubility in the terminal phases of the Nb-Pt system compared to those of Nb alloys with Rh, Ir, Ru and Os. This was confirmed by Waterstrat [1985Wat]. The heat treated and quenched alloys were examined for determination of composition by electron microprobe, XRD and metallography. The terminal solid solution boundary of bcc Nb was established by analysis of equilibrated and quenched alloys in the composition range 10 to 18 at.% Pt. The solubility of Pt in the ( $\alpha Nb$ ) solid solution reaches ~12 at.% at 2040°C, but it decreases at lower temperatures and remains only 5 at.% at 1150°C.

The fcc ( $\alpha Pt$ ) solid solution dissolves ~20 at.% Nb at 2000°C and ~18 at.% Nb at lower temperatures. The metastable coherent structure [1985Wat] of the 80 at.% Pt alloy annealed at 1500°C suggests that the solvus boundary of the ( $\alpha Pt$ ) may be for the metastable alloy. It is quite likely that the true equilibrium boundary is located at lower Nb concentrations.

### Crystal Structures and Lattice Parameters

Crystal structures for the equilibria phases are presented in Table 2.11. The lattice parameters of intermediate phases and terminal solid solutions in the system are presented in Table 2.12.

**Table 2.13. Crystallographic data for Nb-Pt system [1995Tri].**

Phase	Composition, at.% Pt	Pearson Symbol	Space Group	Struktur- bericht Designation	Proto- type	Reference
( $\alpha$ Nb)	0	<i>cI2</i>	<i>Im\bar{3}m</i>	<i>A2</i>	W	[1995Tri]
Nb <sub>3</sub> Pt	19 to 28	<i>cP8</i>	<i>Pm\bar{3}n</i>	<i>A15</i>	Cr <sub>3</sub> Si, $\beta$ W	[1956Gre, 1955Gel]
$\sigma$ (Nb <sub>2</sub> Pt)	31 to 38	<i>tP30</i>	<i>P\bar{4}_2 / mnm</i>	<i>D8<sub>b</sub></i>	$\beta$ W	[1956Gre]
Nb <sub>1-x</sub> Pt <sub>1+x</sub>	51 to 53	<i>oP4</i>	<i>Pmma</i>	<i>B19</i>	AuCd	[1964Gie1, 1964Mal]
$\alpha'$ Pt	57	-	-	-	-	[1964Gie2]
NbPt <sub>2</sub>	~67	<i>oI6</i>	<i>Immm</i>	<i>Immm</i>	MoPt <sub>2</sub>	[1964Gie1, 1964Mal, 1965Gie1]
$\alpha$ NbPt <sub>3</sub>	~75	<i>oP8</i>	<i>Pmnm</i>	<i>D0<sub>a</sub></i>	$\beta$ TiCu <sub>3</sub>	[1964Gie1, 1964Mal]
$\beta$ NbPt <sub>3</sub>	~76	<i>mP48</i>	<i>P\bar{2}_1 / m</i>		$\beta$ NbPt <sub>3</sub>	[1964Gie1, 1965Gie2]
( $\alpha$ Pt)	80 to 100	<i>cF4</i>	<i>Fm\bar{3}m</i>	<i>A1</i>	Cu	[1995Tri]

**Table 2.14. Lattice parameters of intermediate phases and terminal solid solutions in Nb-Pt system – after [1985Wat].**

Phase	Composition, at.% Pt	Lattice Parameters, nm			Reference
		<i>a</i>	<i>b</i>	<i>c</i>	
$\alpha$ Nb	5	0.3277	-	-	[1985Wat]
$\alpha$ Nb	10	0.3260	-	-	[1985Wat]
Nb <sub>3</sub> Pt	20	0.5182	-	-	[1985Wat]
Nb <sub>3</sub> Pt	28	0.5139	-	-	[1985Wat]
$\sigma$	32	0.9940	-	0.5145	[1985Wat]
$\sigma$	38	0.9902	-	0.5132	[1985Wat]
Nb <sub>1-x</sub> Pt <sub>1+x</sub>	50	0.2780	0.4983	0.4611	[1964Gie1]
NbPt <sub>2</sub>	67	0.2801	0.8459	0.3951	[1964Gie1]
$\alpha$ NbPt <sub>3</sub>	75	0.5534	0.4873	0.4564	[1964Gie1]
$\beta$ NbPt <sub>3</sub>	75	0.5537	0.4870	0.2733	[1964Gie1]
$\alpha$ Pt	82	0.3940	-	-	[1985Wat]
$\alpha$ Pt	85	0.3935	-	-	[1985Wat]
$\alpha$ Pt	90	0.3927	-	-	[1985Wat]
$\alpha$ Pt	95	0.3924	-	-	[1985Wat]

## Intermediate Phases

### The Nb<sub>3</sub>Pt Phase

The Nb<sub>3</sub>Pt phase was first discovered by Geller *et al.* [1955Gel] and later identified by Greenfield and Beck [1956Gre] as having a Cr<sub>3</sub>Si-type ( $\beta$ W, A15) structure, as a result of their studies of six alloys in the composition range 25 to 57 at.% Pt, annealed and quenched at 1000°C. The phase was further confirmed by Kimura and Ito [1961Kim], Giessen [1964Gie1] and Waterstrat [1985Wat, 1983Wat]. Waterstrat [1985Wat] found a homogeneity range in Nb<sub>3</sub>Pt with a composition span of 19 to 28 at.% Pt at 1800±10°C. The span narrows at lower temperatures. Nb<sub>3</sub>Pt forms as an ordered structure from the disordered bcc ( $\alpha$ Nb) at 2040°C by peritectic reaction:  $L + (\alpha\text{Nb}) \leftrightarrow \text{Nb}_3\text{Pt}$ .

Nb<sub>3</sub>Pt is a highly ordered phase (order parameter,  $S = 0.93$ ) phase [1955Gel]. The ideal composition is A<sub>3</sub>B, but the phase is also stable at significantly deviating compositions, implying that the crystallographic sites in the lattice are not exclusively occupied by one chemical element [1995Tri]. The remarkable stability of Nb<sub>3</sub>Pt and other A15-type phases [1968Reu] in alloys of

the transition metals is attributed to the intimate involvement of the *d*-electrons in the bonding and the interdependence of the electronic structure and the ability of the atoms to undergo deformation to conform to the geometrical packing requirements.

In an investigation by Robinson [1988Rob] on Nb-Pt alloys with compositions ranging between 16 and 32 at.% Pt, undercooling was reported by as much as 585 K for liquid alloys. The Nb-Pt alloys of 16 to 18 at.% Pt yielded, on undecooling, a single Nb<sub>3</sub>Pt phase in contrast to the ( $\alpha$ Nb) and Nb<sub>3</sub>Pt expected on the basis of Figure 2.12.

### **$\sigma$ Phase**

The  $\sigma$  phase,  $\sim$ Nb<sub>2</sub>Pt, also first reported by Geller *et al.* [1955Gel] together with Nb<sub>3</sub>Pt, was first identified with a tetragonal close-packed crystal structure that was later confirmed by Waterstrat [1985Wat], Giessen [1964Gie1], Maldonado and Schubert [1964Mal] and Kimura and Ito [1961Kim]. Like Nb<sub>3</sub>Pt, the  $\sigma$  phase is also non-stoichiometric and highly stable. It has a homogeneity range of 31 to 38 at.% Pt at 1700°C, narrowing at lower temperatures. The  $\sigma$  crystallises from a mixture of Nb<sub>3</sub>Pt and the melt at 1800 $\pm$ 10°C by the peritectic reaction: L + Nb<sub>3</sub>Pt  $\leftrightarrow$   $\sigma$  phase.

### **Nb<sub>1-x</sub>Pt<sub>1+x</sub> Phase**

Kimura and Ito [1961Kim] found evidence of an equiatomic composition phase which was later identified by Giessen [1964Gie2, 1965Gie1] as having the AuCd-type (*B19*) orthorhombic structure. Waterstrat [1985Wat] reported the phase as being hyper-stoichiometric and is represented as Nb<sub>1-x</sub>Pt<sub>1+x</sub>. It forms at 1700°C with  $\sim$ 43 at.% Pt by a eutectic reaction L  $\leftrightarrow$   $\sigma$  + Nb<sub>1-x</sub>Pt<sub>1+x</sub> and there is agreement between Waterstrat [1985Wat] and Kimura and Ito [1961Kim] for the temperature and nature of the reaction.

### **( $\alpha'$ Pt) Phase**

Giessen [1964Gie1, 1964Gie2, and 1965Gie1] reported a phase with composition close to Nb<sub>1-x</sub>Pt<sub>1+x</sub>, the off-stoichiometric phase. Giessen [1964Gie1] found the phase to be stable only at high temperatures i.e. 1670°C to 1780°C. The temperature of the eutectoid decomposition of  $\alpha'$ Pt

is precisely known from the metallography of 55 at.% and 57.5 at.% Pt alloys quenched from above and below 1670°C.

The crystal structure of ( $\alpha'$ Pt) remains undetermined. By analysis of V-Pt and Nb-Pt, Waterstrat speculated that this phase was an extension of fcc ( $\alpha$ Pt) solid solution. The phase forms from NbPt<sub>2</sub> by a peritectic reaction at 1780±10°C and undergoes another peritectic reaction at 1750±10°C:  $L + (\alpha'\text{Pt}) \leftrightarrow \text{Nb}_{1-x}\text{Pt}_{1+x}$ . On cooling to 1670°C, it decomposes eutectoidally to a mixture of Nb<sub>1-x</sub>Pt<sub>1+x</sub> and NbPt<sub>2</sub>.

### **NbPt<sub>2</sub> Phase**

NbPt<sub>2</sub> is essentially a non-stoichiometric compound having a narrow homogeneity range spanning over 2 to 3 at.% Pt at 1780±10°C [1985Wat]. It forms by the peritectic reaction  $L + \text{NbPt}_3 \leftrightarrow \text{NbPt}_2$  at 1990±10°C as observed in solidification of a 70 at.% Pt alloy. It crystallises with an orthorhombic MoPt<sub>2</sub>-type structure [1964Gie2, 1964Mal and 1965Gie1]. Kimura and Ito [1961Kim] suggested that NbPt<sub>2</sub> is an extension of the ( $\alpha$ Pt) solid solution, but Waterstrat [1985Wat], Maldonado [1964Mal] and Giessen [1965Gie1] assigned NbPt<sub>2</sub> a distinct crystal structure.

### **NbPt<sub>3</sub> Phase**

NbPt<sub>3</sub> solidifies congruently at the composition 75 at.% Pt on cooling to 2040±10°C. Two polymorphs of NbPt<sub>3</sub> were identified and characterised. The low-temperature phase designated as  $\alpha$ NbPt<sub>3</sub> [1964Gie1, 1964Mal] has an orthorhombic Cu<sub>3</sub>Ti-*D0<sub>a</sub>* type structure with a two-layer stacking sequence. The high temperature polymorph is  $\beta$ NbPt<sub>3</sub>, identified as a monoclinic structure, was confirmed by Waterstrat [1985Wat], with a twelve-layer sequence and the same layer type as  $\alpha$ NbPt<sub>3</sub>. Giessen [1964Gie1] suggested that the  $\alpha$ NbPt<sub>3</sub> may be stabilised with respect to  $\beta$ NbPt<sub>3</sub> by trace amounts of interstitial impurities. Maldonado [1964Mal] suggested that  $\alpha$ NbPt<sub>3</sub> is stable below 1000°C and  $\beta$ NbPt<sub>3</sub> has Pt content higher than the stoichiometric composition. NbPt<sub>3</sub> undergoes peritectic reactions at 1990±10°C,  $L + \text{NbPt}_3 \leftrightarrow \text{NbPt}_2$  and at 2010±10°C,  $L + \text{NbPt}_3 \leftrightarrow (\alpha\text{Pt})$ .

### 2.2.2 The Binary Nb-Al System

There are three intermediate phases,  $\text{Nb}_3\text{Al}$ ,  $\text{Nb}_2\text{Al}$  and  $\text{NbAl}_3$ , occurring in this system. Several versions of the conditions leading to formation of the  $\text{Nb}_3\text{Al}$  and  $\text{Nb}_2\text{Al}$  phases have been given. These contradictions are the result of difficulties in obtaining precise information at temperatures above  $1900^\circ\text{C}$ , together with uncertainties in the determination of aluminium content after significant losses [1980Jor]. Table 2.14 presents a summary of the relevant data in literature before Jorda *et al.* [1980Jor] carried out an investigation to try and resolve the contradictions.

**Table 2.15. Summary of results before Jorda [1980Jor] for the Nb-Al system – after [1980Jor].**

Phase	Temperature of formation, °C	Nb-rich limit, at.% Al		Al-rich limit, at.% Al		Reaction type	Reference
		T=1000 <sup>o</sup> C	(High Temp. °C)	T=1000 <sup>o</sup> C	(High Temp. °C)		
(Nb)					18 (2120±10)		[1961Nad]
Nb <sub>3</sub> Al	2120 ±10	22.5	25 (2120)	~29	25 (2120)	Peritectic	[1961Nad]
Nb <sub>2</sub> Al	~1800	35	34 (1650)	~39	~43 (1520)	Congruent	[1961Nad]
NbAl <sub>3</sub>	~1750	73	75 (1750)	77.5	75 (1750)	Congruent	[1961Nad]
(Nb)					23 (1960)		[1966Lun]
Nb <sub>3</sub> Al	1960	17.5	25 (1960)	~22	32 (1870)	Peritectic	[1966Lun]
Nb <sub>2</sub> Al	1870	31.5	33 (1870)	~37	41.3 (1550)	Peritectic	[1966Lun]
NbAl <sub>3</sub>	1605	75	75	75	75	Congruent	[1966Lun]
(Nb)					23 (1850)		[1968Sve]
Nb <sub>3</sub> Al	1750	~17.5	26 (1750)	~22	26 (1750)	Peritectoidal	[1968Sve]
Nb <sub>2</sub> Al	~1850	~33	30 (1750)	~37	~42 (1600)	Peritectic	[1968Sve]
NbAl <sub>3</sub>	1750	75	75	75	75	Congruent	[1968Sve]

An attempt by Jorda *et al.* [1980Jor] to resolve the contradictions resulted in the diagram presented in Figure 2.14. Their findings on the equilibria reactions led to the interpretation of formation of the three intermediate phases as presented in Table 2.15. A more recently calculated phase diagram by Witusiewicz *et al.* [2009Wit] compares the experimental data of Zhu *et al.*, Jorda *et al.*, and Wicker *et al.* [2008Zhu, 1980Jor and 1971Wic] with the diagram in Figure 2.15(a).

**Table 2.16. Equilibria reactions in the Nb-Al system [1980Jor].**

Reaction	Temperature, °C	Reaction type
$(\text{Nb}) + \text{L} \leftrightarrow \text{Nb}_3\text{Al}$	$2060 \pm 10$	Peritectic
$\text{Nb}_3\text{Al} + \text{L} \leftrightarrow \text{Nb}_2\text{Al}$	$1940 \pm 10$	Peritectic
$\text{L} \leftrightarrow \text{NbAl}_3$	1680	Congruent
$\text{L} \leftrightarrow \text{Nb}_2\text{Al} + \text{NbAl}_3$	1590	Eutectic

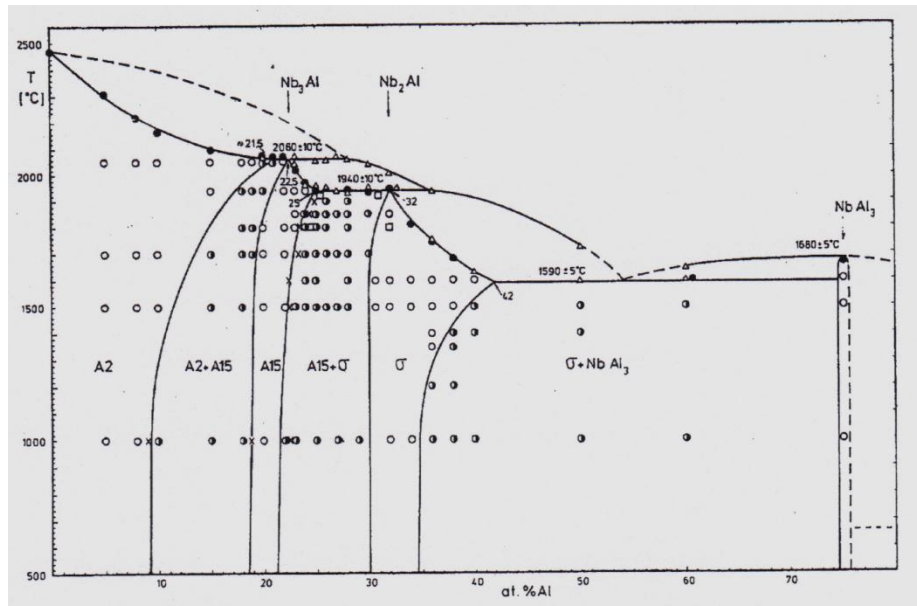


**Figure 2.14. Nb-Al phase diagram after Jorda et al. [1980Jor]: ○, single phase; Φ, two phases; ●, levitation thermal analysis (LTA); Δ, DTA; □, microprobe analysis; x, phase boundary determination by X-ray analysis.**



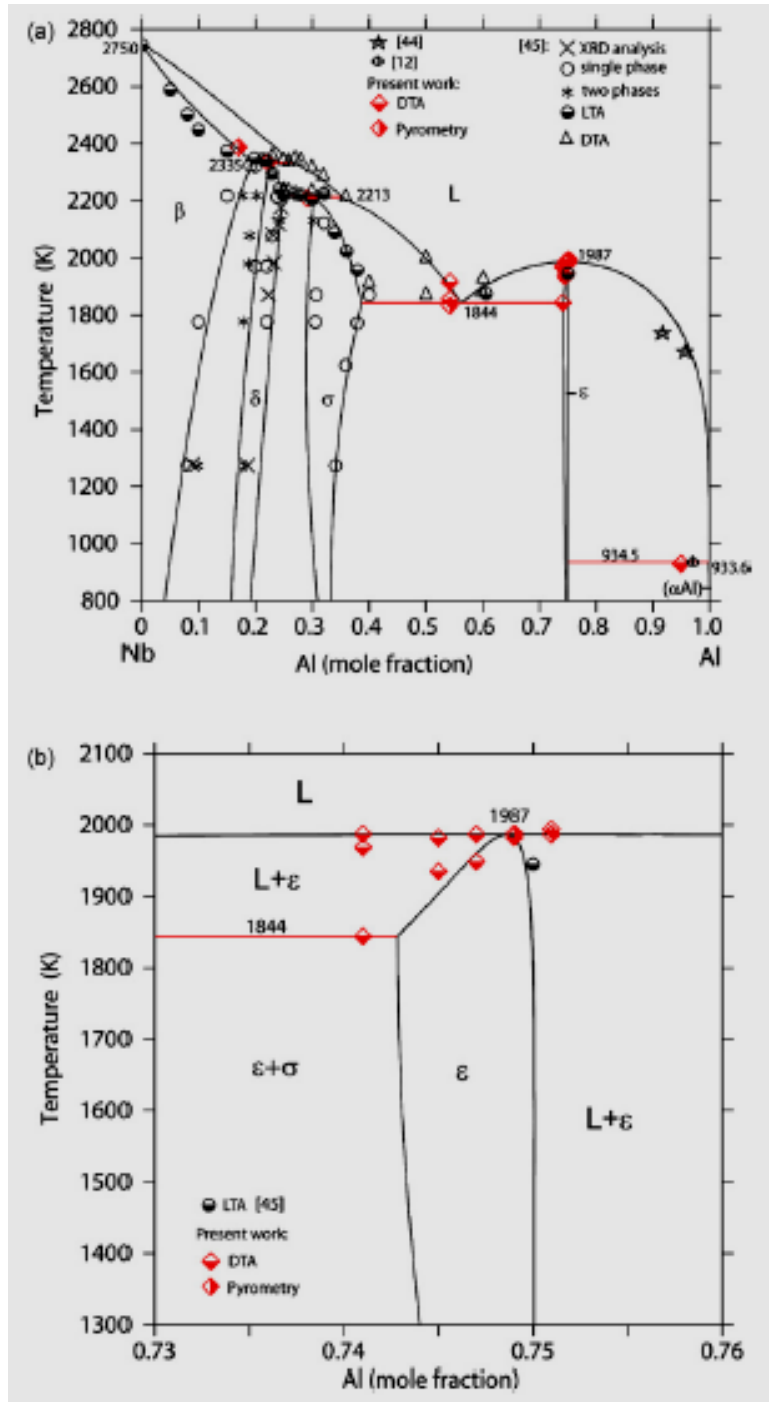


Figure 2.15 (a). Calculated Al-Nb phase diagram [2009Wit] along with experimental data from [2008Zhu], [1980Jor] and [1971Wic]; (b) enlarged part in the vicinity of NbAl<sub>3</sub> ( $\epsilon$ -phase).

### 2.2.3 The Binary Cr-Nb System

The assessed phase diagram presented in Figure 2.14 contains one congruently melting intermediate phase  $\text{Cr}_2\text{Nb}$ . This phase forms a eutectic with each of the terminal solid solutions, (Cr) and (Nb). The phase diagram was assessed by Venkatraman and Neumann [1986Van] and is based on investigations by Kubaschewski and Schneider [1948Kub], Elyutin and Funke [1956Ely], Eremenko *et al.* [1958Ere], Goldschmidt and Brand [1961Gol], Pan [1961Pan1, 1961Pan2], Svechnikov and Pan [1962Sve] and Rudy [1969Rud2].

The temperatures and compositions of the Cr-rich and Nb-rich eutectics according to various investigators are compared in Table 2.15. The assessed values,  $1620 \pm 40^\circ\text{C}$  and  $\sim 12$  at.% Nb and  $1650 \pm 50^\circ\text{C}$  and  $\sim 50$  at.% Nb for the Cr-rich and Nb-rich eutectics, respectively are given in Figure 2.14.

The accepted Calphad assessment of the Cr-Nb system by Costa Neto *et al.* [1993Net] is shown in Figure 2.15(a) with the enlarged area around the vicinity of  $\sim \text{NbCr}_2$  shown in Figure 2.15(b). There are two peritectoids associated with the C14/C15 transitions in this diagram with the first reaction being  $(\text{Cr}) + \text{NbCr}_2 (\text{HT}) \rightarrow \text{NbCr}_2 (\text{LT})$  and the second one,  $(\text{Nb}) + \text{NbCr}_2 \rightarrow \text{NbCr}_2 (\text{LT})$ . The Cr-rich and the Nb-rich eutectic temperatures and compositions are also different from the diagram presented by Jorda *et al.* [1980Jor].

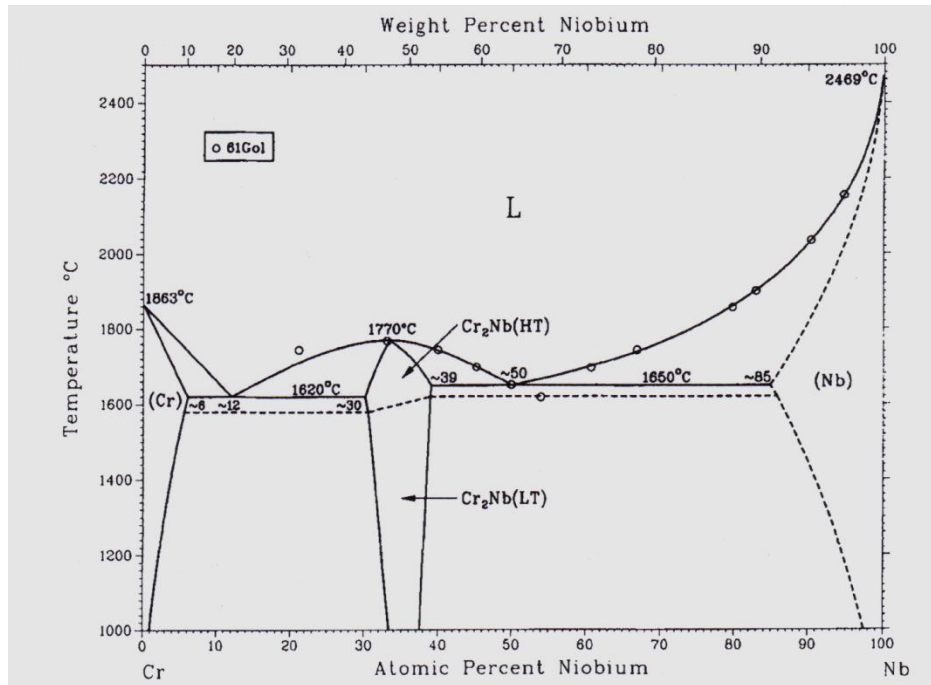


**Figure 2.16. Assessed phase diagram of Cr-Nb after Venkatraman and Neumann [1986Van].**

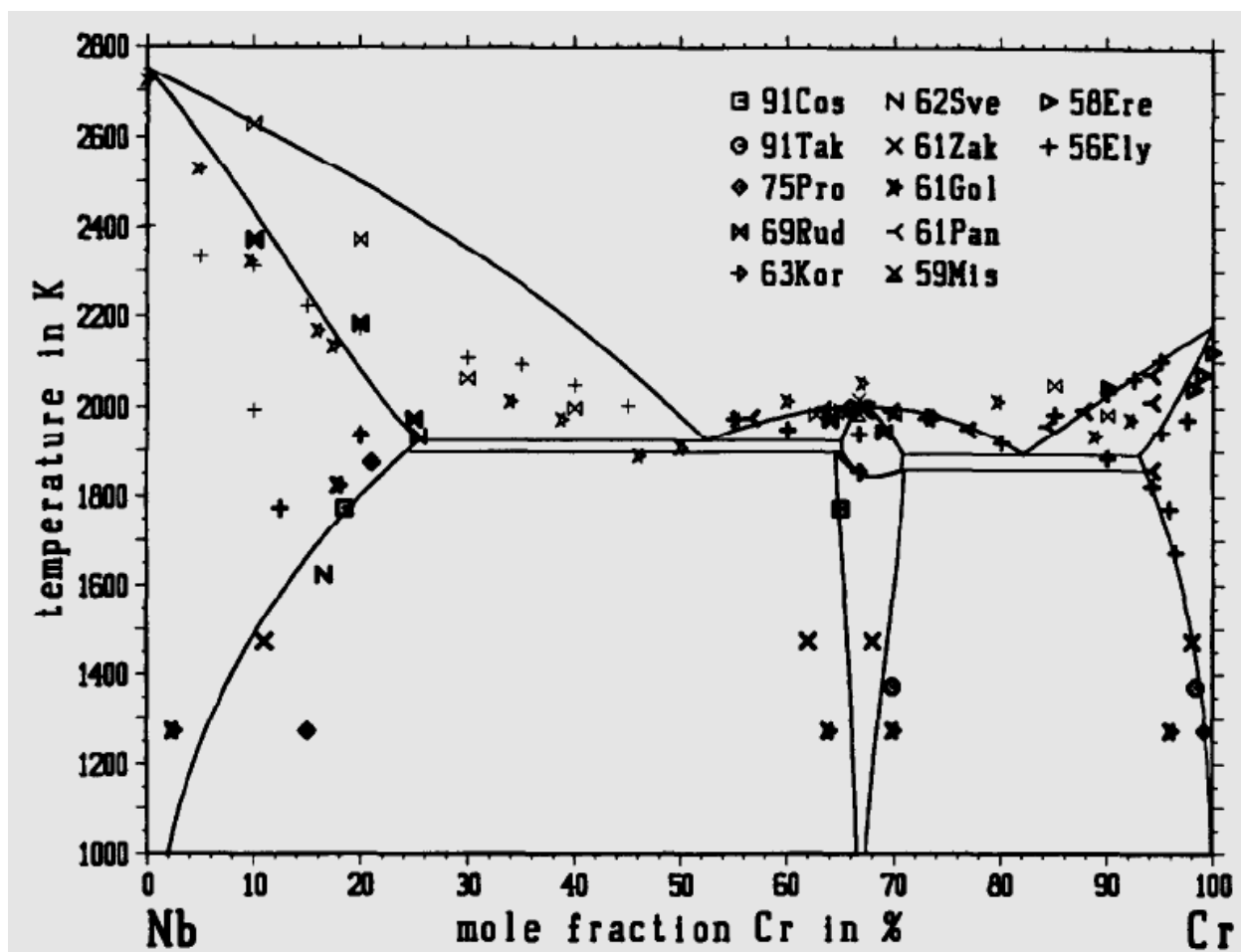


Figure 2.17 (a). Calculated Cr-Nb phase diagram by Costa Neto *et al.* [1993Net] where dark symbols are used in the optimisation and light are not.

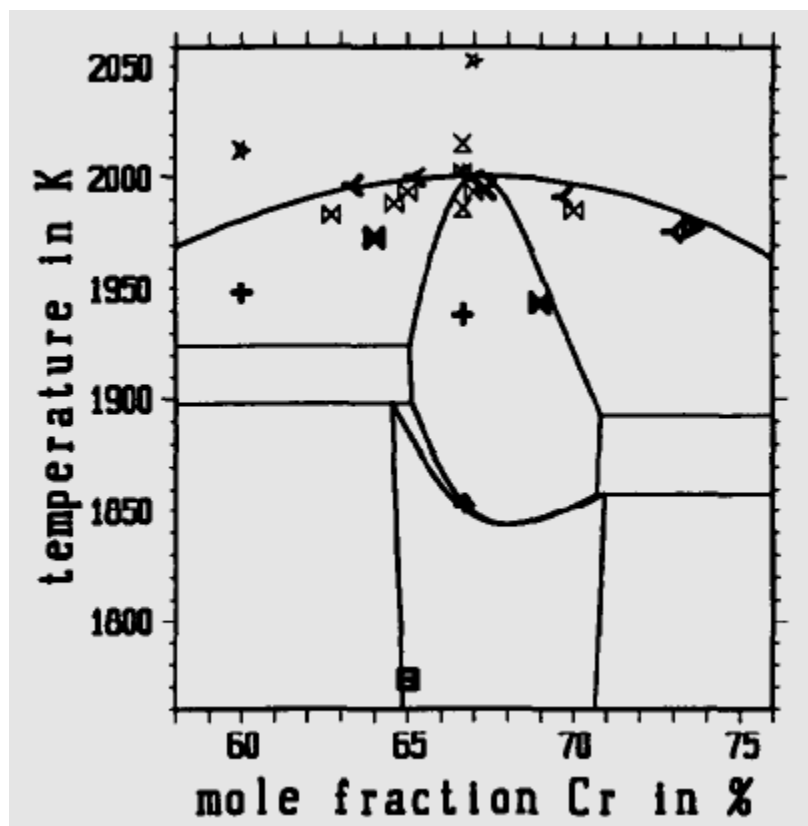


Figure 2.17 (b). Enlarged part of Figure 2.15(a) in the vicinity of NbCr<sub>2</sub> (HT).

Table 2.17. Eutectic temperatures and compositions in the Cr-Nb system [1986Van].

Cr-rich eutectic (a)		Nb-rich eutectic (b)		Reference
Temperature, °C	Composition, at.% Nb	Temperature, °C	Composition, at.% Nb	
1602	21 to 22	1662	38	[1956Ely]
1662	20.1	1713	48.9	[1958Ere]
1620	~12	1602	~53	[1961Pan1]
1642	19.3	1662	49	[1961Pan2]
1668	~19	1703	~48	[1961Zak]
1620 ± 40	~12	1650 ± 50	~50	[1986Van]

The existence of a single Laves-type phase that occurs at the stoichiometric composition NbCr<sub>2</sub> was firmly established [1956Ely, 1958Ere]. There is some disagreement regarding the homogeneity range of NbCr<sub>2</sub>. Elyutin and Funke [1956Ely] and Eremenko *et al.* [1958Ere] claimed that the homogeneity range is extremely small, whereas Goldschmidt and Band [1961Gol], Zakharova and Prokoshkin [1961Zak], Svechnikov and Pan [1962Sve] and Rudy

[1969Rud2] reported homogeneity of several atomic percent. The homogeneity adopted for the assessed phase diagram [1986Van] is based on lattice parameter measurements of Goldschmidt and Band [1961Gol], Zakharova and Prokoshkin [1961Zak] and Rudy [1969Rud2]. All investigators, Duwes and Martens [1952Duw], Elliot and Rostoker [1958Ell], Goldschmidt and Band [1961Gol], Pan [1961Pan1, 1961Pan2], Kornilov *et al.* [1963Kor], Guseva [1965Gus] and Rudy [1969Rud2], agreed that NbCr<sub>2</sub> has the cubic Cu<sub>2</sub>Mg-type (C15) structure, but Pan [1961Pan1, 1961Pan2], Kornilov *et al.* [1963Kor] and Guseva [1965Gus] reported a second modification at high temperatures. According to these investigators, the high-temperature form has the hexagonal MgZn<sub>2</sub>-type (C14) structure. In the temperature range between 1585°C and 1625°C, it transforms to the low-temperature cubic form.

### Crystal Structures

Crystal structure data for the phases in the Cr-Nb system are given in Table 2.16.

**Table 2.18. Crystal structure data for phases in Cr-Nb system [1986Van].**

Phase	Homogeneity, at.% Nb	Pearson symbol	Space group	Struktur- bericht designation	Prototype
(Cr)	0 to 6	<i>cI2</i>	<i>Im<math>\bar{3}m</math></i>	A2	W
NbCr <sub>2</sub> (HT)	30 to 39	<i>hP12</i>	<i>P<math>\bar{6}</math>/mmc</i>	C14	MgZn <sub>2</sub>
NbCr <sub>2</sub> (LT)	30 to 39	<i>cF24</i>	<i>Fd<math>\bar{3}m</math></i>	C15	Cu <sub>2</sub> Mg
(Nb)	85 to 100	<i>cI2</i>	<i>Im<math>\bar{3}m</math></i>	A2	W

According to Pan [1961Pan2], the transformation temperature between the high- and low-temperature NbCr<sub>2</sub> forms increases from 1585°C at the Cr-rich limit to 1625°C at the Nb-rich limit of the homogeneity range. Kornilov [1963Kor] observed the NbCr<sub>2</sub> (HT) form in connection with their study of the Cr<sub>2</sub>Ti-Cr<sub>2</sub>Nb isopleth. According to Guseva [1965Gus], the transformation from the high-temperature to the low-temperature modification is very fast. This might be why the high-temperature modification has not been observed by some investigators.

The atomic volume of Nb is approximately 50% larger than that of Cr ( $0.018 \text{ nm}^3$  per atom as compared to  $0.012 \text{ nm}^3$  per atom). For this reason, the lattice parameter of all phases in the Cr-Nb system increase with increasing Nb content [1956Ely, 1958Ere, 1961Gol, 1969Rud2, 1961Zak].

The lattice parameters of the hexagonal  $\text{Cr}_2\text{Nb}$  (HT) phase were reported as  $a = 0.493 \text{ nm}$  and  $c = 0.812 \text{ nm}$  by Pan [1961Pan1]. The average lattice parameter of the cubic  $\text{Cr}_2\text{Nb}$  (LT) phase is  $0.700 \pm 0.003 \text{ nm}$  [1956Ely, 1961Gol, 1969Rud2, 1961Zak, 1952Duw, 1958Ell]. It increases from  $\sim 0.697 \text{ nm}$  on the Cr-rich side to  $\sim 0.702 \text{ nm}$  on the Nb-rich side [1961Gol, 1969Rud2, 1961Zak].

### **2.3 Review of Selected Quaternary Alloys from the Pt-Al-Cr-Ru System**

The first review selected six alloys based on heat treatment, resulting microstructure, hardness and the precipitate volume fraction. All these six alloys had been investigated at Mintek and/or University of the Witwatersrand at one time or another.

The six alloys are listed in the order of decreasing hardness in Table 2.19. Note that for some of the alloys, different workers obtained different hardness values for the same alloys, probably as a result of different heat treatments, especially cooling rates or some other factor, such as slightly different sample compositions. The alloys are ranked according to the highest hardness value obtained.

**Table 2.19. The six selected alloys with hardness values and precipitate volume percent.**

<b>Alloy, at. %</b>	<b>Hardness, HV<sub>10</sub></b>	<b>Precipitate Vol. % &amp; Reference</b>
Pt <sub>84</sub> :Al <sub>11</sub> :Cr <sub>3</sub> :Ru <sub>2</sub>	472±14 [2002Cor] 395±27 [2008Sho] 361±10 [2006Cor]	12±5 [2008Sho]
Pt <sub>85</sub> :Al <sub>11</sub> :Cr <sub>2</sub> :Ru <sub>2</sub>	430±5 [2003Cor, 2002Cor] 403±20 (After 2 <sup>nd</sup> HT) [2002Cor]	
Pt <sub>78</sub> :Al <sub>15.5</sub> :Cr <sub>4.5</sub> :Ru <sub>2</sub>	421±3 [2003Cor] 164±5 [2008Sho] 428±11 [2002Cor]	Precipitates indiscernible [2008Sho]
Pt <sub>82</sub> :Al <sub>12</sub> :Cr <sub>4</sub> :Ru <sub>2</sub>	378±4 [2008Sho]	10±5 [2008Sho]
Pt <sub>80</sub> :Al <sub>14</sub> :Cr <sub>3</sub> :Ru <sub>3</sub>	361±24 [2008Sho]	Precipitates indiscernible [2008Sho]
Pt <sub>78</sub> :Al <sub>11</sub> :Cr <sub>6</sub> :Ru <sub>5</sub>	357±4 [2008Sho]	24±3 [2008Sho]

Each of the alloys is discussed below with respect to heat treatments, microstructure, hardness, precipitation volume percent and any other findings during investigations at Mintek and/or University of the Witwatersrand.

### **2.3.1 Pt<sub>84</sub>:Al<sub>11</sub>:Cr<sub>3</sub>:Ru<sub>2</sub>**

The Pt<sub>84</sub>:Al<sub>11</sub>:Cr<sub>3</sub>:Ru<sub>2</sub> (at. %) alloy was considered as the first optimum in terms of microstructure and hardness [2002Cor, 2005Pri], although a different alloy has now been identified as such [2008Sho]. It has been given at least three different types of heat treatments by different workers. In one, the alloy was heat treated at 1350°C for 96 h [2002Cor]. The alloy was then furnace cooled resulting in a microstructure composed entirely of a fine two-phase mixture without primary ~Pt<sub>3</sub>Al. The heat treatment gave the highest hardness value of HV<sub>10</sub> = 472±14 [2002Cor] compared to all the Pt-Al-Cr-Ru alloys which had been investigated.



Another heat treatment was ageing in air in a muffle furnace at 1250°C for 100 h then water quenching [2006Cor]. The resulting microstructure was similar to the one above i.e. composed entirely of a fine two-phase mixture without primary  $\sim\text{Pt}_3\text{Al}$  and the hardness value was  $\text{HV}_{10} = 361 \pm 10$  [2006Cor]

A third heat treatment was in air in a furnace at 1500°C for 18 h followed by water quenching, then annealing at 1100°C for 12 h then air cooling [2008Sho]. The microstructure had visible rounded precipitates. The hardness value obtained was  $\text{HV}_{10} = 395 \pm 27$  and the precipitate volume percent was  $12 \pm 5\%$ . In a tensile test at room temperature, the alloy had a maximum UTS value of 722 MPa and elongation % was  $\sim 1\%$  [2006Cor].

### **2.3.2 $\text{Pt}_{85}:\text{Al}_{11}:\text{Cr}_2:\text{Ru}_2$**

In terms of microstructure and hardness, the  $\text{Pt}_{85}:\text{Al}_{11}:\text{Cr}_2:\text{Ru}_2$  (at.%) alloy was second best to  $\text{Pt}_{84}:\text{Al}_{11}:\text{Cr}_3:\text{Ru}_2$ . The alloy has also been subjected to three different types of heat treatments. In the first case, heat treatments were conducted at 1150°C, 1250°C, 1350° and 1450°C to verify that microstructure could be optimised. The highest temperature gave the best microstructure and a hardness value of  $\text{HV}_{10} = 430 \pm 5$  [2003Cor].

The second heat treatment was done at 1350°C for 96 h in argon followed by furnace cooling [2002Cor]. The same hardness value of  $\text{HV}_{10} = 430 \pm 5$  was obtained.

There was a third heat treatment carried out to try and improve the microstructure. This was done at 1350°C for 96 h in air. There was no improvement in the microstructure and the hardness value actually decreased to  $\text{HV}_{10} = 403 \pm 20$ . There was some oxidation resulting in loss of Al due to small sample size [2002Cor].

### **2.3.3 $\text{Pt}_{78}:\text{Al}_{15.5}:\text{Cr}_{4.5}:\text{Ru}_2$**

In one of the investigations [2002Süs], the first heat treatment which was also meant for oxidation an test was done at 1350°C for 10 h in air and the microstructure consisted of large areas of  $\sim\text{Pt}_3\text{Al}$  together with a fine mixture of (Pt) and  $\sim\text{Pt}_3\text{Al}$ . A second heat treatment at 1350°C for 96 h in the same investigation was done to try and improve the microstructure. There was no improvement.

In a second investigation, the alloy was heat treated at 1350°C for 96 h followed by furnace cooling [2002Cor]. The microstructure consisted of large areas of  $\sim\text{Pt}_3\text{Al}$  together with a fine mixture of (Pt) and  $\sim\text{Pt}_3\text{Al}$ .

A third investigation conducted heat treatments at 1150°C, 1250°C, 1350°C and 1450°C to verify whether microstructure could be optimised [2003Cor]. The highest temperature gave the best microstructure which was so fine, that it was difficult to discern the two phases. XRD proved the existence of  $\sim\text{Pt}_3\text{Al}$ . The associated hardness value was  $421 \pm 3 \text{ HV}_{10}$ .

A fourth investigation, conducted heat treatment in air in a furnace at 1500°C for 18 h followed by water quenching, then annealing at 1100°C for 12 h then air cooling [2008Sho]. The resulting microstructure consisted of fine precipitates which was difficult to discern in the HR-SEM. The associated hardness value was  $164 \pm 5 \text{ HV}_{10}$ .

#### **2.3.4 $\text{Pt}_{82}:\text{Al}_{12}:\text{Cr}_4:\text{Ru}_2$**

In the first attempt to improve the microstructure of the  $\text{Pt}_{82}:\text{Al}_{12}:\text{Cr}_4:\text{Ru}_2$  (at.%) alloy, it was heat treated in air in a furnace at 1500°C for 18 h followed by water quenching, then annealing at 1100°C for 12 h finally air cooling. This resulted in a microstructure which had rounded fine precipitate of  $\sim\text{Pt}_3\text{Al}$  in a matrix of (Pt) (Figure 2.15(a)) [2008Sho]. However the SEM-BSE image was unclear. The alloy had a hardness value of  $\text{HV}_{10} = 378 \pm 4$  with a precipitate volume percent of  $10 \pm 5\%$ . The same alloy was later electrolytically etched in HCl/NaCl solution and a microstructure having a eutectic as well as the fine precipitates of  $\sim\text{Pt}_3\text{Al}$  in (Pt) was revealed (Figure 2.15(b)) [2012Ode1].

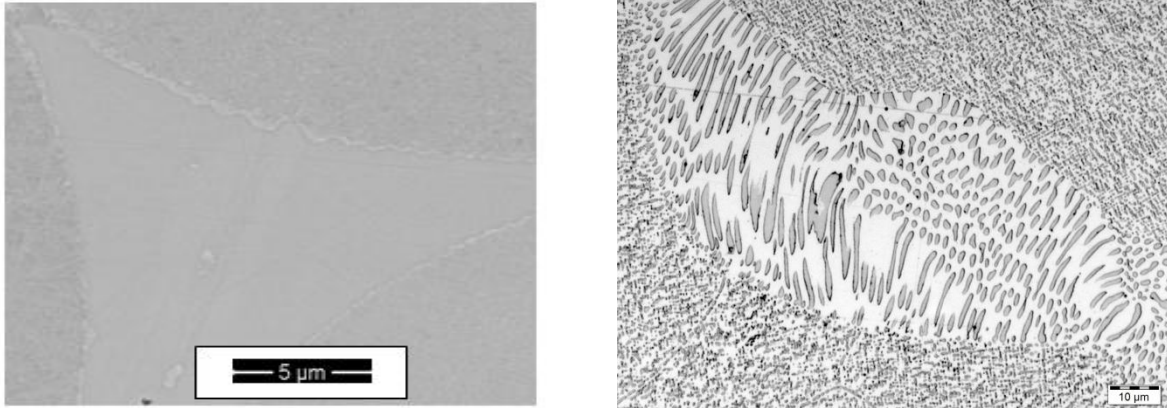


**Figure 2.18 (a).** SEM-BSE image of unetched, annealed  $\text{Pt}_{82}\text{:Al}_{12}\text{:Cr}_4\text{:Ru}_2$  (at.%), showing  $\sim\text{Pt}_3\text{Al}$  precipitates in light (Pt) matrix [2008Sho], (b). Optical microscope image of annealed  $\text{Pt}_{82}\text{:Al}_{12}\text{:Cr}_4\text{:Ru}_2$  (at.%) after electrolytic etching in HCl/NaCl solution, showing  $\sim\text{Pt}_3\text{Al}$  precipitates in light (Pt) matrix as well as a eutectic. The scale is 10  $\mu\text{m}$ . [2012Ode1].

In a second attempt at microstructure improvement, the alloy was homogenised in air in a Lenton muffle furnace at 1500°C for 18 hours and quenched in water, followed by a heat treatment at 1100°C for 120 hours then air cooled. This resulted in a more improved microstructure shown in the TEM micrograph (Figure 2.16) [2012Sho]. The structure and the precipitate volume fraction (estimated using a grid at  $\sim 70\%$ ) was very similar to that of commercial Ni-based superalloys. This alloy was selected as the basis for higher order alloys with results reported in Chapter 6 of this thesis.

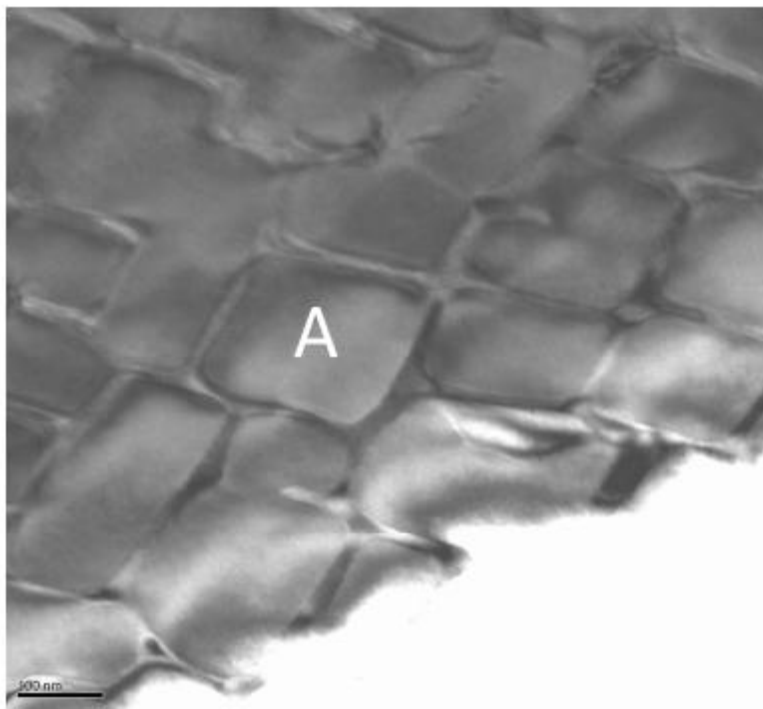


**Figure 2.19. TEM micrograph for nominal  $\text{Pt}_{82}\text{Al}_{12}\text{Cr}_4\text{Ru}_2$  (at.%) showing  $\sim\text{Pt}_3\text{Al}$  (marked A) with channels of (Pt) matrix [2012Sho].**

### 2.3.5 $\text{Pt}_{80}\text{Al}_{14}\text{Cr}_3\text{Ru}_3$

The  $\text{Pt}_{80}\text{Al}_{14}\text{Cr}_3\text{Ru}_3$  (at.%) alloy has also been subjected to several investigations. In one investigation, it was found that the microstructure contained no primary  $\text{L}_{12}$  phase [2001Hil3]. Some precipitates were cuboid, while others had a more irregular morphology. Some had a four clover type or ogdoadically-diced cubes [1958Wes]. There was a bi-modal size distribution with the larger precipitates being 120 to 500nm and the smaller ones a few nm to 70nm. The smaller precipitates had similar morphology to the larger precipitates. The alloy had the best oxidation resistance at that time [2001Hil3].

In an investigation of the oxidation resistance of this alloy in comparison with a ternary alloy, it was observed that there was no transient internal discontinuous oxidation as observed in the ternary alloy  $\text{Pt}_{86}\text{Al}_{10}\text{Cr}_4$  [2001Süs2]. However, subsequently the authors surmised that the alloy could possibly experience severe oxidation in the long term [2002Süs].

In another investigation, the alloy was heat treated in air in a furnace at 1500°C for 18 h followed by water quenching, then annealed at 1100°C for 12 h and finally air cooled [2008Sho]. The

resulting microstructure had fine precipitates which was difficult to discern in the HR-SEM. A Vickers hardness of  $HV_{10} = 361 \pm 24$  was measured, but the precipitate volume percent could not be determined because of the unresolvable precipitates.

### **2.3.6 Pt<sub>78</sub>:Al<sub>11</sub>:Cr<sub>6</sub>:Ru<sub>5</sub>**

The Pt<sub>78</sub>:Al<sub>11</sub>:Cr<sub>6</sub>:Ru<sub>5</sub> (at.%) alloy was recommended as having optimum properties in terms of microstructure, hardness and precipitate volume percent by Shongwe [2008Sho]. It was heat treated in air in a furnace at 1500°C for 18 h followed by water quenching, then annealing at 1100°C for 12 h then air cooling. The resulting microstructure was two-phase, a hardness value of  $HV_{10} = 357 \pm 4$  was measured and the precipitate volume percent was given as  $24 \pm 3\%$ .

## CHAPTER 3: EXPERIMENTAL PROCEDURE

Alloy buttons weighing ~2g each were prepared from four different alloy systems, Pt-Al-V, Pt-Cr-V, Pt-Al-Cr-Ru-V and Pt-Al-Cr-Ru-V-Nb. All the elemental components were of 99.9% purity, except for V which was of 99.6% purity. Each of the alloys was named with respect to its average overall composition in at.%. The samples were manufactured by arc-melting under argon, on a water-cooled copper hearth. Each button was turned over and re-melted three times in an attempt at achieving homogeneity. Titanium was melted in the middle of the copper hearth as an oxygen-getter. There were losses during melting but Pt-Al-V and Pt-Cr-V samples had elemental losses  $\leq 5$  at.% and this was acceptable. However, Ru and Nb losses in the higher order alloys were unacceptably high and efforts should be made to contain these losses in any future work as recommended at the end of the thesis. Nb has a history of big losses during melting [2009Cor].

Each of the samples was halved using a ceramic blade mounted in a Struers Secotom-10 cutting machine. The spindle speed was 3500 rpm and a feed rate of 0.5 m/s was used. One half of each sample was prepared for metallographic examination, in the as-cast condition, by grinding on silicon carbide down to 1200 grit and diamond polishing down to 1 micron. The final polishing was by oxide polishing system (OP-S), by which polishing is achieved through a combination of chemical treatment (the solution has a pH of 8) and gentle abrasive action. It allows selective polishing of softer phases and in many cases subsequent etching was not necessary if the sample was to be analysed using scanning electron microscopy. However, in some cases where the average atomic number for phases in a sample was nearly equal, it became difficult to distinguish between the phases and etching was necessary.

The other halves of the samples were placed in silica glass tubes, 16mm diameter. The glass tubes were then made into vacuum ampoules by evacuating air and sealing while the vacuum pump was running. The ampoules with the samples were placed in a tube furnace and annealed at 1000°C for 1500 hours. Quenching was done by removing the glass ampoules from the

furnace, dropping in water and breaking the glass, as quickly as possible in order to retain the phases existing at 1000°C. The samples were then prepared for metallographic examination in the same way as the as-cast samples.

The microstructures of all the alloys were analysed using a scanning electron microscope (SEM) model HR-NovaNano SEM200 at Mintek. Imaging in all the analyses was done using the backscattered electron (BSE) mode, while overall and phase compositions were determined by energy dispersive X-ray spectroscopy (EDX). Often, it was difficult to discern between some of the phases, even in backscattered electron mode because of the similarity in average atomic number of these phases. There was also the concern that orientation and different electron channelling would also change the contrast [2008Cor], so the morphology of the phases was also used to differentiate them. Since the interaction volume generating the X-rays can be as much as 3  $\mu\text{m}$  across and deep (especially for higher atomic number elements), the analyses for smaller regions than this are for an indication only. Usually, an accuracy of  $\pm 1$  at.% would be expected for this technique. Spot analyses were used on single phases and areal analyses on two-phase regions. The compositions of each phase and overall were determined by taking EDX readings from at least five different areas and reporting the average and the standard deviation.

X-ray diffraction (XRD) was used to confirm the phase identities. A Bruker D2 Phaser Diffractometer with a generator setting of 30 kV and 10 mA was used for all the samples. The analyses on most samples were done using Cu K $\alpha$  radiation of wavelength 1.54 Å. A few of the samples were done using Co K $\alpha$  radiation of wavelength 1.79 Å. The reference database in all the analyses was International Centre for Diffraction Data (ICDD) Powder Diffraction File, PDF-2, Release 2002. All the samples were polished.

Microhardness tests were performed after etching. The specimens were ground on silicon carbide down to 1200 grit and then diamond polished down to 1  $\mu\text{m}$ . The samples were then etched in a solution of 10 g NaCl in 100 cm<sup>3</sup> HCl (32% vol. concentration). Etching was done in a fume cupboard using a DC power supply, and a voltage range of 9V to 12V gave adequate results. The current density in the electrolyte was  $\sim 100 \text{ A.m}^{-2}$ . The counter electrode was a stainless steel wire suspended in the electrolyte solution [2012Ode1].

The hardness of the alloys was measured using a Vickers microhardness tester with a load of 300 g. At least five measurements were carried out to obtain an average hardness value.



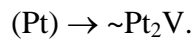
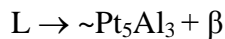
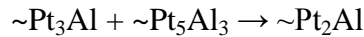
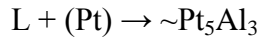
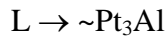
## CHAPTER 4: Pt-Al-V ALLOYS

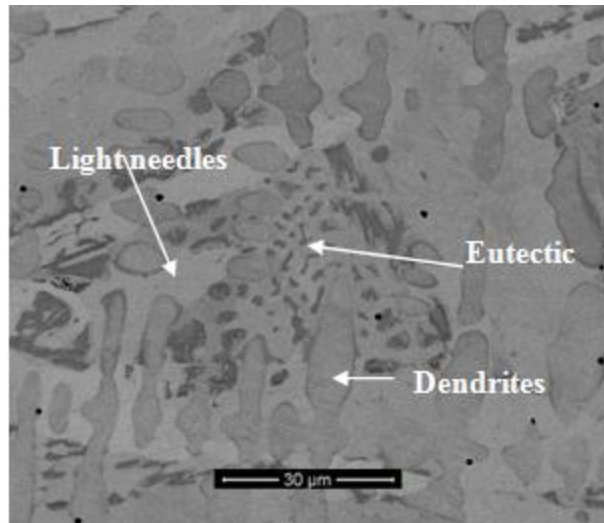
### 4.1 AS-CAST ALLOYS

#### 4.1.1 As-cast Alloy 1, Average Composition $\text{Pt}_{64.3}:\text{Al}_{26.6}:\text{V}_{9.1}$ (at.%)

Figure 4.1 shows the microstructure of the as-cast Alloy 1. It consisted of medium grey dendrites having a dark thin layer around them, light needles, and a eutectic comprising the light phase and a barely resolveable two phase dark region. The compositions of these phases are shown in Table 4.1 and plotted in Figure 4.2. The medium grey dendrites were identified as  $\sim\text{Pt}_3\text{Al}$  (from the EDX plot and the identification by XRD) and the light needles were identified as  $\sim\text{Pt}_5\text{Al}_3$ . The thin dark layer on the dendrites was identified as  $\sim\text{Pt}_2\text{V}$ . XRD confirmed the identities of these phases (Figure 4.3).

Solidification started with the  $\sim\text{Pt}_3\text{Al}$  dendrites, followed by peritectic formation of (Pt). There was a second peritectic reaction between the liquid and (Pt) resulting in  $\sim\text{Pt}_5\text{Al}_3$ , which went on to solidify on its own. A peritectoid reaction followed with the formation of  $\sim\text{Pt}_2\text{Al}$ . The next reaction was a eutectic forming  $\beta + \sim\text{Pt}_5\text{Al}_3$  and the  $\beta$  decomposed eutectoidally to form  $\sim\text{PtAl} + \sim\text{Pt}_5\text{Al}_3$  [1990Mas]. The (Pt) which remained as a thin layer, on  $\sim\text{Pt}_3\text{Al}$ , finally ordered to  $\sim\text{Pt}_2\text{V}$ . The reactions sequence during solidification and cooling were:

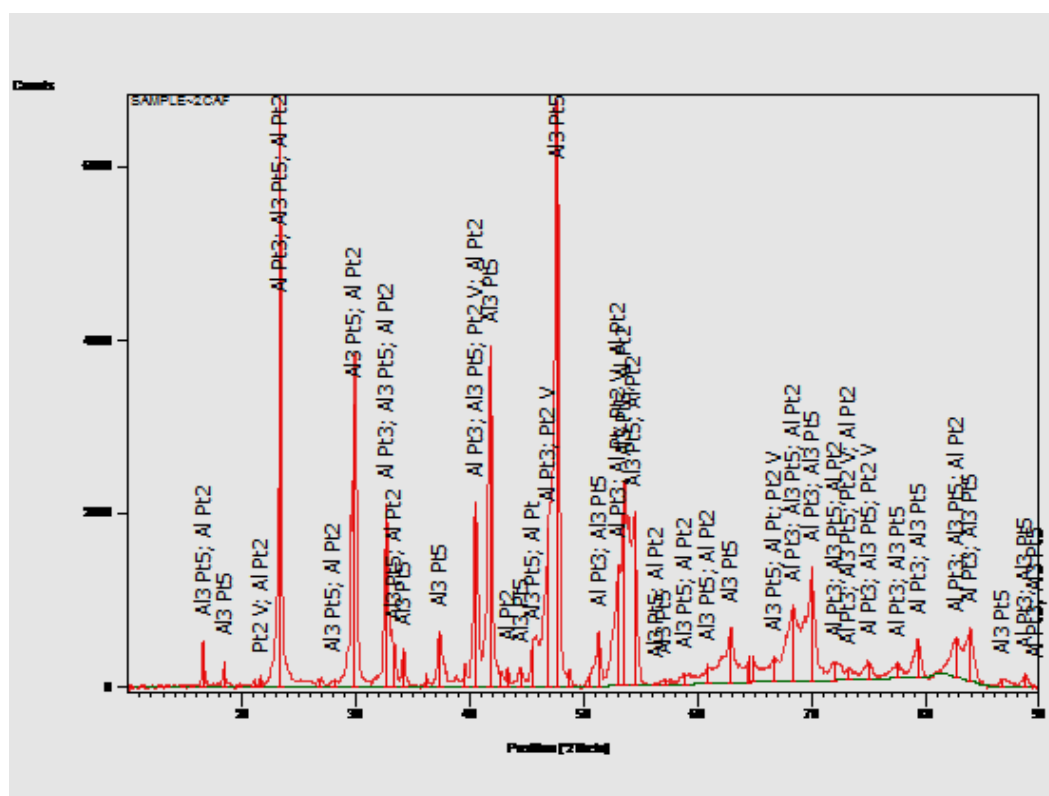
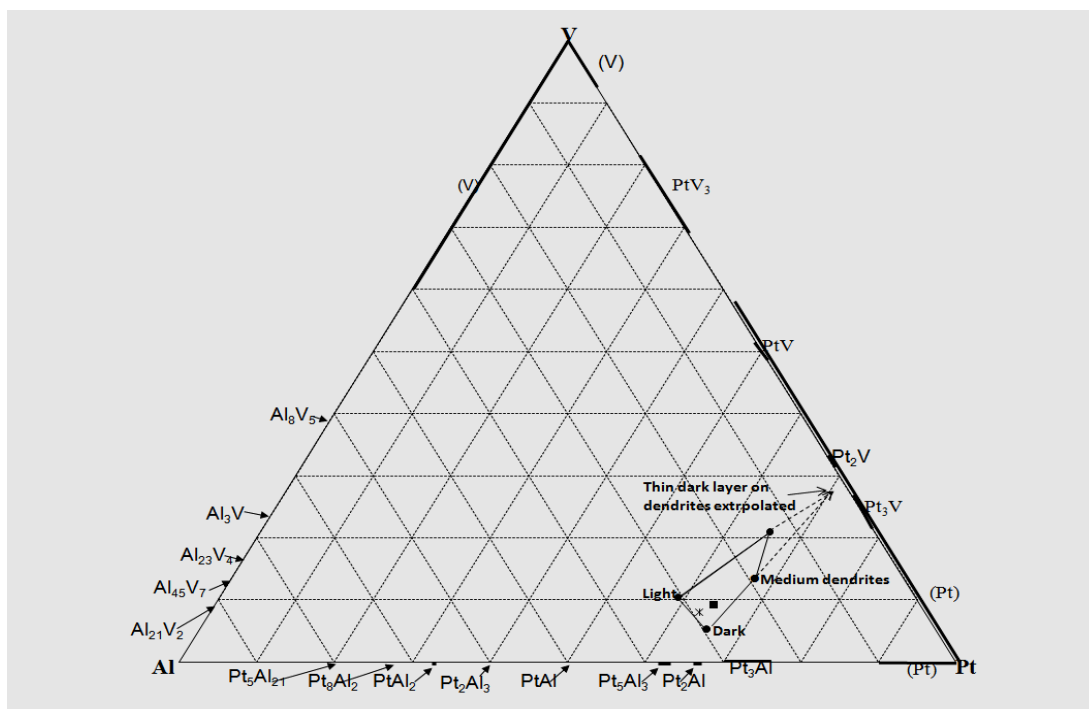




**Figure 4.1. SEM-BSE image of as-cast Alloy 1 showing medium contrast dendrites ( $\sim\text{Pt}_3\text{Al}$ ) with a dark thin layer ( $\sim\text{Pt}_2\text{V}$ ), light needles ( $\sim\text{Pt}_5\text{Al}_3$ ), and a eutectic.**

**Table 4.1. Overall and phase compositions of Alloy 1, average composition  $\text{Pt}_{64.3}:\text{Al}_{26.6}:\text{V}_{9.1}$  (at.%) determined by EDX.**

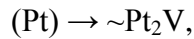
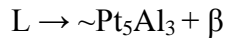
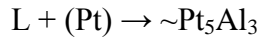
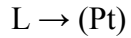
Appearance	Pt	Al	V	Phases
Overall	64.3±0.7	26.6±0.8	9.1±0.4	-
Medium dendrites	67.3±0.6	18.7±0.6	14.0±0.5	$\sim\text{Pt}_3\text{Al}$
Light needles	65.3±0.4	29.4±0.8	5.3±0.5	$\sim\text{Pt}_5\text{Al}_3$
Dark	59.0±1.2	30.7±1.1	10.3±0.4	$\sim\text{Pt}_2\text{Al}$
Thin layer on dendrites	65.5±0.9	13.6±1.1	20.9±1.2	$\sim\text{Pt}_2\text{V}$
Eutectic overall	63.0±0.3	29.0±0.7	8.0±0.5	$\sim\text{PtAl} + \sim\text{Pt}_5\text{Al}_3$



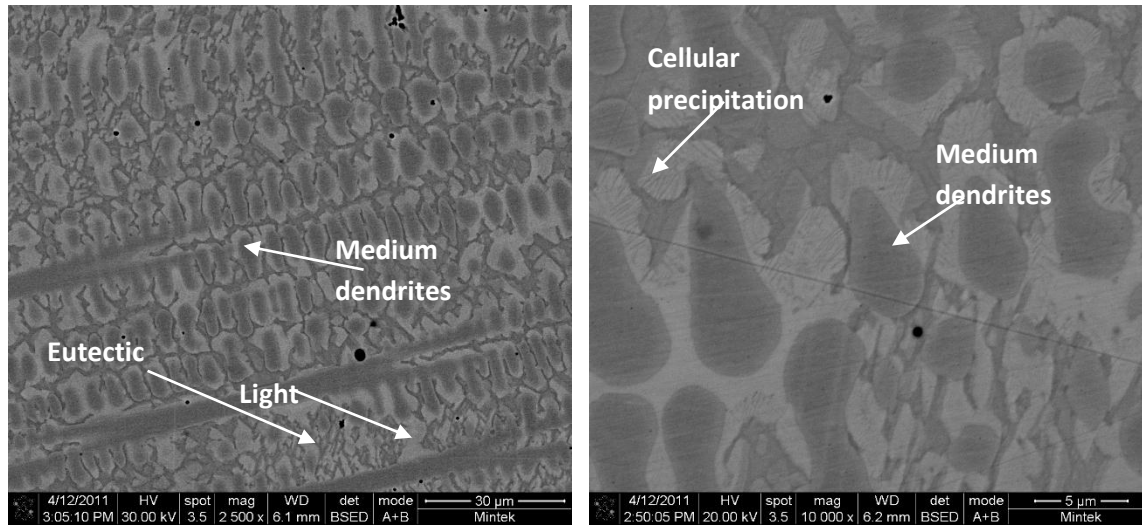
#### 4.1.2 As-cast Alloy 2, Average Composition $\text{Pt}_{59.1}:\text{Al}_{23.1}:\text{V}_{17.8}$ (at.%)

Figure 4.4 shows the microstructure of the as-cast Alloy 2 at different magnifications. There were medium grey dendrites, a light phase surrounding the medium dendrites also appearing dendritic and a complex eutectic. When the compositions of these phases in Table 4.2 were plotted as in Figure 4.5, the medium grey dendrites were identified as  $\sim\text{Pt}_2\text{V}$ , the light phase was identified as  $\sim\text{Pt}_5\text{Al}_3$ , while the dark component of the eutectic was identified as  $\sim\text{PtAl}$ , although the small areas were likely to be affected by the nearby  $\sim\text{Pt}_2\text{V}$  and  $\sim\text{Pt}_5\text{Al}_3$ . XRD confirmed the identities of  $\sim\text{Pt}_2\text{V}$  and  $\sim\text{Pt}_5\text{Al}_3$  and  $\sim\text{PtAl}$ . Solidification started with (Pt). This was followed by a peritectic reaction between the (Pt) and the liquid, resulting in  $\sim\text{Pt}_5\text{Al}_3$ . Then there was a eutectic reaction with the liquid forming  $\sim\text{Pt}_5\text{Al}_3$  and  $\beta$ , and  $\beta$  decomposed at high temperature to form  $\text{PtAl} + \sim\text{Pt}_5\text{Al}_3$  [1990Mas]. The (Pt) dendrites ordered to  $\sim\text{Pt}_2\text{V}$  (identified by unique peaks of those phases amongst the common peaks) (Figure 4.6). There was also a solid state cellular precipitation of  $\sim\text{PtAl}$  in  $\sim\text{Pt}_5\text{Al}_3$  phase, even though these phases were too fine to analyse accurately using SEM-EDX.

The proposed solidification sequence and reactions are:



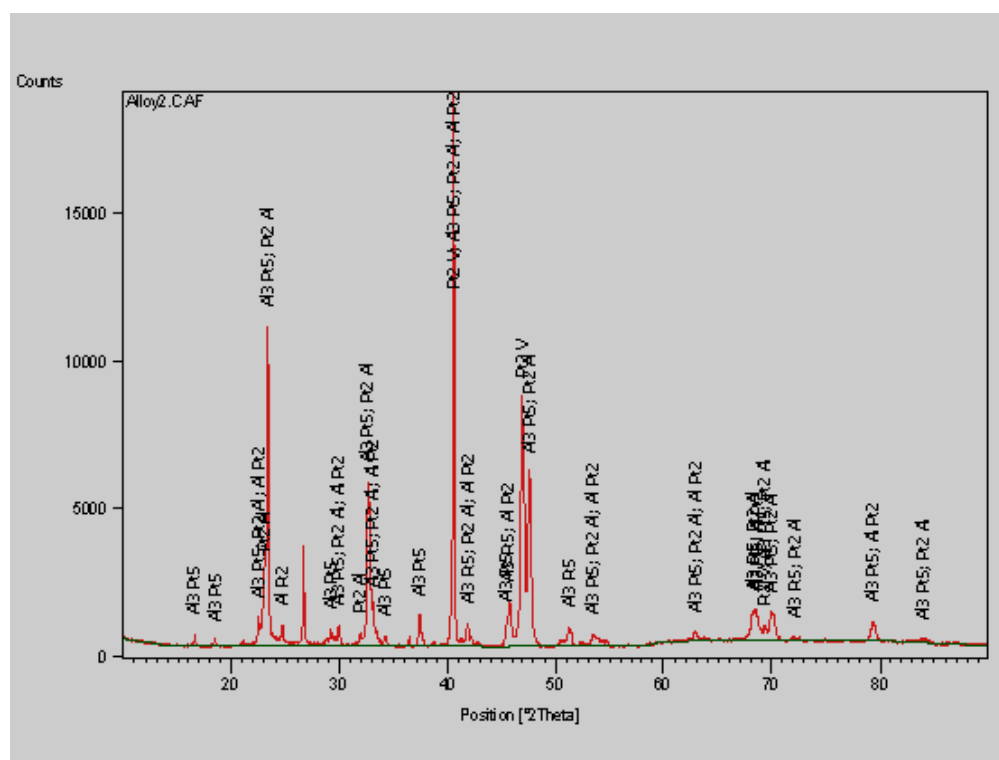
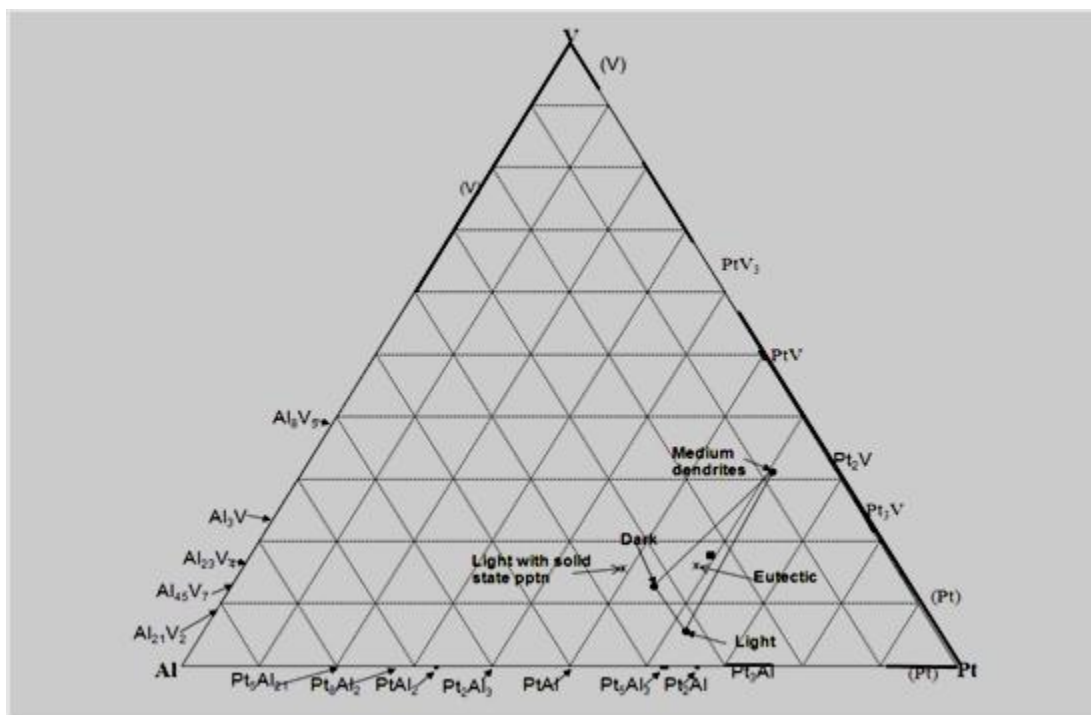
with solid state (cellular) precipitation of  $\sim\text{PtAl}$  in the light  $\sim\text{Pt}_5\text{Al}_3$  phase.



**Figure 4.4 (a).** SEM-BSE image of Alloy 2 showing medium grey dendrites (~Pt<sub>2</sub>V), a light phase (~Pt<sub>5</sub>Al<sub>3</sub>), and a eutectic (~PtAl + ~Pt<sub>5</sub>Al<sub>3</sub>), (b). SEM-BSE image of Alloy 2 showing medium grey dendrites (~Pt<sub>2</sub>V), a light phase (~Pt<sub>5</sub>Al<sub>3</sub>) and the cellular precipitation (~PtAl).

**Table 4.2. Overall and phase compositions of Alloy 2, average composition Pt<sub>59.1</sub>:Al<sub>23.1</sub>:V<sub>17.8</sub> (at.%) determined by EDX.**

Appearance	Pt	Al	V	Phases
Overall	59.1±0.3	23.1±0.4	17.8±0.1	-
Medium dendrites	60.5±0.4	8.3±0.4	31.2±0.4	~Pt <sub>2</sub> V
Light phase	62.0±0.3	32.3±0.3	5.7±0.5	~Pt <sub>5</sub> Al <sub>3</sub>
Light phase with pptn.	49.0±1.9	35.3±5.8	15.7±5.5	~Pt <sub>5</sub> Al <sub>3</sub> with ~PtAl pptn.
Eutectic	58.2±0.4	25.7±1.2	16.1±1.0	~Pt <sub>5</sub> Al <sub>3</sub> + β
Dark eutectic component (2-phase)	54.3±1.7	32.8±1.9	12.9±0.9	~PtAl + ~Pt <sub>5</sub> Al <sub>3</sub>



#### 4.1.3 As-cast Alloy 3, Average Composition $\text{Pt}_{57.3}:\text{Al}_{6.7}:\text{V}_{26}$ (at.%)

Figure 4.7 shows the microstructure of as-cast Alloy 3, average composition  $\text{Pt}_{57.3}:\text{Al}_{6.7}:\text{V}_{26}$  (at.%,) at two different magnifications. There were dark dendrites, a light phase and a dark phase in between the dendrites. When the compositions of the phases in Table 4.3 were plotted as in Figure 4.8, the dendrites were identified as  $\sim\text{Pt}_3\text{V}$  and the light phase was identified as  $\sim\text{Pt}_3\text{Al}$ . The dark phase was identified as  $\sim\text{Pt}_2\text{Al}$  which formed peritectoidally at high temperature from  $\sim\text{Pt}_5\text{Al}_3$  and  $\sim\text{Pt}_3\text{Al}$ . It is assumed that any  $\sim\text{Pt}_5\text{Al}_3$  which had formed had been consumed. Solidification started with (Pt) from the liquid, followed by a transition reaction between the liquid and the (Pt), resulting in a sparse eutectic-like structure with the dark component  $\sim\text{Pt}_2\text{Al}$  in the light  $\sim\text{Pt}_3\text{Al}$ . The final reaction was (Pt) transforming to  $\sim\text{Pt}_3\text{V}$ . XRD confirmed the phase identification as shown in Figure 4.9.

The proposed solidification sequence and reactions are:

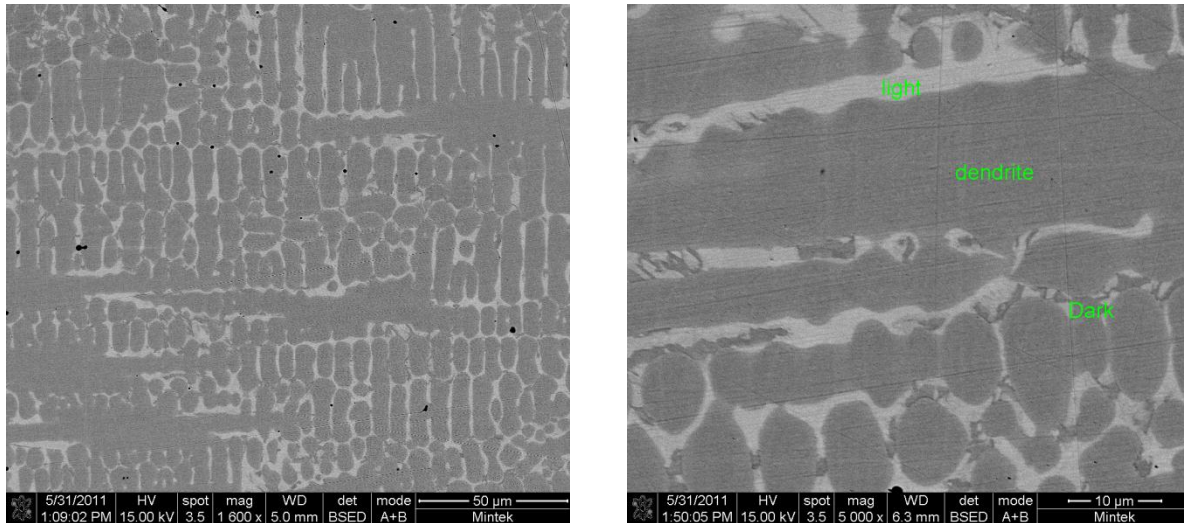
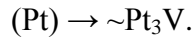
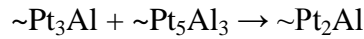
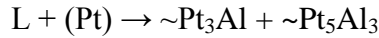
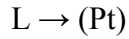


**Figure 4.7. (a). SEM-BSE image of as-cast Alloy 3,  $\text{Pt}_{57.3}:\text{Al}_{6.7}:\text{V}_{26}$  (at.%), showing dendrites ( $\sim\text{Pt}_3\text{V}$ ) and a light phase ( $\sim\text{Pt}_3\text{Al}$ ) and (b). SEM-BSE image of as-cast Alloy  $\text{Pt}_{57.3}:\text{Al}_{6.7}:\text{V}_{26}$  (at.%) dendrites ( $\sim\text{Pt}_3\text{V}$ ), a light phase ( $\sim\text{Pt}_3\text{Al}$ ) and a dark phase ( $\sim\text{Pt}_2\text{Al}$ ) in between the dendrites.**

**Table 4.3. Overall and phase compositions of Alloy 3, average composition Pt<sub>69.3</sub>Al<sub>9.6</sub>V<sub>21.1</sub> (at.%) as determined by EDX.**

Appearance	Pt	Al	V	Phases
Overall	69.3±1.2	9.6±1.0	21.1±1.1	-
Dendrites	69.9±1.3	4.9±1.3	25.2±0.6	~Pt <sub>3</sub> V
Light phase	69.8±0.4	25.5±0.6	4.7±0.6	~Pt <sub>3</sub> Al
Dark	62.8±1.3	27.9±1.2	9.3±0.4	~Pt <sub>2</sub> Al

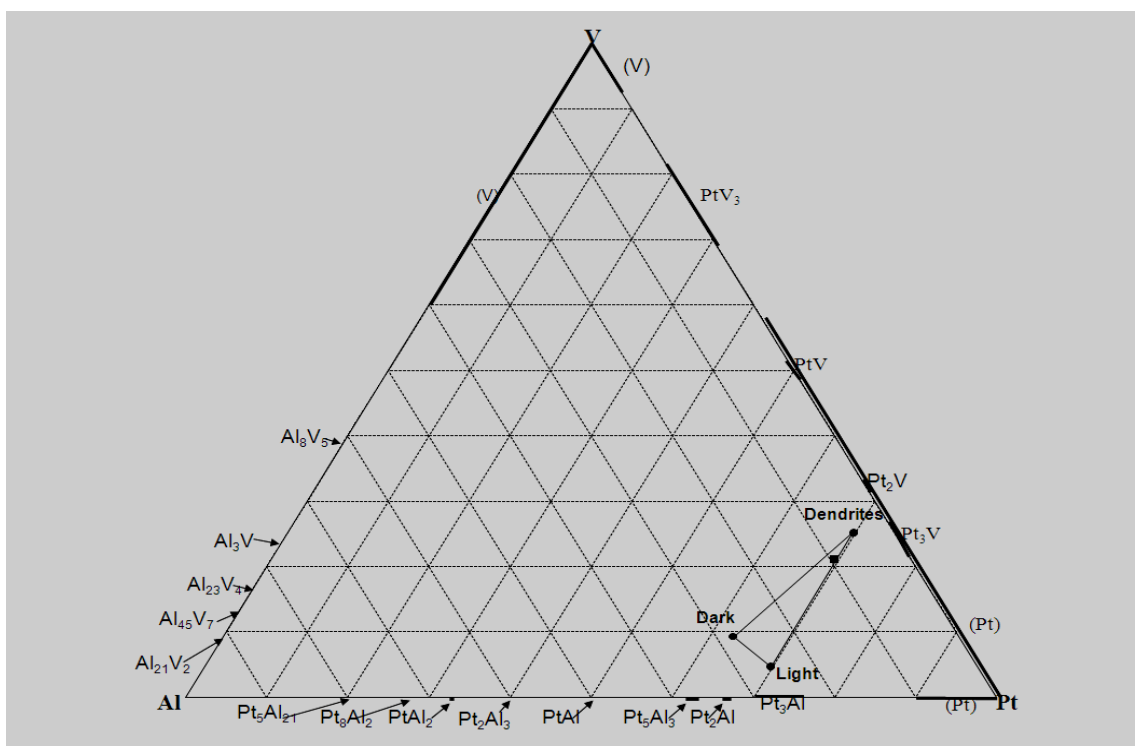


**Figure 4.8. Plot of overall and phase compositions of as-cast Alloy 3, average composition  $\text{Pt}_{57.3}\text{Al}_{6.7}\text{V}_{26}$  (at. %).**





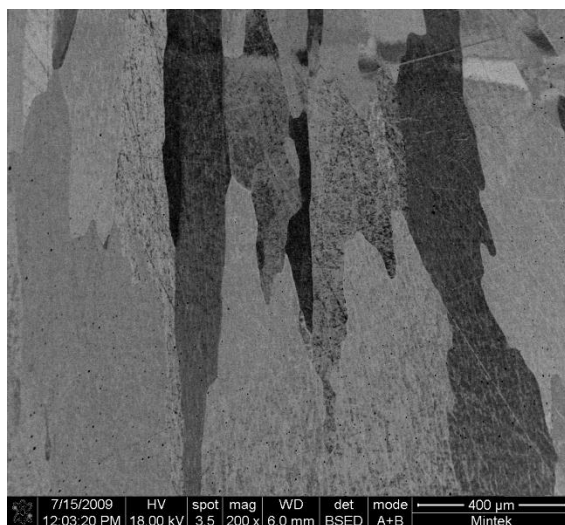


**Figure 4.10. SEM-BSE image of as-cast Alloy 4A, average composition  $\text{Pt}_{76.2}\text{Al}_{17.4}\text{V}_{6.4}$  (at.%), showing a single phase ( $\sim\text{Pt}_3\text{Al}$ ) with grains at different orientations.**

**Table 4.4. Compositions of Alloy 4A, average composition  $\text{Pt}_{76.2}\text{Al}_{17.4}\text{V}_{6.4}$  (at.%) determined by EDX.**

Appearance	Pt	Al	V	Phases
Overall	76.2	17.4	6.4	-
Dark	$75.3 \pm 0.1$	$18.9 \pm 3.7$	$5.8 \pm 2.7$	$\sim\text{Pt}_3\text{Al}$
Medium	$76.4 \pm 0.3$	$16.6 \pm 1.0$	$7.0 \pm 0.9$	$\sim\text{Pt}_3\text{Al}$
Light phase	$75.6 \pm 0.1$	$17.6 \pm 1.5$	$6.8 \pm 1.6$	$\sim\text{Pt}_3\text{Al}$

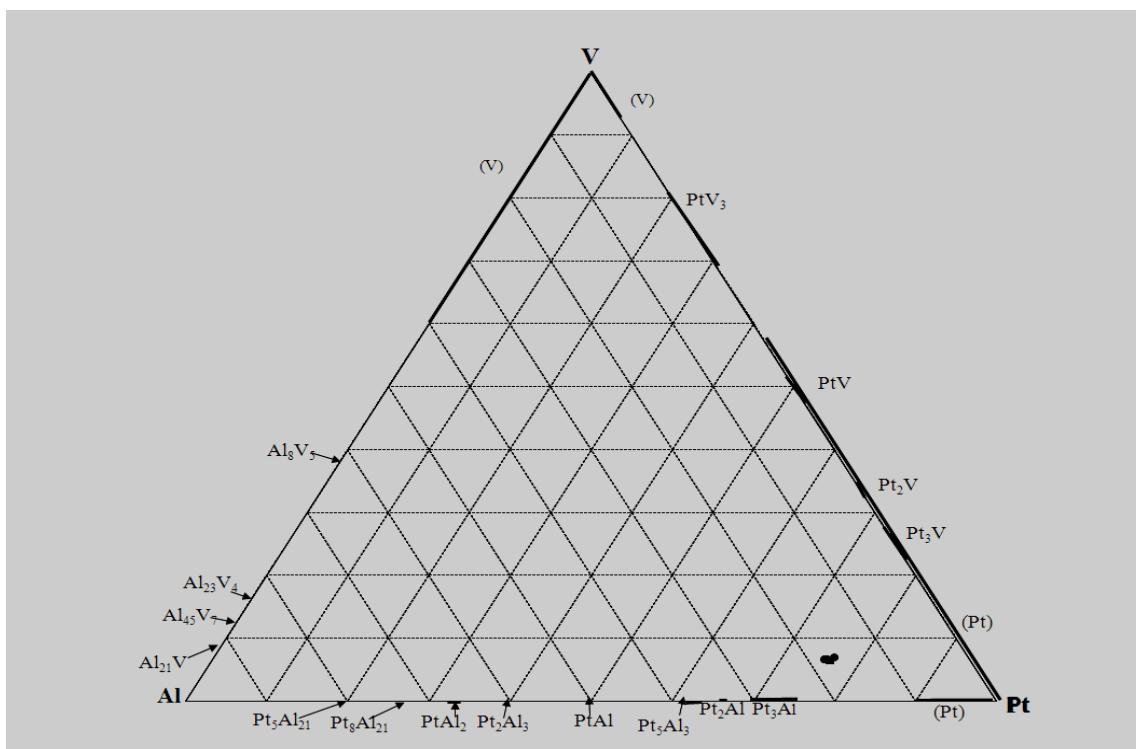
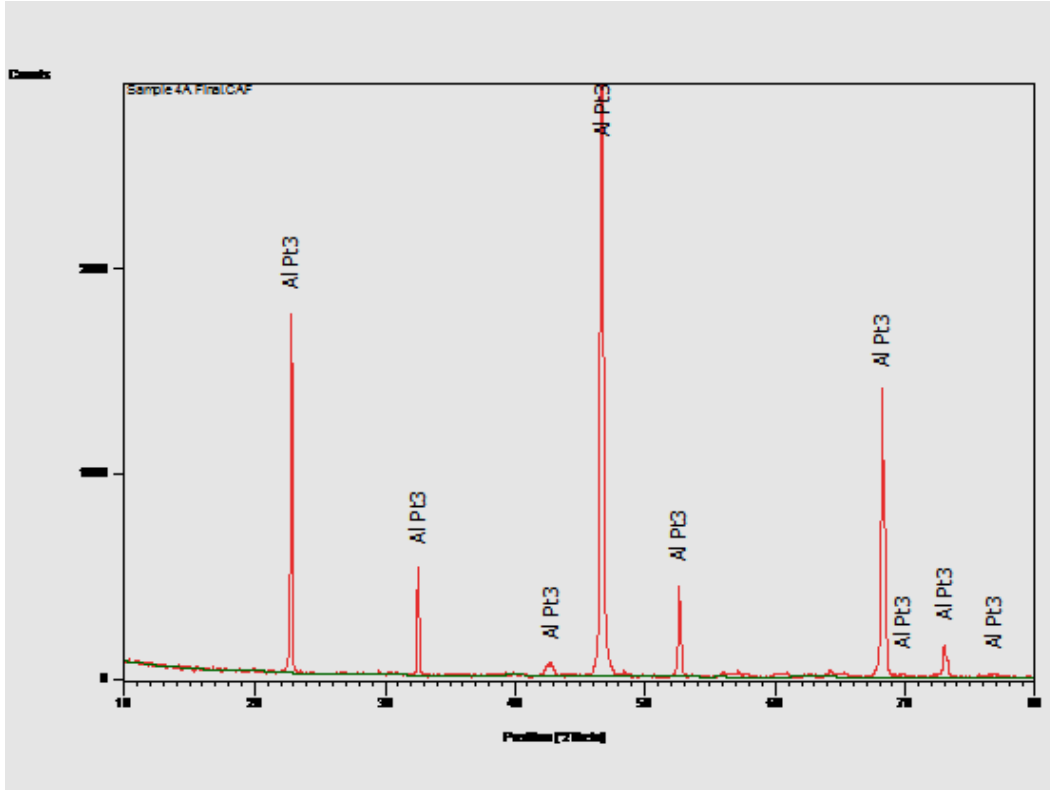


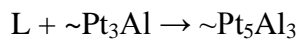
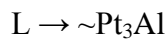
Figure 4.11. Plot of composition of as-cast Alloy 4A, average composition  $\text{Pt}_{76.2}\text{Al}_{17.4}\text{V}_{6.4}$



**Figure 4.12. XRD pattern of as-cast Alloy 4A, average overall composition  $\text{Pt}_{76.2}\text{Al}_{17.4}\text{V}_{6.4}$  (at.%).**

#### **4.1.5 As-cast Alloy 4B, Average Composition $\text{Pt}_{69.8}\text{Al}_{22.3}\text{V}_{7.9}$ (at.%)**

Alloy 4B had the same nominal composition as Alloy 4A, but a different average composition. Figure 4.13 is an SEM-BSE image of the microstructure of as-cast Alloy 4B showing light and medium contrast dendrites with a thin dark contrast phase. Since the average atomic numbers of the phases were similar, the contrast between them was low, giving a poor image. Both the light and medium grey phases were identified as  $\sim\text{Pt}_3\text{Al}$ , from the close compositions and the same dendritic morphology, while the thin dark grey phase was identified as  $\sim\text{Pt}_2\text{Al}$  from the composition. The compositions in Table 4.5 are plotted in Figure 4.14. XRD confirmed the phase identification (Figure 4.15). Solidification started with  $\sim\text{Pt}_3\text{Al}$ , followed by a peritectic formation of a thin layer of  $\sim\text{Pt}_5\text{Al}_3$  which subsequently reacted peritectoidally with  $\sim\text{Pt}_3\text{Al}$  to form  $\sim\text{Pt}_2\text{Al}$ . The proposed solidification sequence and reactions are:



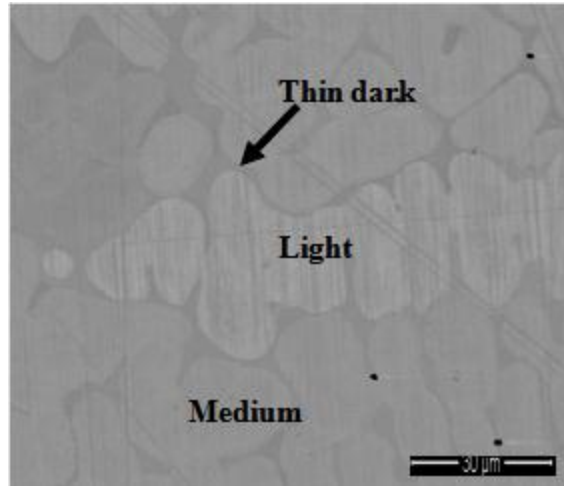
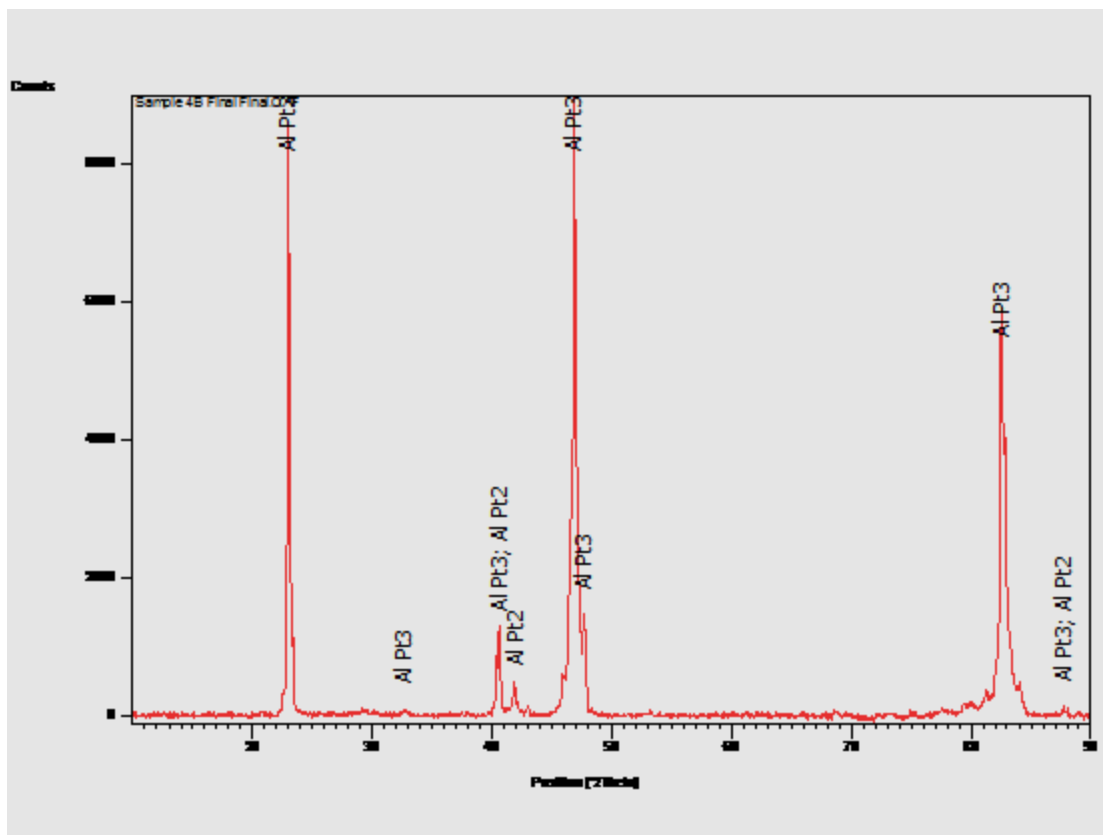


**Figure 4.13.** SEM-BSE image of as-cast Alloy 4B, average composition  $\text{Pt}_{69.8}\text{Al}_{22.3}\text{V}_{7.9}$  (at.%), showing a light grey phase ( $\sim\text{Pt}_3\text{Al}$ ), a medium grey phase ( $\sim\text{Pt}_3\text{Al}$ ) and a thin dark grey phase ( $\sim\text{Pt}_2\text{Al}$ ). The scale bar is 30  $\mu\text{m}$ .

**Table 4.5.** EDX composition analysis data of Alloy 4B, average composition  $\text{Pt}_{69.8}\text{Al}_{22.3}\text{V}_{7.9}$  (at.%).

Appearance	Pt	Al	V	Phases
Overall	$69.8 \pm 0.5$	$22.3 \pm 0.5$	$7.9 \pm 0.5$	-
Light	$70.6 \pm 0.3$	$21.2 \pm 0.1$	$8.2 \pm 0.2$	$\sim\text{Pt}_3\text{Al}$
Medium	$72.2 \pm 1.1$	$18.7 \pm 0.9$	$9.1 \pm 0.4$	$\sim\text{Pt}_3\text{Al}$
Thin dark	$65.8 \pm 0.2$	$30.4 \pm 0.2$	$3.8 \pm 0.3$	$\sim\text{Pt}_2\text{Al}$

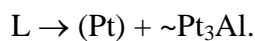
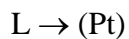




**Figure 4.15. XRD pattern of Alloy 4B, average composition  $\text{Pt}_{69.8}:\text{Al}_{22.3}:\text{V}_{7.9}$  (at.%).**

#### **4.1.6 As-cast Alloy 10, Average Composition $\text{Pt}_{83.9}:\text{Al}_{6.0}:\text{V}_{10.1}$ (at.%)**

Figure 4.16 is an SEM-BSE image of the microstructure of as-cast Alloy 10, average composition  $\text{Pt}_{83.9}:\text{Al}_{6.0}:\text{V}_{10.1}$  (at.%), showing a medium contrast phase which was identified as (Pt) and a fine eutectic. The existence of the eutectic was confirmed after it coarsened during heat treatment for 1500 h at 1000°C (Section 4.2.5). The eutectic and its components were too small to be accurately analysed by EDX, thus the large error. The compositions in Table 4.6 were plotted in Figure 4.17 and the second phase in the eutectic ( $\sim\text{Pt}_3\text{Al}$ ) was identified by extrapolation. XRD confirmed the presence of (Pt) and  $\sim\text{Pt}_3\text{Al}$  (Figure 4.18). The alloy solidified and cooled with the following reactions:



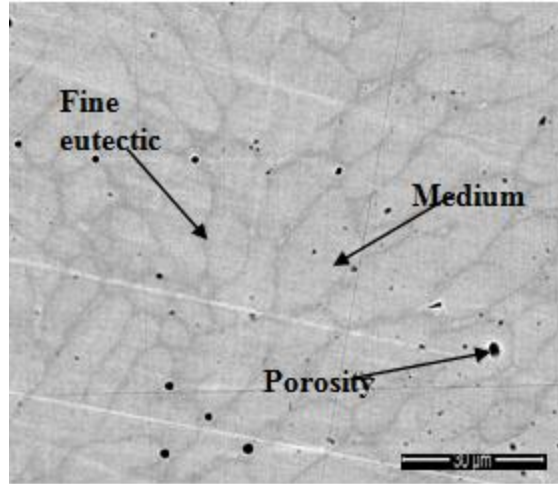


**Figure 4.16.** SEM-BSE image of as-cast Alloy 10, average composition  $\text{Pt}_{83.9}\text{Al}_6\text{V}_{10.1}$  (at.%), showing a medium grey phase (Pt), a fine eutectic ((Pt) +  $\sim\text{Pt}_3\text{Al}$ ) and porosity dark spots, scale bar is 30  $\mu\text{m}$ .

**Table 4.6.** Compositions of as-cast Alloy 10, average composition  $\text{Pt}_{83.9}\text{Al}_6\text{V}_{10.1}$  (at.%) as determined by EDX.

Appearance	Pt	Al	V	Phases
Overall	$83.9 \pm 0.3$	$6.0 \pm 0.3$	$10.1 \pm 0.3$	-
Medium	$88.5 \pm 0.4$	$3.2 \pm 0.51$	$8.3 \pm 0.3$	(Pt)
Eutectic	$78.1 \pm 7.2$	$12.1 \pm 2.1$	$9.8 \pm 5.6$	(Pt) + $\text{Pt}_3\text{Al}$



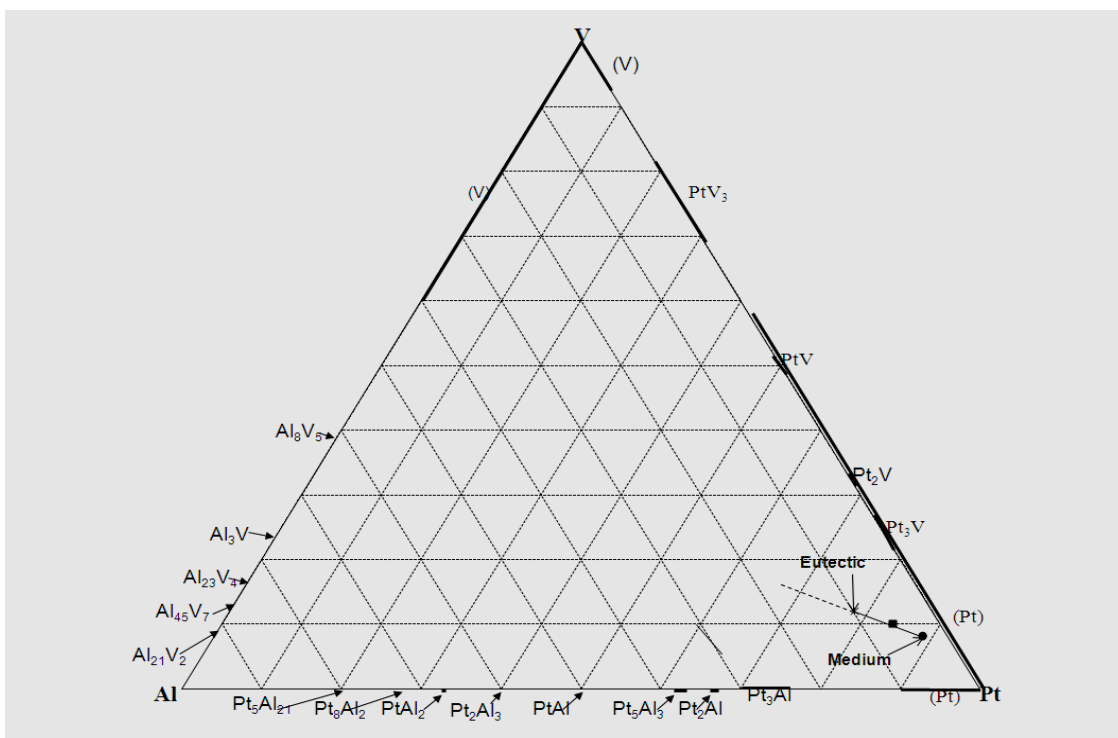


Figure 4.17. Plot of as-cast Alloy 10, average composition  $\text{Pt}_{83.9}\text{Al}_6\text{V}_{10.1}$  (at.%).

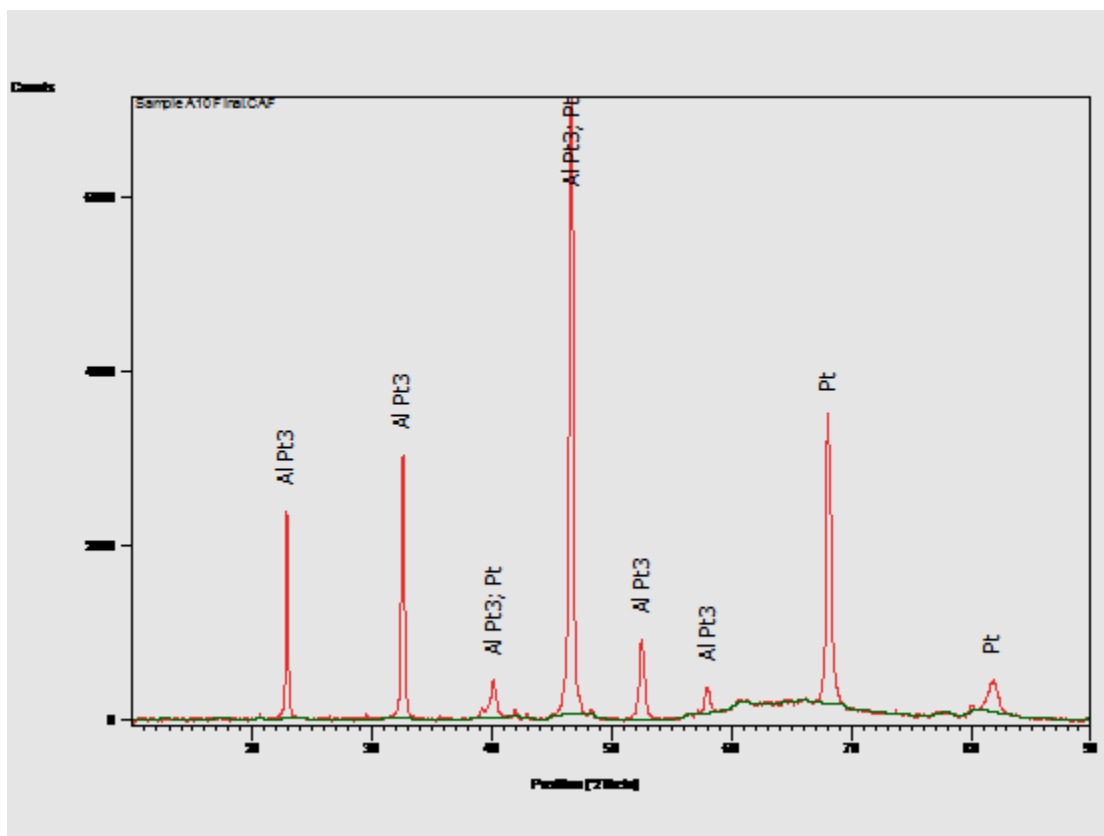
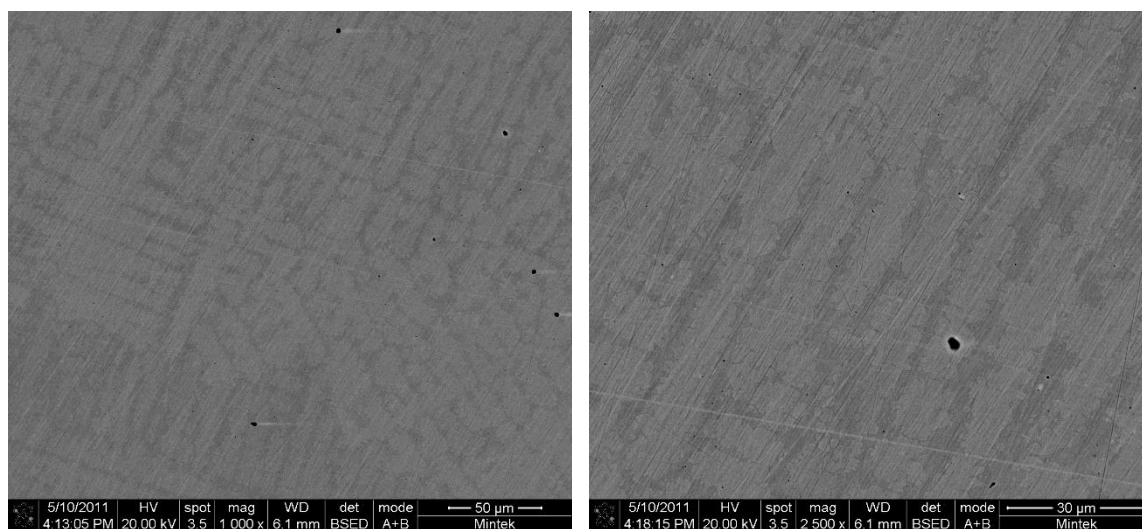
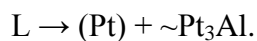
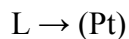


Figure 4.18. XRD pattern of as-cast Alloy 10, average composition  $\text{Pt}_{83.9}\text{Al}_6\text{V}_{10.1}$  (at.%).

#### 4.1.7 As-cast Alloy 11, Average Composition $\text{Pt}_{80.9}\text{Al}_{4.3}\text{V}_{14.8}$ (at.%)

Figures 4.19 shows SEM-BSE images of Alloy 11, average overall composition  $\text{Pt}_{80.9}\text{Al}_{4.3}\text{V}_{14.8}$ , at different magnifications. Both figures show cored medium dendrites and a eutectic. The plot in Figure 4.20 identified the dendrites as (Pt), while the eutectic components are (Pt) and  $\sim\text{Pt}_3\text{Al}$ . XRD confirmed the identities of the phases as shown in the pattern in Figure 4.21.

The solidification sequence and reactions are:



**Figure 4.19 (a).** SEM-BSE image of as-cast Alloy 11,  $\text{Pt}_{80.9}\text{Al}_{4.3}\text{V}_{14.8}$ , showing medium grey dendrites and a eutectic which appears dark and (b). SEM-BSE image of as-cast Alloy 11,  $\text{Pt}_{80.9}\text{Al}_{4.3}\text{V}_{14.8}$ , at a higher magnification, showing medium grey dendrites and a eutectic which appears dark.

**Table 4.7.** Compositions of as-cast Alloy 11, average composition  $\text{Pt}_{80.9}\text{Al}_{4.3}\text{V}_{14.8}$  (at.%), determined by EDX.

Appearance	Pt	Al	V	Phases
Overall	80.9±0.6	4.3±0.4	14.8±0.2	-
Medium	81.8±0.2	1.9±0.2	16.3±0.4	(Pt)
Eutectic	79.4±0.6	8.9±0.8	11.7±0.5	(Pt) + $\text{Pt}_3\text{Al}$

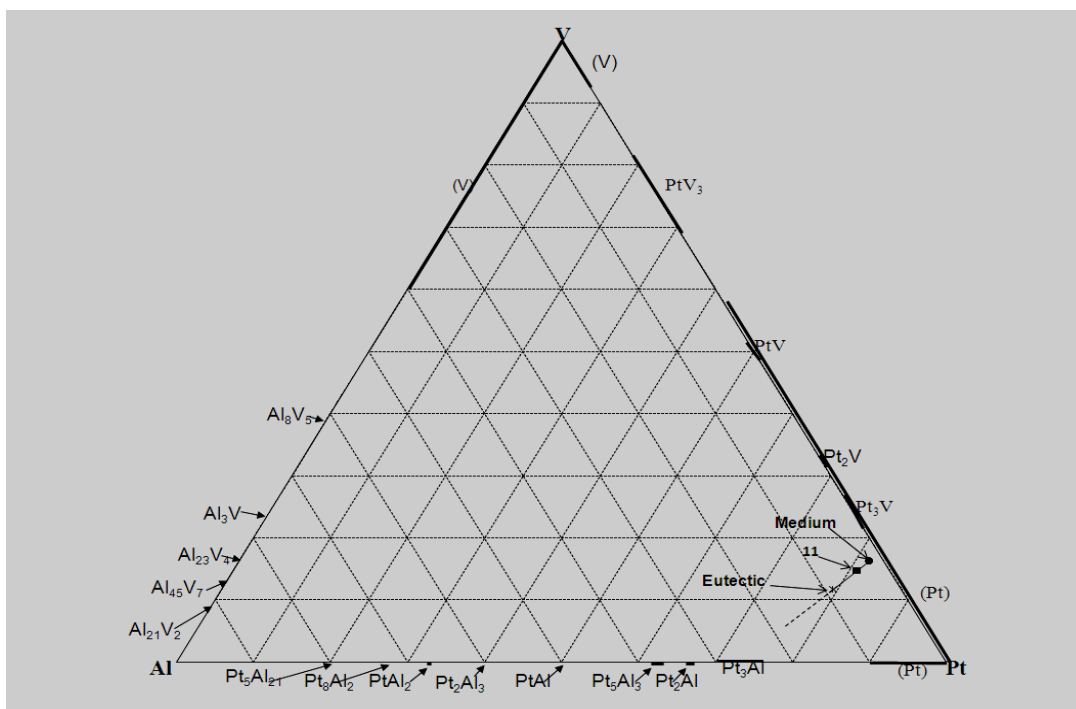


Figure 4.20. Plot of the overall and phase compositions of Alloy 11, average composition  $\text{Pt}_{80.9}\text{Al}_{4.3}\text{V}_{14.8}$  (at.%).

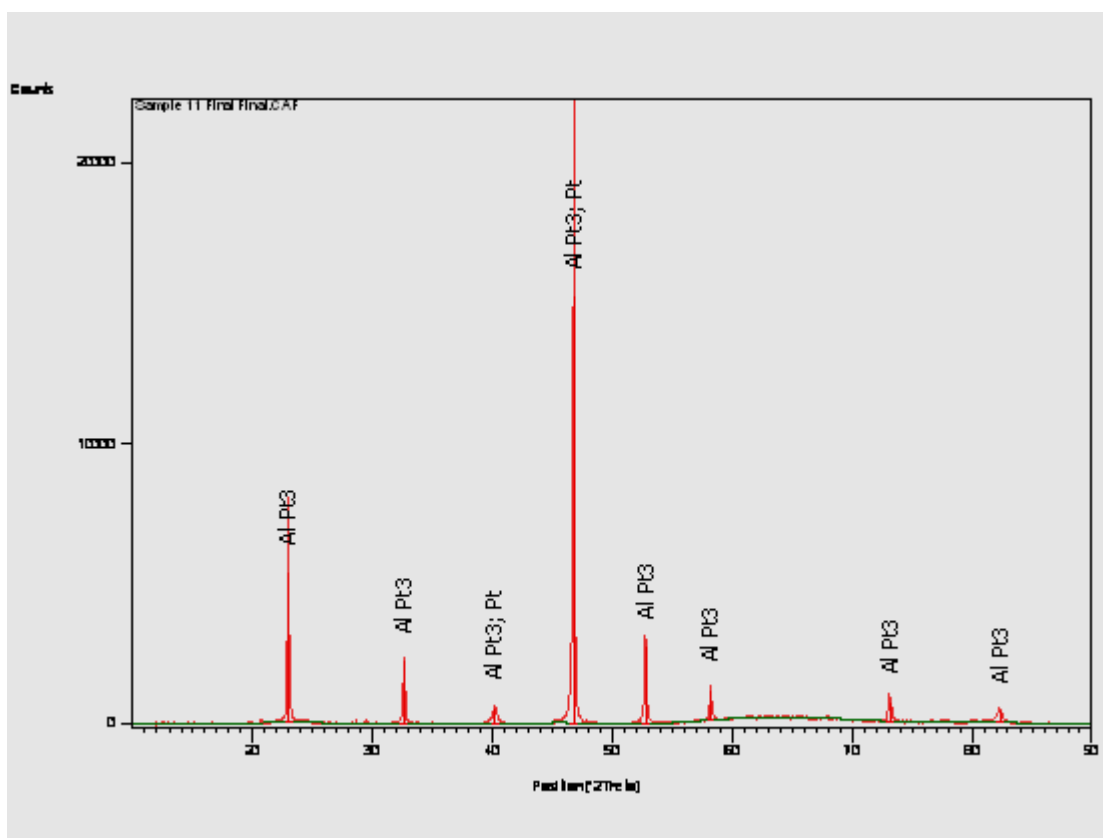
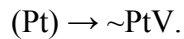
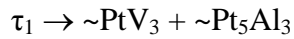
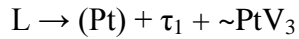
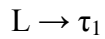
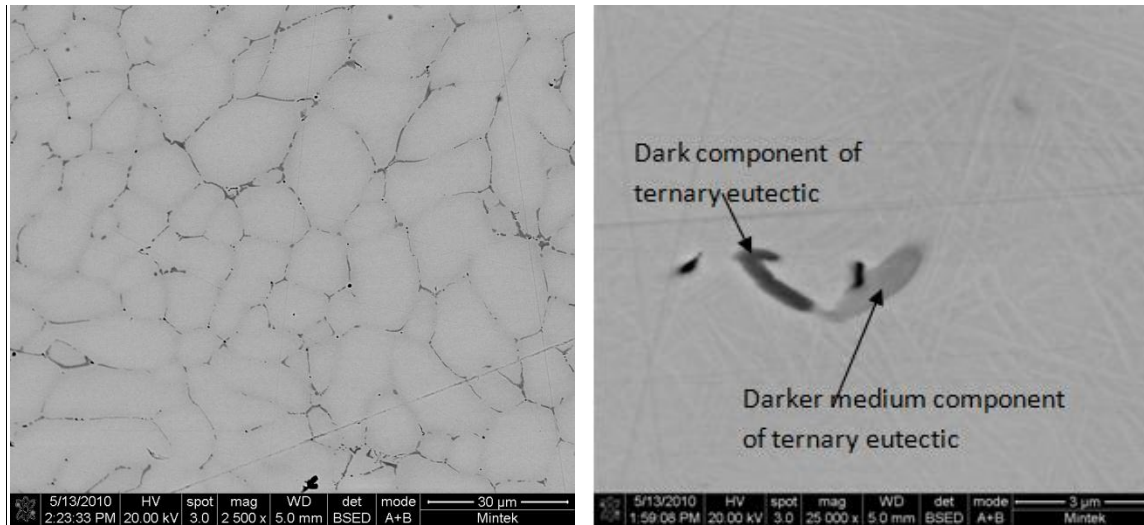


Figure 4.21. XRD pattern of as-cast Alloy 11, average composition  $\text{Pt}_{80.9}\text{Al}_{4.3}\text{V}_{14.8}$  (at.%).

#### 4.1.8 As-cast Alloy 12, Average Composition $\text{Pt}_{52.5}:\text{Al}_{22.6}:\text{V}_{24.9}$ (at.%)

Figure 4.22 is a SEM-BSE image of Alloy 12, average overall composition  $\text{Pt}_{52.5}:\text{Al}_{22.6}:\text{V}_{24.9}$ , showing light medium dendrites and a thin dark interdendritic region, with some pores  $\sim 10\mu\text{m}$  across. The interdendritic regions, which were actually a ternary eutectic, were too small to analyse accurately. At higher magnification (Figure 4.22(b)), the dendrites were seen as a two phase region of fine light needles alternating with a medium phase. This is an indication of a eutectoid reaction whereby the dendrites decomposed into two components. The plot of the areal EDX composition analysis of the two phase dendritic regions indicated that the original dendrites were a possible ternary phase  $\tau_1$  (Figure 4.23). The identification as a possible ternary phase was preferred to simply stating that there was an unknown phase which decomposed eutectoidally. It is recommended that more alloys be made in the vicinity of this sample to either validate the identification or disqualify it. This applies to Sample 13. Extrapolating back from the compositions of  $\sim\text{PtV}_3$  and  $\tau_1$  gives  $\sim\text{Pt}_5\text{Al}_3$  which was confirmed on heat treatment. Higher magnification (Figure 4.22(b)) revealed that the thin dark interdendritic region was a ternary eutectic comprising  $(\text{Pt}) + \tau_1 + \sim\text{PtV}_3$ .  $(\text{Pt})$  subsequently transformed to  $\text{PtV}$  and  $\tau_1$  decomposed eutectoidally to  $\text{PtV}_3 + \sim\text{Pt}_5\text{Al}_3$ . It should be noted that the composition of the thin dark region had a large error and was therefore identified as  $\sim\text{PtV}$  and  $\sim\text{PtV}_3$  by extrapolation away from the composition of the dendritic region (which could have contributed to the analysis of the thin phase). XRD confirmed the phase identification (Figure 4.24). All the  $\tau_1$  decomposed in the eutectoid reaction. Solidification sequence and reactions are:



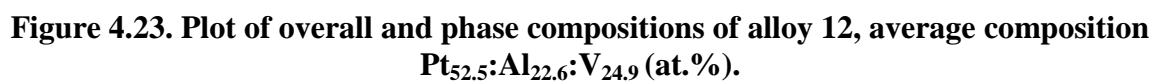


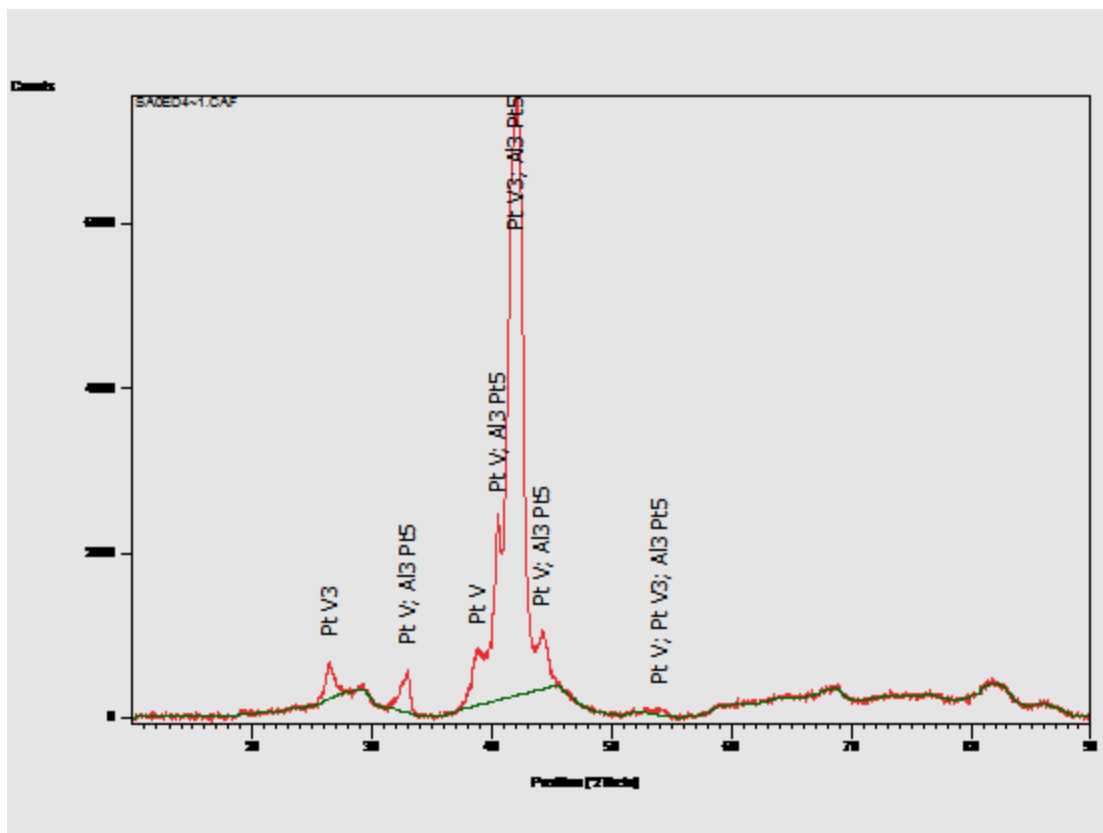
**Figure 4.22. (a). SEM-BSE image of as-cast Alloy 12,  $\text{Pt}_{52.5}:\text{Al}_{22.6}:\text{V}_{24.9}$  showing light medium dendrites and a thin ternary eutectic and (b). SEM-BSE image of as-cast alloy  $\text{Pt}_{52.5}:\text{Al}_{22.6}:\text{V}_{24.9}$ , at a higher magnification showing dark  $\sim\text{PtV}$ , darker medium  $\sim\text{PtV}_3$ , medium and light needles ( $\text{Pt}_5\text{Al}_3$ ).**

**Table 4.8. EDX composition analysis data of as-cast Alloy 12, average composition  $\text{Pt}_{52.5}:\text{Al}_{22.6}:\text{V}_{24.9}$  (at.%).**

Appearance	Pt	Al	V	Phases
Overall	52.5±0.5	22.6±0.3	24.9±0.3	-
Medium + light needles	53.8±0.4	22.2±0.7	24.0±1.1	$\sim\text{PtV}_3 + \sim\text{Pt}_5\text{Al}_3$
Thin dark (ternary eutectic)	47.6±1.8	14.4±2.2	38.0±3.9	$\sim\text{PtV} + \sim\text{PtV}_3 + \tau_1^*$

\* The ternary phase  $\tau_1$  subsequently decomposed in a eutectoid reaction to  $\sim\text{Pt}_5\text{Al}_3 + \sim\text{PtV}_3$ .

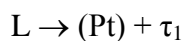
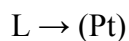


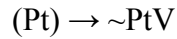
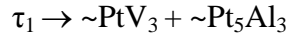


**Figure 4.24. XRD pattern of as-cast Alloy 12, average composition  $\text{Pt}_{52.5}:\text{Al}_{22.6}:\text{V}_{24.9}$  (at.%).**

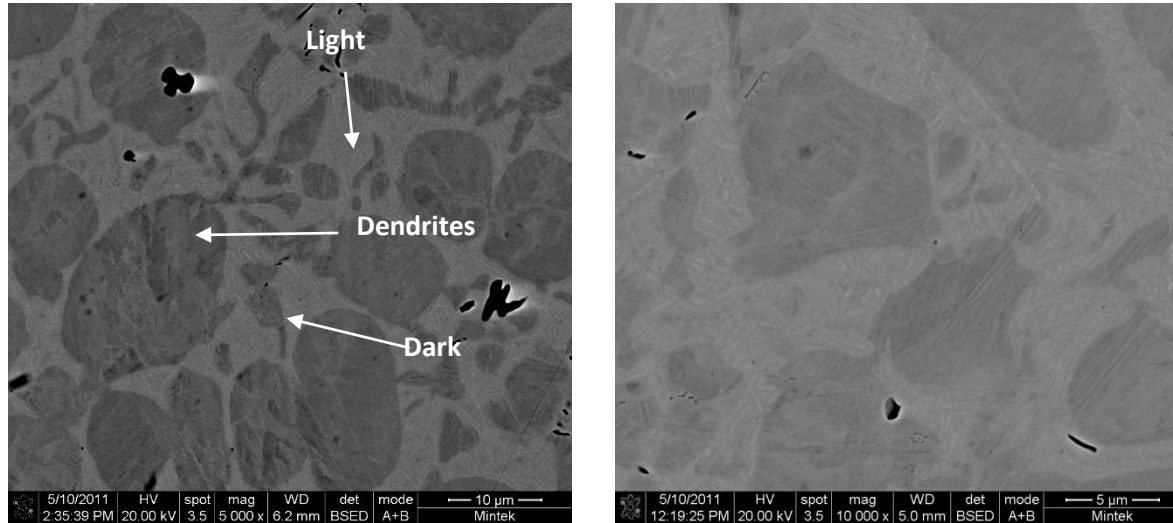
#### **4.1.9 As-cast Alloy 13, Average Composition $\text{Pt}_{53.7}:\text{Al}_{8.8}:\text{V}_{37.5}$ (at.%)**

Figure 4.25 shows SEM-BSE images of Alloy 13, average overall composition  $\text{Pt}_{53.7}:\text{Al}_{8.8}:\text{V}_{37.5}$  (at.%). The images show that the original (Pt) dendrites transformed initially to  $\sim\text{PtV}$  and then the (Pt) went on to decompose eutectoidally to  $\sim\text{PtV} + \sim\text{Pt}_2\text{V}$  as in the binary phase diagram of Pt-V [1990Mas]. A close examination of the dendrites shows a dark phase and a two phase eutectoid region within. There is also a sparse eutectic comprising a light region and the dark which is PtV. At higher magnification (Figure 4.25(b)), the light region was seen as comprising two phases, light and medium. The plot of the areal EDX composition analysis of the two phase light regions indicated that it probably solidified as ternary phase  $\tau_1$  which subsequently decomposed eutectoidally to  $\sim\text{PtV} + \text{Pt}_5\text{Al}_3$ . XRD confirmed the phase identification (Figure 4.27). The solidification sequence and reactions are:





(with the  $\tau_1$  reaction deduced from Sample 12 and also consistent with the heat treated sample).

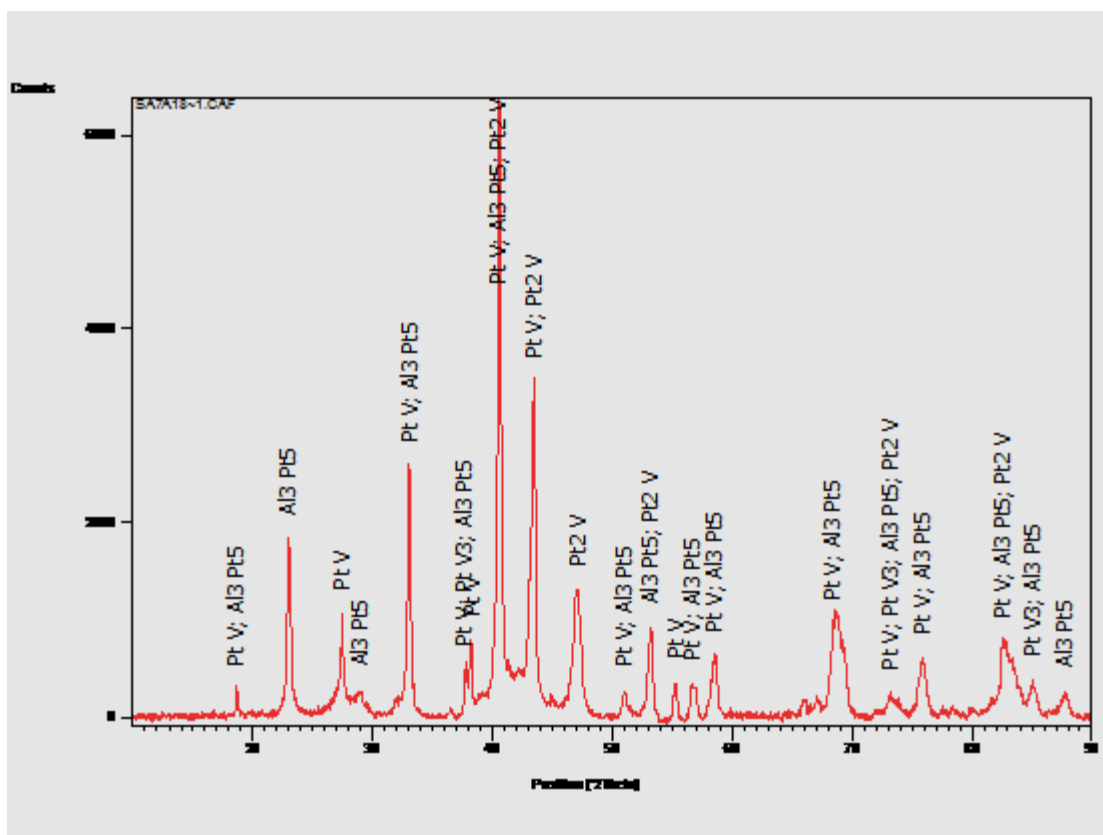
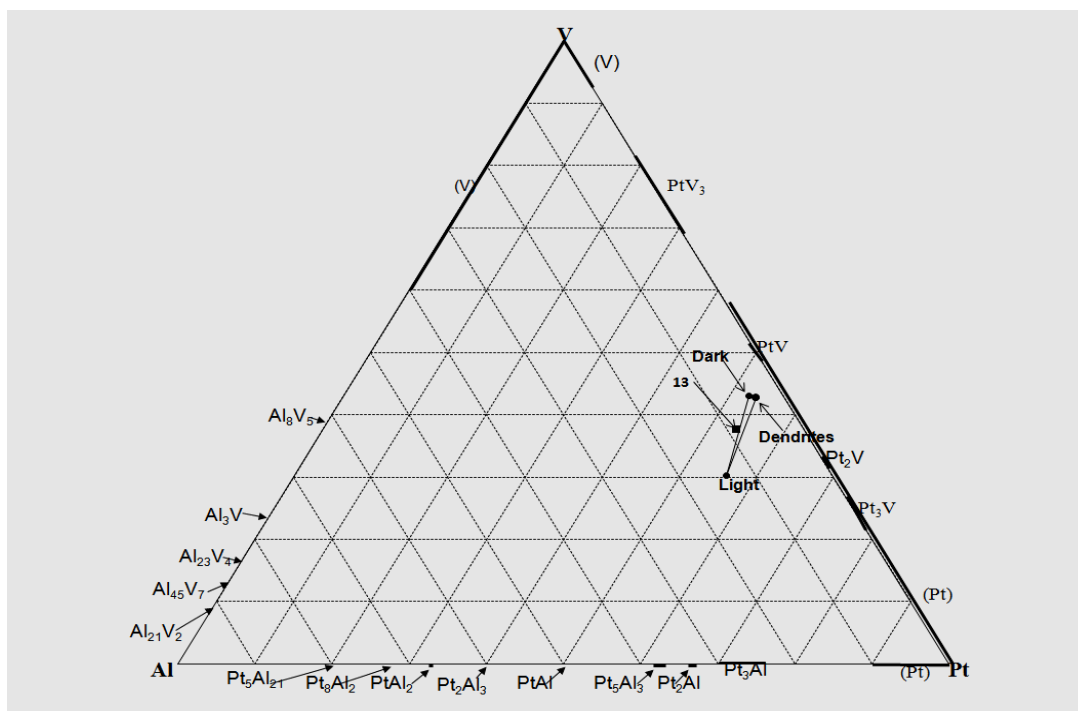


**Figure 4.25 (a).** SEM-BSE image of alloy  $\text{Pt}_{53.7}:\text{Al}_{8.8}:\text{V}_{37.5}$  (at.%) medium dendrites ( $\sim\text{PtV} + \sim\text{PtV}_3$ ), a light phase ( $\tau_1$ ) and dark porosity and (b). SEM-BSE image of Alloy 13,  $\text{Pt}_{53.7}:\text{Al}_{8.8}:\text{V}_{37.5}$  (at.%), at a higher magnification showing medium dendrites ( $\sim\text{PtV} + \sim\text{PtV}_3$ ), a light phase ( $\tau_1$ ) and a sparse eutectic of  $\tau_1$  (which decomposed to  $\sim\text{PtV}_3 + \text{Pt}_5\text{Al}_3$ ) +  $\sim\text{PtV}_3$ .

**Table 4.9. Compositions of as-cast Alloy 13, average composition  $\text{Pt}_{53.7}:\text{Al}_{8.8}:\text{V}_{37.5}$  (at.%) as determined by EDX.**

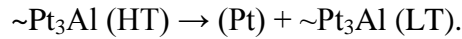
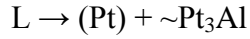
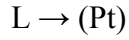
Appearance	Pt	Al	V	Phases
Overall	53.7±0.4	8.8±0.3	37.5±0.2	-
Dendrites (eutectoid)	53.6±0.6	3.7±0.3	42.7±0.3	$\sim\text{PtV} + \sim\text{Pt}_2\text{V}$
Eutectoid of light and medium	55.9±0.4	13.8±0.4	30.3±0.5	$\sim\text{PtV}_3 + \sim\text{Pt}_5\text{Al}_3$
Dark	52.5±0.3	4.5±0.2	43.0±0.4	$\sim\text{PtV}$



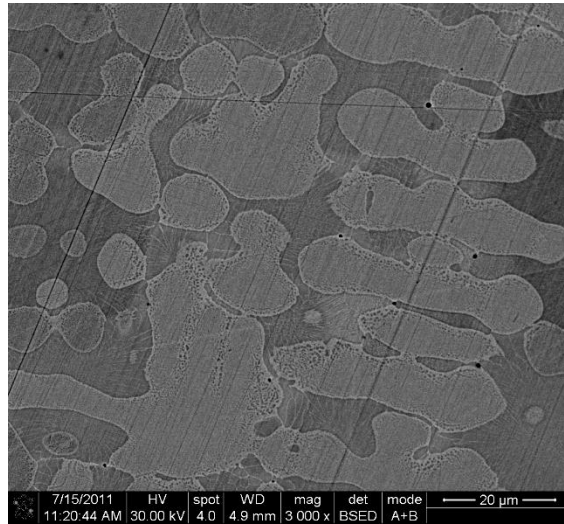


#### 4.1.10 As-cast Alloy 14, Average Composition $\text{Pt}_{84}\text{Al}_{12}\text{V}_4$ (at.%)

Figure 4.28 is a SEM-BSE image of Alloy 14, average composition  $\text{Pt}_{84}\text{Al}_{12}\text{V}_4$  (at.%), showing light (Pt) dendrites having solid state precipitation of  $\sim\text{Pt}_3\text{Al}$  and a eutectic of (Pt) +  $\sim\text{Pt}_3\text{Al}$  (appearing dark) where the  $\text{L}_{12}$  cubic  $\sim\text{Pt}_3\text{Al}$  component decomposed eutectoidally to (Pt) + the tetragonal low temperature  $\sim\text{Pt}_3\text{Al}$ . XRD confirmed the phase identification (Figure 4.30). The proposed solidification and equilibria reactions are:



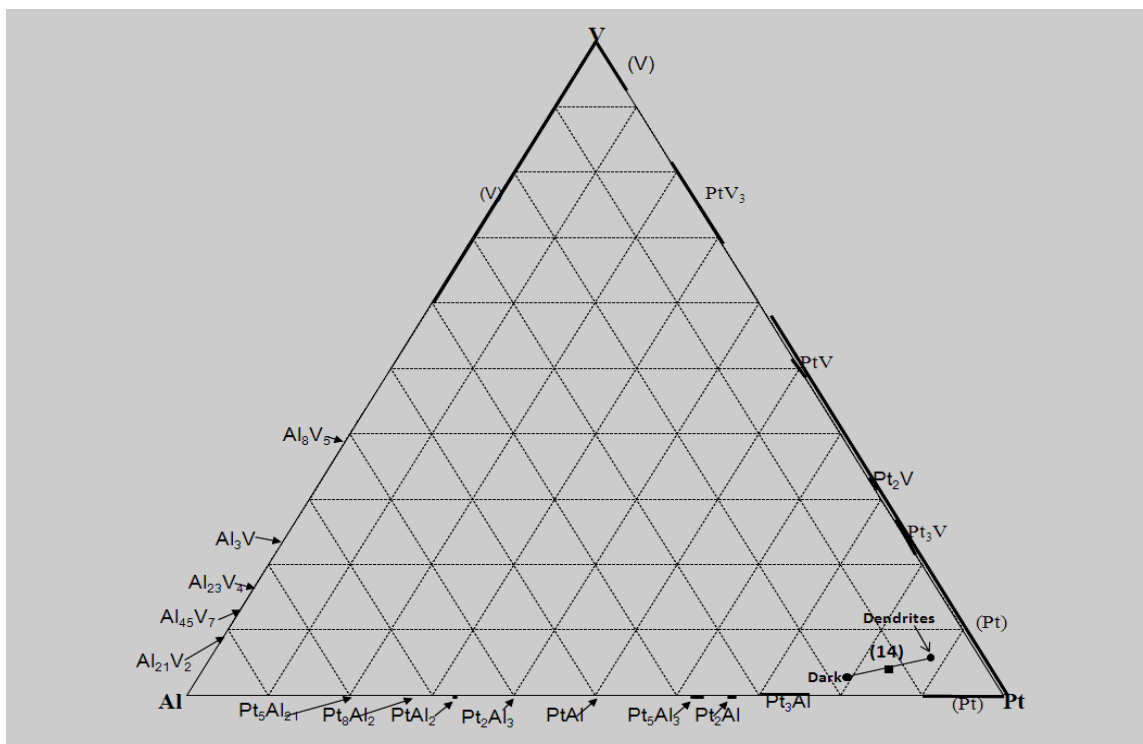
There was also solid state precipitation of  $\sim\text{Pt}_3\text{Al}$  from (Pt) due to a retreating solvus. The eutectoid reaction and the retreating solvus are both in the binary phase diagram [1990Mas].



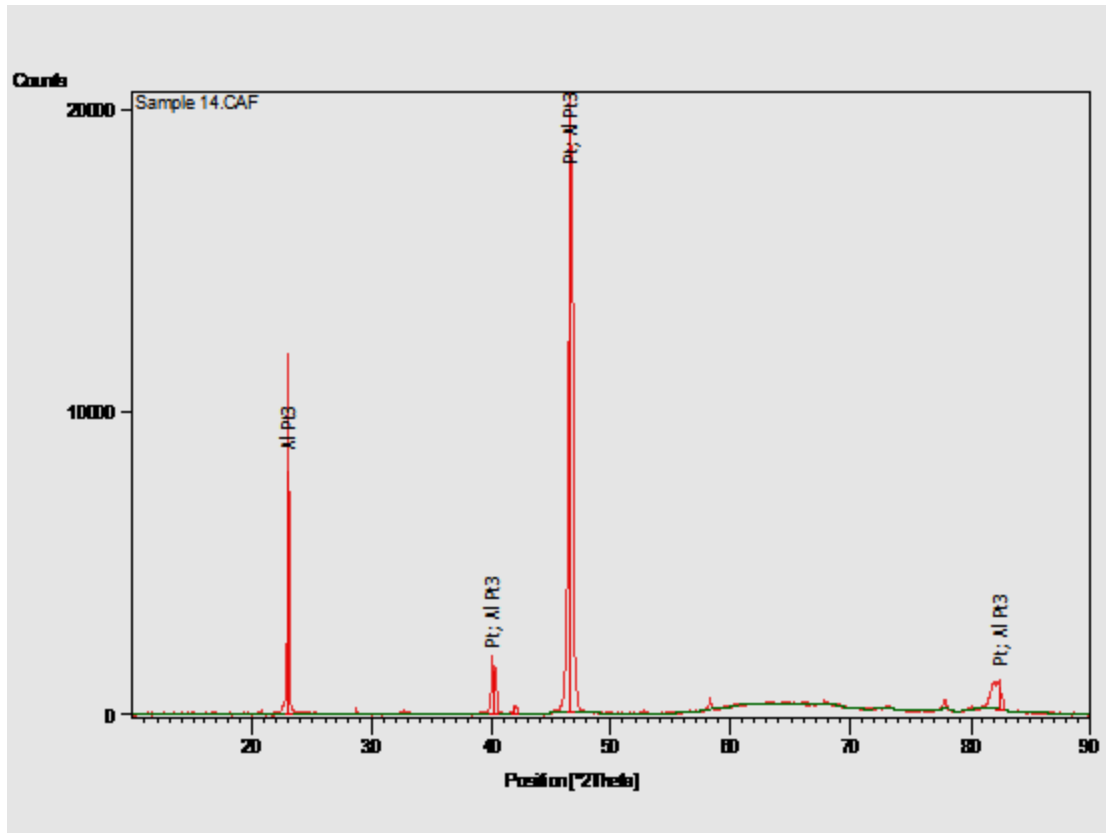
**Figure 4.28. SEM-BSE image of as-cast Alloy 14, average composition  $\text{Pt}_{84}\text{Al}_{12}\text{V}_4$  (at.%), showing light (Pt) dendrites with  $\sim\text{Pt}_3\text{Al}$  pptn. in some areas and a eutectic of (Pt) +  $\sim\text{Pt}_3\text{Al}$ .**

**Table 4.10. Compositions of as-cast Alloy 14, average composition  $\text{Pt}_{84}\text{Al}_{12}\text{V}_4$  (at.%) determined by EDX.**

Appearance	Pt	Al	V	Phase
Overall	84.0±0.7	12.0±0.7	4.0±0.2	-
Dendrites	88.2±0.6	6.1±0.6	5.7±0.5	(Pt)
Eutectoid (Dark)	79.3±0.8	17.9±1.2	2.8±0.7	(Pt) + $\sim\text{Pt}_3\text{Al}$ (LT)



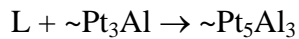
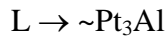
**Figure 4.29. Plot of overall and phase compositions for as-cast Alloy 14, average composition  $\text{Pt}_{84}\text{Al}_{12}\text{V}_4$  (at.%).**



**Figure 4.30. XRD pattern of as-cast Alloy 14, average composition Pt<sub>84</sub>:Al<sub>12</sub>:V<sub>4</sub> (at.%).**

#### **4.1.11 As-cast Alloy 15, Average Composition Pt<sub>72.4</sub>:Al<sub>13.7</sub>:V<sub>13.9</sub> (at.%)**

The SEM-BSE image of Alloy 15, average composition Pt<sub>72.4</sub>:Al<sub>13.7</sub>:V<sub>13.9</sub> (at.%), in Figure 4.31 shows medium contrast ~Pt<sub>3</sub>Al dendrites and light contrast ~Pt<sub>2</sub>Al. All the ~Pt<sub>5</sub>Al<sub>3</sub> which formed from the peritectic reaction,  $L + \sim\text{Pt}_3\text{Al} \rightarrow \sim\text{Pt}_5\text{Al}_3$ , was consumed in the peritectoid reaction,  $\sim\text{Pt}_3\text{Al} + \text{Pt}_5\text{Al}_3 \rightarrow \sim\text{Pt}_2\text{Al}$ . There were light and dark areas due to different orientations of the grains and the grain boundaries were irregular. The data for EDX composition analyses in Table 4.11 were plotted in Figure 4.32. XRD confirmed the phase identification (Figure 4.33). The solidification and cooling reactions were:



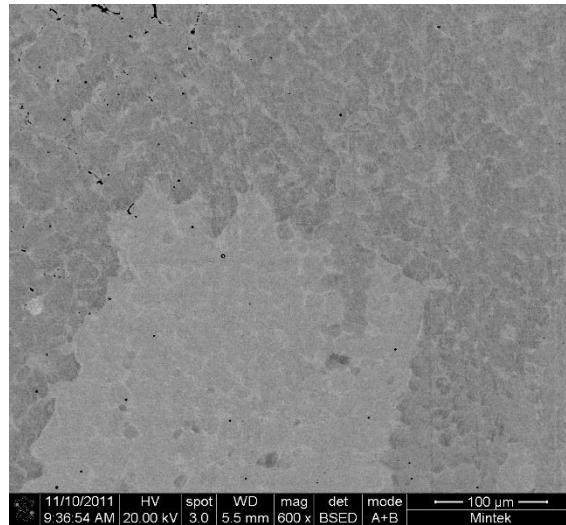
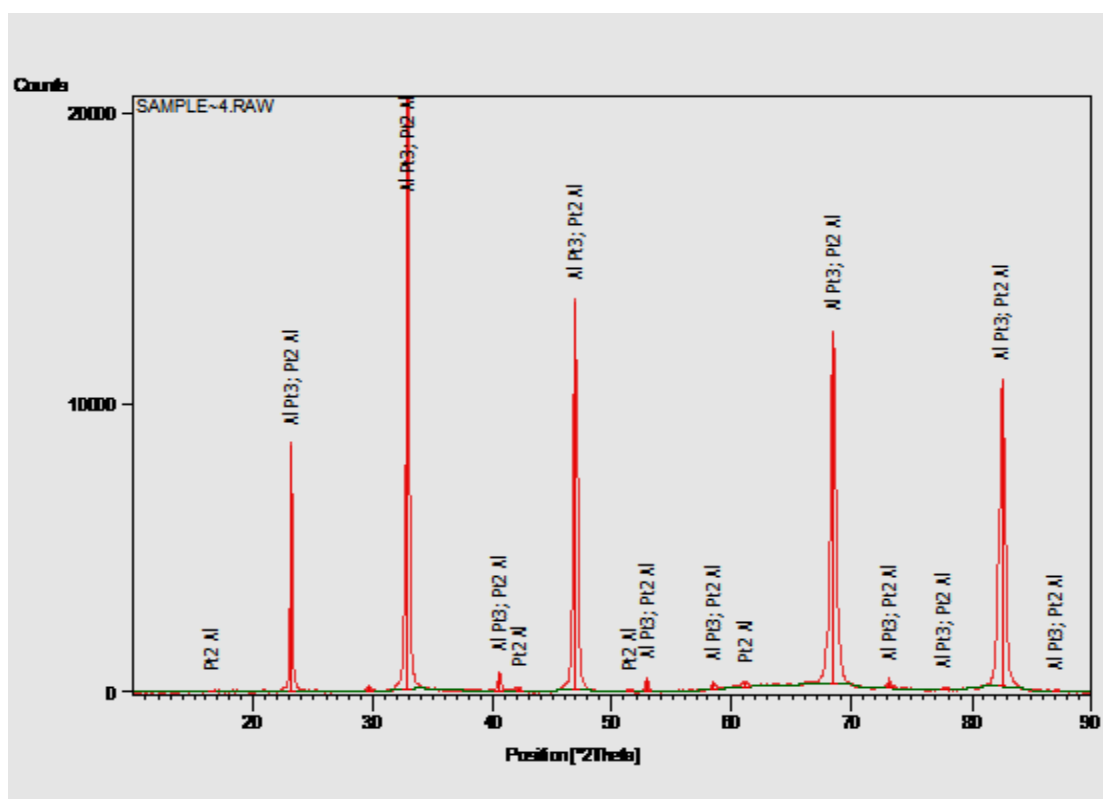
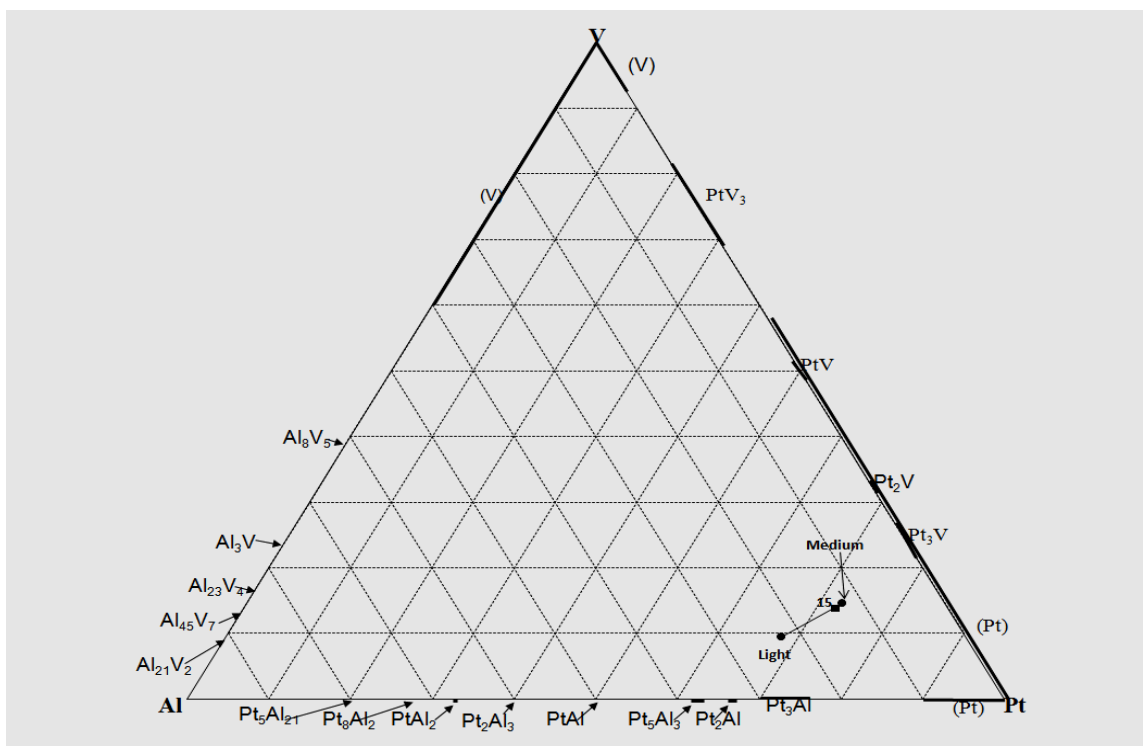


**Figure 4.31. SEM-BSE image of as-cast Alloy 15, average composition  $\text{Pt}_{72.4}:\text{Al}_{13.7}:\text{V}_{13.9}$  (at.%), showing medium contrast  $\sim\text{Pt}_3\text{Al}$  and light contrast  $\sim\text{Pt}_2\text{Al}$ , with light and dark areas due to different grain orientations.**

**Table 4.11. EDX composition analysis data for as-cast Alloy 15, average composition  $\text{Pt}_{72.4}:\text{Al}_{13.7}:\text{V}_{13.9}$  (at.%).**

Appearance	Pt	Al	V	Phase
Overall	$72.4 \pm 0.5$	$13.7 \pm 0.6$	$13.9 \pm 0.7$	-
Medium	$72.8 \pm 0.5$	$12.6 \pm 0.5$	$14.6 \pm 0.8$	$\sim\text{Pt}_3\text{Al}$
Light	$68.0 \pm 1.6$	$22.6 \pm 2.8$	$9.4 \pm 1.6$	$\sim\text{Pt}_2\text{Al}$



#### 4.1.12 As-cast Alloy 16, Average Composition $\text{Pt}_{56.9}\text{Al}_{25.4}\text{V}_{17.7}$ (at.%)

The images of Alloy 16, average composition  $\text{Pt}_{56.9}\text{Al}_{25.4}\text{V}_{17.7}$  (at.%), are shown in Figure 4.34. Figure 4.34(a) is a SEM-BSE image of the alloy and Figure 4.34(b) is an optical microscope image of the same alloy after electrolytic etching in a solution of HCl/NaCl [2012Ode1] (Section 7.1). Unlike the other Pt-Al-V alloys, it was not possible to obtain a contrast with SEM-BSE imaging and contrast was only achieved with the optical microscope after etching. The optical microscope image shows single phase with grains at different orientations. The plot in Figure 4.35 identified the phase as the ternary,  $\tau_2$ . XRD confirmed the phase identification (Figure 4.36) in that the peaks did not match any of the binary phases.

The possible candidate phases are  $\sim\text{PtAl}$ ,  $\sim\text{Pt}_5\text{Al}_3$  and  $\sim\text{Pt}_2\text{Al}$ . When their peaks are included in the presumed pattern of  $\tau_2$  (Figure 4.36(b)), there is overlap in some cases but this is not conclusive as the major peak is not identified with any of these phases. In any case, the fields of these candidate phases are quite far from the plot of Alloy 16 (Figure 4.37). Another reason for the deduction that the alloy is single ternary phase is the grain structure and the cracks in the optical micrograph (Figure 4.34(b)). The cracks indicate extreme brittleness consistent with ternary phases.

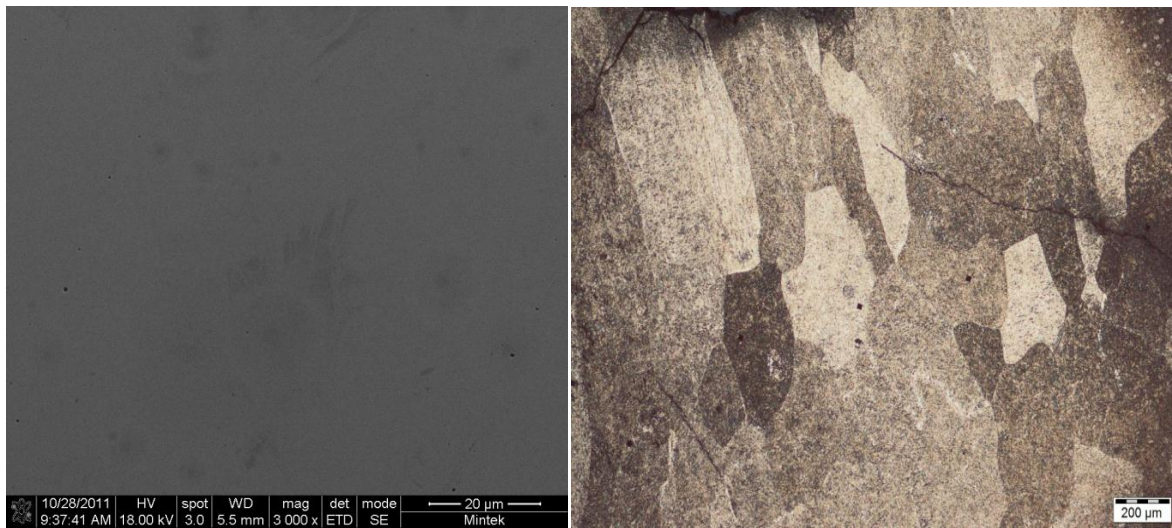


**Figure 4.34. (a). SEM-BSE image of Alloy 16, average composition  $\text{Pt}_{56.9}\text{Al}_{25.4}\text{V}_{17.7}$  (at.%), showing no contrast and (b) optical microscope image of etched Alloy 16, average composition  $\text{Pt}_{56.9}\text{Al}_{25.4}\text{V}_{17.7}$  (at.%), showing single ternary phase,  $\tau_2$ , with grains at different orientations.**

**Table 4.12. EDX composition analysis data for as-cast alloy 16, average composition  $\text{Pt}_{56.9}:\text{Al}_{25.4}:\text{V}_{17.7}$  (at.%).**

	Pt	Al	V	Phase
Overall	$56.9 \pm 0.6$	$25.4 \pm 0.4$	$17.7 \pm 0.3$	$\tau_2$

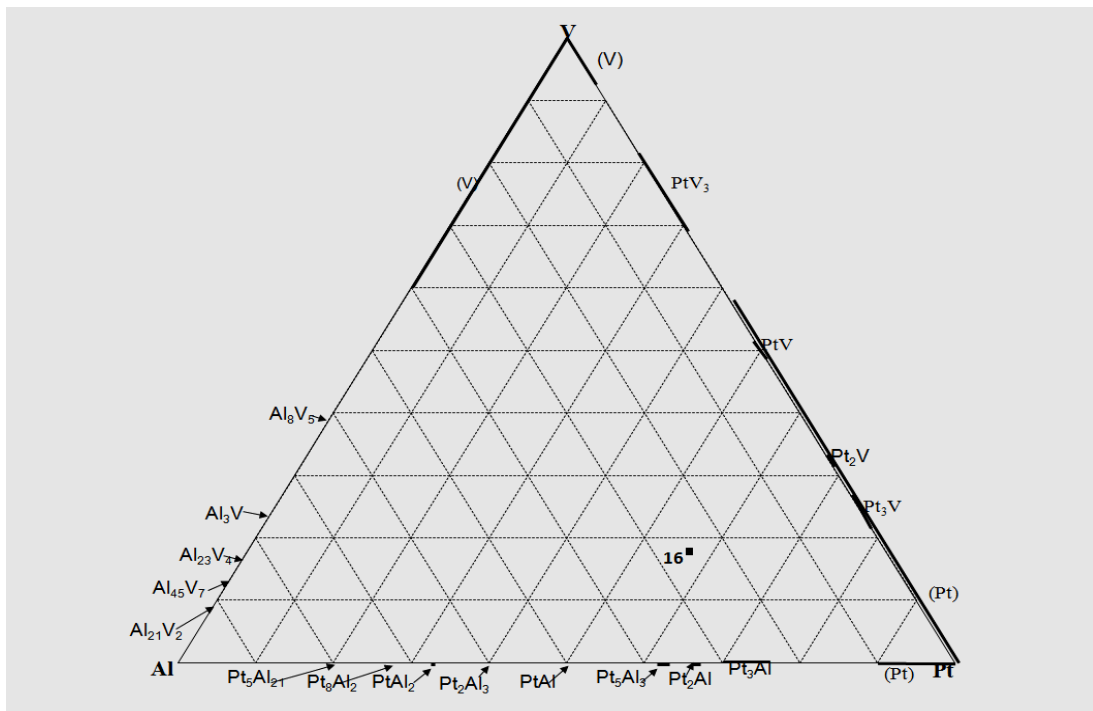


**Figure 4.35. Plot of Alloy 16, average composition  $\text{Pt}_{56.9}:\text{Al}_{25.4}:\text{V}_{17.7}$  (at.%).**



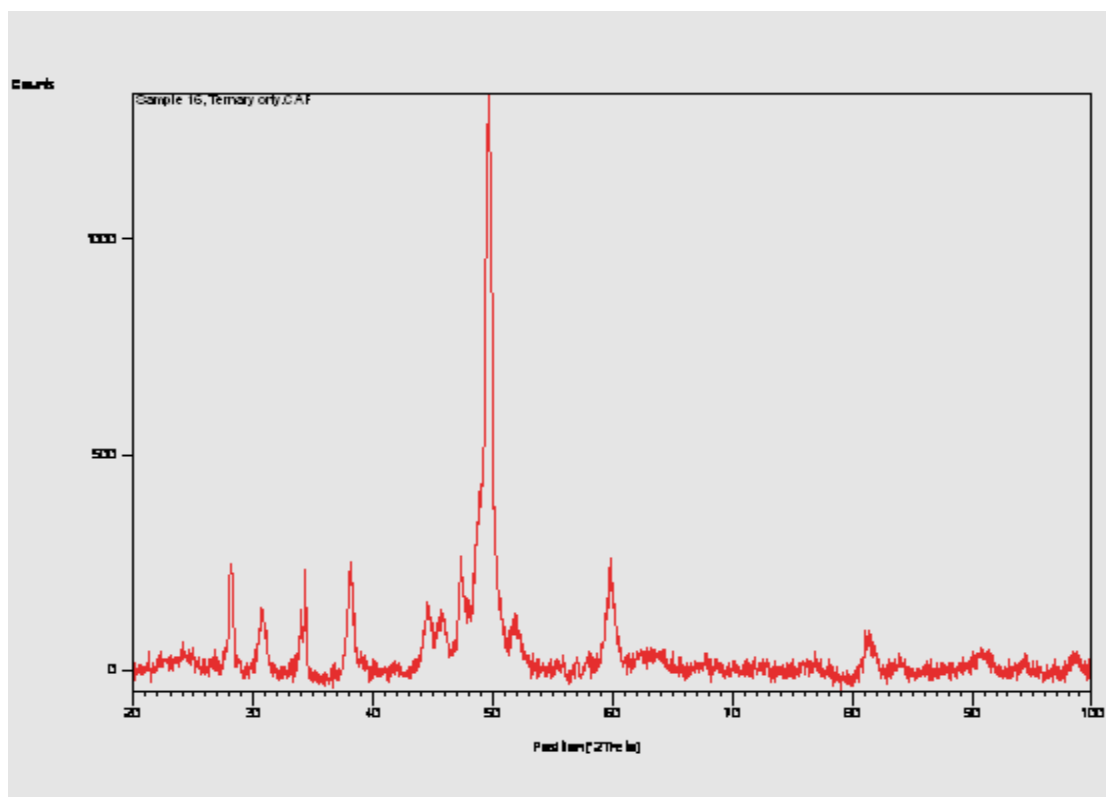


Figure 4.36 (a). XRD pattern of Alloy 16, average composition  $\text{Pt}_{56.9}\text{Al}_{25.4}\text{V}_{17.7}$  (at.%), presumed to be from  $\tau_2$ .



#### 4.1.13 Solidification Projection of the Pt-Al-V System at the Pt-rich corner

The compositions of all the as-cast alloys were plotted, and the phase boundaries deduced on the solidification projection (Figure 4.37). All the Pt-Al phases extended to ~10% V, except ~Pt<sub>3</sub>Al which extended to ~15% V. (Pt) had low extent at low V (with a minimum of ~2 at.% Al, ~82 at.% Pt and ~16 at.% V), and higher extent at higher V content. There were two ternary phases,  $\tau_1$  at ~V<sub>24</sub>Pt<sub>56</sub>Al<sub>20</sub> observed in Alloys 12 and 13 and  $\tau_2$ , ~V<sub>18</sub>Pt<sub>57</sub>Al<sub>25</sub> observed in Alloy 16. In the heat treated samples 12H and 13H, it was confirmed that the eutectoid components, after decomposition of  $\tau_1$ , were ~PtV<sub>3</sub> + ~Pt<sub>5</sub>Al<sub>3</sub>. The confirmation was possible because the components had coarsened substantially and it was possible to get more accurate EDX readings. On the other hand, the ternary phase in sample 16H decomposed to ~PtAl + PtV and the two phases coarsened after the prolonged heat treatment. This was the reason why it was deduced that the two ternary phases were different and hence the different designations  $\tau_1$  and  $\tau_2$ . However there is uncertainty regarding the boundaries of the proposed two phases and therefore there is a recommendation that more samples should be made around the vicinity of these phases and analysed.

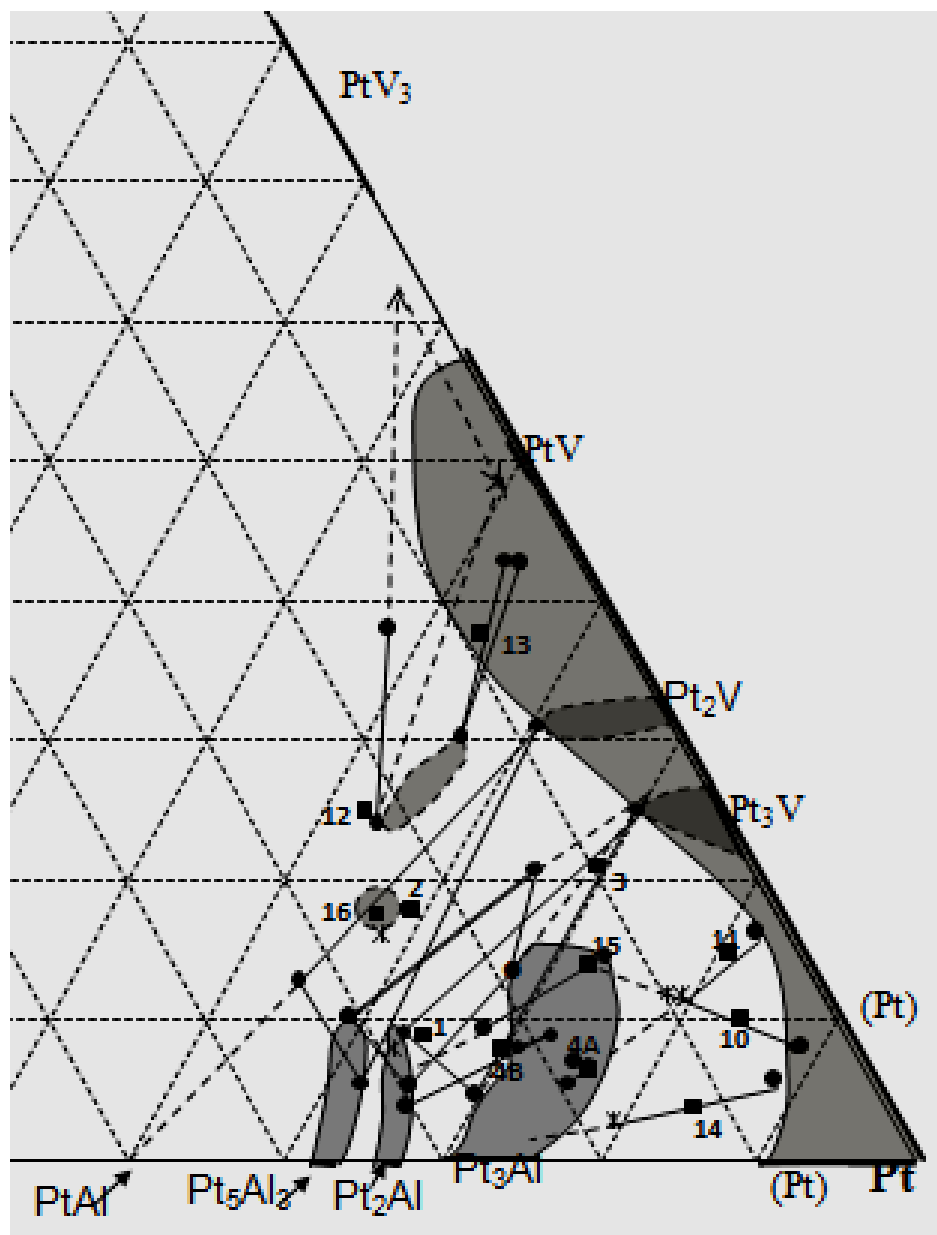


Figure 4.37. Solidification projection of the Pt-Al-V system at the Pt-rich corner (at.%).

Of the reactions observed, all had been reported in the Pt-Al binary [1990Mas], except for the peritectic reactions  $L + (Pt) \rightarrow \sim Pt_5Al_3$  in Alloy 2 and  $L + (Pt) \rightarrow \sim Pt_3Al + \sim Pt_5Al_3$  in Alloy 3 [2012Ode2].

#### 4.1.14 Liquidus Surface Projection of the Pt-Al-V at the Pt-rich Corner

A liquidus surface projection for the Pt-rich corner of the Pt-Al-V was drawn using the overall compositions, primary phases and the solidification sequences. The primary solids on the

liquidus surface (Figure 4.38) are (Pt),  $\sim\text{Pt}_3\text{Al}$ ,  $\sim\text{Pt}_5\text{Al}_3$ ,  $\beta$  and two ternary phases  $\sim\text{V}_{24}\text{Pt}_{56}\text{Al}_{20}$  and  $\sim\text{V}_{18}\text{Pt}_{57}\text{Al}_{25}$  (at.%). Since the reactions in Alloys 12 and 13 showed that the liquidus composition moves in different directions on cooling, there must be a minimum on the reaction involving L,  $\tau_1$  and (Pt). Two ternary phases were deduced from as-cast alloys (Sections 4.1.8, 4.1.9 and 4.1.12). The boundary of the (Pt) liquidus must be complex and have a maximum, as well as a minimum described above, in order for the observed reactions in sample 12 to occur. The maximum has to occur on the  $\tau_2$  – (Pt) in order to avoid impossible reactions (three binary reactions going outwards at an invariant). It is assumed that the  $\tau_1$  surface closes between  $\sim\text{PtV}_3$  and (Pt), given no other data. Figure 4.25(a) could show a ternary eutectic because there appears to be two different dark contrasts (as well as light), but this needs confirmation. Thus the liquidus surface around the ternary phases is speculative, and needs more alloys to be characterised. A simple liquidus surface without a maximum was considered, but this would not give the  $\sim\text{PtV}_3$  in the eutectic of sample 12.

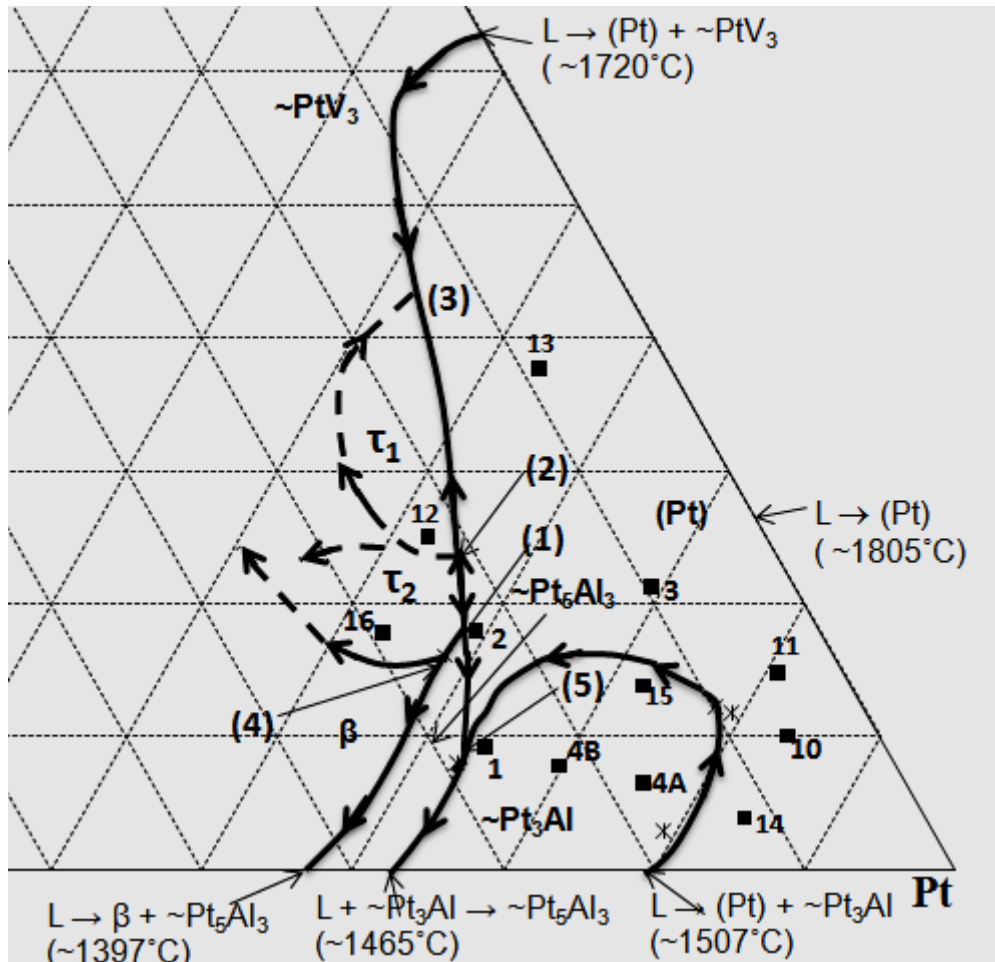


**Figure 4.38. Liquidus surface projection of the Pt-Al-V system at the Pt-rich corner (at.%).**

**Table 4.13. Invariant reactions on the Pt-Al-V liquidus surface at the Pt-rich corner.**

Reaction No.	Liquid Composition (at.%)	Invariant Reaction
(1)	$\sim\text{Pt}_{59}:\text{Al}_{23}:\text{V}_{18}$	$\text{L} + (\text{Pt}) + \tau_2 \rightarrow \sim\text{Pt}_5\text{Al}_3$
(2)	$\sim\text{Pt}_{55}:\text{Al}_{21}:\text{V}_{24}$	$\text{L} + (\text{Pt}) + \tau_2 \rightarrow \tau_1$
(3)	$\sim\text{Pt}_{43}:\text{Al}_{14}:\text{V}_{43}$	$\text{L} \rightarrow (\text{Pt}) + \tau_1 + \sim\text{PtV}_3$
(4)	$\sim\text{Pt}_{58}:\text{Al}_{26}:\text{V}_{16}$	$\text{L} + \tau_2 + \sim\text{Pt}_5\text{Al}_3 \rightarrow \beta$
(5)	$\sim\text{Pt}_{63}:\text{Al}_{28}:\text{V}_9$	$\text{L} + (\text{Pt}) \rightarrow \sim\text{Pt}_3\text{Al} + \sim\text{Pt}_5\text{Al}_3$

## 4.2 ALLOYS ANNEALED AT 1000°C FOR 1500 HOURS

### 4.2.1 Annealed Alloy 1H, Average Composition $\text{Pt}_{64.7}:\text{Al}_{26.2}:\text{V}_{9.1}$ (at.%)

Figure 4.39 is an SEM-BSE image of the microstructure of annealed Alloy 1H, average composition  $\text{Pt}_{64.7}:\text{Al}_{26.2}:\text{V}_{9.1}$  (at.%), showing a medium contrast phase, a light phase, a dark phase and a eutectic. In some cases, the medium contrast phase had a dark thin layer around it, indicating that these were the dendrites in the as-cast alloy although their composition had changed. The original dendrites showed precipitates of a darker phase, presumed to be  $\sim\text{Pt}_2\text{V}$  considering the contrast and the morphology, which varied between coarse (easily visible) and fine (very difficult to resolve). The plot of the compositions in Figure 4.40 suggested the light phase was  $\sim\text{Pt}_5\text{Al}_3$ , the dark phase was either  $\sim\text{PtV}$  or  $\sim\text{Pt}_2\text{V}$ , but XRD confirmed  $\sim\text{Pt}_5\text{Al}_3$  and  $\sim\text{Pt}_2\text{V}$  (Figure 4.41). The medium grey phase was identified as  $\sim\text{Pt}_3\text{Al}$ . The components of the eutectoid were too small to be accurately analysed individually by EDX.

In comparison with the as-cast alloy, the eutectic had coarsened, the light needles could not be seen clearly and most of the dendrites had dark solid state precipitates, showing a retreating solvus.

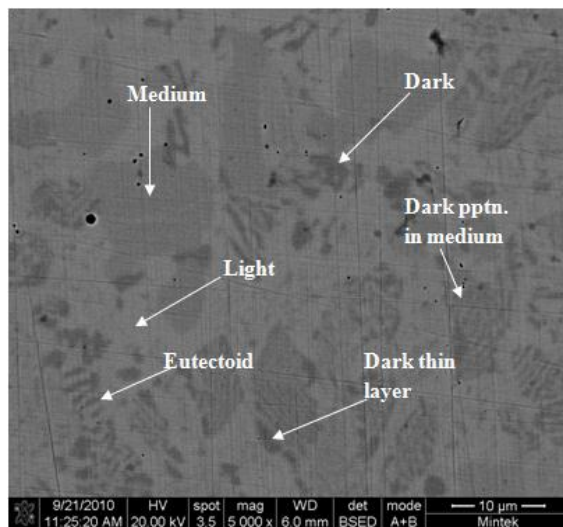


**Figure 4.39. SEM-BSE image of annealed Alloy 1H, average composition  $\text{Pt}_{64.7}:\text{Al}_{26.2}:\text{V}_{9.1}$  (at.%), showing a medium grey phase ( $\sim\text{Pt}_3\text{Al}$ ), a light phase ( $\sim\text{Pt}_5\text{Al}_3$ ), a dark ( $\sim\text{Pt}_2\text{V}$ ) phase, a eutectoid ( $\sim\text{PtAl} + \text{Pt}_5\text{Al}_3$ ).**

**Table 4.14. Overall and phase compositions of annealed Alloy 1H, average composition Pt<sub>64.7</sub>:Al<sub>26.2</sub>:V<sub>9.1</sub> (at.%) as determined by EDX.**

Appearance	Pt	Al	V	Phases
Overall	64.7±0.3	26.2±0.2	9.1±0.2	-
Medium dendrites	65.3±0.4	17.5±0.8	17.2±0.7	~Pt <sub>3</sub> Al
Light phase	65.4±0.9	30.5±1.5	4.1±0.8	~ Pt <sub>5</sub> Al <sub>3</sub>
Dark phase	58.0±1.0	5.3±2.0	36.7±2.5	~Pt <sub>2</sub> V
Eutectoid	63.7±1.2	24.5±2.5	11.8±1.5	~PtAl + ~Pt <sub>5</sub> Al <sub>3</sub>
Two-phase dendrites	66.0±0.5	20.4±1.1	13.6±1.3	~Pt <sub>2</sub> V pptn. within ~Pt <sub>3</sub> Al

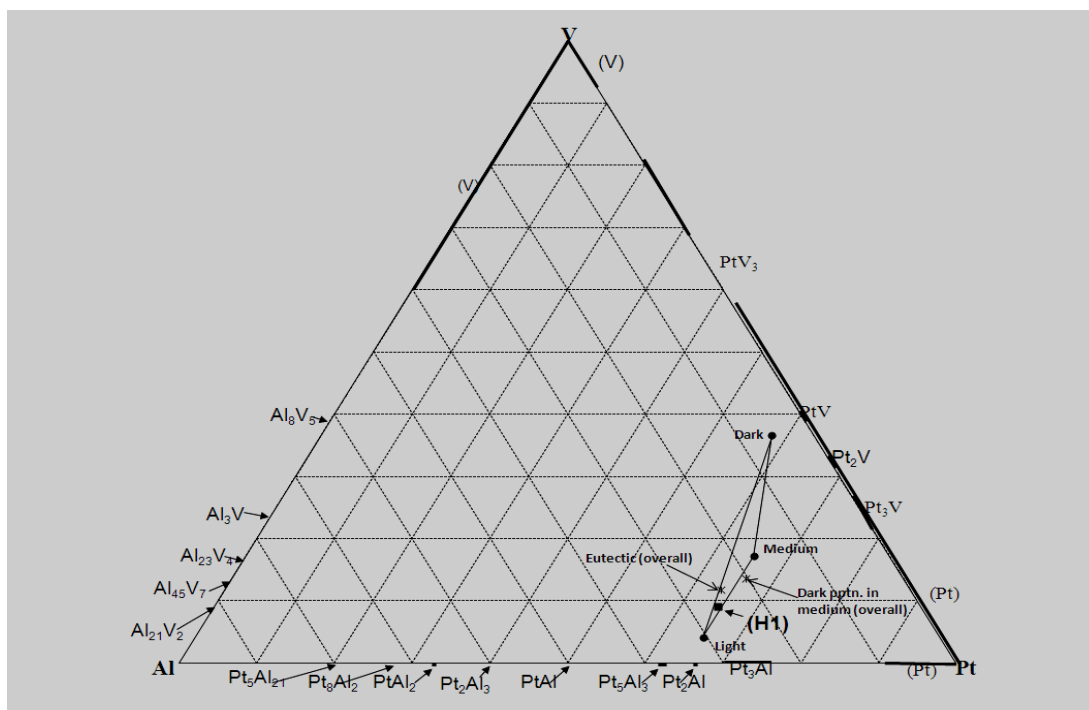


**Figure 4.40. Plot of the overall and phase compositions of the annealed Alloy 1H, average composition Pt<sub>64.7</sub>:Al<sub>26.2</sub>:V<sub>9.1</sub> (at.%).**





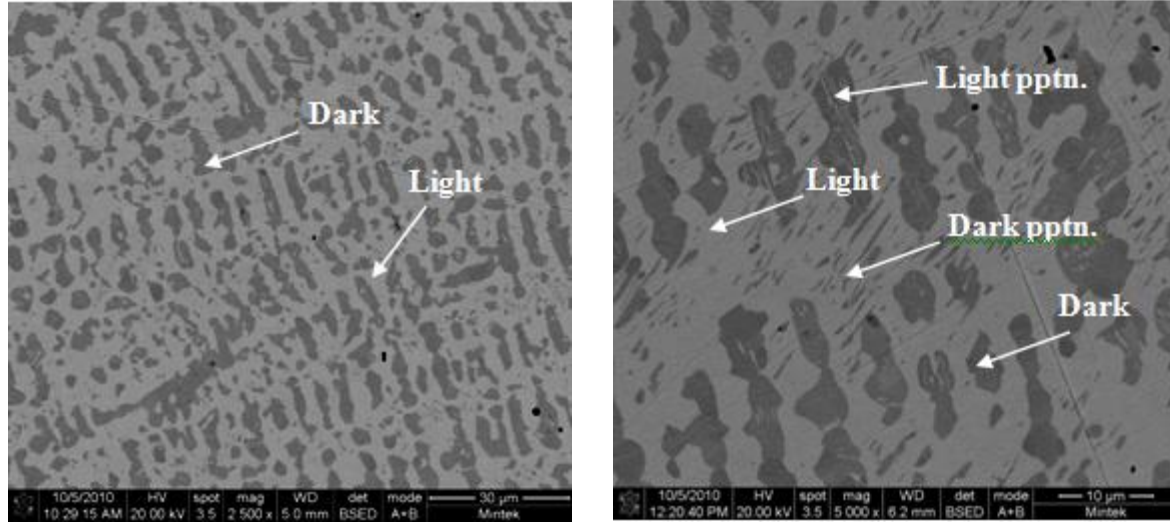
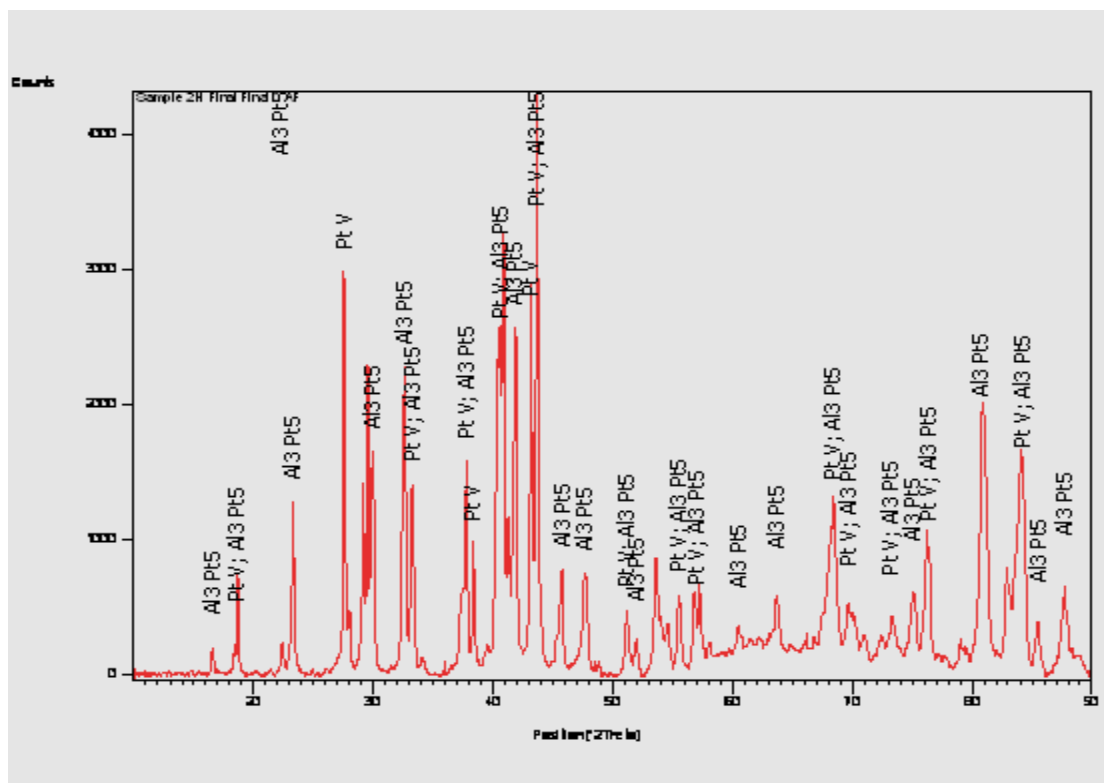
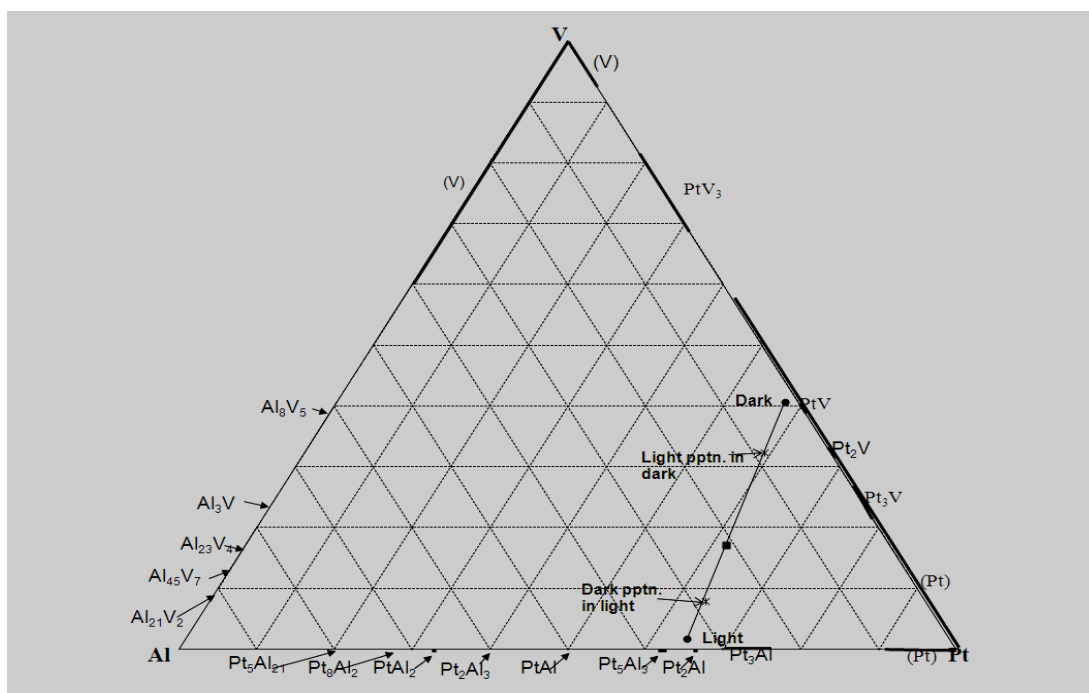


**Figure 4.42. (a). SEM-BSE image of annealed Alloy 2H, average composition  $\text{Pt}_{61.8}:\text{Al}_{21.1}:\text{V}_{17.1}$  (at.%), showing a dark phase ( $\sim\text{PtV}$ ), a light phase ( $\sim\text{Pt}_5\text{Al}_3$ ) and dark precipitates in the light phase, scale bar is 30  $\mu\text{m}$  and (b). SEM-BSE image of annealed Alloy  $\text{Pt}_{61.8}:\text{Al}_{21.1}:\text{V}_{17.1}$  (at.%) showing a dark phase ( $\sim\text{PtV}$ ), a light phase ( $\sim\text{Pt}_5\text{Al}_3$ ), dark precipitates within the light phase and light precipitates in the dark phase, scale bar is 10  $\mu\text{m}$ .**

**Table 4.15. Overall and phase compositions of annealed Alloy 2H, average composition  $\text{Pt}_{61.8}:\text{Al}_{21.1}:\text{V}_{17.1}$  (at.%) as determined by EDX.**

Appearance	Pt	Al	V	Phases
Overall	61.8±0.3	21.1±0.6	17.1±0.3	-
Dark	57.6±0.4	1.8±0.2	40.6±0.2	$\sim\text{PtV}$
Light	64.4±0.3	33.8±0.4	1.8±0.2	$\sim\text{Pt}_5\text{Al}_3$
Dark ppt. within the light matrix (overall)	63.9±0.9	28.2±2.0	7.9±1.2	$\sim\text{PtV}$ pptn. within $\sim\text{Pt}_5\text{Al}_3$
Light ppt. within the dark phase (overall)	58.9±0.9	8.9±0.9	32.2±1.6	$\sim\text{Pt}_5\text{Al}_3$ pptn. within $\sim\text{PtV}$



#### 4.2.3 Annealed Alloy 3H, Average Composition $\text{Pt}_{63.7}:\text{Al}_{10.8}:\text{V}_{25.5}$ (at.%)

Figure 4.45 shows Alloy 3H, average composition  $\text{Pt}_{63.7}:\text{Al}_{10.8}:\text{V}_{25.5}$  (at.%), at different magnifications. Figure 4.45(a) shows a medium grey phase, a light phase and a dark phase. Comparison with the as-cast structure (Figure 4.7) shows that the  $\sim\text{Pt}_2\text{V}$  dendrites had been reduced and had a lighter phase,  $\sim\text{Pt}_3\text{Al}$ , precipitated within (Figure. 4.45(b)). The phase was too small to analyse accurately, although larger areas of the medium phase were analysed. Plotting identified the medium phase as  $\sim\text{Pt}_2\text{V}$ , the dark phase as  $\sim\text{PtV}$ , while the light phase was identified as  $\sim\text{Pt}_3\text{Al}$ , and XRD confirmed these (Figure 4.47). In comparison with the as-cast alloy, the structure coarsened and  $\sim\text{Pt}_2\text{Al}$  disappeared. Instead  $\sim\text{PtV}$  formed in the annealed alloy.

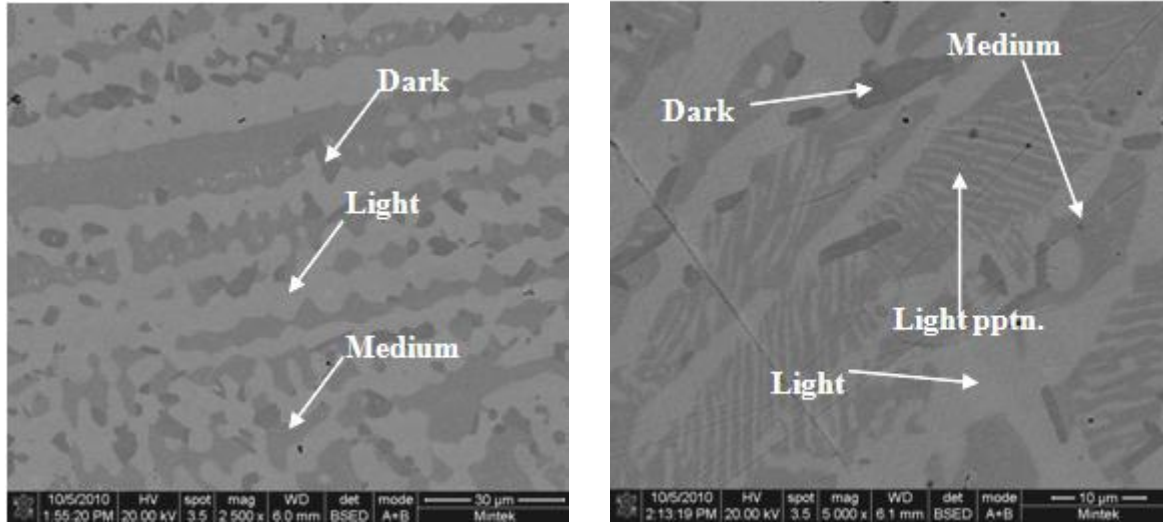


**Figure 4.45. (a). SEM-BSE image of annealed Alloy 3H,  $\text{Pt}_{63.7}:\text{Al}_{10.8}:\text{V}_{25.5}$  (at.%) showing a medium grey phase ( $\sim\text{Pt}_2\text{V}$ ), a light phase ( $\sim\text{Pt}_3\text{Al}$ ) and a dark phase ( $\sim\text{PtV}$ ) and (b). SEM-BSE image of annealed Alloy 3H,  $\text{Pt}_{63.7}:\text{Al}_{10.8}:\text{V}_{25.5}$  (at.%) showing a medium grey phase ( $\sim\text{Pt}_2\text{V}$ ), a light phase ( $\sim\text{Pt}_3\text{Al}$ ), a dark phase ( $\sim\text{PtV}$ ) and 2-phase dendrites.**

**Table 4.16. Overall and phase compositions of annealed Alloy 3H, average composition  $\text{Pt}_{63.7}:\text{Al}_{10.8}:\text{V}_{25.5}$  (at.%) determined by EDX.**

Appearance	Pt	Al	V	Phases
Overall	$63.7 \pm 0.5$	$10.8 \pm 0.6$	$25.5 \pm 0.3$	-
Medium	$64.0 \pm 0.4$	$3.2 \pm 0.5$	$32.8 \pm 0.6$	$\sim \text{Pt}_2\text{V}$
Light	$65.3 \pm 0.8$	$15.9 \pm 1.4$	$18.8 \pm 0.9$	$\sim \text{Pt}_3\text{Al}$
Dark	$58.5 \pm 0.6$	0	$41.5 \pm 0.6$	$\sim \text{PtV}$
2-phase dendrites	$64.3 \pm 0.6$	$7.4 \pm 0.7$	$28.3 \pm 0.3$	$\sim \text{Pt}_3\text{Al}$ pptn. within $\sim \text{Pt}_2\text{V}$

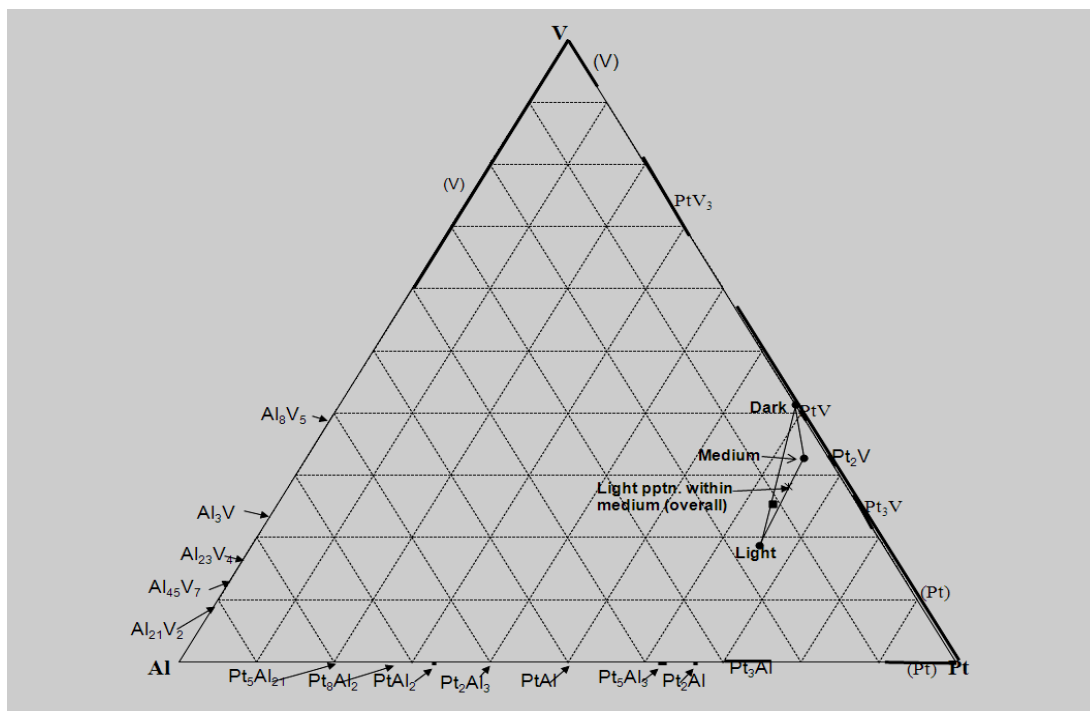


**Figure 4.46. Plot of overall and phase compositions of annealed Alloy 3H, average composition  $\text{Pt}_{63.7}:\text{Al}_{10.8}:\text{V}_{25.5}$  (at.%).**

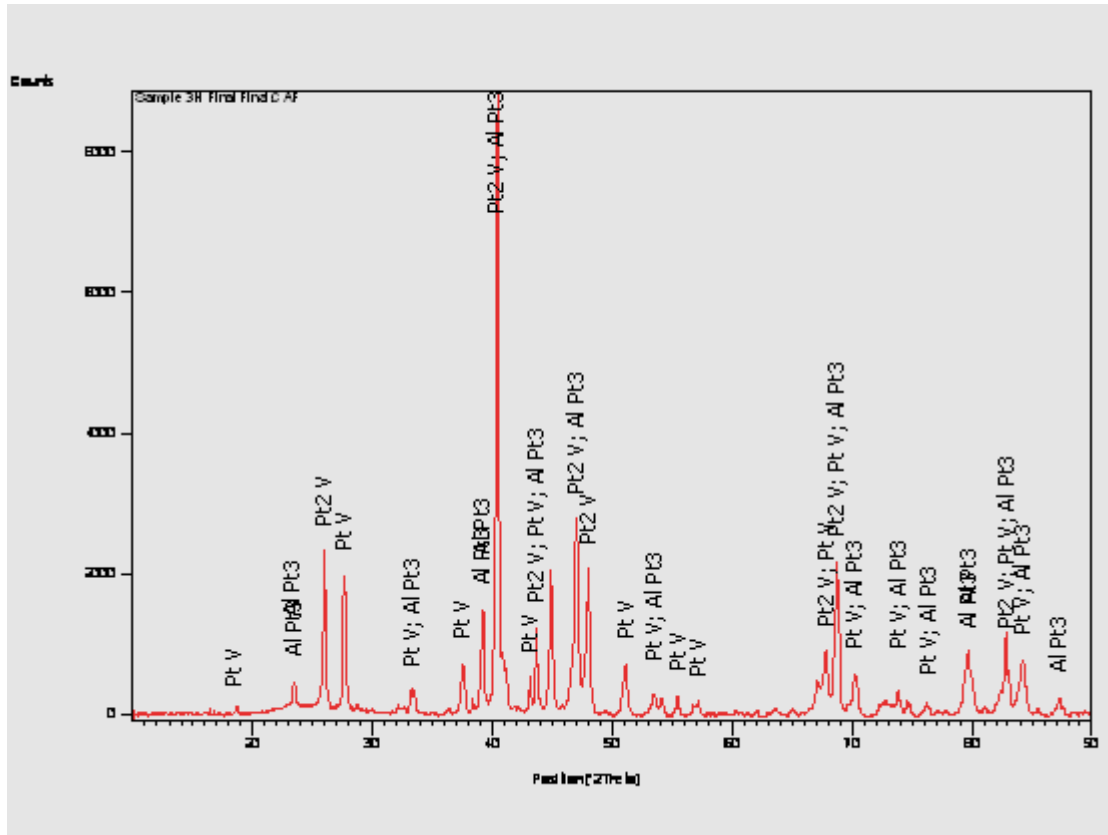


**Figure 4.47. XRD pattern of annealed Alloy 3H, average composition  $\text{Pt}_{63.7}:\text{Al}_{10.8}:\text{V}_{25.5}$  (at.%).**

#### **4.2.4 Annealed Alloy 4BH, Average Composition $\text{Pt}_{69.7}:\text{Al}_{23.2}:\text{V}_{7.1}$ (at.%)**

Figure 4.48 has SEM-BSE images of Alloy 4BH, average composition  $\text{Pt}_{69.7}:\text{Al}_{23.2}:\text{V}_{7.1}$  (at.%), at different magnifications. Both figures show a dark phase, a medium grey phase and a light phase. When the compositions of the phases were plotted as in Figure 4.49, it was determined that the dark and medium grey phase were the same phase  $\sim\text{Pt}_3\text{Al}$ , and the appearance was due to different orientations within the separate grains. The light phase was identified as  $\sim\text{Pt}_2\text{Al}$ . XRD confirmed the presence of both phases, as shown in Figure 4.50. In comparison with the as-cast alloy, the dendrites had more definite boundaries. There is also a new phase,  $\text{Pt}_2\text{Al}$ .

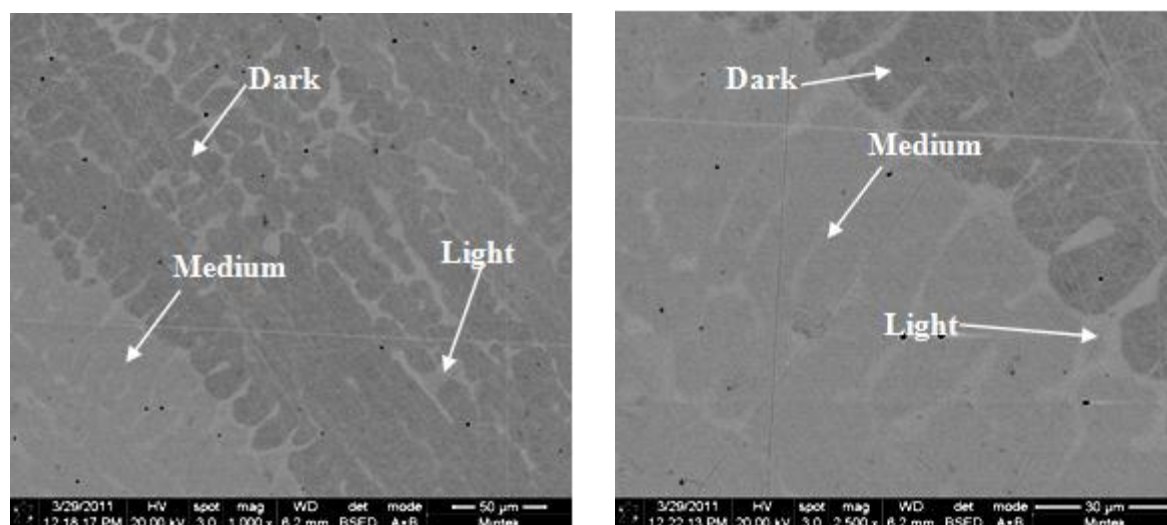
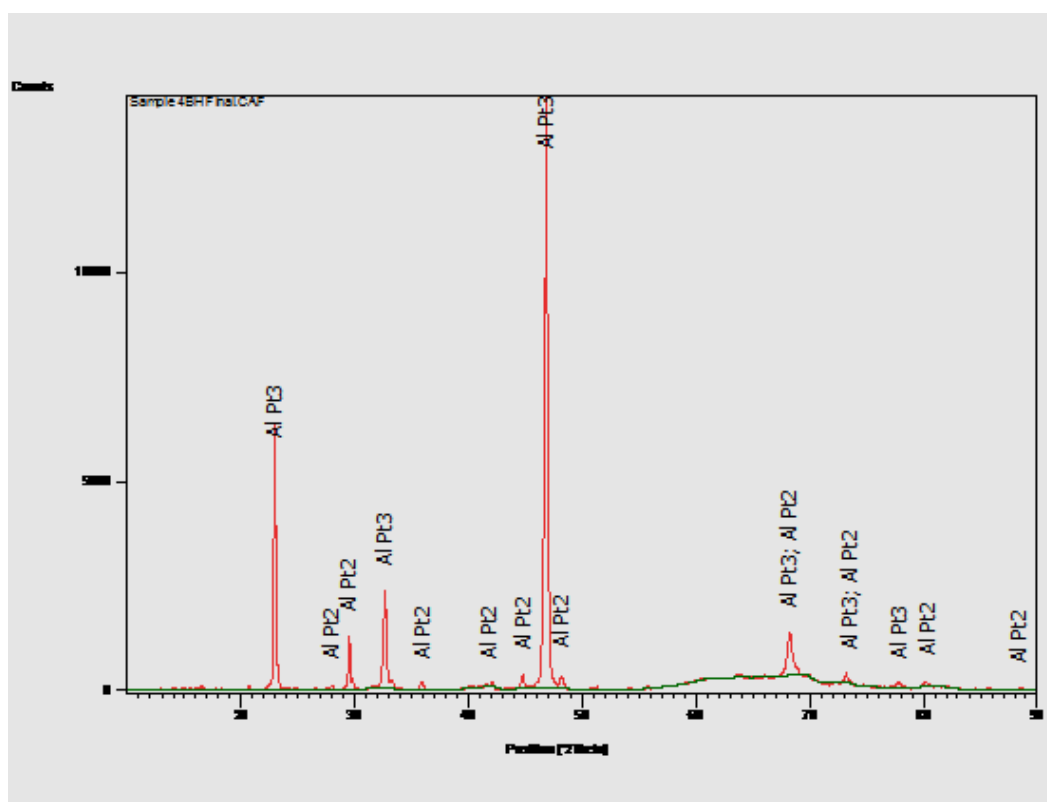
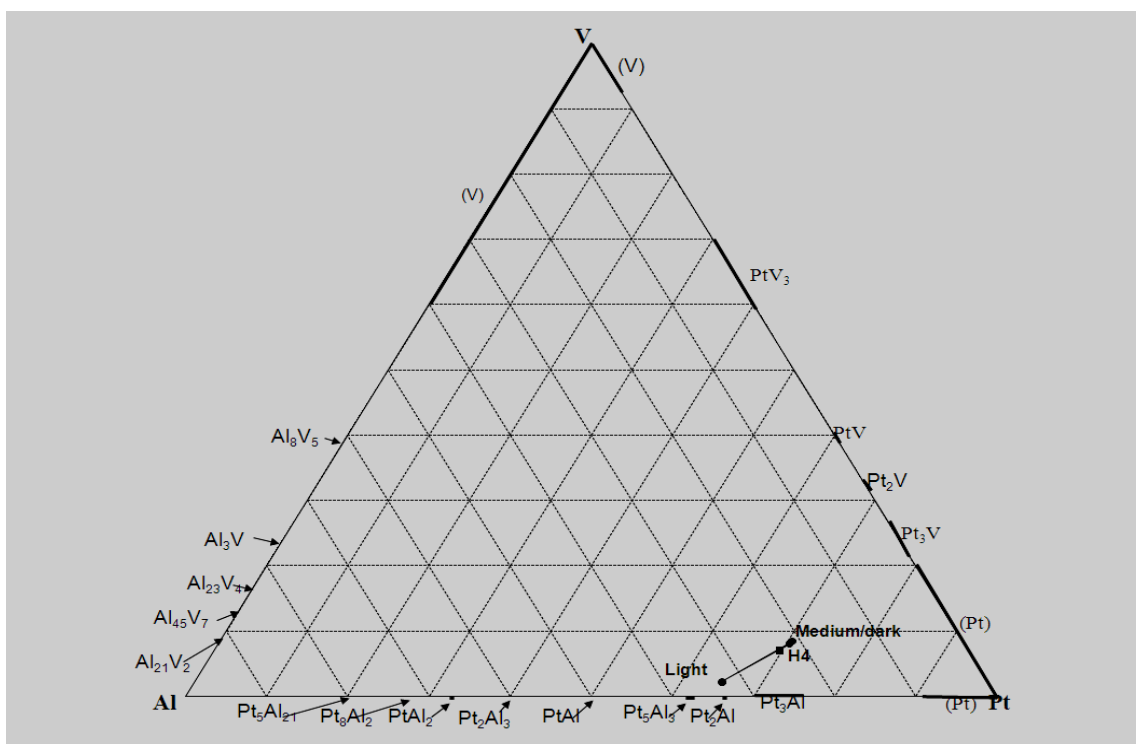


**Figure 4.48. (a).** SEM-BSE image of Alloy 4BH,  $\text{Pt}_{69.7}\text{Al}_{23.2}\text{V}_{7.1}$  (at.%) showing a dark phase, a medium grey phase and a light phase ( $\sim\text{Pt}_2\text{Al}$ ). The dark phase and the medium grey phases are the same phase ( $\sim\text{Pt}_3\text{Al}$ ) seen from different orientations and **(b).** SEM-BSE image of Alloy 4BH,  $\text{Pt}_{69.7}\text{Al}_{23.2}\text{V}_{7.1}$  (at.%) showing a dark phase, a medium grey phase and a light phase at a higher magnification.

**Table 4.17. Overall and phase compositions of annealed Alloy 4BH, average composition  $\text{Pt}_{69.7}\text{Al}_{23.2}\text{V}_{7.1}$  (at.%) as determined by EDX.**

Appearance	Pt	Al	V	Phases
Overall	$69.7 \pm 0.1$	$23.2 \pm 0.3$	$7.1 \pm 0.1$	-
Dark	$70.6 \pm 0.3$	$21.0 \pm 0.2$	$8.4 \pm 0.2$	$\sim\text{Pt}_3\text{Al}$
Medium	$70.3 \pm 0.6$	$21.6 \pm 1.0$	$8.1 \pm 0.7$	$\sim\text{Pt}_3\text{Al}$
Light	$65.1 \pm 0.7$	$32.7 \pm 0.7$	$2.2 \pm 0.2$	$\sim\text{Pt}_2\text{Al}$





#### 4.2.5 Annealed Alloy 10H, Average Composition $\text{Pt}_{83.9}:\text{Al}_{5.8}:\text{V}_{10.3}$ (at.%)

Figure 4.51 shows annealed Alloy 10H, average composition,  $\text{Pt}_{83.9}:\text{Al}_{5.8}:\text{V}_{10.3}$  (at.%), at different magnifications, and both have poor contrast from the close average atomic numbers of the phases. Figure 4.51(a) shows a light contrast phase and a dark phase. From the plotting (Figure 4.52), the light phase was identified as (Pt), the dark phase as  $\sim\text{Pt}_2\text{V}$ , which was not observed in the as-cast sample. The coarsened eutectic could just be discerned in Figure 4.51(a) and was more clearly resolved in Figure 4.51(b). The components of the eutectic were too small to be accurately analysed by EDX. Extrapolation from (Pt) through the eutectic overall indicated that the eutectic also comprised  $\sim\text{Pt}_3\text{Al}$ . XRD confirmed the identities of  $\sim\text{Pt}_2\text{V}$ ,  $\sim\text{Pt}_3\text{Al}$  and (Pt) (Figure 4.53). In comparison with the as-cast alloy, the eutectic coarsened and the dark phase precipitated during annealing.

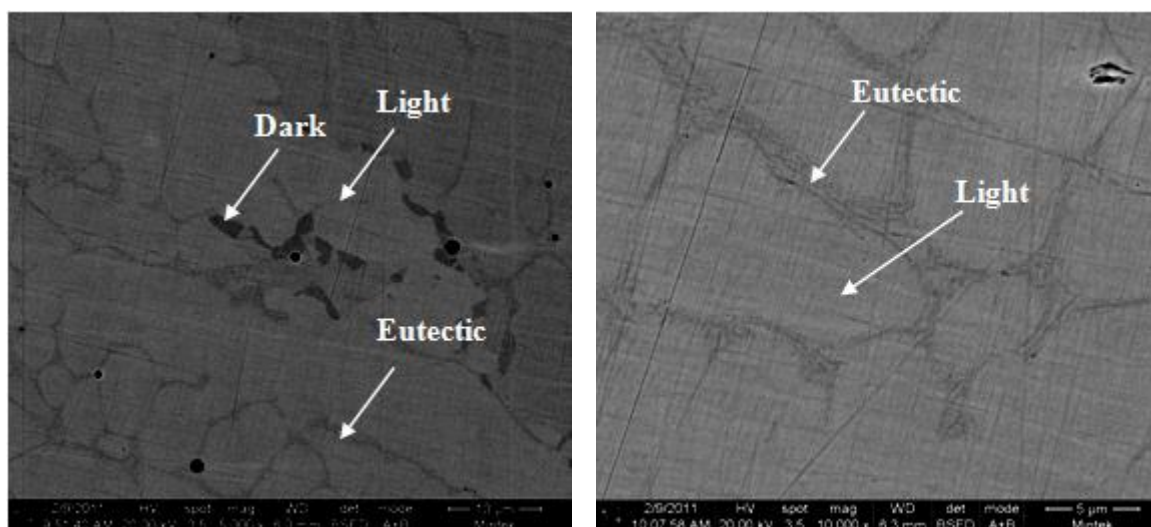


**Figure 4.51 (a). SEM-BSE image of annealed Alloy 10H,  $\text{Pt}_{83.9}:\text{Al}_6:\text{V}_{10.1}$  (at.%) showing a light grey phase, a dark phase and a eutectic and (b). SEM-BSE image of annealed Alloy 10H,  $\text{Pt}_{83.9}:\text{Al}_6:\text{V}_{10.1}$  (at.%) showing a light grey phase and a eutectic at a higher magnification.**

**Table 4.18. Overall and phase compositions of annealed Alloy 10H, average overall composition  $\text{Pt}_{83.9}:\text{Al}_{5.8}:\text{V}_{10.3}$  (at.%) as determined by EDX.**

Appearance	Pt	Al	V	Phases
Overall	83.9±0.9	5.8±0.6	10.3±0.5	-
Light	87.7±0.5	3.7±0.3	8.6±0.5	(Pt)
Dark	70.1±0.7	0	29.9±0.7	~ $\text{Pt}_2\text{V}$
Eutectic	78.4±1.0	6.8±0.2	14.8±1.2	(Pt) + ~ $\text{Pt}_3\text{Al}$

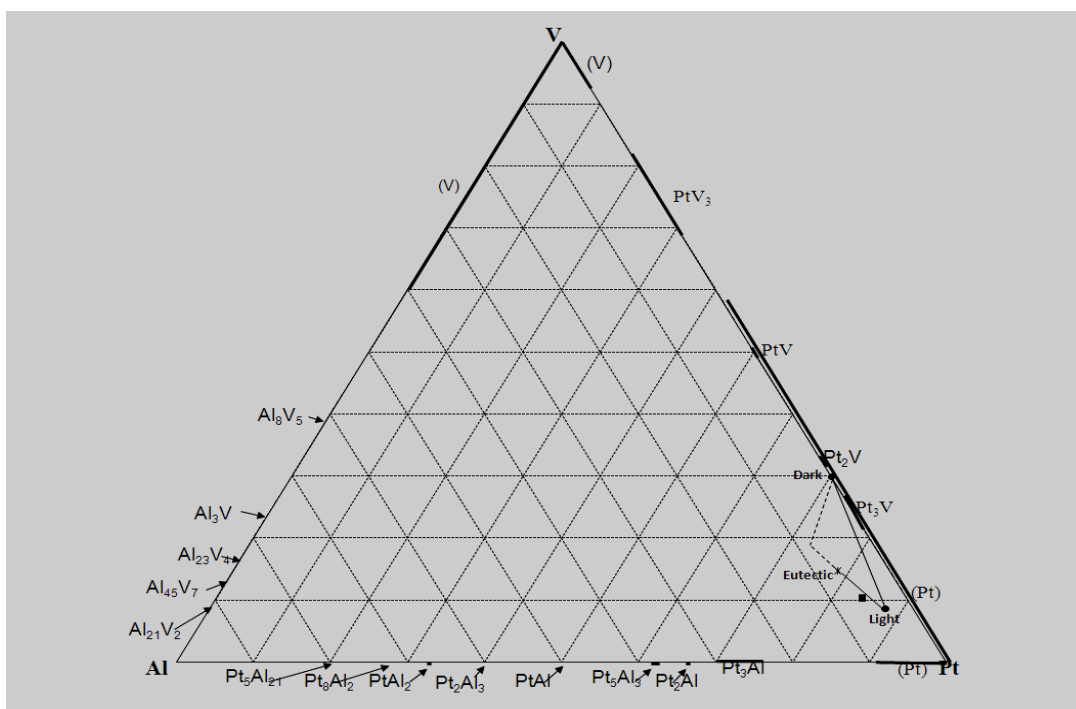


**Figure 4.52. Plot of overall and phase compositions of annealed Alloy 10H, average composition  $\text{Pt}_{83.9}:\text{Al}_{5.8}:\text{V}_{10.3}$  (at.%).**

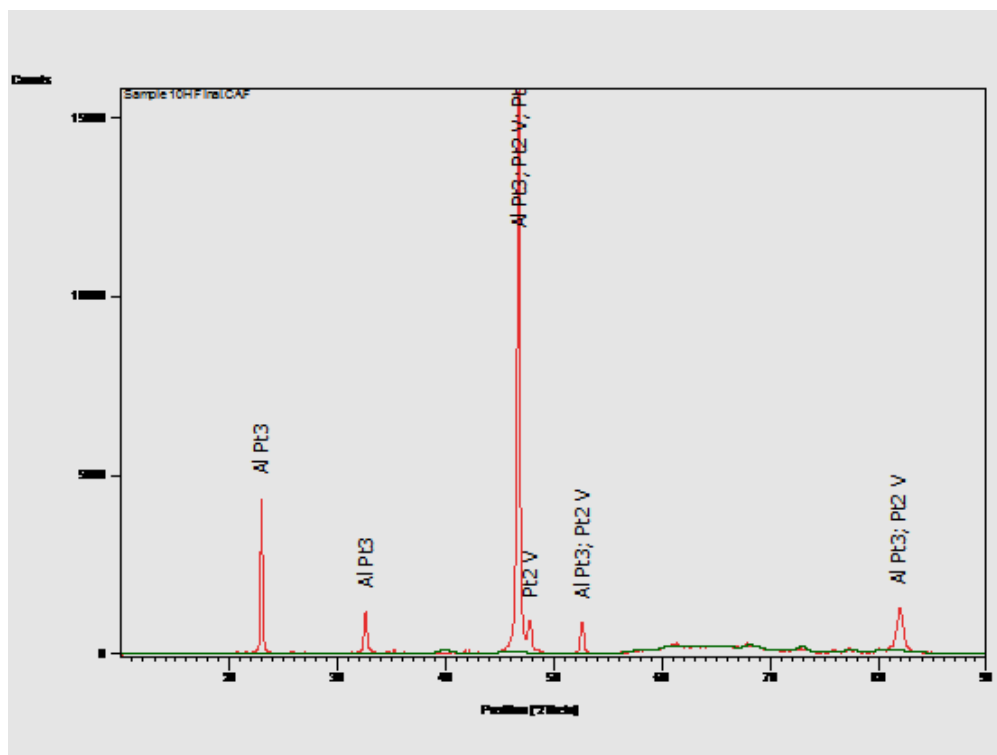


**Figure 4.53. XRD pattern of alloy 10H, average composition  $\text{Pt}_{83.9}\text{Al}_{5.8}\text{V}_{10.3}$  (at.%). The unlabelled peaks are due to the resin mounting (Appendix 1A).**

#### **4.2.6 Annealed Alloy 11H, Average Composition $\text{Pt}_{85.2}\text{Al}_{3.4}\text{V}_{11.4}$ (at.%)**

Figure 4.54 is an SEM-BSE image of annealed Alloy 11H, average composition  $\text{Pt}_{85.2}\text{Al}_{3.4}\text{V}_{11.4}$  (at.%). There was poor contrast because of the close average atomic numbers. There was a light contrast phase and a fine eutectic which appeared dark. The components of the eutectic were too fine to be accurately analysed by EDX even though they had coarsened slightly. Extrapolation from (Pt) indicated that the other component of the eutectic was  $\sim\text{Pt}_3\text{Al}$  (Figure 4.55). The grain boundaries were irregular, but less so than in the as-cast alloy. XRD confirmed the phase identification (Figure 4.56).

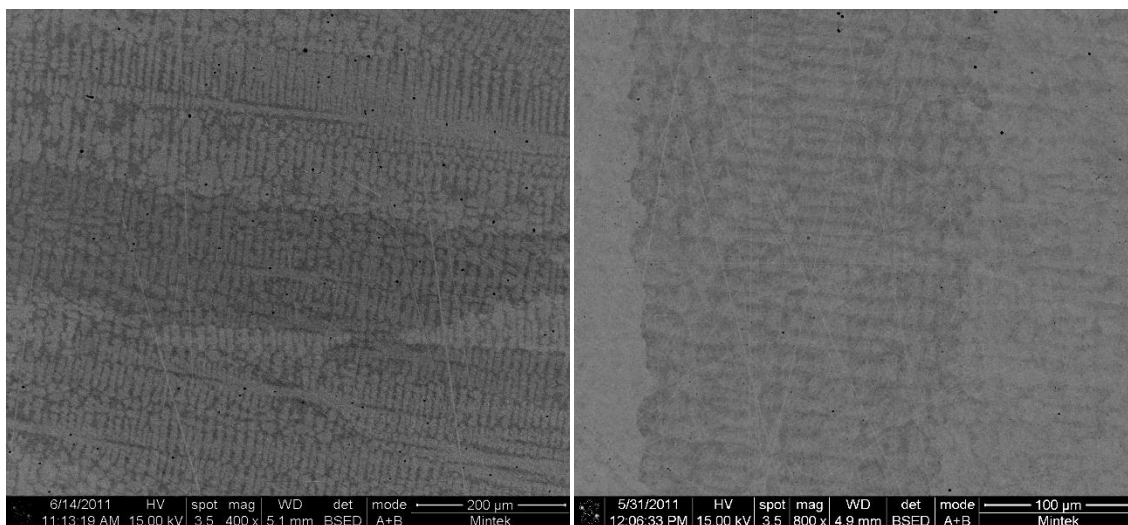


**Figure 4.54. (a). SEM-BSE image of annealed Alloy 11H showing a light phase (Pt) and a dark eutectic, (Pt) +  $\sim$ Pt<sub>3</sub>Al and (b). SEM-BSE image of annealed Alloy 11H at a higher magnification, showing a light phase (Pt) and a dark eutectic, (Pt) +  $\sim$ Pt<sub>3</sub>Al.**

**Table 4.19. Overall and phase compositions of annealed Alloy 11H, average composition Pt<sub>85.2</sub>:Al<sub>3.4</sub>:V<sub>11.4</sub> (at.%), determined by EDX.**

Appearance	Pt	Al	V	Phase
Overall	85.2±1.0	3.4±0.3	11.4±0.7	-
Light	88.1±1.3	1.4±0.4	10.5±1.3	(Pt)
Eutectic (dark)	84.9±1.2	6.3±0.3	8.8±1.0	(Pt) + $\sim$ Pt <sub>3</sub> Al

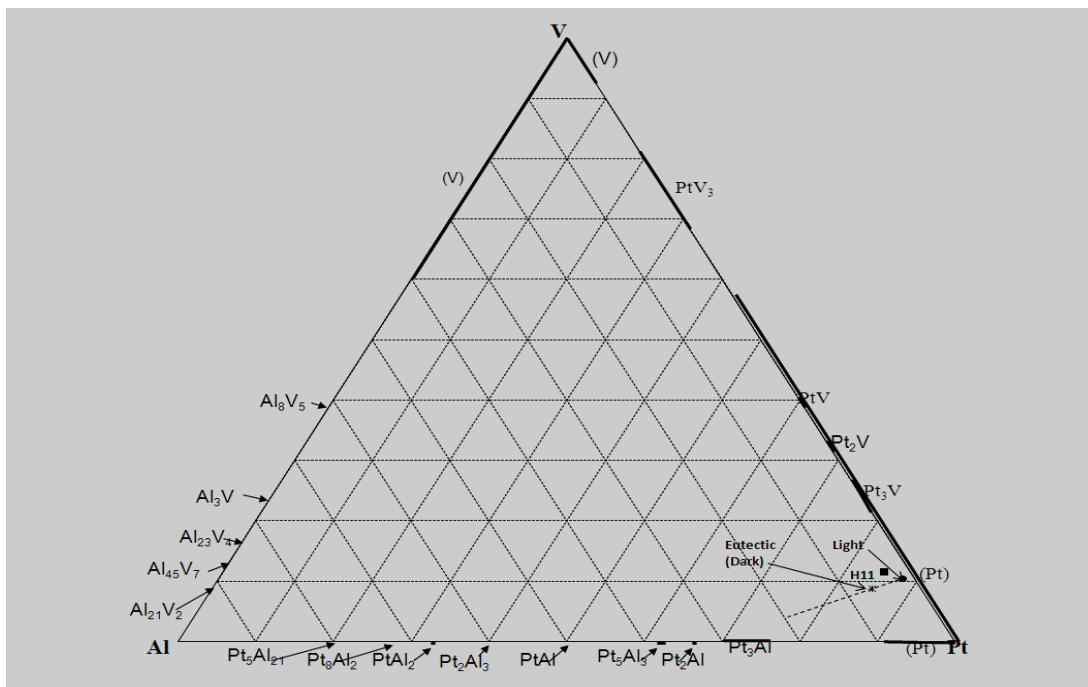


Figure 4.55. Plot of overall and phase compositions of annealed Alloy 11H, average composition  $\text{Pt}_{85.2}\text{Al}_{3.4}\text{V}_{11.4}$  (at.%).

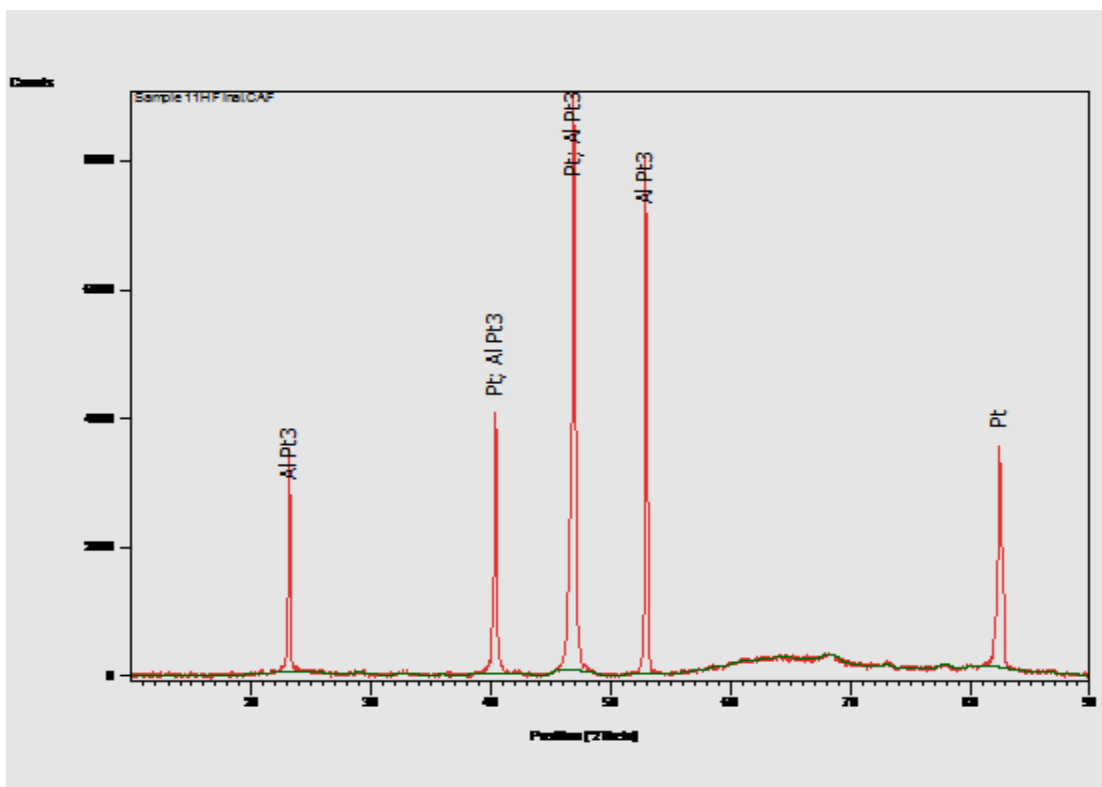
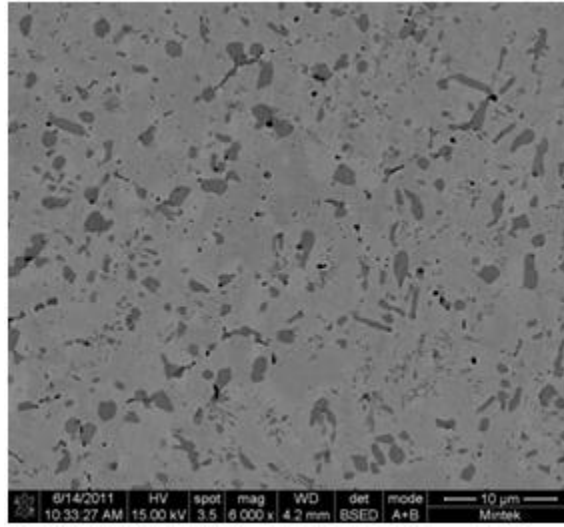


Figure 4.56. XRD pattern of annealed Alloy 11H, average composition  $\text{Pt}_{85.2}\text{Al}_{3.4}\text{V}_{11.4}$  (at.%).

#### 4.2.7 Annealed Alloy 12H, Average Composition $\text{Pt}_{60.5}:\text{Al}_{18.6}:\text{V}_{20.9}$ (at.%)

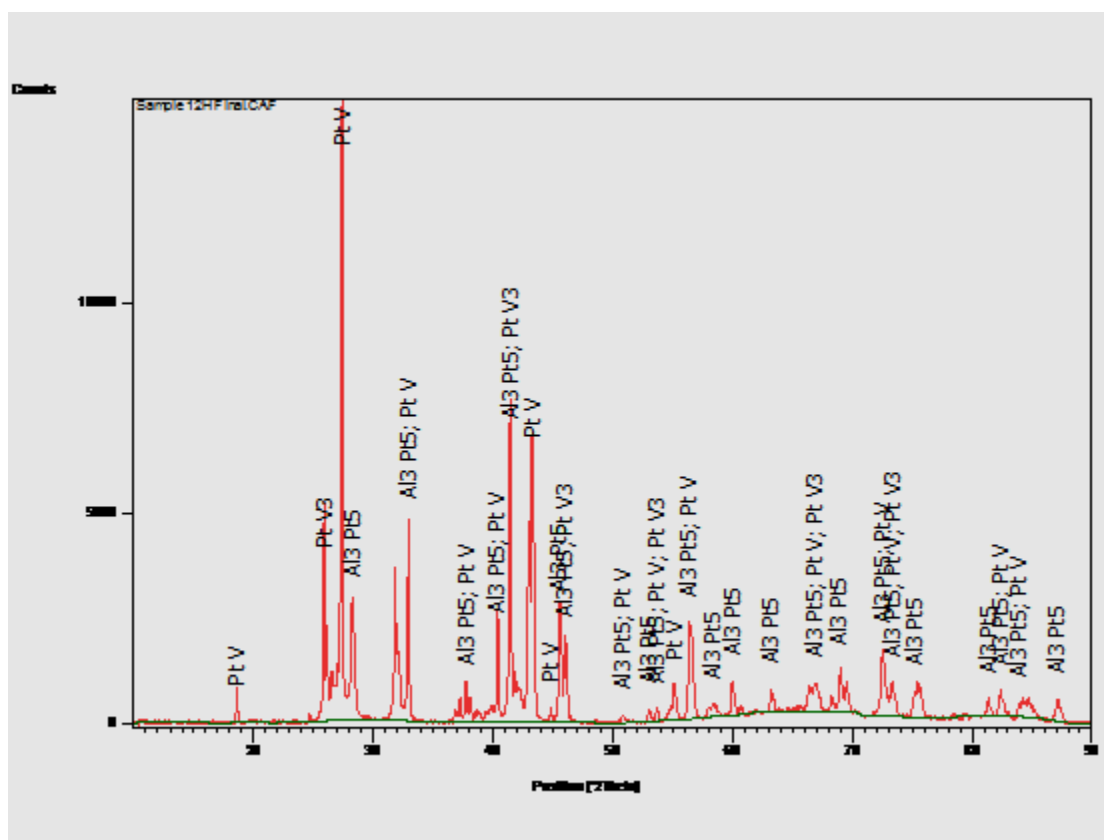
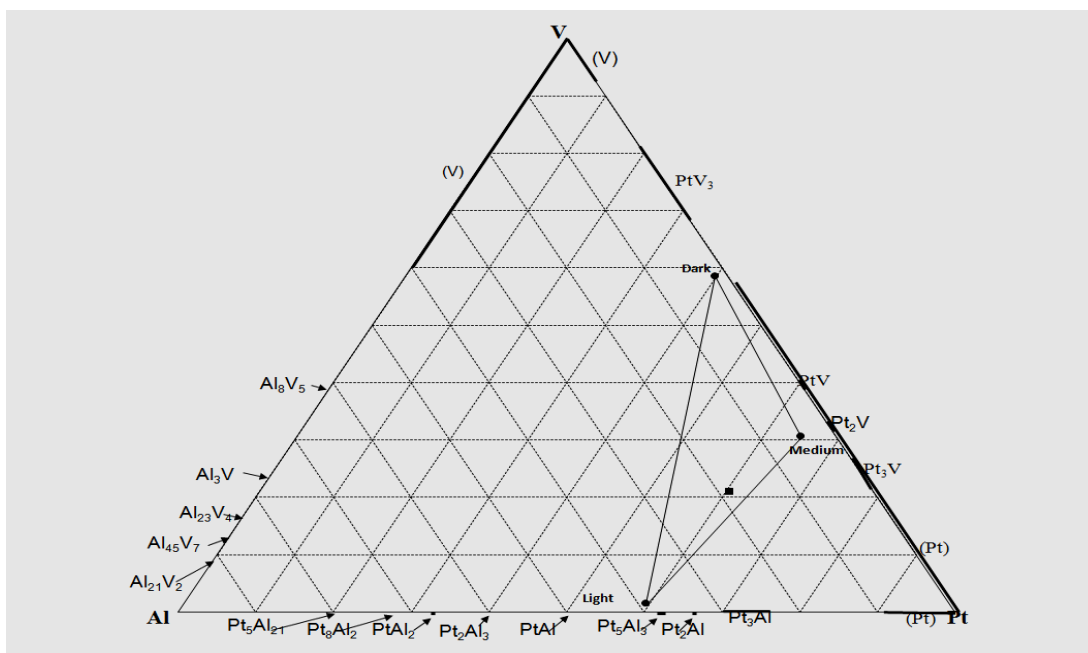
Figure 4.57 is an SEM-BSE image of Alloy 12H, average composition  $\text{Pt}_{60.5}:\text{Al}_{18.6}:\text{V}_{20.9}$  (at.%), showing a light phase, a medium phase and a dark phase. When the overall and phase compositions in Table 4.18 were plotted as in Figure 4.58, the medium phase was identified as  $\sim\text{PtV}$ , the dark phase as  $\sim\text{PtV}_3$  and the light phase as  $\sim\text{Pt}_5\text{Al}_3$ . XRD confirmed the phase identification, as shown in Figure 4.59. In comparison with the as-cast alloy, the ternary phase,  $\tau_1$ , disappeared and  $\sim\text{Pt}_5\text{Al}_3$  formed, showing that the ternary phase existed on casting, but above  $1000^\circ\text{C}$  it transforms to  $\sim\text{Pt}_5\text{Al}_3$ . The alloy also coarsened considerably.



**Figure 4.57. SEM-BSE image of Alloy 12H, average composition  $\text{Pt}_{60.5}:\text{Al}_{18.6}:\text{V}_{20.9}$  (at.%) showing a medium phase ( $\sim\text{PtV}$ ), a dark phase ( $\sim\text{PtV}_3$ ) and the light phase ( $\sim\text{Pt}_5\text{Al}_3$ ).**

**Table 4.20. Overall and phase compositions of Alloy 12H, average composition  $\text{Pt}_{60.5}:\text{Al}_{18.6}:\text{V}_{20.9}$  (at.%), determined by EDX.**

Appearance	Pt	Al	V	Phase
Overall	60.5±1.2	18.6±1.0	20.9±0.8	-
Medium	64.9±0.5	4.5±0.5	30.6±0.6	$\sim\text{PtV}$
Dark	39.9±2.0	1.5±0.2	58.6±2.0	$\sim\text{PtV}_3$
Light	59.4±1.0	39.1±1.2	1.5±0.3	$\sim\text{Pt}_5\text{Al}_3$



#### 4.2.8 Annealed Alloy 13H, Average Composition $\text{Pt}_{59.2}:\text{Al}_{8.4}:\text{V}_{32.4}$ (at.%)

Figure 4.60 is a SEM-BSE image of Alloy 13H, average composition  $\text{Pt}_{59.2}:\text{Al}_{8.4}:\text{V}_{32.4}$  (at.%), showing a medium contrast phase, a light contrast phase and a dark phase. When the compositions in Table 4.19 were plotted as in Figure 4.61, the medium contrast phase was identified as  $\sim\text{PtV}$ , the dark phase was identified as  $\text{PtV}_3$  and the light contrast phase was identified as  $\sim\text{Pt}_5\text{Al}_3$ . XRD confirmed the phase identification (Figure 4.62). The alloy lost its dendritic structure after annealing and there was more of the dark phase and less of the light phase. The ternary phase,  $\tau_1$ , also went through a solid state transformation with the reaction  $\tau_1 \rightarrow \sim\text{PtV} + \sim\text{PtV}_3 + \sim\text{Pt}_5\text{Al}_3$ . Thus  $\tau_1$  forms on solidification and is stable to a temperature above  $1000^\circ\text{C}$ , where it transforms to the three phases.

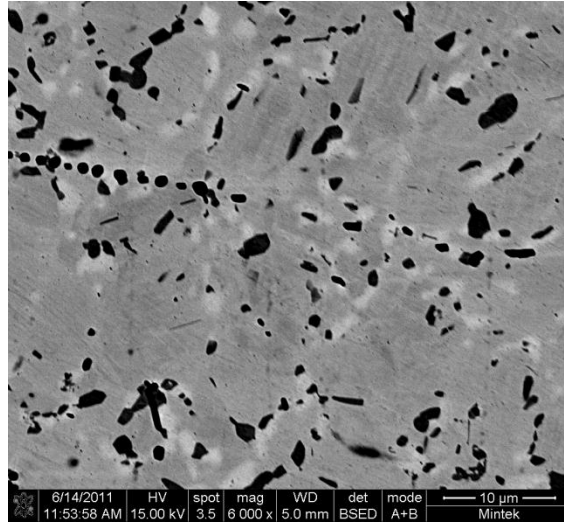
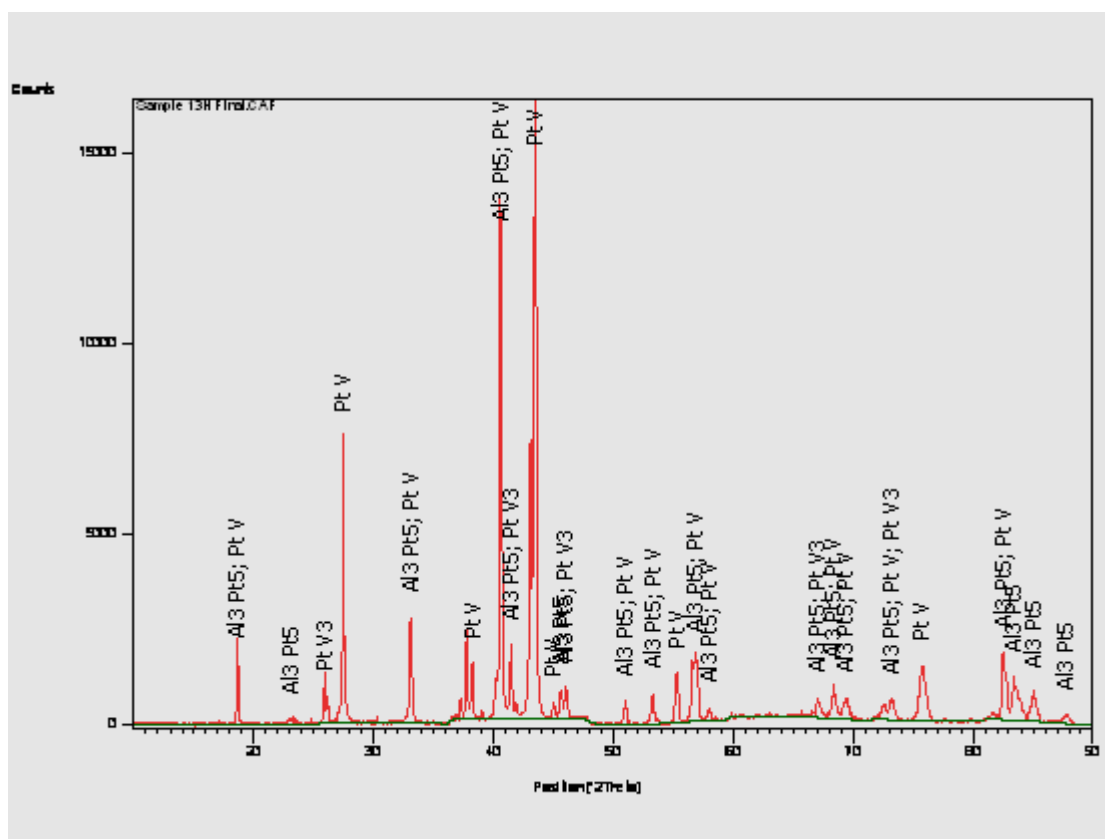
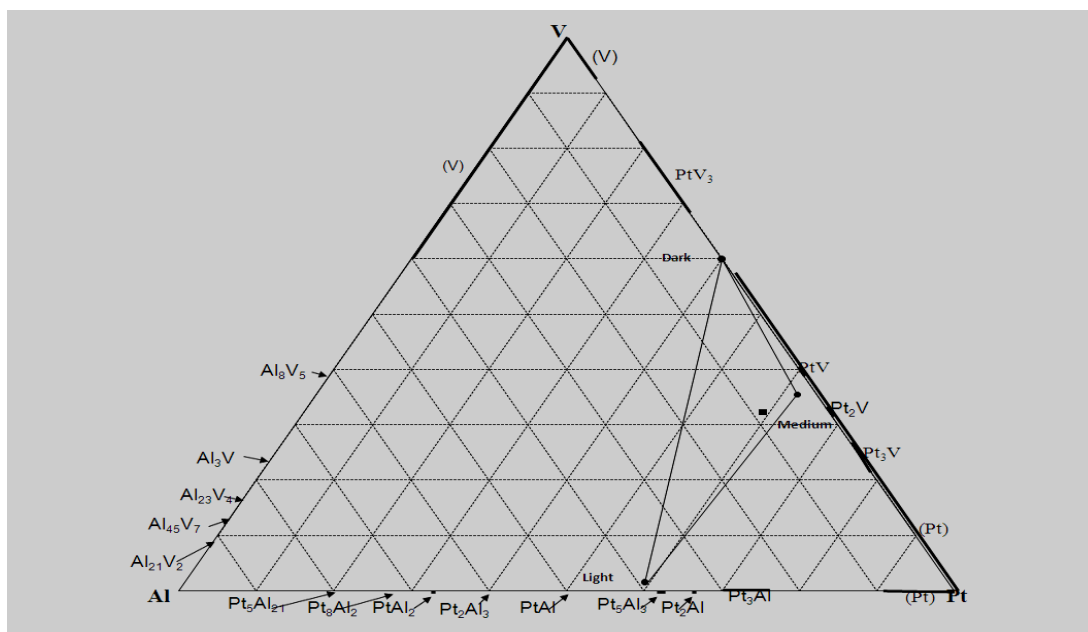


**Figure 4. 60.** SEM-BSE image of annealed Alloy 13H, average composition  $\text{Pt}_{59.2}:\text{Al}_{8.4}:\text{V}_{32.4}$  (at.%) showing a medium contrast phase  $\sim\text{PtV}$ , a dark phase  $\sim\text{PtV}_3$  and a light phase ( $\sim\text{Pt}_5\text{Al}_3$ ).

**Table 4.21.** Overall and phase compositions of Alloy 13H, average composition  $\text{Pt}_{59.2}:\text{Al}_{8.4}:\text{V}_{32.4}$  (at.%), determined by EDX.

Appearance	Pt	Al	V	Phase
Overall	$59.2 \pm 1.0$	$8.4 \pm 1.0$	$32.4 \pm 0.6$	-
Medium	$62.0 \pm 0.8$	$2.5 \pm 0.2$	$35.5 \pm 0.8$	$\sim\text{PtV}$
Dark	$40.2 \pm 1.9$	0	$59.8 \pm 1.9$	$\sim\text{PtV}_3$
Light	$62.6 \pm 0.6$	$33.9 \pm 0.8$	$3.5 \pm 0.3$	$\sim\text{Pt}_5\text{Al}_3$





#### 4.2.9 Annealed Alloy 14H, Average Composition $\text{Pt}_{81.6}:\text{Al}_{14.5}:\text{V}_{3.7}$ (at.%)

Figure 4.63 is a SEM-BSE image of Alloy 14H, average composition  $\text{Pt}_{81.6}:\text{Al}_{14.5}:\text{V}_{3.7}$  (at.%), showing light dendrites (Pt) having dark solid state precipitates ( $\sim\text{Pt}_3\text{Al}$ ) with the interdendritic dark  $\sim\text{Pt}_3\text{Al}$ . The dark precipitates which had been observed in the as-cast condition coarsened during heat treatment. The dark  $\sim\text{Pt}_3\text{Al}$  also had light (Pt) solid state precipitation, which had not been evident in the as-cast condition. The solid state precipitates indicate the retreating solvi of (Pt) and  $\sim\text{Pt}_3\text{Al}$ . The  $\sim\text{Pt}_3\text{Al}$  phase had lighter areas which was referred to as “medium” and darker areas which was referred to as “dark layer” (Table 4.20). EDX analysis was done on both the “medium” and “dark layer” separately to determine if there was coring. The plots for both were so close that it could not be conclusively stated that there was coring, or of so, it was minimal. XRD confirmed the phase identification (Figure 4.65). There were minor peaks in the spectrum which did not match either of the identified phases.

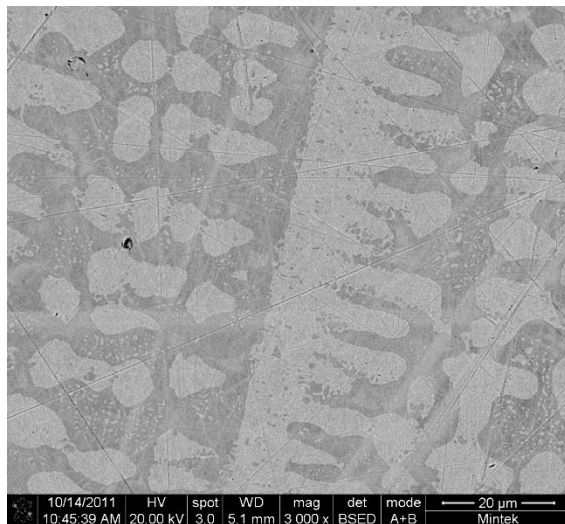


**Figure 4.63. SEM-BSE image of Alloy 14H, average composition  $\text{Pt}_{81.6}:\text{Al}_{14.5}:\text{V}_{3.7}$  (at.%), showing light dendrites, ( $\sim\text{Pt}$ ), having dark pptn. within, medium phase ( $\sim\text{Pt}_3\text{Al}$ ) with light pptn. ( $\sim\text{Pt}_3\text{Al}$ ) within.**

**Table 4.22. Overall and phase compositions of Alloy 14H, average composition Pt<sub>81.6</sub>:Al<sub>14.5</sub>:V<sub>3.7</sub> (at.%), determined by EDX.**

Appearance	Pt	Al	V	Phase
Overall	81.8±0.7	14.5±0.4	3.7±0.8	-
Light dendrites	88.8±0.4	6.1±0.5	5.1±0.3	(Pt)
Medium	74.0±0.2	23.9±0.6	2.1±0.3	~Pt <sub>3</sub> Al
Dark layer	75.3±0.7	21.8±0.6	2.9±0.3	~Pt <sub>3</sub> Al
Dark pptn. in light	76.9±0.9	19.3±0.9	3.8±0.9	~Pt <sub>3</sub> Al

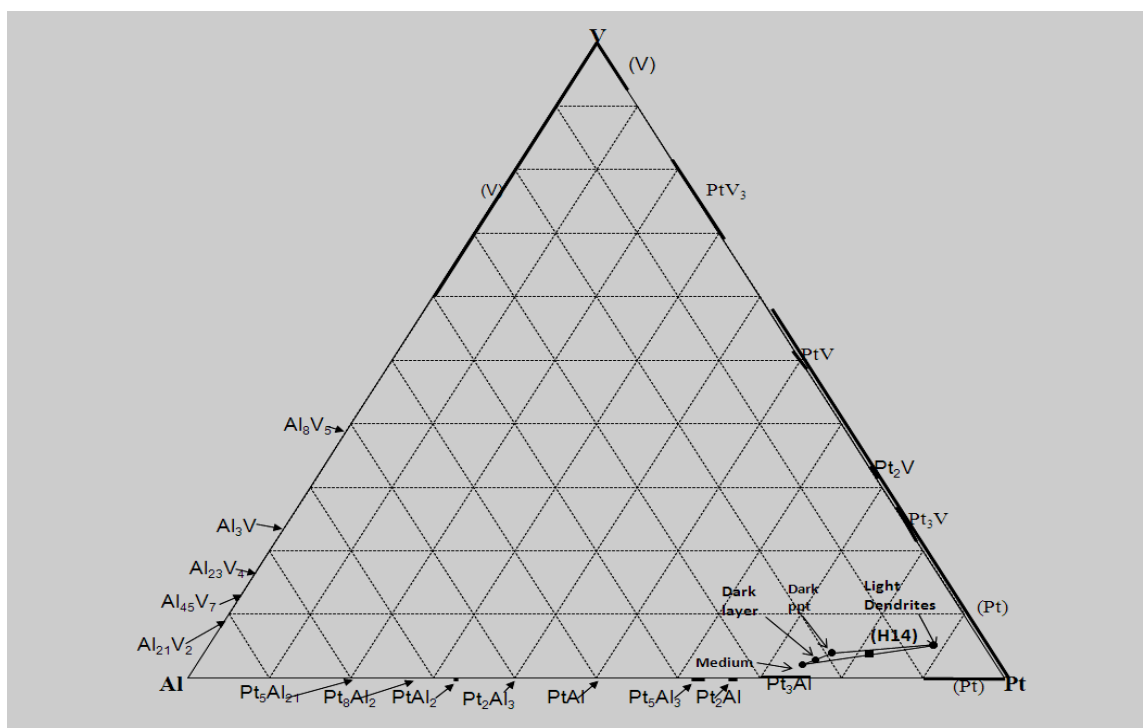


**Figure 4.64. Plot of the overall and phase compositions of annealed Alloy 14H, average composition  $\text{Pt}_{81.6}\text{Al}_{14.5}\text{V}_{3.7}$  (at.%).**

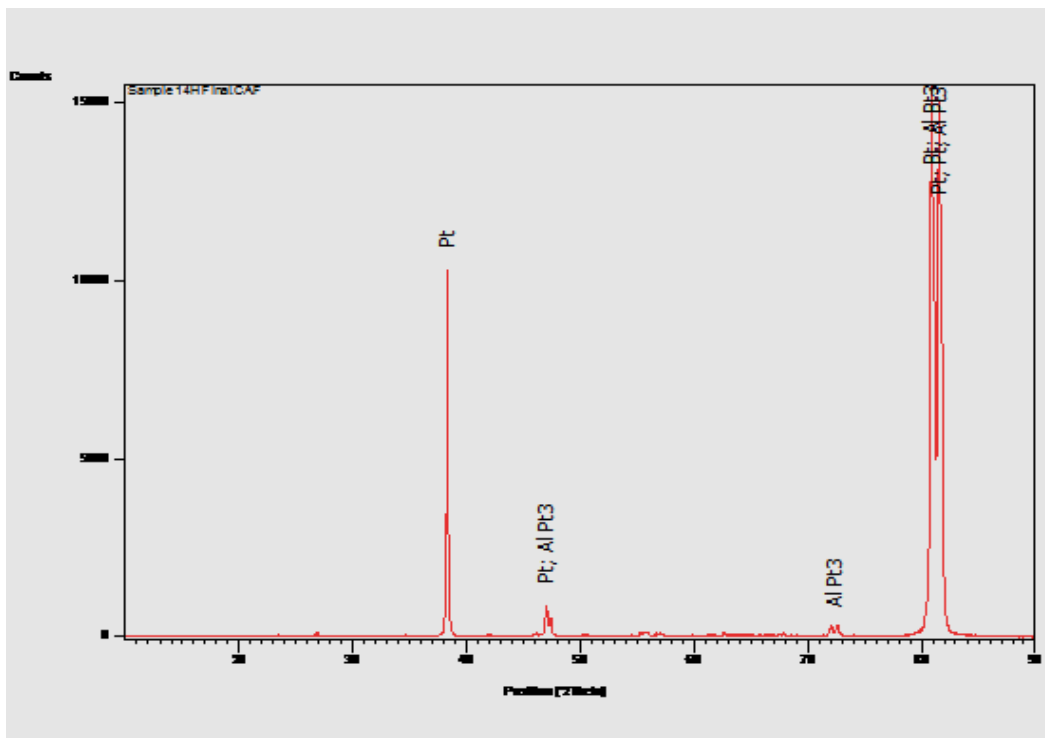


**Figure 4.65. XRD pattern of annealed Alloy 14H, average composition  $\text{Pt}_{81.6}:\text{Al}_{14.5}:\text{V}_{3.7}$  (at.%).**

#### **4.2.10 Annealed Alloy 15H, Average Overall Composition $\text{Pt}_{72.3}:\text{Al}_{13.5}:\text{V}_{14.2}$ (at.%)**

The SEM-BSE image of annealed Alloy 15H, average composition  $\text{Pt}_{72.3}:\text{Al}_{13.5}:\text{V}_{14.2}$  (at.%), in Figure 4.66 shows single phase  $\sim\text{Pt}_3\text{Al}$  with grains at different orientations. The data for EDX composition analysis in Table 2.21 are plotted in Figure 4.67. XRD confirmed the phase identification (Figure 4.68). The microstructure changed from a two-phase structure in the as-cast condition to a single phase structure in the annealed condition.

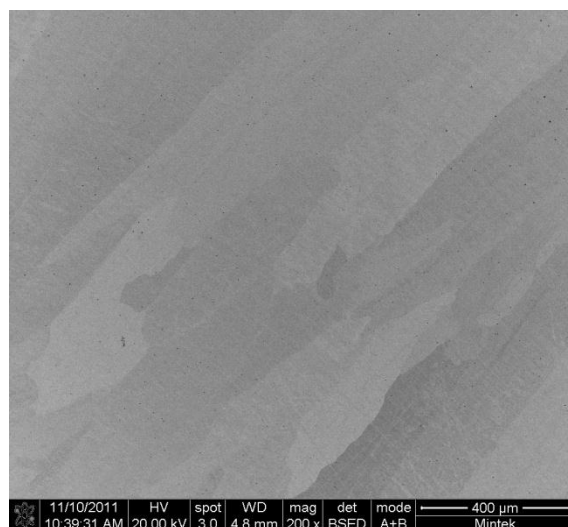
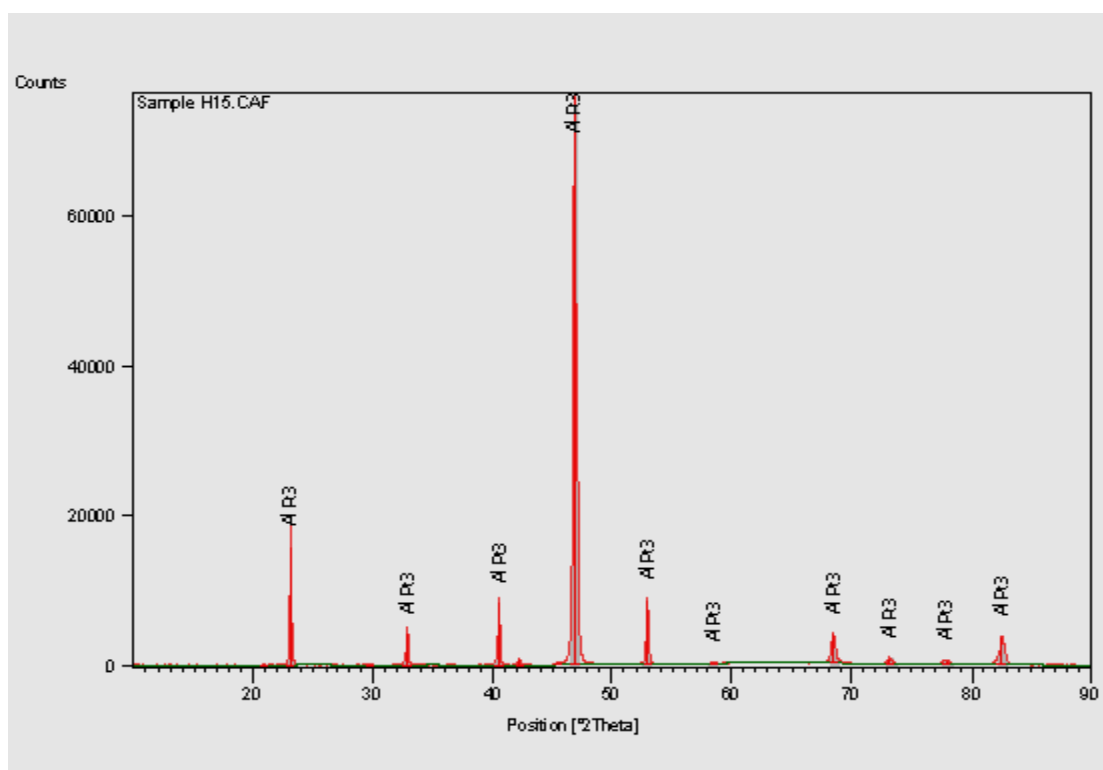
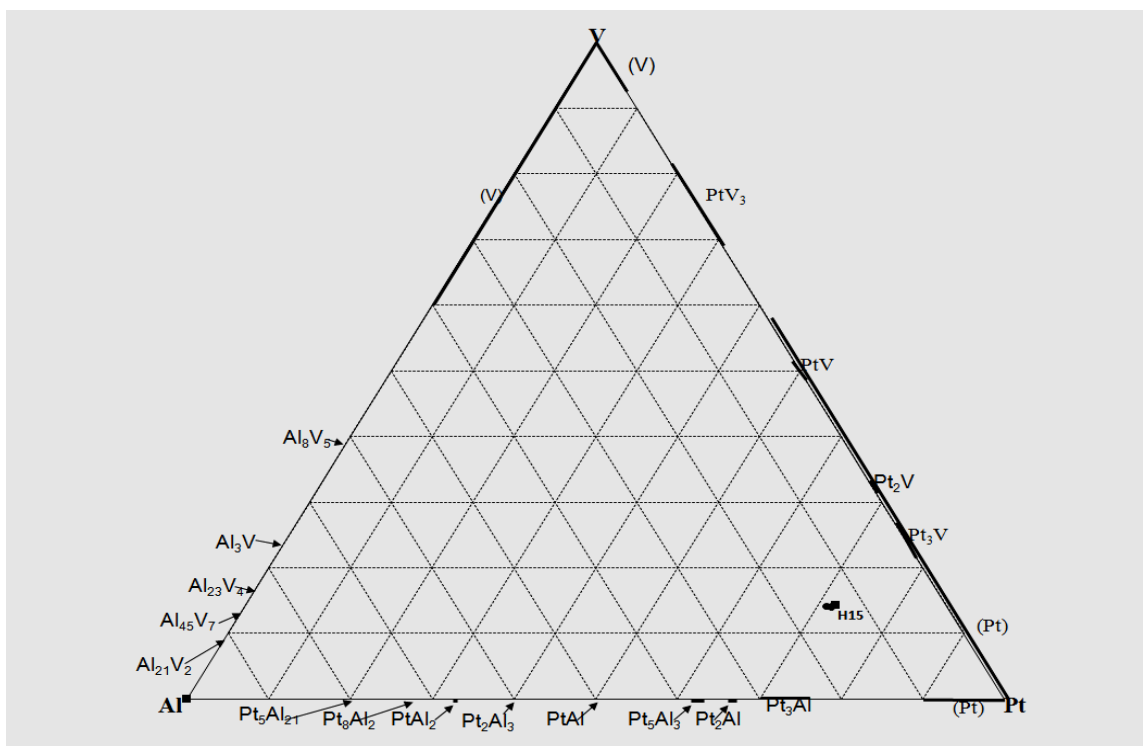


**Figure 4.66. SEM-BSE image of annealed Alloy 15H, average composition  $\text{Pt}_{72.3}\text{Al}_{13.5}\text{V}_{14.2}$  (at.%), showing single phase  $\sim\text{Pt}_3\text{Al}$  with grains at different orientations.**

**Table 4.23. EDX composition analysis for annealed Alloy 15H, average composition  $\text{Pt}_{72.3}\text{Al}_{13.5}\text{V}_{14.2}$  (at.%).**

Appearance	Pt	Al	V	Phase
Overall	72.3±0.6	13.5±0.5	14.2±0.4	-
Dark	71.3±0.9	14.6±0.7	14.1±0.4	$\sim\text{Pt}_3\text{Al}$
Medium	71.8±0.5	14.3±0.5	13.9±0.3	$\sim\text{Pt}_3\text{Al}$



#### 4.2.11 Annealed Alloy 16H, Average Composition $\text{Pt}_{51.0}:\text{Al}_{31.1}:\text{V}_{17.9}$ (at.%)

Figure 4.69 is an SEM-BSE image of annealed Alloy 16H, average composition  $\text{Pt}_{51.0}:\text{Al}_{31.1}:\text{V}_{17.9}$  (at.%), showing dark  $\sim\text{PtV}$  and light  $\sim\text{PtAl}$ . The EDX composition analysis data in Table 4.23 are plotted in Figure 4.70. XRD confirmed the phase identification as shown by the pattern in Figure 4.71. The microstructure changed from a single ternary phase,  $\tau_2$ , in the as-cast condition to a two-phase structure of  $\sim\text{PtAl}$  and  $\sim\text{PtV}$  indicating that there a solid state transformation  $\tau_2 \rightarrow \sim\text{PtAl} + \sim\text{PtV}$  at some temperature between  $1000^\circ\text{C}$  and the solidification temperature.

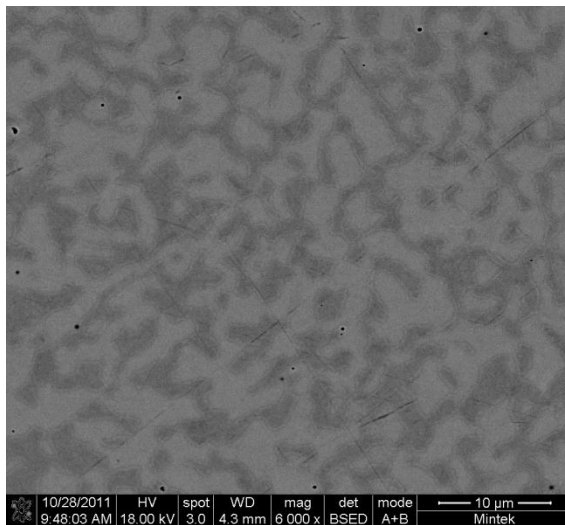
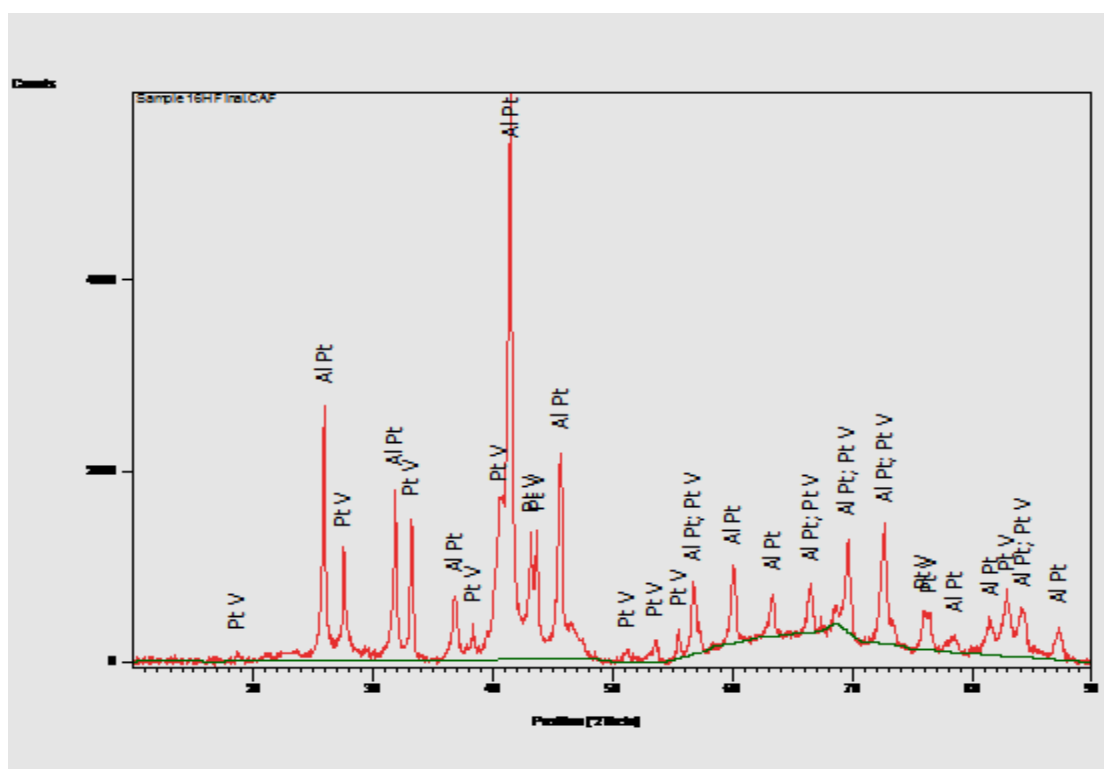
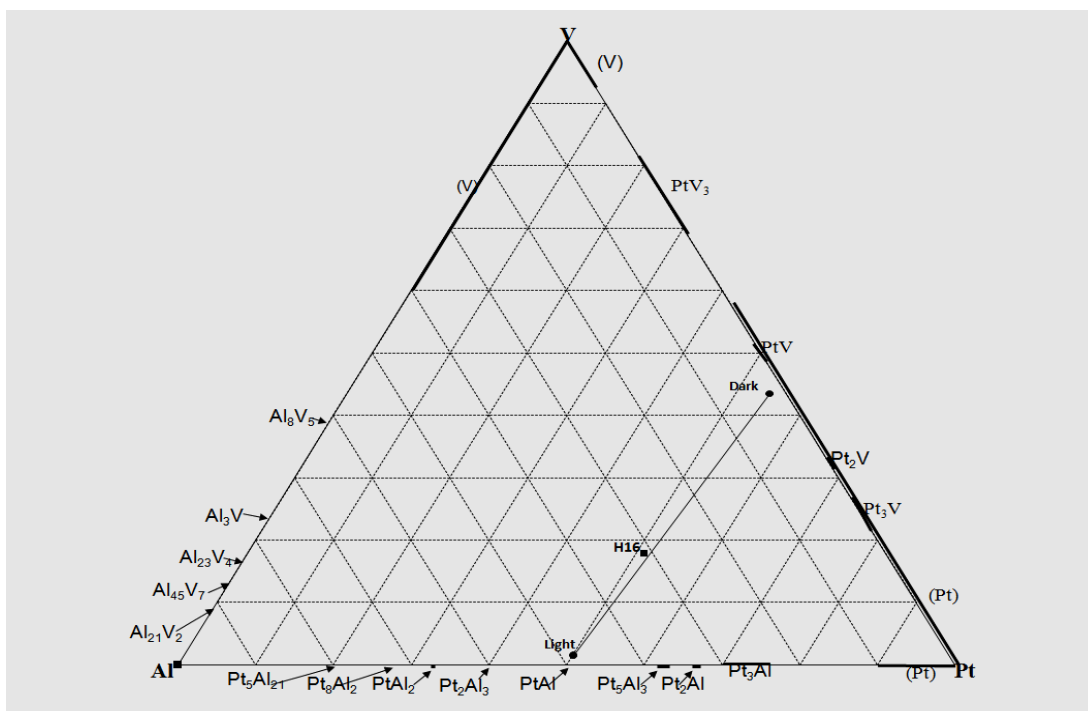


**Figure 4 69. SEM-BSE image of annealed Alloy 16H, average composition  $\text{Pt}_{51.0}:\text{Al}_{31.1}:\text{V}_{17.9}$  (at.%), showing dark  $\sim\text{PtV}$  and light  $\sim\text{PtAl}$ .**

**Table 4.24. EDX composition analysis data for annealed Alloy 16H, average composition  $\text{Pt}_{51.0}:\text{Al}_{31.1}:\text{V}_{17.9}$  (at.%).**

Appearance	Pt	Al	V	Phase
Overall	$51.0 \pm 0.4$	$31.1 \pm 0.4$	$17.9 \pm 0.7$	-
Light	$50.2 \pm 0.6$	$48.3 \pm 0.5$	$1.5 \pm 0.2$	$\sim\text{PtAl}$
Dark	$54.4 \pm 1.0$	$2.1 \pm 0.7$	$43.5 \pm 0.5$	$\sim\text{PtV}$





#### 4.2.12 Combined Plot and isothermal section of the Pt-Al-V System at 1000°C at the Pt-rich corner

The combined plot in Figure 4.73 shows tie-lines of Alloys 12H and 13H crossing tie-lines of the other alloys. It was deduced that the two alloys were quenched from a relatively lower temperature compared to the other alloys because of their outer positions in the furnace. This had resulted from the difficulty in removing them from the tube furnace during the quenching process. When the two alloys were left out, it was possible to draw an isothermal section as in Figure 4.74 which was consistent with both the solidification and liquidus surface projections.

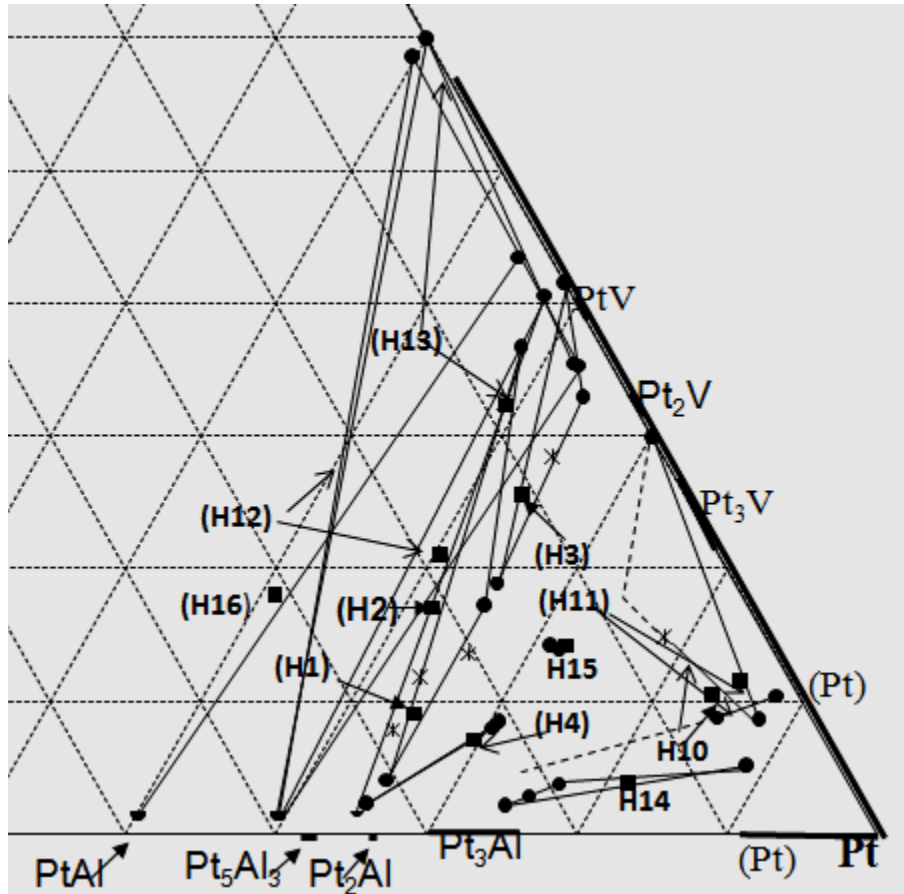
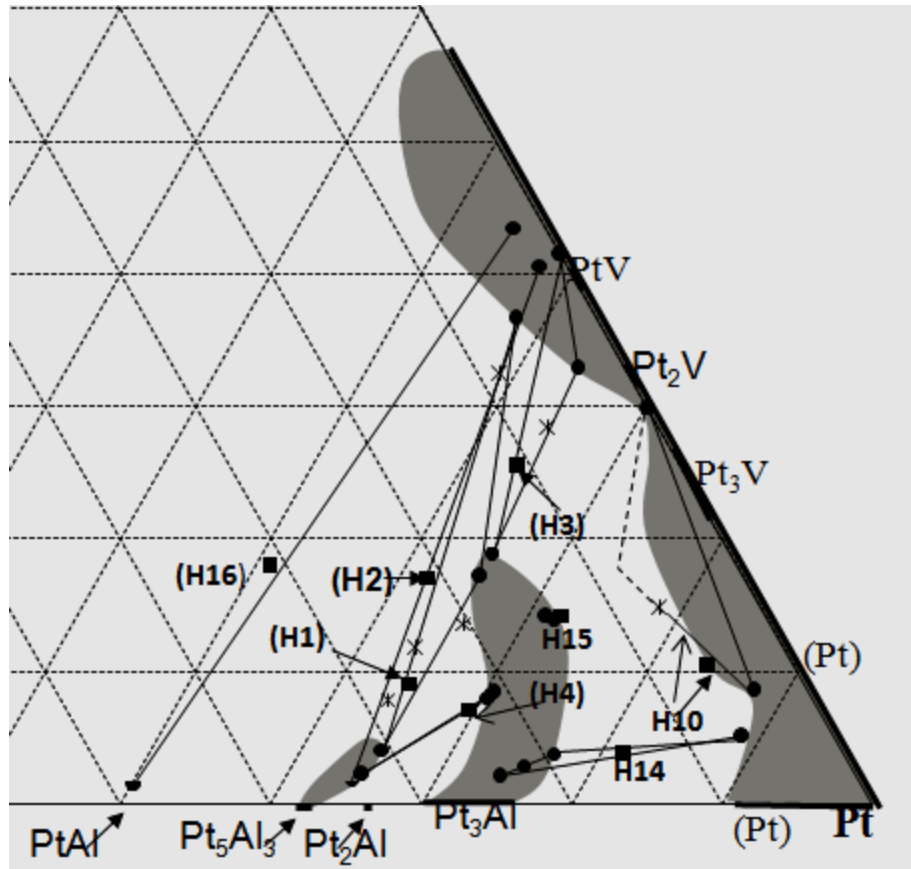


Figure 4.72. Combined plot of the Pt-Al-V system at 1000°C at the Pt-rich corner.



**Figure 4.73. Isothermal section of the Pt-Al-V system at 1000°C at the Pt-rich corner.**

Figure 4.75 shows the plot of the two Alloys 12H and 13H. The  $\tau_1$  in the as-cast condition had decomposed eutectoidally into fine light needles of  $\sim\text{Pt}_5\text{Al}_3$  and darker  $\sim\text{PtV}_3$  while the (Pt) had transformed to  $\sim\text{PtV}$ . On heat treatment, the three phases coarsened and it was possible to do reasonable EDX analyses, which confirmed the presence of the three phases,  $\sim\text{Pt}_5\text{Al}_3$  and  $\sim\text{PtV}_3$  and  $\sim\text{PtV}$ , in the as-cast and in the annealed conditions. Alloy 16 was single ternary phase,  $\tau_2$ , in the as-cast condition and transformed to  $\sim\text{PtAl} + \sim\text{PtV}$ , suggesting that it was actually a different ternary phase.



**Table 4.25. Position (2 Theta) and corresponding  $d$  spacing of the  $\tau_1$  peaks in the XRD pattern of Alloys 12 and 13.**

Alloy 12		Alloy 13	
$d$ spacing	$2\theta$	$d$ spacing	$2\theta$
2.7	32.9	2.7	33.1
2.2	40.5	2.2	40.6
2.1	42.1	2.1	43.5
1.7	54.0	1.7	53.2

**Table 4.26. Solidification and cooling reactions of the Pt-Al-V alloys.**

Alloy ID	Composition, at.%	Solidification and Cooling Reactions
1	Pt <sub>64.3</sub> :Al <sub>26.6</sub> :V <sub>9.1</sub>	$L \rightarrow \sim\text{Pt}_3\text{Al}$ $L + \sim\text{Pt}_3\text{Al} \rightarrow (\text{Pt})$ $L + (\text{Pt}) \rightarrow \sim\text{Pt}_5\text{Al}_3$ $\sim\text{Pt}_3\text{Al} + \sim\text{Pt}_5\text{Al}_3 \rightarrow \sim\text{Pt}_2\text{Al}$ $L \rightarrow \sim\text{Pt}_5\text{Al}_3 + \beta$ $\beta \rightarrow \sim\text{Pt}_5\text{Al}_3 + \sim\text{PtAl}$ $(\text{Pt}) \rightarrow \sim\text{Pt}_2\text{V}$
2	Pt <sub>59.1</sub> :Al <sub>23.1</sub> :V <sub>17.8</sub>	$L \rightarrow (\text{Pt})$ $L + (\text{Pt}) \rightarrow \sim\text{Pt}_5\text{Al}_3$ $L \rightarrow \sim\text{Pt}_5\text{Al}_3 + \beta$ $\beta \rightarrow \sim\text{PtAl} + \sim\text{Pt}_5\text{Al}_3$ $(\text{Pt}) \rightarrow \sim\text{Pt}_2\text{V}$
3	Pt <sub>57.3</sub> :Al <sub>6.7</sub> :V <sub>26</sub>	$L \rightarrow (\text{Pt})$ $L + (\text{Pt}) \rightarrow \sim\text{Pt}_3\text{Al} + \sim\text{Pt}_5\text{Al}_3$ $\sim\text{Pt}_3\text{Al} + \sim\text{Pt}_5\text{Al}_3 \rightarrow \sim\text{Pt}_2\text{Al}$ $(\text{Pt}) \rightarrow \sim\text{Pt}_3\text{V}$
4A	Pt <sub>76.2</sub> Al <sub>17.4</sub> V <sub>6.4</sub>	$L \rightarrow \sim\text{Pt}_3\text{Al}$
4B	Pt <sub>69.8</sub> :Al <sub>22.3</sub> :V <sub>7.9</sub>	$L \rightarrow \sim\text{Pt}_3\text{Al}$ $L + \sim\text{Pt}_3\text{Al} \rightarrow \sim\text{Pt}_5\text{Al}_3$ $\sim\text{Pt}_3\text{Al} + \sim\text{Pt}_5\text{Al}_3 \rightarrow \sim\text{Pt}_2\text{Al}$
10	Pt <sub>83.9</sub> :Al <sub>16.0</sub> :V <sub>10.1</sub>	$L \rightarrow (\text{Pt})$ $L \rightarrow (\text{Pt}) + \sim\text{Pt}_3\text{Al}$
11	Pt <sub>80.9</sub> :Al <sub>4.3</sub> :V <sub>14.8</sub>	$L \rightarrow (\text{Pt})$ $L \rightarrow (\text{Pt}) + \sim\text{Pt}_3\text{Al}$
12	Pt <sub>52.5</sub> :Al <sub>22.6</sub> :V <sub>24.9</sub>	$L \rightarrow \tau_1$ $L \rightarrow (\text{Pt}) + \tau_1 + \sim\text{PtV}_3$ $\tau_1 \rightarrow \sim\text{PtV}_3 + \sim\text{Pt}_5\text{Al}_3$

		$(Pt) \rightarrow \sim PtV.$
13	$Pt_{53.7}:Al_{8.8}:V_{37.5}$	$L \rightarrow (Pt)$ $L \rightarrow (Pt) + \tau_1$ $\tau_1 \rightarrow \sim PtV_3 + \sim Pt_5Al_3$ $(Pt) \rightarrow \sim PtV$ $(Pt) \rightarrow \sim PtV + \sim Pt_2V,$
14	$Pt_{84}:Al_{12}:V_4$	$L \rightarrow (Pt)$ $L \rightarrow (Pt) + \sim Pt_3Al$ $\sim Pt_3Al (HT) \rightarrow (Pt) + \sim Pt_3Al (LT).$
15	$Pt_{72.4}:Al_{13.7}:V_{13.9}$	$L \rightarrow \sim Pt_3Al$ $L + \sim Pt_3Al \rightarrow \sim Pt_5Al_3$ $\sim Pt_3Al + \sim Pt_5Al_3 \rightarrow \sim Pt_2Al.$
16	$Pt_{56.9}:Al_{25.4}:V_{17.7}$	$L \rightarrow \tau_2$

## CHAPTER 5: Pt-Cr-V ALLOYS

### 5.1 AS-CAST ALLOYS

#### 5.1.1 As-cast Alloy 5, Average Composition $\text{Pt}_{73.8}\text{Cr}_{16.9}\text{V}_{9.3}$ (at.%)

Figure 5.1 shows that Alloy 5, average composition  $\text{Pt}_{73.8}\text{Cr}_{16.9}\text{V}_{9.3}$  (at.%) was mainly single phase with grains at different orientations. The compositions in Table 5.1 are for various shades of contrast as seen in the image. The plot of these compositions in Figure 5.2 confirms that the alloy is single phase. XRD gave the identity of the phase as seen in the pattern in Figure 5.3. The alloy solidified and cooled with the following reactions:

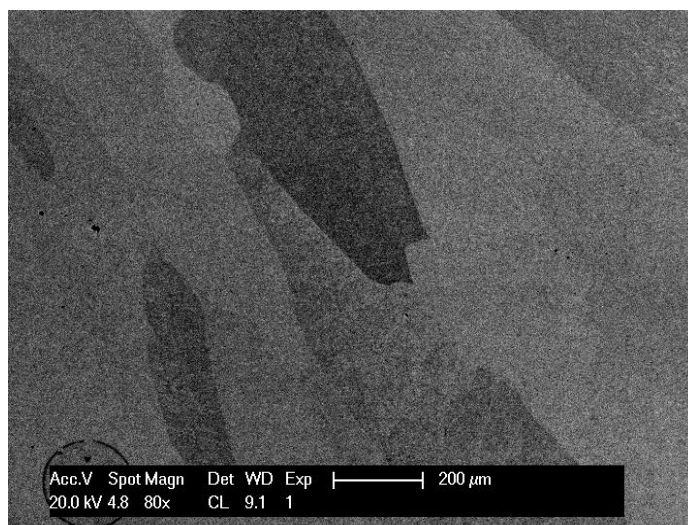
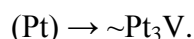
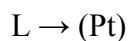


**Figure 5.1. SEM-BSE image of as-cast Alloy 5, average composition  $\text{Pt}_{73.8}\text{Cr}_{16.9}\text{V}_{9.3}$  (at.%), showing single phase,  $\sim\text{Pt}_3\text{V}$ , with grains at different orientations.**

**Table 5.1. Compositions of Alloy 5, average composition  $\text{Pt}_{73.8}\text{Cr}_{16.9}\text{V}_{9.3}$  (at.%) as determined by EDX.**

Appearance	Pt	Cr	V	Phases
Overall	73.8±0.6	16.9±0.4	9.3±0.5	-
Dark	73.9±0.1	16.6±0.1	9.5±0.1	$\sim\text{Pt}_3\text{V}$
Light	73.9±0.6	16.9±0.6	9.2±0.3	$\sim\text{Pt}_3\text{V}$

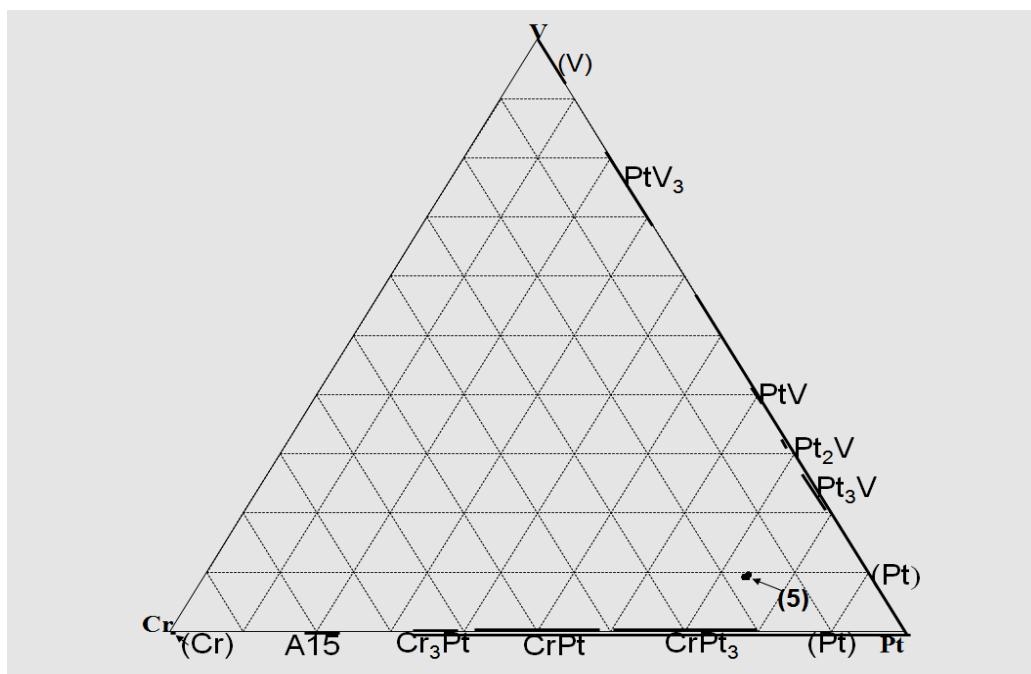


Figure 5.2. Plot of compositions of Alloy 5, average overall composition  $Pt_{73.8}:Cr_{16.9}:V_{9.3}$  (at.%).

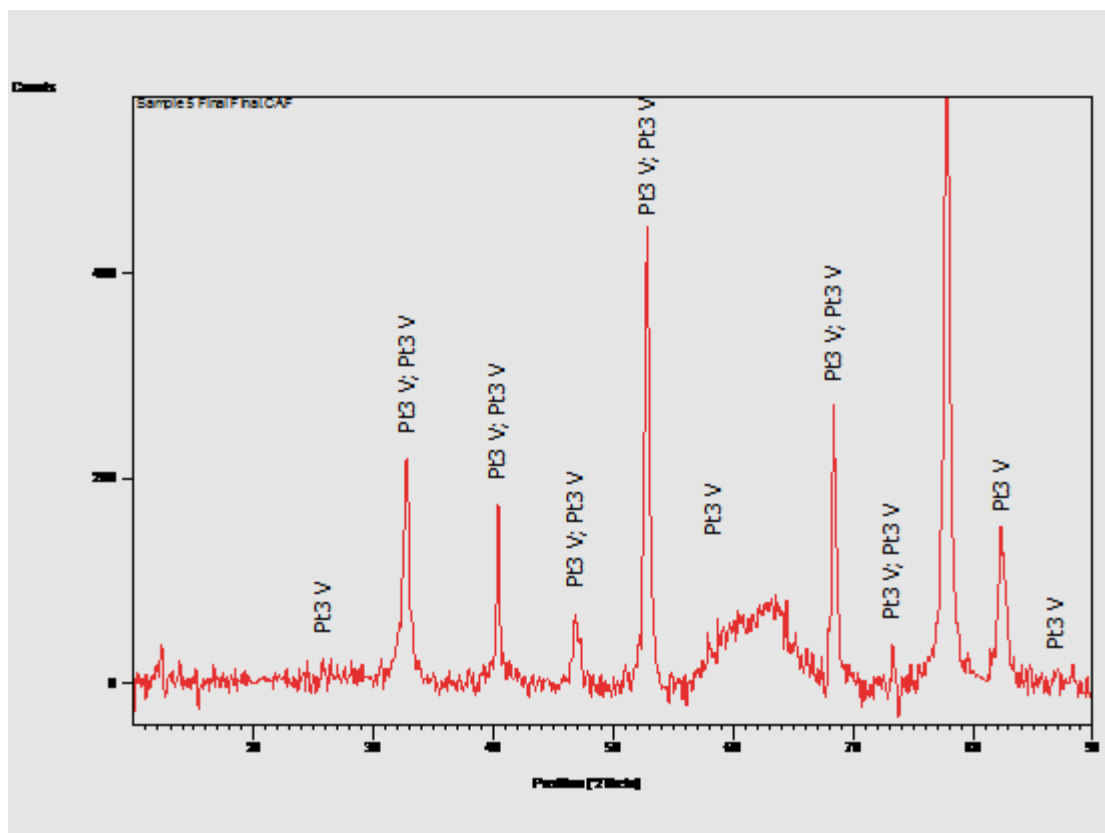
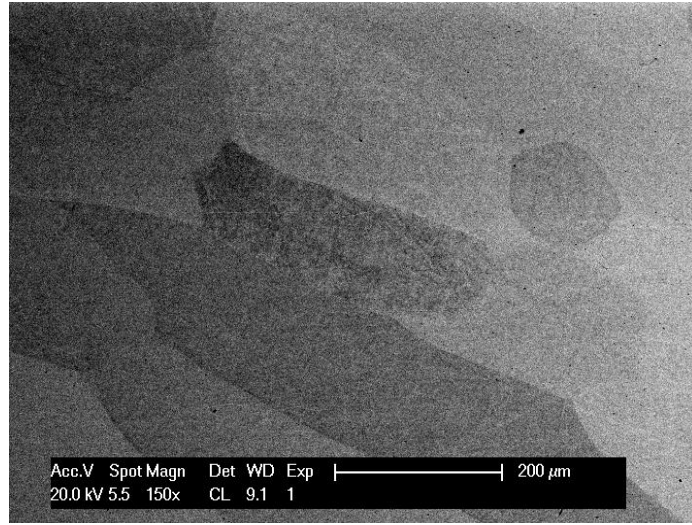
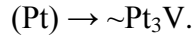
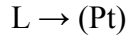


Figure 5.3. XRD pattern of Alloy 5, average composition  $Pt_{73.8}:Cr_{16.9}:V_{9.3}$  (at.%).

### 5.1.2 As-cast Alloy 6, Average Composition $\text{Pt}_{72.3}\text{Cr}_{8.3}\text{V}_{19.4}$ (at.%)

Figure 5.4 shows an SEM-BSE image of Alloy 6, average composition  $\text{Pt}_{72.3}\text{Cr}_{8.3}\text{V}_{19.4}$  (at.%).

The alloy was also single phase  $\sim\text{Pt}_3\text{V}$  and the different contrasts seen in the image were due to grains of different orientations. The EDX composition analyses of the different shades of contrast are given in Table 5.2 and plotted in Figure 5.5. XRD confirmed the identity of the phase as shown in the pattern in Figure 5.6. The alloy cooled with the following reactions:



**Figure 5.4. SEM-BSE image of Alloy 6, average composition  $\text{Pt}_{72.3}\text{Cr}_{8.3}\text{V}_{19.4}$  (at.%) showing single phase  $\sim\text{Pt}_3\text{V}$  with grains at different orientations.**

**Table 5.2. EDX composition analysis of Alloy 6, average overall composition  $\text{Pt}_{72.3}\text{Cr}_{8.3}\text{V}_{19.4}$  (at.%).**

Appearance	Pt	Cr	V	Phase
Overall	$72.3 \pm 0.2$	$8.3 \pm 0.2$	$19.4 \pm 0.2$	-
Dark	$72.3 \pm 0.3$	$8.4 \pm 0.1$	$19.3 \pm 0.5$	$\sim\text{Pt}_3\text{V}$
Light	$72.8 \pm 0.5$	$8.1 \pm 0.1$	$19.1 \pm 0.3$	$\sim\text{Pt}_3\text{V}$



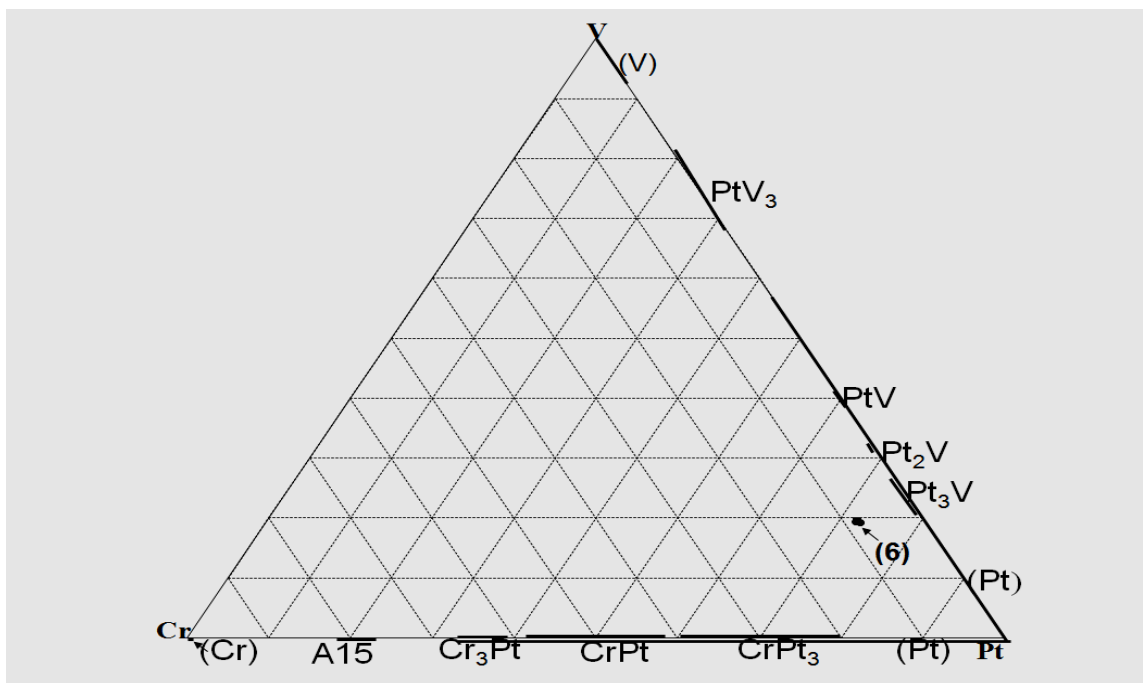


Figure 5.5. Plot of composition of Alloy 6, average composition  $Pt_{72.3}:Cr_{8.3}:V_{19.4}$  (at.%).

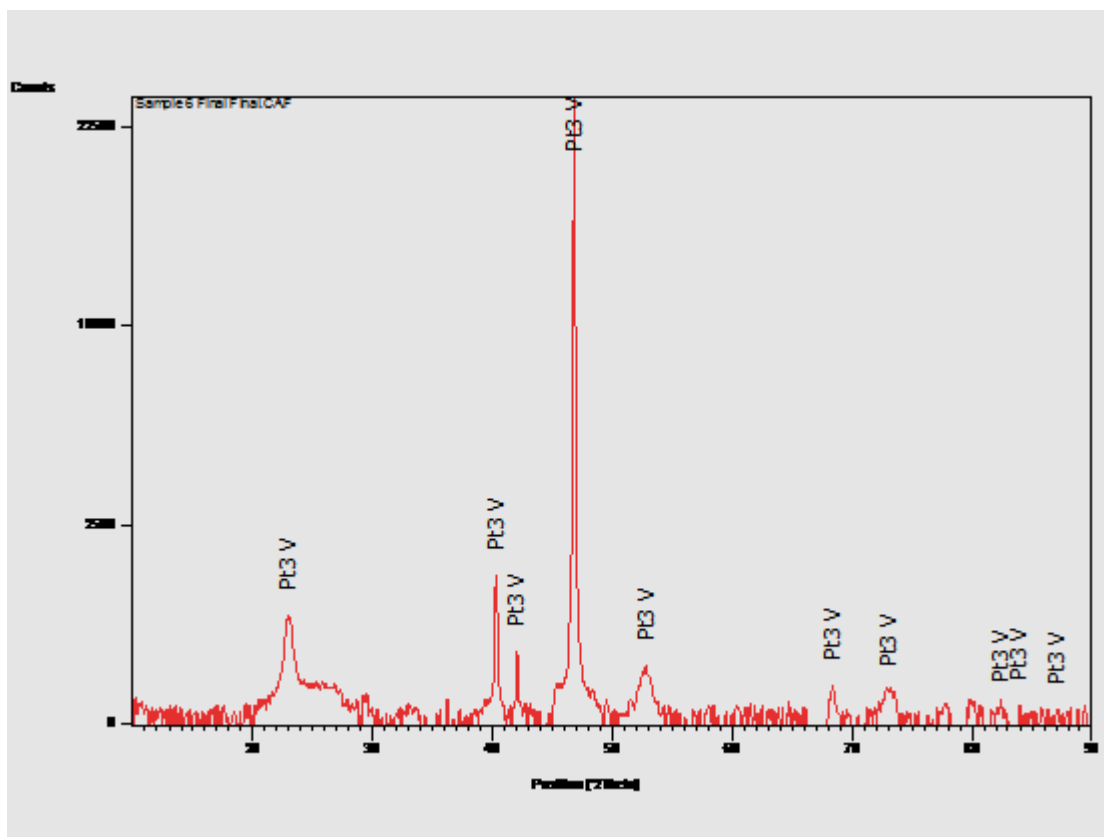
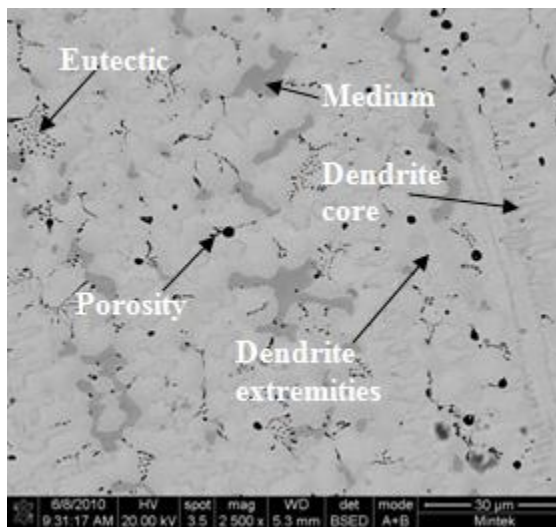
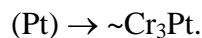
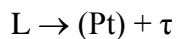
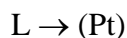


Figure 5.6. XRD pattern of Alloy 6, average composition  $Pt_{72.3}:Cr_{8.3}:V_{19.4}$  (at.%).

### 5.1.3 As-cast Alloy 7, Average Composition $\text{Pt}_{33.4}\text{Cr}_{45.8}\text{V}_{20.8}$ (at.%)

An SEM-BSE image of as-cast Alloy 7 is shown in Figure 5.7. There were cored  $\sim\text{Cr}_3\text{Pt}$  dendrites, medium contrast  $\text{A15}(\sim\text{Cr}_3\text{Pt})$ , a eutectic comprising  $\sim\text{Cr}_3\text{Pt} + \text{ternary phase } \tau$  and porosity. As stated in page 28, in this investigation, the A15 phase will be designated  $\text{A15}(\sim\text{Cr}_3\text{Pt})$  to distinguish it from the  $\sim\text{Cr}_3\text{Pt}$  formed by ordering of (Pt). The compositions of the phases, from EDX analysis are given in Table 5.3 and plotted in Figure 5.8. XRD analysis confirmed the identities of the phases, as shown in Figure 5.9. The unidentified peaks originated from the ternary phase (which was not in the database). The alloy went through the following reactions during solidification and cooling:



**Figure 5.7. SEM-BSE image of as-cast Alloy 7, average composition  $\text{Pt}_{33.4}\text{Cr}_{45.8}\text{V}_{20.8}$  (at.%) showing  $\sim\text{Cr}_3\text{Pt}$  dendrites, medium contrast  $\text{A15}(\sim\text{Cr}_3\text{Pt})$ , a eutectic of  $\sim\text{Cr}_3\text{Pt} + \tau$  and porosity.**

**Table 5.3. EDX composition analysis of Alloy 7, average composition  $\text{Pt}_{33.4}:\text{Cr}_{45.8}:\text{V}_{20.8}$  (at.%).**

Appearance	Pt	Cr	V	Phase
Overall	$33.4 \pm 0.3$	$45.8 \pm 0.2$	$20.8 \pm 0.1$	-
Dendrite core	$36.1 \pm 0.5$	$41.7 \pm 0.4$	$22.2 \pm 0.3$	$\sim\text{Cr}_3\text{Pt}$
Dendrite extremities	$36.8 \pm 0.9$	$43.2 \pm 0.5$	$20.0 \pm 0.2$	$\sim\text{Cr}_3\text{Pt}$
Medium	$26.2 \pm 0.4$	$55.9 \pm 0.5$	$17.9 \pm 0.2$	A15 ( $\sim\text{Cr}_3\text{Pt}$ )
Eutectic	$34.2 \pm 0.4$	$43.9 \pm 0.6$	$21.9 \pm 0.4$	$\tau + \sim\text{Cr}_3\text{Pt}$

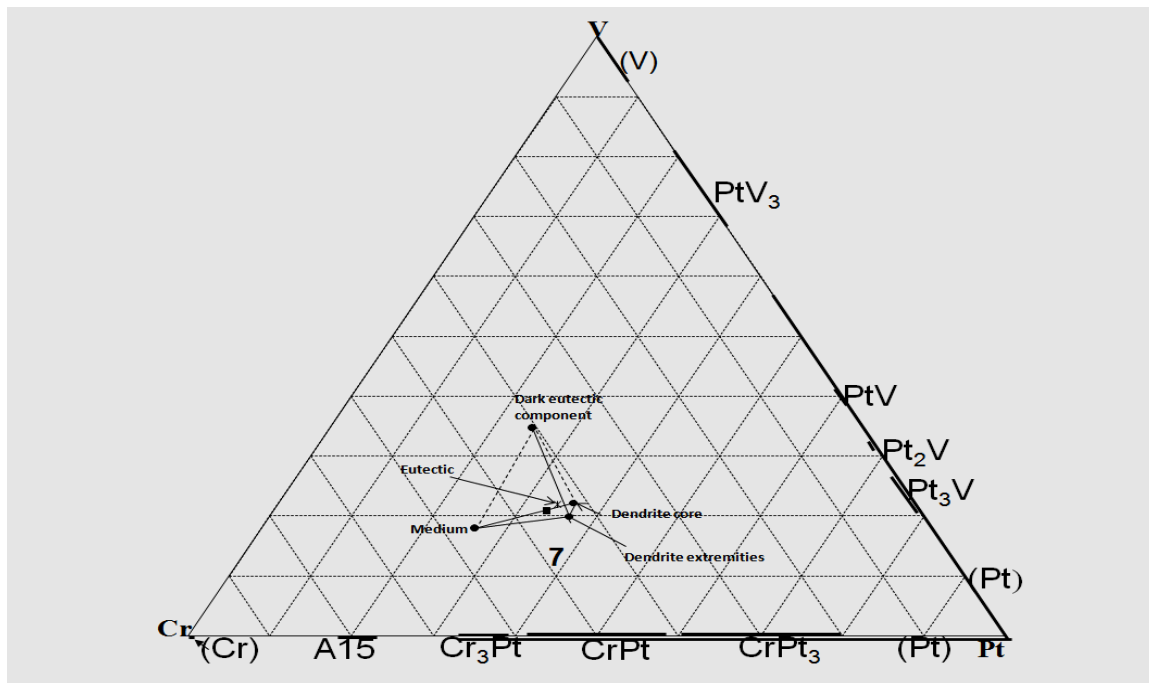


**Figure 5.8. Plot of composition of Alloy 7, average composition  $\text{Pt}_{33.4}:\text{Cr}_{45.8}:\text{V}_{20.8}$  (at.%).**

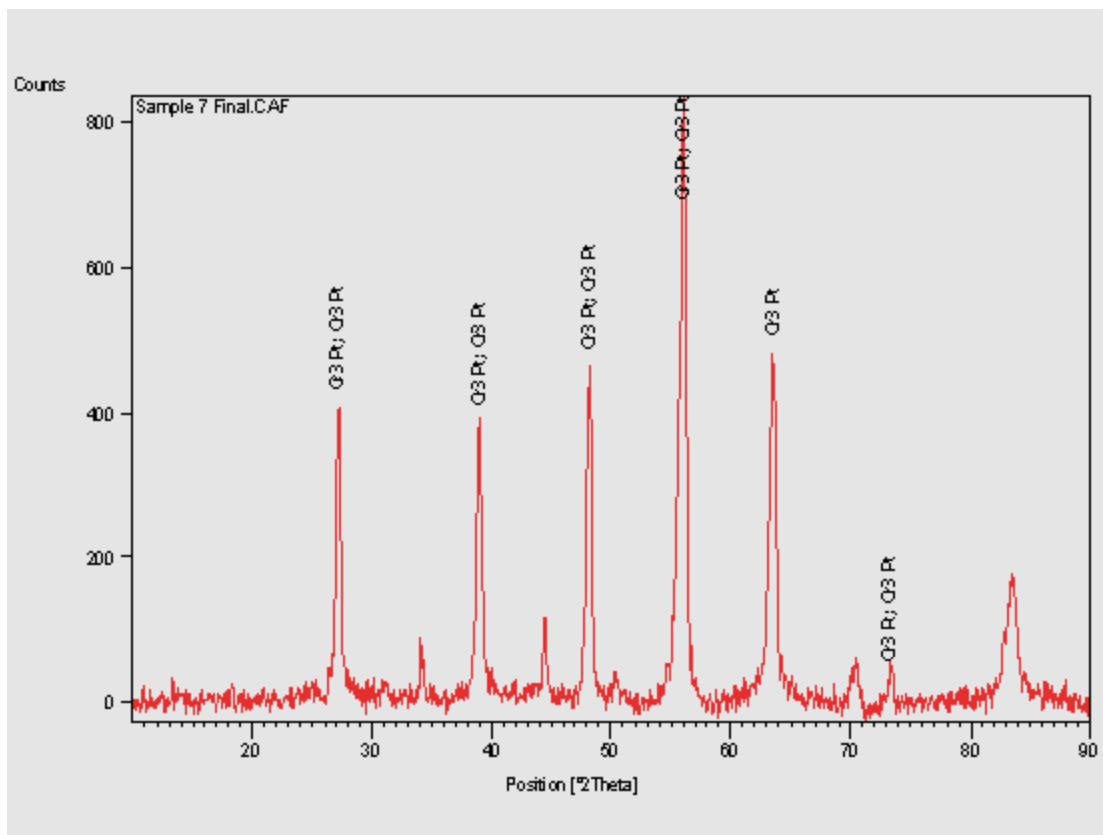


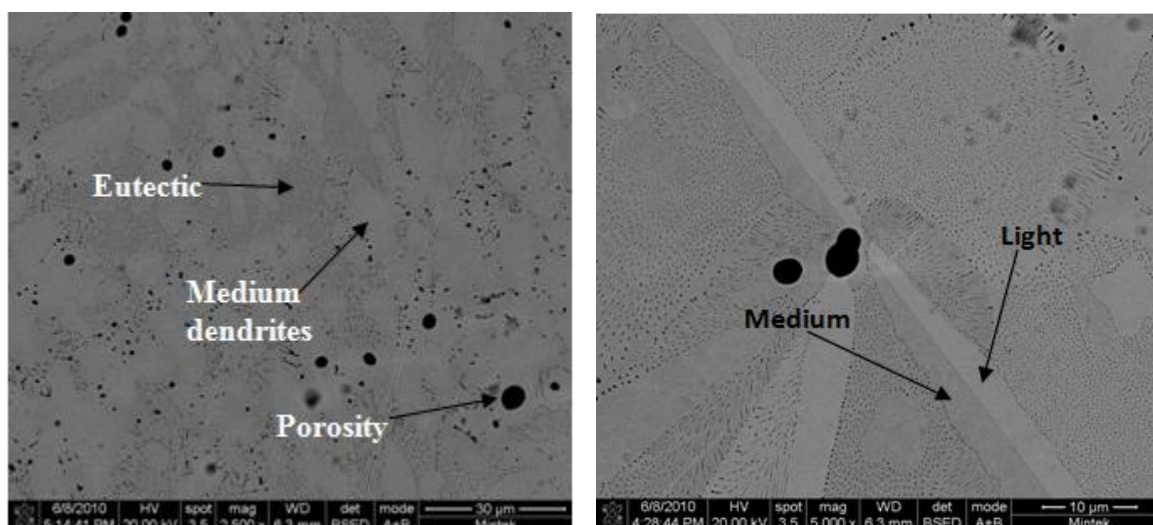
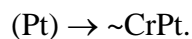
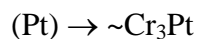
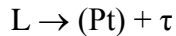
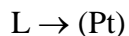
**Figure 5.9. XRD pattern of as-cast Alloy 7, average composition  $\text{Pt}_{33.4}\text{:Cr}_{45.8}\text{:V}_{20.8}$  (at.%).**

#### **5.1.4 As-cast Alloy 8, Average Composition $\text{Pt}_{53.0}\text{:Cr}_{22.4}\text{:V}_{24.5}$ (at.%)**

The SEM-BSE image in Figure 5.10 shows Alloy 8 having dendrites that were originally (Pt) and transformed to medium  $\sim\text{Cr}_3\text{Pt}$  initially. However, before the transformation was complete, the remaining (Pt) became richer in Pt sufficiently to start transforming to lighter  $\sim\text{CrPt}$ . This is possible with the binary Cr-Pt phase diagram proposed by Okamoto [2009Oka]. A eutectic of a ternary phase  $\tau + \sim\text{Cr}_3\text{Pt}$  (or  $\sim\text{CrPt}$ ) also formed as well as porosity. The  $\tau$  in the eutectic partially oxidised and most of it fell out during preparation. Table 5.4 has the data for EDX composition analysis. The compositions were plotted in Figure 5.11. The compositions of  $\sim\text{Cr}_3\text{Pt}$ ,  $\sim\text{CrPt}$  and the eutectic were very close and were nearly co-incident in the plot. Extrapolation, in conjunction with the plot of Alloys 7 and 22, which had similar eutectics, determined that the dark phase in the eutectic is a ternary phase,  $\tau$ . Some (proportion unknown) of the ternary phase was pulled out during preparation due to brittleness and this is the explanation for the position of the plot of the overall composition falling within the solid solution field. The plot for the overall composition also fell outside the dotted line of extrapolation joining the two phases because the dendrites were cored. XRD confirmed the identity of the  $\sim\text{Cr}_3\text{Pt}$  and  $\sim\text{CrPt}$  phases as shown in Figure 5.12.

The peaks for  $\tau$  are not seen in the pattern probably because they are overlapped by the other peaks. Since most of the  $\tau$  fell out, there would have been little of the phase remaining to allow it to be detected by the XRD.

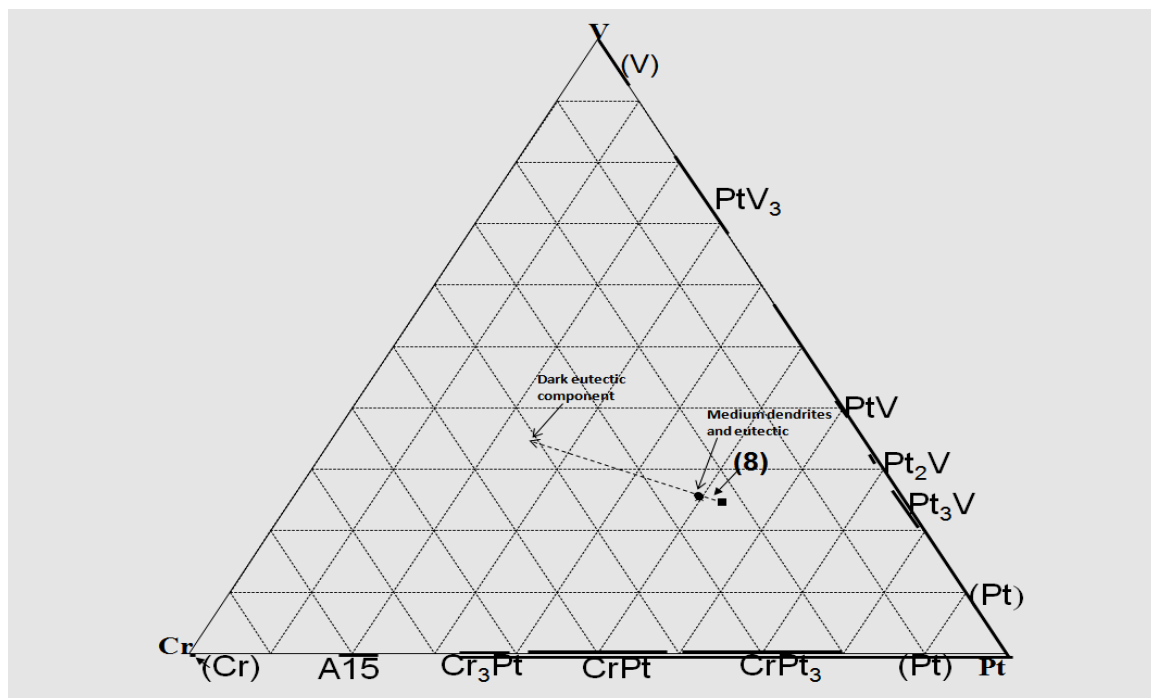
The alloy solidified and cooled with following reactions:



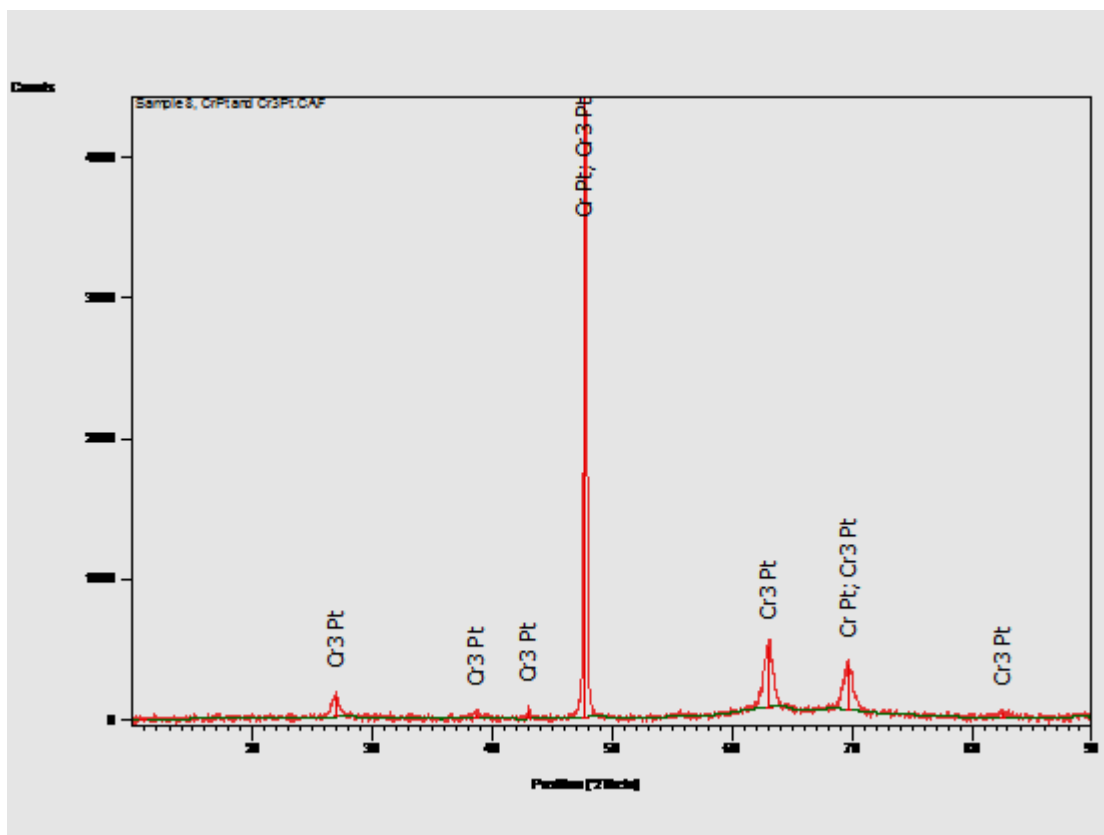
**Figure 5.10(a).** SEM-BSE image of Alloy 8, average composition  $Pt_{53.0}:Cr_{22.4}:V_{24.5}$  (at.%) showing medium  $\sim Cr_3Pt$  and light  $\sim CrPt$  dendrites, a eutectic of  $\tau + \sim CrPt$  and  $\tau + \sim Cr_3Pt$  and porosity. **(b).** SEM-BSE image of Alloy 8, average composition  $Pt_{53.0}:Cr_{22.4}:V_{24.5}$  (at.%), at higher magnification, showing medium  $\sim Cr_3Pt$  and light  $\sim CrPt$  dendrites and a eutectic of  $\tau + \sim CrPt$  and  $\tau + \sim Cr_3Pt$  and porosity.

**Table 5.4. EDX composition analysis of Alloy 8, average composition  $\text{Pt}_{53.0}:\text{Cr}_{22.4}:\text{V}_{24.5}$  (at.%).**

Appearance	Pt	Cr	V	Phase
Overall	$53.1 \pm 0.4$	$22.4 \pm 0.2$	$24.5 \pm 0.1$	-
Medium dendrites	$49.3 \pm 0.5$	$24.8 \pm 0.7$	$25.9 \pm 0.4$	$\sim \text{Cr}_3\text{Pt}$
Light dendrites	$49.7 \pm 0.7$	$24.8 \pm 0.3$	$25.5 \pm 0.5$	$\text{CrPt}$
Eutectic	$49.8 \pm 0.6$	$24.8 \pm 0.3$	$25.4 \pm 0.6$	$\tau + \sim \text{Cr}_3\text{Pt}$ (or $\sim \text{CrPt}$ )



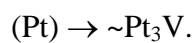
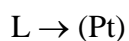
**Figure 5.11. Plot of Alloy 8, average composition  $\text{Pt}_{53.0}:\text{Cr}_{22.4}:\text{V}_{24.5}$  (at.%).**



**Figure 5.12. XRD pattern of Alloy 8, average composition  $\text{Pt}_{53.0}:\text{Cr}_{22.4}:\text{V}_{24.5}$  (at.%).**

#### **5.1.5 As-cast Alloy 17, Average Composition, $\text{Pt}_{68.5}:\text{Cr}_{16.2}:\text{V}_{15.3}$ (at.%)**

Figure 5.13 is a SEM-BSE image of Alloy 17, average composition  $\text{Pt}_{68.5}:\text{Cr}_{16.2}:\text{V}_{15.3}$  (at.%), showing single phase  $\sim\text{Pt}_3\text{V}$  with grains at different orientations. EDX composition analysis was done on the different shades of contrast and the data shown in Table 5.5 were plotted in Figure 5.14. XRD confirmed the identity of the single phase as  $\sim\text{Pt}_3\text{V}$  as shown in the pattern in Figure 5.15. However, ordering was not complete as some (Pt) was detected by XRD. The alloy solidified and cooled with the following reactions:



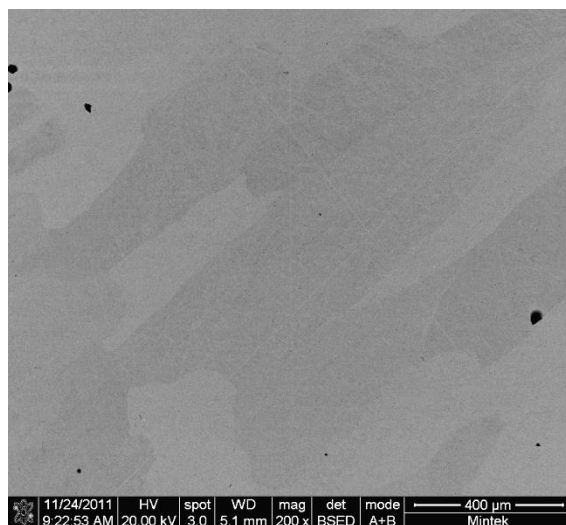
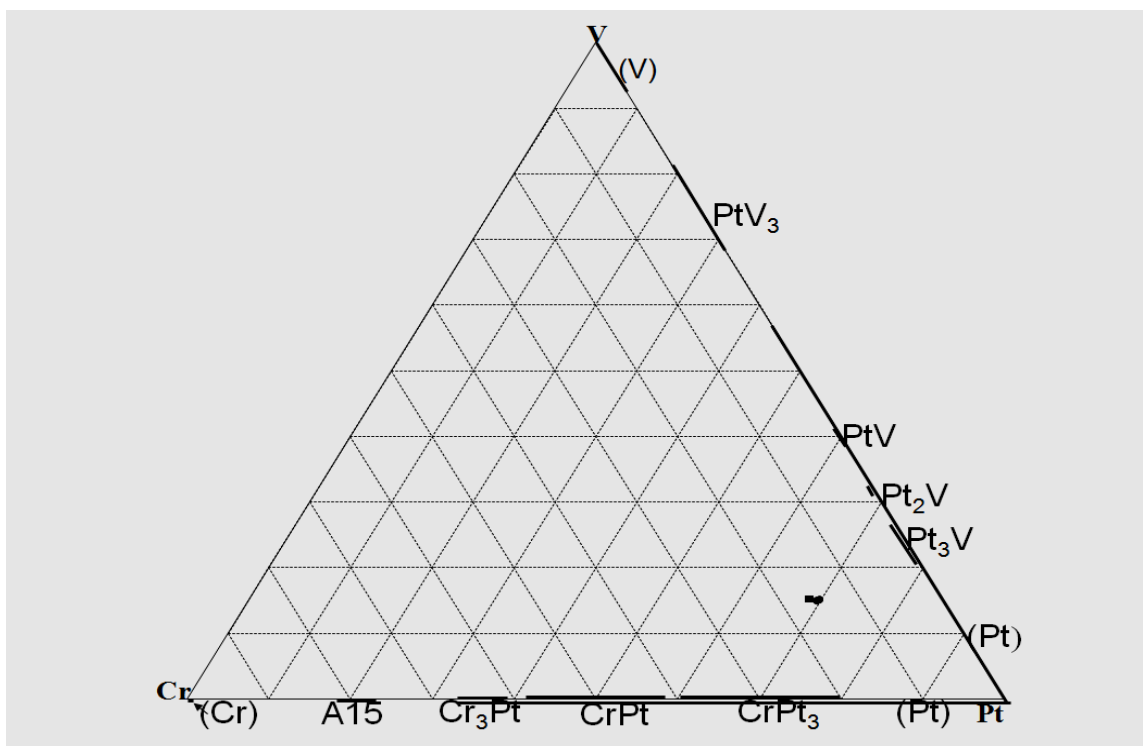


**Figure 5.13. SEM-BSE image of Alloy 17, average composition  $\text{Pt}_{68.5}\text{Cr}_{16.2}\text{V}_{15.3}$  (at.%) showing single phase  $\sim\text{Pt}_3\text{V}$  with grains at different orientations.**

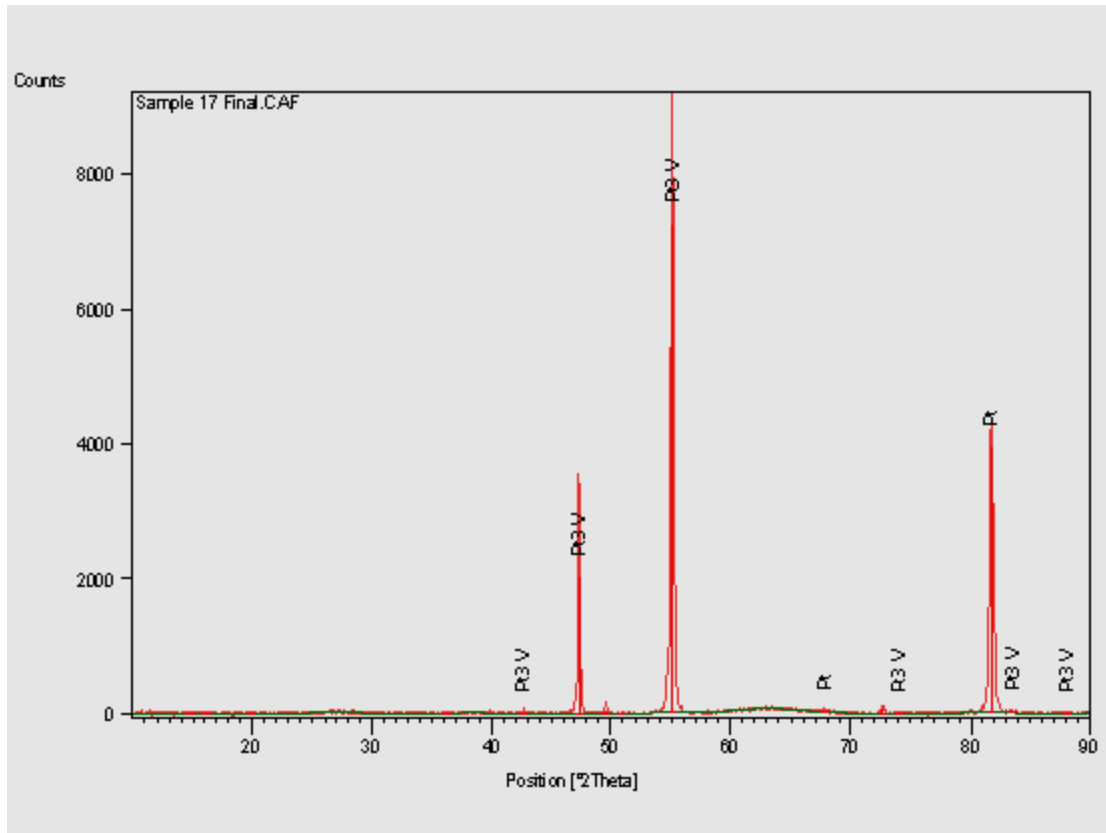
**Table 5.5. EDX composition analysis of Alloy 17, average composition  $\text{Pt}_{68.5}\text{Cr}_{16.2}\text{V}_{15.3}$  (at.%).**

Appearance	Pt	Cr	V	Phase
Overall	$68.5 \pm 0.9$	$16.2 \pm 0.5$	$15.3 \pm 0.8$	-
Dark	$69.6 \pm 0.8$	$15.5 \pm 0.5$	$14.9 \pm 0.3$	$\sim\text{Pt}_3\text{V}$
Light	$69.7 \pm 0.5$	$15.2 \pm 0.4$	$15.1 \pm 0.6$	$\sim\text{Pt}_3\text{V}$





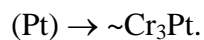
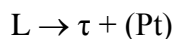
**Figure 5.14. Plot of Alloy 17, average composition  $\text{Pt}_{68.5}\text{Cr}_{16.2}\text{V}_{15.3}$  (at.%).**



**Figure 5.15.**XRD pattern of Alloy 17, average composition  $\text{Pt}_{68.5}\text{:Cr}_{16.2}\text{:V}_{15.3}$  (at.%).

#### **5.1.6 As-cast Alloy 18, Average Composition $\text{Pt}_{32.8}\text{:Cr}_{28.6}\text{:V}_{38.6}$ (at.%)**

Figure 5.16 is an SEM-BSE image of Alloy 18, average composition  $\text{Pt}_{32.8}\text{:Cr}_{28.6}\text{:V}_{38.6}$  (at.%), showing dark ternary phase dendrites,  $\tau$  and a sparse eutectic comprising light  $\sim\text{Cr}_3\text{Pt} + \tau$ . There could have been some solidification of (Pt) only before the eutectic formed properly (this can happen with fast cooling). The EDX composition analysis data in Table 5.6 are plotted in Figure 5.17. XRD confirmed the phase identities as shown in the pattern in Figure 5.18 and it was deduced that the unidentified peaks originated from the ternary phase, which is not in the database [2002ICDD]. The alloy solidified and cooled with the following reactions:



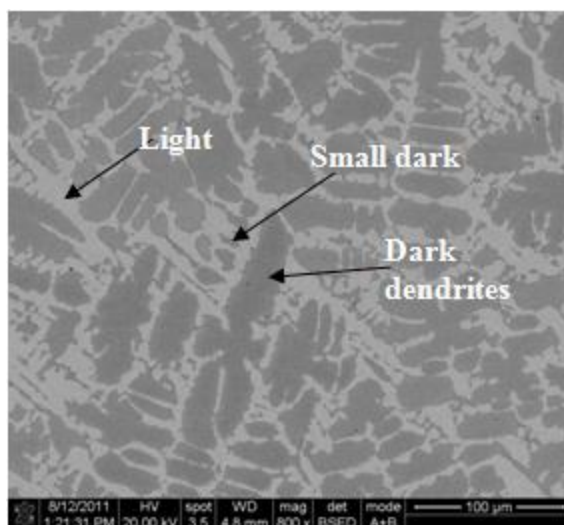


**Figure 5.16. SEM-BSE image of Alloy 18, average composition  $\text{Pt}_{32.8}\text{Cr}_{28.6}\text{V}_{38.6}$  (at.%), showing dark  $\tau$  dendrites, light  $\sim\text{Cr}_3\text{Pt}$ , and a sparse eutectic of small dark  $\tau$  +  $\sim\text{Cr}_3\text{Pt}$ .**

**Table 5.6. EDX composition analysis of Alloy 18, average composition  $\text{Pt}_{32.8}\text{Cr}_{28.6}\text{V}_{38.6}$  (at.%).**

Appearance	Pt	Cr	V	Phases
Overall	32.8±0.5	28.6±0.3	38.6±0.5	-
Dark dendrites	29.9±0.9	27.4±0.4	42.7±1.0	$\tau$
Light	38.8±0.7	28.0±1.5	33.2±1.3	$\sim\text{Cr}_3\text{Pt}$
Small dark in eutectic	30.8±0.9	30.6±1.5	38.6±0.9	$\tau$
Eutectic	36.0±1.3	29.0±0.9	35.0±0.5	$\tau$ + $\sim\text{Cr}_3\text{Pt}$

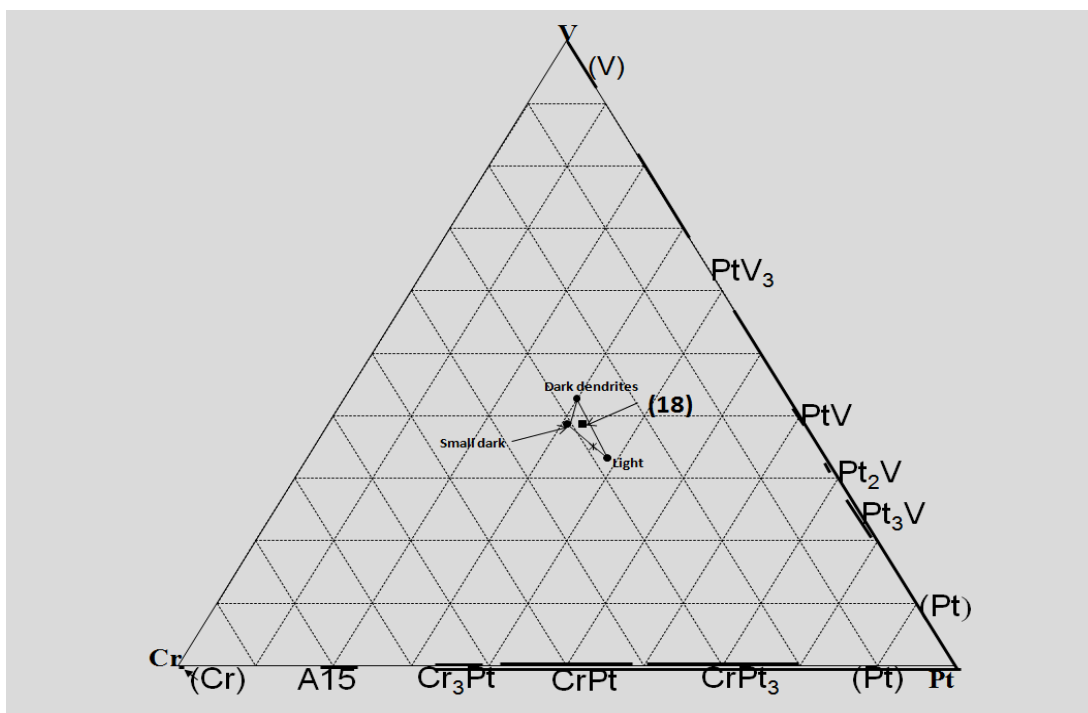


Figure 5.17. Plot of Alloy 18, average composition  $Pt_{32.8}:Cr_{28.6}:V_{38.6}$  (at.%).

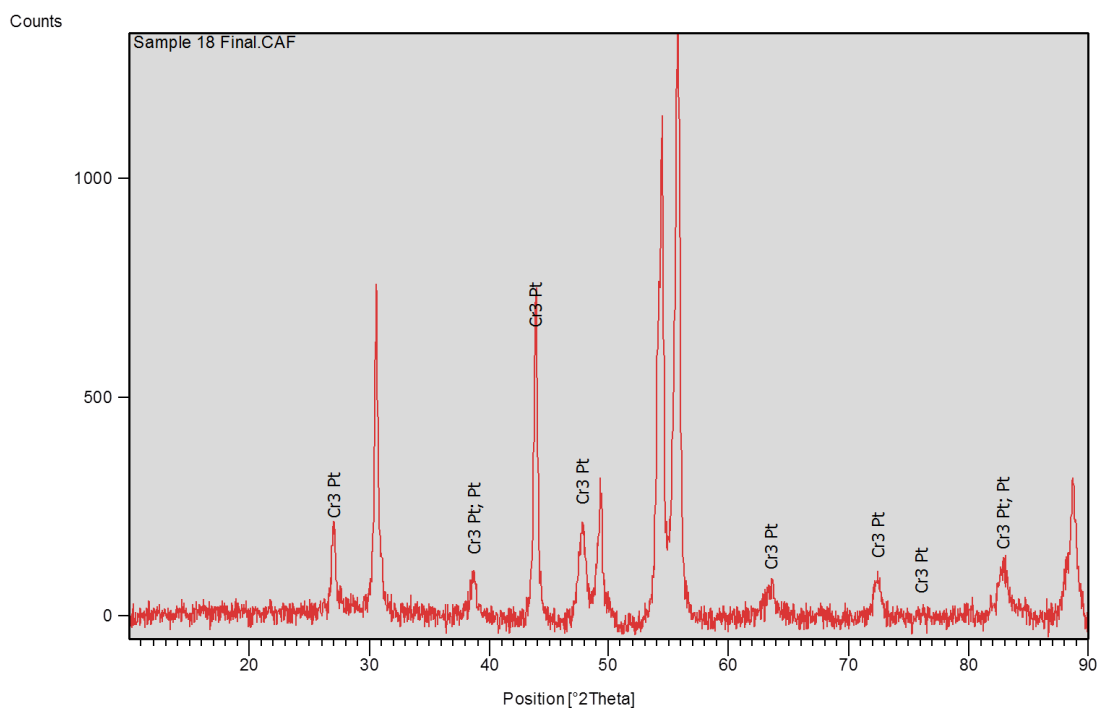
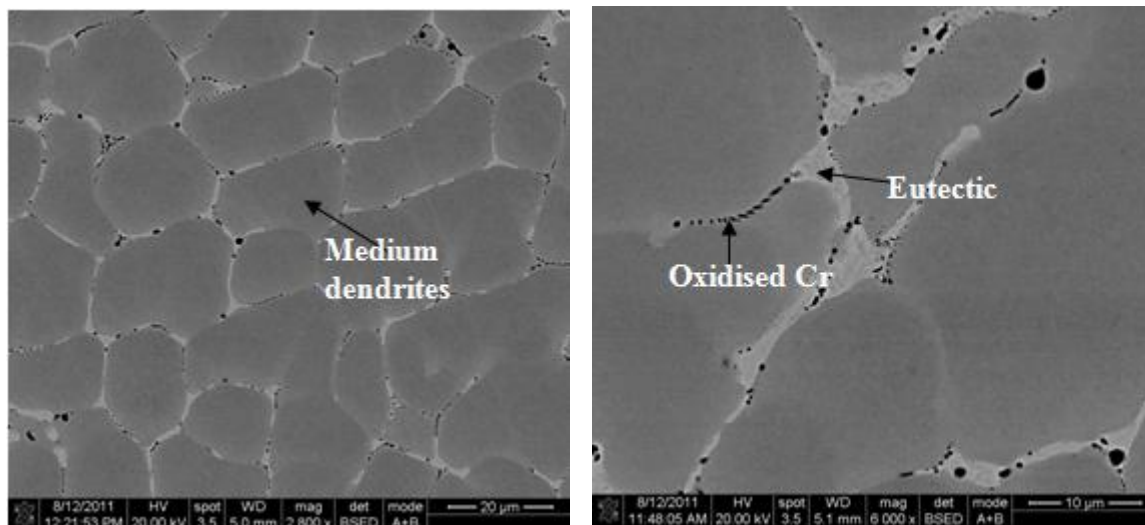
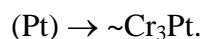
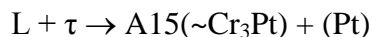


Figure 5.18. XRD pattern of Alloy 18, average composition  $Pt_{32.8}:Cr_{28.6}:V_{38.6}$  (at.%).

### 5.1.7 As-cast Alloy 19, Average Composition $\text{Pt}_{25.8}:\text{Cr}_{42.9}:\text{V}_{31.3}$ (at.%)

Figure 5.19(a) shows an SEM-BSE image of Alloy 19, average composition  $\text{Pt}_{25.8}:\text{Cr}_{42.9}:\text{V}_{31.3}$  (at.%) and Figure 5.19(b) shows a higher magnification. There were ternary,  $\tau$ , dendrites, and an apparently light single phase at low magnification, which was actually A15 ( $\sim\text{Cr}_3\text{Pt}$ ) +  $\sim\text{Cr}_3\text{Pt}$  eutectic, as shown at higher magnification. There were also dark porosity and oxides. It was not possible to measure a eutectic overall area because the region was too narrow, allowing only a spot analysis. The position of the overall composition in the plot in Figure 5.20 is explained by the fact that a Cr-rich phase is missing. XRD confirmed the phase identification and the unidentified peaks originated from the ternary phase (Figure 5.21). The alloy solidified and cooled with the following reactions:



**Figure 5.19(a).** SEM-BSE image of Alloy 19, average composition  $\text{Pt}_{25.8}:\text{Cr}_{42.9}:\text{V}_{31.3}$  (at.%), showing medium  $\tau$  dendrites, light  $\sim\text{Cr}_3\text{Pt}$  and dark porosity and oxide (b). SEM-BSE image of Alloy 19, at a higher magnification, showing a eutectic between the light and a light medium phase.

**Table 5.7. EDX composition analysis of Alloy 19, average composition  $\text{Pt}_{25.8}:\text{Cr}_{42.9}:\text{V}_{31.3}$  (at.%).**

Appearance	Pt	Cr	V	Phase
Overall	25.8±0.8	42.9±0.5	31.3±0.5	-
Dark medium dendrites	24.9±0.2	40.5±0.5	34.6±0.6	$\tau$
Light (Eutectic)	33.3±1.0	44.3±1.0	22.4±0.9	$\text{A15}(\sim\text{Cr}_3\text{Pt}) + \sim\text{Cr}_3\text{Pt}$

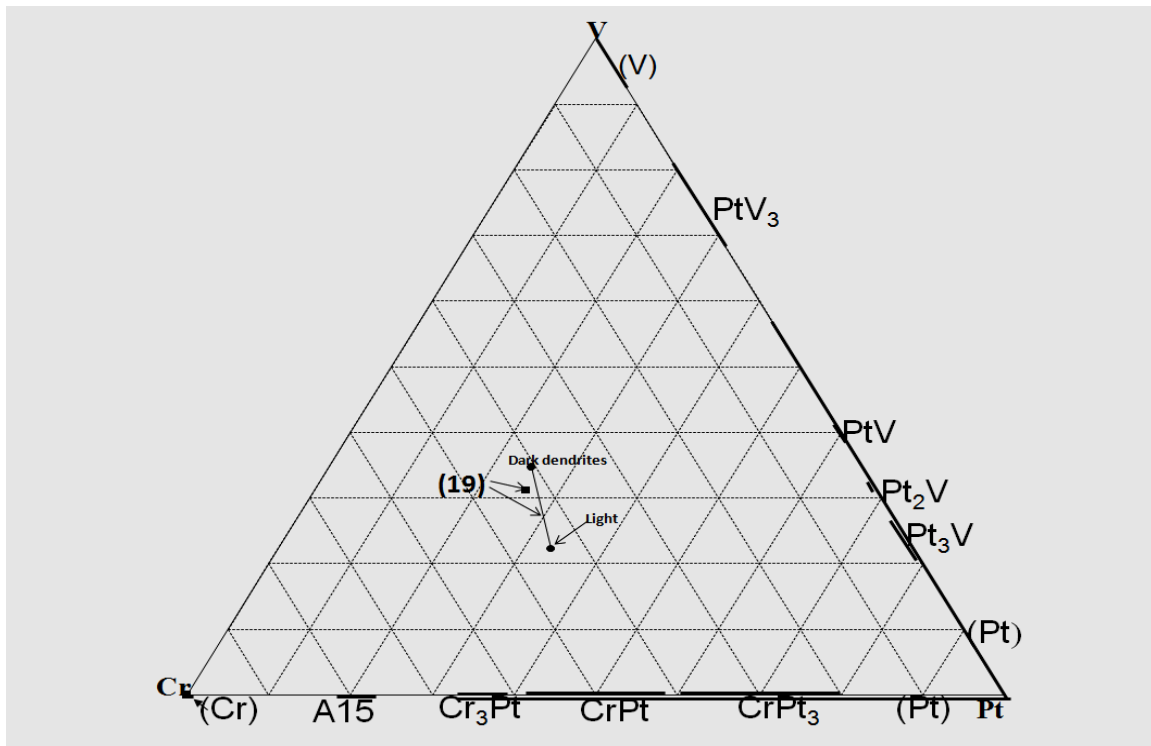


**Figure 5.20. Plot of Alloy 19, average composition  $\text{Pt}_{25.8}:\text{Cr}_{42.9}:\text{V}_{31.3}$  (at.%).**

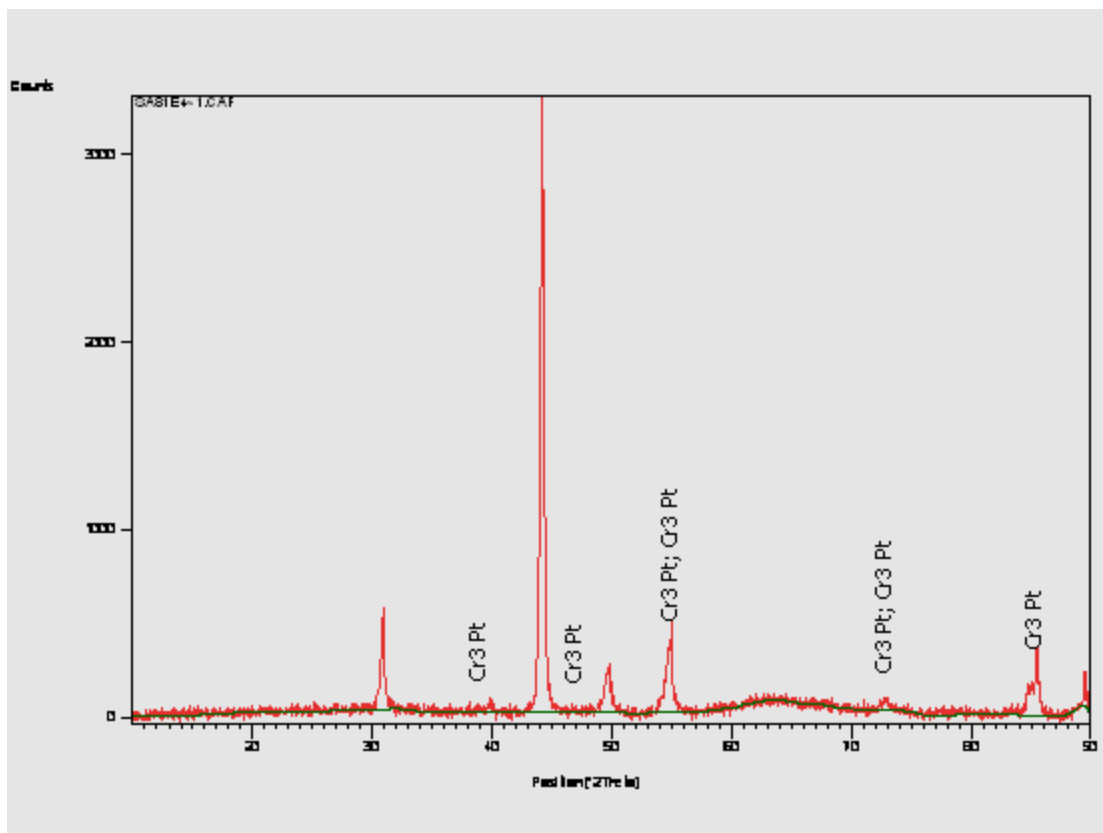


**Figure 5.21. XRD pattern of Alloy 19, average composition  $\text{Pt}_{25.8}\text{Cr}_{42.9}\text{V}_{31.3}$  (at.%).**

### **5.1.8 As-cast Alloy 20, Average Composition $\text{Pt}_{38.8}\text{Cr}_{14.2}\text{V}_{47.0}$ (at.%)**

Figure 5.22 is an SEM-BSE image of Alloy 20, average composition  $\text{Pt}_{38.8}\text{Cr}_{14.2}\text{V}_{47.0}$  (at.%), showing light cored dendrites, a medium phase and a eutectic. The cored light dendrites were identified as  $\sim\text{PtV}$  while the medium phase was identified as  $\sim\text{PtV}_3$ . The medium phase also appeared dendritic; this is because it was growing (after forming peritectically) independently between the dendrite arms of the primary light phase. The light phase was identified as the primary phase, because the central stem and arms can be clearly seen in Figure 5.22, and were lighter in the centre, showing that these dendrites were more developed, so they were first, and the others formed on them. The eutectic comprised the medium  $\sim\text{PtV}_3$  phase and was mainly holes where the second component was inadvertently removed on sample preparation. XRD confirmed the identities of the phases (Figure 5.24). The unidentified peaks are those for the ternary phase,  $\tau$ , in the eutectic.

The alloy solidified and cooled with the following reactions:

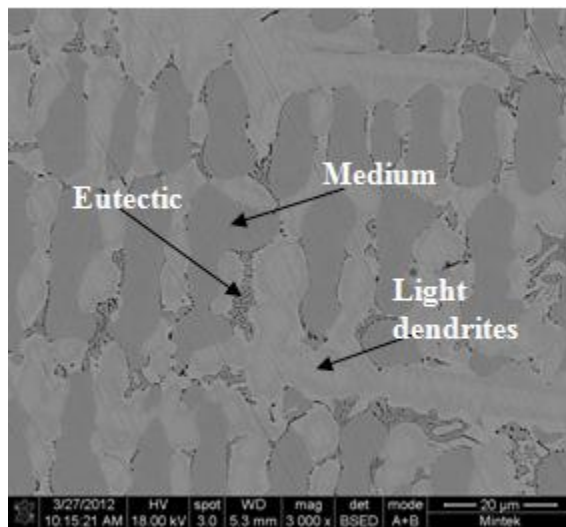
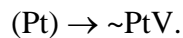
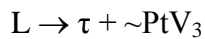
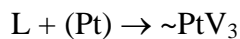
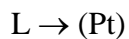


**Figure 5.22. SEM-BSE image of Alloy 20, average composition  $Pt_{38.8}:Cr_{14.2}:V_{47.0}$  (at.%), showing light cored  $\sim PtV$  dendrites, medium  $\sim PtV_3$  and a eutectic of dark  $\tau$  + medium  $PtV_3$ .**

**Table 5.8. EDX composition analysis of Alloy 20, average composition  $Pt_{38.8}:Cr_{14.2}:V_{47.0}$  (at.%).**

Appearance	Pt	Cr	V	Phase
Overall	38.8±0.5	14.2±0.4	47.0±0.5	-
Light dendrite core	42.4±1.3	13.0±0.5	44.6±0.9	$\sim PtV$
Light dendrite extremities	41.1±0.7	13.0±0.8	45.9±0.9	$\sim PtV$
Medium	34.4±0.8	14.70.4	50.9±0.8	$\sim PtV_3$
Eutectic	33.8±0.9	15.7±0.5	50.5±1.0	$\tau + \sim PtV_3$



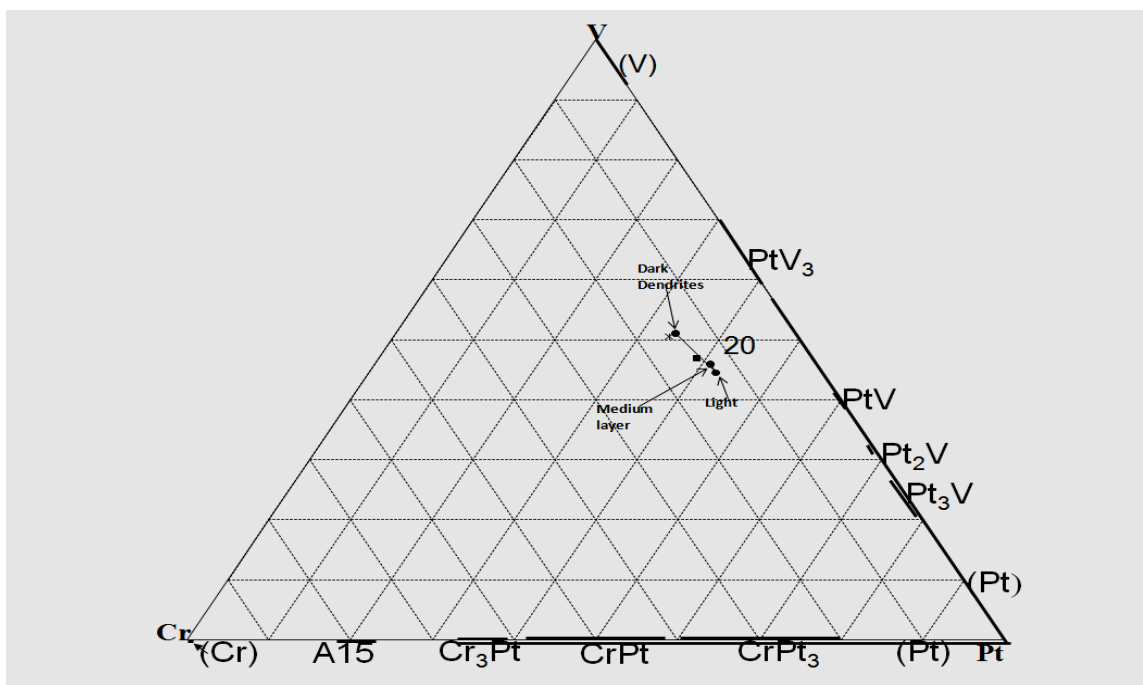


Figure 5.23. Plot of Alloy 20, average composition Pt<sub>38.8</sub>:Cr<sub>14.2</sub>:V<sub>47.0</sub> (at.%).

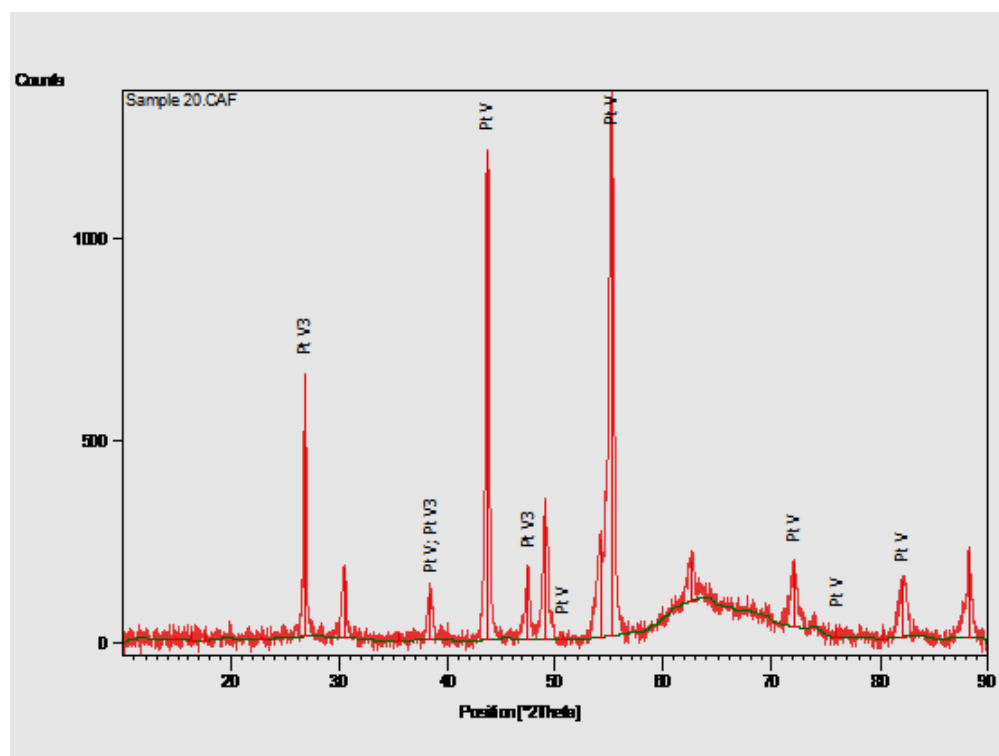
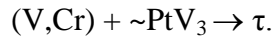
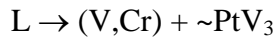
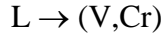


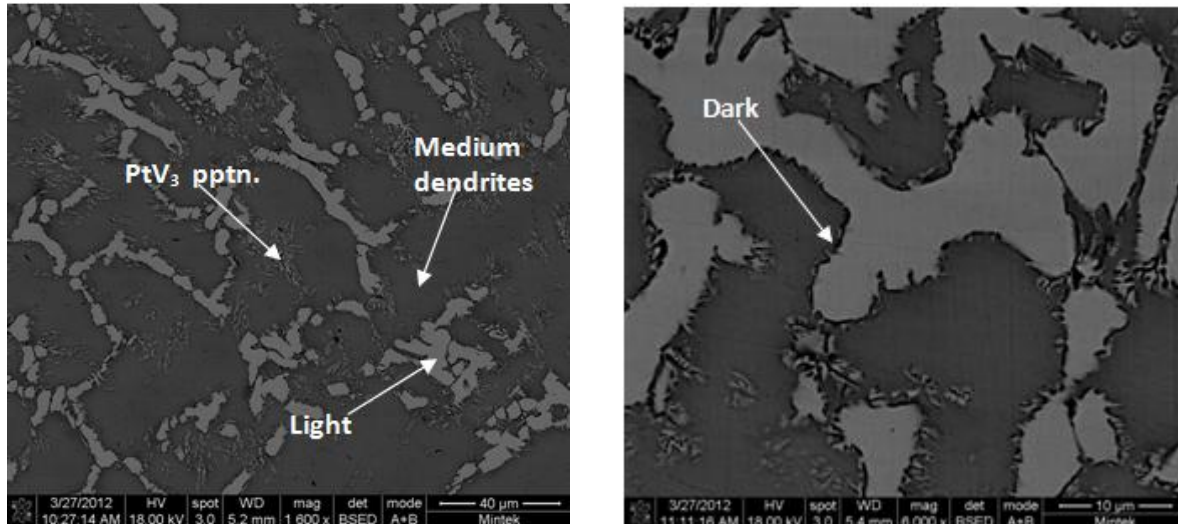
Figure 5.24. XRD pattern for Alloy 20, average overall composition Pt<sub>38.8</sub>:Cr<sub>14.2</sub>:V<sub>47.0</sub> (at.%).

### 5.1.9 As-cast Alloy 21, Average Composition $\text{Pt}_{16.8}\text{Cr}_{13.4}\text{V}_{69.8}$ (at.%)

The SEM-BSE image in Figure 5.25 is for Alloy 21, average composition  $\text{Pt}_{16.8}\text{Cr}_{13.4}\text{V}_{69.8}$  (at.%). The image shows (V,Cr) dendrites,  $\sim\text{PtV}_3$  which is part of a eutectic whose other component is (V,Cr), and  $\sim\text{PtV}_3$  which precipitated from (V,Cr) in the solid state, due to a retreating (V,Cr) solvus. There is a thin dark phase at the boundary of (V,Cr) and  $\sim\text{PtV}_3$  and because of its limited growth it is deduced that it formed after solidification was complete from a peritectoid reaction between (V,Cr) and  $\sim\text{PtV}_3$ . XRD confirmed the identities of the phases (Figure 5.27). The position of some of the unidentified peaks corresponded with that of  $\tau$  in the XRD patterns of the other alloys, which had the ternary phase. It was therefore concluded that the thin dark phase is the ternary phase,  $\tau$ . The alloy solidified and cooled with the following reactions:



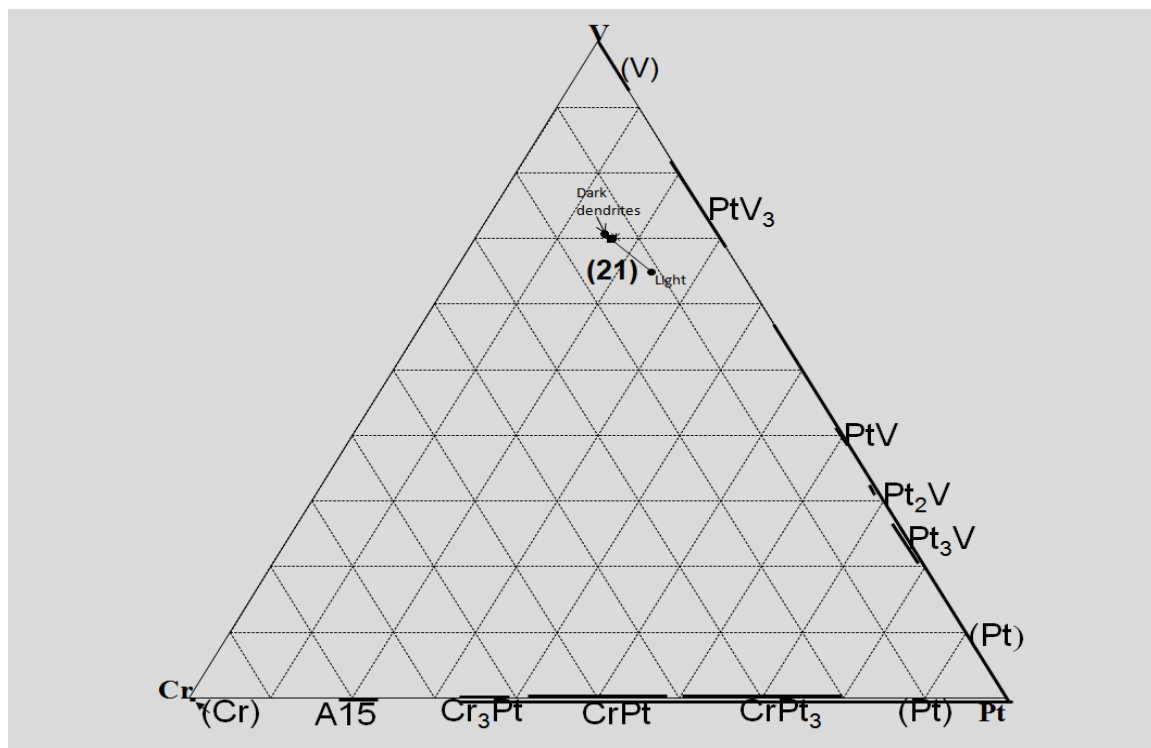
The last reaction was solid state precipitation of  $\sim\text{PtV}_3$  from (V) due to a retreating solvus.



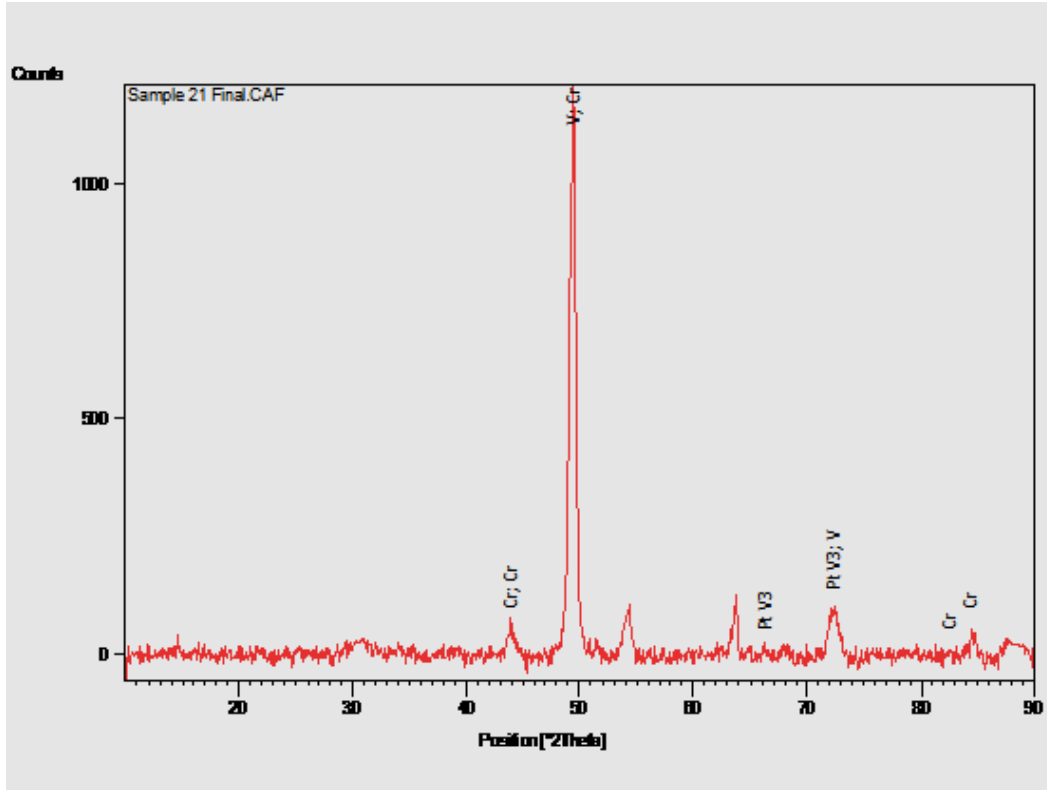
**Figure 5.25(a).** SEM-BSE image of Alloy 21, average composition  $\text{Pt}_{16.8}\text{Cr}_{13.4}\text{V}_{69.8}$  (at.%) showing medium contrast (V,Cr) dendrites, light contrast  $\sim\text{PtV}_3$  and solid state precipitates  $\sim\text{PtV}_3$  in (V,Cr). **(b).** SEM-BSE image of Alloy 21, average composition  $\text{Pt}_{16.8}\text{Cr}_{13.4}\text{V}_{69.8}$  (at.%) showing medium contrast (V,Cr) dendrites, light contrast  $\sim\text{PtV}_3$ , solid state precipitates  $\sim\text{PtV}_3$  in (V,Cr) and a thin dark ternary phase,  $\tau$ , at the boundary of (V,Cr) and  $\sim\text{PtV}_3$

**Table 5.9. EDX composition analysis of Alloy 21, average composition  $\text{Pt}_{16.8}\text{Cr}_{13.4}\text{V}_{69.8}$  (at.%).**

Appearance	Pt	Cr	V	Phase
Overall	$16.8 \pm 0.7$	$13.4 \pm 0.5$	$69.8 \pm 0.6$	-
Medium dendrites	$15.6 \pm 0.3$	$13.8 \pm 0.5$	$70.6 \pm 0.7$	(V,Cr)
Dendrites with light pptn.	$17.2 \pm 1.3$	$12.7 \pm 0.9$	$70.1 \pm 1.0$	(V,Cr) with $\sim\text{PtV}_3$ pptn.
Light	$24.2 \pm 0.8$	$10.9 \pm 0.2$	$64.9 \pm 0.7$	$\sim\text{PtV}_3$



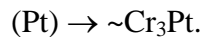
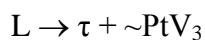
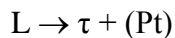
**Figure 5.26. Plot of Alloy 21, average composition  $\text{Pt}_{16.8}\text{Cr}_{13.4}\text{V}_{69.8}$  (at.%).**



**Figure 5.27. XRD pattern of Alloy 21, average composition  $\text{Pt}_{16.8}\text{:Cr}_{13.4}\text{:V}_{69.8}$  (at.%).**

#### **5.1.10 As-cast Alloy 22, Average Composition $\text{Pt}_{28.7}\text{:Cr}_{27.2}\text{:V}_{44.1}$ (at.%)**

Figure 5.28(a) is an SEM-BSE image of Alloy 22, average composition  $\text{Pt}_{28.7}\text{:Cr}_{27.2}\text{:V}_{44.1}$  (at.%), showing medium  $\tau$  dendrites, light  $\sim\text{Cr}_3\text{Pt}$ , darker medium  $\sim\text{PtV}_3$  and a dark discrete component of a eutectic. The light  $\sim\text{Cr}_3\text{Pt}$  and darker medium  $\sim\text{PtV}_3$  are components of coarse eutectics while the dark phase is a component of a ternary eutectic. Most of the dark component of the ternary eutectic oxidized (proportion unknown), and fell out due to brittleness and this is responsible for the positions of the plots of the overall compositions of the alloy and ternary eutectic falling outside the upper portion of the triangle (Figure 5.29). XRD confirmed the phases as shown in the pattern in Figure 5.30. The unidentified peaks were for  $\tau$ . The alloy solidified and cooled with the following reactions:



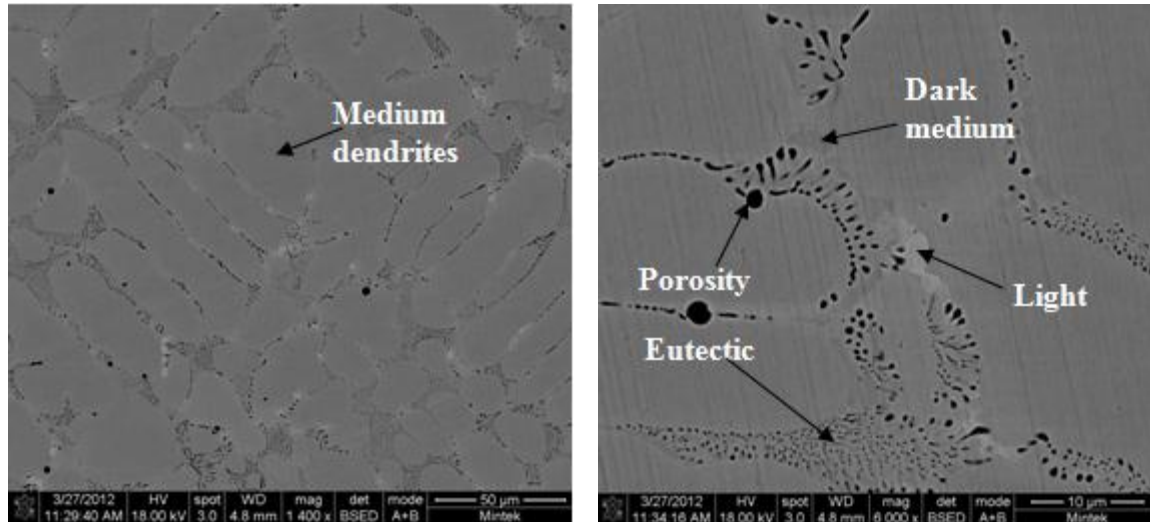
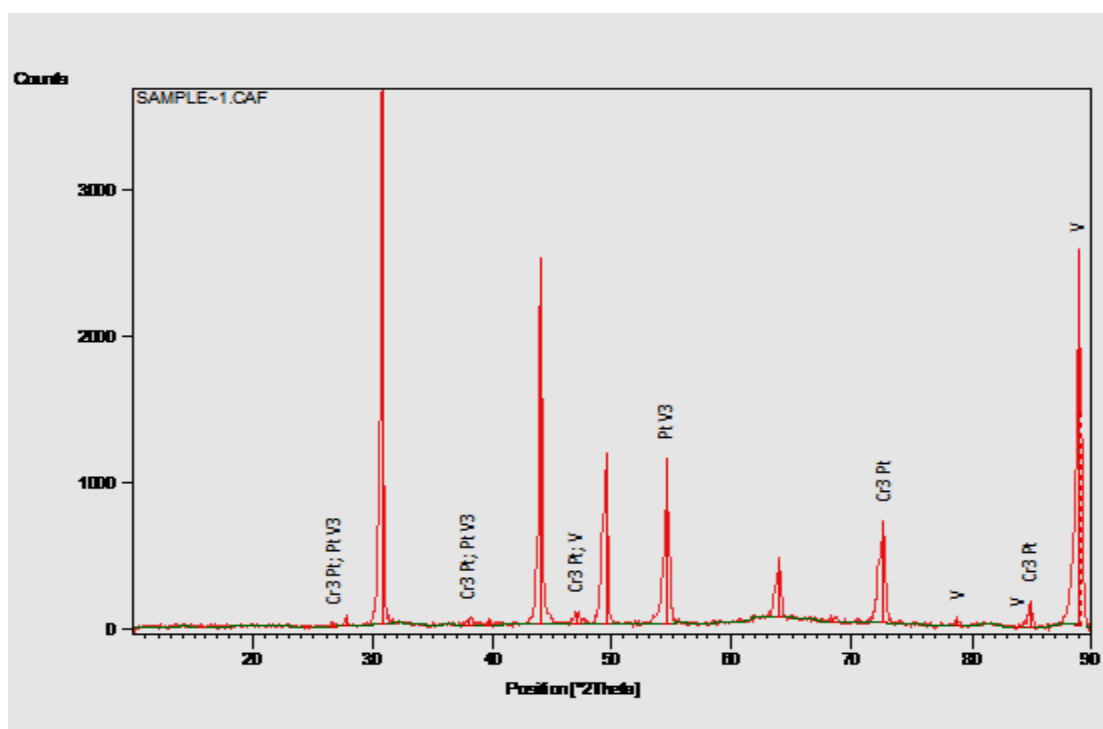
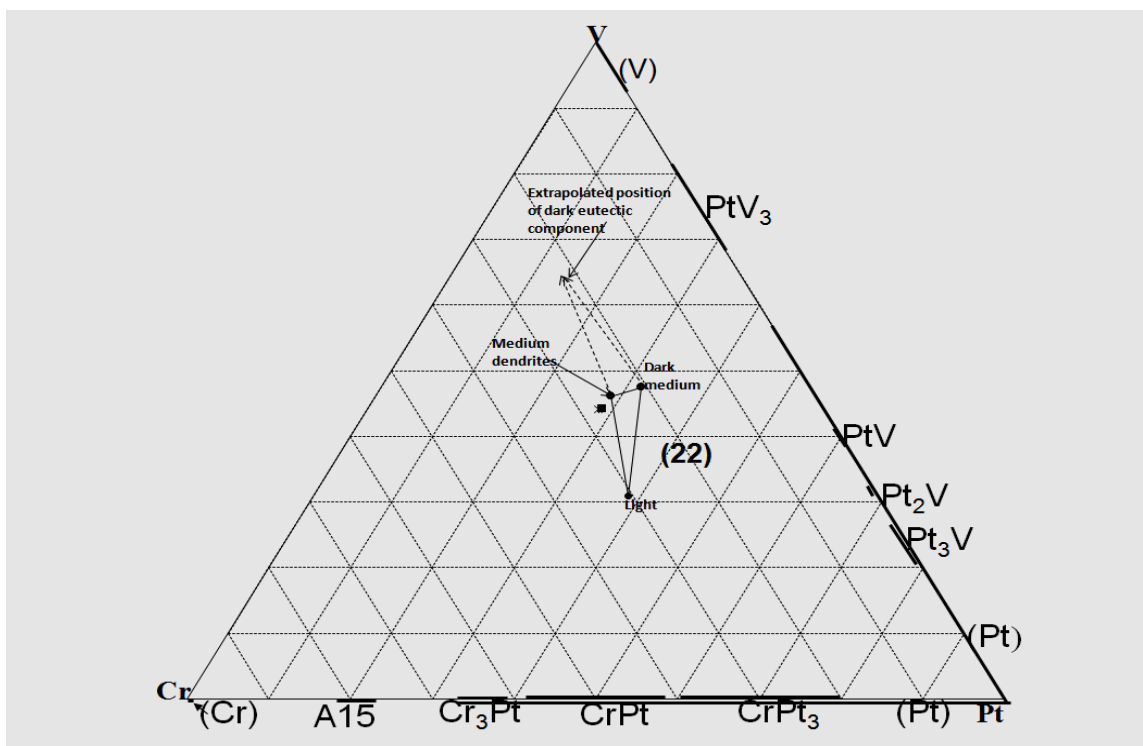


**Figure 5.28(a).** SEM-BSE image of Alloy 22, average composition  $\text{Pt}_{28.7}\text{Cr}_{27.2}\text{V}_{44.1}$  (at.%) showing medium dendrites, a light phase and a eutectic. (b). SEM-BSE image of Alloy 22 at a higher magnification showing a different shade of medium contrast at the extremities of dendrites.

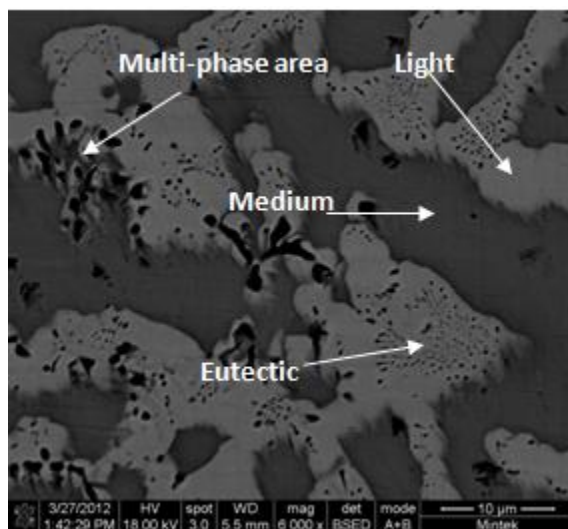
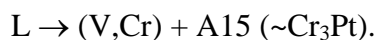
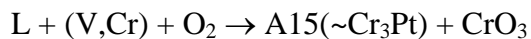
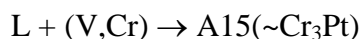
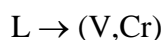
**Table 5.10. EDX composition analysis of Alloy 22, average composition  $\text{Pt}_{28.7}\text{Cr}_{27.2}\text{V}_{44.1}$  (at.%).**

Appearance	Pt	Cr	V	Phase
Overall	$28.7 \pm 0.7$	$27.2 \pm 0.4$	$44.1 \pm 0.7$	-
Dendrites	$28.8 \pm 0.4$	$28.1 \pm 0.3$	$43.1 \pm 0.4$	$\tau_3$
Dark medium	$31.8 \pm 0.7$	$20.6 \pm 0.4$	$47.6 \pm 0.9$	$\sim \text{PtV}_3$
Light	$38.5 \pm 0.8$	$30.5 \pm 1.1$	$31.0 \pm 1.3$	$\sim \text{Cr}_3\text{Pt}$
Eutectic	$28.4 \pm 1.1$	$27.6 \pm 0.9$	$44.0 \pm 1.3$	$\tau + \sim \text{PtV}_3 + (\text{V}, \text{Cr})$



#### 5.1.11 As-cast Alloy 23, Average Composition $\text{Pt}_{16.5}:\text{Cr}_{56.1}:\text{V}_{27.4}$ (at.%)

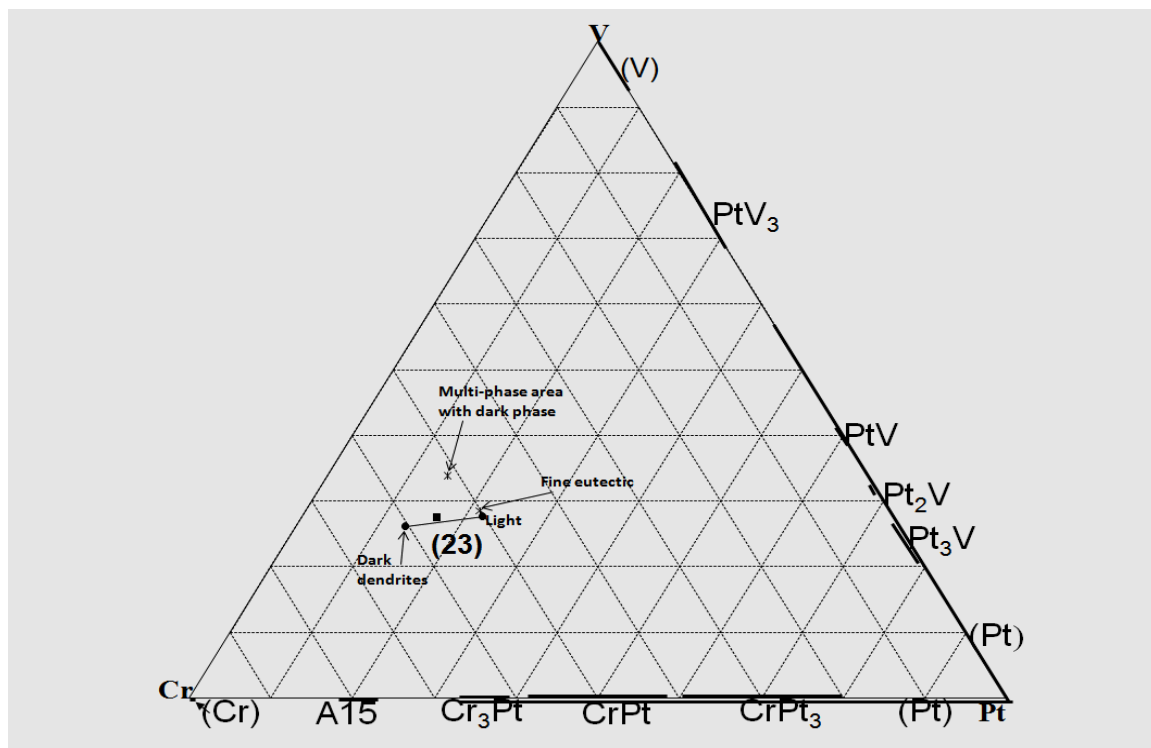
An SEM-BSE image of Alloy 23, average overall composition  $\text{Pt}_{16.5}:\text{Cr}_{56.1}:\text{V}_{27.4}$  (at.%), in Figure 5.31 shows medium (V,Cr) dendrites, light A15 ( $\sim\text{Cr}_3\text{Pt}$ ), a eutectic consisting of A15( $\sim\text{Cr}_3\text{Pt}$ ) + (V,Cr) and a multi-phase area with a dark component. The EDX composition analysis data in Table 5.11 were plotted in Figure 5.32. XRD confirmed the phase identities as shown in the pattern in Figure 5.33 and that an oxide,  $\text{CrO}_3$ , formed. The oxide is the dark component of the multi-phase area. Although oxygen was the fourth component in the system, it was felt that the results could still be used for ternary interpretation, because oxygen only reacted with Cr. The reactions during solidification and cooling are:



**Figure 5.31. SEM-BSE image of Alloy 23, average composition  $\text{Pt}_{16.5}:\text{Cr}_{56.1}:\text{V}_{27.4}$  (at.%), showing medium contrast (Cr) dendrites, light A15( $\sim\text{Cr}_3\text{Pt}$ ), A15( $\sim\text{Cr}_3\text{Pt}$ ) + (Cr) eutectic and dark oxide.**

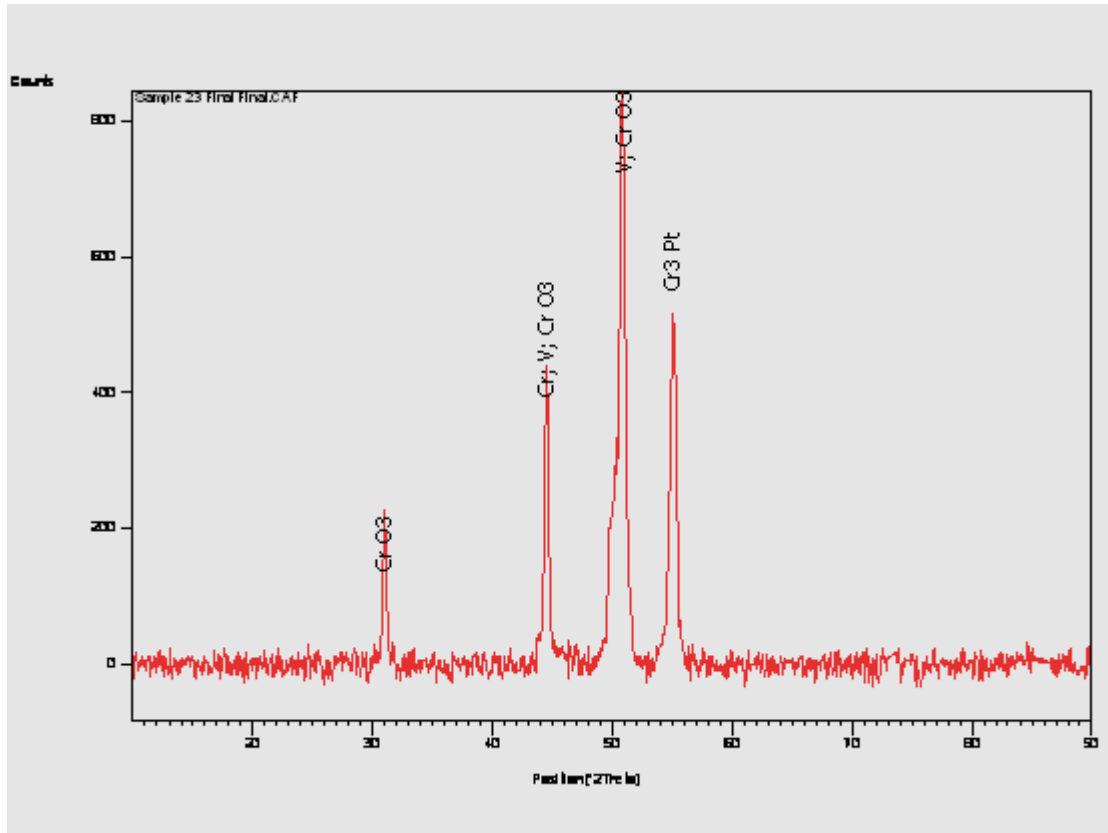
**Table 5.11. EDX composition analysis of Alloy 23, average composition  $\text{Pt}_{16.5}:\text{Cr}_{56.1}:\text{V}_{27.4}$  (at.%).**

Appearance	Pt	Cr	V	Phase
Overall	$16.5 \pm 0.6$	$56.1 \pm 0.5$	$27.4 \pm 0.3$	-
Medium dendrites	$13.4 \pm 0.9$	$60.6 \pm 0.6$	$26.0 \pm 0.3$	(V,Cr)
Light	$22.1 \pm 0.5$	$50.3 \pm 0.3$	$27.6 \pm 0.4$	A15 ( $\sim\text{Cr}_3\text{Pt}$ )
Multi-phase area with dark phase	$14.7 \pm 1.2$	$51.5 \pm 1.5$	$33.8 \pm 2.0$	(V,Cr) + A15 ( $\sim\text{Cr}_3\text{Pt}$ ) + $\text{CrO}_3$
Fine eutectic	$21.3 \pm 0.5$	$50.2 \pm 0.9$	$28.5 \pm 0.9$	A15 ( $\sim\text{Cr}_3\text{Pt}$ ) + (V,Cr)



**Figure 5.32. Plot of Alloy 23, average composition  $\text{Pt}_{16.5}:\text{Cr}_{56.1}:\text{V}_{27.4}$  (at.%).**

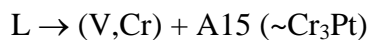
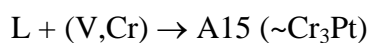
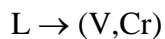




**Figure 5.33. XRD pattern of Alloy 23, average composition  $\text{Pt}_{16.5}\text{:Cr}_{56.1}\text{:V}_{27.4}$  (at.%).**

#### **5.1.12 As-cast Alloy 24, Average Composition $\text{Pt}_{14.9}\text{:Cr}_{73.7}\text{:V}_{11.4}$ (at.%)**

Figure 5.34 is a SEM-BSE image of Alloy 24, average composition  $\text{Pt}_{14.9}\text{:Cr}_{73.7}\text{:V}_{11.4}$  (at.%), showing medium cored dendrites, (Cr), light A15( $\sim\text{Cr}_3\text{Pt}$ ), a sparse eutectic of (V,Cr) + A15 ( $\sim\text{Cr}_3\text{Pt}$ ) and small dark oxides. There is also a multi-phase area with a dark component which turned out to be the oxide  $\text{CrO}_3$  from XRD analysis. The data for EDX composition analysis in Table 5.12 are plotted in Figure 5.35. It was not possible to do an overall composition analysis of the sparse eutectic. XRD which confirmed the identities of the phases as shown in the pattern in Figure 5.36 also detected the oxide  $\text{CrO}_3$ , despite the precaution of a Ti-getter being used. The alloy solidified and cooled with the following reactions taking place:



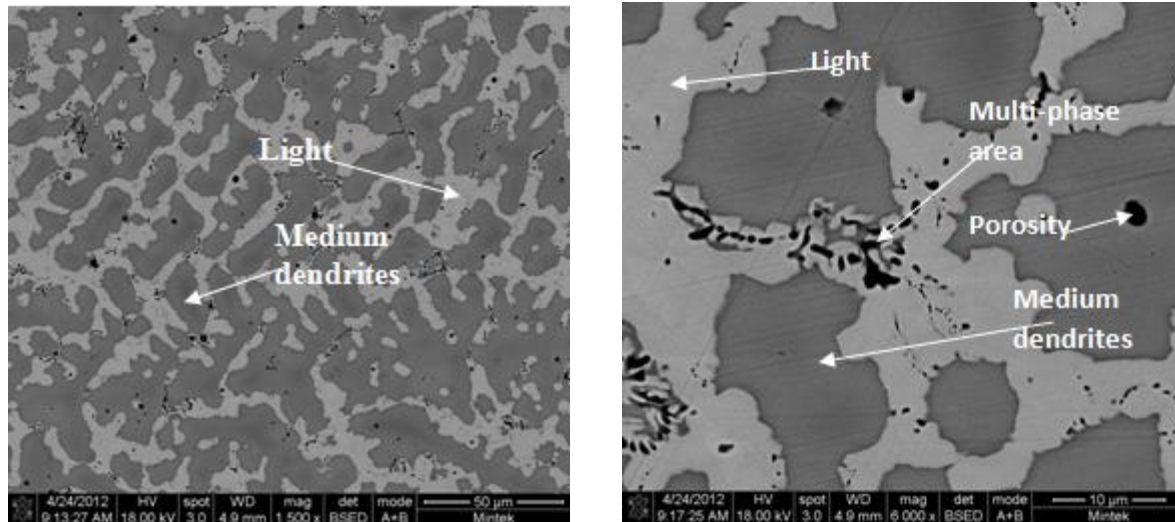


**Figure 5.34 (a).** SEM-BSE image of Alloy 24, average composition  $\text{Pt}_{14.9}:\text{Cr}_{73.7}:\text{V}_{11.4}$  (at.%), showing medium cored dendrites, (V,Cr), light A15( $\sim\text{Cr}_3\text{Pt}$ ), sparse eutectic of (Cr) + A15( $\sim\text{Cr}_3\text{Pt}$ ) and rounded dark porosity and oxides. **(b).** SEM-BSE image of Alloy 24, average composition  $\text{Pt}_{14.9}:\text{Cr}_{73.7}:\text{V}_{11.4}$  (at.%), showing medium cored dendrites, (V,Cr), light A15( $\sim\text{Cr}_3\text{Pt}$ ), multi-phase area with a dark component and rounded dark porosity and oxides.

**Table 5.12. EDX composition analysis of Alloy 24, average overall composition  $\text{Pt}_{14.9}:\text{Cr}_{73.7}:\text{V}_{11.4}$  (at.%).**

Appearance	Pt	Cr	V	Phase
Overall	14.9±0.7	73.7±0.6	11.4±0.2	-
Dark dendrite core	8.1±0.2	80.9±0.2	11.0±0.04	(V,Cr)
Dendrite extremities	12.7±0.5	76.4±0.6	10.9±0.3	(V,Cr)
Light	22.4±0.7	66.2±0.7	11.4±0.7	A15 ( $\sim\text{Cr}_3\text{Pt}$ )

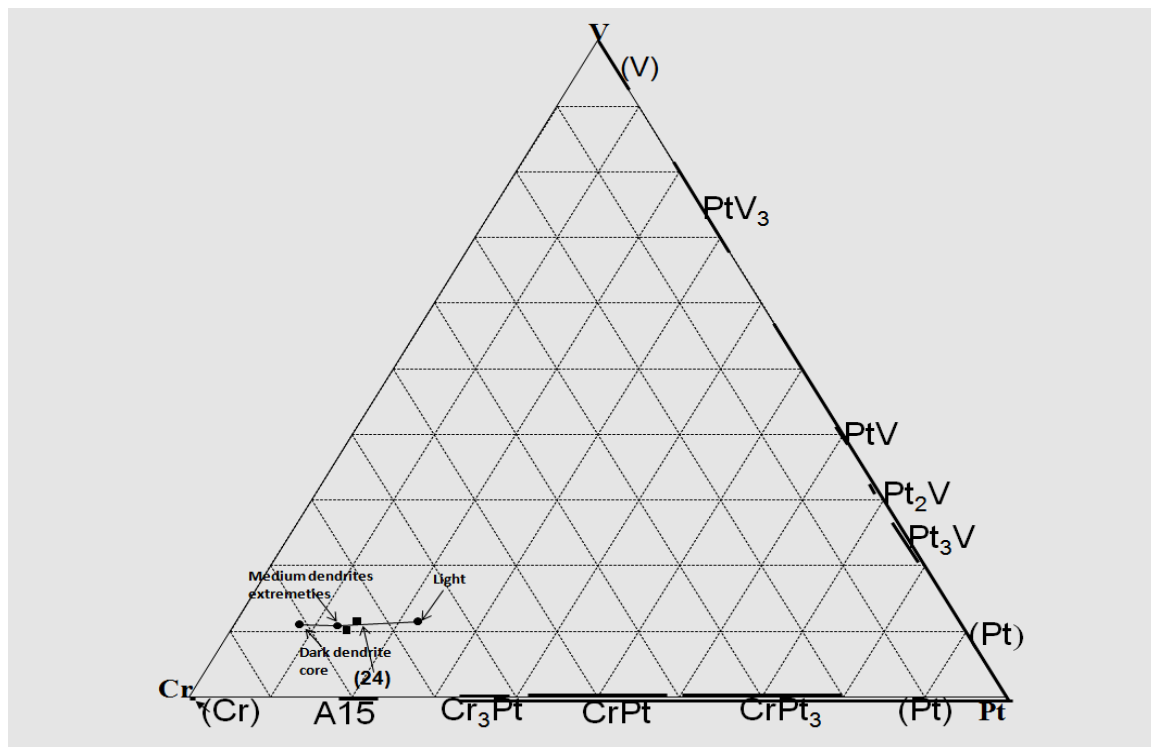
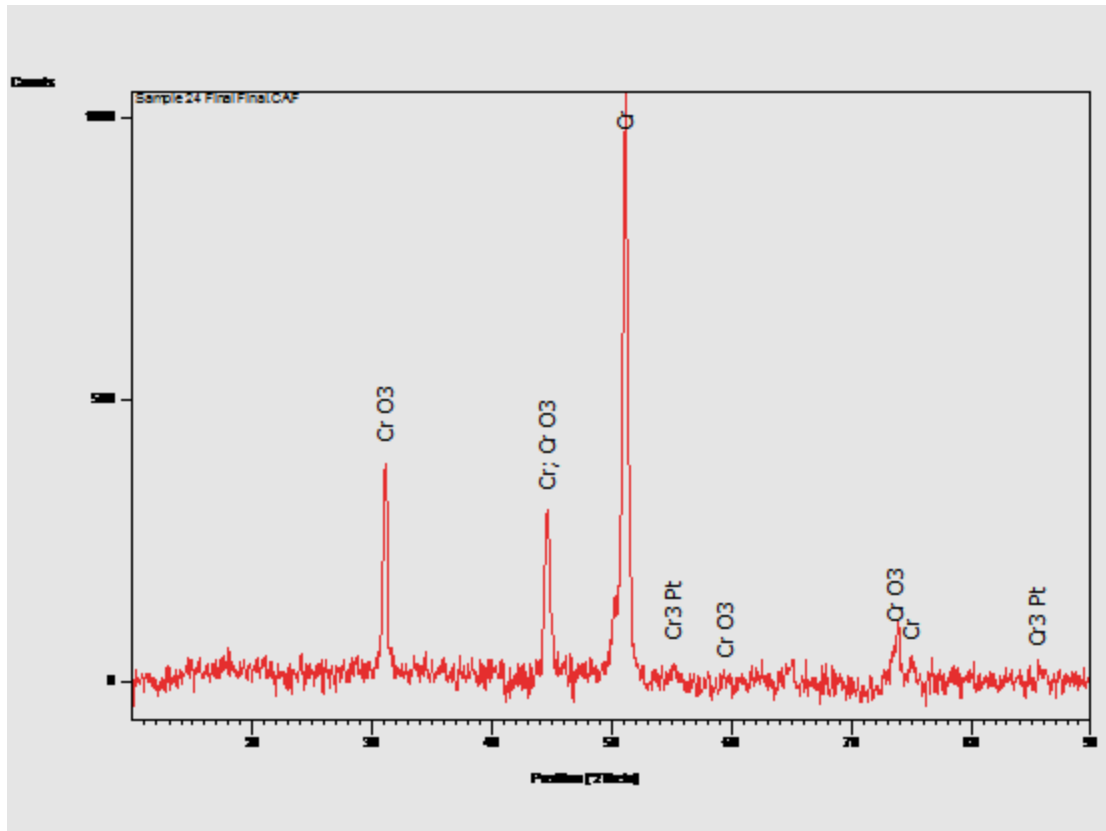


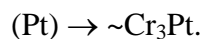
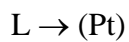
Figure 5.35. Plot of Alloy 24, average composition  $\text{Pt}_{14.9}\text{:Cr}_{73.7}\text{:V}_{11.4}$  (at.%).



**Figure 5.36. XRD pattern of Alloy 24, average composition  $\text{Pt}_{14.9}:\text{Cr}_{73.7}:\text{V}_{11.4}$  (at.%).**

### **5.1.13 As-cast Alloy 25, Average Composition $\text{Pt}_{34.1}:\text{Cr}_{57.4}:\text{V}_{8.5}$ (at.%)**

The SEM-BSE image of Alloy 25, average composition  $\text{Pt}_{34.1}:\text{Cr}_{57.4}:\text{V}_{8.5}$  (at.%), in Figure 5.37, shows cored light  $\sim\text{Cr}_3\text{Pt}$  dendrites, medium A15( $\sim\text{Cr}_3\text{Pt}$ ), which formed a sparse eutectic with  $\sim\text{Cr}_3\text{Pt}$ , and small dark oxides. The EDX composition analysis data in Table 5.13 were plotted in Figure 5.38. XRD, which confirmed the identity of the phases as shown in the pattern in Figure 5.39, also detected the presence of the oxide  $\text{CrO}_3$ . The alloy solidified and cooled with the following reactions:



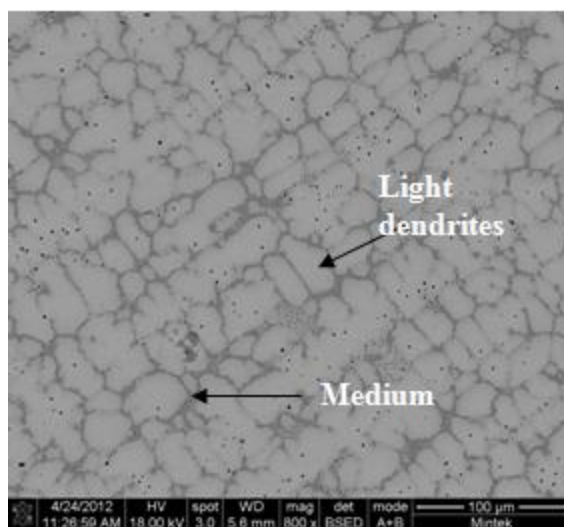


**Figure 5.37. SEM-BSE image of Alloy 25, average composition  $\text{Pt}_{34.1}:\text{Cr}_{57.4}:\text{V}_{8.5}$  (at.%), showing light  $\sim\text{Cr}_3\text{Pt}$  cored dendrites, medium contrast A15( $\sim\text{Cr}_3\text{Pt}$ ) and dark oxide.**

**Table 5.13. EDX composition analysis of Alloy 25, average composition  $\text{Pt}_{34.1}:\text{Cr}_{57.4}:\text{V}_{8.5}$  (at.%).**

Appearance	Pt	Cr	V	Phase
Overall	34.1±1.0	57.4±1.0	8.5±0.2	-
Light dendrite core	37.7±0.5	53.7±0.7	8.6±0.4	$\sim\text{Cr}_3\text{Pt}$
Dendrite extremities	33.2±0.6	58.5±0.4	8.3±0.6	$\sim\text{Cr}_3\text{Pt}$
Medium	25.4±0.3	65.9±0.3	8.7±0.2	A15( $\sim\text{Cr}_3\text{Pt}$ )

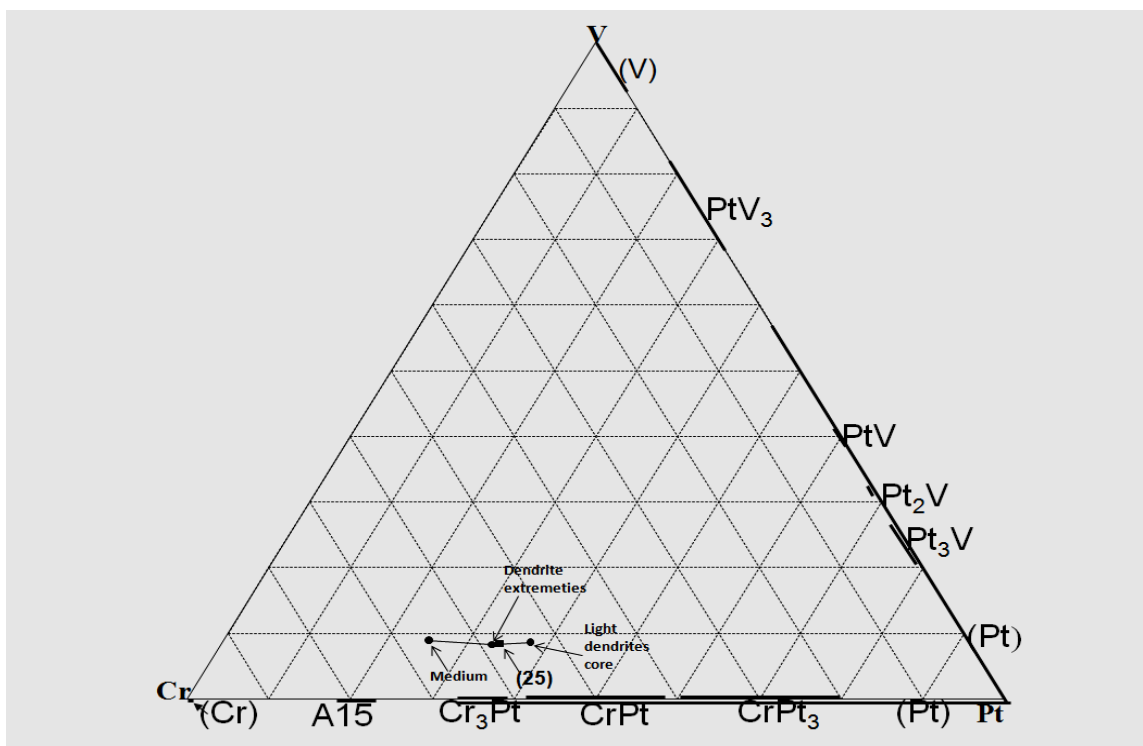


Figure 5.38. Plot of Alloy 25, average composition  $Pt_{34.1}:Cr_{57.4}:V_{8.5}$  (at.%).

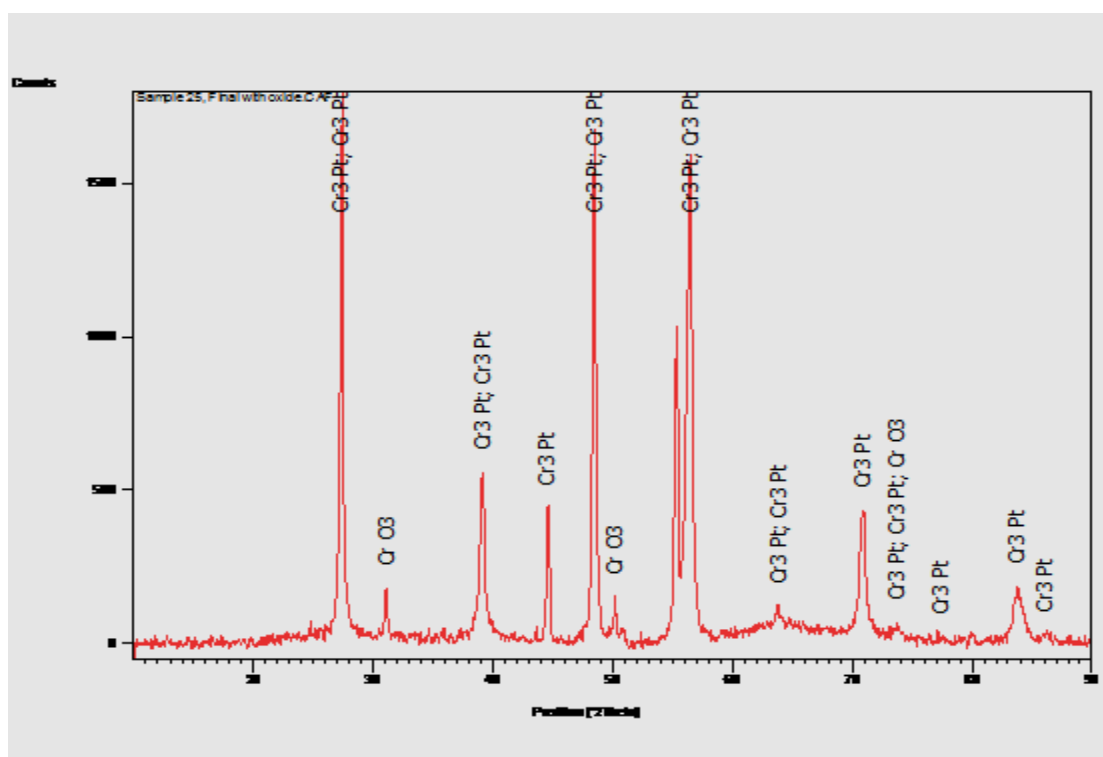


Figure 5.39. XRD pattern of Alloy 25, average composition  $Pt_{34.1}:Cr_{57.4}:V_{8.5}$  (at.%).

#### 5.1.14 Solidification Projection of the Pt-Cr-V System

The solidification projection obtained from the as-cast samples is given in Figure 5.40. The A15 ( $\sim\text{Cr}_3\text{Pt}$ ) phase extended in the ternary to  $\sim 28$  at.% V, and  $\sim\text{PtV}_3$  extended to  $\sim 21$  at.% Cr. A ternary phase was found in some of the as-cast alloys, between  $\sim\text{V}_{39}\text{Cr}_{31}\text{Pt}_{30}$  (at.%) to  $\sim\text{V}_{46}\text{Cr}_{25}\text{Pt}_{29}$  (at.%). Alloy 21 showed solid state precipitation, indicating that the solvus of the solid solution (V,Cr) retreats noticeably with decreasing temperature.

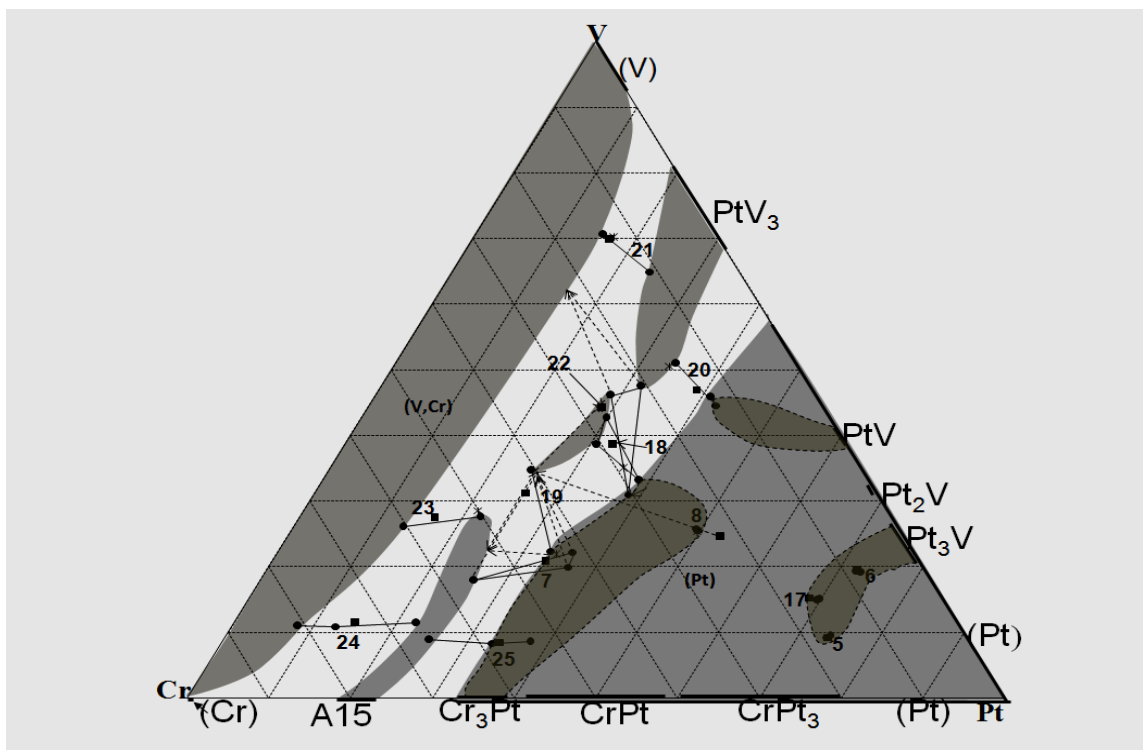
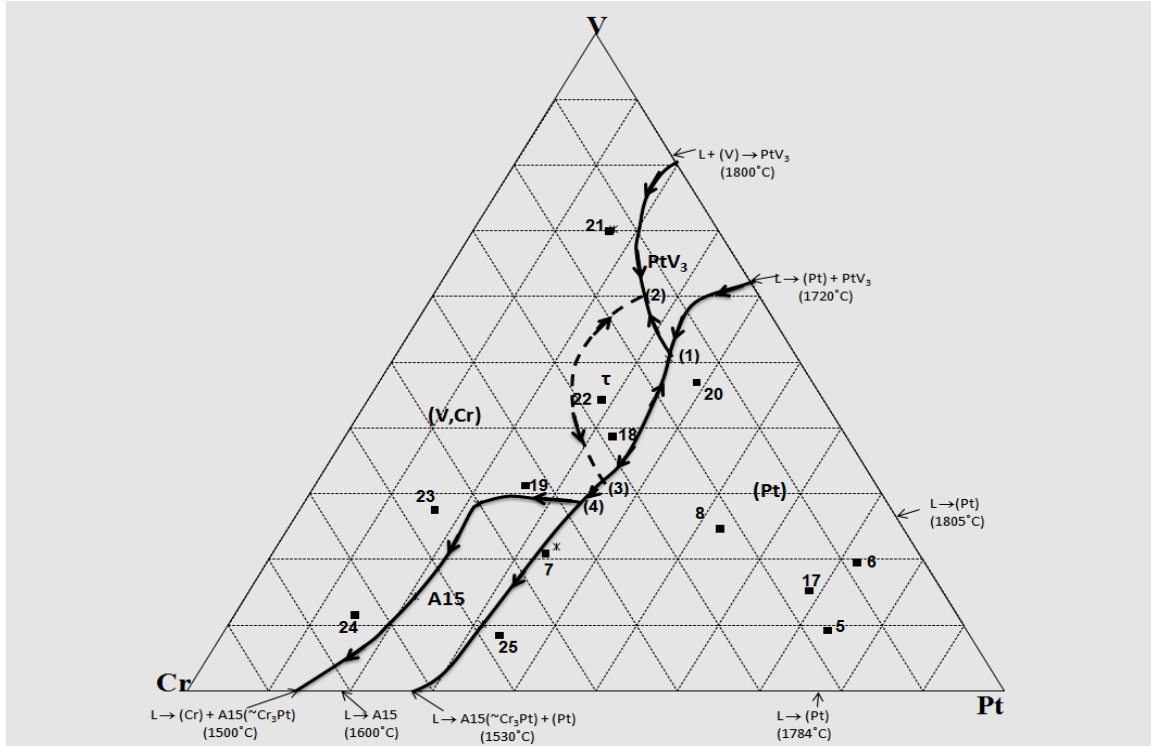


Figure 5.40. Solidification projection of the Pt-Cr-V system (at.%).

#### 5.1.15 Liquidus Surface Projection of the Pt-Cr-V System

The liquidus surface projection is shown in Figure 5.41 and is mainly the surfaces of (Pt) and (V,Cr) solid solutions. It was derived from the solidification sequences of the phases and their morphologies. Solidification starts with the composition moving directly away from the primary solid (on that primary liquidus surface), until a boundary with another liquidus surface is met, and the liquid composition then follows the boundary between the two liquidus surfaces for either a eutectic or a peritectic reaction, allowing for the fact that on non-equilibrium cooling, the liquid composition can sometimes run across the surface of the peritectic component. The

boundary between the (V,Cr) solid solution and  $\tau$  is dotted because more alloys need to be studied in that area to determine the exact boundary.



**Figure 5.41. Liquidus surface projection of the Pt-Cr-V system (at.%).**

Four ternary invariant reactions were identified as follows:

Reaction No.	Liquid Composition (at.%)	Reaction
(1)	$\sim\text{Pt}_{34}\text{Cr}_{15}\text{V}_{51}$	$\text{L} + (\text{Pt}) \rightarrow \sim\text{PtV}_3 \rightarrow \tau$
(2)	$\sim\text{Pt}_{26}\text{Cr}_{14}\text{V}_{60}$	$\text{L} \rightarrow (\text{V,Cr}) + \sim\text{PtV}_3 + \tau$
(3)	$\sim\text{Pt}_{35}\text{Cr}_{33}\text{V}_{32}$	$\text{L} + \tau_3 \rightarrow (\text{Pt}) + (\text{V,Cr})$
(4)	$\sim\text{Pt}_{34}\text{Cr}_{38}\text{V}_{28}$	$\text{L} + (\text{Pt}) + (\text{V,Cr}) \rightarrow \text{A15}(\sim\text{Cr}_3\text{Pt})$

After reaction 4, the liquid composition flows to the Cr-Pt binary edge at the eutectic

$\text{L} \rightarrow (\text{Cr}) + \text{A15}(\sim\text{Cr}_3\text{Pt})$  and  $\text{L} \rightarrow \text{A15}(\sim\text{Cr}_3\text{Pt}) + (\text{Pt})$ . It is worthwhile to note direct evidence of Reaction (2) was found in Alloy 22.



## 5.2 ALLOYS ANNEALED AT 1000°C FOR 1500 HOURS

### 5.2.1 Annealed Alloy 5H, Average Composition $\text{Pt}_{76.2}:\text{Cr}_{16.1}:\text{V}_{7.7}$ (at.%)

The SEM-BSE image of annealed Alloy 5H, average composition  $\text{Pt}_{76.2}:\text{Cr}_{16.1}:\text{V}_{7.7}$  (at.%), in Figure 5.42 shows single phase  $\sim\text{Pt}_3\text{V}$ , with grains at different orientations. EDX composition analysis was done on different shades of contrast and the data in Table 5.14 are plotted in Figure 5.43. The plot was used to identify the phase and XRD confirmed the identity as shown by the pattern in Figure 5.44.

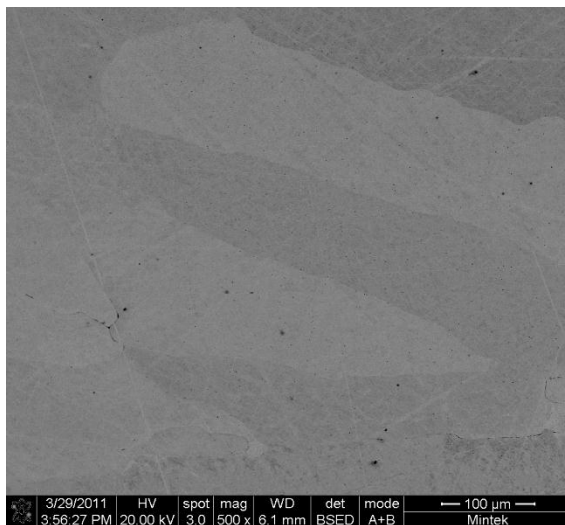


**Figure 5.42.** SEM-BSE image of annealed Alloy 5H, average composition  $\text{Pt}_{76.2}:\text{Cr}_{16.1}:\text{V}_{7.7}$  (at.%), showing single phase  $\sim\text{Pt}_3\text{V}$  with grains at different orientations.

**Table 5.14.** EDX composition analysis data for annealed Alloy 5H, average composition  $\text{Pt}_{76.2}:\text{Cr}_{16.1}:\text{V}_{7.7}$  (at.%).

Appearance	Pt	Cr	V	Phase
Overall	76.2±0.4	16.1±0.4	7.7±0.2	-
Dark	76.1±0.2	16.0±0.4	7.9±0.2	$\sim\text{Pt}_3\text{V}$
Light	75.7±0.5	16.5±0.5	7.8±0.3	$\sim\text{Pt}_3\text{V}$

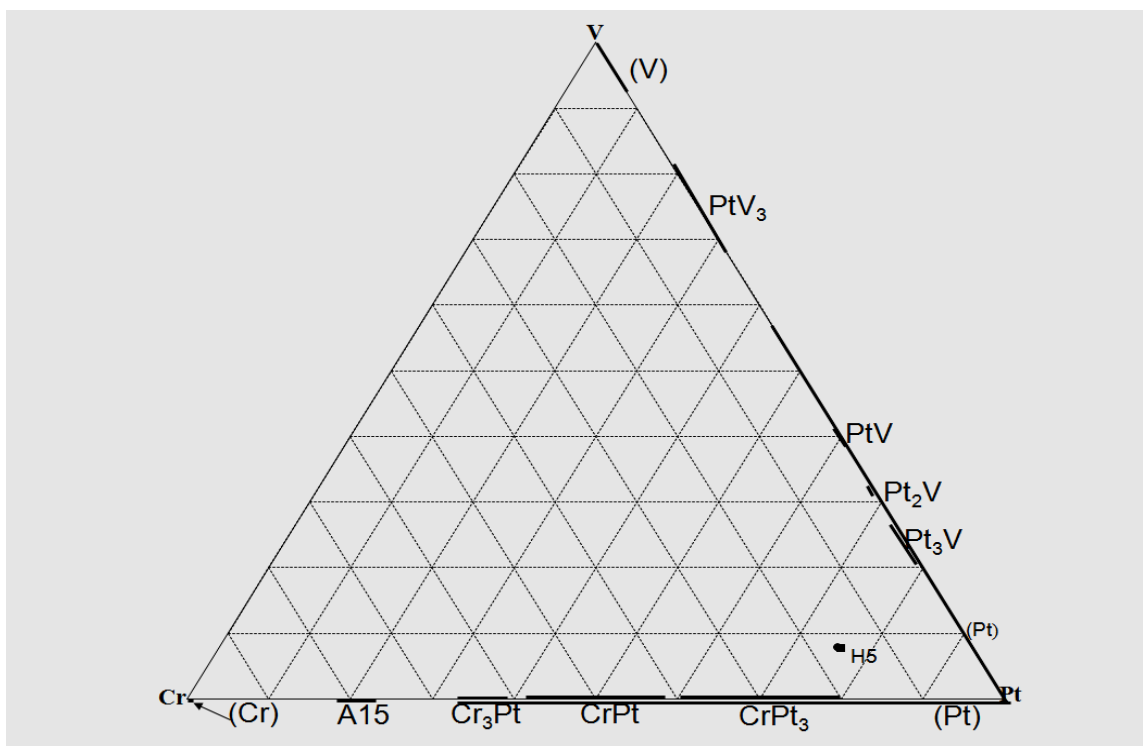


Figure 5.43. Plot of annealed Alloy 5H, average composition  $\text{Pt}_{76.2}:\text{Cr}_{16.1}:\text{V}_{7.7}$  (at.%).

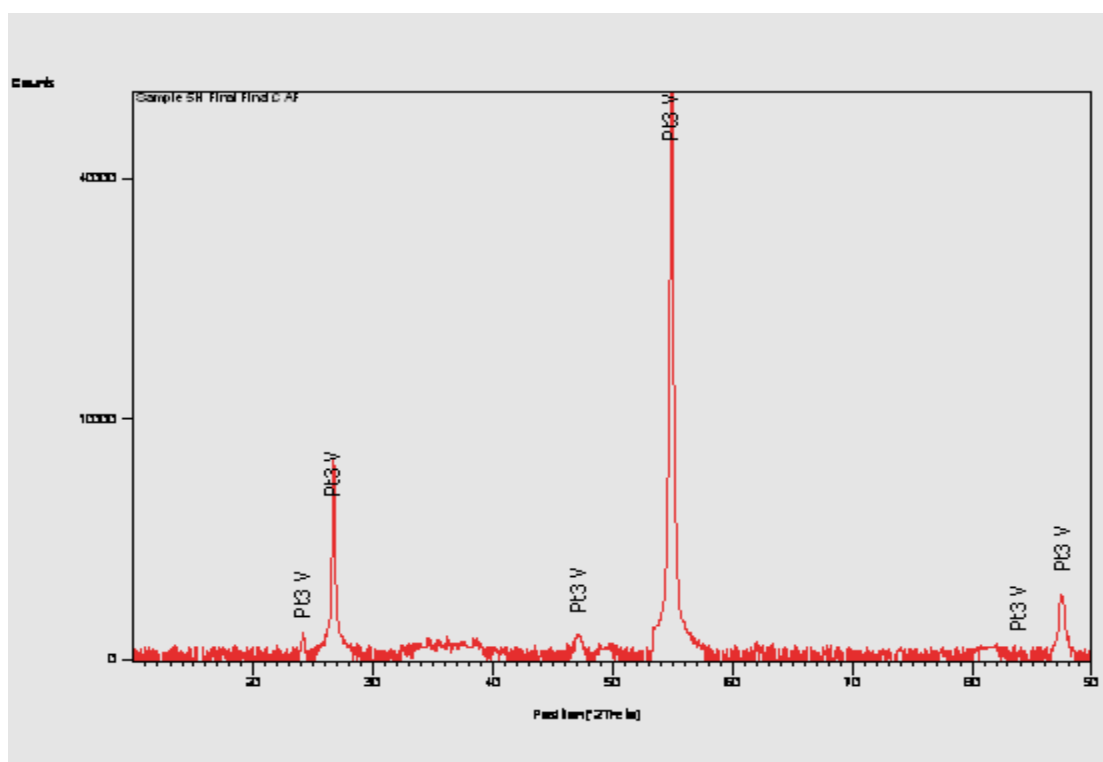
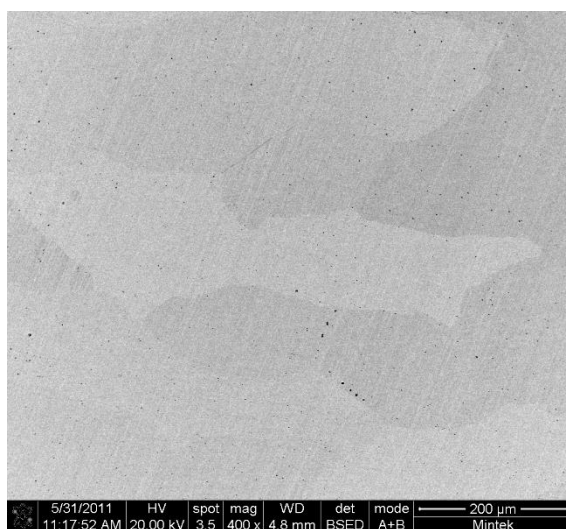


Figure 5.44. XRD pattern of annealed Alloy 5H, average composition  $\text{Pt}_{76.2}:\text{Cr}_{16.1}:\text{V}_{7.7}$  (at.%).

### 5.2.2 Annealed Alloy 6H, Average Composition $\text{Pt}_{77.3}\text{Cr}_{6.6}\text{V}_{16.1}$ (at.%)

Figure 5.45 is a SEM-BSE image of annealed Alloy 6H, average composition  $\text{Pt}_{77.3}\text{Cr}_{6.6}\text{V}_{16.1}$  (at.%), showing single phase  $\sim\text{Pt}_3\text{V}$  with grains at different orientations. The data in Table 5.15 are EDX composition analyses done on different shades of contrast seen in Figure 5.45 and plotted in Figure 5.46. XRD confirmed the alloy was predominantly single phase  $\sim\text{Pt}_3\text{V}$ , although some peaks were for  $\sim\text{Pt}_2\text{V}$ . This indicates that the eutectoid reaction at  $\sim 970^\circ\text{C}$ ,  $(\text{Pt}) \rightarrow \sim\text{Pt}_2\text{V} + \sim\text{Pt}_3\text{V}$ , in the binary phase diagram of Pt-V [1990Mas] may have taken place locally (possibly at a different temperature in the ternary), although the eutectoid is not shown in the SEM-BSE image.



**Figure 5.45. SEM-BSE image of annealed Alloy 6H, average composition  $\text{Pt}_{77.3}\text{Cr}_{6.6}\text{V}_{16.1}$  (at.%), showing single phase  $\sim\text{Pt}_3\text{V}$  with grains at different orientations.**

**Table 5.15. EDX composition analysis data for annealed Alloy 6H, average composition  $\text{Pt}_{77.3}\text{Cr}_{6.6}\text{V}_{16.1}$  (at.%).**

Appearance	Pt	Cr	V	Phase
Overall	$77.3 \pm 0.5$	$6.6 \pm 0.4$	$16.1 \pm 0.2$	-
Dark	$76.5 \pm 0.4$	$7.2 \pm 0.3$	$16.3 \pm 0.3$	$\sim\text{Pt}_3\text{V}$
Light	$76.5 \pm 0.5$	$7.1 \pm 0.3$	$16.4 \pm 0.5$	$\sim\text{Pt}_3\text{V}$

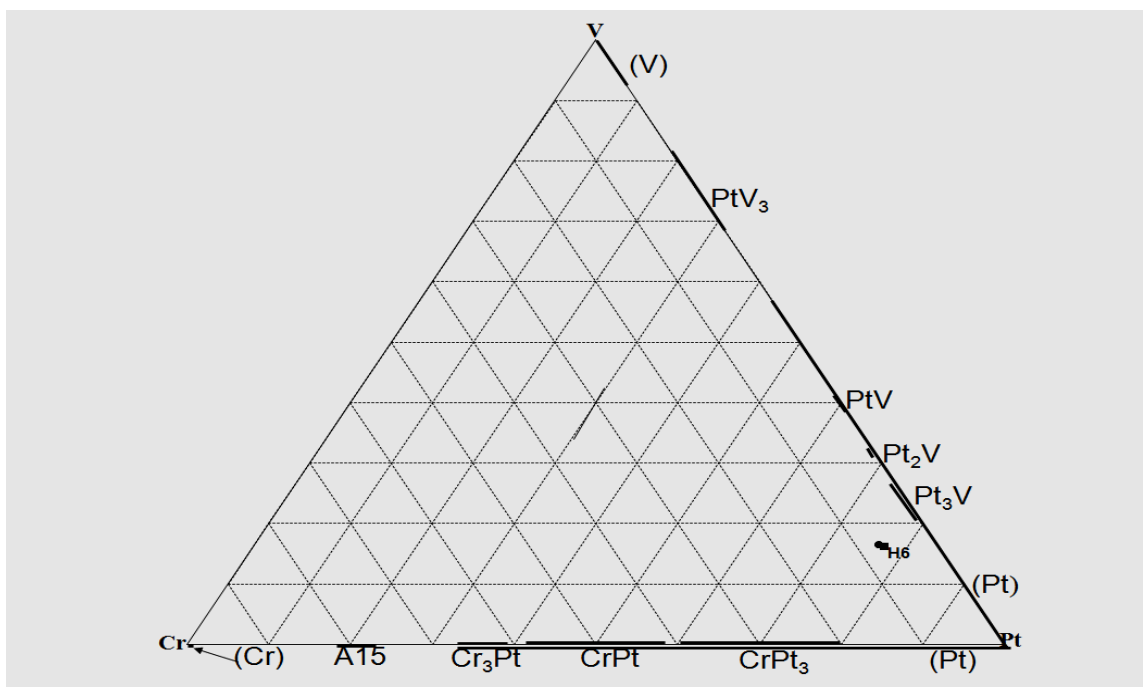


Figure 5.46. Plot of annealed Alloy 6H, average composition  $\text{Pt}_{77.3}:\text{Cr}_{6.6}:\text{V}_{16.1}$  (at.%).

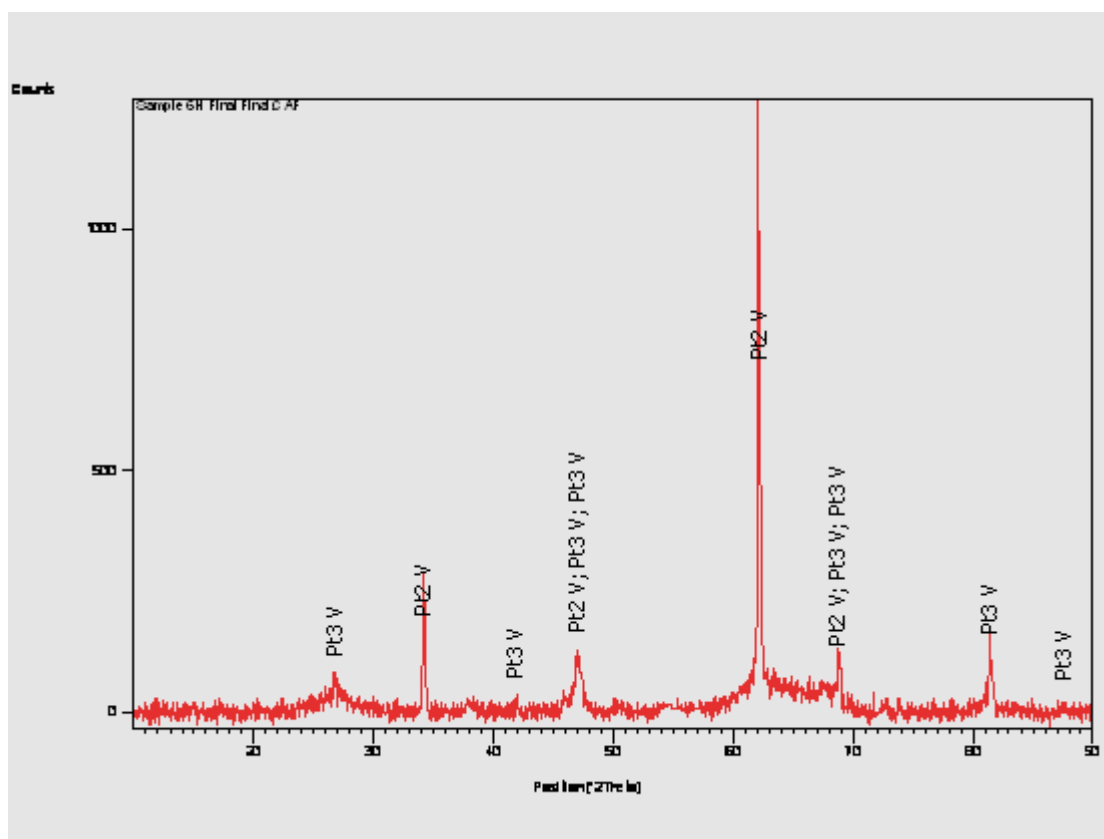
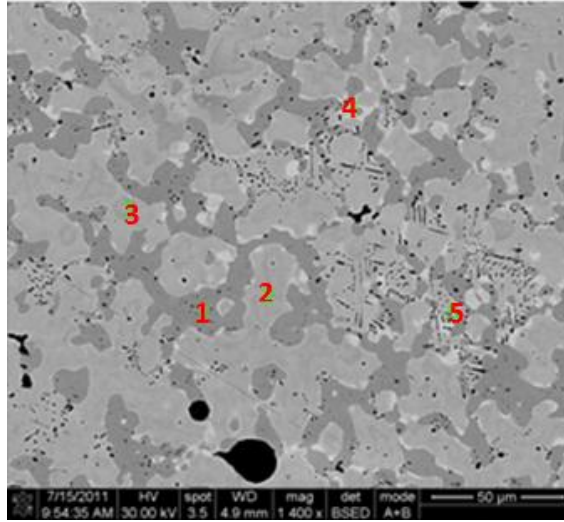


Figure 5.47. XRD pattern of annealed Alloy 6H, average composition  $\text{Pt}_{77.3}:\text{Cr}_{6.6}:\text{V}_{16.1}$  (at.%).

### 5.2.3 Annealed Alloy 7H, Average Composition $\text{Pt}_{35.7}:\text{Cr}_{45.1}:\text{V}_{19.2}$ (at.%)

The SEM-BSE image in Figure 5.48 is that of annealed Alloy 7H, average composition  $\text{Pt}_{35.7}:\text{Cr}_{45.1}:\text{V}_{19.2}$  (at.%), shows dark medium A15( $\sim\text{Cr}_3\text{Pt}$ ) (1), light medium contrast  $\sim\text{CrPt}$  (2), medium  $\sim\text{Cr}_3\text{Pt}$  (3), light contrast (Pt) (4) and a eutectic of the ternary phase,  $\tau + \sim\text{Cr}_3\text{Pt}$  (5). XRD confirmed the identity of the phases as shown in the pattern in Figure 19. XRD detected the presence of (Pt), indicating that quenching prevented transformation from going to completion. The unidentified peaks originated from the ternary phase  $\tau$ . Compared to the as-cast structure, the alloy had coarsened, and a new phase,  $\sim\text{CrPt}$ , had appeared.



**Figure 5.48.** SEM-BSE image of annealed Alloy 7H, average composition  $\text{Pt}_{35.7}:\text{Cr}_{45.1}:\text{V}_{19.2}$  (at.%), showing darker medium contrast A15( $\sim\text{Cr}_3\text{Pt}$ ) (1), light medium contrast  $\sim\text{CrPt}$  (2), medium contrast  $\sim\text{Cr}_3\text{Pt}$  (3), light contrast (Pt) (4) and a eutectic of  $\tau + \sim\text{Cr}_3\text{Pt}$  (5).

**Table 5.16. EDX composition analysis for annealed Alloy 7H, average composition  $\text{Pt}_{35.7}:\text{Cr}_{45.1}:\text{V}_{19.2}$  (at.%).**

Appearance	Pt	Cr	V	Phase
Overall	$35.7 \pm 0.4$	$45.1 \pm 0.6$	$19.2 \pm 0.4$	-
Dark medium (1)	$33.2 \pm 0.8$	$50.4 \pm 0.8$	$16.4 \pm 0.6$	A15 ( $\sim\text{Cr}_3\text{Pt}$ )
Light medium (2)	$42.6 \pm 2.2$	$39.2 \pm 1.8$	$18.2 \pm 1.7$	$\sim\text{CrPt}$
Medium (3)	$38.9 \pm 0.4$	$37.0 \pm 0.6$	$24.1 \pm 1.1$	$\sim\text{CrPt}$
Light (4)	$48.6 \pm 0.4$	$35.2 \pm 0.5$	$16.2 \pm 0.3$	$\sim\text{CrPt}_3$
Eutectic (5)	$40.3 \pm 1.3$	$39.6 \pm 1.5$	$20.1 \pm 0.3$	$\tau + \sim\text{CrPt}_3$

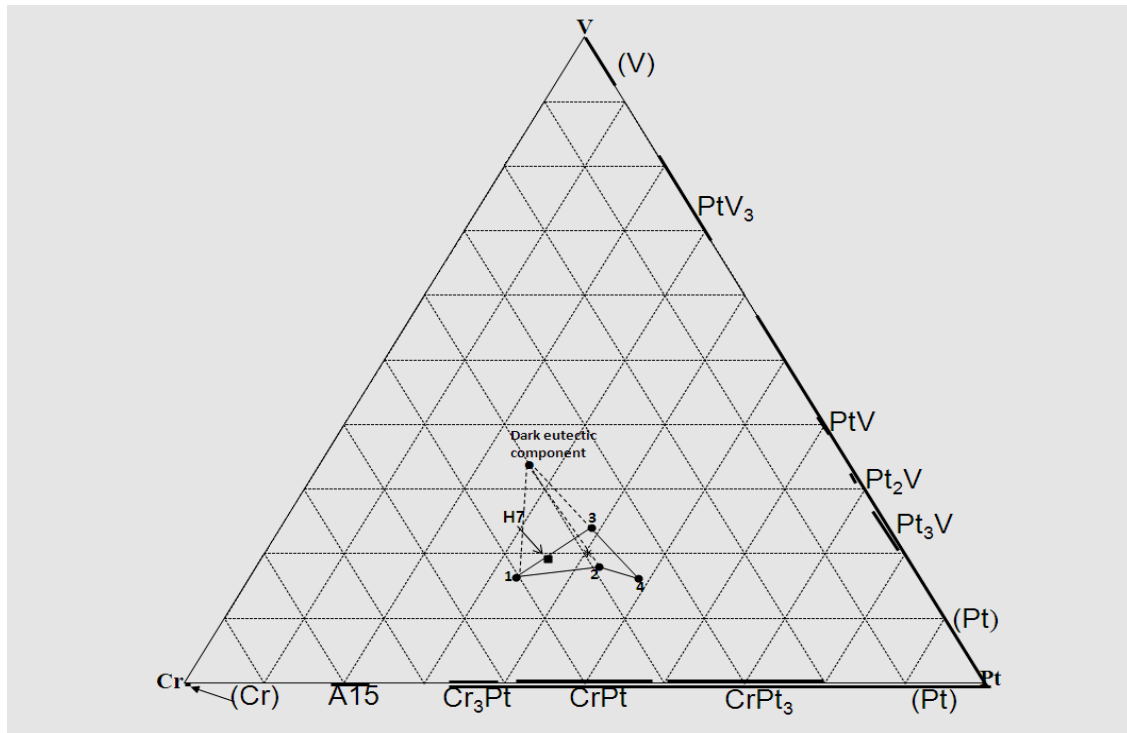


**Figure 5.49. Plot of annealed Alloy 7H, average composition  $\text{Pt}_{35.7}:\text{Cr}_{45.1}:\text{V}_{19.2}$  (at.%).**

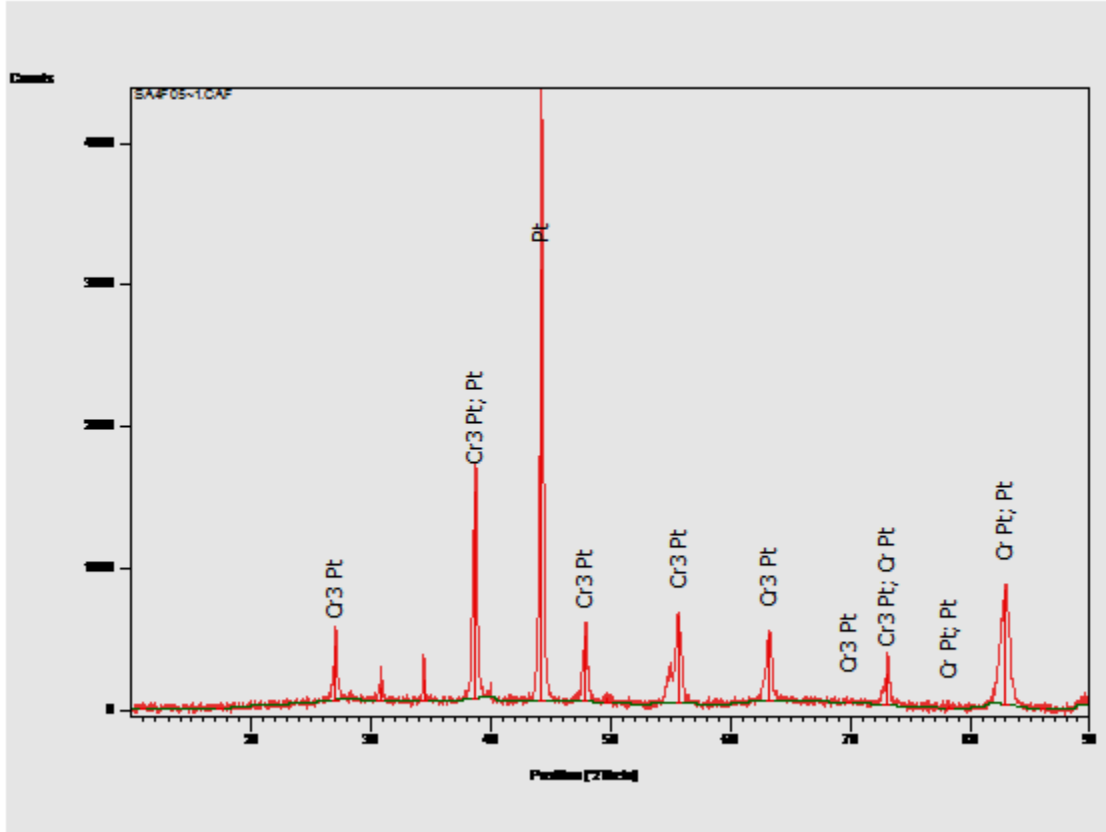


**Figure 5.50. XRD pattern of annealed Alloy 7H, average composition  $\text{Pt}_{35.7}:\text{Cr}_{45.1}:\text{V}_{19.2}$  (at.%), with unidentified peaks from  $\tau$ .**

#### **5.2.4 Annealed Alloy 8H, Average Composition $\text{Pt}_{52.3}:\text{Cr}_{23.4}:\text{V}_{24.3}$ (at.%)**

Figure 5.51 is a SEM-BSE image of annealed Alloy 8H, average composition  $\text{Pt}_{52.3}:\text{Cr}_{23.4}:\text{V}_{24.3}$  (at.%), showing medium contrast  $\sim\text{Cr}_3\text{Pt}$ , a eutectic of  $\sim\text{Cr}_3\text{Pt} +$  the ternary phase,  $\tau$  and dark porosity. Table 5.17 has the data for EDX composition analysis, which are plotted in Figure 5.52. The identity of the dark component in the eutectic was determined as  $\tau$  by extrapolation. XRD confirmed the phase identification, as can be seen in the pattern in Figure 5.53. The unidentified peaks originated from the ternary phase  $\tau$ . After, annealing the structure coarsened and there was more apparently more porosity (although a slightly different section had been analysed). Most of the dark component of the eutectic fell out during preparation, indicating that it was brittle.

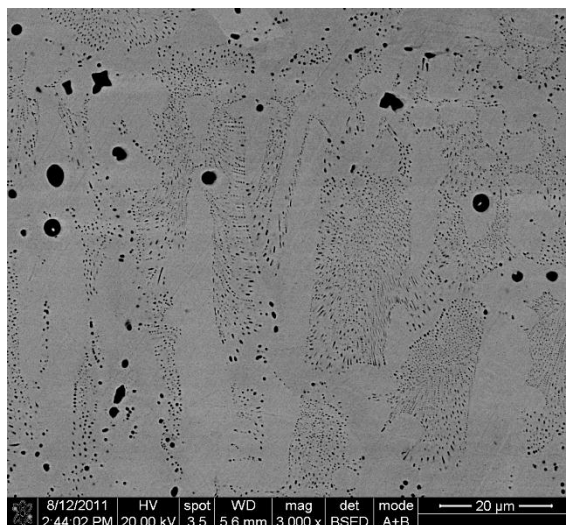


**Figure 5.51. SEM-BSE image of annealed Alloy 8H, average composition  $\text{Pt}_{52.3}:\text{Cr}_{23.4}:\text{V}_{24.3}$  (at.%), showing medium contrast  $\sim\text{Cr}_3\text{Pt}$ , a eutectic of  $\sim\text{Cr}_3\text{Pt} + \tau$  and dark porosity.**

**Table 5.17. EDX composition analysis data for annealed Alloy 8H, average composition  $\text{Pt}_{52.3}:\text{Cr}_{23.4}:\text{V}_{24.3}$  (at.%).**

Appearance	Pt	Cr	V	Phase
Overall	$52.3 \pm 1.2$	$23.4 \pm 0.7$	$24.3 \pm 0.6$	-
Medium	$53.7 \pm 0.7$	$23.0 \pm 1.1$	$23.3 \pm 0.6$	$\sim\text{Cr}_3\text{Pt}$
Eutectic	$52.0 \pm 0.4$	$23.2 \pm 0.4$	$24.8 \pm 0.3$	$\tau + \sim\text{Cr}_3\text{Pt}$



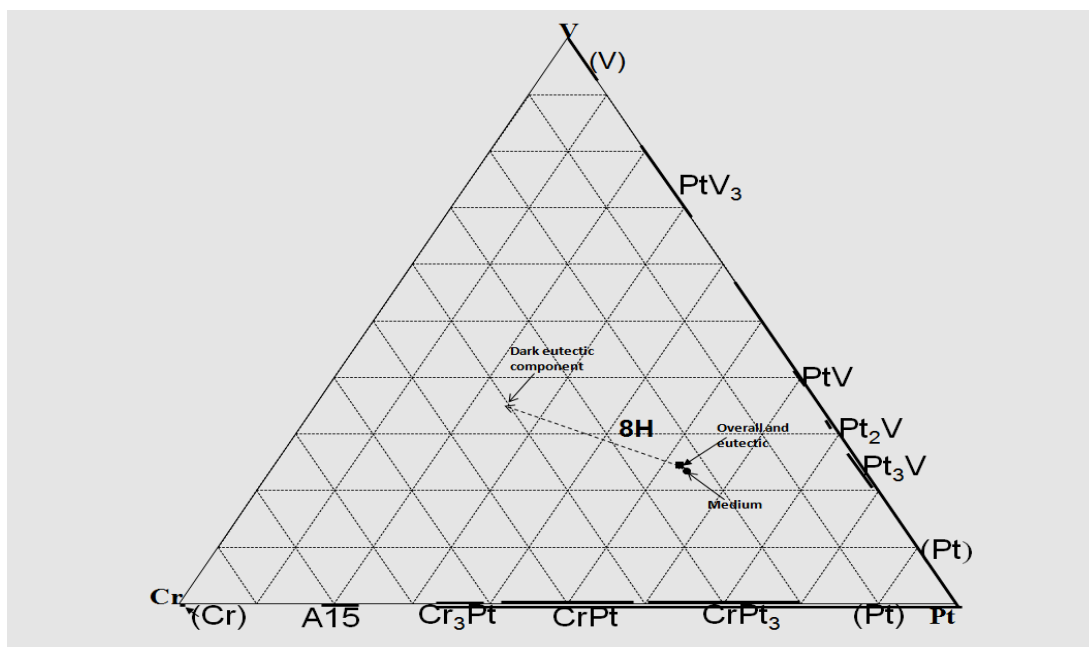


Figure 5.52. Plot of annealed Alloy 8H, average composition  $\text{Pt}_{52.3}:\text{Cr}_{23.4}:\text{V}_{24.3}$  (at.%).

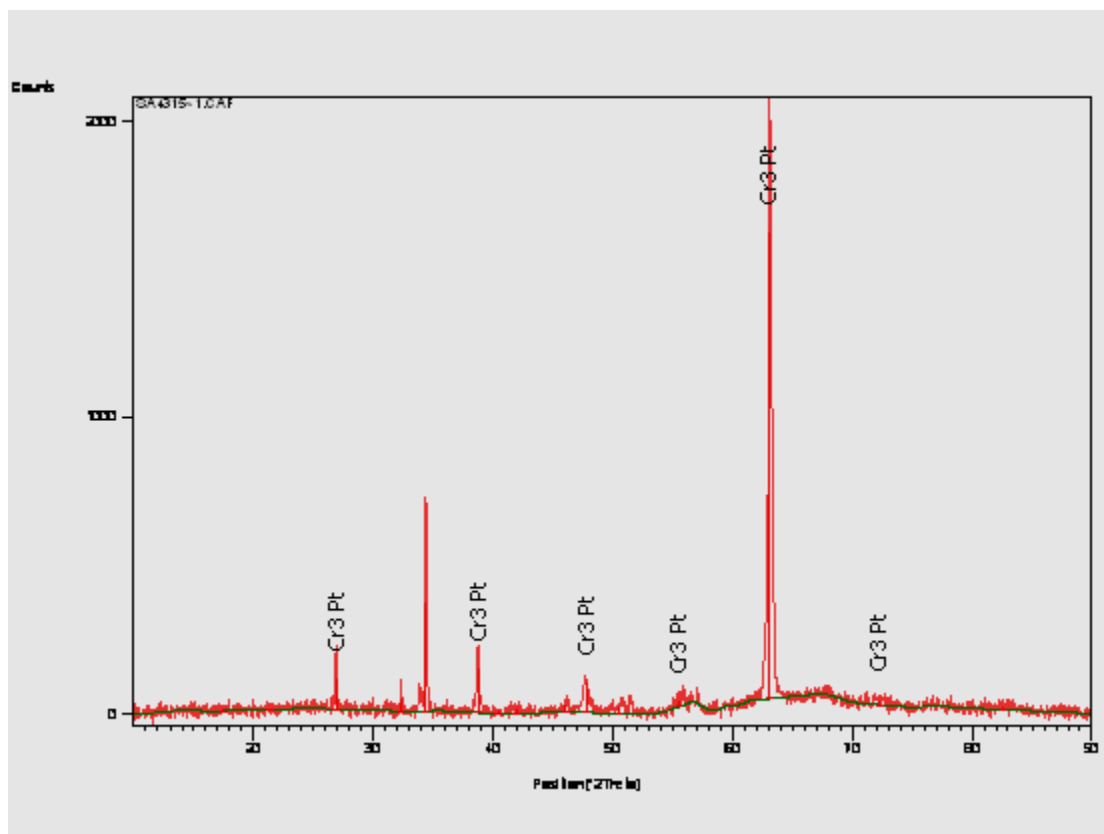
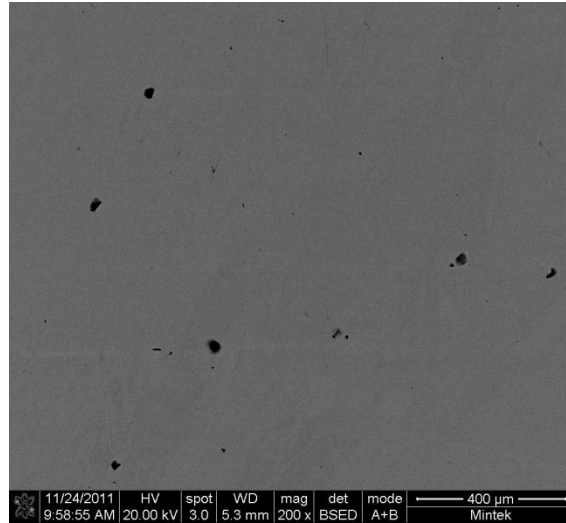


Figure 5.53. XRD pattern of annealed Alloy 8H, average composition  $\text{Pt}_{52.3}:\text{Cr}_{23.4}:\text{V}_{24.3}$  (at.%), with unidentified peaks from  $\tau$ .

### 5.2.5 Annealed Alloy 17H, Average Composition $\text{Pt}_{70.2}:\text{Cr}_{15.4}:\text{V}_{14.4}$ (at.%)

The SEM-BSE image of Alloy 17H, average composition  $\text{Pt}_{70.2}:\text{Cr}_{15.4}:\text{V}_{14.4}$  (at.%), in Figure 5.54 shows single phase  $\sim\text{Pt}_3\text{V}$  and dark porosity. Table 5.18 has the EDX composition analysis data, which are plotted in Figure 5.55. XRD confirmed the phase identification (Figure 5.56).



**Figure 5.54. SEM-BSE image of annealed Alloy 17H, average composition  $\text{Pt}_{70.2}:\text{Cr}_{15.4}:\text{V}_{14.4}$  (at.%), showing single phase  $\sim\text{Pt}_3\text{V}$  and dark porosity.**

**Table 5.18. EDX composition analysis data for annealed Alloy 17H, average composition  $\text{Pt}_{70.2}:\text{Cr}_{15.4}:\text{V}_{14.4}$  (at.%).**

	Pt	Cr	V	Phase
Overall	$70.2\pm0.6$	$15.4\pm0.8$	$14.4\pm0.7$	$\sim\text{Pt}_3\text{V}$

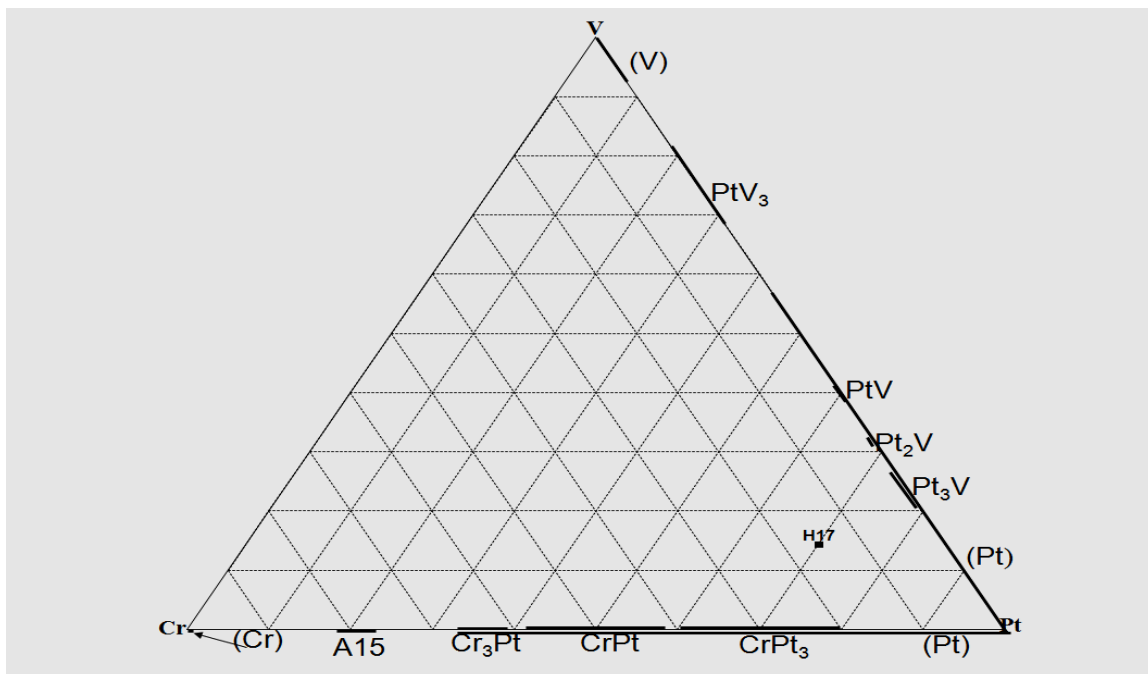


Figure 5.55. Plot of annealed Alloy 17H, average composition  $Pt_{70.2}:Cr_{15.4}:V_{14.4}$  (at.%).

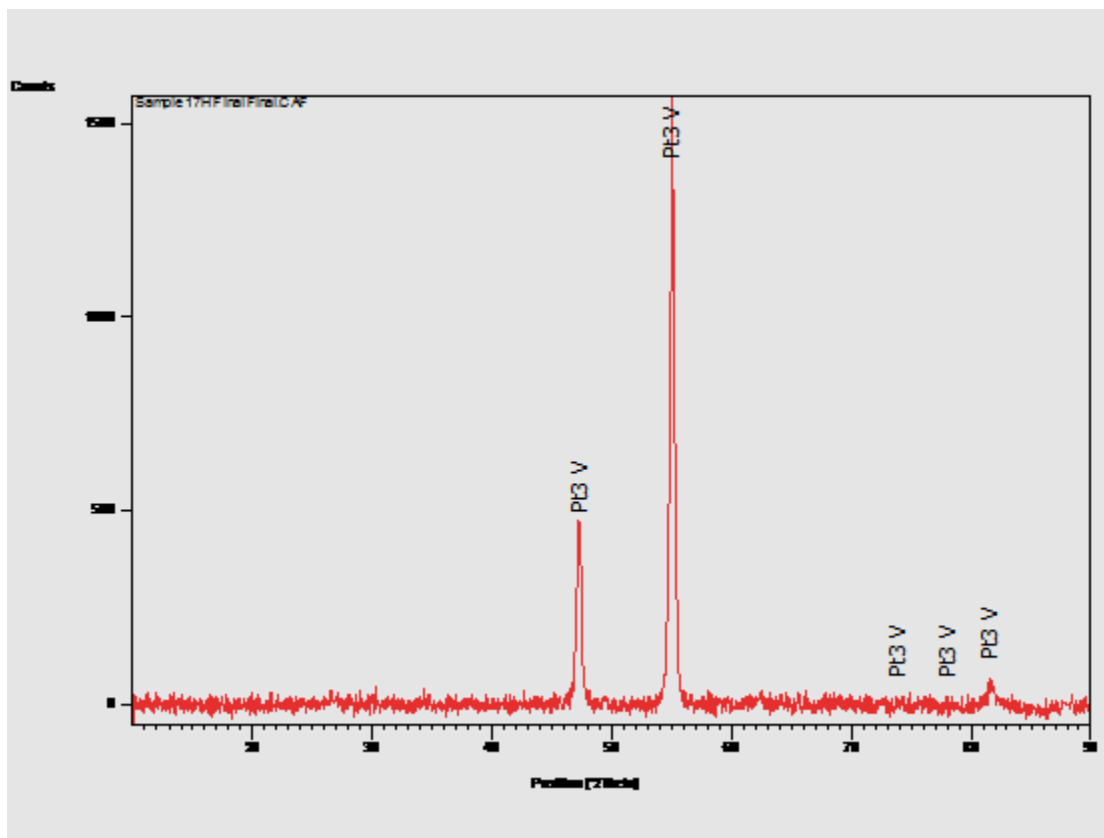
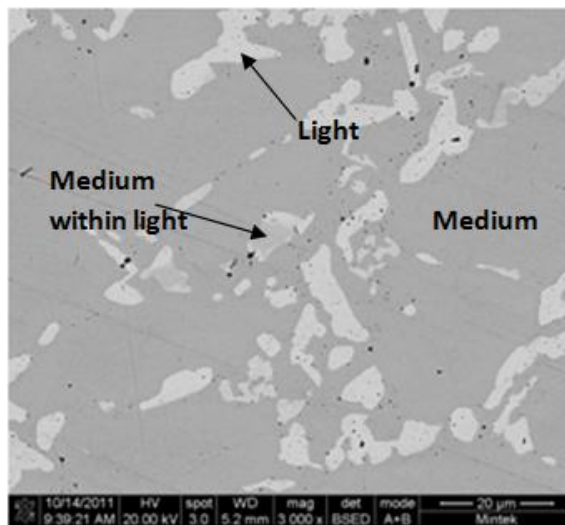


Figure 5.56. XRD pattern of annealed Alloy 17H, average composition  $Pt_{70.2}:Cr_{15.4}:V_{14.4}$  (at.%).

### 5.2.6 Annealed Alloy 18H, Average Composition $\text{Pt}_{34.0}:\text{Cr}_{28.3}:\text{V}_{37.7}$ (at.%)

Figure 5.57 is an SEM-BSE image of annealed Alloy 18H, average composition  $\text{Pt}_{34.0}:\text{Cr}_{28.3}:\text{V}_{37.7}$  (at.%), showing a medium contrast ternary phase, light  $\sim\text{PtV}$ , and a another medium phase  $\sim\text{CrPt}$  within the light  $\sim\text{PtV}$ . The microstructure had coarsened and a new phase  $\sim\text{PtV}$  had formed. The EDX composition analysis data in Table 5.19 are plotted in Figure 5.58. XRD confirmed the phase identification as shown in the pattern in Figure 5.59. The unidentified peaks originated from the ternary phase.



**Figure 5.57.** SEM-BSE image of annealed Alloy 18H, average composition  $\text{Pt}_{34.0}:\text{Cr}_{28.3}:\text{V}_{37.7}$  (at.%), showing a medium ternary phase,  $\tau$ , light  $\sim\text{PtV}$ , and medium  $\sim\text{CrPt}$  within  $\sim\text{PtV}$ .

**Table 5.19.** EDX composition analysis data for annealed Alloy 18H, average composition  $\text{Pt}_{34.0}:\text{Cr}_{28.3}:\text{V}_{37.7}$  (at.%).

Appearance	Pt	Cr	V	Phase
Overall	$34.0 \pm 0.8$	$28.3 \pm 0.4$	$37.7 \pm 0.7$	-
Medium	$30.2 \pm 0.6$	$27.3 \pm 0.5$	$42.5 \pm 0.6$	$\tau$
Light	$51.1 \pm 1.2$	$15.8 \pm 0.6$	$33.1 \pm 0.7$	$\sim\text{PtV}$
Medium in light	$39.3 \pm 1.0$	$28.7 \pm 0.8$	$32.0 \pm 1.2$	$\sim\text{CrPt}$

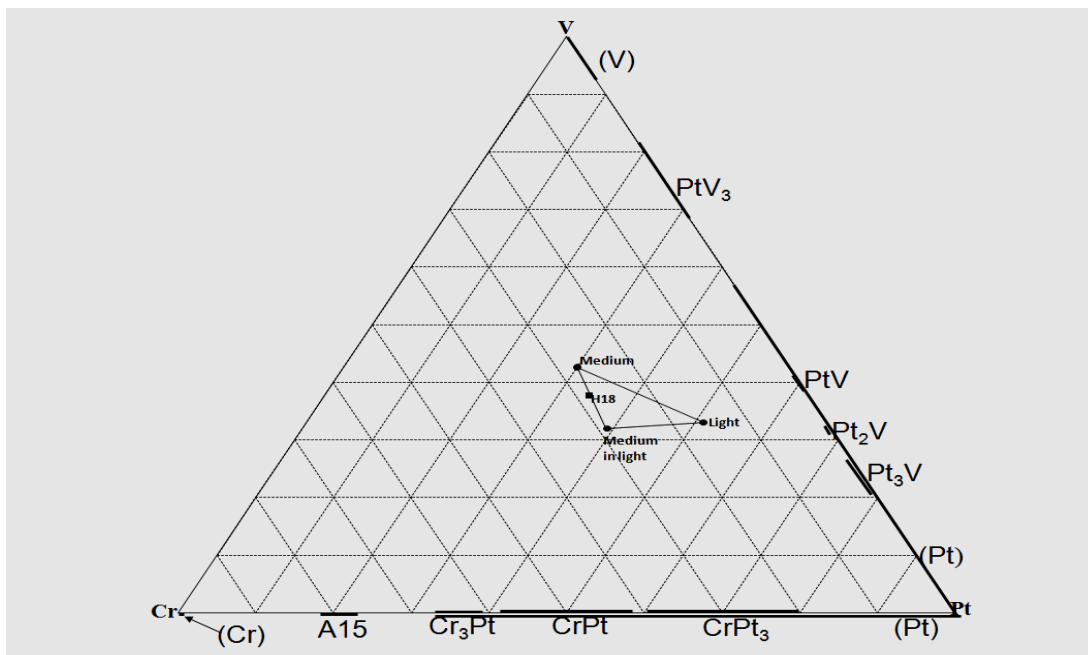


Figure 5.58. Plot of annealed Alloy 18H, average composition  $\text{Pt}_{34.0}:\text{Cr}_{28.3}:\text{V}_{37.7}$  (at.%).

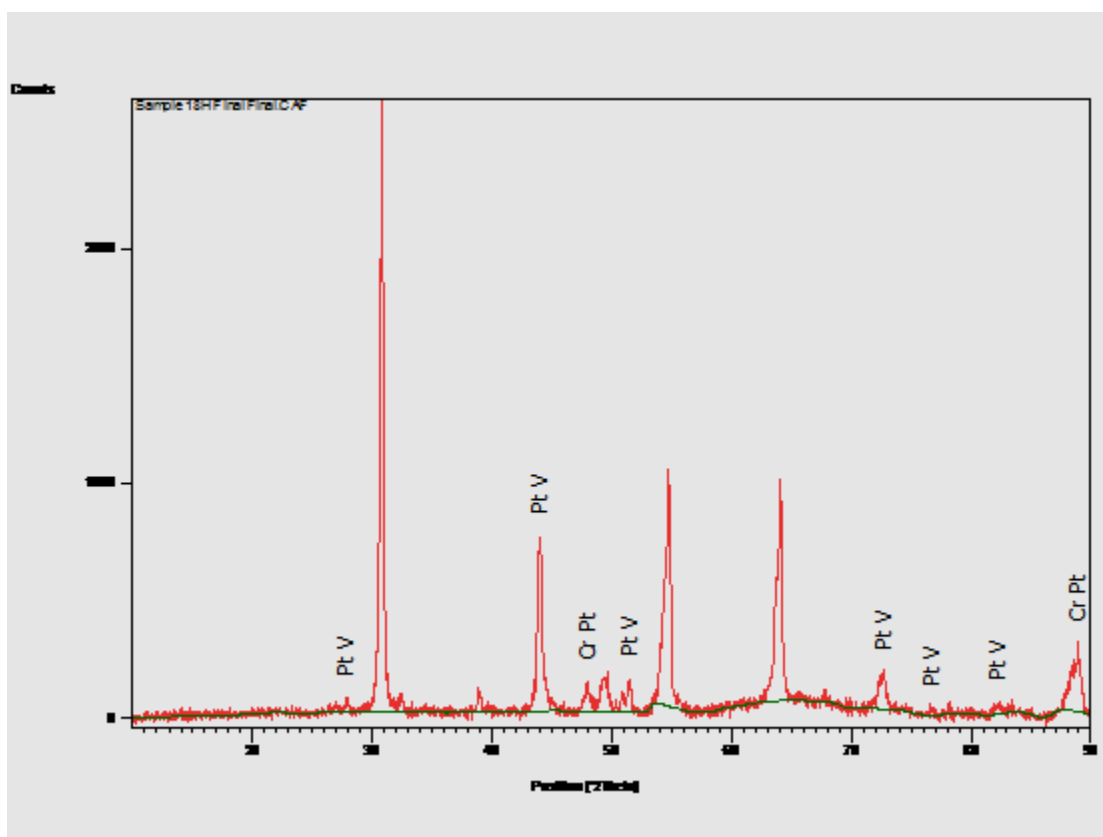
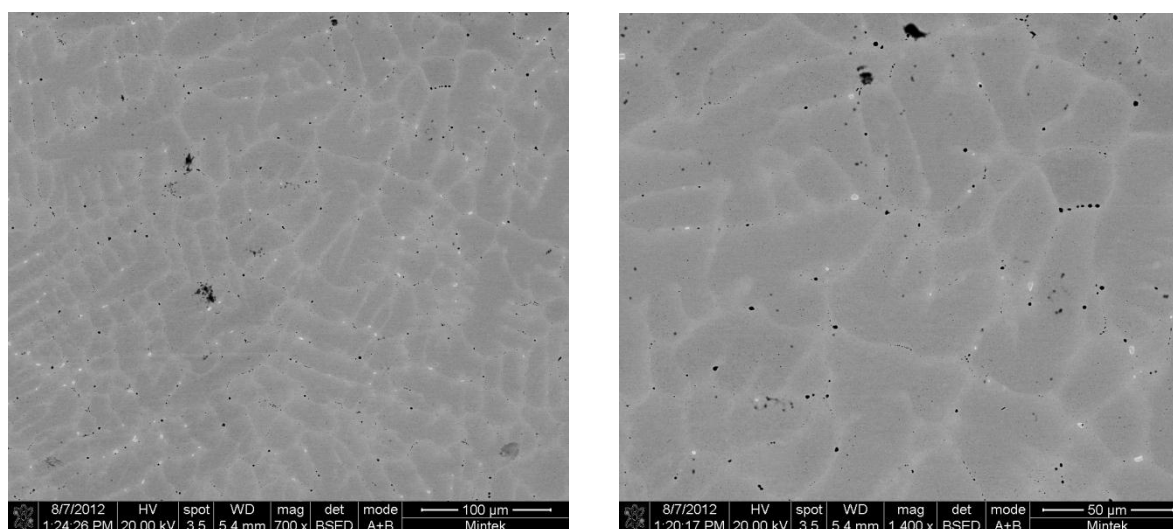


Figure 5.59. XRD pattern of annealed Alloy 18H, average composition  $\text{Pt}_{34.0}:\text{Cr}_{28.3}:\text{V}_{37.7}$  (at.%). The unidentified peaks originated from  $\tau$ .

### 5.2.7 Annealed Alloy 19H, Average Composition $\text{Pt}_{25.1}:\text{Cr}_{43.5}:\text{V}_{31.5}$ (at.%)

The SEM-BSE image of Alloy 19H, average composition  $\text{Pt}_{25.1}:\text{Cr}_{43.5}:\text{V}_{31.5}$  (at.%), in Figure 5.60 shows dark,  $\tau$ , dendrites, light A15( $\sim\text{Cr}_3\text{Pt}$ ) and lightest  $\sim\text{Cr}_3\text{Pt}$ . The structure coarsened on annealing. In the as-cast condition there was the ternary phase,  $\tau$  and a eutectic, while in the annealed condition there is  $\tau$ , and two discrete phases, light A15( $\sim\text{Cr}_3\text{Pt}$ ) and lightest  $\sim\text{Cr}_3\text{Pt}$ . The presence of the ternary phase was deduced from the similarity in structure with the as-cast alloy and also from the position of the plot. The alloy was so brittle that it disintegrated while being removed from the resin mounting before it could be analysed by XRD.



**Figure 5.60(a).** SEM-BSE image of Alloy 19H, average composition  $\text{Pt}_{25.1}:\text{Cr}_{43.5}:\text{V}_{31.5}$  (at.%), showing dark dendrites,  $\tau$ , light A15( $\sim\text{Cr}_3\text{Pt}$ ), and lightest  $\sim\text{Cr}_3\text{Pt}$ . **(b).** SEM-BSE image of Alloy 19H, average composition  $\text{Pt}_{25.1}:\text{Cr}_{43.5}:\text{V}_{31.5}$  (at.%), at a higher magnification showing dark dendrites,  $\tau$ , light A15( $\sim\text{Cr}_3\text{Pt}$ ), and lightest  $\sim\text{Cr}_3\text{Pt}$

**Table 5.20. EDX composition analysis data for Alloy 19H, average composition  $\text{Pt}_{25.1}:\text{Cr}_{43.5}:\text{V}_{31.5}$  (at.%).**

Appearance	Pt	Cr	V	Phase
Overall	25.1 $\pm$ 0.2	43.4 $\pm$ 0.7	31.5 $\pm$ 0.5	-
Dark	24.2 $\pm$ 0.7	41.0 $\pm$ 0.7	34.8 $\pm$ 0.9	$\tau$
Light	27.2 $\pm$ 0.6	47.1 $\pm$ 0.9	25.7 $\pm$ 0.3	A15( $\sim\text{Cr}_3\text{Pt}$ )
Lightest	35.4 $\pm$ 1.1	38.9 $\pm$ 0.9	25.7 $\pm$ 0.2	$\sim\text{Cr}_3\text{Pt}$

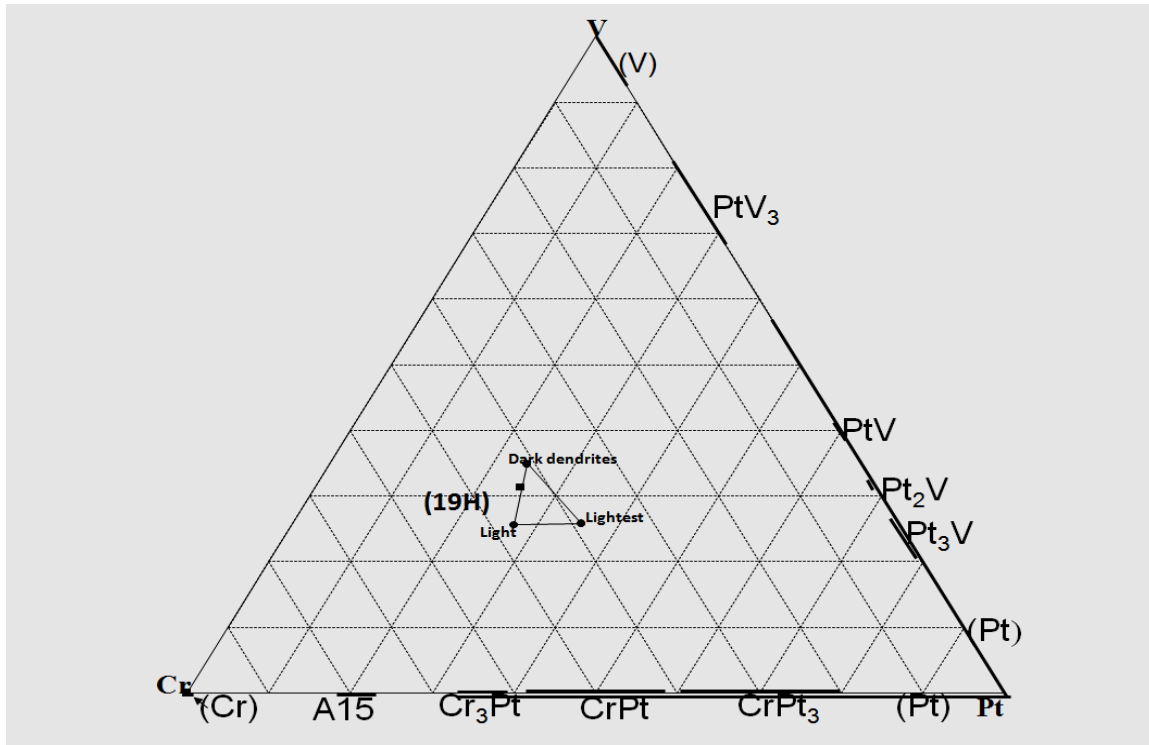


**Figure 5.61. Plot of Alloy annealed 19H, average composition  $\text{Pt}_{25.1}:\text{Cr}_{43.5}:\text{V}_{31.5}$  (at.%).**

### **5.2.8 Annealed Alloy 20H, Average Composition $\text{Pt}_{37.2}:\text{Cr}_{14.6}:\text{V}_{48.2}$ (at.%)**

An SEM-BSE image of annealed Alloy 20H in Figure 5.62, average composition  $\text{Pt}_{37.2}:\text{Cr}_{14.6}:\text{V}_{48.2}$  (at.%), shows medium contrast  $\sim\text{PtV}_3$ , light  $\sim\text{PtV}$  and a eutectic of dark  $\tau_1 + \sim\text{PtV}_3$ . Porosity and oxides, also with dark contrast, can be seen in the figure. The data for EDX composition analysis in Table 5.21 were plotted in Figure 5.63 and used to identify the phases. XRD was used to confirm the identity of the phases and the pattern is shown in Figure 5.64. The  $\sim\text{PtV}$  light phase, which was cored in the as-cast condition, homogenised during heat treatment and consequently its composition shifted substantially towards  $\sim\text{PtV}$ . The composition of the other phases remained similar to what they were in the as-cast condition, although the morphology of the light phase had changed considerably and there was more porosity. The medium phase had also homogenised and its morphology changed as well. There was a phase within the medium phase with a contrast between that of the medium phase and the light phase and is designated the light medium phase. The plot of its composition fell on the straight line joining the light and the medium phase and it was therefore concluded that it is the light phase just underneath the medium phase.

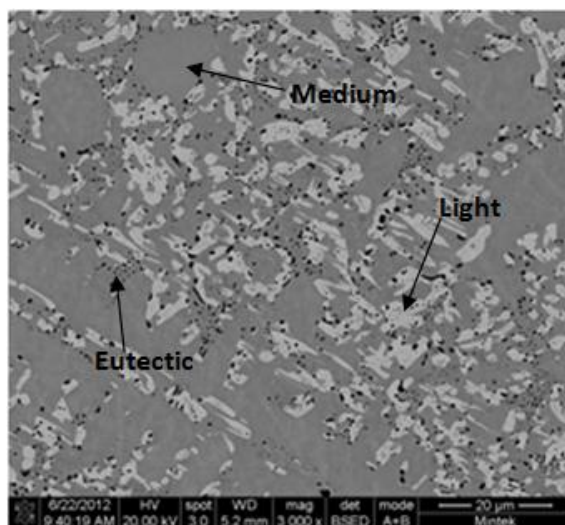


**Figure 5.62. SEM-BSE image of annealed Alloy 20H, average composition  $\text{Pt}_{37.2}\text{:Cr}_{14.6}\text{:V}_{48.2}$  (at.%), showing medium contrast  $\sim\text{PtV}_3$ , light PtV and a eutectic of dark  $\tau + \text{PtV}_3$ . Porosity and oxides are also of dark contrast.**

**Table 5.21. EDX composition analysis data for annealed Alloy 20H, average composition  $\text{Pt}_{37.2}\text{:Cr}_{14.6}\text{:V}_{48.2}$  (at.%).**

Appearance	Pt	Cr	V	Phase
Overall	$37.2 \pm 0.6$	$14.6 \pm 0.5$	$48.2 \pm 0.5$	-
Medium	$33.7 \pm 0.6$	$15.2 \pm 1.3$	$51.1 \pm 1.5$	$\sim\text{PtV}_3$
Light	$52.2 \pm 1.0$	$40.9 \pm 1.1$	$6.9 \pm 1.3$	$\sim\text{PtV}$
Light medium	$42.8 \pm 0.6$	$11.5 \pm 0.7$	$45.7 \pm 0.5$	$\sim\text{PtV}$ beneath $\sim\text{PtV}_3$
Eutectic	$33.7 \pm 1.1$	$15.5 \pm 0.6$	$50.8 \pm 1.3$	$\tau + \sim\text{PtV}_3$



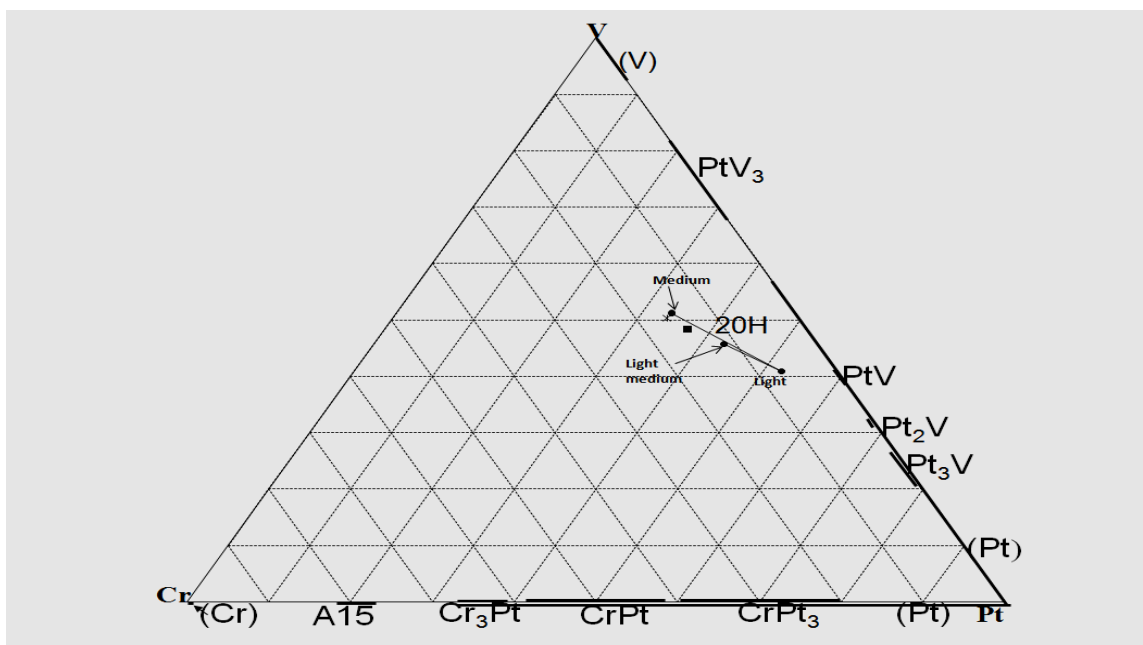


Figure 5.63. Plot of annealed Alloy 20H, average composition  $Pt_{37.2}:Cr_{14.6}:V_{48.2}$  (at.%).

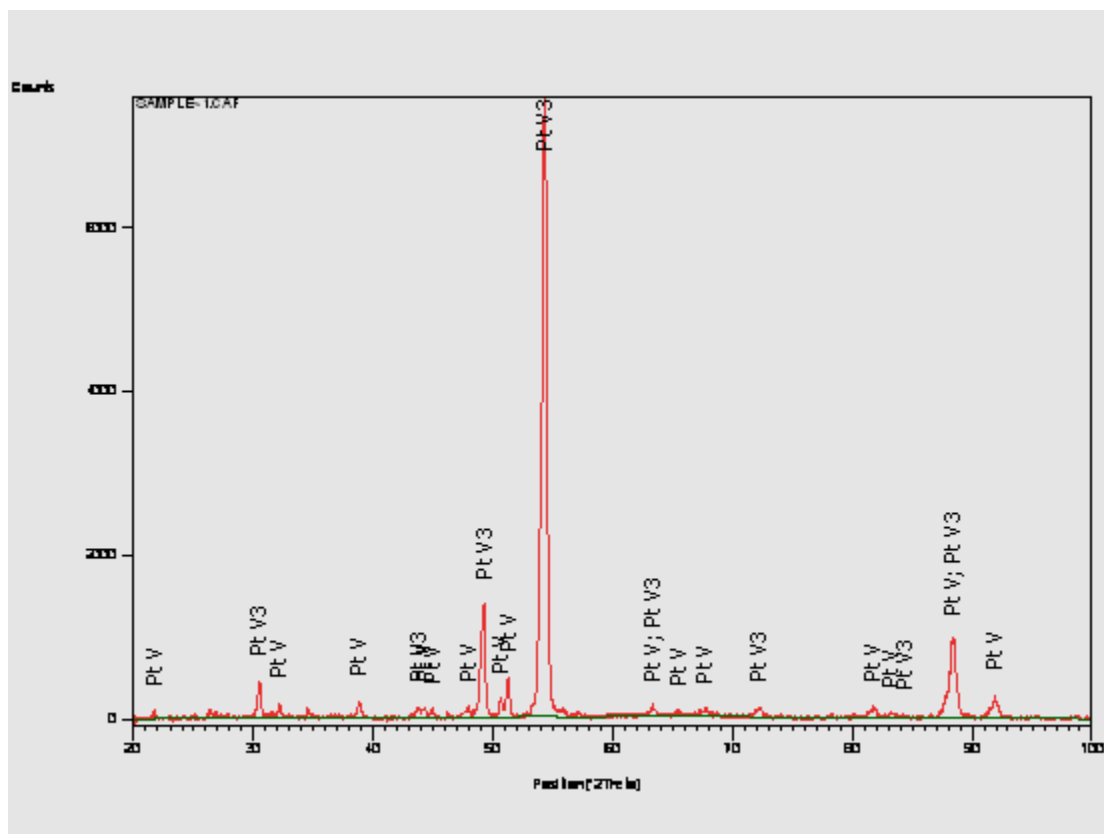
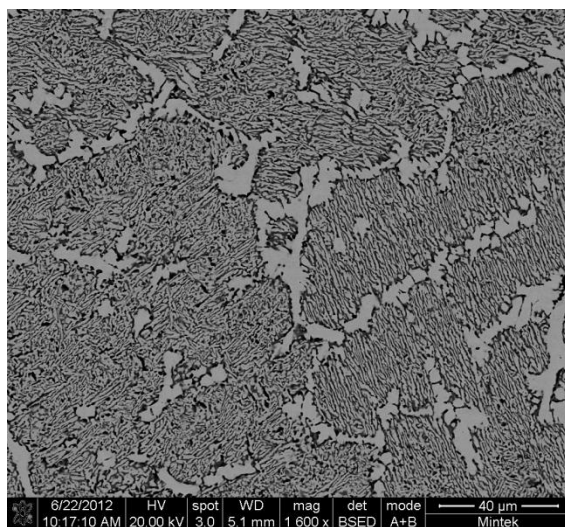


Figure 5.64. XRD pattern of annealed Alloy 20H, average composition  $Pt_{37.2}:Cr_{14.6}:V_{48.2}$  (at.%).

### 5.2.9 Annealed Alloy 21H, Average Composition $\text{Pt}_{16.5}\text{:Cr}_{13.2}\text{:V}_{70.3}$ (at.%)

Figure 5.65 is a SEM-BSE image of annealed Alloy 21H, average composition  $\text{Pt}_{16.5}\text{:Cr}_{13.2}\text{:V}_{70.3}$  (at.%), showing light  $\sim\text{PtV}_3$  and light  $\sim\text{PtV}_3$  solid state precipitates in the medium solid solution (V,Cr), which were the dendrites. The composition of the two-phase region (solid state precipitates and the solid solution) was taken as an area. The eutectic had rounded and coarsened and the dendrites had much precipitation indicating a steep (V,Cr) solvus. The data for the EDX composition analysis in Table 5.22 were plotted in Figure 5.66. The alloy became very brittle after heat treatment; it broke into small pieces during removal from the resin mounting. Consequently, XRD was not done.



**Figure 5.65. SEM-BSE image of annealed Alloy 21H, average composition  $\text{Pt}_{16.5}\text{:Cr}_{13.2}\text{:V}_{70.3}$  (at.%), showing light  $\sim\text{PtV}_3$  and light  $\sim\text{PtV}_3$  solid state precipitates from medium contrast solid solution dendrites (V, Cr).**

**Table 5. 22. EDX composition analysis data for annealed Alloy 21H, average composition  $\text{Pt}_{16.5}\text{:Cr}_{13.2}\text{:V}_{70.3}$  (at.%).**

Appearance	Pt	Cr	V	Phase
Overall	16.5±0.5	13.2±0.5	70.3±0.8	-
Light	24.1±0.8	10.6±0.4	65.3±0.9	$\sim\text{PtV}_3$
Dendrites + Solid state pptn. area	15.6±0.3	13.8±0.3	70.6±0.2	(V,Cr) + $\sim\text{PtV}_3$

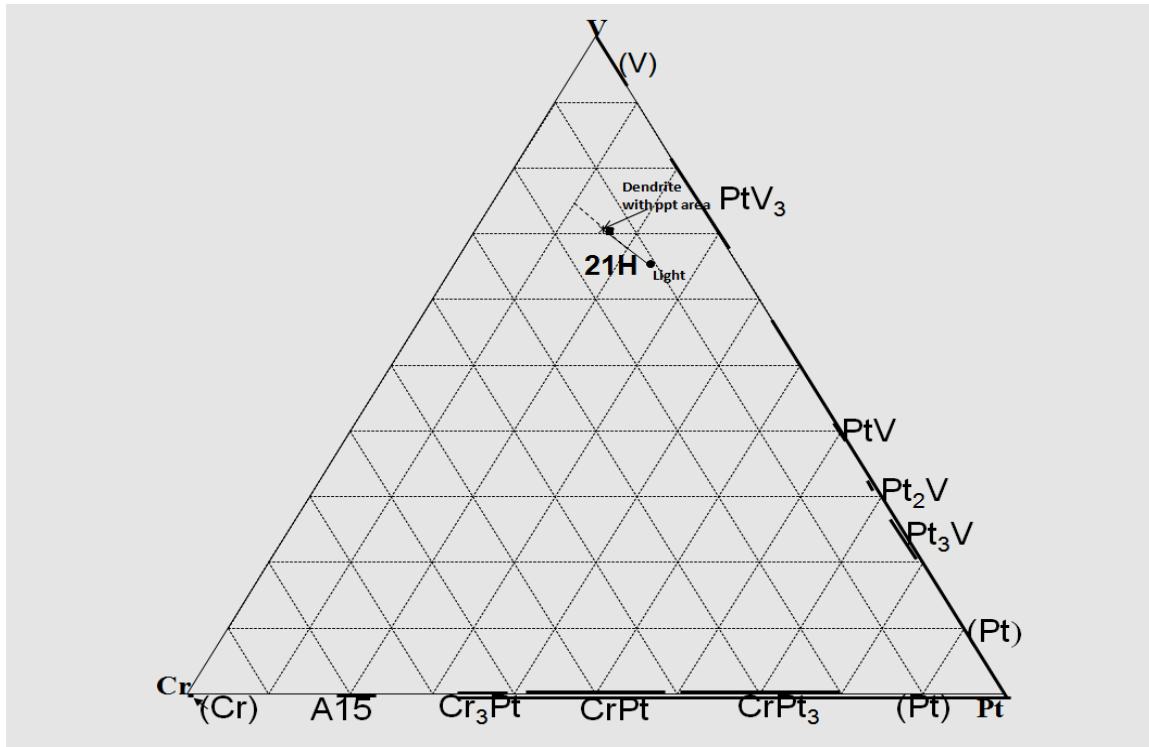


**Figure 5.66.**Plot of annealed Alloy 21H, average composition  $\text{Pt}_{16.5}:\text{Cr}_{13.2}:\text{V}_{70.3}$  (at.%).

#### **5.2.10 Annealed Alloy 22H, Average Composition $\text{Pt}_{27.1}:\text{Cr}_{26.8}:\text{V}_{46.1}$ (at.%)**

An SEM-BSE image of annealed Alloy 22H, average composition  $\text{Pt}_{27.1}:\text{Cr}_{26.8}:\text{V}_{46.1}$  (at.%), in Figure 5.67 shows medium contrast dendrites ( $\tau$ ) having fine solid state precipitates of  $\sim\text{PtV}_3$ , medium phase ( $\sim\text{PtV}_3$ ), a coarsened eutectic of  $\tau + \sim\text{PtV}_3$ , dark oxides and porosity. The EDX composition analyses in Table 5.23 are plotted in Figure 5.68 and used to identify the phases. The alloy was very brittle after heat treatment and broke into small pieces during removal from resin mounting. The brittleness was due to the ternary phase,  $\tau$ . Consequently, XRD was not done. Compared to the as-cast sample, the  $\sim\text{Cr}_3\text{Pt}$  had disappeared, and there was  $\sim\text{PtV}_3$  precipitation in  $\tau$ , indicating a  $\tau$  sloping solvus. Part of the eutectic had also fallen out, probably due to brittleness as a result of oxidation.

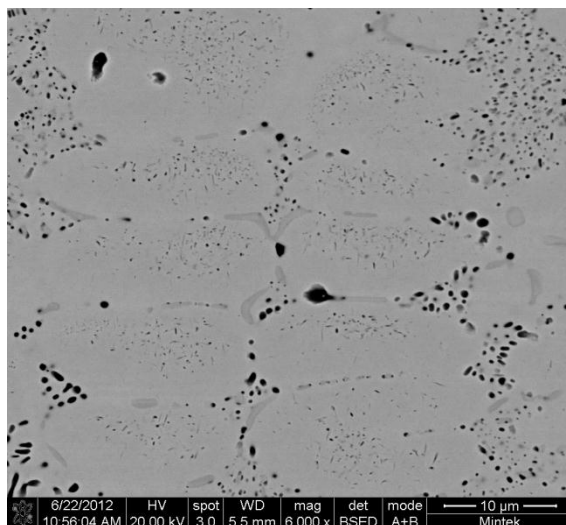


**Figure 5.67. SEM-BSE image of annealed Alloy 22H, average composition  $\text{Pt}_{27.1}:\text{Cr}_{26.8}:\text{V}_{46.1}$  (at.%), showing medium contrast dendrites ( $\tau$ ) with fine dark solid state precipitates (Cr), a medium phase ( $\sim\text{PtV}_3$ ), a eutectic of  $\tau + (\text{Cr})$  and dark porosity.**

**Table 5.23. EDX composition analysis data of annealed Alloy 22H, average composition  $\text{Pt}_{27.1}:\text{Cr}_{26.8}:\text{V}_{46.1}$  (at.%).**

Appearance	Pt	Cr	V	Phase
Overall	27.1±0.3	26.8±0.4	46.1±0.5	-
Dendrite area (with pptn.)	26.2±0.7	25.8±0.4	48.0±0.8	$\tau$ with $\sim\text{PtV}_3$ pptn.
Medium	27.8±0.7	12.9±1.7	59.3±1.1	$\sim\text{PtV}_3$
Eutectic	25.5±1.0	27.2±1.1	47.3±1.6	$\tau + (\text{V,Cr})$

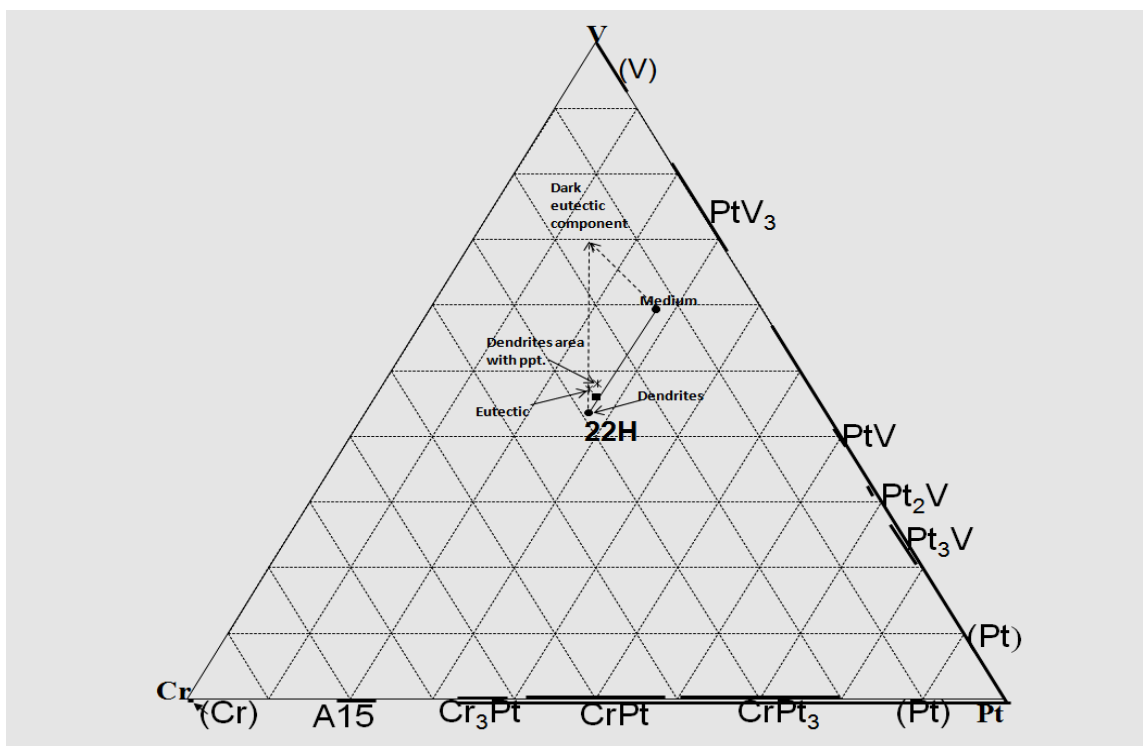


**Figure 5.68. Plot of annealed Alloy 22H, average composition  $\text{Pt}_{27.1}:\text{Cr}_{26.8}:\text{V}_{46.1}$  (at.%).**

### 5.2.11 Annealed Alloy 23H, Average Composition $\text{Pt}_{14.5}:\text{Cr}_{58.1}:\text{V}_{27.4}$ (at.%)

Figure 5.69 is an SEM-BSE image of annealed Alloy 23H, average composition  $\text{Pt}_{14.5}:\text{Cr}_{58.1}:\text{V}_{27.4}$  (at.%), showing (V,Cr) medium dendrites having light A15 ( $\sim\text{Cr}_3\text{Pt}$ ) solid state precipitates, light A15( $\sim\text{Cr}_3\text{Pt}$ ) and a eutectic of A15( $\sim\text{Cr}_3\text{Pt}$ ) + (V,Cr). Table 5.24 has the data for EDX composition analysis, which are plotted in Figure 5.70. The XRD pattern, which did not have many peaks, confirmed the phase identities and the presence of oxides as shown in Figure 5.71.

After annealing, there had been precipitation in the (V,Cr) dendrites, and the A15( $\sim\text{Cr}_3\text{Pt}$ ) had noticeably coarsened. The dark component of the eutectic partly fell out during preparation, probably, due to brittleness as a result of oxidation.

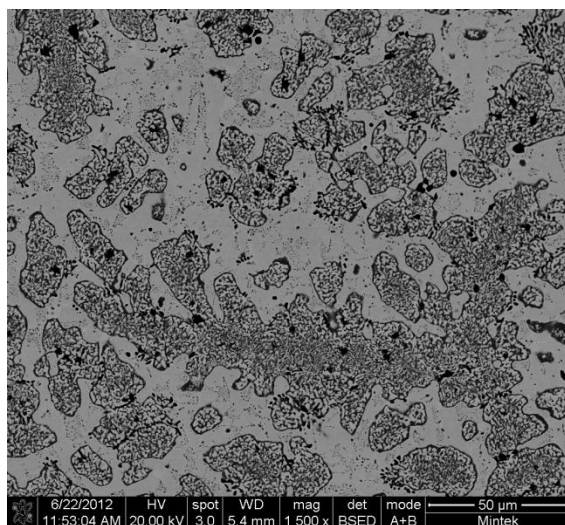


**Figure 5.69. SEM-BSE image of annealed Alloy 23H, average composition  $\text{Pt}_{14.5}\text{:Cr}_{58.1}\text{:V}_{27.4}$  (at.%), showing (Cr) dendrites having light A15 ( $\sim\text{Cr}_3\text{Pt}$ ) solid state precipitates, light A15 ( $\sim\text{Cr}_3\text{Pt}$ ) and a eutectic of A15 ( $\sim\text{Cr}_3\text{Pt}$ ) and (V,Cr).**

**Table 5.24. EDX composition analysis data for annealed Alloy 23H, average composition  $\text{Pt}_{14.5}\text{:Cr}_{58.1}\text{:V}_{27.4}$  (at.%).**

Appearance	Pt	Cr	V	Phase
Overall	14.5±0.7	58.1±0.4	27.4±0.3	-
Dendrite area with ppt.	11.2±1.1	63.0±1.8	25.8±0.8	(V,Cr) + A15( $\sim\text{Cr}_3\text{Pt}$ )
Light	19.5±0.4	50.9±0.3	29.6±0.3	A15( $\sim\text{Cr}_3\text{Pt}$ )
Eutectic	21.2±0.8	50.3±0.5	28.5±1.2	A15( $\sim\text{Cr}_3\text{Pt}$ ) + (V,Cr)

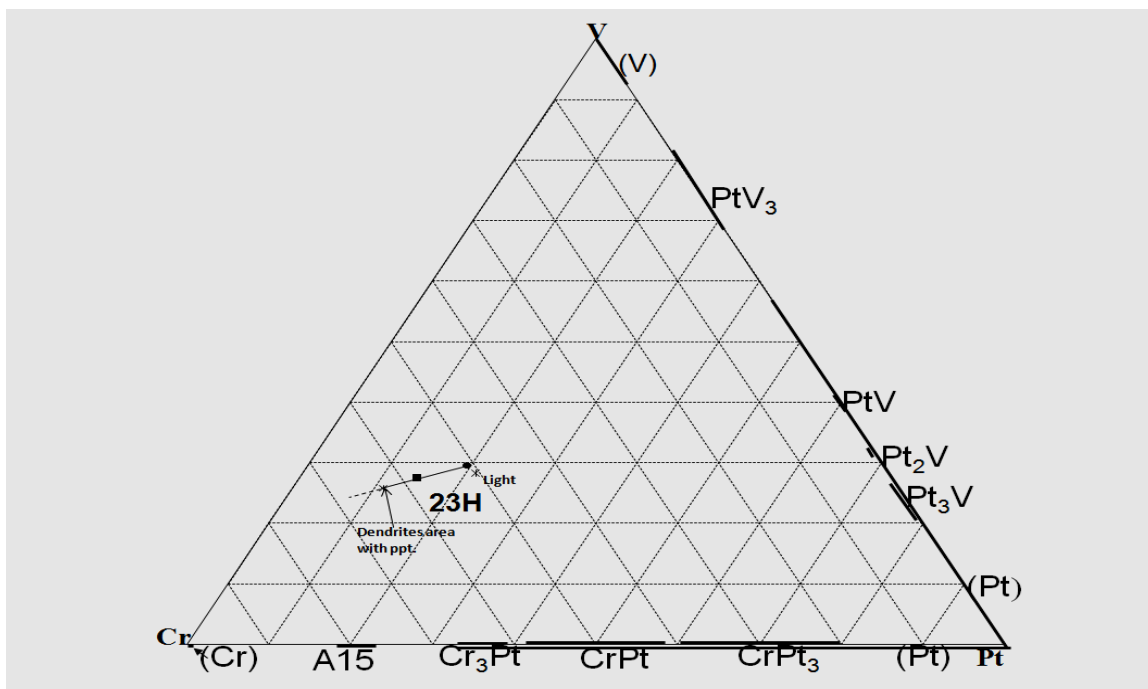


Figure 5.70. Plot of annealed Alloy 23H, average composition  $\text{Pt}_{14.5}\text{Cr}_{58.1}\text{V}_{27.4}$  (at.%).

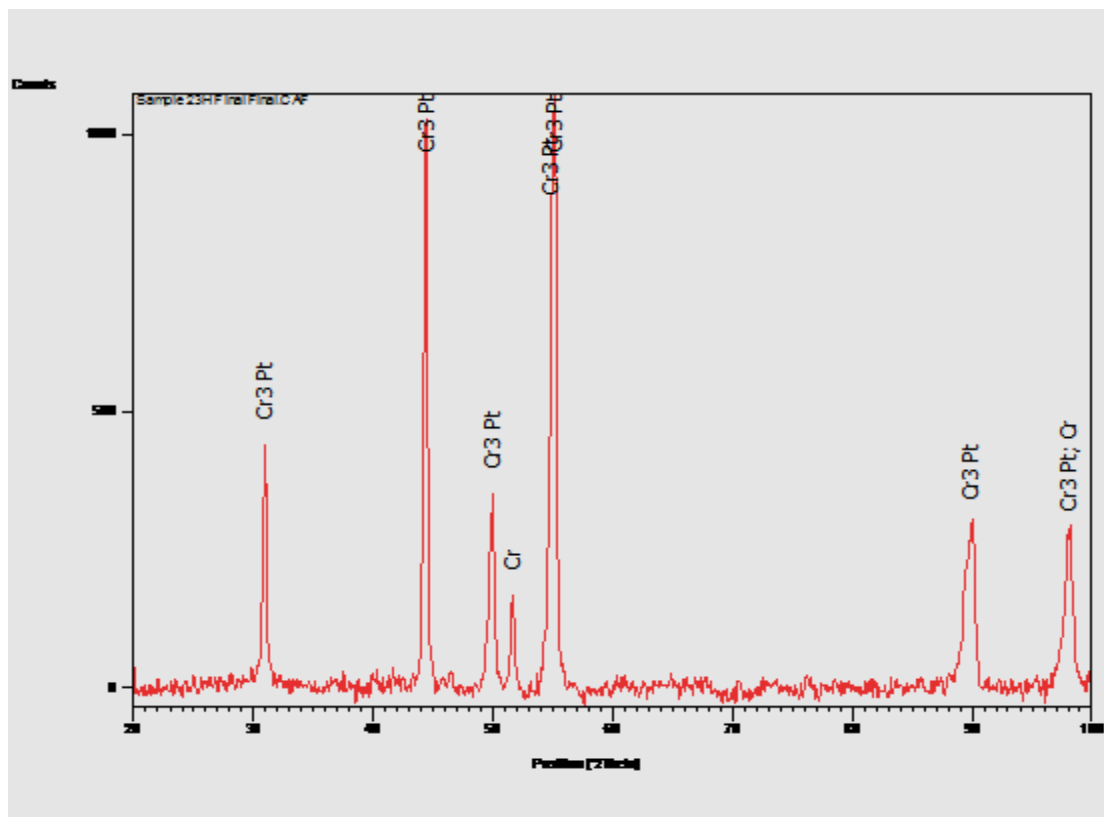
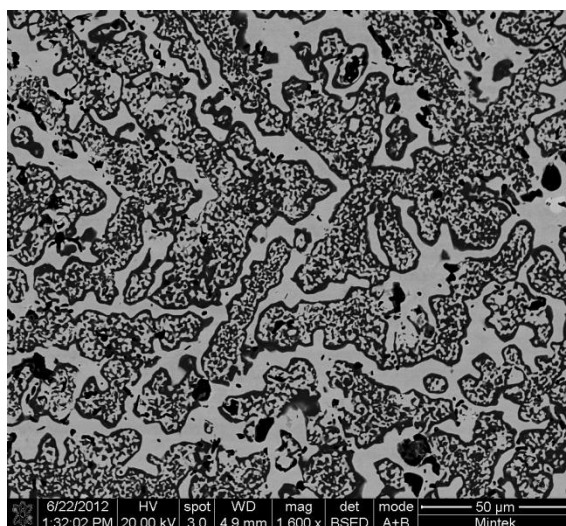


Figure 5.71. XRD pattern of annealed Alloy 23H, average composition  $\text{Pt}_{14.5}\text{Cr}_{58.1}\text{V}_{27.4}$  (at.%).

### 5.2.12 Annealed Alloy 24H, Average Composition $\text{Pt}_{14.2}:\text{Cr}_{75.8}:\text{V}_{10.0}$ (at.%)

The SEM-BSE image of annealed Alloy 24H, average composition  $\text{Pt}_{14.2}:\text{Cr}_{75.8}:\text{V}_{10.0}$  (at.%), in Figure 5.72 shows medium contrast (Cr) dendrites having light A15( $\sim\text{Cr}_3\text{Pt}$ ) solid state precipitates and surrounding light contrast A15( $\sim\text{Cr}_3\text{Pt}$ ). Table 5.26 contains data for EDX composition analysis, which are plotted in Figure 5.73. The plot was used to identify the phases. XRD confirmed the phase identities, as shown in the pattern in Figure 5.74. Compared to the as-cast microstructure, there was a precipitation within the (V,Cr) dendrites and the eutectic had disappeared.  $\sim\text{Cr}_3\text{Pt}$  which had not been in the as-cast sample, formed during annealing.



**Figure 5.72. SEM-BSE image of annealed Alloy 24H, average composition  $\text{Pt}_{14.2}:\text{Cr}_{75.8}:\text{V}_{10.0}$  (at.%), showing medium contrast (Cr) dendrites having light A15 ( $\sim\text{Cr}_3\text{Pt}$ ) solid state precipitates, light contrast A15( $\sim\text{Cr}_3\text{Pt}$ ) and lightest contrast  $\sim\text{Cr}_3\text{Pt}$ .**

**Table 5.25. EDX composition analysis data for annealed Alloy 24H, average composition  $\text{Pt}_{14.2}:\text{Cr}_{75.8}:\text{V}_{10.0}$  (at.%).**

Appearance	Pt	Cr	V	Phase
Overall	14.2±0.4	75.8±0.4	10.0±0.2	-
Dendrite area with ppt.	10.8±1.7	79.8±1.9	9.4±0.3	(V,Cr) + A15( $\sim\text{Cr}_3\text{Pt}$ )
Light	25.6±0.5	63.6±1.3	10.8±1.1	A15( $\sim\text{Cr}_3\text{Pt}$ )
Lightest	36.2±0.6	55.2±1.2	8.6±1.0	$\sim\text{Cr}_3\text{Pt}$



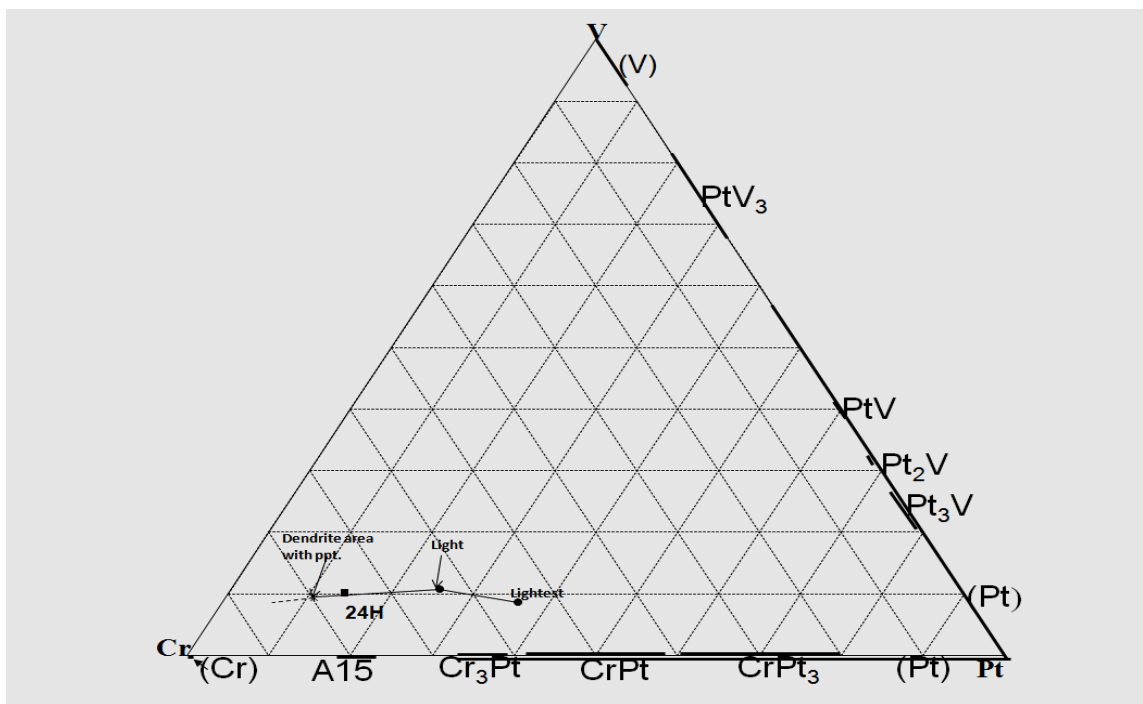


Figure 5.73. Plot of annealed Alloy 24H, average composition  $Pt_{14.2}:Cr_{75.8}:V_{10.0}$  (at.%).

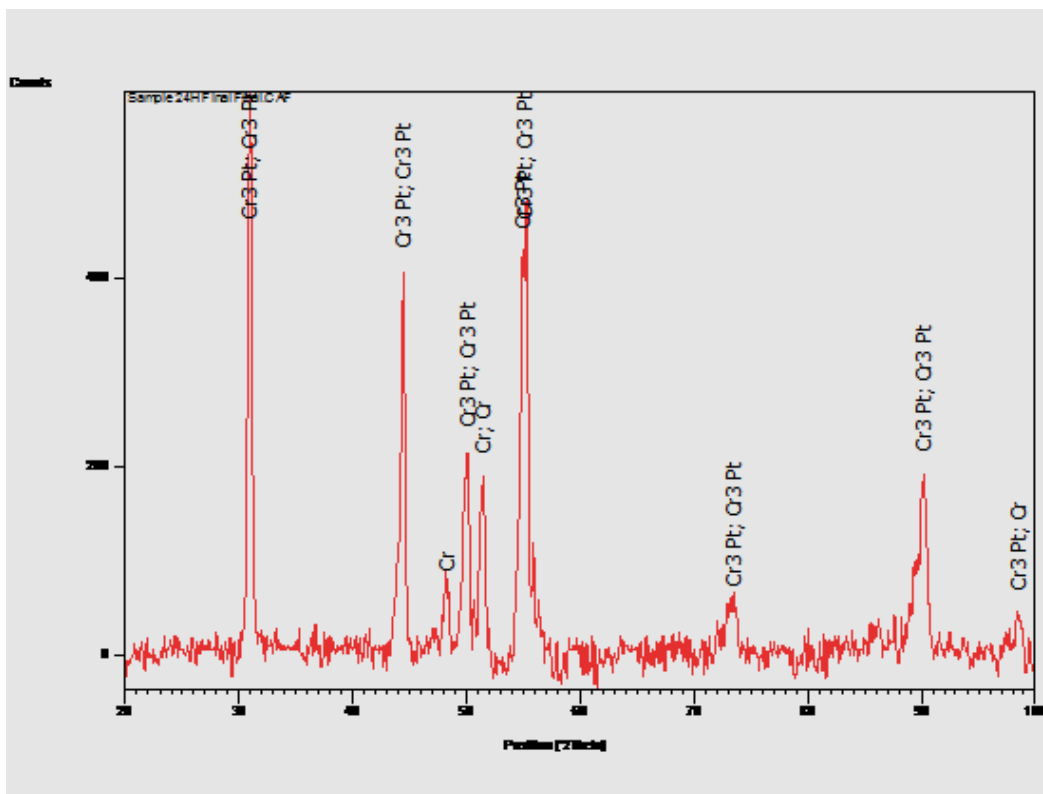
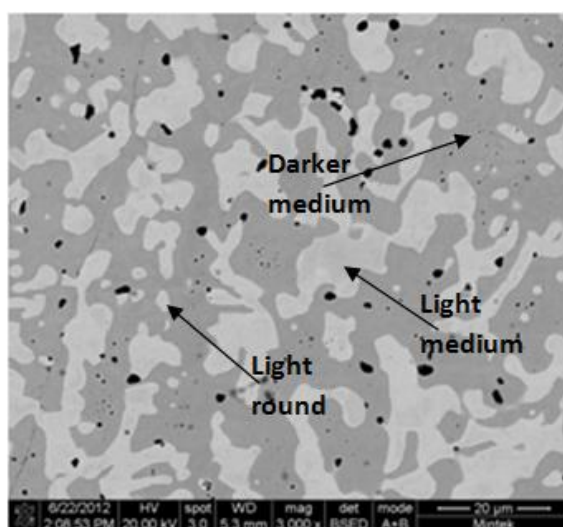


Figure 5.74. XRD pattern of annealed Alloy 24H, average composition  $Pt_{14.2}:Cr_{75.8}:V_{10.0}$  (at.%).

### 5.2.13 Annealed Alloy 25H, Average Composition $\text{Pt}_{33.6}:\text{Cr}_{57.7}:\text{V}_{8.7}$ (at.%)

Figure 5.75 is an SEM-BSE image of annealed Alloy 25H, average composition  $\text{Pt}_{33.6}:\text{Cr}_{57.7}:\text{V}_{8.7}$  (at.%), showing light round CrPt, light medium  $\sim\text{Cr}_3\text{Pt}$ , darker medium A15( $\sim\text{Cr}_3\text{Pt}$ ), dark oxides and porosity. There was evidence of some coring after annealing in the  $\sim\text{Cr}_3\text{Pt}$  dendrites but not as much as it was in the as-cast alloy. The dendritic structure had nearly been lost, and there was much rounded porosity. The eutectic had nearly disappeared. The EDX composition analysis data in Table 5.26, which are plotted in Figure 5.76, were used to identify the phases. XRD confirmed the phase identities as shown in Figure 5.77.



**Figure 5.75. SEM-BSE image of annealed Alloy 25H, average composition  $\text{Pt}_{33.6}:\text{Cr}_{57.7}:\text{V}_{8.7}$  (at.%), showing light  $\sim\text{CrPt}$ , light medium  $\sim\text{Cr}_3\text{Pt}$ , darker medium A15 ( $\sim\text{Cr}_3\text{Pt}$ ), dark oxides and porosity.**

**Table 5.26. EDX composition analysis data for Alloy 25H, average composition  $\text{Pt}_{33.6}:\text{Cr}_{57.7}:\text{V}_{8.7}$  (at.%).**

Appearance	Pt	Cr	V	Phase
Overall	33.6±0.4	57.7±0.3	8.7±0.1	-
Light	44.0±0.6	48.1±0.4	7.9±0.3	$\sim\text{CrPt}$
Light medium	39.7±1.1	52.5±0.9	7.8±0.2	$\sim\text{Cr}_3\text{Pt}$
Dark medium	28.0±0.7	63.0±0.4	9.0±0.4	A15( $\sim\text{Cr}_3\text{Pt}$ )

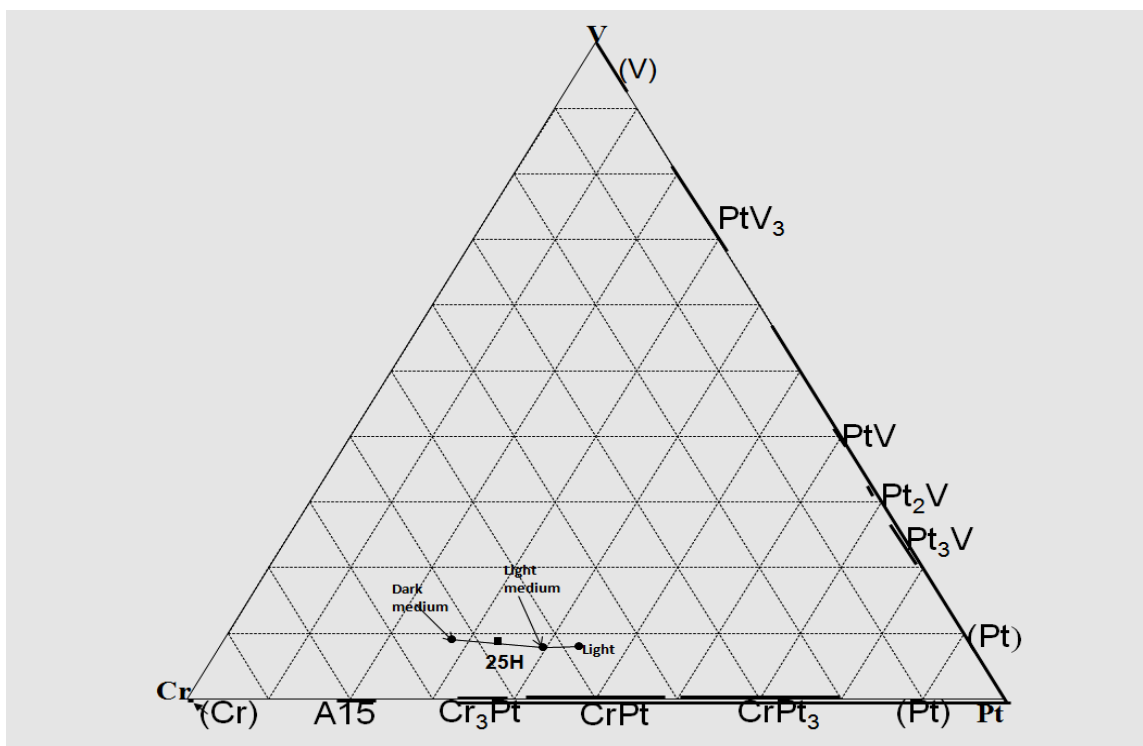


Figure 5.76. Plot of annealed Alloy 25H, average composition  $Pt_{33.6}:Cr_{57.7}:V_{8.7}$  (at.%).

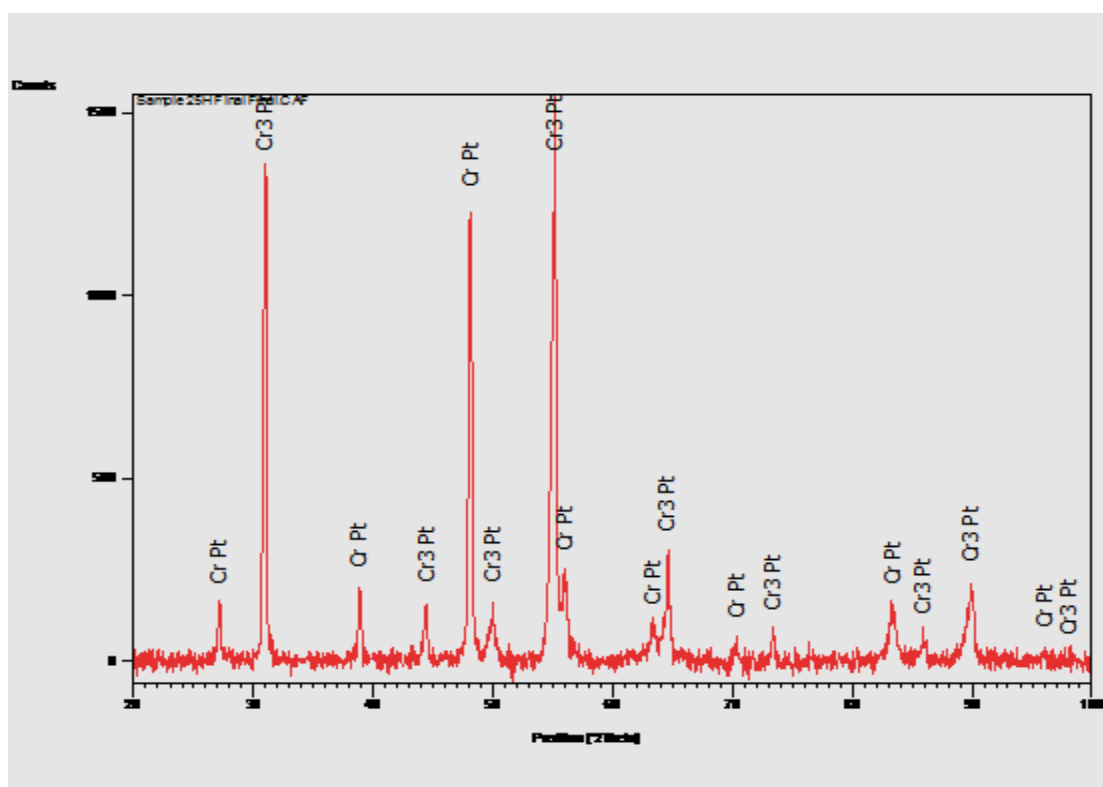


Figure 5.77. XRD pattern of annealed Alloy 25H, average composition  $Pt_{33.6}:Cr_{57.7}:V_{8.7}$  (at.%).

#### 5.2.14 Isothermal Section of the Pt-Cr-V System at 1000°C

The isothermal section for the Pt-Cr-V system at 1000°C was drawn as shown in Figure 5.78. A large part of the projected surface area was covered by the phase field of the solid solution (Pt), followed by the solid solution (V,Cr), although the boundary could not be derived accurately. The phases A15( $\sim\text{Cr}_3\text{Pt}$ ),  $\sim\text{PtV}_3$  and the ternary phase,  $\tau$ , were also in the alloys at 1000°C. The isothermal section is consistent with the solidification projection, especially considering the shape of Pt, and liquidus surface projections. The boundary of the phase field of A15( $\sim\text{Cr}_3\text{Pt}$ ) on the left side requires more alloys in its vicinity, so that it can be more accurately defined. Therefore, it is partly dotted and the curvature was drawn to conform to the opposite side.

Although the (V,Cr) boundary could not be accurately drawn, because of the precipitation within, that precipitation showed that the solvus had retreated rapidly by 1000°C. The ordered phases  $\sim\text{Cr}_3\text{Pt}$  and  $\text{Pt}_2\text{V}$  were found, showing that they formed above 1000°C.

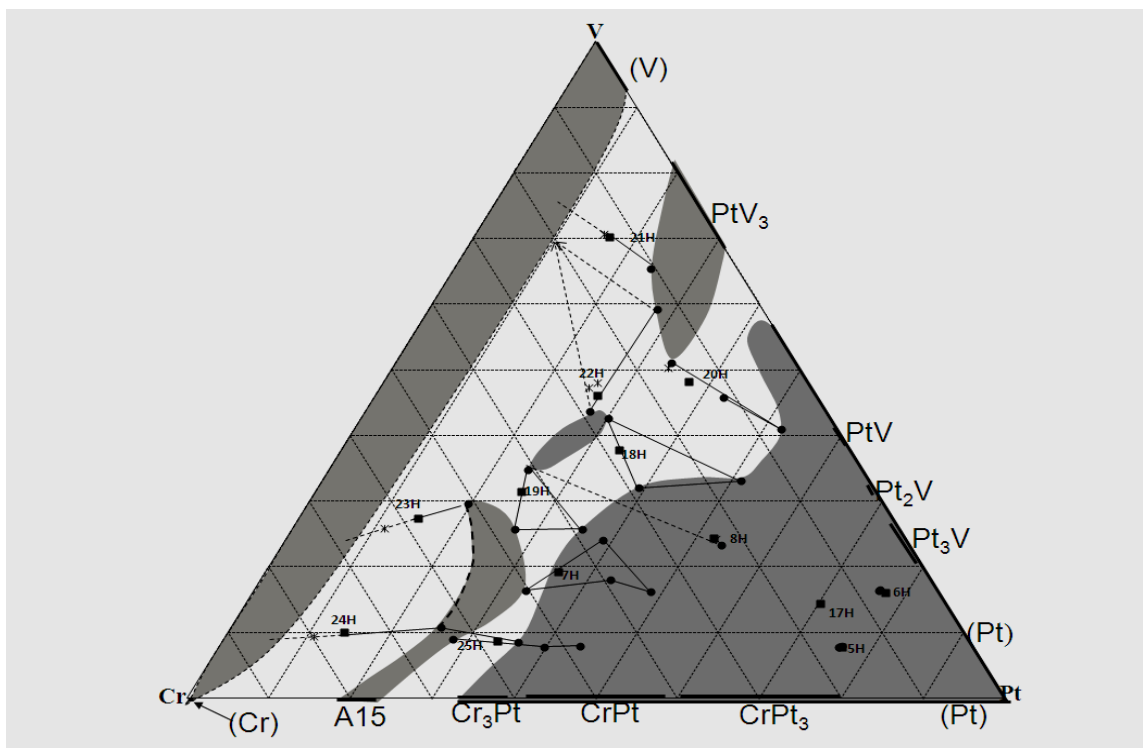


Figure 5.78. Isothermal section of the Pt-Cr-V system at 1000°C (at.%).

### 5.2.15 Tabulated Positions of the Ternary Phase, $\tau$ , in the XRD Pattern

Table 5.27 shows the positions (2Theta) of the ternary phase,  $\tau$ , for the various alloys in which it appears. Apart from sample 8, there is good agreement, considering that  $\tau$  had a range of compositions.

**Table 5.27. Positions (2 Theta) of the ternary phase,  $\tau$ , in the XRD pattern**

Sample ID	2 Theta (deg.)				
	1	2	3	4	5
22	30.6	49.5	54.6	78.8	83.9
19	30.8	44.2* 49.6	54.8	78.9	83.5
18	30.6	49.3	54.4	80.0	-
18H	30.8	49.4	54.7	-	82.2
8	<b>27.0</b>	<b>43.0</b>	<b>63.1</b>	-	82.6
8H	32.3	50.6	-	-	82.5
7	31.0	50.3	-	78.9	83.5
7H	30.7	49.7	-	78.3	82.9

\* The  $2\theta = 44.2^\circ$  is actually the second unidentified peak in the XRD pattern of sample 19 and  $49.6^\circ$  the third peak. However,  $49.6^\circ$  is similar in value to second unidentified peaks in the patterns of the other samples and is therefore included in the second column.

Sample 8 had slightly different peaks (shown in bold in Table 7.27), but this would be expected since it was at the opposite side of the  $\tau$  phase field and had much different composition. Thus, there would be more peak shift. If  $\tau$  was not cubic, the peaks would shift in different directions, making matching even more difficult.

**Table 5.28. Solidification and cooling reactions of the Pt-Cr-V alloys.**

<b>Alloy ID</b>	<b>Composition, at. %</b>	<b>Solidification and Cooling Reactions</b>
5	Pt <sub>73.8</sub> :Cr <sub>16.9</sub> :V <sub>9.3</sub>	L → (Pt) (Pt) → ~Pt <sub>3</sub> V
6	Pt <sub>72.3</sub> :Cr <sub>8.3</sub> :V <sub>19.4</sub>	L → (Pt) (Pt) → ~Pt <sub>3</sub> V
7	Pt <sub>33.4</sub> :Cr <sub>45.8</sub> :V <sub>20.8</sub>	L → (Pt) L + (Pt) → A15(~Cr <sub>3</sub> Pt) L → (Pt) + τ (Pt) → ~Cr <sub>3</sub> Pt
8	Pt <sub>53.0</sub> :Cr <sub>22.4</sub> :V <sub>24.5</sub>	L → (Pt) L → (Pt) + τ (Pt) → ~Cr <sub>3</sub> Pt (Pt) → ~CrPt
17	Pt <sub>68.5</sub> :Cr <sub>16.2</sub> :V <sub>15.3</sub>	L → (Pt) (Pt) → ~Pt <sub>3</sub> V
18	Pt <sub>32.8</sub> :Cr <sub>28.6</sub> :V <sub>38.6</sub>	L → τ L → τ + (Pt) (Pt) → ~Cr <sub>3</sub> Pt
19	Pt <sub>25.8</sub> :Cr <sub>42.9</sub> :V <sub>31.3</sub>	L → τ L + τ → A15(~Cr <sub>3</sub> Pt) + (Pt) (Pt) → ~Cr <sub>3</sub> Pt
20	Pt <sub>38.8</sub> :Cr <sub>14.2</sub> :V <sub>47.0</sub>	L → (Pt) L + (Pt) → ~PtV <sub>3</sub> L → τ + ~PtV <sub>3</sub> (Pt) → ~PtV
21	Pt <sub>28.7</sub> :Cr <sub>27.2</sub> :V <sub>44.1</sub>	L → (V,Cr) L → (V,Cr) + ~PtV <sub>3</sub> (V,Cr) + ~PtV <sub>3</sub> → τ.
22	Pt <sub>28.7</sub> :Cr <sub>27.2</sub> :V <sub>44.1</sub>	L → τ L → τ + (Pt) L → τ + ~PtV <sub>3</sub> L → τ + ~PtV <sub>3</sub> + (V,Cr) (Pt) → ~Cr <sub>3</sub> Pt
23	Pt <sub>16.5</sub> :Cr <sub>56.1</sub> :V <sub>27.4</sub>	L → (V,Cr) L + (V,Cr) → A15(~Cr <sub>3</sub> Pt) L + (V,Cr) + O <sub>2</sub> → A15(~Cr <sub>3</sub> Pt) + CrO <sub>3</sub> L → (V,Cr) + A15 (~Cr <sub>3</sub> Pt)
24	Pt <sub>14.9</sub> :Cr <sub>73.7</sub> :V <sub>11.4</sub>	L → (V,Cr) L + (V,Cr) → A15 (~Cr <sub>3</sub> Pt) L → (V,Cr) + A15 (~Cr <sub>3</sub> Pt) L + (V,Cr) + O <sub>2</sub> → A15 (~Cr <sub>3</sub> Pt) + CrO <sub>3</sub>

25	Pt <sub>34.1</sub> :Cr <sub>57.4</sub> :V <sub>8.5</sub>	$L \rightarrow (Pt)$ $L \rightarrow (Pt) + A15(\sim Cr_3Pt)$ $(Pt) \rightarrow \sim Cr_3Pt$
----	--	---

## CHAPTER 6: HIGHER ORDER ALLOYS OF THE Pt-Al-Cr-Ru-V AND Pt-Al-Cr-Ru-V-Nb SYSTEMS

### 6.1 AS-CAST ALLOYS

#### 6.1.1 As-cast Alloy 26, Average Composition Pt<sub>63.9</sub>:Al<sub>12.2</sub>:Cr<sub>4.3</sub>:Ru<sub>0.7</sub>:V<sub>18.9</sub> (at.%)

The SEM-BSE image of as-cast Alloy 26, average composition Pt<sub>63.9</sub>:Al<sub>12.2</sub>:Cr<sub>4.3</sub>:Ru<sub>0.7</sub>:V<sub>18.9</sub> (at.%), in Figure 6.1 shows a dendritic structure of two phases, dark dendrites and a light matrix. The targeted eutectic is not apparent in the image, and might have been too fine to discern. Table 6.1 has the data for EDX composition analysis. The dark phase was identified as the solid solution (Pt) and the light phase as  $\sim Pt_3Al$ , with all of the alloy's  $\sim 19$  at.% V in solution. This identification was done so that (Pt) had the highest Pt content, the lowest Al content, the highest Ru content and the highest V content. This was consistent with the Pt-Al-V ternary system (Chapter 4) regarding the change in contrast ((Pt) being darker instead of lighter than  $\sim Pt_3Al$ ). The V partitioned preferentially to the (Pt) at  $\sim 23.5$  at.% V compared to  $\sim 7.8$  at.% V in  $\sim Pt_3Al$ .

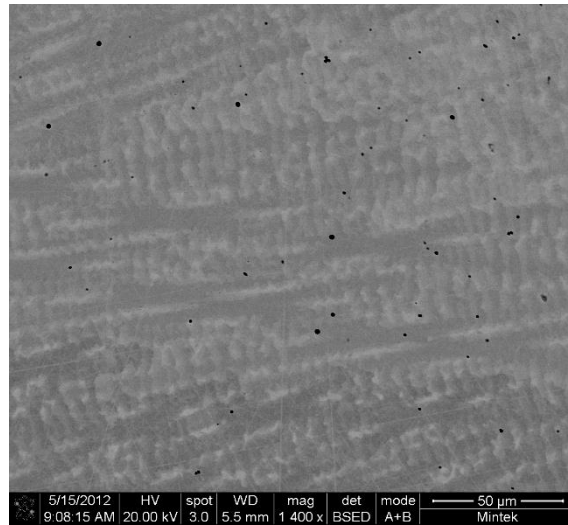


**Figure 6.1. SEM-BSE image of as-cast Alloy 26, average composition  $\text{Pt}_{63.9}:\text{Al}_{12.2}:\text{Cr}_{4.3}:\text{Ru}_{0.7}:\text{V}_{18.9}$  (at. %), showing dark (Pt) and light  $\sim\text{Pt}_3\text{Al}$ .**



**Table 6.1. EDX composition analysis data for as-cast Alloy 26, average composition  $\text{Pt}_{63.9}:\text{Al}_{12.2}:\text{Cr}_{4.3}:\text{Ru}_{0.7}:\text{V}_{18.9}$  (at.%).**

Appearance	Pt	Al	Cr	Ru	V	Phase
Overall	63.9±1.0	12.2±0.4	4.3±0.5	0.7±0.4	18.9±0.9	-
Dark	65.2±0.7	5.0±1.1	4.9±0.2	1.4±0.3	23.5±0.7	(Pt)
Light	62.3±1.2	27.4±1.9	2.5±0.3	0	7.8±0.7	~Pt <sub>3</sub> Al

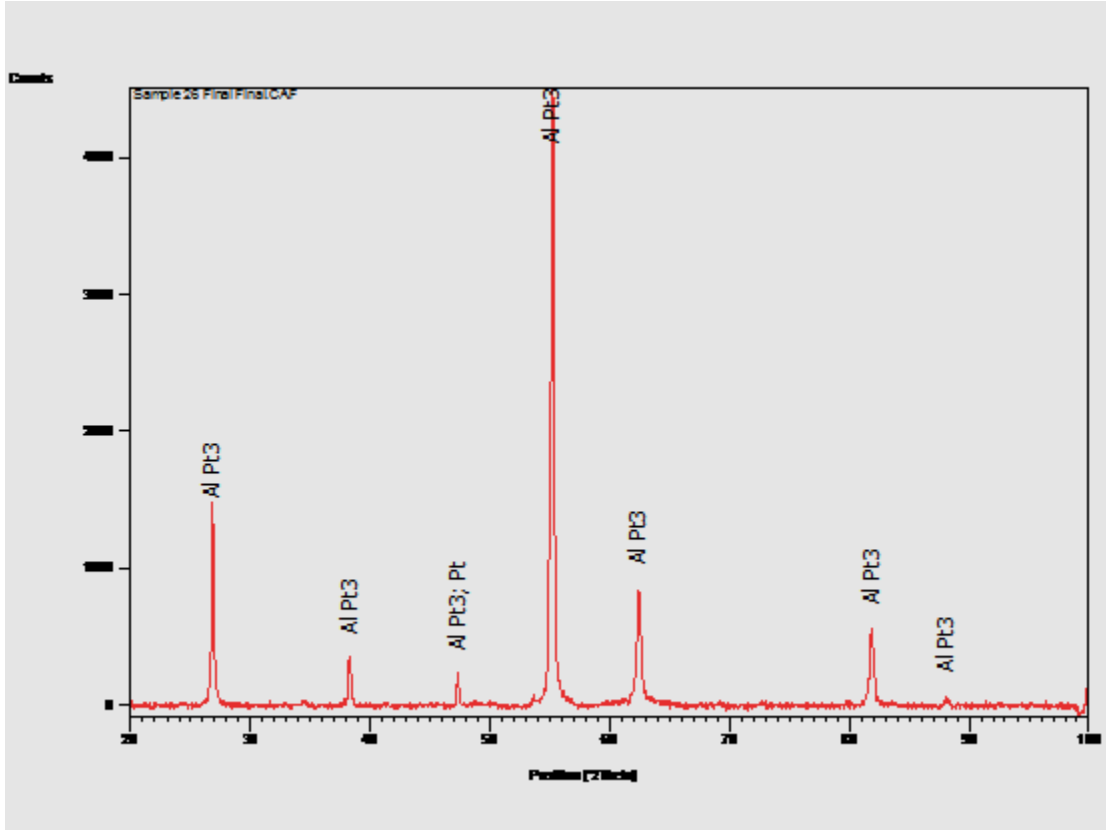
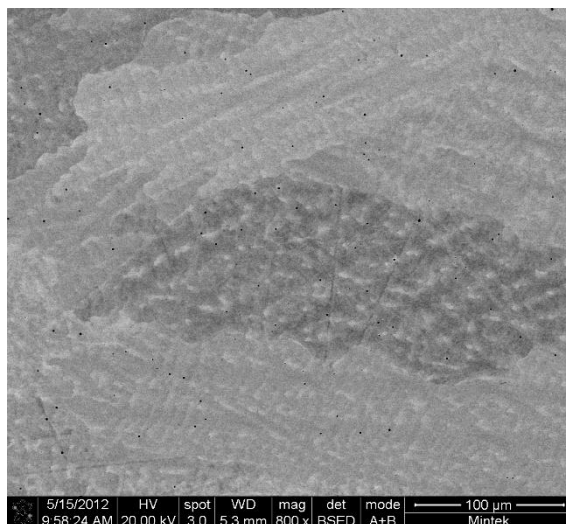


Figure 6.2. XRD pattern of Alloy 26, average composition  $\text{Pt}_{63.9}:\text{Al}_{12.2}:\text{Cr}_{4.3}:\text{Ru}_{0.7}:\text{V}_{18.9}$  (at.%).

### 6.1.2 As-cast Alloy 27, Average Overall Composition $\text{Pt}_{69.5}:\text{Al}_{11.5}:\text{Cr}_{4.2}:\text{Ru}_{0.6}:\text{V}_{14.2}$ (at.%)

Figure 6.3(a) is a SEM-BSE image of as-cast Alloy 27, average composition  $\text{Pt}_{69.5}:\text{Al}_{11.5}:\text{Cr}_{4.2}:\text{Ru}_{0.6}:\text{V}_{14.2}$  (at.%), showing a two-phase structure with some areas appearing lighter than the others due to different orientations. The image does not show the expected eutectic. Composition analysis was done for the two phases in the light area and the darker area in the SEM-BSE image. Comparison of the composition data shows that the two phases in the two areas were the same, and the difference in contrast is due to different orientations. The EDX

composition analysis data are in Table 6.2. The dark phase was identified as the solid solution (Pt) and the light phase was  $\sim\text{Pt}_3\text{Al}$ . Most of the V went into solution in the (Pt). The XRD pattern in Figure 6.4 shows the identity of the phases.



**Figure 6.3. SEM-BSE image of as-cast Alloy 27, average composition  $\text{Pt}_{69.5}\text{:Al}_{11.5}\text{:Cr}_{4.2}\text{:Ru}_{0.6}\text{:V}_{14.2}$  (at.%), showing dark  $\sim\text{Pt}_3\text{Al}$  and light (Pt). There are dark and light areas due to different orientations and irregular grain boundaries.**

**Table 6.2. EDX composition analysis data for as-cast Alloy 27, average composition  $\text{Pt}_{69.5}\text{:Al}_{11.5}\text{:Cr}_{4.2}\text{:Ru}_{0.6}\text{:V}_{14.2}$  (at.%).**

Appearance	Pt	Al	Cr	Ru	V	Phase
Overall	69.5±0.5	11.5±0.5	4.2±0.3	0.6±0.3	14.2±0.5	-
Dark in dark area	70.5±1.4	7.7±1.1	4.5±0.2	0.9±0.3	16.4±1.1	(Pt)
Light in dark area	66.1±1.6	26.1±3.7	2.8±0.3	0	5.0±2.1	$\sim\text{Pt}_3\text{Al}$
Dark in light area	69.8±0.9	9.1±1.1	4.3±0.3	1.0±0.6	15.8±0.5	(Pt)
Light in light area	67.7±0.8	18.8±2.2	3.6±0.2	0	9.9±1.2	$\sim\text{Pt}_3\text{Al}$

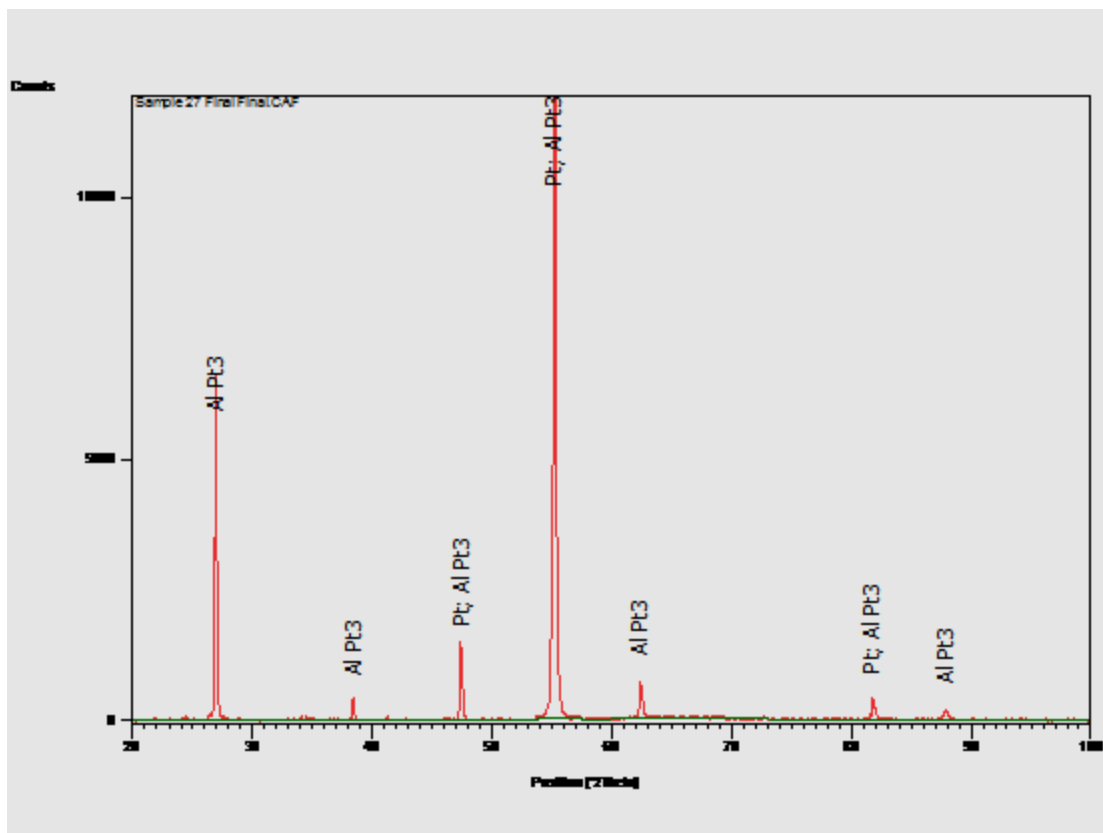


**Figure 6.4. XRD pattern of Alloy 27, average composition  $\text{Pt}_{69.5}\text{Al}_{11.5}\text{Cr}_{4.2}\text{Ru}_{0.6}\text{V}_{14.2}$  (at.%)**

### **6.1.3 As-cast Alloy 28, Average Composition $\text{Pt}_{75.2}\text{Al}_{11.2}\text{Cr}_{4.0}\text{Ru}_{0.6}\text{V}_{9.5}$ (at.%)**

The SEM-BSE image of as-cast Alloy 28, average composition  $\text{Pt}_{75.2}\text{Al}_{11.2}\text{Cr}_{4.0}\text{Ru}_{0.6}\text{V}_{9.5}$  (at.%), in Figure 6.5 shows a single phase with grains at different orientations. Table 6.3 contains the data for EDX composition analysis. All the ~10 at.% V in the alloy went into solution in the one visible phase. The XRD pattern in Figure 6.6 shows all the major peaks originated from ~ $\text{Pt}_3\text{Al}$ , so this was taken to be the identity even with all the Ru and V in solution.

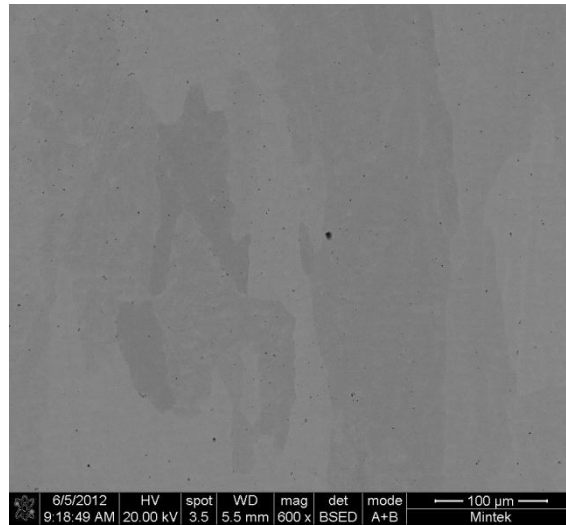


**Figure 6.5. SEM-BSE image of as-cast Alloy 28, average composition  $\text{Pt}_{75.2}\text{:Al}_{11.2}\text{:Cr}_{4.0}\text{:Ru}_{0.6}\text{:V}_{9.5}$  (at.%), showing single phase,  $\sim\text{Pt}_3\text{Al}$ , with grains at different orientations.**

**Table 6.3. EDX composition analysis data for as-cast Alloy 28, average composition  $\text{Pt}_{75.2}\text{:Al}_{11.2}\text{:Cr}_{4.0}\text{:Ru}_{0.6}\text{:V}_{9.5}$  (at.%).**

Appearance	Pt	Al	Cr	Ru	V	Phase
Overall	74.7±0.6	11.2±0.4	4.0±0.2	0.6±0.4	9.5±0.2	-
Dark	73.2±2.2	13.6±3.5	4.1±0.4	0.8±0.6	8.3±2.4	$\sim\text{Pt}_3\text{Al}$
Medium	73.1±0.4	11.1±1.3	4.5±0.1	0.7±0.5	10.6±1.2	$\sim\text{Pt}_3\text{Al}$

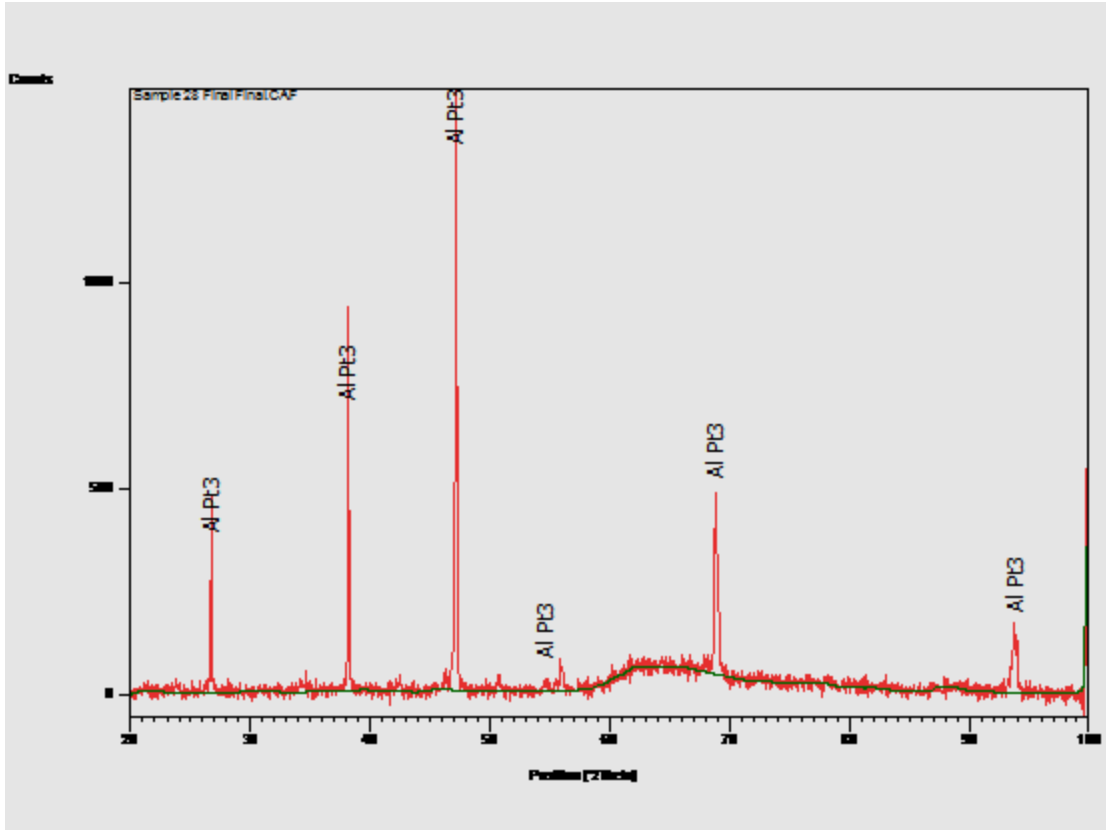


**Figure 6.6. XRD pattern of Alloy 28, average composition  $\text{Pt}_{75.2}:\text{Al}_{11.2}:\text{Cr}_{4.0}:\text{Ru}_{0.6}:\text{V}_{9.5}$  (at.%).**

#### **6.1.4 As-cast Alloy 29, Average Composition $\text{Pt}_{78.7}:\text{Al}_{12.2}:\text{Cr}_{3.8}:\text{Ru}_{0.6}:\text{V}_{5.2}$ (at.%)**

Figure 6.6 is an SEM-BSE image of as-cast Alloy 29, average composition  $\text{Pt}_{78.7}:\text{Al}_{12.2}:\text{Cr}_{3.8}:\text{Ru}_{0.6}:\text{V}_{5.2}$  (at.%), showing a single phase with grains at different orientations with irregular grain boundaries. Table 6.4 contains data for EDX composition analysis. The single phase was identified as  $\sim\text{Pt}_3\text{Al}$ , as shown in the XRD pattern of Figure 6.7. All the  $\sim 5$  at.% V went into solution in the  $\sim\text{Pt}_3\text{Al}$ , as well as the Ru.

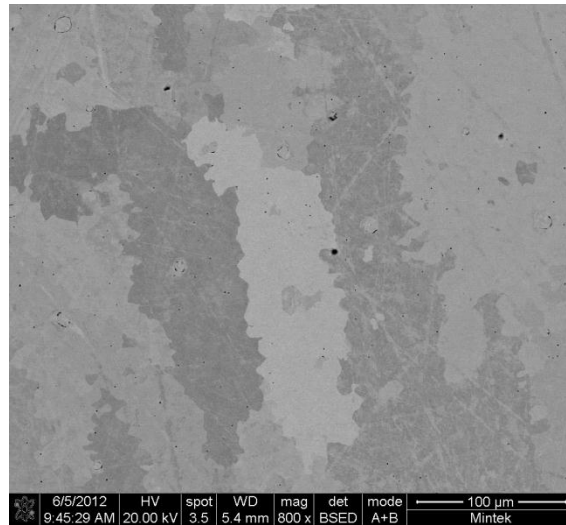


**Figure 6.7. SEM-BSE image of as-cast Alloy 29, average composition  $\text{Pt}_{78.7}\text{:Al}_{12.2}\text{:Cr}_{3.8}\text{:Ru}_{0.6}\text{:V}_{5.2}$  (at.%), showing single phase,  $\sim\text{Pt}_3\text{Al}$ , with irregular grains at different orientations.**

**Table 6.4. EDX composition analysis data for as-cast Alloy 29, average composition  $\text{Pt}_{78.7}\text{:Al}_{12.2}\text{:Cr}_{3.8}\text{:Ru}_{0.6}\text{:V}_{5.2}$  (at.%).**

Appearance	Pt	Al	Cr	Ru	V	Phase
Overall	78.2±0.9	12.2±0.7	3.8±0.2	0.6±0.1	5.2±0.3	-
Dark	79.4±1.9	10.6±2.8	4.3±0.5	0.1±0.2	5.6±0.8	$\sim\text{Pt}_3\text{Al}$
Medium	80.8±0.5	7.0±0.9	4.4±0.3	1.1±0.4	6.7±0.3	$\sim\text{Pt}_3\text{Al}$
Light	78.7±2.8	12.5±3.3	3.8±0.4	0.1±0.2	4.9±0.6	$\sim\text{Pt}_3\text{Al}$

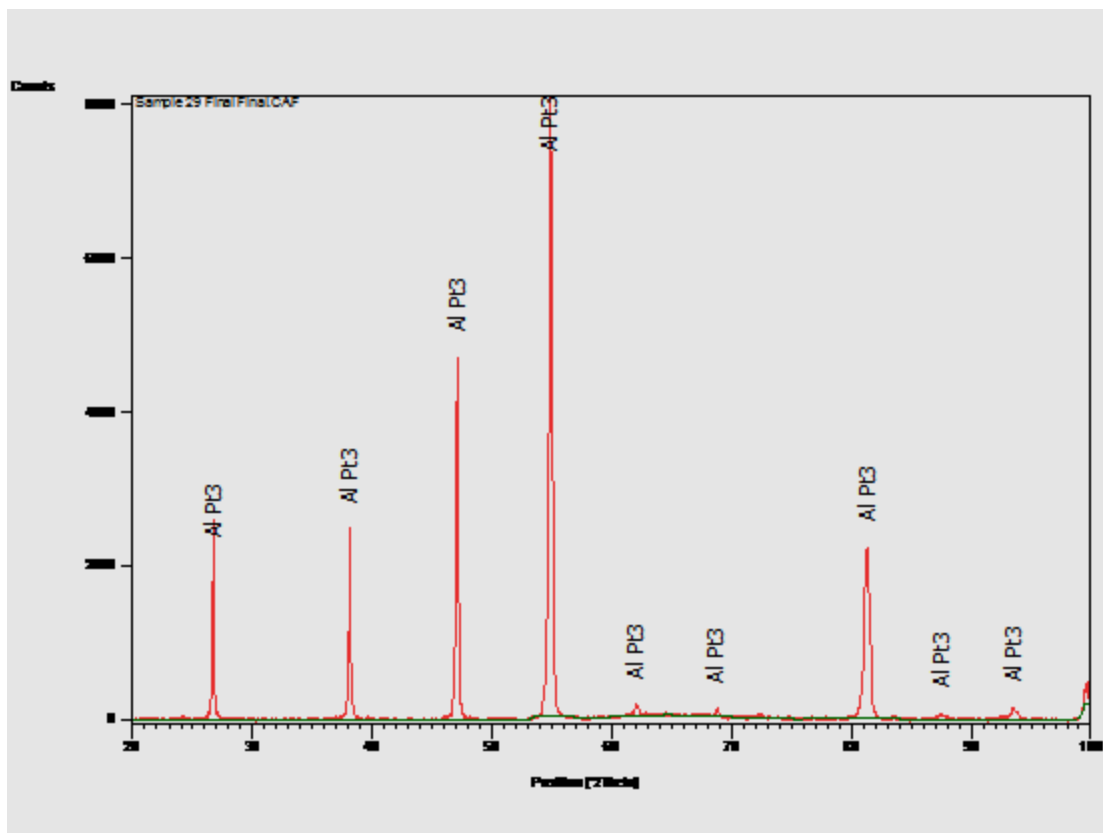


**Figure 6.8. XRD pattern of Alloy 29, average composition  $\text{Pt}_{78.7}:\text{Al}_{12.2}:\text{Cr}_{3.8}:\text{Ru}_{0.6}:\text{V}_{5.2}$  (at.%).**

#### **6.1.5 As-cast Alloy 30, Average Composition $\text{Pt}_{63.2}:\text{Al}_{12.9}:\text{Cr}_{4.0}:\text{Ru}_{0.7}:\text{V}_{19.0}:\text{Nb}_{0.6}$ (at.%)**

The SEM-BSE image of as-cast Alloy 30, average composition  $\text{Pt}_{63.2}:\text{Al}_{12.9}:\text{Cr}_{4.0}:\text{Ru}_{0.7}:\text{V}_{19.0}:\text{Nb}_{0.6}$  (at.%), in Figure 6.8 shows dark dendrites and an irregular eutectic similar to the microstructure in Alloy 2. Table 6.5 has the data for EDX composition analysis. The dark dendrites were identified as (Pt) (having higher Pt, Ru, and V and lower Al) and the eutectic components as  $\sim\text{Pt}_3\text{Al} + (\text{Pt})$ . The targeted Nb content in the alloy was 5 at.%, but the Nb was lost during melting, leaving only an average content of 0.6 at.%. The XRD pattern for the alloy is shown in Figure 6.10.

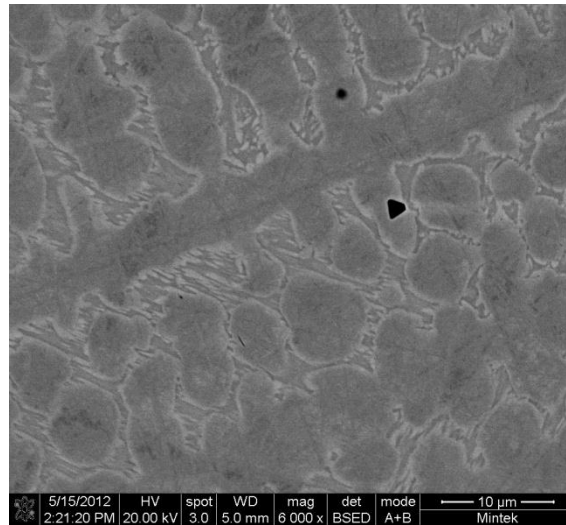


**Figure 6.9. SEM-BSE image of as-cast Alloy 30, average composition  $\text{Pt}_{63.2}\text{:Al}_{12.9}\text{:Cr}_{4.0}\text{:Ru}_{0.7}\text{:V}_{19.0}\text{:Nb}_{0.6}$  (at. %), showing dark (Pt) dendrites and a eutectic of  $\sim\text{Pt}_3\text{Al} + (\text{Pt})$ .**

**Table 6.5. EDX composition analysis data for as-cast Alloy 30, average composition  $\text{Pt}_{63.2}\text{:Al}_{12.9}\text{:Cr}_{4.0}\text{:Ru}_{0.7}\text{:V}_{19.0}\text{:Nb}_{0.6}$  (at. %).**

Appearance	Pt	Al	Cr	Ru	V	Nb	Phase
Overall	63.4±1.1	12.9±1.7	4.0±0.1	0.7±0.3	19.0±0.9	0.6±0.4	-
Dark	62.7±0.6	6.3±0.6	5.1±0.4	1.0±0.4	23.3±0.9	1.6±0.7	(Pt)
Eutectic	56.1±0.8	31.1±0.9	3.9±0.3	0.1±0.1	8.8±0.4	0	$\sim\text{Pt}_3\text{Al} + (\text{Pt})$



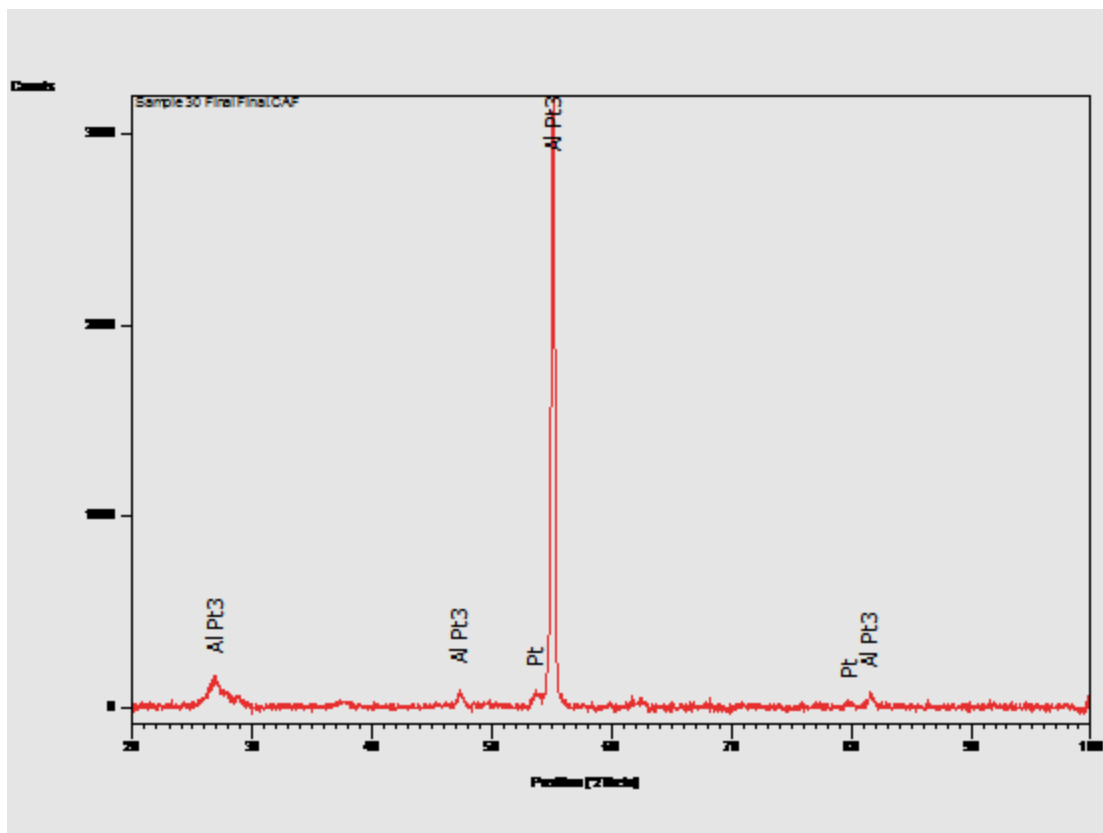


**Figure 6.10. XRD pattern of Alloy 30, average composition  $\text{Pt}_{63.2}\text{:Al}_{12.9}\text{:Cr}_{4.0}\text{:Ru}_{0.7}\text{:V}_{19.0}\text{:Nb}_{0.6}$  (at.%).**

#### **6.1.6 As-cast Alloy 31, Average Composition $\text{Pt}_{71.7}\text{:Al}_{12.8}\text{:Cr}_{4.9}\text{:Ru}_{1.1}\text{:V}_{9.9}\text{:Nb}_{0.3}$ (at.%)**

Figure 6.11 is an SEM-BSE image of as-cast Alloy 31, average composition  $\text{Pt}_{71.7}\text{:Al}_{12.8}\text{:Cr}_{4.9}\text{:Ru}_{1.1}\text{:V}_{9.9}\text{:Nb}_{0.3}$  (at.%), showing a two-phase structure with areas appearing light and dark, due to different orientations and there were also irregular grain boundaries. The expected eutectic was not apparent. Table 6.6 contains the EDX composition analysis data. The dark phase was identified as (Pt) and the light phase as  $\sim\text{Pt}_3\text{Al}$ . The V was more soluble in (Pt) compared to  $\sim\text{Pt}_3\text{Al}$ . The XRD pattern is shown in Figure 6.12.

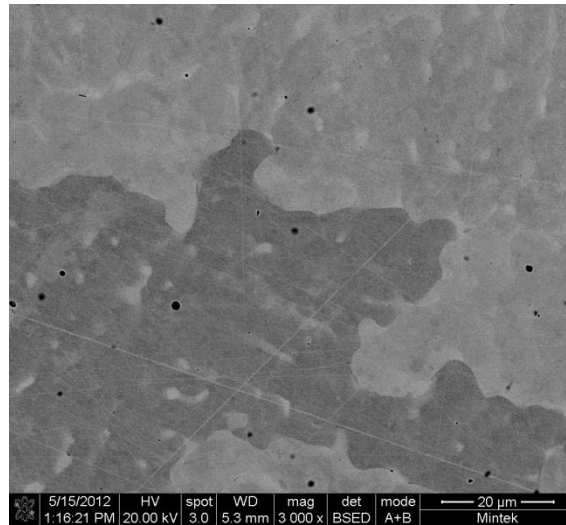


**Figure 6.11. SEM-BSE image of as-cast Alloy 31, average composition  $\text{Pt}_{71.7}:\text{Al}_{12.8}:\text{Cr}_{4.9}:\text{Ru}_{1.1}:\text{V}_{9.9}:\text{Nb}_{0.3}$  (at.%), showing dark  $\sim\text{Pt}_3\text{Al}$  and light (Pt). There are light and dark areas due to different orientations.**

**Table 6.6. EDX composition analysis data for as-cast Alloy 31, average composition  $\text{Pt}_{71.7}:\text{Al}_{12.8}:\text{Cr}_{4.9}:\text{Ru}_{1.1}:\text{V}_{9.9}:\text{Nb}_{0.3}$  (at.%).**

Appearance	Pt	Al	Cr	Ru	V	Nb	Phase
Overall	71.0±2.1	12.8±1.8	4.9±0.4	1.1±0.8	9.9±0.5	0.3±0.1	-
Dark in light area	73.8±1.6	9.0±2.0	4.3±0.4	0.9±0.6	11.2±1.3	0.8±0.4	(Pt)
Light in light area	64.2±0.9	29.5±1.0	2.8±0.2	0	3.5±0.5	0	$\sim\text{Pt}_3\text{Al}$
Dark in dark area	73.8±1.3	8.6±1.1	4.6±0.4	1.0±0.8	10.6±0.8	1.4±0.8	(Pt)
Light in dark area	64.6±1.2	29.3±0.6	2.5±0.2	0	3.6±0.4	0	$\sim\text{Pt}_3\text{Al}$

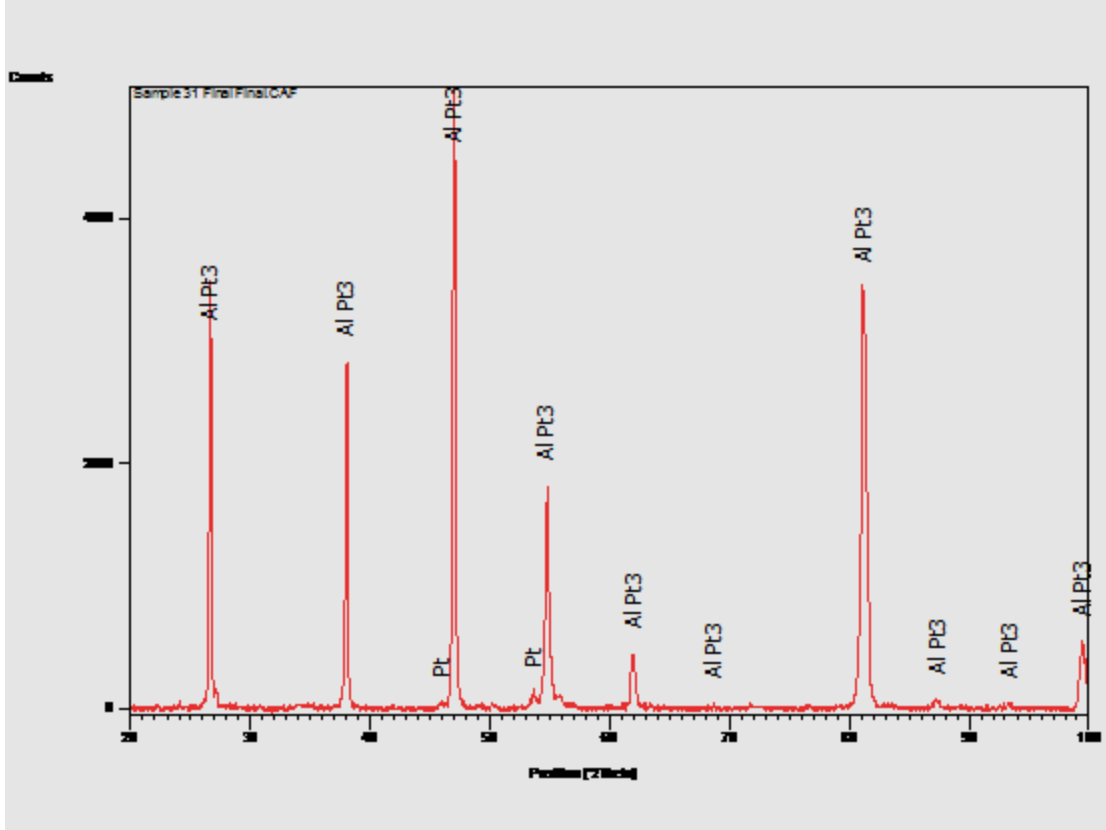


**Figure 6.12. XRD pattern of Alloy 31, average composition  $\text{Pt}_{71.7}\text{Al}_{12.8}\text{Cr}_{4.9}\text{Ru}_{1.1}\text{V}_{9.9}\text{Nb}_{0.3}$  (at.%).**

## 6.2 ALLOYS ANNEALED AT 1000°C FOR 1500 HOURS

### 6.2.1 Annealed Alloy 26H, Average Composition $\text{Pt}_{61.7}\text{Al}_{13.9}\text{Cr}_{4.1}\text{Ru}_{0.6}\text{V}_{19.6}$ (at.%)

The SEM-BSE image of annealed Alloy 26H average composition  $\text{Pt}_{61.7}\text{Al}_{13.9}\text{Cr}_{4.1}\text{Ru}_{0.6}\text{V}_{19.6}$  (at.%), in Figure 6.13 shows a two-phase structure of a dark and a light phase. The EDX composition analysis data are in Table 6.7. The dark phase was identified as  $\sim\text{Pt}_2\text{V}$  and the light area as  $\sim\text{Pt}_3\text{Al}$ . The prolonged heat treatment resulted in (Pt), which had been the second phase in the as-cast alloy, transformed to  $\sim\text{Pt}_2\text{V}$  as indicated in the binary phase diagram of Pt-V [1990Mas]. The XRD pattern is shown in Figure 6.14.

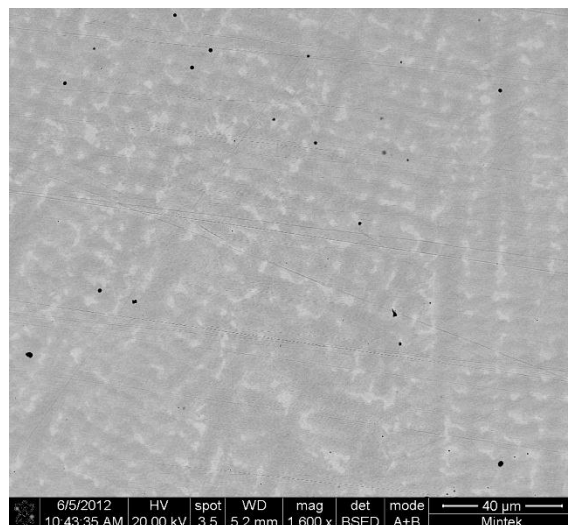


**Figure 6.13. SEM-BSE image of annealed Alloy 26H, average composition  $\text{Pt}_{61.7}\text{Al}_{13.9}\text{Cr}_{4.1}\text{Ru}_{0.6}\text{V}_{19.6}$  (at.%), showing a two phase structure of dark  $\sim\text{Pt}_2\text{V}$  and light  $\sim\text{Pt}_3\text{Al}$ .**

**Table 6.7. EDX composition analysis data for annealed Alloy 26H, average composition  $\text{Pt}_{61.7}\text{Al}_{13.9}\text{Cr}_{4.1}\text{Ru}_{0.6}\text{V}_{19.6}$  (at.%).**

Appearance	Pt	Al	Cr	Ru	V	Phase
Overall	61.8±0.7	13.9±0.9	4.1±0.3	0.6±0.2	19.6±0.4	-
Dark	61.8±1.3	7.1±1.3	4.7±0.2	1.4±0.4	25.0±1.4	$\sim\text{Pt}_2\text{V}$
Light	57.9±0.4	37.6±0.8	1.8±0.3	0	2.7±0.4	$\sim\text{Pt}_3\text{Al}$

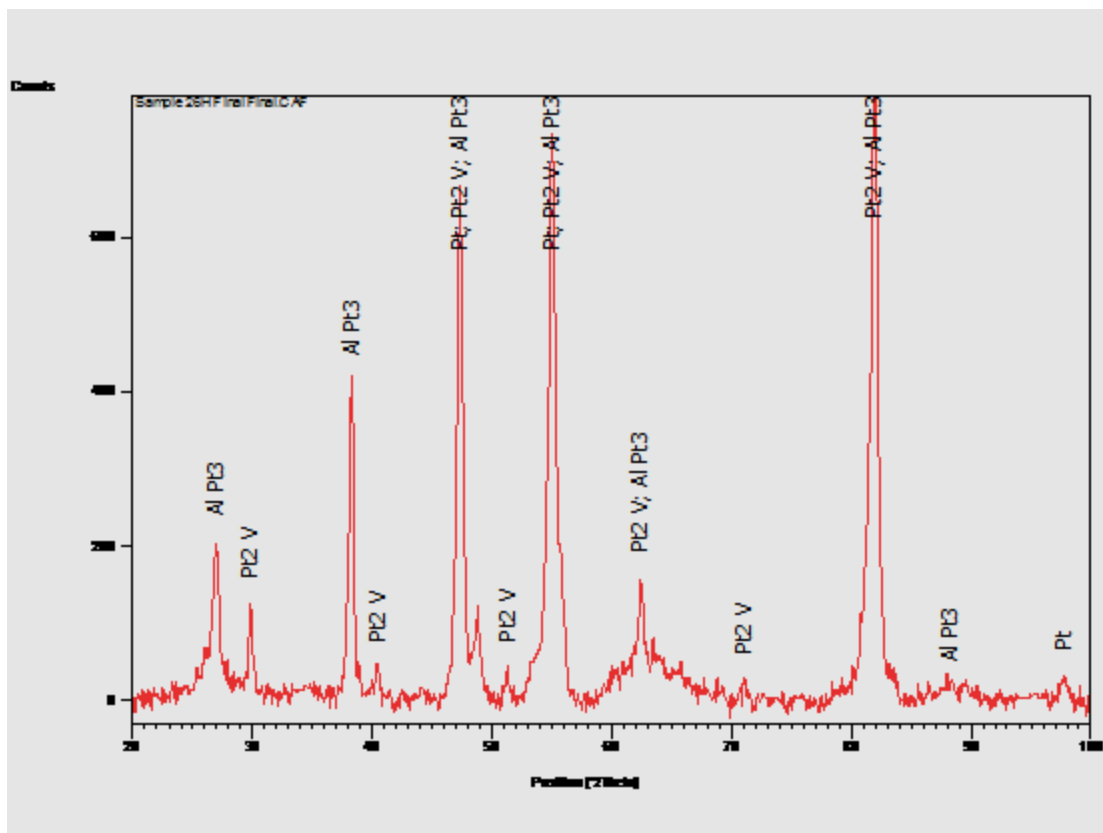


**Figure 6.14. XRD pattern of annealed Alloy 26H, average composition  $\text{Pt}_{61.7}:\text{Al}_{13.9}:\text{Cr}_{4.1}:\text{Ru}_{0.6}:\text{V}_{19.6}$  (at.%).**

### **6.2.2 Annealed Alloy 27H, Average Composition $\text{Pt}_{69.8}:\text{Al}_{11.4}:\text{Cr}_{4.4}:\text{Ru}_{0.5}:\text{V}_{14.1}$ (at.%)**

Figure 6.15 is an SEM-BSE image of Alloy 27H, average composition  $\text{Pt}_{69.8}:\text{Al}_{11.4}:\text{Cr}_{4.4}:\text{Ru}_{0.5}:\text{V}_{14.1}$  (at.%), showing single phase  $\sim\text{Pt}_3\text{Al}$  with grains at different orientations. The EDX composition analysis data are in Table 6.8. The single phase was identified as  $\sim\text{Pt}_3\text{Al}$ . All the  $\sim 14$  at.% V remained in solution in the existing phase after the heat treatment. The alloy had been two-phase,  $\sim\text{Pt}_3\text{Al}$  and (Pt) in the as-cast condition. The XRD pattern is shown in Figure 6.16 and shows some (Pt).

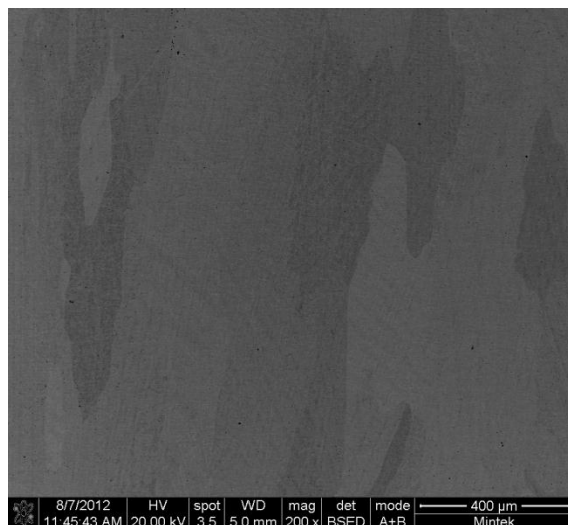


**Figure 6.15. SEM-BSE image of annealed Alloy 27H, average composition  $\text{Pt}_{69.8}\text{Al}_{11.4}\text{Cr}_{4.4}\text{Ru}_{0.5}\text{V}_{14.1}$  (at. %), showing single phase  $\sim\text{Pt}_3\text{Al}$  with grains at different orientations.**

**Table 6.8. EDX composition analysis data for Alloy 27H, average composition  $\text{Pt}_{69.8}\text{Al}_{11.4}\text{Cr}_{4.4}\text{Ru}_{0.5}\text{V}_{14.1}$  (at. %).**

Appearance	Pt	Al	Cr	Ru	V	Phase
Overall	69.6±1.3	11.4±1.0	4.4±0.2	0.5±0.4	14.1±0.7	-
Dark	69.5±0.4	11.4±0.2	4.2±0.2	0.4±0.1	14.5±0.2	$\sim\text{Pt}_3\text{Al}$
Light	69.6±0.7	11.2±0.4	4.5±0.4	0.5±0.4	14.2±0.1	$\sim\text{Pt}_3\text{Al}$

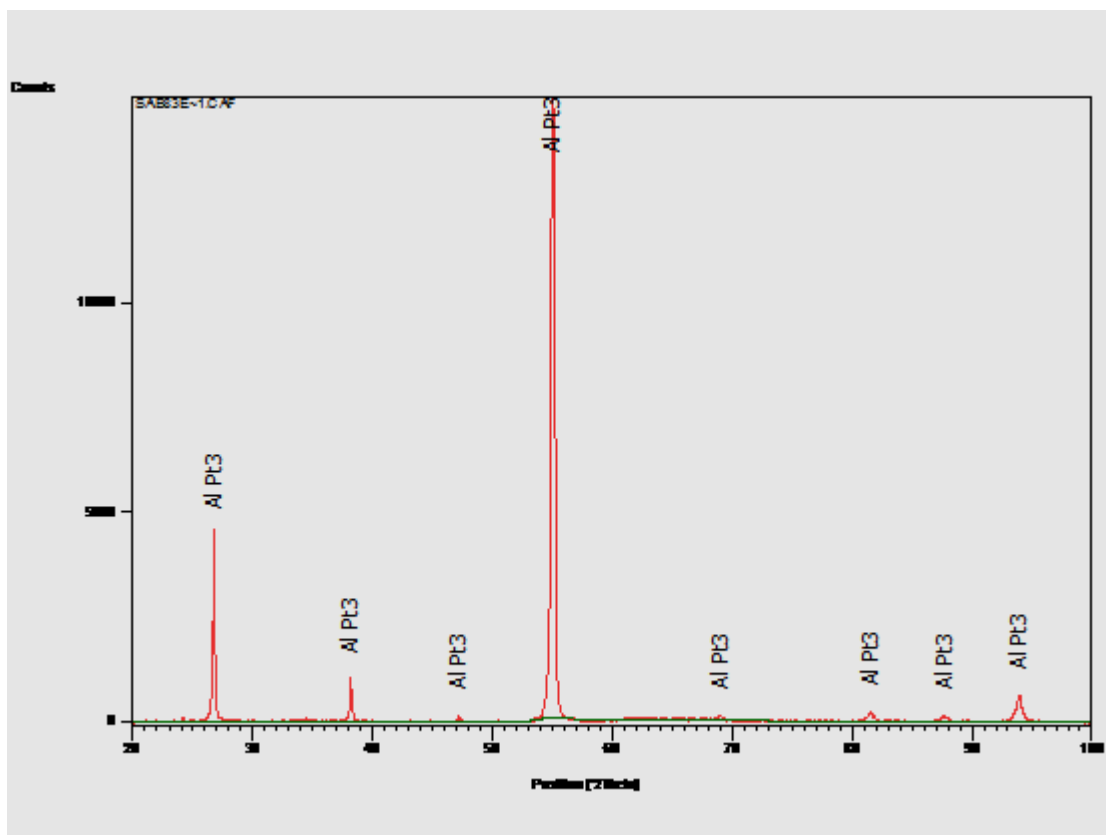


**Figure 6.16. XRD pattern of annealed Alloy 27H, average composition  $\text{Pt}_{69.8}\text{:Al}_{11.4}\text{:Cr}_{4.4}\text{:Ru}_{0.5}\text{:V}_{14.1}$  (at.%).**

### **6.2.3 Annealed Alloy 28H, Average Composition $\text{Pt}_{83.0}\text{:Al}_{10.1}\text{:Cr}_{3.7}\text{:Ru}_{0.8}\text{:V}_{9.0}$ (at.%)**

The SEM-BSE image of annealed Alloy 28H, average composition  $\text{Pt}_{83.0}\text{:Al}_{10.1}\text{:Cr}_{3.7}\text{:Ru}_{0.8}\text{:V}_{9.0}$  (at.%), in Figure 6.17, shows single phase  $\sim\text{Pt}_3\text{Al}$  with grains at different orientations. The EDX composition analysis data are in Table 6.9. The single phase was identified as  $\sim\text{Pt}_3\text{Al}$ . All the  $\sim 9$  at.% V went into solution in  $\sim\text{Pt}_3\text{Al}$ . The XRD pattern is shown in Figure 6.18.

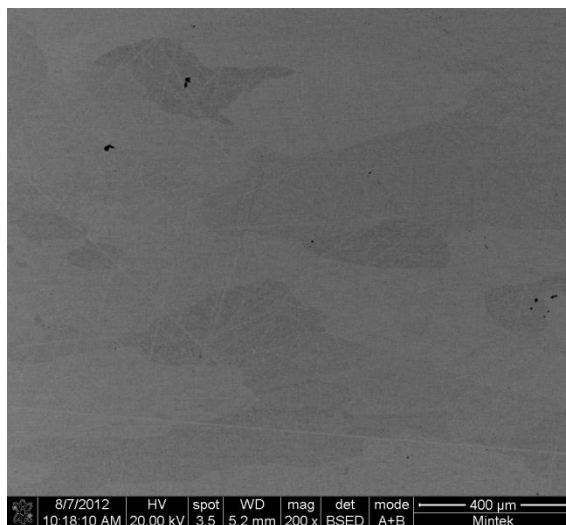


**Figure 6.17. SEM-BSE image of annealed Alloy 28H, average composition  $\text{Pt}_{83.0}:\text{Al}_{10.1}:\text{Cr}_{3.7}:\text{Ru}_{0.8}:\text{V}_{9.0}$  (at.%), showing single phase  $\sim\text{Pt}_3\text{Al}$  with grains at different orientations.**

**Table 6.9. EDX composition analysis data for Alloy 28H, average composition  $\text{Pt}_{83.0}:\text{Al}_{10.1}:\text{Cr}_{3.7}:\text{Ru}_{0.8}:\text{V}_{9.0}$  (at.%).**

Appearance	Pt	Al	Cr	Ru	V	Phase
Overall	76.4±1.0	10.1±0.3	3.7±0.6	0.8±0.1	9.0±0.4	-
Dark	75.8±1.0	10.4±0.6	4.3±0.3	0.8±0.2	8.7±0.3	$\sim\text{Pt}_3\text{Al}$
Light	75.8±2.0	10.5±1.4	4.2±0.5	0.5±0.1	9.0±0.4	$\sim\text{Pt}_3\text{Al}$



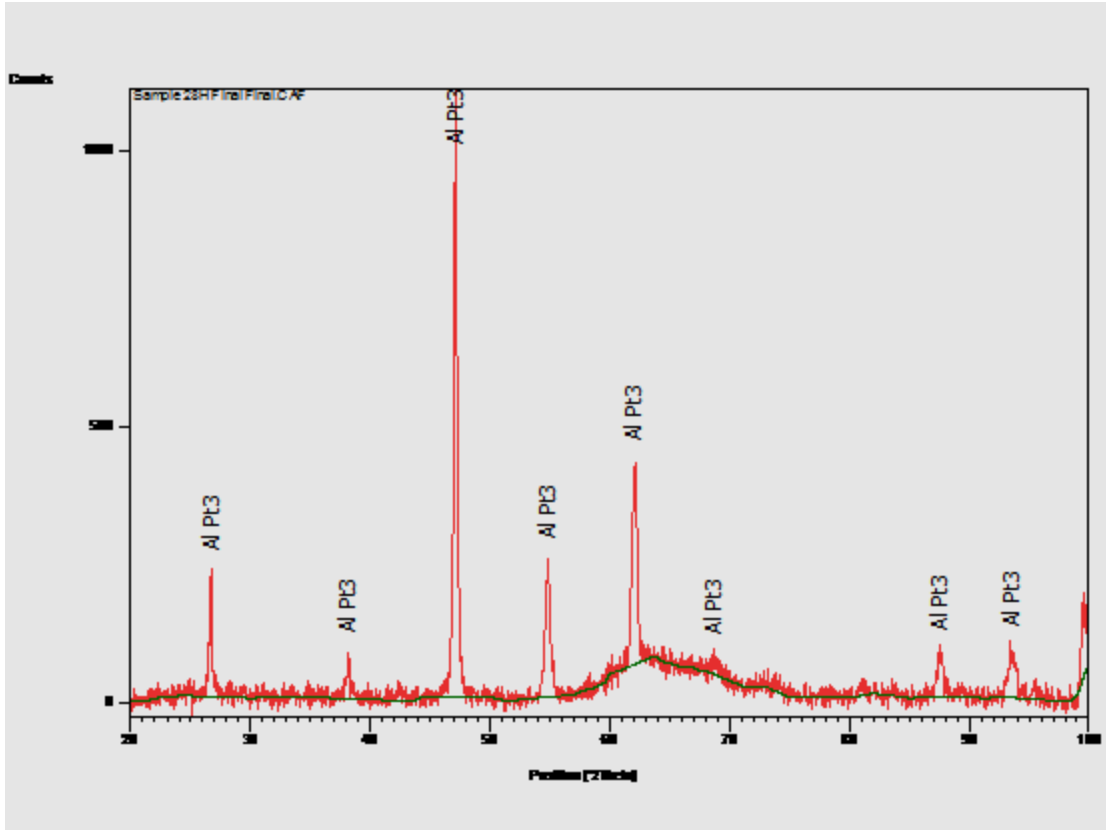


**Figure 6.18. XRD pattern of annealed Alloy 28H, average composition  $\text{Pt}_{83.0}:\text{Al}_{10.1}:\text{Cr}_{3.7}:\text{Ru}_{0.8}:\text{V}_{9.0}$  (at.%).**

#### **6.2.4 Annealed Alloy 29H, Average Composition $\text{Pt}_{83.0}:\text{Al}_{18.7}:\text{Cr}_{3.7}:\text{Ru}_{0.8}:\text{V}_{4.3}$ (at.%)**

Figure 6.19 is a SEM-BSE image of Alloy 29H, average composition  $\text{Pt}_{83.0}:\text{Al}_{18.7}:\text{Cr}_{3.7}:\text{Ru}_{0.8}:\text{V}_{4.3}$  (at.%), showing dark contrast  $\sim\text{Pt}_3\text{Al}$  with light solid state precipitation of (Pt), and light contrast (Pt) with dark solid state precipitation of  $\sim\text{Pt}_3\text{Al}$ . There was very low contrast between the phases and it was difficult to interpret. Additionally, both of the analysed phases had precipitates of the other phase, bringing their overall compositions closer. The phases were distinguished on the basis of composition ((Pt) having higher Pt, Ru and V with lower Al). Unlike the other samples, (Pt) was the light phase, because it had less V. The EDX composition analysis data are in Table 6.10. The solid state precipitations indicate retreating solvi of  $\sim\text{Pt}_3\text{Al}$  and (Pt). The XRD pattern is shown in Figure 6.20.

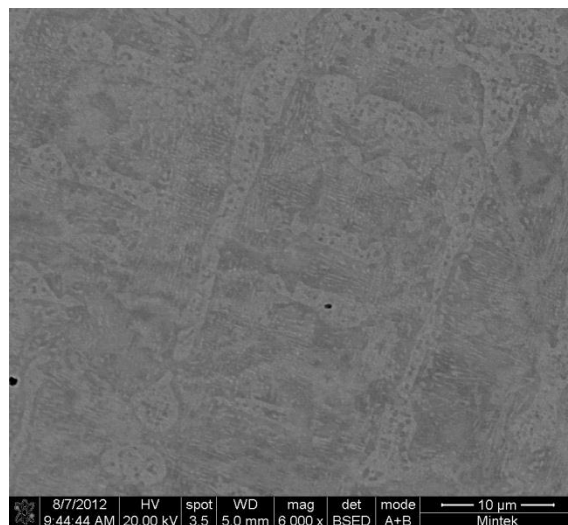


**Figure 6.19. SEM-BSE image of annealed Alloy 29H, average composition  $\text{Pt}_{83.0}:\text{Al}_{8.7}:\text{Cr}_{3.7}:\text{Ru}_{0.8}:\text{V}_{4.3}$  (at.%).**

**Table 6.10. EDX composition analysis data for Alloy 29H, average composition  $\text{Pt}_{83.0}:\text{Al}_{8.7}:\text{Cr}_{3.7}:\text{Ru}_{0.8}:\text{V}_{4.3}$  (at.%).**

Appearance	Pt	Al	Cr	Ru	V	Phase
Overall	82.5±0.7	8.7±0.6	3.7±0.4	0.8	4.3±0.6	-
Light with dark pptn.	82.6±2.0	6.8±1.5	4.1±0.5	1.6±1.3	4.9±0.4	(Pt) with ~Pt <sub>3</sub> Al pptn.
Dark with light pptn.	80.4±2.0	10.1±1.7	3.9±0.4	1.2±0.8	4.4±0.5	~Pt <sub>3</sub> Al with (Pt) pptn

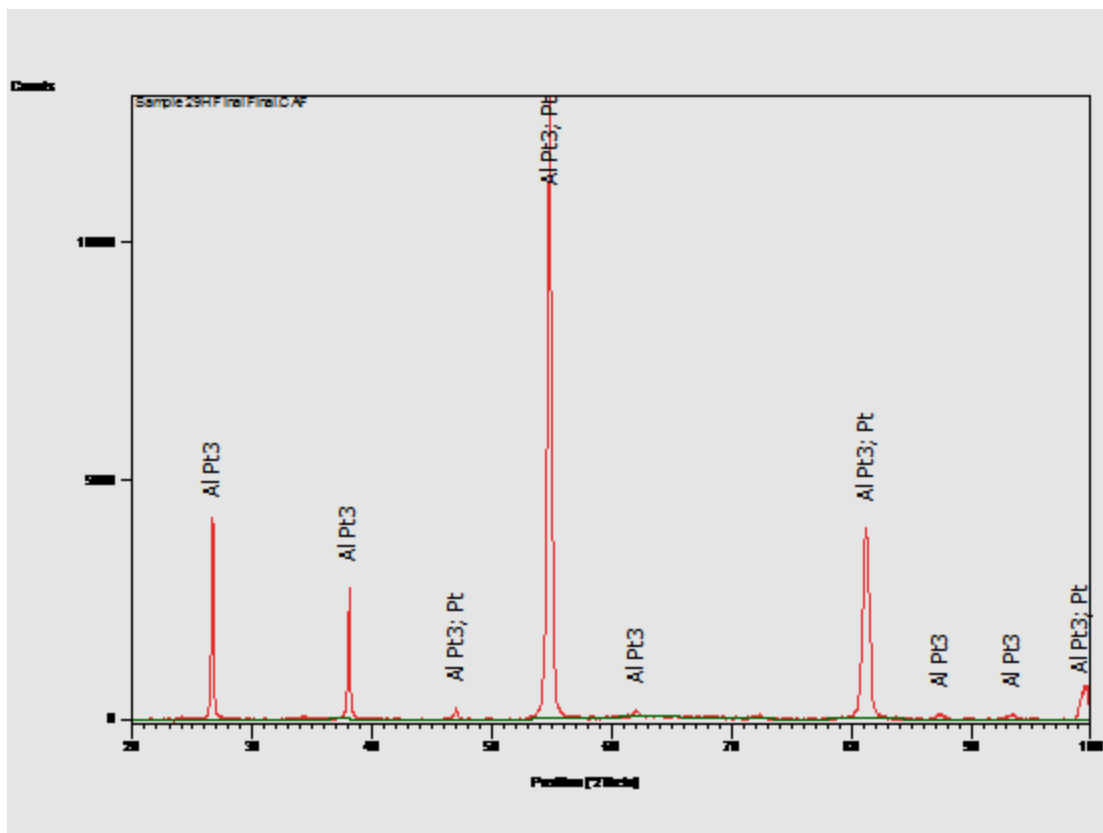


**Figure 6.20. XRD pattern for annealed Alloy 29H, average composition  $\text{Pt}_{83.0}:\text{Al}_{8.7}:\text{Cr}_{3.7}:\text{Ru}_{0.8}:\text{V}_{4.3}$  (at.%).**

### **6.2.5 Annealed Alloy 30H, Average Composition $\text{Pt}_{53.9}:\text{Al}_{18.0}:\text{Cr}_{4.3}:\text{Ru}_{1.4}:\text{V}_{21.9}:\text{Nb}_{1.0}$ (at.%)**

Figure 6.21 is an SEM-BSE image of annealed Alloy 30H, average composition  $\text{Pt}_{53.9}:\text{Al}_{18.0}:\text{Cr}_{4.3}:\text{Ru}_{1.4}:\text{V}_{21.9}:\text{Nb}_{1.0}$  (at.%), showing a medium contrast phase with light solid state precipitates, a light phase, a dark phase and a coarsened eutectoid of light and dark. The medium phase was identified as  $\sim\text{Pt}_2\text{V}$ , the light phase as  $\sim\text{Pt}_3\text{Al}$  and the dark phase as  $\sim\text{PtV}$  (although its composition was fairly similar to  $\tau_1$  of Pt-Al-V). The components of the coarsened eutectoid were  $\sim\text{PtV}$  and  $\sim\text{Pt}_2\text{V}$ . The XRD pattern is shown in Figure 6.22. In the as-cast Alloy 30, there were only two phases, (Pt) and  $\sim\text{Pt}_3\text{Al}$ . Since there was no melting during heat treatment, any new phase formation must have involved solid state transformation of one or both phases. Since  $\sim\text{Pt}_3\text{Al}$  was retained in the heat treated structure, then any new phase must have resulted from solid state transformation of (Pt). Thus the search for phase identity was simplified to what (Pt) may transform to, especially in the component binary systems, at around the heat treatment temperature.

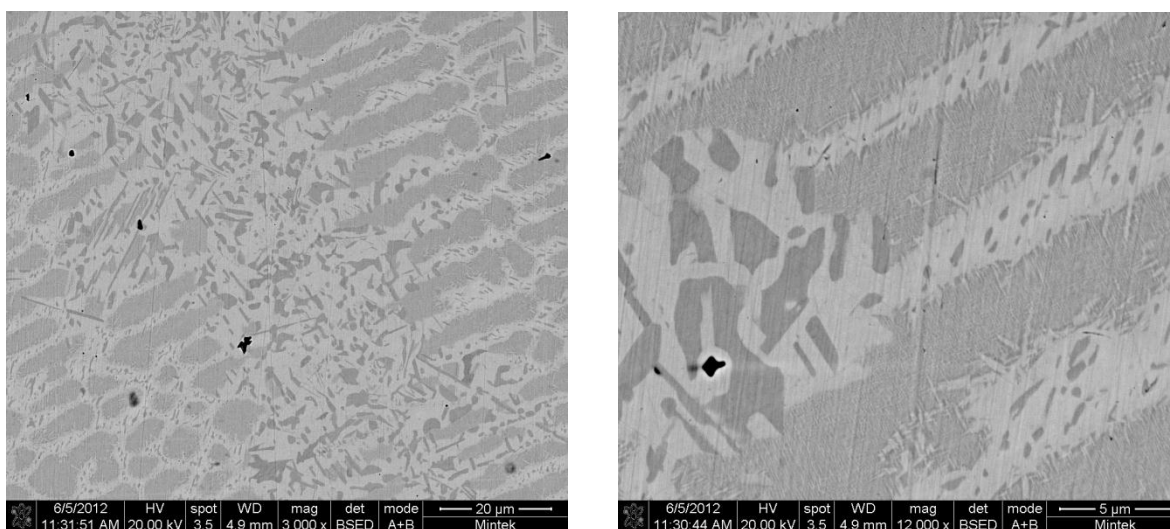


**Figure 6.21(a).** SEM-BSE image of annealed Alloy 30H, average composition  $\text{Pt}_{53.9}:\text{Al}_{18.0}:\text{Cr}_{4.3}:\text{Ru}_{1.4}:\text{V}_{21.9}:\text{Nb}_{1.0}$  (at. %), showing a medium  $\sim\text{Pt}_2\text{V}$  with a light solid state precipitate, dark  $\sim\text{PtV}$ , coarsened eutectoid of  $\sim\text{PtV} + \sim\text{Pt}_2\text{V}$ . **(b).** SEM-BSE image of annealed Alloy 30H, average composition  $\text{Pt}_{53.9}:\text{Al}_{18.0}:\text{Cr}_{4.3}:\text{Ru}_{1.4}:\text{V}_{21.9}:\text{Nb}_{1.0}$  (at. %), at a higher magnification, showing a medium  $\sim\text{Pt}_2\text{V}$  with a light solid state precipitate, dark  $\sim\text{PtV}$ , coarsened eutectoid of  $\sim\text{PtV} + \sim\text{Pt}_2\text{V}$ .

**Table 6.11. EDX composition analysis data for annealed Alloy 30H, average composition  $\text{Pt}_{53.9}:\text{Al}_{18.0}:\text{Cr}_{4.3}:\text{Ru}_{1.4}:\text{V}_{21.9}:\text{Nb}_{1.0}$  (at. %).**

Appearance	Pt	Al	Cr	Ru	V	Nb	Phase
Overall	53.4± 1.8	18.0± 1.4	4.3± 0.3	1.4± 0.9	21.9± 1.3	1.0± 0.8	-
Medium dendrites	56.4± 1.6	8.1± 1.9	5.1± 0.5	2.2± 0.6	26.9± 0.3	1.3± 0.8	$\sim\text{Pt}_2\text{V}$
Light	57.3± 1.3	24.8± 1.6	2.4± 0.3	0.2	14.8± 1.7	0.5± 0.1	$\sim\text{Pt}_3\text{Al}$
Dark	47.8± 1.9	7.7± 2.4	7.6± 0.9	2.6± 0.1	34.3± 3.4	0	$\sim\text{PtV}$
Eutectoid	55.6± 0.3	17.0± 1.3	4.5± 0.5	1.3± 0.3	21.6± 0.9	0	$\sim\text{PtV} + \sim\text{Pt}_2\text{V}$



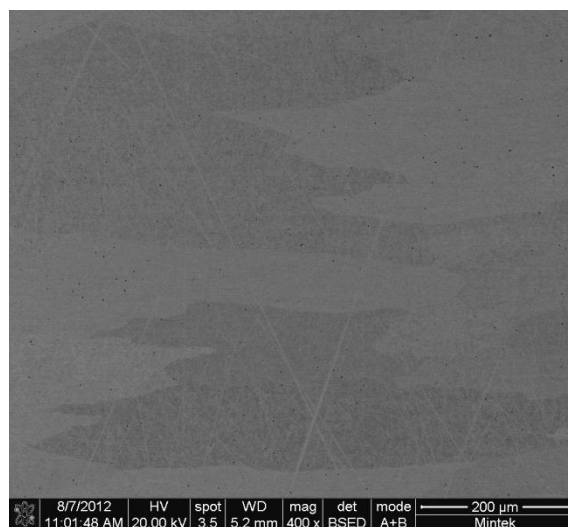


**Figure 6.23. SEM-BSE image of annealed Alloy 31H, average composition  $\text{Pt}_{74.1}:\text{Al}_{11.5}:\text{Cr}_{4.5}:\text{Ru}_{0.5}:\text{V}_{9.3}:\text{Nb}_{0.3}$  (at. %), showing single phase  $\sim\text{Pt}_3\text{Al}$  with grains at different orientations.**

**Table 6.12. EDX composition annealed analysis for Alloy 31H, average composition  $\text{Pt}_{74.1}:\text{Al}_{11.5}:\text{Cr}_{4.5}:\text{Ru}_{0.5}:\text{V}_{9.3}:\text{Nb}_{0.3}$  (at. %).**

Appearance	Pt	Al	Cr	Ru	V	Nb	Phase
Overall	73.9±0.6	11.5±0.6	4.5±0.3	0.5±0.2	9.3±0.3	0.3±0.1	-
Dark	73.2±0.7	11.3±0.7	4.1±0.4	0.6±0.4	9.4±0.4	1.4±0.4	$\sim\text{Pt}_3\text{Al}$
Light	73.3±0.4	11.1±1.0	4.4±0.3	1.0±0.4	9.3±0.4	0.9±0.5	$\sim\text{Pt}_3\text{Al}$

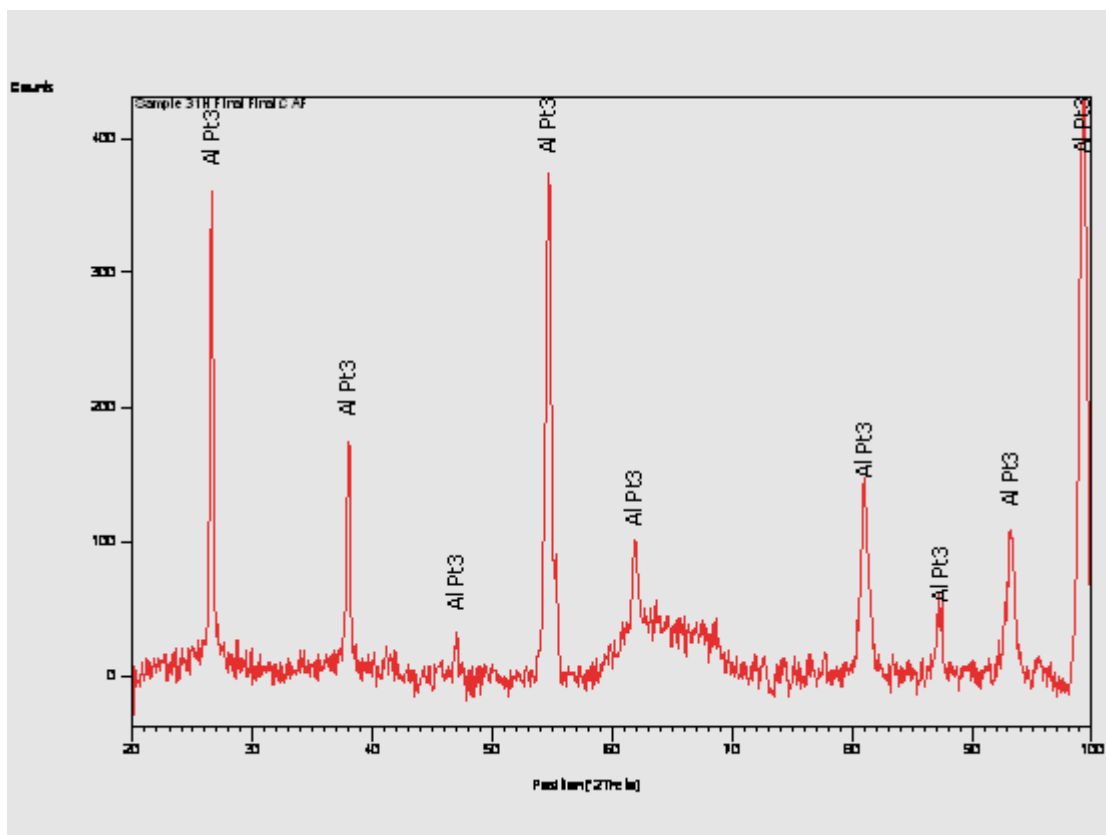


**Figure 6.24. XRD pattern of annealed Alloy 31H, average composition  $\text{Pt}_{74.1}:\text{Al}_{11.5}:\text{Cr}_{4.5}:\text{Ru}_{0.5}:\text{V}_{9.3}:\text{Nb}_{0.3}$  (at.%).**

## CHAPTER 7: MICROHARDNESS

There is an empirical relationship between hardness and strength of a metal. Since a hardness test is easier to perform compared to tensile strength test, it is often used to get an indication of the strength of a metal, especially when only small samples are available [1988Smi, 1990Die].

### 7.1 Experimental Procedure

The specimens were ground on silicon carbide down to 1200 grit and then diamond polished down to 1  $\mu\text{m}$ . The samples were then etched in a solution of 10 g NaCl in 100  $\text{cm}^3$  HCl (32% vol. concentration). Etching was done in a fume cupboard using a DC power supply, and a voltage range of 9V to 12V gave adequate results. The current density in the electrolyte was  $\sim 100 \text{ A.m}^{-2}$ . The counter electrode was a stainless steel wire suspended in the electrolyte solution [2012Ode1]. The microhardness indenter used incorporates an optical microscope, with a maximum magnification of 1000x, and only an etched surface could be seen clearly in the machine. If not etched, then sometimes it was difficult to differentiate between the sample and the mounting resin surface.

The hardness of the alloys was measured using a Vickers microhardness tester with a load of 300 g. At least five measurements were carried out to obtain an average hardness value. A 5 kg load was tried but it could only indent around the centre of the sample. An attempt to indent away from the centre resulted in the sample tilting and being driven out of the resin mounting.

### 7.2 Alloys of the Pt-Al-V System

#### 7.2.1 As-cast Alloys of the Pt-Al-V System

The results of hardness measurements of the as-cast Pt-Al-V samples are given in Table 7.1. The hardness values are superposed on the solidification projection in Figure 7.1. The images of the indentations are shown in the micrographs in Figures 7.2 to 7.11.



Alloys having Pt content more than 70 at.% had the lowest hardness values (less than 500 HV<sub>0.3</sub>), while 64% of the alloys had a relatively high hardness values of more than 500 HV<sub>0.3</sub>. The single ternary phase Alloy 16 had the highest hardness of 886 HV<sub>0.3</sub>, which would be expected, as would likely to be brittle. The images of the indentations are shown in the micrographs (Figures 7.2 to 7.10). Generally the load of 300 g used was too low to cause substantial cracks during indentation on these particular alloys. However, Alloy 16 had cracks before indentation confirming its brittle nature.

Hill [2001Hil2] reported Vickers macrohardness measurements of several Pt-based ternary alloys, at room temperature. Eight of these were Pt-Al-Z alloys (where Z was Ni, Ru or Re). Six of the alloys had Vickers hardness less than 500 HV in the as-cast and annealed conditions and the highest value was 530 HV. In his investigation of Pt-Al-Cr alloys, Süss [2007Süs] found that 75% of the alloys in the as-cast condition had Vickers hardness over 600 HV<sub>10</sub> at room temperature.

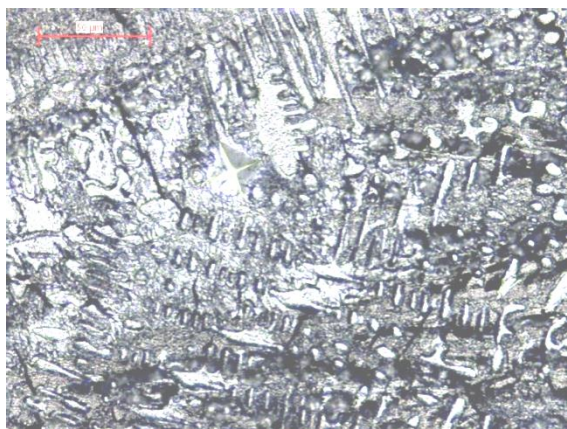


**Figure 7.1 Vickers hardness indentation on as-cast Alloy 1, average composition Pt<sub>64.3</sub>:Al<sub>26.6</sub>:V<sub>9.1</sub> (at.%).**

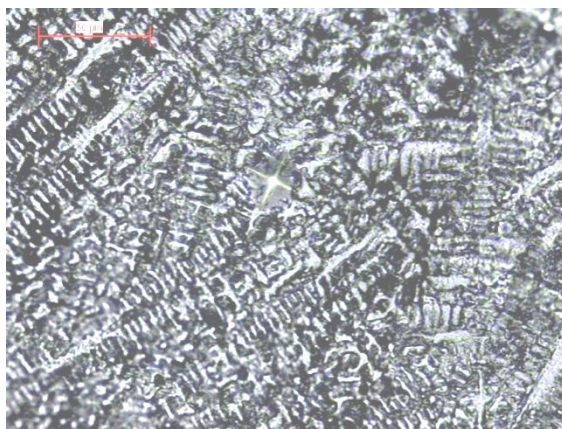


**Figure 7.2. Vickers hardness indentation on as-cast Alloy 2, average composition Pt<sub>59.1</sub>:Al<sub>23.1</sub>:V<sub>17.8</sub> (at.%).**

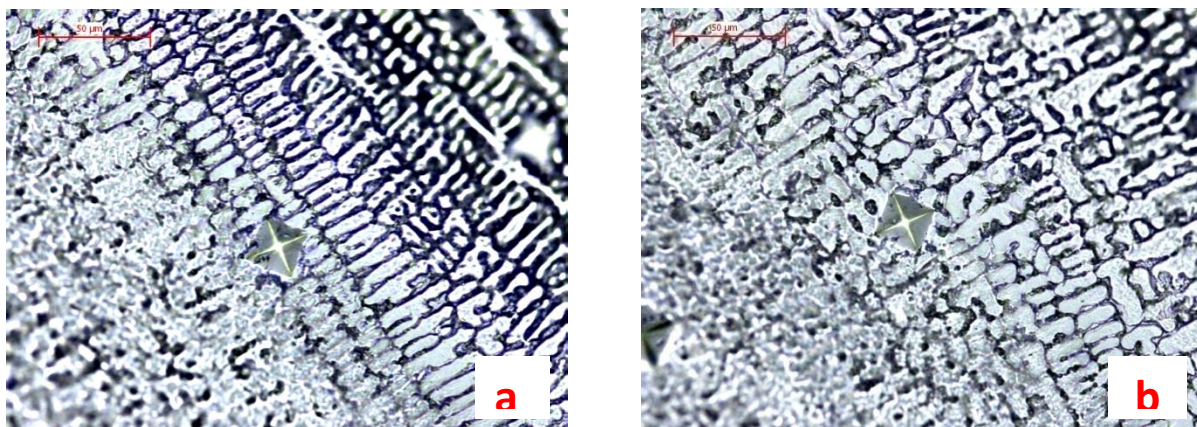


**Figure 7.3. Vickers hardness indentation on as-cast Alloy 3, average composition  $\text{Pt}_{69.3}:\text{Al}_{9.6}:\text{V}_{21.1}$  (at.%) (a) one area (b) image from a different area**

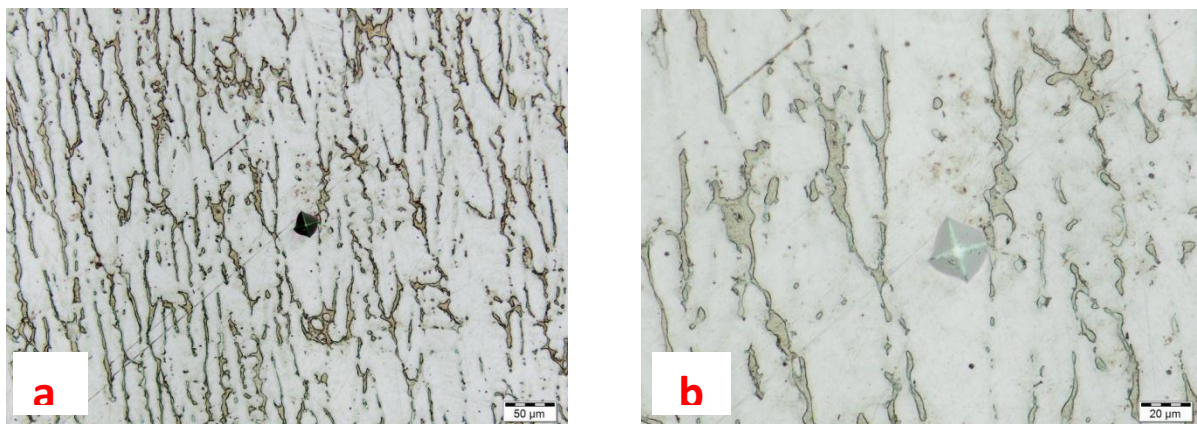


**Figure 7.4. Vickers hardness indentation on as-cast Alloy 4B average composition  $\text{Pt}_{69.8}:\text{Al}_{22.3}:\text{V}_{7.9}$  (at.%) (a) low magnification (b) higher magnification.**



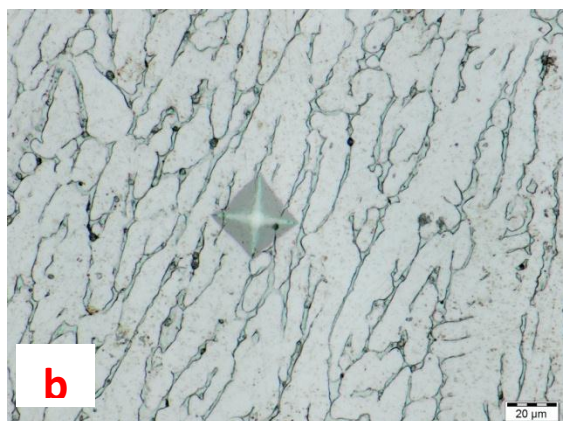
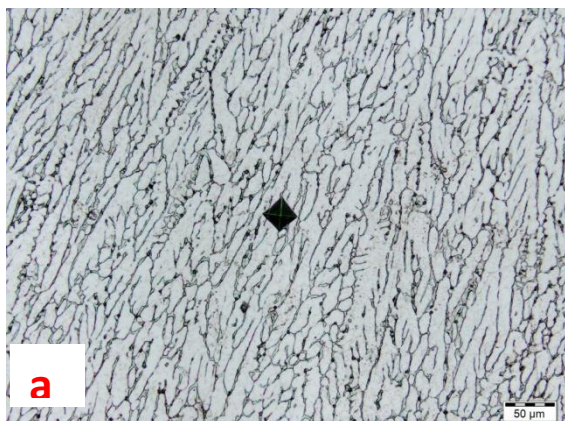


**Figure 7.5. Vickers hardness indentation on as-cast Alloy 10, average composition  $\text{Pt}_{83.9}:\text{Al}_6:\text{V}_{10.1}$  (at.%) (a) low magnification (b) higher magnification.**

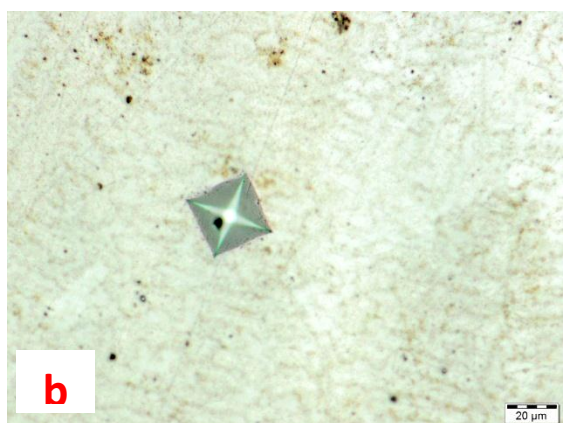
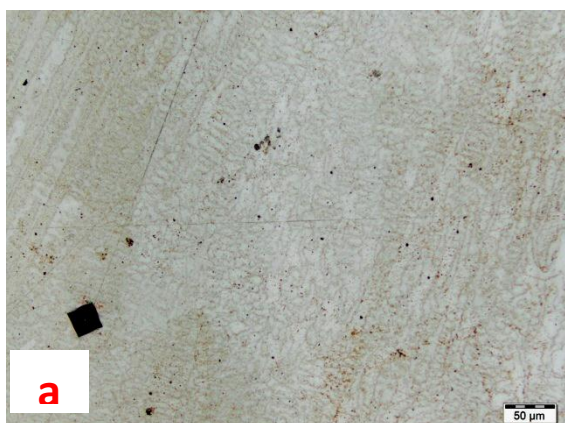


**Figure 7.6. Vickers hardness indentation on as-cast Alloy 11, average composition  $\text{Pt}_{80.9}:\text{Al}_{4.3}:\text{V}_{14.8}$  (at.%) (a) low magnification (b) higher magnification.**

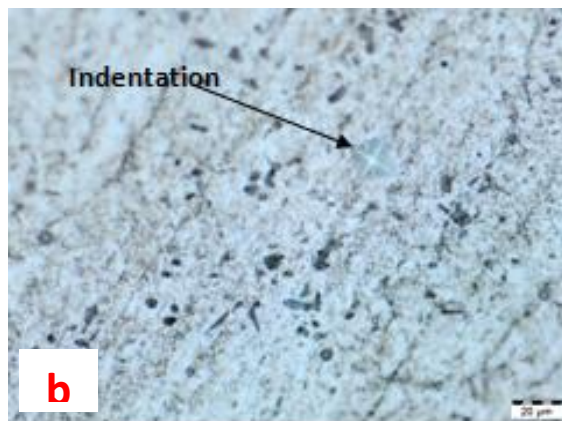
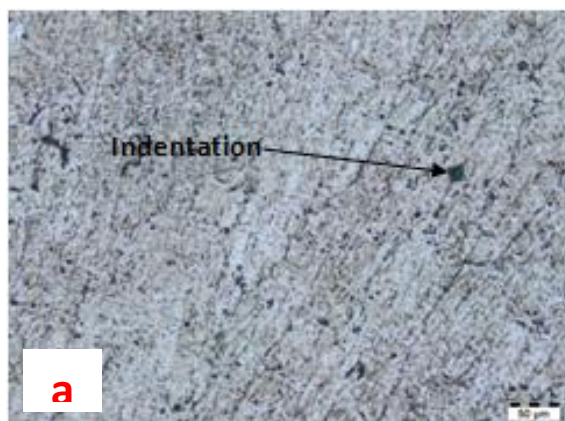


**Figure 7.7. Vickers hardness indentation on as-cast Alloy 12, average composition  $\text{Pt}_{52.5}:\text{Al}_{22.6}:\text{V}_{24.9}$  (at.%) (a) low magnification (b) higher magnification.**

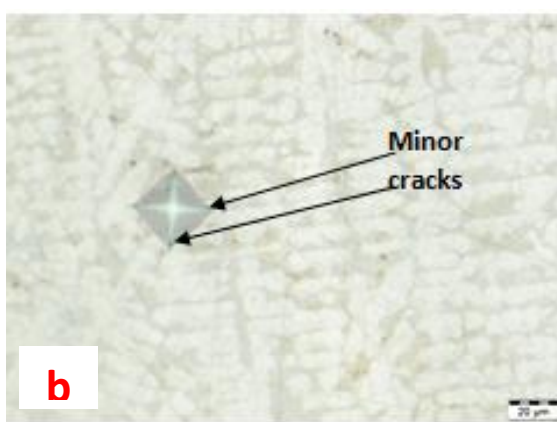
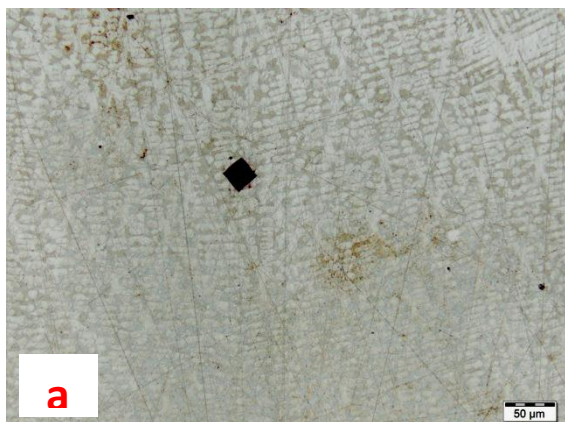


**Figure 7.8. Vickers hardness indentation on as-cast Alloy 14, average composition  $\text{Pt}_{84}:\text{Al}_2:\text{V}_4$  (at.%) (a) low magnification (b) higher magnification.**



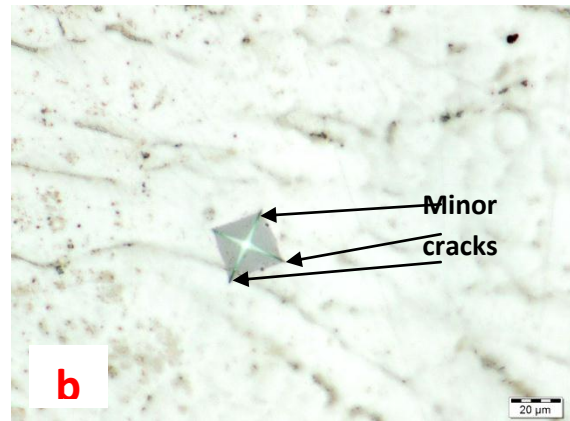
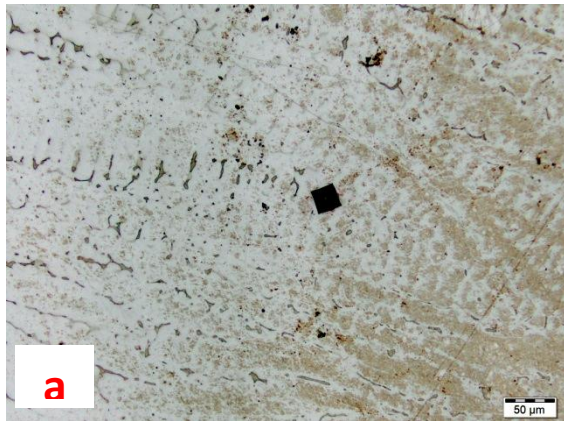


**Figure 7.9.** Vickers hardness indentation on as-cast Alloy 15, average composition  $\text{Pt}_{72.4}:\text{Al}_{13.7}:\text{V}_{13.9}$  (at.%) with (a) low magnification (b) higher magnification showing minor cracks at three corners.



**Figure 7.10.** Vickers hardness indentation on as-cast Alloy 16, average composition  $\text{Pt}_{56.9}:\text{Al}_{25.4}:\text{V}_{17.7}$  (at.%) with (a) low magnification (b) higher magnification showing minor cracks at three corners.

**Table 7.1. Hardness values (HV<sub>0.3</sub>) of annealed Pt-Al-V alloys compared to as-cast alloys.**

<b>Alloy ID No.</b>	<b>Average composition (at.%)</b>	<b>As-cast hardness (HV<sub>0.3</sub>)</b>	<b>Annealed hardness (HV<sub>0.3</sub>)</b>	<b>Phases present in the as-cast alloys</b>	<b>Phases present in the annealed alloys</b>
1	Pt <sub>64.3</sub> :Al <sub>26.6</sub> :V <sub>9.1</sub>	655±27	635±13	~Pt <sub>3</sub> Al, ~Pt <sub>5</sub> Al <sub>3</sub> , ~Pt <sub>2</sub> Al, ~Pt <sub>3</sub> V, PtAl	~Pt <sub>3</sub> Al, Pt <sub>5</sub> Al <sub>3</sub> , ~Pt <sub>2</sub> V, PtAl
2	Pt <sub>59.1</sub> :Al <sub>23.1</sub> :V <sub>17.8</sub>	746±35	624±26	~Pt <sub>2</sub> V, ~Pt <sub>5</sub> Al <sub>3</sub> , PtAl	~PtV, ~Pt <sub>5</sub> Al <sub>3</sub>
3	Pt <sub>69.3</sub> :Al <sub>9.6</sub> :V <sub>21.1</sub>	519±34	516±17	~Pt <sub>3</sub> V, ~Pt <sub>3</sub> Al, ~Pt <sub>2</sub> Al	~Pt <sub>2</sub> V, ~Pt <sub>3</sub> Al, ~PtV
4B	Pt <sub>69.8</sub> :Al <sub>22.3</sub> :V <sub>7.9</sub>	671±23	696±20	~Pt <sub>3</sub> Al, ~Pt <sub>2</sub> Al	~Pt <sub>3</sub> Al, ~Pt <sub>2</sub> Al
10	Pt <sub>83.9</sub> :Al <sub>6</sub> :V <sub>10.1</sub>	420±20	482±14	(Pt), ~Pt <sub>3</sub> Al	(Pt), ~Pt <sub>2</sub> V, ~Pt <sub>3</sub> Al
11	Pt <sub>80.9</sub> :Al <sub>4.3</sub> :V <sub>14.8</sub>	381±13	378±16	(Pt), ~Pt <sub>3</sub> Al	(Pt), ~Pt <sub>3</sub> Al
12	Pt <sub>52.5</sub> :Al <sub>22.6</sub> :V <sub>24.9</sub>	767±37	733±18	~PtV, ~PtV <sub>3</sub> , ~Pt <sub>5</sub> Al <sub>3</sub>	~PtV, ~PtV <sub>3</sub> , ~Pt <sub>5</sub> Al <sub>3</sub>
13	Pt <sub>53.7</sub> :Al <sub>8.8</sub> :V <sub>37.5</sub>	584±19	585±19	~PtV, ~PtV <sub>3</sub> , ~Pt <sub>5</sub> Al <sub>3</sub>	~PtV, ~PtV <sub>3</sub> , ~Pt <sub>5</sub> Al <sub>3</sub>
14	Pt <sub>84</sub> :Al <sub>12</sub> :V <sub>4</sub>	475±9	347±10	(Pt), ~Pt <sub>3</sub> Al	(Pt), ~Pt <sub>3</sub> Al
15	Pt <sub>72.4</sub> :Al <sub>13.7</sub> :V <sub>13.9</sub>	462±14	535±23	~Pt <sub>3</sub> Al, ~Pt <sub>2</sub> Al	~Pt <sub>3</sub> Al
16	Pt <sub>56.9</sub> :Al <sub>25.4</sub> :V <sub>17.7</sub>	886±23	-	τ <sub>2</sub>	~PtAl, ~PtV

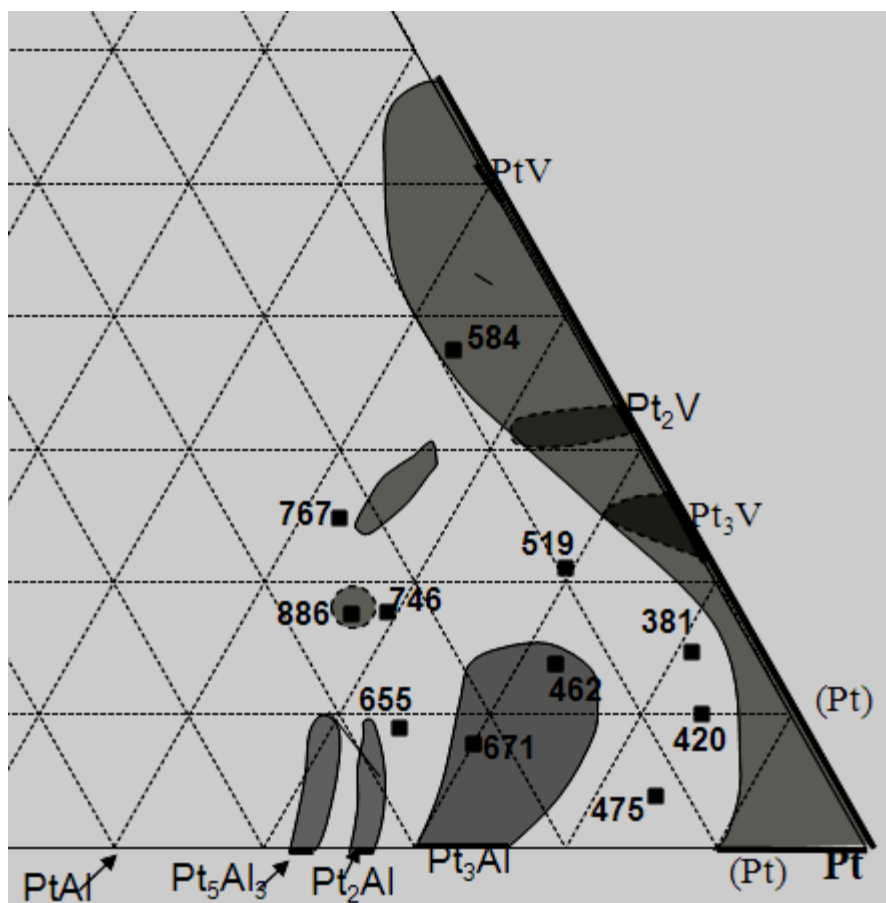


**Figure 7.11. Hardness values ( $HV_{0.3}$ ) of as-cast Pt-Al-V alloys superposed on solidification projection (at.%).**

### 7.2.2 Pt-Al-V Alloys Annealed at 1000°C for 1500 Hours

The hardness values for annealed alloys of the Pt-Al-V system are given in Table 7.1. The values are superposed on the isothermal section in Figure 7.2.

Seventy percent of the annealed alloys have hardness values higher than 500  $HV_{0.3}$  and the rest, which have a relatively high Pt content above 80 at.%, have hardness values below 500  $HV_{0.3}$ . About 45% of the alloys had hardness values over 600  $HV_{0.3}$ . Annealed Alloy 16H cracked and disintegrated while being ground in preparation for polishing and etching, indicating that it was very brittle and it also had the ternary phase in as-cast condition. In all the alloys (Figures 7.1 to 7.21), there was no cracking or noticeable deformation around the indentations, therefore their toughness could not be quantitatively assessed, although the toughness must have been reasonable (except for Alloy 16 which had comprised the ternary phase in the as-cast condition

and had cracks before indentation). However, this can be attributed to the relatively small load used in the microhardness testing. The small load was chosen because of the small size of the samples (~1 g). However, these hardness values for the alloys whether in the as-cast or annealed condition are very high compared to that of pure platinum which is very soft and ductile with a Vickers hardness of 50 HV (the load was not specified) [2008Mur].

These results are comparable to what Süß [2007Süs] found in his investigation of Pt-Al-Cr alloys, where just over half of the annealed alloys had hardness values above 600 HV<sub>10</sub>. Only one of the Pt-Al based alloys, Pt<sub>62</sub>:Al<sub>19</sub>:Ni<sub>19</sub>, investigated by Hill [2001Hil2] had a hardness value of 530 HV (the load used was not specified). The rest had hardness below 500 HV. The quaternary alloys discussed in Section 2.3 of this thesis also had much lower hardness values, with the highest being 430 HV<sub>10</sub>.

The phase ~Pt<sub>2</sub>Al disappeared during annealing of Alloy 1H, but the hardness remained more or less the same. In Alloy 2H, two phases, ~Pt<sub>2</sub>V and ~PtAl disappeared and a new phase, ~PtV formed, while ~Pt<sub>5</sub>Al<sub>3</sub> was present both in the as-cast and annealed condition. The hardness of Alloy 2H reduced by ~100 HV<sub>0.3</sub>, suggesting that the either or both of the two phases which disappeared contributed to the higher hardness in the as-cast condition.

The hardness of Alloys 3 and 4B remained more or less the same after annealing. In Alloy 3, the two phases ~Pt<sub>3</sub>V and ~Pt<sub>2</sub>Al disappeared and two new phases, ~Pt<sub>2</sub>V and ~PtV formed, while in Alloy 4B there was no change in the phases.

In Alloy 10, a new phase ~Pt<sub>2</sub>V formed during annealing, while the two phases (Pt) and ~Pt<sub>3</sub>Al were retained. There was a slight increase of hardness from 420 HV<sub>0.3</sub> to 482 HV<sub>0.3</sub> suggesting that the new phase, as expected, was responsible for the increase. The phases in Alloy 11 remained the same and, as expected, the hardness also remained the same after annealing.

The hardness of Alloys 12 and 13 remained the same after annealing if the standard deviations are taken into account. In both alloys, the ternary phase  $\tau_1$  disappeared during annealing and two



new phases  $\sim\text{PtV}_3$  and  $\sim\text{Pt}_5\text{Al}_3$  formed. This is not surprising as ternary phases are expected to be hard and the Pt-V intermetallics are also generally hard.

The hardness of Alloy 14 decreased by  $\sim 100$  HV while the two phases (Pt) and  $\sim\text{Pt}_3\text{Al}$  remained the same in the as-cast and annealed conditions. The decrease in hardness may be explained by coarsening of the phases during annealing. Alloy 15 changed from two-phase,  $\sim\text{Pt}_3\text{Al}$  and  $\sim\text{Pt}_2\text{Al}$ , to single phase,  $\sim\text{Pt}_3\text{Al}$ , while the hardness increased from 462 HV<sub>0.3</sub> to 535 HV<sub>0.3</sub>. This suggests that  $\sim\text{Pt}_2\text{Al}$  is a soft phase compared to  $\sim\text{Pt}_3\text{Al}$  and its disappearance contributed to the increase in hardness.

Alloy 16 was single ternary phase,  $\tau_2$ , and was the hardest alloy, even in the as-cast condition with Vickers hardness of 886 HV<sub>0.3</sub>. Further evidence of its hardness and brittleness were the visible cracks in the as-cast condition. It disintegrated while being removed from the resin mounting and it was not possible to measure the hardness in the annealed condition.



**Figure 7.12. Vickers hardness indentation on annealed Alloy 1H, average composition  $\text{Pt}_{64.3}:\text{Al}_{26.6}:\text{V}_{9.1}$  (at. %).**



**Figure 7.13. Vickers hardness indentation on annealed Alloy 2H, average composition  $\text{Pt}_{59.1}:\text{Al}_{23.1}:\text{V}_{17.8}$  (at. %).**

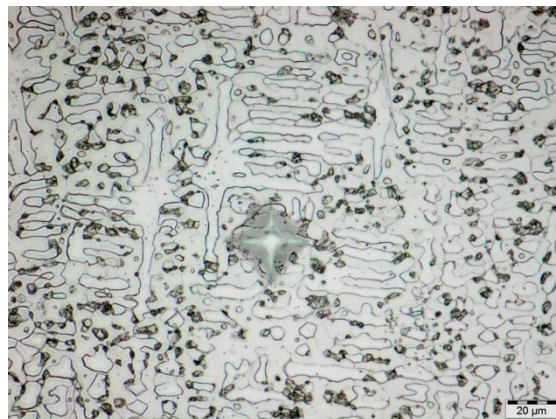


**Figure 7.14. Vickers hardness indentation on annealed Alloy 3H, average composition  $\text{Pt}_{69.3}:\text{Al}_{9.6}:\text{V}_{21.1}$  (at. %).**

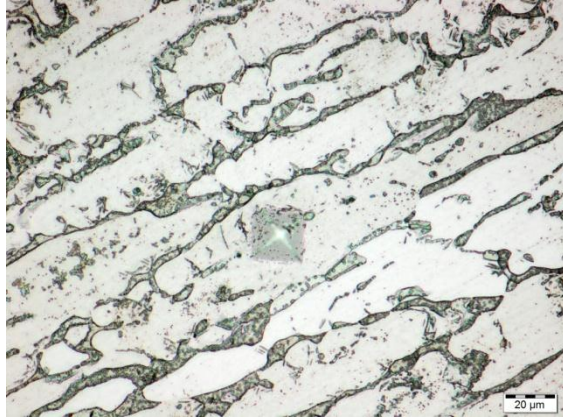


**Figure 7.15. Vickers hardness indentation on annealed Alloy 4BH, average composition  $\text{Pt}_{69.8}:\text{Al}_{22.3}:\text{V}_{7.9}$  (at. %).**

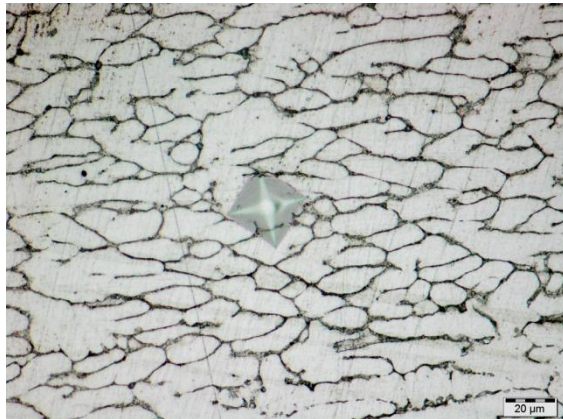


**Figure 7.16. Vickers hardness indentation on annealed Alloy 10H, average composition  $\text{Pt}_{83.9}:\text{Al}_6:\text{V}_{10.1}$  (at. %).**

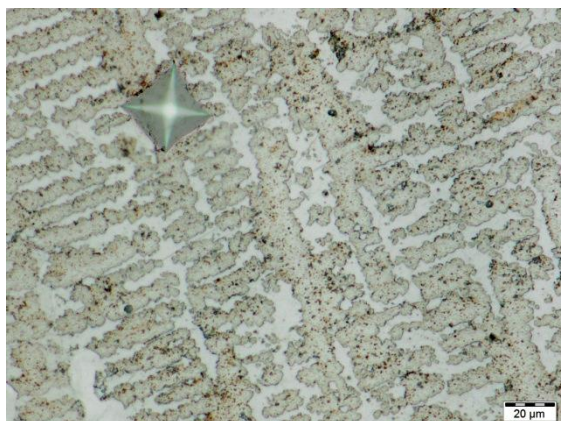


**Figure 7.17. Vickers hardness indentation on annealed Alloy 11H, average composition  $\text{Pt}_{80.9}:\text{Al}_{4.3}$ :**



**Figure 7.18. Vickers hardness indentation on annealed Alloy 12H, average composition  $\text{Pt}_{52.5}:\text{Al}_{22.6}:\text{V}_{24.9}$  (at.%).**



**Figure 7.19. Vickers hardness indentation on annealed Alloy 13H, average composition  $\text{Pt}_{53.7}:\text{Al}_{8.8}:\text{V}_{37.5}$  (at.%).**





**Figure 7.20. Vickers hardness indentation on annealed Alloy 14H, average composition  $\text{Pt}_{81.6}:\text{Al}_{14.5}:\text{V}_{3.7}$  (at.%).**

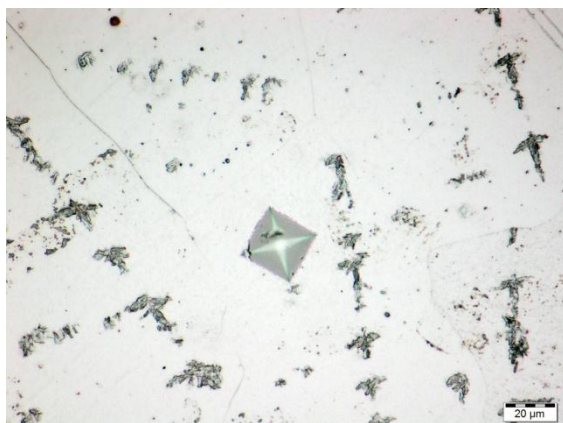


**Figure 7.21. Vickers hardness indentation on annealed Alloy 15H, average composition  $\text{Pt}_{72.4}:\text{Al}_{13.7}:\text{V}_{13.9}$  (at.%).**

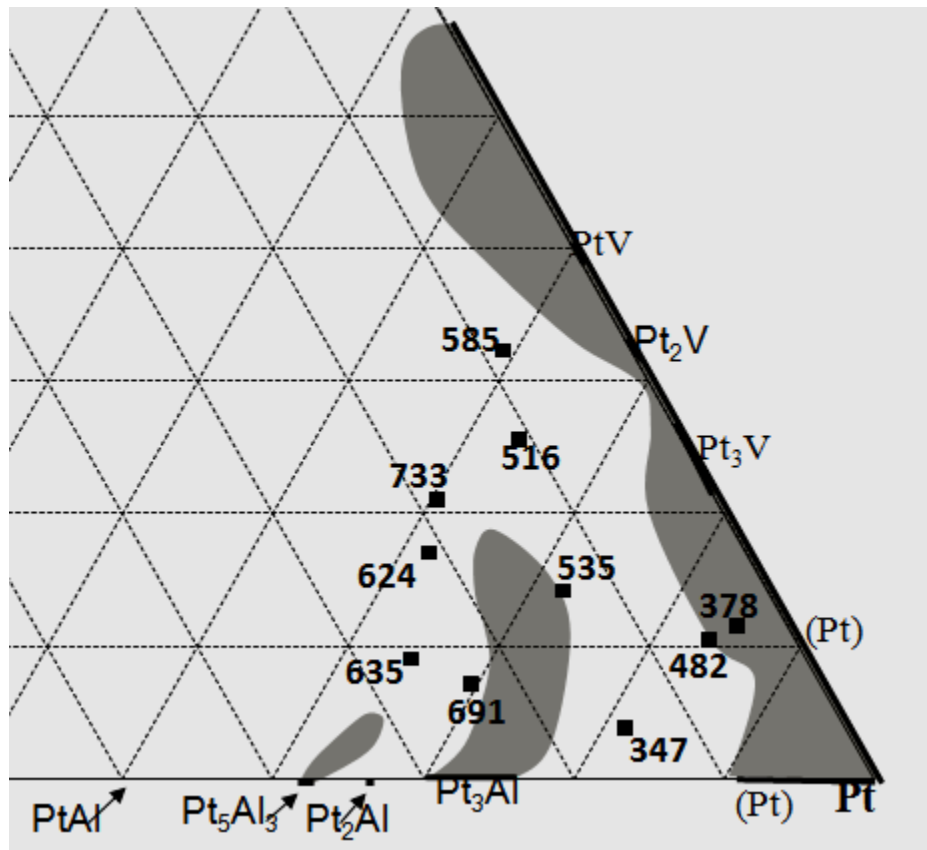


**Figure 7.22.** Hardness values ( $HV_{0.3}$ ) of annealed Pt-Al-V alloys superposed on isothermal section at 1000°C (at.%).

### 7.3 Alloys of the Pt-Cr-V System

#### 7.3.1 As-cast Pt-Cr-V Alloys

The results of microhardness tests of Pt-Cr-V alloys are given in Table 7.3. The values are superposed on the solidification projection in Figure 7.4.

The alloys having ternary phase dendrites (Alloys 18, 19 and 22) had very high hardness values, as expected. Alloy 19 had the highest hardness value ( $1109 \pm 25 HV_{0.3}$ ). The second hardest alloy was Alloy 22 which had a hardness of  $1086 \pm 28 HV_{0.3}$ . All the indentations on Alloy 8 were on the eutectic areas and the high hardness value of  $936 HV_{0.3}$  reflects the high hardness of the ternary phase component of the eutectic, rather than the solid solution component (Figure 7.27(a) and (b)). The single phase Alloys 5 and 6 which had high Pt content had the lowest hardness

values. Alloy 17 which also had high Pt content had a similarly low hardness. The SEM-BSE image of Alloy 17 and its plot indicated single phase alloy. However, the XRD analysis indicated that though the alloy had predominantly  $\sim\text{Pt}_3\text{V}$ , there was a small amount of (Pt) (Figure 5.15). The etched optical microscope image shows fine precipitates at the grain boundaries. The inward curvature of the edge of the indentation shows that these dark precipitates in the grain boundaries are harder than the lighter phase (Figure 7.27(b)).

The rest of the alloys all had relatively high hardness values, except for Alloy 25 which had a low hardness value of 358  $\text{HV}_{0.3}$ . The images of the indentations are shown in Figures 7.24 to 7.36. There were no cracks or deformation around the indentations, probably due to the low indentation load of 300 g.

The hardness values were comparable to those obtained by Süß [2007Süs] in his investigation of Pt-Al-Cr alloys. Süß used a load of 10 kg and many of the alloys cracked and deformed around the indentations. However, the highest Vickers hardness values obtained by Süß were between 800  $\text{HV}_{10}$  to 900  $\text{HV}_{10}$ . The hardness of the Pt-Cr-V alloys investigated in this work were also generally much higher than the ternary Pt-Al based alloys investigated by Hill [2001Hil2] which had the highest hardness value of 530 HV (the load used was not specified). The quaternary alloys discussed in Section 2.3 of this thesis also had much lower hardness values with highest being 430  $\text{HV}_{10}$ . However, these hardness values for the alloys whether in the as-cast or annealed condition, are very high compared to that of pure platinum which is very soft and ductile with a Vickers hardness of 50 HV [2008Mur].

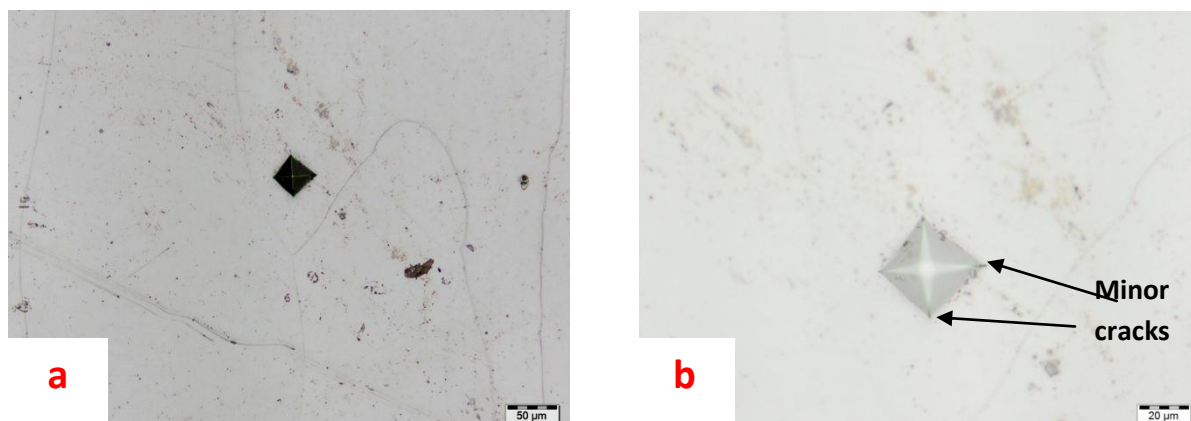


**Figure 7.23. Vickers hardness indentation on as-cast Alloy 5, average composition  $\text{Pt}_{73.8}\text{Cr}_{16.9}\text{V}_{9.3}$  (at.%), with (a) low magnification (b) a higher magnification showing two minor cracks at the corners.**

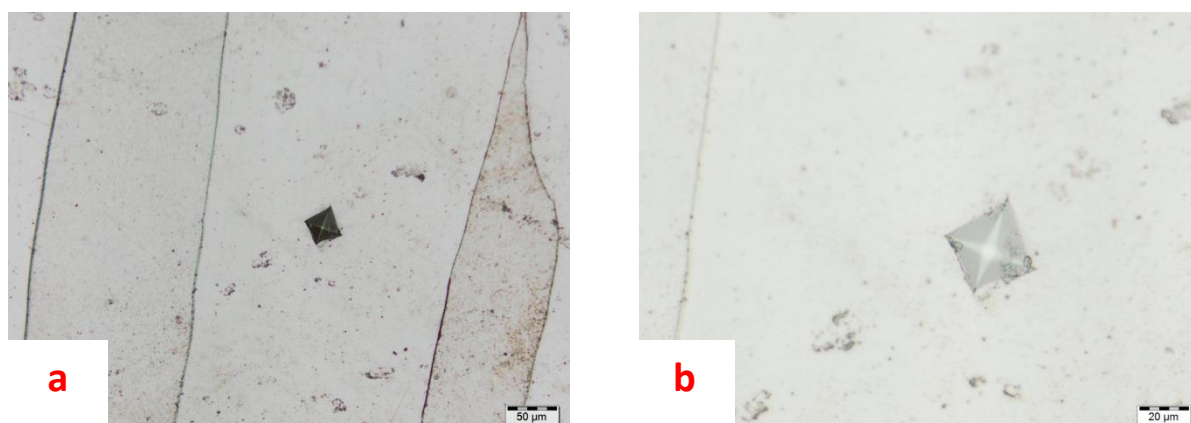


**Figure 7.24. Vickers hardness indentation on as-cast Alloy 6, average composition  $\text{Pt}_{72.3}\text{Cr}_{8.3}\text{V}_{19.4}$  (at.%), with (a) low magnification (b) a higher magnification.**



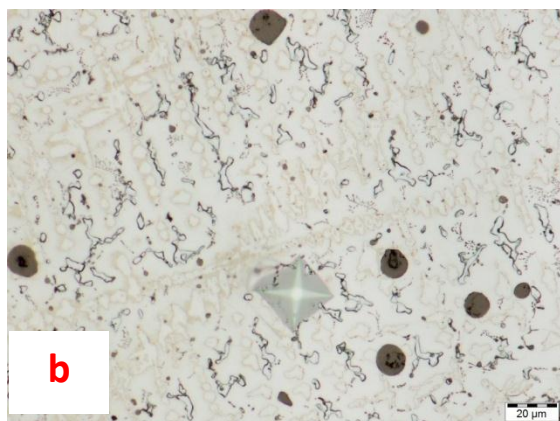
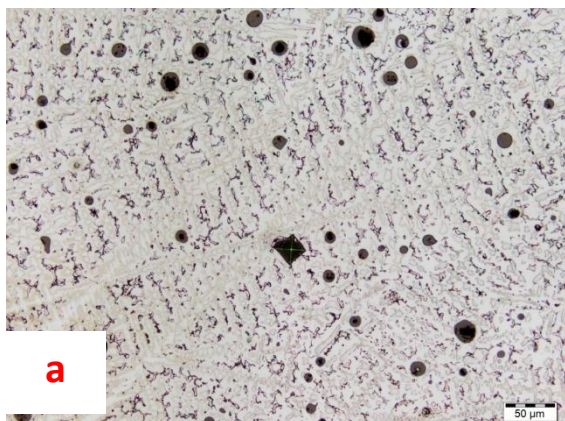


**Figure 7.25. Vickers hardness indentation on as-cast Alloy 7, average composition  $\text{Pt}_{33.4}:\text{Cr}_{45.8}:\text{V}_{20.8}$  (at.%), with (a) low magnification (b) a higher magnification.**

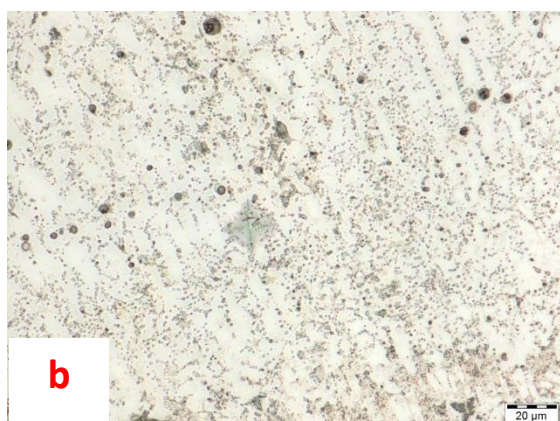
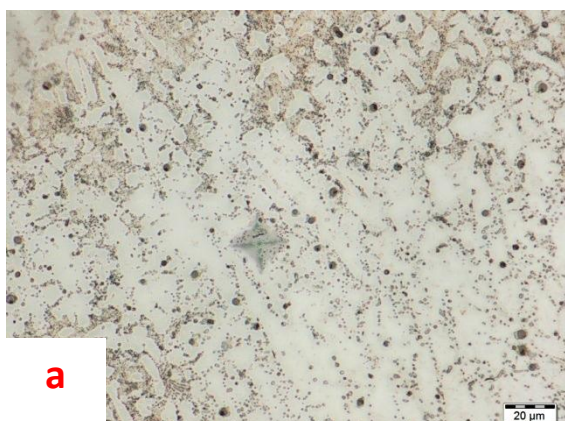


**Figure 7.26. Vickers hardness indentation on as-cast Alloy 8, average composition  $\text{Pt}_{53.0}:\text{Cr}_{22.4}:\text{V}_{24.5}$  (at.%), with (a) one area (b) a different area**

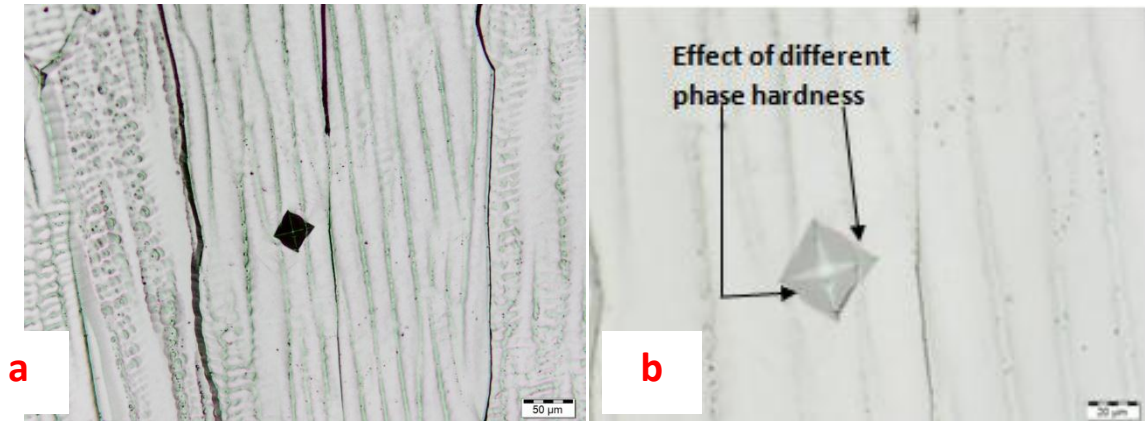


**Figure 7.27. Vickers hardness indentation on as-cast Alloy 17, average composition  $\text{Pt}_{68.5}:\text{Cr}_{16.2}:\text{V}_{15.3}$  (at.%), with (a) low magnification (b) a higher magnification.**

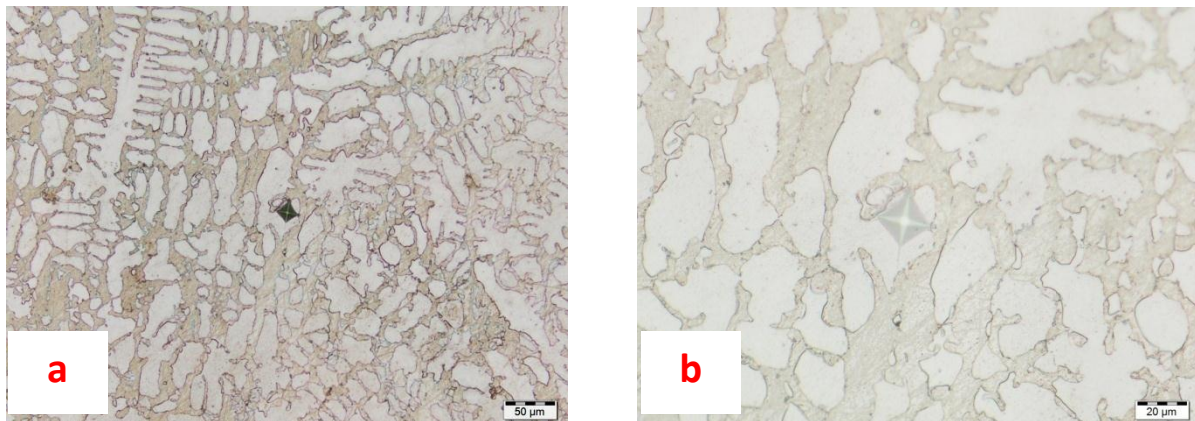


**Figure 7.28. Vickers hardness indentation on as-cast Alloy 18, average composition  $\text{Pt}_{32.8}:\text{Cr}_{28.6}:\text{V}_{38.6}$  (at.%), with (a) low magnification (b) a higher magnification.**



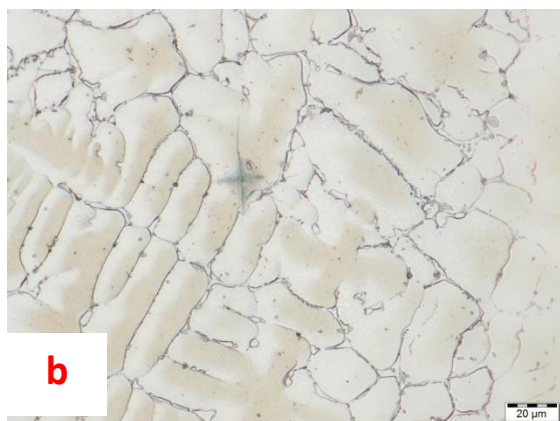
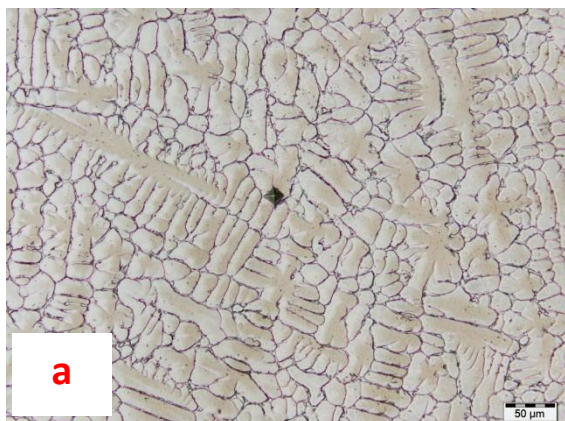


**Figure 7.29. Vickers hardness indentation on as-cast Alloy 19, average composition  $\text{Pt}_{25.8}\text{Cr}_{42.9}\text{V}_{31.3}$  (at.%), (a) low magnification (b) a higher magnification.**

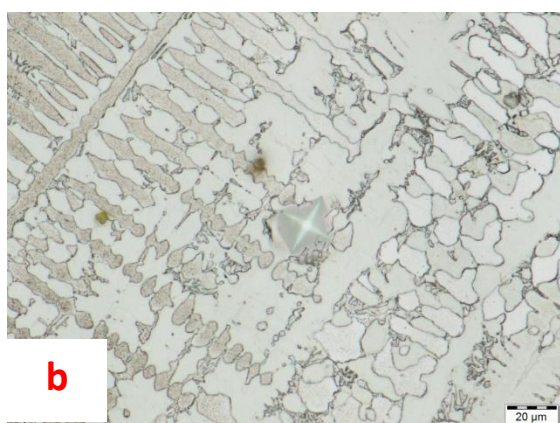
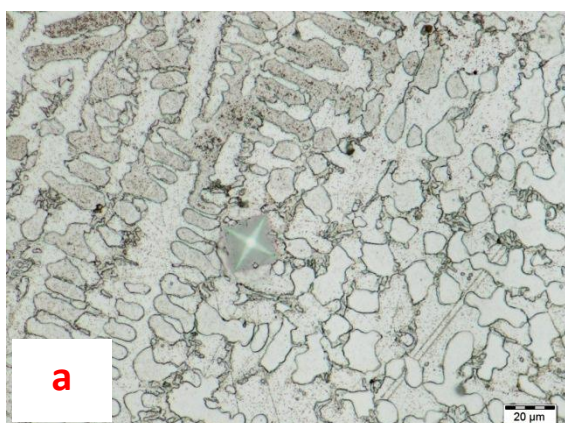


**Figure 7.30. Vickers hardness indentation on as-cast Alloy 20, average composition  $\text{Pt}_{16.8}\text{Cr}_{13.4}\text{V}_{69.8}$  (at.%), (a) one area (b) a different area**

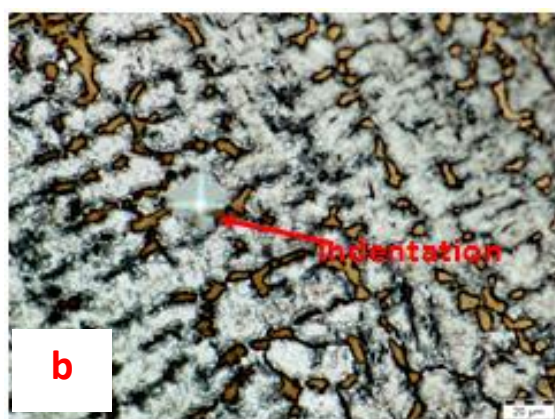
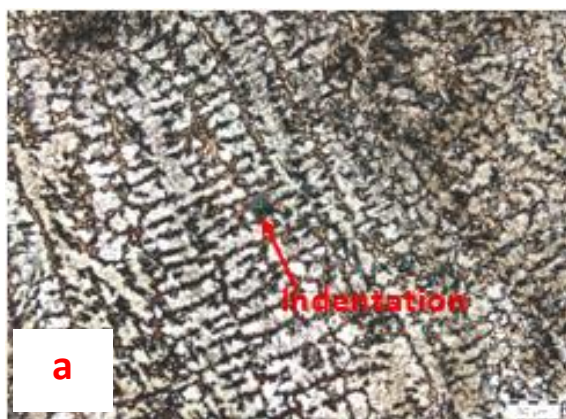


**Figure 7.31. Vickers hardness indentation on as-cast Alloy 21, average composition  $\text{Pt}_{16.8}:\text{Cr}_{13.4}:\text{V}_{69.8}$  (at.%), (a) low magnification (b) a higher magnification.**

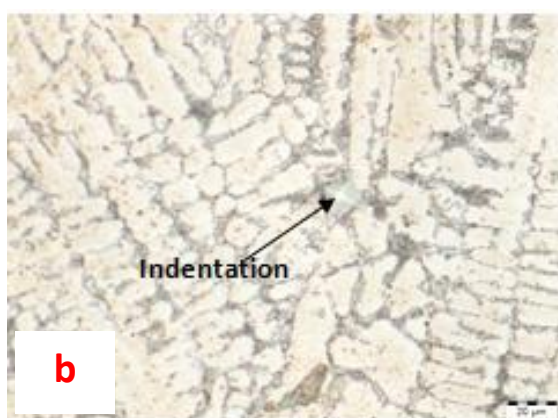


**Figure 7.32. Vickers hardness indentation on as-cast Alloy 22, average composition  $\text{Pt}_{28.7}:\text{Cr}_{27.2}:\text{V}_{44.1}$  (at.%), (a) low magnification (b) a higher magnification.**



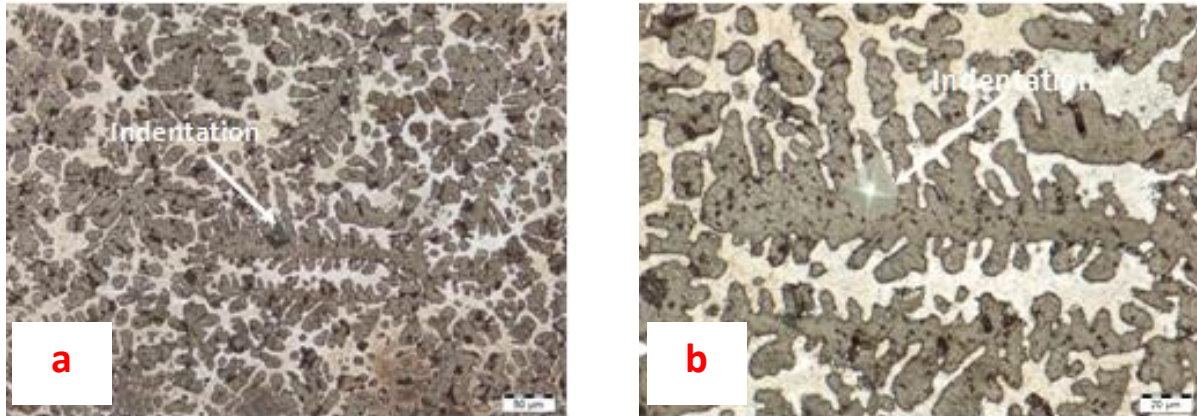


**Figure 7.33. Vickers hardness indentation on as-cast Alloy 23, average composition  $\text{Pt}_{16.5}:\text{Cr}_{56.1}:\text{V}_{27.4}$  (at.%), (a) low magnification (b) a higher magnification.**

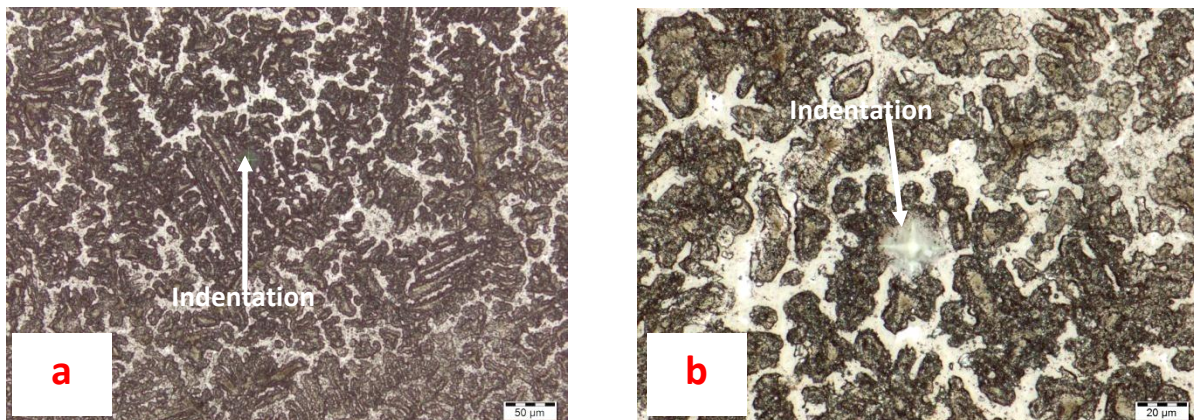


**Figure 7.34. Vickers hardness indentation on as-cast Alloy 24, average composition  $\text{Pt}_{14.9}:\text{Cr}_{73.7}:\text{V}_{11.4}$  (at.%), with (a) low magnification (b) a higher magnification.**

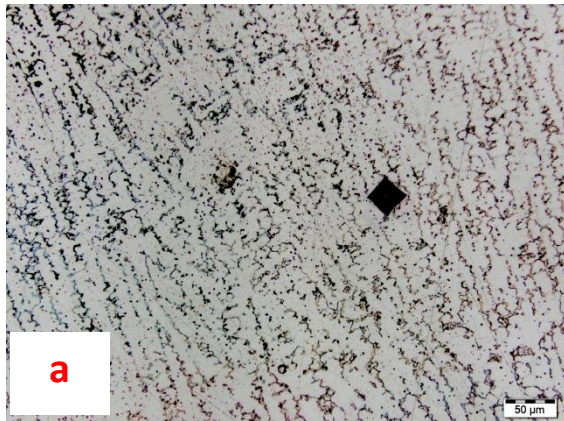


**Figure 7.35. Vickers hardness indentation on as-cast Alloy 25, average composition  $\text{Pt}_{34.1}:\text{Cr}_{57.4}:\text{V}_{8.5}$  (at.%), (a) low magnification (b) a higher magnification.**

**Table 7.2. Hardness values (HV<sub>0.3</sub>) of annealed Pt-Cr-V alloys compared to as-cast alloys.**

<b>Alloy ID No.</b>	<b>Average composition (at.%)</b>	<b>As-cast hardness (HV<sub>0.3</sub>)</b>	<b>Annealed hardness (HV<sub>0.3</sub>)</b>	<b>Phases present in the as-cast alloys</b>	<b>Phases present in the annealed alloys</b>
5	Pt <sub>73.8</sub> :Cr <sub>16.9</sub> :V <sub>9.3</sub>	272±8	280±26	~Pt <sub>3</sub> V	~Pt <sub>3</sub> V
6	Pt <sub>72.3</sub> :Cr <sub>8.3</sub> :V <sub>19.4</sub>	317±8	330±17	~Pt <sub>3</sub> V	~Pt <sub>2</sub> V, Pt <sub>3</sub> V
7	Pt <sub>33.4</sub> :Cr <sub>45.8</sub> :V <sub>20.8</sub>	527±28	589±23	~Cr <sub>3</sub> Pt, A15(~Cr <sub>3</sub> Pt), τ	~Cr <sub>3</sub> Pt, ~CrPt A15(~Cr <sub>3</sub> Pt), τ
8	Pt <sub>53.0</sub> :Cr <sub>22.4</sub> :V <sub>24.5</sub>	936±59	637±28	~CrPt, τ	~Cr <sub>3</sub> Pt, τ
17	Pt <sub>68.5</sub> :Cr <sub>16.2</sub> :V <sub>15.3</sub>	291±19	350±8	~Pt <sub>3</sub> V	~Pt <sub>3</sub> V
18	Pt <sub>32.8</sub> :Cr <sub>28.6</sub> :V <sub>38.6</sub>	854±30	1086±46	~Cr <sub>3</sub> Pt, τ	~Pt <sub>2</sub> V, τ, ~CrPt
19	Pt <sub>25.8</sub> :Cr <sub>42.9</sub> :V <sub>31.3</sub>	1109±25	-	τ, A15(~Cr <sub>3</sub> Pt), ~Cr <sub>3</sub> Pt	A15(~Cr <sub>3</sub> Pt), ~Cr <sub>3</sub> Pt, τ
20	Pt <sub>38.8</sub> :Cr <sub>14.2</sub> :V <sub>47.0</sub>	796±35	923±57	~PtV <sub>3</sub> , ~PtV, τ	~PtV <sub>3</sub> , ~PtV, τ
21	Pt <sub>16.8</sub> :Cr <sub>13.4</sub> :V <sub>69.8</sub>	618±25	-	(V,Cr), ~PtV <sub>3</sub>	(V,Cr), ~PtV <sub>3</sub>
22	Pt <sub>28.7</sub> :Cr <sub>27.2</sub> :V <sub>44.1</sub>	1086±28	-	~Cr <sub>3</sub> Pt, ~PtV <sub>3</sub> , τ, (V,Cr)	~PtV <sub>3</sub> , τ, (V,Cr)
23	Pt <sub>16.5</sub> :Cr <sub>56.1</sub> :V <sub>27.4</sub>	707±41	837±46	(V,Cr), A15(~Cr <sub>3</sub> Pt)	(V,Cr), A15(~Cr <sub>3</sub> Pt)
24	Pt <sub>14.9</sub> :Cr <sub>73.7</sub> :V <sub>11.4</sub>	692±73	544±20	(V,Cr), A15(~Cr <sub>3</sub> Pt)	(V,Cr), A15(~Cr <sub>3</sub> Pt)
25	Pt <sub>34.1</sub> :Cr <sub>57.4</sub> :V <sub>8.5</sub>	358±9	838±27	~Cr <sub>3</sub> Pt, A15(~Cr <sub>3</sub> Pt)	~Cr <sub>3</sub> Pt, A15(~Cr <sub>3</sub> Pt)

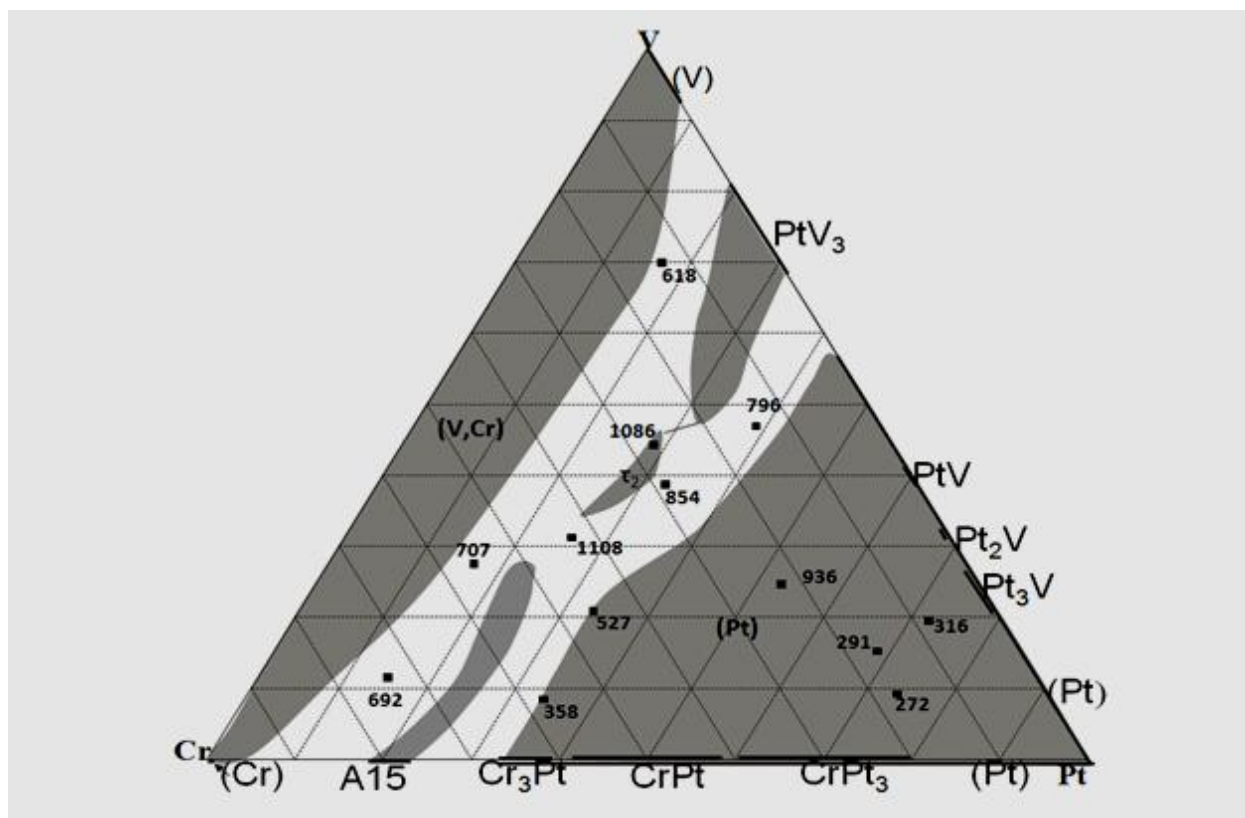


**Figure 7.36. Hardness values ( $HV_{0.3}$ ) of as-cast Pt-Cr-V alloys superposed on the solidification projection (at.%).**

### 7.3.2 Pt-Cr-V Alloys Annealed at 1000°C for 1500 Hours

The hardness values of annealed Pt-Cr-V alloys are given in Table 7.4. The values are superposed on the isothermal section at 1000°C in Figure 7.4. Alloys 19H, 21H and 22H cracked and disintegrated, due to extreme brittleness, before hardness values could be measured.

There was a general increase in hardness values after annealing the Pt-Cr-V alloys except for Alloys, 8H and 24H which had lower values, and this was probably due to coarsening. Alloys 18, 19 and 22 (as-cast) had ternary phase dendrites with high hardness values, in the as-cast condition, as expected. The three alloys also exhibited extreme brittleness. The annealed Alloys 19H and 22H cracked and disintegrated while being removed from the resin mounting. Alloy 18H cracked, but stayed as one piece, and therefore it was possible to undertake microhardness testing. The annealed Alloy 21H also cracked and disintegrated while being removed from the resin mounting. The alloys with high Pt content had the lowest hardness values.



If the three annealed alloys, which disintegrated, are included among those with hardness values exceeding 600 HV<sub>0.3</sub>, then ~62% of the alloys had Vickers hardness higher than 600 HV<sub>0.3</sub>. This shows that the alloys were generally harder than those investigated by Süß [2007Süs], where just over half of the alloys had Vickers hardness higher than 600 HV<sub>10</sub>. Again if the same three alloys are included among those that had hardness values higher than 750 HV<sub>0.3</sub>, then slightly more than half the alloys had hardness values more than 750 HV<sub>0.3</sub> compared to those investigated by Süß [2007Süs], where only three of the alloys (~17%) had hardness values higher than 750 HV<sub>10</sub>. The assumption that the three alloys which disintegrated had hardness values higher than 750 HV<sub>0.3</sub> is valid because the hardest annealed alloy whose hardness was measured is Alloy 18H with a hardness value of 1086 HV<sub>0.3</sub>, and there were other three alloys with hardness values exceeding 800 HV<sub>0.3</sub>.

These alloys were much harder than Pt-Al based alloys investigated by Hill [2001Hil2] where the hardest alloy had a Vickers hardness of 530 HV (the load used was not specified). They were also much harder than the quaternary alloys discussed in Section 2.3 of this thesis where the hardest alloy had a Vickers hardness of 430 HV<sub>10</sub>.

The hardness of Alloys 5H and 6H remained more or less the same after annealing. Alloy 5H remained single phase ~Pt<sub>3</sub>V after annealing, while Alloy 6H changed from a single phase structure of ~Pt<sub>3</sub>V to a two-phase structure of ~Pt<sub>2</sub>V and ~Pt<sub>3</sub>V. This shows that the hardness of the two phases ~Pt<sub>2</sub>V and Pt<sub>3</sub>V are nearly the same. Alloy 17H, which had also been single phase ~Pt<sub>3</sub>V in the as-cast condition, retained the same phase after annealing. There was a slight increase in its hardness.

The phases in Alloy 7H stayed the same before and after annealing and there was not much change in the hardness as expected. However, there was a substantial decrease in the hardness of Alloy 8H after annealing, although the phases were the same. This decrease is attributed to coarsening.

In Alloy 18H, the phase ~Cr<sub>3</sub>Pt disappeared and ~Pt<sub>2</sub>V formed after annealing, while the ternary phase,  $\tau_3$ , was present both in the as-cast and annealed condition. The increase of hardness from

854 HV<sub>0.3</sub> to 1085 HV<sub>0.3</sub> is therefore attributed to  $\sim\text{Pt}_2\text{V}$ , as expected. Alloy 19, which had the highest hardness value at 1109 HV<sub>0.3</sub> in the as-cast condition, disintegrated while being removed from the resin mounting, therefore hardness was not measured. However, the phases,  $\tau_3$ , A15( $\sim\text{Cr}_3\text{Pt}$ ) and  $\sim\text{Cr}_3\text{Pt}$ , remained the same in the as-cast and annealed conditions and the disintegration indicated extreme hardness and brittleness.

The phases in Alloy 20H did not change after annealing, but the hardness increased from 796 HV<sub>0.3</sub> to 923 HV<sub>0.3</sub>. This was the same with Alloy 21H where the phases (V,Cr) and  $\sim\text{PtV}_3$  remained the same in the as-cast and annealed conditions. However, Alloy 21H disintegrated while being removed from the resin mounting and it was not possible to measure its hardness after annealing. But the disintegration indicated extreme hardness and brittleness.

Alloy 22 had a hardness value 1086 HV<sub>0.3</sub>, making it the second hardest in the as-cast condition. It had the same phases  $\sim\text{Cr}_3\text{Pt}$ ,  $\sim\text{PtV}_3$ ,  $\tau_3$  and (V,Cr) in the as-cast and annealed conditions. It disintegrated while being removed from the resin mounting, and as such, its annealed hardness was not measured. The disintegration indicated extreme hardness and brittleness. The phases, (V,Cr) and A15( $\sim\text{Cr}_3\text{Pt}$ ), in Alloy 23H remained the same in the as-cast and annealed conditions, but the hardness increased from 707 HV<sub>0.3</sub> to 837 HV<sub>0.3</sub>.

Alloy 24H had the same phases, (V,Cr) and A15( $\sim\text{Cr}_3\text{Pt}$ ) in the as-cast and annealed conditions, but the hardness decreased from 692 HV<sub>0.3</sub> to 544 HV<sub>0.3</sub>. This is not the same trend seen with the most of the alloys in this system. Alloy 25H also retained the same phases,  $\sim\text{Cr}_3\text{Pt}$  and A15( $\sim\text{Cr}_3\text{Pt}$ ), in the as-cast and annealed conditions, but there was a substantial increase in hardness from 358 HV<sub>0.3</sub> to 838 HV<sub>0.3</sub>. This was because heat treatment produced more of the A15( $\sim\text{Cr}_3\text{Pt}$ ) which would be expected to be harder, being an intermetallic phase.

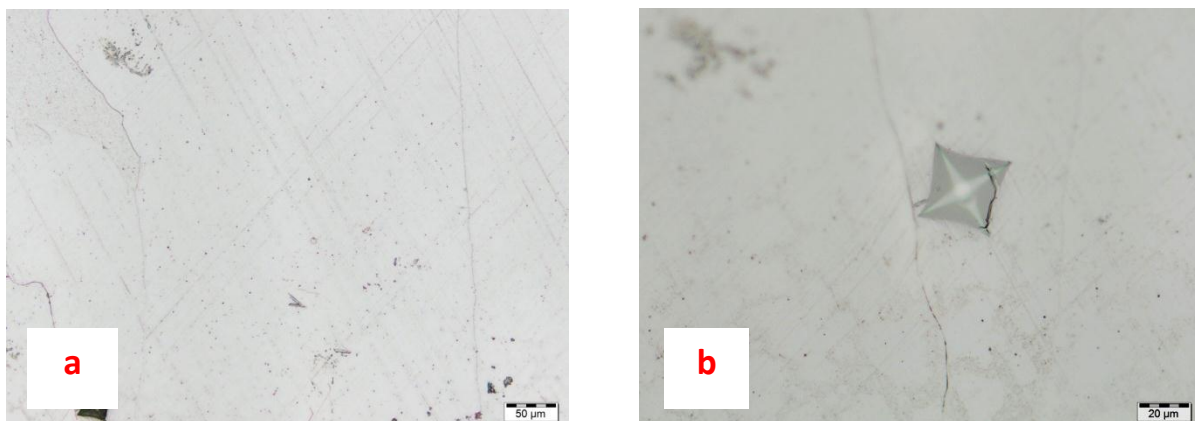


**Figure 7.37. Vickers hardness indentation on annealed Alloy 5H, average composition  $\text{Pt}_{73.8}\text{Cr}_{16.9}\text{V}_{9.3}$  (at.%), (a) low magnification with the indentation showing pin cushioning, (b) a higher magnification with the indentation showing that the diamond indenter is damaged.**

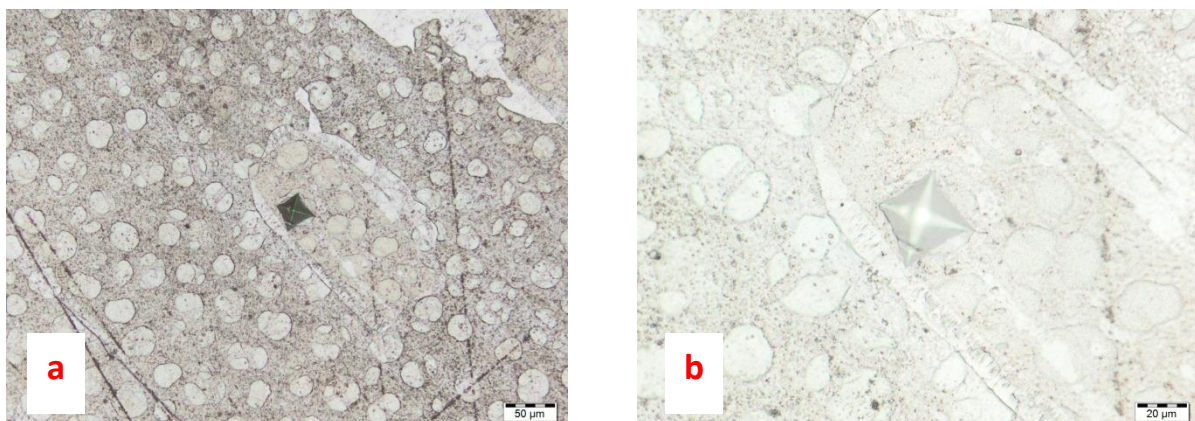


**Figure 7.38. Vickers hardness indentation on annealed Alloy 6H, average composition  $\text{Pt}_{72.3}\text{Cr}_{8.3}\text{V}_{19.4}$  (at.%), (a) low magnification with the indentation showing pin cushioning, (b) at a higher magnification with the indentation showing that the diamond indenter is damaged.**

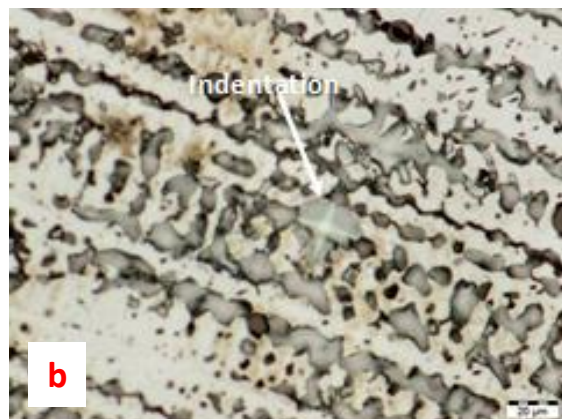


**Figure 7.39. Vickers hardness indentation on annealed Alloy 7H, average composition  $\text{Pt}_{33.4}:\text{Cr}_{45.8}:\text{V}_{20.8}$  (at.%), (a) low magnification (b) a higher magnification.**

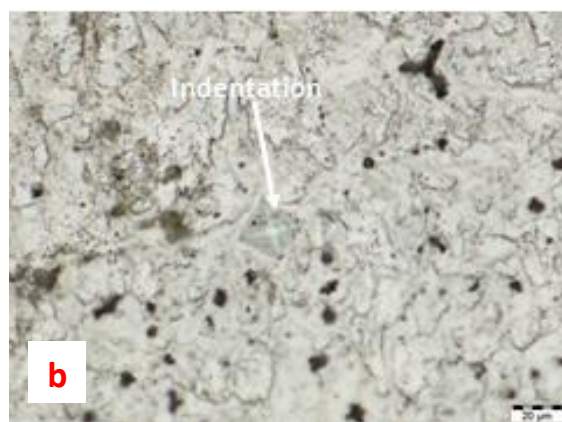


**Figure 7.40. Vickers hardness indentation on annealed Alloy 8H, average composition  $\text{Pt}_{53.0}:\text{Cr}_{22.4}:\text{V}_{24.5}$  (at.%), (a) low magnification (b) a higher magnification.**



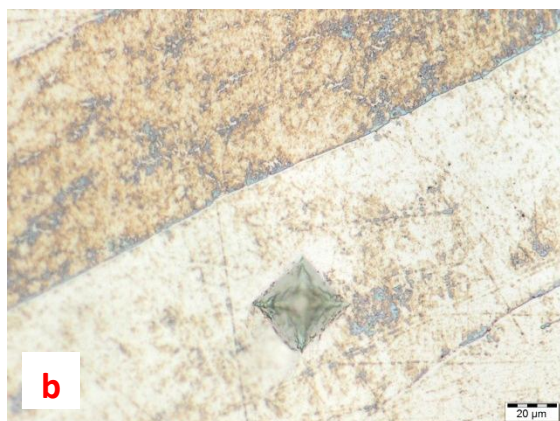
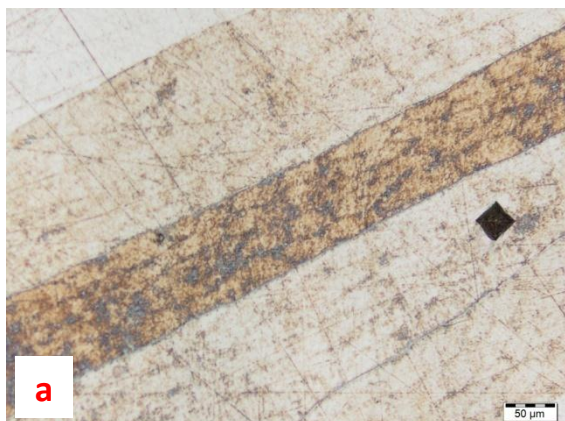


**Figure 7.41. Vickers hardness indentation on annealed Alloy 17H, average composition  $\text{Pt}_{68.5}:\text{Cr}_{16.2}:\text{V}_{15.3}$  (at.%), (a) low magnification (b) a higher magnification.**

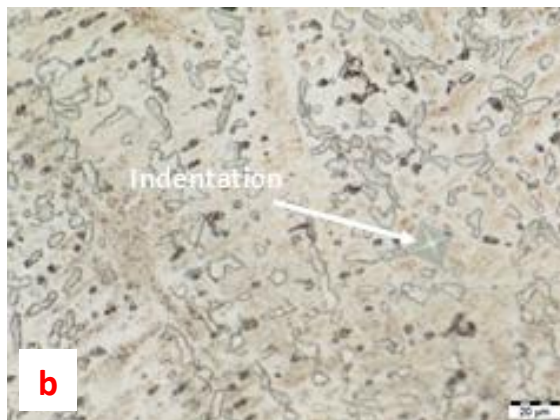


**Figure 7.42. Vickers hardness indentation on annealed Alloy 18H, average composition  $\text{Pt}_{32.8}:\text{Cr}_{28.6}:\text{V}_{38.6}$  (at.%) with (a) low magnification and (b) higher magnification.**

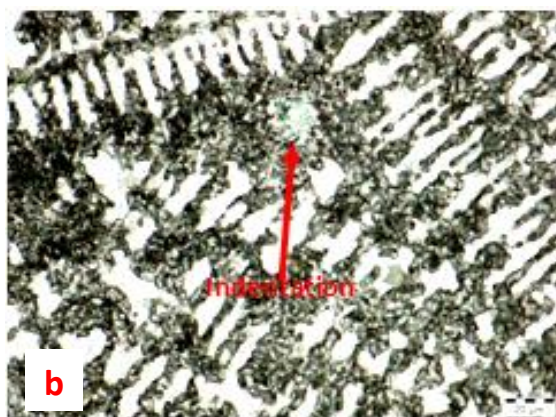
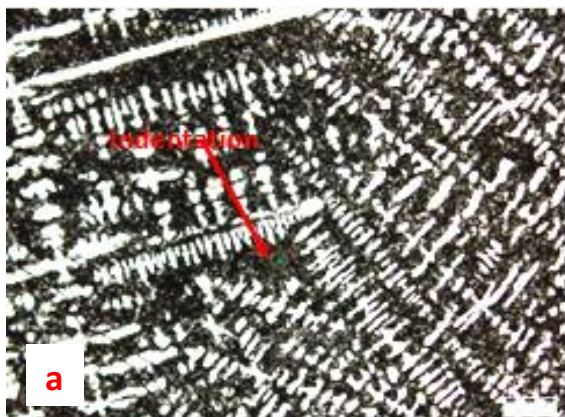


**Figure 7.43. Vickers hardness indentation on annealed Alloy 20H, average composition  $\text{Pt}_{38.8}:\text{Cr}_{14.2}:\text{V}_{47.0}$  (at.%) with (a) low magnification and (b) higher magnification.**

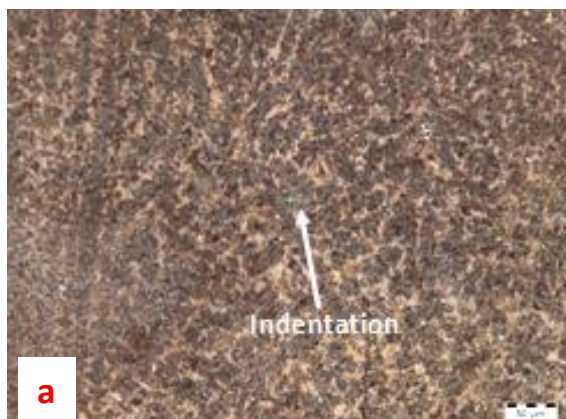


**Figure 7.44. Vickers hardness indentation on annealed Alloy 23H, average composition  $\text{Pt}_{16.5}:\text{Cr}_{56.1}:\text{V}_{27.4}$  (at.%) with (a) low magnification and (b) higher magnification.**



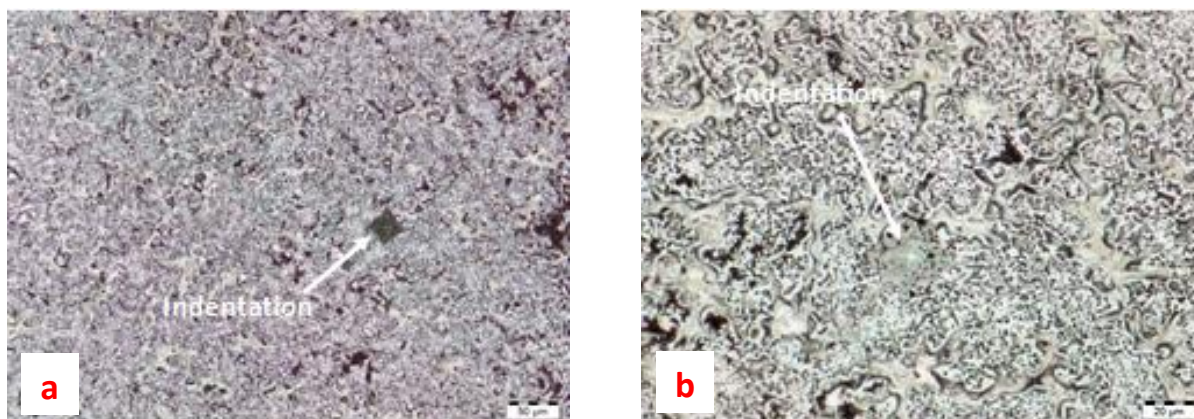


**Figure 7.45. Vickers hardness indentation on annealed Alloy 24H, average composition  $\text{Pt}_{14.9}:\text{Cr}_{73.7}:\text{V}_{11.4}$  (at.%) with (a) low magnification and (b) higher magnification.**

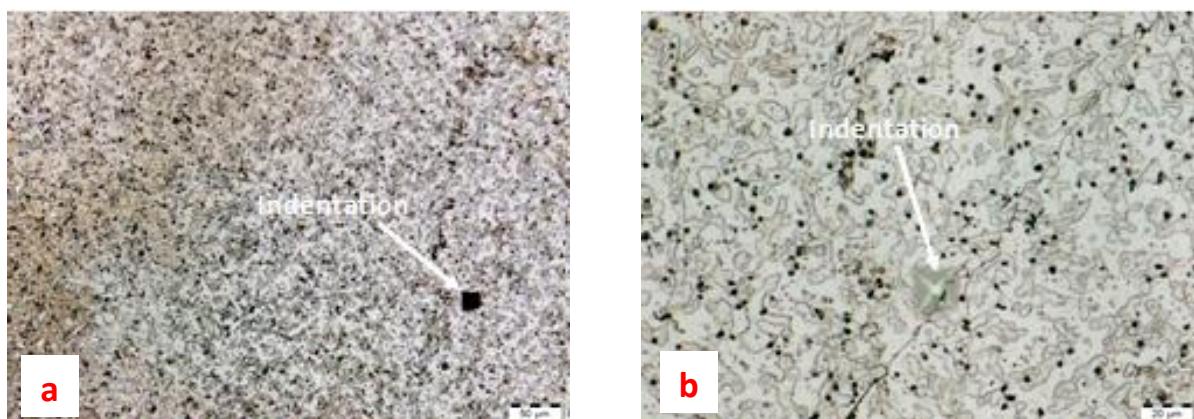


**Figure 7.46. Vickers hardness indentation on annealed Alloy 25H, average composition  $\text{Pt}_{34.1}:\text{Cr}_{57.4}:\text{V}_{8.5}$  (at.%) with (a) low magnification and (b) higher magnification.**

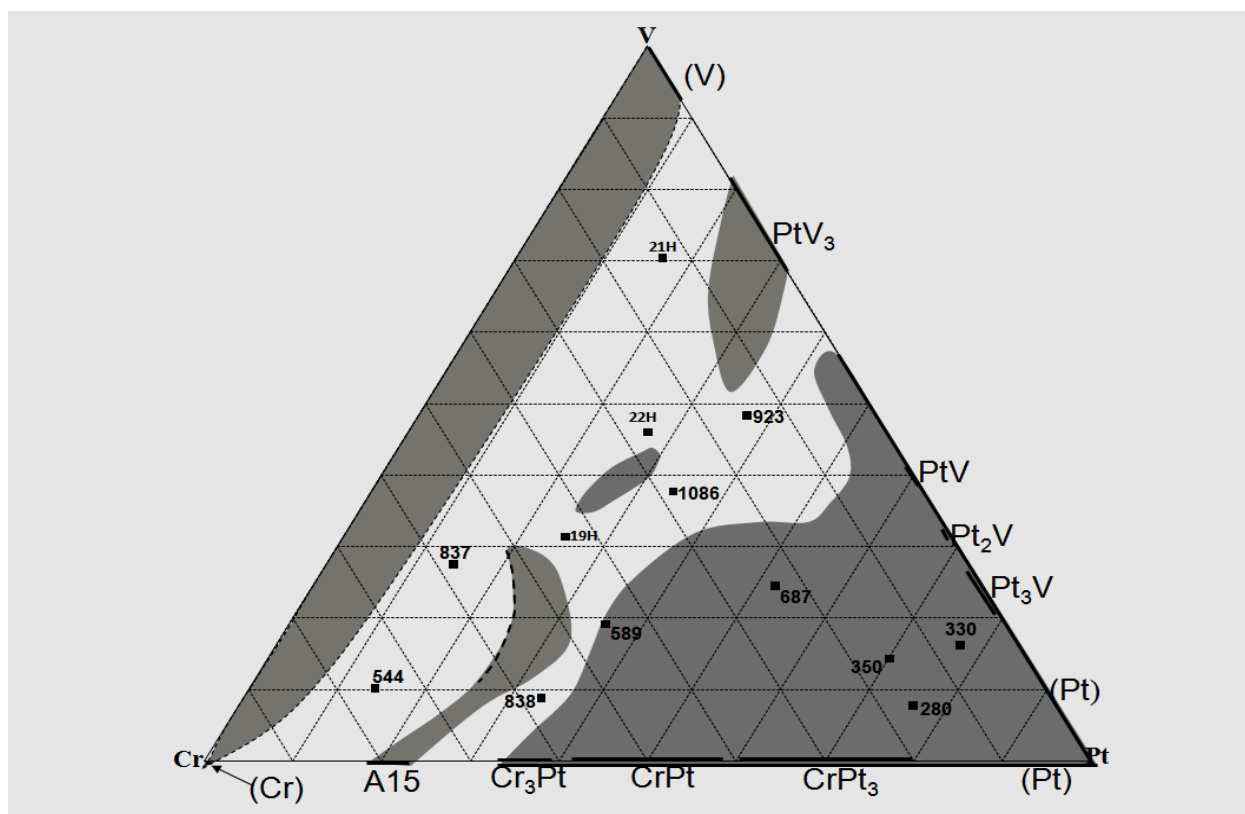


**Figure 7.47. Hardness values (HV<sub>0.3</sub>) of annealed Pt-Cr-V alloys superposed on isothermal section at 1000°C (at.%).**

## 7.4 Higher Order Alloys

### 7.4.1 As-cast Higher Order Alloys

The images of the indentations on as-cast higher order alloys are shown in Figures 7.48 to 7.53. The hardness values are given in Table 7.3. There were no cracks or noticeable slip lines around the edges of the indentations. However, pin-cushioning can be seen in the indentations on Alloys 27 and 30.

Half of the as-cast higher order alloys had hardness above 500 HV<sub>0.3</sub>. Alloy 30 had the highest hardness value of 603 HV<sub>0.3</sub>. As-cast alloys with two-phase structure (~Pt<sub>3</sub>Al and (Pt)) are generally harder than the single phase structure (~Pt<sub>3</sub>Al). This higher hardness cannot be attributed to (Pt) as it has been shown in Sections 7.2 and 7.3 that higher Pt content lowers hardness of alloys and that pure platinum is very soft and ductile with a hardness value of only



~50 HV [2008Mur]. Only the alloys with higher V content had a two-phase structure of (Pt) and ~Pt<sub>3</sub>Al. Therefore, the high V content could be the major contributing factor to higher hardness. This is further confirmed in Section 7.4.3 of this thesis where variation of hardness with vanadium content is analysed graphically.

All the six higher order alloys were based on the quaternary alloy Pt<sub>82</sub>:Al<sub>12</sub>:Cr<sub>4</sub>:Ru<sub>2</sub> (at.%) and both V and Nb were added to replace Pt, while the content of the other elemental components were meant to remain constant. However, because of losses during melting, the actual average compositions are used to designate the alloys. After a heat treatment at 1500°C for 18 h followed by water quenching and then at 1100°C followed by air cooling, the hardness of Alloy Pt<sub>82</sub>:Al<sub>12</sub>:Cr<sub>4</sub>:Ru<sub>2</sub> was 378 HV<sub>10</sub> with a precipitate volume percent of 10±5. This shows that the addition of V, and in the case of Alloys 30 and 31, V and Nb, had substantially increased the hardness and possibly the precipitate volume fraction, even in the as-cast condition.

The as-cast higher order alloys still did not have the right microstructure as noted in Chapter 6. However, they were generally harder than the six quaternary alloys discussed in Section 2.3 where the hardest is Alloy Pt<sub>84</sub>:Al<sub>11</sub>:Cr<sub>3</sub>:Ru<sub>2</sub> with a hardness of 472 HV<sub>10</sub>. They are also harder than the eight ternary Pt-Al based alloys investigated by Hill [2001Hil2] where the hardest alloy had a Vickers hardness of 530 HV (the load used was not specified). However, the ternary alloys in the Pt-Al-V system (Chapter 4), Pt-Cr-V system (Chapter 5) and the Pt-Al-Cr system [2007Süs] are generally much harder than the as-cast higher order alloys, because of their microstructures.

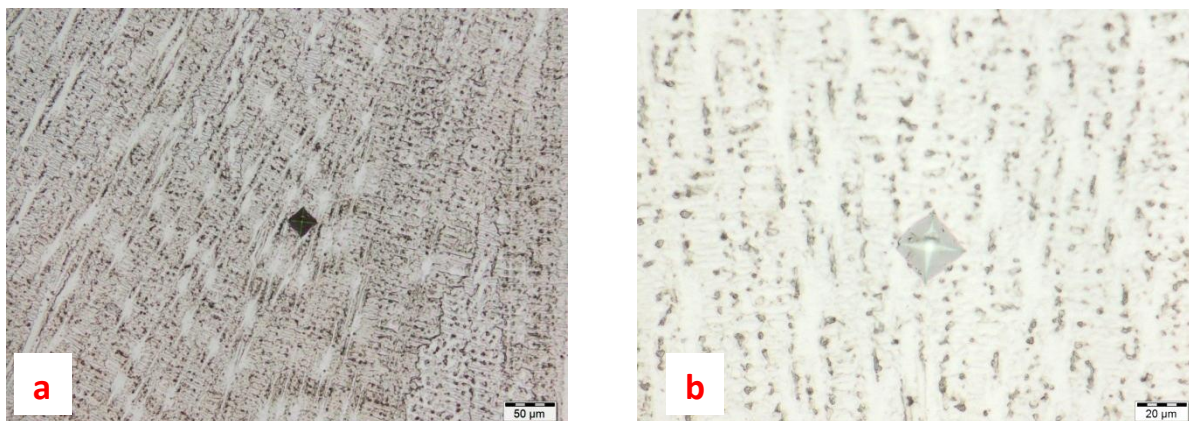


**Figure 7.48. Vickers hardness indentation on as-cast Alloy 26, average composition  $\text{Pt}_{63.9}:\text{Al}_{12.2}:\text{Cr}_{4.3}:\text{Ru}_{0.7}:\text{V}_{18.9}$  (at.%) with (a) low magnification and (b) higher magnification.**

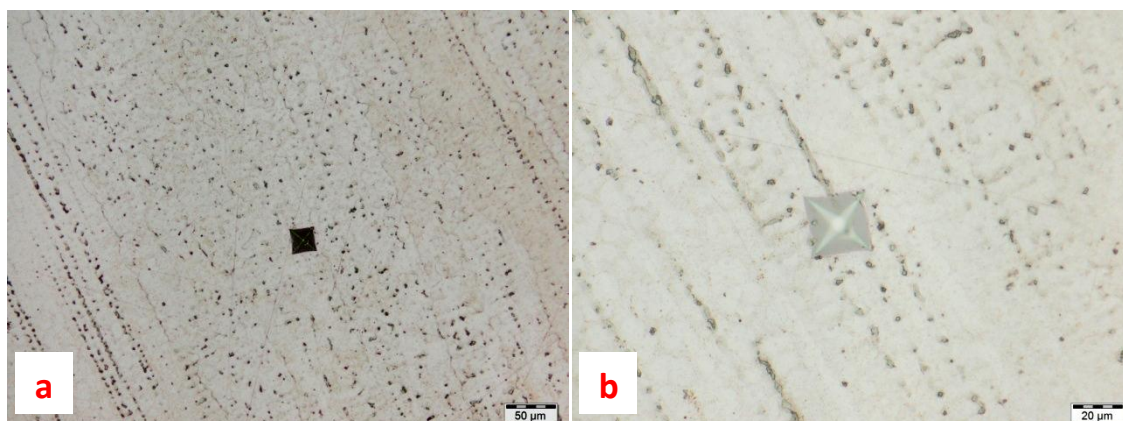


**Figure 7.49. Vickers hardness indentation on as-cast Alloy 27, average composition  $\text{Pt}_{69.5}:\text{Al}_{11.5}:\text{Cr}_{4.2}:\text{Ru}_{0.6}:\text{V}_{14.2}$  (at.%) with (a) low magnification and (b) higher magnification with indentation showing pin-cushioning.**



**Figure 7.50. Vickers hardness indentation on as-cast Alloy 28, average composition  $\text{Pt}_{75.2}:\text{Al}_{11.2}:\text{Cr}_{4.0}:\text{Ru}_{0.6}:\text{V}_{9.5}$  (at.%) with (a) low magnification and (b) higher magnification.**

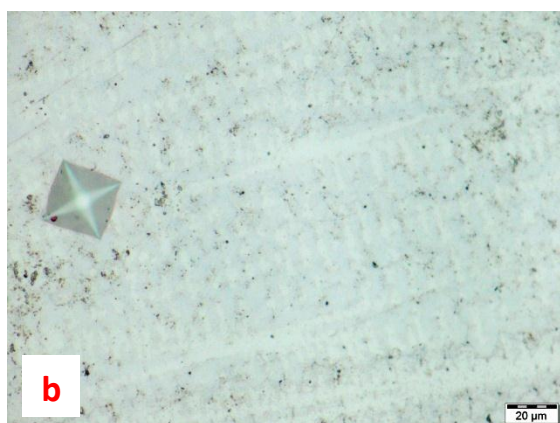
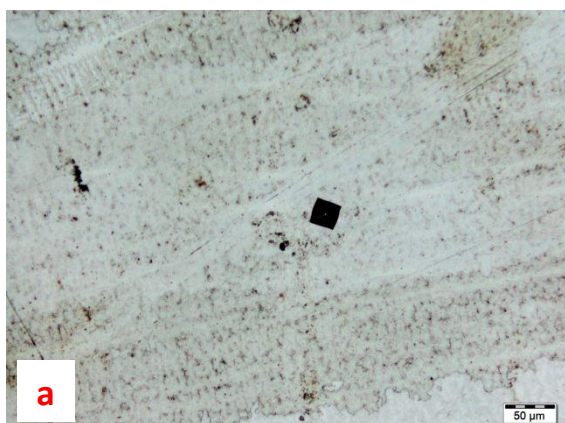


**Figure 7.51. Vickers hardness indentation on as-cast Alloy 29, average composition  $\text{Pt}_{78.7}:\text{Al}_{12.2}:\text{Cr}_{3.8}:\text{Ru}_{0.6}:\text{V}_{5.2}$  (at.%) with (a) low magnification and (b) higher magnification.**





**Figure 7.52. Vickers hardness indentation on as-cast Alloy 30, average composition  $\text{Pt}_{63.2}:\text{Al}_{12.9}:\text{Cr}_{4.0}:\text{Ru}_{0.7}:\text{V}_{19.0}:\text{Nb}_{0.6}$  (at.%) with (a) low magnification and (b) higher magnification with the indentation showing pin-cushioning.**

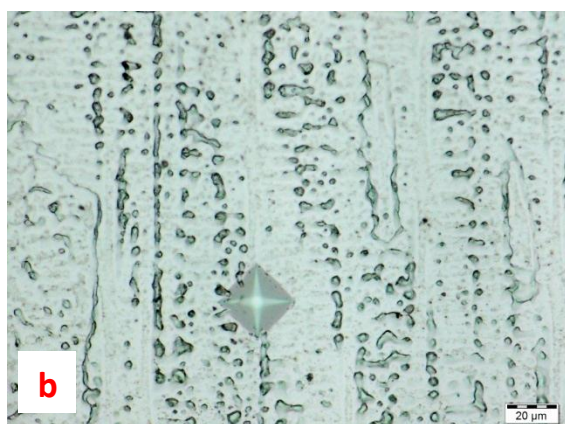
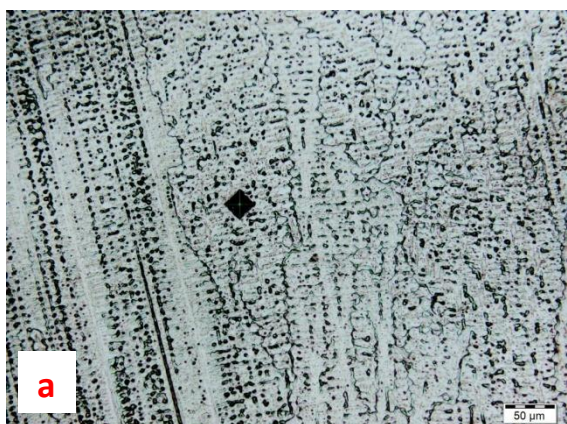


**Figure 7.53. Vickers hardness indentation on as-cast Alloy 31, average composition  $\text{Pt}_{71.7}:\text{Al}_{12.8}:\text{Cr}_{4.9}:\text{Ru}_{1.1}:\text{V}_{9.9}:\text{Nb}_{0.3}$  (at.%) with (a) low magnification and (b) higher magnification.**

**Table 7.3. Hardness values (HV<sub>0.3</sub>) of annealed higher order alloys compared to as-cast alloys.**

<b>Alloy ID No.</b>	<b>Average composition (at.%)</b>	<b>As-cast hardness (HV<sub>0.3</sub>)</b>	<b>Annealed hardness (HV<sub>0.3</sub>)</b>	<b>Phases present in the as-cast alloys</b>	<b>Phases present in the annealed alloys</b>
26	Pt <sub>63.9</sub> :Al <sub>12.2</sub> :Cr <sub>4.3</sub> :Ru <sub>0.7</sub> :V <sub>18.9</sub>	537±13	700±20	~Pt <sub>3</sub> Al, (Pt)	~Pt <sub>3</sub> Al, ~Pt <sub>2</sub> V
27	Pt <sub>69.5</sub> :Al <sub>11.5</sub> :Cr <sub>4.2</sub> :Ru <sub>0.6</sub> :V <sub>14.2</sub>	428±11	482±24	~Pt <sub>3</sub> Al, (Pt)	~Pt <sub>3</sub> Al
28	Pt <sub>75.2</sub> :Al <sub>11.2</sub> :Cr <sub>4.0</sub> :Ru <sub>0.6</sub> :V <sub>9.5</sub>	377±8	359±9	~Pt <sub>3</sub> Al	~Pt <sub>3</sub> Al
29	Pt <sub>78.7</sub> :Al <sub>12.2</sub> :Cr <sub>3.8</sub> :Ru <sub>0.6</sub> :V <sub>5.2</sub>	422±9	-	~Pt <sub>3</sub> Al	~Pt <sub>3</sub> Al, (Pt)
30	Pt <sub>63.2</sub> :Al <sub>12.9</sub> :Cr <sub>4.0</sub> :Ru <sub>0.7</sub> :V <sub>19.0</sub> :Nb <sub>0.6</sub>	603±21	821±32	~Pt <sub>3</sub> Al, (Pt)	~Pt <sub>3</sub> Al, ~PtV, ~Pt <sub>2</sub> V
31	Pt <sub>71.7</sub> :Al <sub>12.8</sub> :Cr <sub>4.9</sub> :Ru <sub>1.1</sub> :V <sub>9.9</sub> :Nb <sub>0.3</sub>	545±12	535±15	~Pt <sub>3</sub> Al, (Pt)	~Pt <sub>3</sub> Al

#### **7.4.2 Higher Order Alloys Annealed at 1000°C for 1500 Hours**

The hardness values of annealed higher order alloys compared to as-cast alloys is given in Table 7.3. The images of the indentations on the annealed are shown in Figures 7.54 to 7.58. The indentation on Alloy 26H has slight pin-cushioning. There were no cracks or noticeable slip lines around the edges of the indentations.

There was a general increase in the hardness values after annealing, except for Alloy 31H which had the same value statistically, and Alloy 28H which reduced marginally. Alloy 29H cracked and disintegrated while being ground, and as such, hardness could not be measured. This suggested extreme brittleness and a large increase in hardness, even though the as-cast hardness was fairly low compared to the other higher order alloys.

The hardness of Alloy 26 increased from 537 HV<sub>0.3</sub> to 700 HV<sub>0.3</sub> and this was expected as the (Pt) solid solution, which had been in the as-cast alloy, ordered to  $\sim\text{Pt}_2\text{V}$  during annealing. Alloy 27 was two-phase ( $\sim\text{Pt}_3\text{Al}$  and (Pt)) in the as-cast condition but changed to single phase ( $\sim\text{Pt}_3\text{Al}$ ) after annealing and the hardness increased slightly from 428 HV<sub>0.3</sub> to 482 HV<sub>0.3</sub>.

Alloy 28 was single phase ( $\sim\text{Pt}_3\text{Al}$ ) in the as-cast condition and remained single phase in the annealed condition and the hardness also stayed the same. Alloy 29 was single phase ( $\sim\text{Pt}_3\text{Al}$ ) in the as-cast condition but changed to two-phase ( $\sim\text{Pt}_3\text{Al}$  and (Pt)). The alloy disintegrated while being ground indicating a substantial increase in hardness after annealing.

Alloy 30 had two phases,  $\sim\text{Pt}_3\text{Al}$  and (Pt), in the as-cast condition but during annealing the solid solution transformed to  $\sim\text{PtV}$  and  $\sim\text{Pt}_2\text{V}$ . Consequently, the hardness increased from 603 HV<sub>0.3</sub> to 821 HV<sub>0.3</sub>. The two Pt-V intermetallic compounds were responsible for the large increase in hardness. Alloy 31 had two phases,  $\sim\text{Pt}_3\text{Al}$  and (Pt) but changed to single phase,  $\sim\text{Pt}_3\text{Al}$  during annealing. The hardness stayed statistically the same.

The hardness of the annealed alloys was higher than the quaternary alloys discussed in Section 2.3, but within the range of hardness of the alloys in the three ternary systems, Pt-Al-V (Chapter 4), Pt-Cr-V (Chapter 5) and Pt-Al-Cr [2007Süs]. This is excluding the extremely hard alloys which had ternary phases. They were also generally harder than the Pt-Al based alloys investigated by Hill [2001Hil2], although some of them were within the same range.

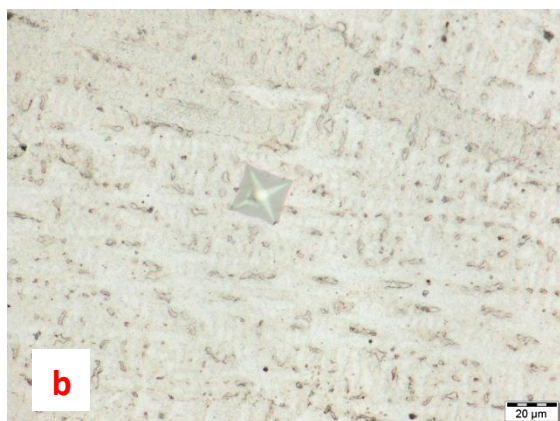
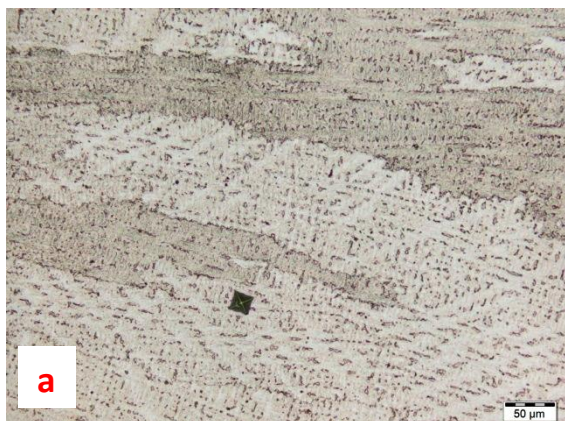


**Figure 7.54. Vickers hardness indentation on Alloy 26H, average composition  $\text{Pt}_{63.9}:\text{Al}_{12.2}:\text{Cr}_{4.3}:\text{Ru}_{0.7}:\text{V}_{18.9}$  (at.%) with (a) low magnification and (b) higher magnification with pin-cushioning.**

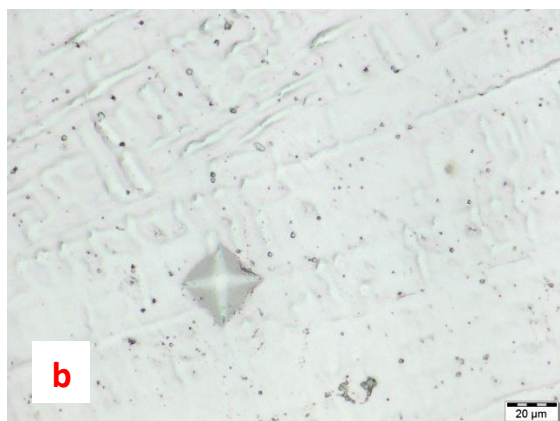
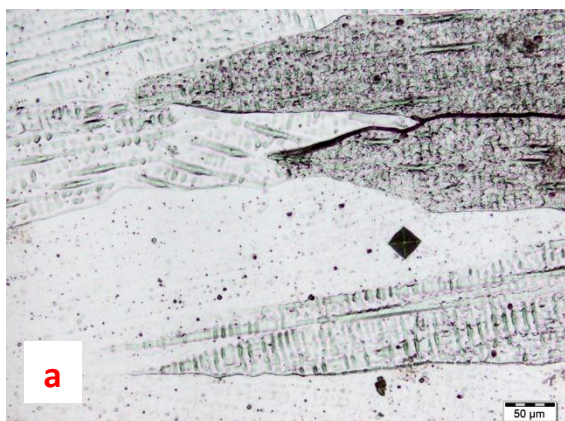


**Figure 7.55. Vickers hardness indentation on annealed Alloy 27H, average composition  $\text{Pt}_{69.5}:\text{Al}_{11.5}:\text{Cr}_{4.2}:\text{Ru}_{0.6}:\text{V}_{14.2}$  (at.%) with (a) low magnification and (b) higher magnification.**



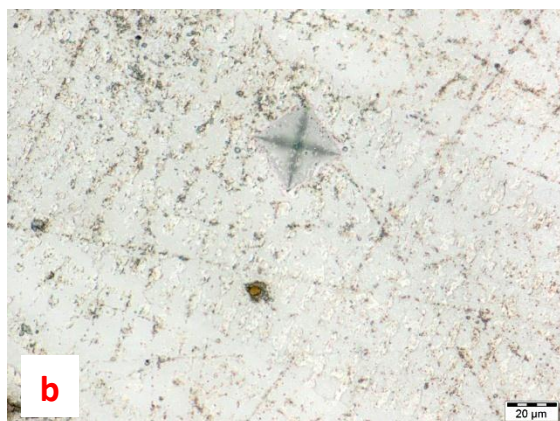
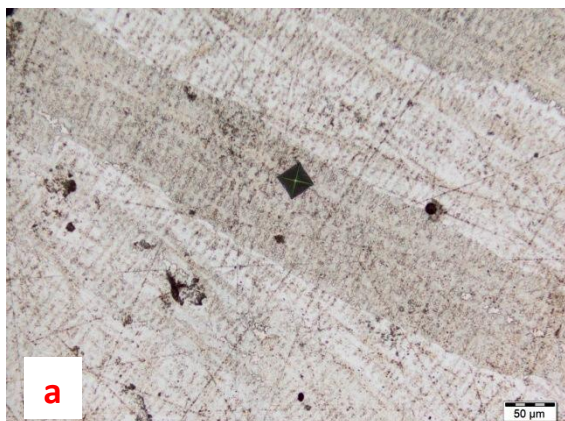


**Figure 7.56. Vickers hardness indentation on annealed Alloy 28H, average composition  $\text{Pt}_{75.2}:\text{Al}_{111.2}:\text{Cr}_{4.0}:\text{Ru}_{0.6}:\text{V}_{9.5}$  (at.%) with (a) low magnification and (b) higher magnification**



**Figure 7.57. Vickers hardness indentation on annealed Alloy 30H, average composition  $\text{Pt}_{63.2}:\text{Al}_{12.9}:\text{Cr}_{4.0}:\text{Ru}_{0.7}:\text{V}_{19.0}:\text{Nb}_{0.6}$  (at.%) with (a) lower magnification and (b) higher magnification.**



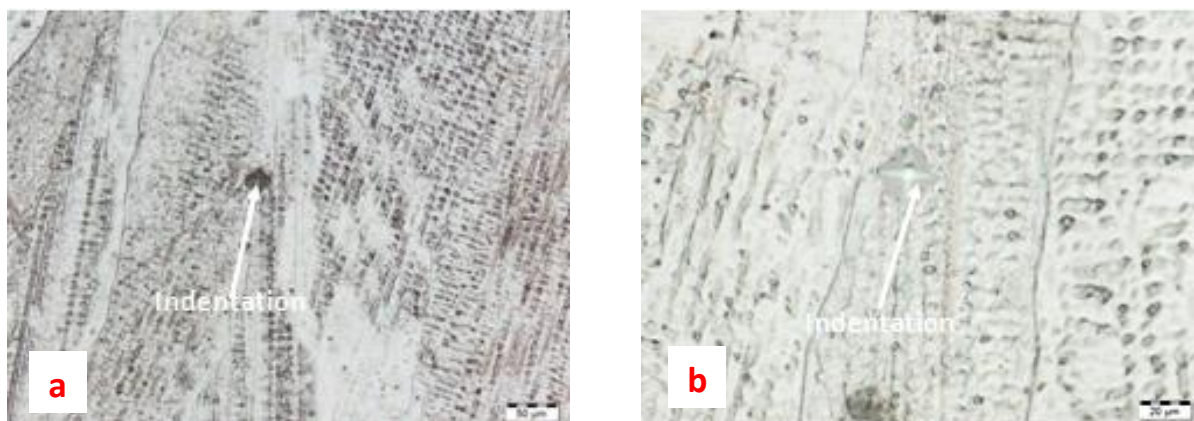


**Figure 7.58. Vickers hardness indentation on annealed Alloy 31H, average composition  $\text{Pt}_{71.7}:\text{Al}_{12.8}:\text{Cr}_{4.9}:\text{Ru}_{1.1}:\text{V}_{9.9}:\text{Nb}_{0.3}$  (at.%) with (a) low magnification and (b) higher magnification.**

### **7.4.3 Variation of Hardness Values with Vanadium Content**

Figure 7.59 shows hardness values plotted against vanadium content for both as-cast and annealed alloys. The general trend is that hardness increased as vanadium content increased for both as-cast and annealed alloys. Also, the hardness values for annealed alloys were generally higher compared to as-cast alloys. However, the samples were few, and definite conclusions can only be made after similar work is done on more samples.

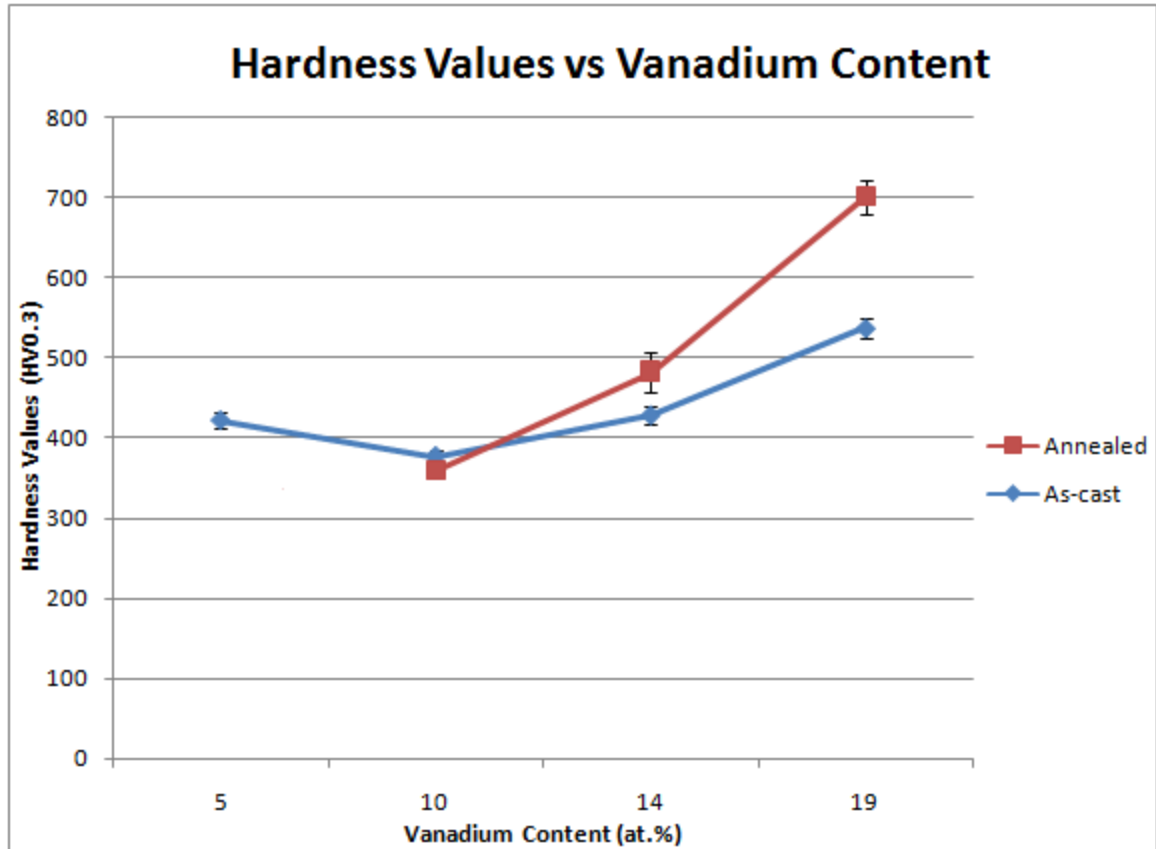


**Figure 7.59. Hardness values (HV<sub>0.3</sub>) plotted against vanadium content (at.%) for as-cast and annealed higher order alloys.**

## CHAPTER 8:DISCUSSION

### 8.1 Pt-Al-V ALLOYS

Alloy 1, average composition  $\text{Pt}_{64.3}:\text{Al}_{26.6}:\text{V}_{9.1}$  (at.%), had a complex structure and solidified to  $\sim\text{Pt}_3\text{Al}$  initially, as in the binary phase diagram of Pt-Al [1990Mas]. This was followed by a peritectic reaction which formed a dark layer, (Pt). Another peritectic reaction between the dark layer and the liquid formed light needles ( $\sim\text{Pt}_5\text{Al}_3$ ), which solidified and grew on their own. A peritectoid reaction then took place between the light needles and the  $\sim\text{Pt}_3\text{Al}$  to form dark  $\sim\text{Pt}_2\text{Al}$ . This was followed by a eutectic reaction which formed the metastable  $\beta$  phase and  $\sim\text{Pt}_5\text{Al}_3$ . The  $\beta$  phase decomposed eutectoidally to form  $\sim\text{PtAl}$  and  $\sim\text{Pt}_5\text{Al}_3$ . Finally, (Pt) which now remained as a thin dark layer on  $\sim\text{Pt}_3\text{Al}$  transformed to  $\sim\text{Pt}_2\text{V}$ .

After annealing at  $1000^\circ\text{C}$  for 1500 h, the alloy was designated as 1H. It had  $\sim\text{Pt}_3\text{Al}$ ,  $\sim\text{Pt}_5\text{Al}_3$ ,  $\sim\text{Pt}_2\text{V}$ , a eutectic of  $\sim\text{PtAl} + \sim\text{Pt}_5\text{Al}_3$  and solid state precipitation of  $\sim\text{Pt}_2\text{V}$  within  $\sim\text{Pt}_3\text{Al}$ . In comparison with the as-cast alloy, the eutectic coarsened, the light needles could not be seen clearly and most of the dendrites had dark solid state precipitates, showing a retreating solvus.

The phase  $\sim\text{Pt}_2\text{Al}$  disappeared during annealing of Alloy 1H, but the hardness remained more or less the same with the as-cast hardness being  $655\pm 27 \text{ HV}_{0.3}$  and the annealed hardness  $635\pm 13 \text{ HV}_{0.3}$ .

Alloy 2, average composition  $\text{Pt}_{59.1}:\text{Al}_{23.1}:\text{V}_{17.8}$  (at.%), also had a complex structure and solidified with (Pt) which later ordered to  $\sim\text{Pt}_2\text{V}$ . A peritectic reaction between the liquid and the (Pt) followed, forming  $\sim\text{Pt}_5\text{Al}_3$ . The next reaction was a eutectic, which formed  $\sim\text{Pt}_5\text{Al}_3$  and  $\beta$  followed by a eutectoid decomposition of  $\beta$  to form  $\sim\text{PtAl}$  and  $\sim\text{Pt}_5\text{Al}_3$ . Finally, there was a solid state precipitation of  $\sim\text{PtAl}$  in  $\sim\text{Pt}_5\text{Al}_3$ , showing that the  $\sim\text{Pt}_5\text{Al}_3$  solvus retreated substantially.

After annealing, the alloy was designated as 2H and had  $\sim\text{PtV}$ ,  $\sim\text{Pt}_5\text{Al}_3$ , solid state precipitation of  $\sim\text{PtV}$  within  $\sim\text{Pt}_5\text{Al}_3$  and solid state precipitation of  $\sim\text{Pt}_5\text{Al}_3$  within  $\sim\text{PtV}$ . This showed that the solvi of  $\sim\text{Pt}_5\text{Al}_3$  and  $\sim\text{PtV}$  retreat substantially. Compared to the as-cast sample, the  $\sim\text{Pt}_2\text{V}$

dendrites had transformed to  $\sim\text{PtV}$  and reduced in proportion, and  $\sim\text{Pt}_5\text{Al}_3$  precipitated within. The light matrix had aligned precipitates of  $\sim\text{PtV}$ , from solid state precipitation. The dark component of the eutectic seen in the as-cast sample was not evident in the annealed alloy, unless it became the aligned precipitates.

The hardness decreased from  $746\pm35 \text{ HV}_{0.3}$  in the as-cast condition to  $624\pm26 \text{ HV}_{0.3}$  in the annealed condition, and the decrease may be attributed to the disappearance of  $\sim\text{PtAl}$  and  $\sim\text{Pt}_2\text{V}$  during annealing.

Alloy 3, average composition  $\text{Pt}_{57.3}:\text{Al}_{16.7}:\text{V}_{26}$  (at.%), solidified with (Pt) which later ordered to  $\sim\text{Pt}_2\text{V}$ . A peritectic reaction between the liquid and the (Pt) followed, forming  $\sim\text{Pt}_3\text{Al}$  and  $\sim\text{Pt}_5\text{Al}_3$ . The  $\sim\text{Pt}_3\text{Al}$  then reacted peritectoidally with  $\sim\text{Pt}_5\text{Al}_3$  to form  $\sim\text{Pt}_2\text{Al}$ . All the  $\sim\text{Pt}_5\text{Al}_3$  was consumed in the peritectoid reaction.

After annealing, the alloy had  $\sim\text{Pt}_2\text{V}$ ,  $\sim\text{Pt}_3\text{Al}$ ,  $\sim\text{PtV}$  and solid state precipitation of  $\sim\text{Pt}_3\text{Al}$  within  $\sim\text{Pt}_2\text{V}$ , showing that the solvus of  $\sim\text{Pt}_2\text{V}$  retreats substantially. In comparison with the as-cast alloy, the structure coarsened and  $\sim\text{Pt}_2\text{Al}$  disappeared. Instead  $\sim\text{PtV}$  formed in the annealed alloy.

The hardness of the as-cast alloy was  $519\pm34 \text{ HV}_{0.3}$  and that of the annealed was  $516\pm17 \text{ HV}_{0.3}$ , which shows that the changes in the structure did not alter the hardness.

Alloy 4B, average composition  $\text{Pt}_{69.8}:\text{Al}_{22.3}:\text{V}_{7.9}$  (at.%), solidified to form first  $\sim\text{Pt}_3\text{Al}$  followed by a peritectic reaction between the liquid and the  $\sim\text{Pt}_3\text{Al}$  to form  $\sim\text{Pt}_5\text{Al}_3$ . The last reaction was peritectoid between  $\sim\text{Pt}_3\text{Al}$  and  $\sim\text{Pt}_5\text{Al}_3$  forming  $\sim\text{Pt}_2\text{Al}$ .

After annealing, the alloy had the same phases  $\sim\text{Pt}_3\text{Al}$  and  $\sim\text{Pt}_2\text{Al}$  and the hardness stayed the same with the as-cast alloy having a hardness of  $671\pm23 \text{ HV}_{0.3}$  and that of the annealed alloy being  $696\pm20 \text{ HV}_{0.3}$ .

Alloy 10, average composition  $\text{Pt}_{83.9}:\text{Al}_6:\text{V}_{10.1}$  (at.%), solidified with (Pt), followed by a eutectic reaction which formed (Pt) and  $\sim\text{Pt}_3\text{Al}$ . After annealing, the alloy had (Pt),  $\sim\text{Pt}_2\text{V}$  and  $\sim\text{Pt}_3\text{Al}$ . In comparison with the as-cast alloy, the eutectic coarsened and the dark phase precipitated during annealing. The hardness increased marginally from  $420\pm 20 \text{ HV}_{0.3}$  to  $482\pm 14 \text{ HV}_{0.3}$  and this slight increase can be attributed to the formation of  $\sim\text{Pt}_2\text{V}$ .

Alloy 11, average composition  $\text{Pt}_{80.9}:\text{Al}_{4.3}:\text{V}_{14.8}$  (at.%), also solidified with (Pt), followed by a eutectic reaction which formed (Pt) and  $\sim\text{Pt}_3\text{Al}$ . After annealing, the alloy had the same phases and the hardness stayed the same with the as-cast alloy's hardness being  $381\pm 13 \text{ HV}_{0.3}$  and that of the annealed being  $378\pm 16 \text{ HV}_{0.3}$ . There was less coring in the annealed alloy compared to the as-cast sample.

Alloy 12, average composition  $\text{Pt}_{52.5}:\text{Al}_{22.6}:\text{V}_{24.9}$  (at.%), had a two phase dendritic region and a thin dark region which revealed a ternary eutectic at higher magnification. When the areal composition of the dendritic region was plotted, its position was far from any of the binary phase fields and the original dendrites, which decomposed eutectoidally into the two phases  $\sim\text{PtV}_3$  and  $\sim\text{Pt}_5\text{Al}_3$ , was identified as a possible ternary phase,  $\tau_1$ . However, more alloys with compositions in the vicinity of this proposed ternary phase need to be analysed. Thus, the alloy solidified with the ternary phase  $\tau_1$  followed by reaction forming a ternary eutectic comprising (Pt) +  $\tau_1$  +  $\sim\text{PtV}_3$ . The  $\tau_1$  then decomposed eutectoidally to  $\sim\text{PtV}_3$  +  $\sim\text{Pt}_5\text{Al}_3$  and finally ((Pt) transformed to  $\sim\text{PtV}$ . The annealed alloy had  $\sim\text{Pt}_5\text{Al}_3$ ,  $\sim\text{PtV}$  and  $\sim\text{PtV}_3$ , which confirmed the presence of these phases in the as-cast sample. In comparison with the as-cast alloy, the annealed alloy had coarsened considerably. The as-cast hardness ( $767\pm 37 \text{ HV}_{0.3}$ ) and the annealed hardness ( $733\pm 18 \text{ HV}_{0.3}$ ) were similar.

Alloy 13, average composition  $\text{Pt}_{53.7}:\text{Al}_{8.8}:\text{V}_{37.5}$  (at.%), solidified with (Pt), followed by a eutectic reaction resulting in the formation of (Pt) +  $\tau_1$ . The identity of  $\tau_1$  was deduced in a similar manner to the way it was deduced in Alloy 12. Then there was a eutectoid decomposition of  $\tau_1$  to form  $\sim\text{PtV}_3$  +  $\text{Pt}_5\text{Al}_3$ . The original (Pt) dendrites transformed initially to  $\sim\text{PtV}$  and then the (Pt) went on to decompose eutectoidally to  $\sim\text{PtV}$  +  $\sim\text{Pt}_2\text{V}$  as in the binary phase diagram of Pt-V

[1990Mas]. The annealed alloy had  $\sim\text{PtV}$ ,  $\sim\text{PtV}_3$  and  $\sim\text{Pt}_5\text{Al}_3$ . The hardness stayed the same as the as-cast alloy being  $584\pm 19 \text{ HV}_{0.3}$  and that of the annealed alloy being  $585\pm 19 \text{ HV}_{0.3}$ .

Alloy 14, average composition  $\text{Pt}_{84}:\text{Al}_{12}:\text{V}_4$  (at.%), solidified with (Pt) followed by a eutectic reaction which formed (Pt) +  $\sim\text{Pt}_3\text{Al}$ . Finally, a eutectoid decomposition of the high temperature cubic  $\sim\text{Pt}_3\text{Al}$  formed the low temperature tetragonal  $\sim\text{Pt}_3\text{Al}$  and (Pt) [1990Mas]. After annealing, there was solid state precipitation of  $\sim\text{Pt}_3\text{Al}$  within (Pt) and (Pt) within  $\sim\text{Pt}_3\text{Al}$ . The hardness decreased from  $475\pm 9 \text{ HV}_{0.3}$ , in the as-cast condition, to  $347\pm 10 \text{ HV}_{0.3}$  in the annealed condition. The decrease in hardness can be attributed to the change in the structure.

Alloy 15, average composition  $\text{Pt}_{72.4}:\text{Al}_{13.7}:\text{V}_{13.9}$  (at.%), solidified with primary  $\sim\text{Pt}_3\text{Al}$ , followed by a peritectic reaction between the liquid and the  $\sim\text{Pt}_3\text{Al}$  forming  $\sim\text{Pt}_5\text{Al}_3$ . The last reaction was a peritectoid reaction between the  $\sim\text{Pt}_3\text{Al}$  and the  $\sim\text{Pt}_5\text{Al}_3$ , forming  $\sim\text{Pt}_2\text{Al}$ . After annealing, the alloy became single phase  $\sim\text{Pt}_3\text{Al}$ , and the hardness increased from  $462\pm 14 \text{ HV}_{0.3}$  to  $535\pm 23 \text{ HV}_{0.3}$ . The slight increase may be attributed to change in structure.

Alloy 16, average composition  $\text{Pt}_{56.9}:\text{Al}_{25.4}:\text{V}_{17.7}$  (at.%), solidified with a single ternary phase designated as  $\tau_2$ . It was not possible to obtain sufficient contrast using SEM in the BSE mode. Contrast between grains of different orientations was only achieved after etching in an HCl/NaCl solution and viewed through an optical microscope [2012Ode1]. The alloy was brittle in the as-cast condition and there was evidence of cracking. It was annealed like all the others and SEM analysis was done.

The alloy had  $\sim\text{PtAl}$  and  $\sim\text{PtV}$  after annealing which showed that at temperatures much above  $1000^\circ\text{C}$  (on solidification) it exists as single ternary phase,  $\tau_2$ , but decomposes to the two phases above  $1000^\circ\text{C}$ . An attempt to remove the sample from the resin mounting, resulted in its disintegration and consequently, XRD analysis could not be performed on the annealed sample. It had the highest hardness ( $886\pm 23 \text{ HV}_{0.3}$ ).

The compositions were plotted, and the phase boundaries deduced on the solidification projection (Figure 4.37). All the Pt-Al phases extended to  $\sim 10\% \text{ V}$ , except  $\sim\text{Pt}_3\text{Al}$  which

extended to ~15% V. (Pt) had low extent at low V (with a minimum of ~2 at.% Al, ~82 at.% Pt and ~16 at.% V), and higher extent at higher V. There were two ternary phases,  $\tau_1$  at  $\sim V_{24}Pt_{56}Al_{20}$  (at.%) observed in two samples and  $\tau_2$ ,  $\sim V_{18}Pt_{57}Al_{25}$  (at.%) observed in a third sample.

Of the reactions observed, all had been reported in the Pt-Al binary [1990Mas], except for the peritectic reactions  $L + (Pt) \rightarrow \sim Pt_5Al_3$  in Alloy 2 and  $L + (Pt) \rightarrow \sim Pt_3Al + \sim Pt_5Al_3$  in Alloy 3 [2012Ode2].

A liquidus surface projection for the Pt-rich corner of the Pt-Al-V was drawn using the overall compositions, primary phases and the solidification sequences. The primary solids on the liquidus surface (Figure 4.38) are (Pt),  $\sim Pt_3Al$ ,  $\sim Pt_5Al_3$ ,  $\beta$  and two ternary phases  $\tau_1$  and  $\tau_2$ . Since the reactions in Alloys 12 and 13 showed that the liquidus composition moves in different directions on cooling, there must be a minimum on the reaction involving L,  $\sim V_{24}Pt_{56}Al_{20}$  and (Pt).

## 8.2 Pt-Cr-V ALLOYS

Alloy 5, average composition  $Pt_{73.8}:Cr_{16.9}:V_{9.3}$  (at.%), solidified with single phase  $\sim Pt_3V$  and stayed single phase  $\sim Pt_3V$  after annealing. There was also no change in hardness, which was  $272 \pm 8$  HV<sub>0.3</sub> in the as-cast condition and  $280 \pm 26$  HV<sub>0.3</sub> after annealing.

Alloy 6, average composition  $Pt_{72.3}:Cr_{8.3}:V_{19.4}$  (at.%), was single phase  $\sim Pt_3V$  in the as-cast condition but changed to two-phase,  $\sim Pt_2V$  and  $Pt_3V$ , after annealing. The hardness stayed the same,  $317 \pm 8$  HV<sub>0.3</sub> in the as-cast condition and  $330 \pm 17$  HV<sub>0.3</sub> in the annealed condition.

Alloy 7, average composition  $Pt_{33.4}:Cr_{45.8}:V_{20.8}$  (at.%), had three phases in the as-cast condition,  $\sim Cr_3Pt$ , A15( $\sim Cr_3Pt$ ) and a ternary phase designated as  $\tau$ . After annealing, both SEM/EDX and XRD analyses showed that the alloy had the same three phases. Hardness increased marginally from  $527 \pm 28$  HV<sub>0.3</sub> in the as-cast condition to  $589 \pm 23$  HV<sub>0.3</sub> in the annealed condition.

Alloy 8, average composition  $\text{Pt}_{53.0}:\text{Cr}_{22.4}:\text{V}_{24.5}$  (at.%), had  $\sim\text{CrPt}$  dendrites and a eutectic of  $\sim\text{CrPt}$  and a ternary phase,  $\tau$ . After annealing, the alloy still had the same  $\sim\text{CrPt}$  dendrites and the eutectic, but the structure had coarsened. During hardness measurements, the indentations were located on the eutectic areas resulting in a high hardness value because of the ternary phase component. The hardness decreased after annealing, probably because of coarsening.

The SEM-BSE image of Alloy 17, average composition  $\text{Pt}_{68.5}:\text{Cr}_{16.2}:\text{V}_{15.3}$  (at.%), and its plot indicated a single phase alloy, in the as-cast and annealed conditions. However, the XRD analysis indicated that the alloy was predominantly  $\sim\text{Pt}_3\text{V}$  with a small amount (Pt) (Figure 5.15). The etched, optical microscope, images show fine precipitates at the grain boundaries. The inward curvature of the edge of the indentation shows that these dark precipitates in the etched image are harder than the lighter phase (Figure 7.27(b)). The hardness increased slightly from  $291\pm19 \text{ HV}_{0.3}$  to  $350\pm8 \text{ HV}_{0.3}$  after annealing.

Alloy 18, average composition  $\text{Pt}_{32.8}:\text{Cr}_{28.6}:\text{V}_{38.6}$  (at.%), had a ternary phase,  $\tau_3$ , dendrites and a sparse eutectic comprising  $\tau + \sim\text{Cr}_3\text{Pt}$ . After annealing, the alloy had  $\sim\text{PtV}$ ,  $\sim\text{CrPt}$  and  $\tau$ . The hardness was  $854\pm30 \text{ HV}_{0.3}$  in the as-cast condition and increased to  $1086\pm46 \text{ HV}_{0.3}$  in the annealed condition. The high hardness is attributed to the ternary phase, as well the intermetallic phase  $\sim\text{PtV}$ .

Alloy 19, average composition  $\text{Pt}_{25.8}:\text{Cr}_{42.9}:\text{V}_{31.3}$ , had  $\tau_3$  dendrites, A15( $\sim\text{Cr}_3\text{Pt}$ ) and  $\sim\text{Cr}_3\text{Pt}$  in the as-cast condition and the same phases after heat treatment. It had the highest hardness ( $1109\pm25 \text{ HV}_{0.3}$ ) in the as-cast condition. Due to brittleness, it disintegrated while being removed from the resin mounting before the annealed hardness was measured. However, the brittleness and disintegration is an indication of extreme hardness.

Alloy 20, average composition  $\text{Pt}_{38.8}:\text{Cr}_{14.2}:\text{V}_{47.0}$  (at.%), had cored  $\sim\text{PtV}$  dendrites and  $\sim\text{PtV}_3$  which also appeared dendritic; this is because it was solidifying independently (after forming peritectically) between the dendrite arms of the primary  $\sim\text{PtV}$ . The  $\sim\text{PtV}$  phase was identified as the primary phase, because the central stem and arms could be clearly seen. There was a eutectic which comprised the medium  $\sim\text{PtV}_3$  phase and mainly holes, where the second component,  $\tau_3$ , was inadvertently removed on sample preparation. After annealing, the alloy had the same



phases. However, the  $\sim\text{PtV}$  phase, which was cored in the as-cast condition, homogenised during heat treatment and consequently its composition shifted substantially towards  $\sim\text{PtV}$ . The morphology of both  $\sim\text{PtV}$  and  $\sim\text{PtV}_3$  changed considerably, and there was more porosity. The hardness increased from  $796\pm35 \text{ HV}_{0.3}$  in the as-cast condition to  $923\pm57 \text{ HV}_{0.3}$  in the annealed condition and the change was attributed to the change in microstructure.

Alloy 21, average composition  $\text{Pt}_{16.8}:\text{Cr}_{13.4}:\text{V}_{69.8}$  (at.%), had (V,Cr) dendrites and a sparse eutectic of (V,Cr) and  $\sim\text{PtV}_3$ . There was a ternary phase,  $\tau_3$ , which had formed from a peritectoid reaction between (V,Cr) and  $\sim\text{PtV}_3$ . There was also solid state precipitates of  $\sim\text{PtV}_3$  within (V,Cr), showing that (V,Cr) had a retreating solvus. After annealing, the eutectic had rounded and coarsened and the dendrites had much precipitation, indicating a very sloping (V,Cr) solvus. The alloy became very brittle after heat treatment; it broke into small pieces during removal from the resin mounting. Consequently, XRD was not done. The disintegration is an indication of extreme brittleness. The as-cast hardness was  $618\pm25 \text{ HV}_{0.3}$ . The presence of a ternary phase and the intermetallic compound  $\sim\text{PtV}_3$  in the alloy could be the contributing factor to the high hardness especially after annealing.

Alloy 22, average composition  $\text{Pt}_{28.7}:\text{Cr}_{27.2}:\text{V}_{44.1}$  (at.%), had  $\tau_3$  dendrites,  $\sim\text{PtV}_3$ ,  $\sim\text{Cr}_3\text{Pt}$  and a ternary eutectic comprising  $\tau_3 + \sim\text{PtV}_3 + (\text{V,Cr})$ . After annealing, the alloy had solid state  $\sim\text{PtV}_3$  precipitation within  $\tau_3$  (evidence of a retreating  $\tau_3$  solvus),  $\sim\text{PtV}_3$  and a eutectic of  $\tau_3 + (\text{V,Cr})$ . The as-cast hardness was  $1086\pm28$  and this high hardness was attributed to the ternary phase. The alloy cracked and disintegrated while being removed from the resin and hardness in the annealed condition was not measured. The disintegration is an indication of extreme brittleness which can be attributed to the ternary phase and the intermetallic compound  $\sim\text{PtV}_3$ .

Alloy 23, average composition  $\text{Pt}_{16.5}:\text{Cr}_{56.1}:\text{V}_{27.4}$  (at.%), had (V,Cr) dendrites,  $\text{A15}(\sim\text{Cr}_3\text{Pt})$ , a eutectic consisting of  $\text{A15}(\sim\text{Cr}_3\text{Pt}) + (\text{V,Cr})$  and a small amount of  $\text{CrO}_3$ . After annealing, the alloy had solid state precipitation of  $\text{A15}(\sim\text{Cr}_3\text{Pt})$  in the (V,Cr) dendrites,  $\text{A15}(\sim\text{Cr}_3\text{Pt})$ , a eutectic of  $\text{A15}(\sim\text{Cr}_3\text{Pt}) + (\text{V,Cr})$ , and a small amount of  $\text{CrO}_3$ . The solid state precipitation showed that (V,Cr) retreated substantially. The hardness increased from  $707\pm41 \text{ HV}_{0.3}$  in the as-

cast condition to  $837 \pm 46$  HV<sub>0.3</sub> in the annealed condition. The increase in the hardness is attributed to the change in the microstructure.

Alloy 24, average composition Pt<sub>14.9</sub>:Cr<sub>73.7</sub>:V<sub>11.4</sub> (at.%), had cored dendrites, (V,Cr), A15(~Cr<sub>3</sub>Pt), a sparse eutectic of (V,Cr) + A15(~Cr<sub>3</sub>Pt) and a multi-phase area with a dark component. XRD analysis confirmed the presence of a small amount of CrO<sub>3</sub>. Compared to the as-cast microstructure, there was precipitation within the (V,Cr) dendrites and the eutectic had disappeared. ~Cr<sub>3</sub>Pt, which had not been in the as-cast sample, formed during annealing. The hardness decreased from  $692 \pm 73$  HV<sub>0.3</sub> in the as-cast condition to  $544 \pm 20$  HV<sub>0.3</sub> in the annealed condition. The decrease in the hardness is attributed to the coarseness in the microstructure after annealing.

Alloy 25, average composition Pt<sub>34.1</sub>:Cr<sub>57.4</sub>:V<sub>8.5</sub> (at.%), had cored ~Cr<sub>3</sub>Pt dendrites, medium A15(~Cr<sub>3</sub>Pt) which formed a sparse eutectic with ~Cr<sub>3</sub>Pt. A small amount of CrO<sub>3</sub> was detected by XRD analysis. After annealing, the alloy had light round and light medium ~Cr<sub>3</sub>Pt, darker medium A15(~Cr<sub>3</sub>Pt), dark oxides and porosity. Although some coring was still present after annealing, the dendritic structure had nearly been lost, and there was much rounded porosity. The eutectic had nearly disappeared. There was a substantial increase in hardness, from  $358 \pm 9$  HV<sub>0.3</sub> in the as-cast condition to  $838 \pm 27$  HV<sub>0.3</sub> in the annealed condition. This increase is attributed to the change in microstructure.

## 8.3 HIGHER ORDER ALLOYS

### As-cast Alloys

Alloy 26, average composition Pt<sub>63.9</sub>:Al<sub>12.2</sub>:Cr<sub>4.3</sub>:Ru<sub>0.7</sub>:V<sub>18.9</sub> (at.%), and Alloy 27, average composition Pt<sub>69.5</sub>:Al<sub>11.5</sub>:Cr<sub>4.2</sub>:Ru<sub>0.6</sub>:V<sub>14.2</sub> (at.%) had a two-phase dendritic structure of (Pt) dendrites and ~Pt<sub>3</sub>Al. In both alloys, V partitioned preferentially to the (Pt), with Alloy 26 having ~23.5 at.% V in (Pt) compared to ~7.8 at.% V in ~Pt<sub>3</sub>Al, and Alloy 27 having ~16 at.% V in (Pt) compared to ~10 at.% V in ~Pt<sub>3</sub>Al.

Alloy 31, average composition  $\text{Pt}_{71.7}:\text{Al}_{12.8}:\text{Cr}_{4.9}:\text{Ru}_{1.1}:\text{V}_{9.9}:\text{Nb}_{0.3}$  (at.%), also had a two-phase dendritic structure of (Pt) dendrites and  $\sim\text{Pt}_3\text{Al}$  and V partitioned preferentially to (Pt). There was  $\sim 11$  at.% V in (Pt) and  $\sim 3.5$  at.% V in  $\sim\text{Pt}_3\text{Al}$ . The entire Nb in the alloy went into solution in (Pt).

Alloy 28, average composition  $\text{Pt}_{75.2}:\text{Al}_{11.2}:\text{Cr}_{4.0}:\text{Ru}_{0.6}:\text{V}_{9.5}$  (at.%), and Alloy 29, average composition  $\text{Pt}_{78.7}:\text{Al}_{12.2}:\text{Cr}_{3.8}:\text{Ru}_{0.6}:\text{V}_{5.2}$  (at.%) were both single phase  $\sim\text{Pt}_3\text{Al}$  with all the  $\sim 10$  at.% V in Alloy 28 and  $\sim 5$  at.% V in Alloy 29 in solution in the  $\sim\text{Pt}_3\text{Al}$ .

Alloy 30, average composition  $\text{Pt}_{63.2}:\text{Al}_{12.9}:\text{Cr}_{4.0}:\text{Ru}_{0.7}:\text{V}_{19.0}:\text{Nb}_{0.6}$  (at.%), had (Pt) dendrites and a eutectic of  $\sim\text{Pt}_3\text{Al} + (\text{Pt})$ . There was  $\sim 23$  at.% V in the (Pt) dendrites and  $\sim 9$  at.% V in the eutectic. The entire Nb went into solution in the (Pt), and none was detected in the eutectic.

One of the reasons why V was selected as an addition to Pt-Al based alloys was its high solubility in the solid solution (Pt). It was postulated that V had the potential to act as a solid solution strengthener. The results show that this may be case since hardnesses were substantially increased.

### **Alloys Annealed at 1000°C for 1500 Hours**

The choice of the compositions of the higher order alloys was aimed at identifying two-phase microstructure analogues to nickel-based superalloys. The solid solution phase, (Pt) in Alloy 26, which is denoted Alloy 26H after annealing transformed by ordering to  $\sim\text{Pt}_2\text{V}$  during heat treatment. Alloy 27H had a similar two-phase structure to Alloy 26H in the as-cast condition but became single phase  $\sim\text{Pt}_3\text{Al}$  after heat treatment.

Alloy 28H remained single phase,  $\sim\text{Pt}_3\text{Al}$ , after heat treatment while Alloy 29H changed from single phase,  $\sim\text{Pt}_3\text{Al}$ , in the as-cast condition to a two-phase structure of  $\sim\text{Pt}_3\text{Al}$  and (Pt). Each of the phases in Alloy 29H had solid state precipitation of the other phase indicating retreating solvi for both phases. This would be beneficial for precipitation strengthening, because it would potentially allow more precipitation and higher volume fraction to occur.

The structure of Alloy 30H changed substantially from that in the as-cast condition. The solid solution (Pt), which had been part of a eutectic in the as-cast condition, transformed to two phases  $\sim\text{Pt}_2\text{V}$  and  $\sim\text{Pt}_3\text{Al}$  during heat treatment. There was also solid state precipitation in the  $\sim\text{Pt}_3\text{Al}$  dendrites. The morphology of the  $\sim\text{Pt}_3\text{Al}$  component of the eutectic also changed and were smaller and more rounded.

Alloy 31H which had a two-phase structure in the as-cast condition, became single phase  $\sim\text{Pt}_3\text{Al}$  after heat treatment.

The required microstructure of fine precipitates of  $\sim\text{Pt}_3\text{Al}$  in a matrix of (Pt) is obtained when an alloy solidifies to (Pt) followed by solid state precipitation of  $\sim\text{Pt}_3\text{Al}$ . Any other phases, especially a eutectic could be detrimental. All the six alloys had solidified with either (Pt) dendrites or single phase  $\sim\text{Pt}_3\text{Al}$ . Annealing also did not produce the required microstructure. It is then possible that the compositions and/or the annealing procedure were not right.

Alloy 26 had the highest V content of  $\sim 19$  at.% and although it retained a two-phase structure after annealing, the (Pt) transformed to  $\sim\text{Pt}_2\text{V}$  which is not desirable. The next highest V content was that of Alloy 27 at  $\sim 15$  at.%. It was also two-phase with  $\sim\text{Pt}_3\text{Al}$  dendrites and (Pt) but transformed to single phase  $\sim\text{Pt}_3\text{Al}$  on annealing. It is possible that tweaking the compositions of alloys with V content around  $\sim 15$  at.% may result in the right microstructure. For the alloys which had single phase  $\sim\text{Pt}_3\text{Al}$ , rather than (Pt) dendrites, it appears that V additions change the boundaries, so that to have an alloy based on (Pt), less Al should be present.

El-Bagoury measured hardness of aged experimental NBSAs. The specimens were aged at  $845^\circ\text{C}$  for 24 h and then solution treated at  $1120^\circ\text{C}$  and  $1180^\circ\text{C}$ . The Vickers hardness for the specimens solution treated at  $1120^\circ\text{C}$  were 472 HV and those at  $1180^\circ\text{C}$  were 450. These values compared very well with those of the higher order alloys.

## **9. CONCLUSIONS AND RECOMMENDATIONS**

### **9.1 CONCLUSIONS**

#### **9.1.1 The Pt-Al-V System at the Pt-rich Corner**

- The following diagrams were successfully constructed for the Pt-Al-V system at the Pt-rich corner after using SEM, EDX and XRD:
  - Solidification projection,
  - Liquidus surface projection and
  - Isothermal section at 1000°C
- It was concluded that all the phase fields were determined accurately since the diagrams were consistent with each other.
- Two ternary phases were found, designated  $\tau_1$  and  $\tau_2$ .
- The boundary enclosing the ternary phases on one side, in the solidification projection, was speculative because more alloys are required in the vicinity for accurate determination.
- Alloys with low V and high Pt content had the lowest hardness values, while alloys having ternary phases had the highest hardnesses.
- Examination of the indentations did not reveal the brittleness or toughness of the alloys. There were very few cracks or slip lines around the edges of the indentations because of the low load (300 g) used.
- Five ternary invariant reactions were identified at the Pt-rich corner of the system.

#### **9.1.2 The Pt-Cr-V System**

- The following diagrams were successfully constructed for the Pt-Cr-V system
  - Solidification projection
  - Liquidus surface projection
  - Isothermal section at 1000°C
- It was concluded that all the phases were determined accurately since all the three diagrams were consistent with each other
- The liquidus surface was mainly the two solid solutions (Pt) and (V,Cr).

- A ternary phase was found in the Pt-Cr-V system.
- Four ternary invariant reactions were identified in the system.
- The boundary enclosing the (V,Cr) phase field on one side was speculative because all the phases used to determine that boundary had solid state precipitation and compositions plotted were areal for the two-phase regions.
- Alloys with low V and high Pt content had the lowest hardness values while alloys having the ternary phase had the highest hardnesses.
- Examination of the indentations did not reveal the brittleness or toughness of the alloys. There were very few cracks or slip lines around the edges of the indentations because of the low load (300 g) used.

### 9.1.3 Higher Order Alloys

- The best addition of V is ~15 at.%; higher additions would result in the formation of the brittle intermetallic phases of the Pt-V system.
- The hardness of the alloys investigated was higher than that of the quaternary alloys which had been investigated and previously considered as optimum.
- It is possible to get two phase structures of (Pt) and ~Pt<sub>3</sub>Al with addition of V and Nb.

## 9.2 RECOMMENDATIONS

- More alloys in the vicinity of the two ternary phases in the Pt-Al-V system should be investigated to determine the phase field boundaries more accurately.
- It is recommended that Al content be reduced with addition of V to the higher order alloys so as to get the required microstructure of ~Pt<sub>3</sub>Al precipitates within (Pt).
- The heat treatment of 1000°C for 1500 h did not transform the higher order alloys to the intended structure of fine ~Pt<sub>3</sub>Al precipitates in a matrix of (Pt) and in some cases homogenisation was not achieved. A different heat treatment similar to the one done by Wenderoth *et al.* [2005Wen] is recommended. Specifically, a two stage process where homogenisation is done at a higher temperature of 1500°C for a shorter period of 12 hours followed by water quenching. The second step is a precipitation heat treatment at 1000°C for 120 hours also followed by water quenching. The heat treatment is done in a conventional chamber furnace under flowing argon.

It is hoped that the results and data from this study will be used to improve and expand the existing thermodynamic databases of the Pt-based superalloys, especially with regard to the inclusion of vanadium. There have been several attempts to build thermodynamic databases for the prediction of phase equilibria of Pt-base superalloys. Watson *et al.* [2006Wat] undertook a preliminary assessment of the Cr-Pt-Ru system using a combination of Pandat and MTDATA software. In their review, Cornish *et al.* [2007Cor] reported on the work being undertaken at Mintek, the University of Leeds and the University of Bayreuth to build up a thermodynamic database for Pt-Al-Cr-Ru system. At the University of Bayreuth, Preussner *et al.* [2008Pre] used thermodynamic calculations based on first principles to deal with the problem of sparse data.

## REFERENCES

- [1930Mul] L. Müller: *Ann. Phys.*, (Leipzig), 7(5) (1930) 9-47.
- [1934Nem] W.A. Nemilov: *Z. Anorg. Allg. Chem.*, 218 (1934) 33-44.
- [1935Fri] E. Friederich and A. Kussman: *Phys. Z.*, 36 (1935) 185-192.
- [1940Geb] E. Gebhart and W. Koster: *Z. Metallkd.*, 32 (1940) 253-264.
- [1940Rau] E. Raub and W. Mahler: *Z. Metallkd.*, 32 (1940) 262-264.
- [1948Kub] O. Kubaschewski and A. Schneider: *J. Inst. Met.*, 75 (1948) 403-416.
- [1952Duw] P. Duwez and H. Martens: Crystal structure of TaCr<sub>2</sub> and NbCr<sub>2</sub>, *Trans. AIME*, 194 (1952) 72-74.
- [1952Mar] H. Martens and P. Duwez: *Trans. ASM*, 44 (1952) 484-493.
- [1954Ros] W. Rostoker and A. Yamamoto: A survey of vanadium binary systems, *Trans. ASM*, 46 (1954) 1136-1167.
- [1955Car] O.N. Carlson, D.J. Kenney and H. A. Wilhelm: *Trans. ASM*, 47 (1955) 1-20.
- [1955Ell] R.P. Elliot: *Trans. ASM*, 47 (1955) 538-540.
- [1955Gel] S. Geller, T.B. Mathias and R. Goldstein: *J. Amer. Chem. Soc.*, 77 (1955) 210.
- [1956Ely] V.P. Elyutin and V.F. Funke: *Izv. Akad. Nauk SSSR, Otd. Tekh. Nauk*, 3 (1956) 68-76 in Russian: Brucher Translation No. 4304, available from ASM.
- [1956Gre] P. Greenfield and P. A. Beck: *Trans. AIME*, 206 (1956) 265-276.
- [1958Ell] R.P. Elliot and W. Rostoker: *Trans. ASM*, 50 (1958) 617-633.
- [1958Ere] V.N. Eremenko, G.V. Zudilova and L.A. Gaevskaya: *Metalloved. Term. Obrab. Met.*, 1 (1958) 11-16, in Russian: Brucher Translation No. 4108, available from ASM.
- [1958Wes] J.H. Westbrook: Precipitation of Ni<sub>3</sub>Al from nickel solid solution as octogonally diced cubes, *Zeitschrift für Kristallographie*, 110 (1958) 21-29.



- [1959Bai] D.M. Bailey, O.N. Carlson and J.F. Smith: *Trans. ASM*, 51 (1959) 1097-1102.
- [1959Car] O.N. Carlson, D.T. Eash and A.L. Eustice: *Reactive Metals*, W.R. Claugh, Ed., Interscience Publishers, New York, 2 (1959) 277-295.
- [1959Sve] V.N. Svetsnikov, Y. A. Kocherzhinskii, V.M. Pan, E.E. Emaistrenko and A.K. Shurin, *Izled. Zharopr. Splav., Akad. Nauk SSSR, Inst. Met.*, 4, (1959) 248-256.
- [1960Kna] A.G. Knapton: *J. Less-Common Met.*, 2 (1960) 113-124.
- [1961Geb] E. Gebhart and G. Joseph: *Z. Metallkd.*, (1961) 310-317.
- [1961Gol] H.J. Goldschmidt and J.A. Brand: *J. Less-Common Met.*, 3 (1961) 44-61.
- [1961Kim] H. Kimura and A. Ito: *Trans. Natl. Inst. Res. Met. (Jpn)*, 3 (1961) 27-34.
- [1961Nad] A. Nadumov and B.I. Rabiezova: *Izv. Akad. Nauk SSSR, Otd. Tekn. Nauk, Metall. Topl.*, 4 (1961) 68.
- [1961Pan1] V.M. Pan: *Fiz. Met. Metalloved.*, 12 (3) (1961) 455-457, in Russian; translation in *Phys. Met. Metallogr.*, 12 (1961) 139-141.
- [1961Pan2] V.M. Pan: *Dapov. Akad. Nauk Ukr. RSR.*, (1961) 332-334, in Ukrainian.
- [1961Zak] M.I. Zakharova and D.A. Prokoshkin: *Izv. Akad. Nauk SSSR, Otd. Tekh. Nauk, Metall. Topl.*, 4 (1961) 59-67, in Russian.
- [1962Bro] W. Bronger and W. Klemm: *Z. Anorg. Alg. Chem.*, 319 (1962) 58.
- [1962Sve] V.M. Svechnikov and V.M. Pan: *Issled. Zharoprochn. Splavam.*, 8 (1962) 47-56, in Russian.
- [1963Kor] I.I. Kornilov, K.I. Shakhova, P.B. Budberg and N.A. Nedumov: *Dokl. Akad. Nauk SSSR*, 149 (6) (1963) 1340-1342, in Russian; translation in *Dokl. Chem.*, 149 (1963) 362-364.
- [1963Hol] H. Holleck, F. Benesovsky and H. Nowotny: *Monatsh. Chem.*, 94 (1963) 477-481.

- [1963Pic] S.J. Pickart and R. Nathans: *J. Appl. Phys.*, 34 (4) (1963) 1203-1204.
- [1964Huc] R. Huch and W. Klemm: *Z. Anorg. Alg. Chem.*, 329 (1964) 123-135.
- [1964Gie1] B.C. Giessen, D. Parker and N.J. Grant: *Acta Crystallgr.*, 17 (1964) 615-616.
- [1964Gie2] B.C. Giessen, D. Parker and N.J. Grant: *J. Met.*, (*abstract*), 16 (1964) 92-93.
- [1964Mal] A. Maldonado and K. Schubert: *Z. Metallkd.*, 55 (1964) 619-626.
- [1964Ram] A. Raman and K. Schubert: *Z. Metallkd.*, 55 (1964) 798-804.
- [1965Gie1] B.C. Giessen and N.J. Grant: *J. of Less-Common Metals*, 8 (1965) 114-119.
- [1965Gie2] B.C. Giessen, R.H. Kane and N.J. Grant: *Trans. TMS-AIME*, 233 (1965) 855-864.
- [1965Gus] L.N. Guseva: *Izv. Akad Nauk SSSR, Neorg. Mater.*, 1(10) (1965) 1743-1747, in Russian; translation in *Inorg. Mater.*, 1(10) (1965) 1581-1583.
- [1966Lun] C.F. Lundin and S. Yamamoto: *Trans. Metall. Soc., AIME*, 236 (1966) 863-872.
- [1967Wil] L.A. Wiley: Aluminium, Appendix 1, Phase Diagrams, K.B. Van Horn (Ed.), *Am. Soc. Met.*, (1967) 359-381.
- [1968Eds] L. Edshammer: *Acta Chem. Scand.*, 22 (1968) 2374-2375.
- [1968Kus] A. Kussman, K. Müller and E. Raub, *Z. Metallkd.*, 59 (1968) 859-863.
- [1968Mos] M. Moss: *Acta. Metall.*, 16 (1968) 321-326.
- [1968Sve] V.N. Svechnikov, B.M. Pan and B.I. Latiesheva: *Metallofizika* 2 (1968) 54.
- [1968Tan] L.E. Tanner: *Phys. Status Solid*, 30 (1968) 685.
- [1968Reu] E.C. Van Reuth and R.M. Waterstrat: *Acta Crystallogr. B*, 24 (1968) 186-196.
- [1969Rud1] E. Rudy: *Compendium of phase diagram data, Air Force Materials Laboratory, Part V, TR-65-2, Cr-V system*, Wright-Patterson AFB, Ohio, 21 (1969) 116-117.

- [1969Rud2] E. Rudy: *Compendium of phase diagram data, Air Force Materials Laboratory, Part V, TR-65-2, Cr-Nb system*, Wright-Patterson AFB, 21 (1969) 127-130.
- [1969Var] N.I Varich, L.M. Burov, K. Ye. Kolesnichenko and A.P. Maksimenko: *Phys. Met. Metallogr.*, 15 (2) (1969) 111-113.
- [1970Dar] A. S. Darling, G. L. Selman and R. Rushforth: *Plat. Met. Rev.*, 14 (1970) 124-130.
- [1970Shi] A.Ya. Shinayev and D.B. Butrymowicz: *Metall. Trans.*, 1 (1970)1905-1907.
- [1971Har] L.D. Hartsough and R.H. Hammond: *Solid State Commun.*, 9 (1971) 885-889.
- [1971Wic] A. Wicker, C. Albert and J. Droile: *C.R. Acad. Sci.*, 272C (1971) 1711-1713.
- [1973Bes] M.J. Besnus and A.J.P. Meyer: *Phys. Status Solidi (B)* (58) (1973) 533-542.
- [1973Hat] B.A. Hatt, J.K.R. Page and V.G. Rivlin: *J. Low Temp. Phys.*, 10(3/4) (1973) 271-284.
- [1973Leg] J.M. Leger and T.H. Hall: *J. Less-Common Met.*, 32 (1973) 181-187.
- [1973Wat1] R.M. Waterstrat: *Metall. Trans.*, 4 (1973) 455-466.
- [1973Wat2] R.M. Waterstrat: *Metall. Trans.*, 4 (1973) 1585-1592.
- [1975Cha] T. Chattopadhyay and K. Schubert: *J. Less-Common Met.*, 41 (1975) 19-32.
- [1976Bag] J. Baglin, F. d'Heurle and S. Zirinsky: *J. Electrochemical Soc.*, 125 (1976) 1854.
- [1976Cha] T. Chattopadhyay and K. Schubert: *J. Less-Common Met.*, 45 (1976) 79-83.
- [1976Gue] P. Guex and P Feschotte: *J. Less-Common Met.*, 46 (1976) 101-116.
- [1977Bha] K.K. Bhandary and K. Girgis: *Acta. Crystallogr. A*, 33 (1977) 903-913.
- [1977Got] T. Goto: *J. Phys. Soc., Jpn*, 43 (1977) 341-359.
- [1977Koc] Yu.A. Kocherzhinskii and H. Unal, *High Temp. – High Press.*, 9 (1977) 361-365.

- [1977Mol] V.V. Molokanov, D.B. Chernov and P.B. Budberg, *Russ. J. Phys. Chem.*, 51 (1977) 1181-1183.
- [1978Bag] J. Baglin, J. Dempsey, F. d'Heurle, W. Hammer and S. Zirinsky: *Proc. Electrochem. Soc.*, 125 (1978) 185-198.
- [1978Bha] S. Bhan and S. Kudielka: *Z. Metallkd.*, 69 (1978) 333-334.
- [1978Sch] K. Schubert: *Z. Krist.* 148 (1978) 221-236.
- [1979Sch] M.J. Schaller: *Z. Metallkd.* 70 (1979) 318-321.
- [1980Pia] G. Piatti and G. Pellegrini: *J. Mater. Sci.* 15 (1980) 2403-2408.
- [1980Jor] J.L. Jorda, R. Flükiger and J. Müller: *J. Less-Common Met.*, 75 (1980) 227-239.
- [1981Ere] V.N. Eremenko, Y.V. Natanzon, V.P. Titov: *Russ. Metall.*, 5 (1981) 34-37.
- [1981Goo] D.A. Goodman, J.W. Cahn and L.H. Bennet: *Bull. Alloy Phase Diagr.* 2(1), (1981) 29-34.
- [1982Smi] J.F. Smith, D.M. Bailey and O.N. Carlson: *Bull. Alloy Phase Diagr.*, 2(4) (1982) 469-473.
- [1982Ell] M. Ellner, U. Kattner and B. Predel: *J. Less-Common Met.*, 87 (1982) 305-325.
- [1983Wat] R.M. Waterstrat and B.C. Giessen: *Alloy Phase Diagrams, MRS Proc.*, L.H. Bennett, T.B. Massalski and B.C. Giessen, (Eds.), North Holland, NY, 19, (1983) 423-428.
- [1985Vil1] P. Villars, L.D. Calvert (Eds.): *Pearson's Handbook of Crystallographic Data for Intermetallic Phases*, Ohio, USA, ASM, 2 (1985) 1850.
- [1985Vil2] P. Villars and L.D. Calvert (Eds.): *Pearson's Handbook of Crystallographic Data for Intermetallic Phases*, Ohio, USA, ASM, 3 (1985) 3044.
- [1985Vil3] P. Villars and L.D. Calvert (Eds.): *Pearson's Handbook of Crystallographic Data for Intermetallic Phases*, Ohio, USA, ASM, 2 (1985) 1890.

- [1985Wat] R.M. Waterstrat and B.C. Giessen: *Metall. Trans. A*, 16A (1985) 1943-1949.
- [1986Ino] A. Inoue, L. Arnberg, B. Lehtinen, M. Oguchi and T. Masumoto: *Metall. Trans. A*, 17 (1986) 1657-1664.
- [1986McA] A.J. McAlister and D. J. Kahan: *Bull. Alloy Phase Diagr.*, 7(1) (1986) 47-51.
- [1986Mis] Y. Mishima, Y. Oya and T. Suzuki: *Proc. of the International Conference on Martensitic Transformations*, The Japan Institute of Metals, Japan, (1986) 1009 – 1014.
- [1986Sch] D. Schryvers, S. Amelinckx: *Acta Metall.*, 34 (1986) 43
- [1986Van] M. Vankatraman and J.P. Neumann: *Bull. Alloy Phase Diagr.*, 7(5) (1986) 462-466.
- [1987Kim] Y.W. Kim and F.H. Froes: *6<sup>th</sup> Int. Conf. Rapidly Quenched Met. (RQ6)*, Montreal, Quebec, 3-7 Aug. (1987).
- [1987Oya] Y. Oya, Y. Mishima and T. Suzuki: *Z. Metallkd.* 78 (1987) 485-490.
- [1987Sim] C.T. Sims, N. S. Stoloff and W. C. Hagel: *Superalloys II: High Temperature Materials for Aerospace and Industrial Power*: Wiley-Interscience, New York, NY, (1987) 27-57, 66-78, 538-543.
- [1988Rob] M.B. Robinson: *The effect of undercooling on niobium-platinum and niobium-silicon systems*, Dissertation, Vanderbilt Univ., Diss. Absts. Int. 49(5) (1988) 222.
- [1988Smi] William F. Smith: *Principles of Materials Science and Engineering*, 2<sup>nd</sup> ed., McGraw-Hill, Singapore (1988), p 272.
- [1989Mur] J.L. Murray: *Bull. Alloy Phase Diagr.* vol. 10(4) (1989) 351-357.
- [1989Smi] J.F. Smith: *Phase diagrams of binary vanadium alloys*. ASM International, (1989) 223.
- [1990Die] George E. Dieter: *Mechanical Metallurgy*, SI Metric Edn., McGraw-Hill, London (1990) 325.

- [1990Mas] T.B. Massalski: *Binary Alloy Phase Diagrams*. vol. 1, 2<sup>nd</sup> Edn., ASM International, Materials Park, OH, (1990).
- [1990Ven] M. Venkatram and J.P. Neumann: *Bull. Alloy Phase Diagr.*, 11(1) (1990) 16-21.
- [1991Vil] P. Villars and L.D. Calvert (Eds.): *Pearson's Handbook of Crystallographic Data for Intermetallic Phases*, ASM International, Materials Park, OH, 1991.
- [1993Net] J.G. Costa Neto, S.G. Fries, H.L. Lukas, S. Gama, G. Effenberg: Thermodynamic optimisation of the Nb-Cr system, *CALPHAD*, 17(3) (1993) 219-228.
- [1994Bri] C.L. Briant, J.J. Petrovic, B.P. Belaway, A.K. Vasudevan, and H.A. Lipsitt (Eds.): High-Temperature Silicides and Refractory Alloys, *Proc. Mat. Res. Soc. Symp.*, 322, Pittsburg, (1994) 305.
- [1995Tri] S.N. Tripathi, S.R. Bharadwaj and S.R. Dharwadkar: *J. Phase Equilibria*, 16(5) (1995) 465-470.
- [1996Wol] I.M. Wolff and G. Sauthoff: *Metall. Mat. Trans. A*, 27A (1996) 2642-2652.
- [1996Yam] Y. Yamabe, Y. Koizumi, H. Murakami, Y. Ro, T. Maruko and H. Harada: *Scripta Mater.*, 35 (1996) 211-215.
- [1997Yam1] Y. Yamabe-Mitarai, Y. Koizumi, H. Murakami, Y. Ro, T. Maruko and H. Harada: *Scripta Mater.* 36 (1997) 393-398.
- [1997Yam2] Y. Yamabe-Mitarai, Y. Koizumi, H. Murakami, Y. Ro, T. Maruko and H. Harada: *High Ordered Intermetallic Alloys VII*, edited by C.C. Koch, C.T. Liu, N.S. Stoloff and A. Warner. *Mater. Res. Soc. Symp. Proc.* 460, Warrendale, PA, (1997) 701.
- [1997Yam3] Y. Yamabe-Mitarai, Y. Ro, T. Maruko and H. Harada: *Structural Intermetallics*. The Minerals, Metals and Materials Society, Warrendale, PA, (1997) 805.
- [1998Gow] G.W. Goward: *Sur. Coat. Technol.* 108-109 (1998) 73-79.

- [1998Gu] Y. Gu, Y. Yamabe-Mitarai, Y. Ro, T. Yokokawa and T. Harada: *Scripta Mater.*, 39(6) (1998) 723-728.
- [1998Mur] J.L. Murray: *J. Phase Equilibria*, Vol. 19, No. 4 (1998) 368-375.
- [1998Yam] Y. Yamabe-Mitarai, Y. Ro, T. Maruko and H. Harada: *Metall. Mater. Trans. A* 29A (1998) 537-549.
- [2000Car] T. Carneiro and G. Tither: Niobium plays role in strengthening superalloys. *American Metal Market(USA)* 108 (2000) 8.
- [2000Yu] X. Yu, Y. Yamabe-Mitarai, Y. Ro and H. Harada: *Intermetallics*, 8 (2000) 619-622.
- [2000Wol] I.M. Wolff and P. J. Hill: *Plat. Met. Rev.*, (44) 4 (2000) 158-166.
- [2001Big] T. Biggs, P.J. Hill, L.A. Cornish and M.J. Witcomb: *J. Phase Equilibria*, 22 (2001) 214-218.
- [2001Hil1] P.J. Hill, T. Biggs, P. Ellis, J. Hohls, S. Taylor and I.M. Wolff: *Mater. Sci. Eng. A*, 301(2) (2001) 167-179.
- [2001Hil2] P.J. Hill: *Superalloy analogues based on platinum for ultra-high temperature applications*. PhD Dissertation, University of the Witwatersrand, Johannesburg, 2001.
- [2001Hil3] P.J. Hill, L. A. Cornish and M.J. Witcomb: *Proc. Microsc. Soc. South. Afr*, 31 (2001) 22.
- [2001Oik] K. Oikawa, G.W. Qin, T. Ikeshoji, O. Kitakami, Y. Shimada, K. Ishida and K. Fukamishi: *J. Magnetism and Magnetic Mat.* 236 (2001) 220-233.
- [2001Süs1] R. Süß, P.J. Hill, P. Ellis and I.M. Wolff: *Proc. 7<sup>th</sup> European Conference on Advanced Materials and Processes*, Rimini, Italy, 2001. CD-ROM: ISBN 8885298397.

- [2001Süs2] R. Süß, P.J. Hill, P. Ellis and L.A. Cornish: *Proc. Microsc. Soc. South. Afr.*, Johannesburg, 5<sup>th</sup> -7<sup>th</sup> December, 31 (2001) 21.
- [2002Cor] L.A. Cornish, J. Hohls, P. J. Hill, S. Prins, R. Süß and D.N. Compton: *J. Mining and Metall.*, 38 (3-4) (2002) 197-204.
- [2002Hil] P.J. Hill, Y. Yamabe-Mitarai, H. Murakami, L. A. Cornish, M.J. Witcomb, I.M. Wolff and H. Harada: *Third International Symposium on Structural Intermetallics, TMS*, Jackson Hole, Wyoming, USA, rescheduled to April 28-May 2, (2002) 527-533.
- [2002ICDD] International Centre for Diffraction Data (ICDD) Powder Diffraction File, PDF-2, Release 2002.
- [2002Süs] R. Süß, L.A. Cornish, P.J. Hill, J. Hohls and D.N. Compton: *Properties of a New Series of Superalloys Based on Pt<sub>80</sub>:Al<sub>14</sub>:Cr<sub>3</sub>:Ru<sub>3</sub>*, Advanced Materials and Processes for Gas Turbines, Eds. G.E. Fuchs, A.W. James, T. Gabb, M. McLean and H. Harada, TMS, The Minerals, Metals and Materials Society, 22nd - 26th September 2002, Copper Mountain, Colorado, USA. (2003) 301-307.
- [2002Tia] W.H. Tian and M. Nemoto: *Mater. Sci. Eng., A*, 653 (2002) 329-331.
- [2003Cor] L. A. Cornish, B. Fischer and R. Volkl: Development of platinum-group-metal superalloys for high temperature use. *MRS Bulletin* September 2003, 28(9) (2003) 632-638.
- [2003Hua] C. Huang, Y. Yamabe-Mitarai, K. Nishida and H. Harada: *Intermetallics*, 11 (2003) 917-926.
- [2004Hua] C. Huang, Y. Yamabe-Mitarai and H. Harada: *J. Alloys and Compounds* 366 (2004) 217-221.
- [2005Pri] S.N. Prins, L.A. Cornish and P.S. Boucher: *J. Alloys and Compounds* 403 (2005) 245-257.
- [2005Vol] R. Völkl, Y. Yamabe-Mitarai, C. Huang and H. Harada: *Metall. Mat. Trans. A*, 36A(11) (2005) 2881-2892.



- [2005Wen] M. Wenderoth, L.A. Cornish, R. Süss, S. Vorberg, B. Fischer, U. Glatzel and R. Völkl: *Metall. Mat. Trans. A*, 36A (2005) 567-575.
- [2005Zha] J.-C. Zhao, X. Zheng and D. Cahill: *Materials Today*, October, (2005) 28-37.
- [2006Cor] L.A. Cornish, R. Süss, L.H. Chown, A. Douglas, M. Matema, L. Glaner and G. Williams: *New Pt-based alloys for high temperature application in aggressive environments: The next stage*. Proc. International Southern Africa Institute of Mining and Metallurgy conference “Platinum Surges Ahead”, Sun City, Symposium Series S45, 57-66, 8<sup>th</sup> – 12<sup>th</sup> October 2006, 57-66.
- [2006Ndl] G.F. Ndlovu: *Microstructural investigation of the Pt-Al-Nb system*, M.Sc. dissertation, University of Western Cape, December 2006.
- [2006Wat] A. Watson, L.A. Cornish and R. Süss: *Rare Metals*, 25 (5) (2006) 597-607.
- [2007Cor] L.A. Cornish, R. Süss and A. Watson: *Plat. Met. Rev.* 51 (3) (2007) 104-115.
- [2007Dou] A. Douglas, J. H. Neethling, R. Santamarta, D. Schryvers and L.A. Cornish: *J. Alloys Compd.*, 432 (2007) 96-102.
- [2006Nxu] S. Nxumalo, C.I. Lang: *J. Alloys Compd.*, 425 (2006) 181.
- [2006Süs] R. Süss, L.A. Cornish and M.J. Witcomb: *Investigation of as-cast alloys in the Pt-Cr-Ru system. J. Alloys and compounds* 416 (2006) 80-92.
- [2007Süs] R. Süss: *Investigation of the Pt-Al-Cr system as part of the development of the Pt-Al-Cr-Ru thermodynamic database*. PhD Thesis, University of the Witwatersrand, 2007.
- [2008Cor] L.A. Cornish, M.J. Witcomb, S. Coetzee, W. Tshawe and S. Prins: Anomalies and pitfalls in phase analysis using BSE, *Proceedings of Microscopy Society of Southern Africa Conference*, 38 (2008) 9.
- [2008Had] F. Haddad, S.E. Amara and R. Kesri: *Metall. Mat. Trans. A*, 39A (2008) 1026-1033.

- [2008Mur] T. Murakami, R. Sahara, D. Harako, M. Akiba, T. Narushima and C. Ouchi: *Mater. Trans.*, 49(3) (2008) 538-547.
- [2008Pre] J. Preussner, S.N. Prins, M. Wenderoth, R. Völkl, U. Glatzel: Building a thermodynamic database for platinum-based superalloys. *Plat. Met. Rev.*, 52(1), (2008) 48-51.
- [2008Sho] B.M. Shongwe, L. A. Cornish and R. Süss: *Advanced Metals Initiative Conference*, Johannesburg, 18<sup>th</sup> – 19<sup>th</sup> November, 2008, on CD.
- [2008Wan] C.P. Wang, A.Q. Zheng and X.J. Liu: *Intermetallics* 16 (2008) 544-549.
- [2008Wen] M. Wenderoth, S. Voberg, B. Fischer, Y. Yamabe-Mitarai, H. Harada, U. Glatzel, R. Völkl: *Mat. Sci. Eng. A* 483-484, (2008), 509-511.
- [2008Zha] C. Zhang, J. Zhu, A. Bengston, D. Morgan, F. Zhang, Y. Yang and Y.A. Chang: *Acta Materialia*, 56 (2008) 5796-5803.
- [2008Zhu] Z. Zhu, Y. Du, L. Zhang, H. Chen, H. Xu, C. Tang: *J. Alloys Compd.*, 460 (2008) 632-638.
- [2009Cor] L. A. Cornish, R. Süss, A. Douglas, L. H. Chown and L. Glaner: The Platinum Development Initiative: Platinum-based alloys for high temperature and special applications: Part I. *Plat. Met. Rev.*, 53(1) (2009) 2-10.
- [2009Dou] A. Douglas, P.J. Hill, T. Murakumo, L.A. Cornish and R. Süss: The Platinum Development Initiative: Platinum-based alloys for high temperature and special applications: Part II. *Plat. Met. Rev.*, 53(2) (2009) 69-77.
- [2009Mul] F.M. Mulaudzi: *Constitution of the Pt-Cr-Nb system*, M.Sc. dissertation, University of the Witwatersrand, 2009.
- [2009Oka] H. Okamoto: *J. Phase Equilibria and Diffusion*, 30 (3) (2009) 295-296.
- [2009Süs] R. Süss, A. Watson, L. A. Cornish and D. N. Compton: Development of a data base for the prediction of phases in Pt-Al-Cr-Ru for high temperature and corrosive environment: Al-Cr-Ru. *J. Alloys and Compounds* 476 (2009) 176-186.

- [2009Wit] V.T. Witusiewicz, A.A. Bondar, U.Hecht, T.Ya. Velikanova: *J. Alloys Compd.*, 472 (2009) 133-161.
- [2010Sam] S. Samal and L.A. Cornish: Characterisation of the Pt-rich alloys in the Pt-Al-Nb system. *Proc. Microsc. Soc. South. Afr.*, Bela Bela, South Africa, 26<sup>th</sup> -29<sup>th</sup> October, 40 (2010) 50.
- [2011Cor1] L.A. Cornish and L.H. Chown, “Platinum-based alloys and coatings: materials for the future?”, *Advances in Gas Turbines, Chapter 15*, (2011) 337-370.
- [2011Cor2] L.A. Cornish and L.H. Chown: Platinum-based alloys and coatings: Materials for the future? *Advances in Gas Turbine Technology* InTech Europe, University Campus, STeP Ri, 5100 Rijeka, Croatia (2011) 337-370.
- [2011Bag] N. El-Bagoury: Microstructure and Mechanical Properties of Aged Nickel Base Superalloy, *Archives of Applied Science Research*, , 3 (2) (2011) 266-276
- [2011Tsh] W. Tshawe, L.A. Cornish, L.H. Chown, M.J. Papo: A study of the Pt-Al phase diagram. *Proceedings of African Materials Research Society Conference*, Victoria Falls, Zimbabwe, December 11-16, 2011. Submitted to MRS.
- [2012Ode1] B.O. Odera and L.A. Cornish, M.J. Papo, G.O. Rading: Electrolytic etching of platinum-aluminium based alloys. *Plat. Met. Rev.*, 56(4) (2012) pp 257-261.
- [2012Ode2] B.O. Odera, L.A. Cornish, M.B. Shongwe, G.O. Rading, M.J. Papo: As-cast and heat-treated alloys of the Pt-Al-V system at the Pt-rich corner. *The Journal of Southern African Institute of Mining and Metallurgy (SAIMM)*, 7A (2012) 505-515.
- [2012Sho] M.B. Shongwe, M.J. Witcomb, L.A. Cornish and M.J. Papo: TEM studies of Pt-Al-Cr-Ru alloys. *The Journal of Southern African Institute of Mining and Metallurgy (SAIMM)*, 7A, (2012) 551-558.

**APPENDIX      PAPERS PRESENTED AND PUBLISHED DURING THE  
COURSE OF THIS Ph.D.**

1. B.O. Odera, L.A. Cornish, M.J. Papo and G.O. Rading: *Electrolytic etching of platinum-aluminium based alloys*. Platinum Metals Review, 56(4) 2012 pp 257-261. E-ISSN 1471-0676.
2. B.O. Odera, L.A. Cornish, M.B. Shongwe, G.O. Rading, M.J. Papo: *As-cast and heat-treated alloys of the Pt-Al-V system at the Pt-rich corner*. The Journal of Southern African Institute of Mining and Metallurgy (SAIMM), vol. 7A, 2012 pp 505-515.
3. B.O. Odera, L.A. Cornish, M.J. Papo and G.O. Rading: *Microstructural investigation of some as-cast alloys of the Pt-Cr-V system*. Proceedings of the Ferrous and Base Metals Development Network Conference, Magaliesburg, South Africa, October 15-17, 2012, pp 291-308. ISBN 978-1-920410-33-9.
4. B.O. Odera, L.A. Cornish, G.O. Rading, M.J. Papo: *Solidification projection of the Pt-Al-V system at the Pt-rich corner*. Proceedings of the Microscopic Society of Southern Africa Conference, Pretoria, South Africa, December 5-9, Vol. 41, p 72, 2011, ISSN 0250-0418: ISBN 0-620-35056-3.
5. B.O. Odera, L.A. Cornish, M.B. Shongwe, G.O. Rading, M.J. Papo: *A study of some as-cast and heat treated alloys of the Pt-Al-V system at the Pt-rich corner*. Proceedings of the ZrTa New Metals Development Network Conference at Mount Grace Country House and Spa, Magaliesburg. The Southern African Institute of Mining and Metallurgy, Advanced Metals Initiative, 12-14 October 2011, p 46 (Abstract book), ISBN 978-1-920410-23-0.
6. B.O. Odera, L.A. Cornish, R. Suss, G.O. Rading: *A study of as-cast alloys of the Pt-Cr-V system*. Proceedings of the Microscopic Society of Southern Africa Conference held at Warmbaths Forever Resorts, South Africa, October 26-29, Vol 40, p 52, 2010, ISSN 0250-0418: ISBN 0-620-35056-3.
7. B.O. Odera, L.A. Cornish, R. Suss, G.O. Rading: *A study of phases in as-cast alloys from the Pt-Al-V system at the Pt-rich corner*. Proceedings of Microscopic Society of Southern Africa Conference at University of Kwazulu-Natal, Durban, South Africa, December 8-11, Vol. 39, p 61, 2009, ISSN 0250-0418: ISBN 0-620-35056-3.